

AD-A247 719

AGARD-R-783

1

AGARD-R-783

AGARD

ADVISORY GROUP FOR AEROSPACE RESEARCH & DEVELOPMENT

7 RUE ANCELLE 92200 NEUILLY SUR SEINE FRANCE

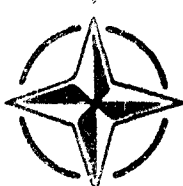
AGARD REPORT 783

FBI

Special Course on Engineering Methods in Aerodynamic Analysis and Design of Aircraft

(Les Méthodes d'Ingénierie Employée lors de
l'Analyse et de la Conception des Aéronefs)

The material assembled in this book was prepared under the combined sponsorship of the Fluid Dynamics Panel, the Consultant and Exchange Programme of AGARD, and the von Kármán Institute, and was presented as an AGARD Special Course at the Middle East Technical University, Ankara, Turkey, 6th–10th May 1991, at the von Kármán Institute for Fluid Dynamics, Rhode-St-Genèse, Belgium 13th–17th May 1991 and at the Universidad Politécnica de Madrid, Spain 20th–24th May 1991.



NORTH ATLANTIC TREATY ORGANIZATION

92-06961



Published January 1992

Distribution and Availability on Back Cover

**Best
Available
Copy**

AGARD

ADVISORY GROUP FOR AEROSPACE RESEARCH & DEVELOPMENT

7 RUE ANCELLE 92200 NEUILLY SUR SEINE FRANCE

AGARD REPORT 783

Special Course on Engineering Methods in Aerodynamic Analysis and Design of Aircraft

(Les Méthodes d'Ingénierie Employée lors de
l'Analyse et de la Conception des Aéronefs)



Accession No.	
NTIS Serial	50
DTIC Tab	
Issue Date	
Justification	
By	
Distribution	
Availability	000
Available On	
Dist	Special
A-1	

The material assembled in this book was prepared under the combined sponsorship of the Fluid Dynamics Panel, the Consultant and Exchange Programme of AGARD, and the von Kármán Institute, and was presented as an AGARD Special Course at the Middle East Technical University, Ankara, Turkey, 6th–10th May 1991, at the von Kármán Institute for Fluid Dynamics, Rhode-St-Genèse, Belgium 13th–17th May 1991 and at the Universidad Politécnica de Madrid, Spain 20th–24th May 1991.



North Atlantic Treaty Organization
Organisation du Traité de l'Atlantique Nord

The Mission of AGARD

According to its Charter, the mission of AGARD is to bring together the leading personalities of the NATO nations in the fields of science and technology relating to aerospace for the following purposes.

- Recommending effective ways for the member nations to use their research and development capabilities for the common benefit of the NATO community;
- Providing scientific and technical advice and assistance to the Military Committee in the field of aerospace research and development (with particular regard to its military application);
- Continuously stimulating advances in the aerospace sciences relevant to strengthening the common defence posture;
- Improving the co-operation among member nations in aerospace research and development;
- Exchange of scientific and technical information;
- Providing assistance to member nations for the purpose of increasing their scientific and technical potential;
- Rendering scientific and technical assistance, as requested, to other NATO bodies and to member nations in connection with research and development problems in the aerospace field

The highest authority within AGARD is the National Delegates Board consisting of officially appointed senior representatives from each member nation. The mission of AGARD is carried out through the Panels which are composed of experts appointed by the National Delegates, the Consultant and Exchange Programme and the Aerospace Applications Studies Programme. The results of AGARD work are reported to the member nations and the NATO Authorities through the AGARD series of publications of which this is one.

Participation in AGARD activities is by invitation only and is normally limited to citizens of the NATO nations.

The content of this publication has been reproduced
directly from material supplied by AGARD or the authors

Published January 1992

Copyright © AGARD 1992
All Rights Reserved

ISBN 92-835-0652-9



Printed by Specialised Printing Services Limited
40 Chigwell Lane, Loughton, Essex IG10 3TZ

Recent Publications of the Fluid Dynamics Panel

AGARDOGRAPHS (AG)

Design and Testing of High-Performance Parachutes
AGARD AG-319, November 1991

Experimental Techniques in the Field of Low Density Aerodynamics
AGARD AG-318 (E), April 1991

Techniques Expérimentales Liées à l'Aérodynamique à Basse Densité
AGARD AG-318 (FR), April 1990

A Survey of Measurements and Measuring Techniques in Rapidly Distorted Compressible Turbulent Boundary Layers
AGARD AG-315, May 1989

Reynolds Number Effects in Transonic Flows
AGARD AG-303, December 1988

REPORTS (R)

Aircraft Dynamics at High Angles of Attack: Experiments and Modelling
AGARD R-776, Special Course Notes, March 1991

Inverse Methods in Airfoil Design for Aeronautical and Turbomachinery Applications
AGARD R-780, Special Course Notes, November 1990

Aerodynamics of Rotorcraft
AGARD R-781, Special Course Notes, November 1990

Three-Dimensional Supersonic/Hypersonic Flows Including Separation
AGARD R-764, Special Course Notes, January 1990

Advances in Cryogenic Wind Tunnel Technology
AGARD R-774, Special Course Notes, November 1989

ADVISORY REPORTS (AR)

Air Intakes for High Speed Vehicles
AGARD AR-270, September 1991

Appraisal of the Suitability of Turbulence Models in Flow Calculations
AGARD AR-291, Technical Status Review, July 1991

Rotary-Balance Testing for Aircraft Dynamics
AGARD AR-265, Report of WG 11, December 1990

Calculation of 3D Separated Turbulent Flows in Boundary Layer Limit
AGARD AR-255, Report of WG10, May 1990

Adaptive Wind Tunnel Walls: Technology and Applications
AGARD AR-269, Report of WG12, April 1990

CONFERENCE PROCEEDINGS (CP)

Effects of Adverse Weather on Aerodynamics
AGARD CP-496, December 1991

Manoeuvring Aerodynamics
AGARD CP-497, November 1991

Vortex Flow Aerodynamics
AGARD CP-494, July 1991

Missile Aerodynamics
AGARD CP-493 October 1990

- Aerodynamics of Combat Aircraft Controls and of Ground Effects**
AGARD CP-465, April 1990
- Computational Methods for Aerodynamic Design: (Inverse) and Optimization**
AGARD-CP-463, March 1990
- Applications of Mesh Generation to Complex 3-D Configurations**
AGARD CP-464, March 1990
- Fluid Dynamics of Three-Dimensional Turbulent Shear Flows and Transition**
AGARD CP-438, April 1989
- Validation of Computational Fluid Dynamics**
AGARD CP-437, December 1988
- Aerodynamic Data Accuracy and Quality: Requirements and Capabilities in Wind Tunnel Testing**
AGARD CP-429, July 1988
- Aerodynamics of Hypersonic Lifting Vehicles**
AGARD CP-428, November 1987
- Aerodynamic and Related Hydrodynamic Studies Using Water Facilities**
AGARD CP-413, June 1987
- Applications of Computational Fluid Dynamics in Aeronautics**
AGARD CP-412, November 1986
- Store Airframe Aerodynamics**
AGARD CP-389, August 1986
- Unsteady Aerodynamics -- Fundamentals and Applications to Aircraft Dynamics**
AGARD CP-386, November 1985
- Aerodynamics and Acoustics of Propellers**
AGARD CP-366, February 1985
- Improvement of Aerodynamic Performance through Boundary Layer Control and High Lift Systems**
AGARD CP-365, August 1984
- Wind Tunnels and Testing Techniques**
AGARD CP-348, February 1984
- Aerodynamics of Vortical Type Flows in Three Dimensions**
AGARD CP-342, July 1983
- Missile Aerodynamics**
AGARD CP-336, February 1983
- Prediction of Aerodynamic Loads on Rotorcraft**
AGARD CP-334, September 1982
- Wall Interference in Wind Tunnels**
AGARD CP-335, September 1982
- Fluid Dynamics of Jets with Applications to V/STOL**
AGARD CP-308, January 1982
- Aerodynamics of Power Plant Installation**
AGARD CP-301, September 1981
- Computation of Viscous-Inviscid Interactions**
AGARD CP-291, February 1981
- Subsonic/Transonic Configuration Aerodynamics**
AGARD CP-285, September 1980
- Turbulent Boundary Layers Experiments, Theory and Modelling**
AGARD CP-271, January 1980
- Aerodynamic Characteristics of Controls**
AGARD CP-262, September 1979
- High Angle of Attack Aerodynamics**
AGARD CP-247, January 1979

Foreword

Engineering work in preliminary design of new projects is based, to a large degree, on basic fundamental experimental tests, empirical procedures, and low level (fast, inexpensive, and easy-to-handle) computer codes restricted to potential flow with simple correction terms for viscous effects. There is a need for training young engineers joining industry to work with these simple engineering tools. Without skillful use of these tools, the art of cost-effective preliminary design of new aircraft will be jeopardized.

The objective of this special course is to present proven engineering methods used during conceptual and preliminary design and development of new aircraft concepts. The course will focus on simple computational procedures for conceptual and preliminary design, low-level analysis, computer codes, and experimental techniques for aircraft performance predictions.

P.W.Sacher
Special Course Director

Avant-Propos

Les travaux d'ingénierie entrepris au niveau des études préliminaires d'un nouveau projet sont basés, en grande partie, sur des essais expérimentaux fondamentaux, des procédures empiriques, et des codes de machine du premier échelon (rapides, peu coûteux et conviviaux) limités aux écoulements potentiels, avec des simples facteurs de correction pour les effets visqueux.

Les jeunes ingénieurs qui débutent dans l'industrie doivent être formés à l'emploi de ces outils simples d'aide à la conception. Sinon, l'étude préliminaire des nouveaux avions dans des conditions de rentabilité acceptables sera fortement compromise.

L'objet de ce cours spécial est de présenter des méthodes d'ingénierie qui ont fait leurs preuves lors d'études préliminaires et conceptuelles entreprises en vue de développer des nouveaux concepts d'avion. Le cours mettra l'accent sur des procédures de calcul simples pour l'étude préliminaire et conceptuelle, des codes machine d'analyse initiale et des techniques expérimentales pour la prévision des performances des aéronaves.

P.W.Sacher

Special Course Staff

Special Course Director: Dipl. Ing. P.W.Sacher
Deutsche Aerospace
Messerschmitt-Bolkow-Blohm GmbH
Military Aircraft Division
Advanced Design Dept.
PO. Box 80 11 60
D-8000 Munich 80
Germany

LECTURERS

Mr P.Perner Aviation Marcel Dassault Breguet Aviation 78 Quai Carnot 92214 St. Cloud France	Mr C W.Boppe Manager — Technology Development B/35/35 Grumman Corporation Bethpage, NY 11787 United States
Mr H.W.M Hoeijmakers National Aerospace Laboratory NLR Anthony Fokkerweg 2 PO Box 90502 1006 BM Amsterdam The Netherlands	Dr J E Lamar Mail Stop 361 NASA Langley Research Center Hampton, VA 23665 United States
Mr B Haines 3 Bromham Road Buddenham Bedford MK40 4AF United Kingdom	Mr D P Raymer President, Conceptual Research, PO Box 923156 Sylmar, CA 91342-3156 United States

LOCAL COORDINATORS

Professor M Carbonato von Karman Institute for Fluid Dynamics Chausse de Waterloo, 72 1640 Rhode-St-Genese Belgium	Professor R. Martinez-Val Universidad Politecnica de Madrid E.T.S.I. Aeronauticos Plaza Cardenal Cisneros 3 28040 Madrid Spain	Professor C. Çiray Aeronautical Eng Dept Middle East Technical University Inonu Bu'vari Pk. 06531 Ankara Turkey
---	---	--

PANEL EXECUTIVE

Dr W Goodrich

Mail from Europe: AGARD—OTAN Attn: FDP Executive 7, rue Ancelle 92200 Neuilly-sur-Seine France	Mail from US and Canada: AGARD—NATO Attn: FDP Executive Unit 21551 APO AE 09777 Tel. 33(1) 47 38 57 75 Telex. 610176 (France) Telefax 33(1) 47 38 57 99
---	--

Contents

	Page
Recent Publications of the Fluid Dynamics Panel	iii
Foreword/Avant-Propos	v
Special Course Staff	vi
	Reference
Introduction by P.W Sacher	1
Computational Procedures for Preliminary Design by P.Perner	2
Configuration Development by D.P Raymer	3
Survey of Experimental Techniques for Performance Prediction by B.Hanes	4
Panel Methods for Aerodynamic Analysis and Design by H W M Hoedjmakers	5
High Angle of Attack — Aerodynamics by J E Lamar	6
Aircraft Drag Analysis Methods by C W Boppe	7

INTRODUCTION

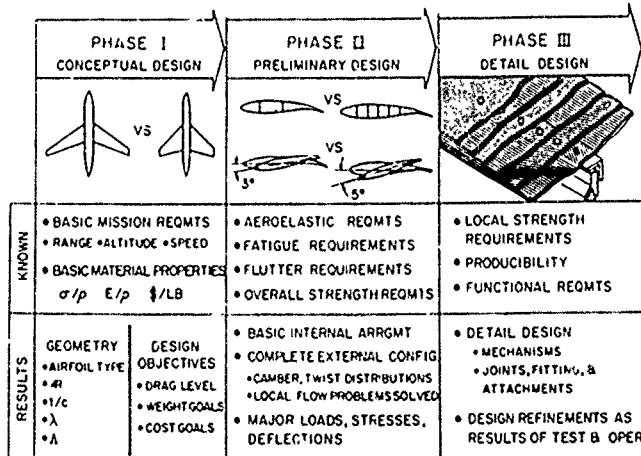
by
 P.W.Sacher
 Deutsche Aerospace
 Messerschmitt-Bölkow-Blohm-GmbH
 Military Aircraft Division
 Advanced Design Dept.
 P.O.Box 801160
 D-8000 Munich 80
 Germany

1. Rationale for the special course

In 1986 the AGARD Fluid Dynamics Panel organized a special course on the subject of "Fundamentals of Fighter Aircraft Design" at the V.K.I. Brussels, the AF Academy Athens and at the METU Ankara. More than 200 young engineers attended this course. It seems to be timely to repeat a similar approach within the AGARD technical programme and with respect to the scope of the previous course three major modifications were approved :

- (a) Aerodynamic analysis tools used in conceptual and preliminary aircraft design should be included
- (b) Extension to civil aircraft should be allowed and
- (c) Addressing mostly conceptual and preliminary design, the scope of the course should be restricted to fast, inexpensive and easy-to-handle design and analysis tools.

First the terminus "Engineering Methods" should be defined more in detail. It is understood that this methods shall represent proven engineering procedures most commonly used in industry during the conceptual and preliminary design and development of any new aircraft concept.



Ref.: Fundamentals of Aircraft Design (L.M.Nicolai)

Fig. 1 Major design phases in aircraft development

In this sense engineering methods are characterized by :

- basically fundamental orientation
- they have to be fast, inexpensive, easy to operate, flexible and validated in the limits of its applicability and mostly for the last reason
- their efficiency is strongly dependent on skill and experience of trained personnel.

In consequence young engineers, starting their professional career in industry have to get acquainted to work with this "Workhorses" of the aircraft design business. This course shall contribute to this "Training Process".

It is left to describe the state of "Conceptual Design" and "Preliminary Design" of a new aircraft project. As Fig. 1 outlines schematically, conceptual design is phase I in the overall design process. Based on desired mission requirements, the first impression of the new vehicle is achieved by using iterative design-sizing programmes starting from existing similar "Baseline" designs with known performance. In the following phase II, an optimization process follows resulting in the complete definition of the external configuration and the database for geometry, major loads, stresses and performance. This geometric shape will be "frozen" for the detailed design (phase III) and more sophisticated design tools, e.g. complex viscous CFD, will be applied.

According to the restriction to conceptual and preliminary design, contributions to the special course have been selected. In addition to preliminary design (Chap. 2) and configuration finding (Chap. 3), surveys on basic potential flow codes and experimental verification techniques follow in Chap. 4 and 5. Due to progress in using more and more the extended nonlinear range of angle of attack, Chap. 6 was included, taking also account for high speed aircraft designs, having large leading edge sweep and vortical type leading edge flow separation. The aircraft drag analysis methods conclude this selection of fundamental surveys on engineering methods for the daily work of the aeronautical engineer during conceptual and preliminary design in Chap. 7.

2 Levels of aerodynamic flow simulation

The classical way to get confidence on a new aircraft design is the experiment using windtunnels. This "experimental flow simulation" has led to the development of the aircraft of today. But in recent years the extension of the flight envelope of new projects has reached flow regimes where the flow simulation in ground test facilities has become questionable. For small Reynolds numbers, achieved in windtunnels have always been a problem, but now, in addition, the flow simulation for high speed concerning temperature, "real-gas" chemistry and hot model test techniques play an important role. So more and more numerical flow simulation contributes to the extrapolation from windtunnel to real flight data.

It has to be understood clearly, that CFD will never replace windtunnel experimental work, but CFD will give a strong support to analyze windtunnel data in a complementary way. The result is more confidence in a new design before first flight. There is a long list of attractive features provided by CFD when applied parallel to experimental work .

- (1) Increase of design broadness. An increased number of configurations will be investigated by using CFD in addition to baseline experiments.
- (2) The guarantee of compatibility of derived similar vehicles.
- (3) Quality assurance of data obtained will be independent of personal skill.
- (4) Reproducibility, transparency and standardization of the overall design process will be achieved.
- (5) Last not least the complementary use of CFD will result in a considerable reduction of the design risk

Fig. 2 shows some major characteristics of experimental and numerical flow simulation.

Computational flow simulation

- + real geometry
- + no limits for variation of parameters
- + known boundary conditions
- + real Re-number
- + short response
- + cost decreasing with time
- errors not known
- systematical errors (equation)
- good reproducibility /objectivity
- flow representation by model approximation
- computer speed and memory limited

Experimental flow simulation

- scaled geometry
- model flexibility limited
- not always defined
- Re-number too low
- long term (time consuming)
- cost increasing
- + accuracy of measuring technique known
- ? sometimes hidden
- ? questionable (experimental "skill")
- + real flow (flow quality?)

Fig. 2 Compilation of major characteristic features in computational (CFD) and experimental (EFD) flow simulation

Experimental investigations during an early design phase require modular models with a high degree of flexibility to get all effects of major geometric parameters. As Fig. 3 demonstrates, such a modular model requires an extensive test campaign

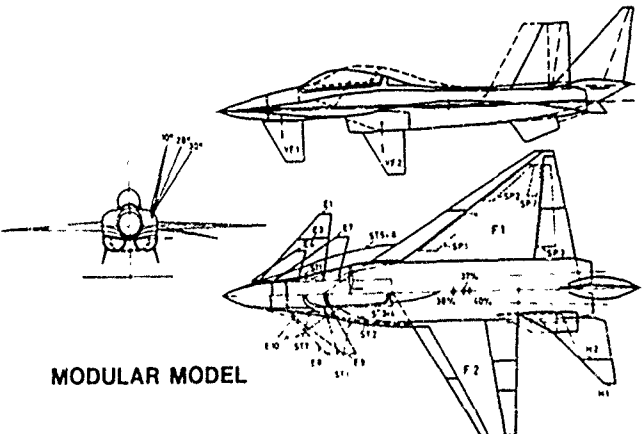


Fig. 3 Complexity of modular models during experimental configuration optimization

Therefor a number of good arguments speak for the increasing importance of computational flow simulation but the big "unknown" today is the demand for "code-validation" or the question of confidence in predicted data.

Aerodynamic computational codes used in aircraft industry for analysis and design can be grouped into three major categories. Fig. 4 shows a somewhat arbitrary, but nevertheless representative collection of codes used in the MBB advanced design department.

SIMPLE/CHEAP/FAST	ADVANCED	COMPLEX/EXPENSIVE
DATCOM - handbook method SCHEMENSKY - handbook method for empirical based induced drag PS105 - sub-,super-,hyperersonic panel method derivatives and loads LAMAR - vortex lattice method Ind. drag minimization vortex lift HARRIS - wave drag analysis optimization	HYP3 - modified newtonian theory HISS - higher order sub- and supersonic panelmethod HIDFS - design option of HISS potential flow theory HIVISC - extension to boundary layer	EUFLEX - numerical flow simulation INviscid - vortical type flow coupling to bound.Layer INFLEX - unsteady flow - EULER equations NSFLEX - NAVIER-STOKES - viscous vortical type flow - laminar, turbulent - separated flow - viscous/inviscid interactions - shock-viscous interactions - zonal version

Fig. 4 Aerodynamic computational tools for analysis and design

Some general comments on Fig. 4 :

- (1) Empirical methods have to be simple, cheap, fast and easy-to-handle. These are handbook methods but also simple linear 1. order singularity methods like linear 1. order panel and vortex lattice methods. In many cases this simple codes are based on engineering experience and "rules", (e.g. "area rule", "leading edge-suction analogy"). Viscous flow corrections, slender body approximations and propulsion system induced effects may often be pre-estimated within this category.
- (2) "Advanced" higher order (still linearized) potential flow codes take account for vortical separated flow, nonlinear wake interactions and corrections for boundary layer development.
- (3) On the "Highest level", full potential flow codes, Euler solvers and Navier Stokes codes belong to the third category, often understood as the real domain of CFD. This last category of codes may not be used during conceptual and preliminary design because of the need of timeconsuming input requirements and computational cost. Supercritical wing design, high angle of attack aerodynamics and flows with strong viscous/inviscid interactions can only be simulated using such complex CFD codes.

Following the terms of reference of this special course the content will be restricted to procedures of the first group, the simple, cheap and fast methods (1).

3. Level of confidence in EFD and CFD

Using computer codes a general remark has to made on the status of computational tools. We distinguish :

(1) Research codes

They produce test results which have to be validated by test or flight data. In general this codes could be used only by the originators.

(2) Pilot codes

Are ready for in-house applications by several engineers having the possibility to discuss questionable results with the originator of the code.

(3) Production codes

Ready for transfer to other places. They have already been validated and detailed documentation is available for external applications.

Our empirical methods in most cases belong to the third category. But the validation of the codes has been often replaced by "calibration". Sofar some remarks on the problem of code "Validation" have to be made. It is understood that code validation is to insure that the mathematical and numerical schemes employed in the code

accurately model the critical physics of the flow field. This may not be necessarily the case for empirical methods where the mathematical model representing the flow physics is poor. Effects of mesh resolutions mathematical algorithms turbulence models and gas models are often negligible. Fig. 5 identifies some of the major sources of errors in computational procedures.

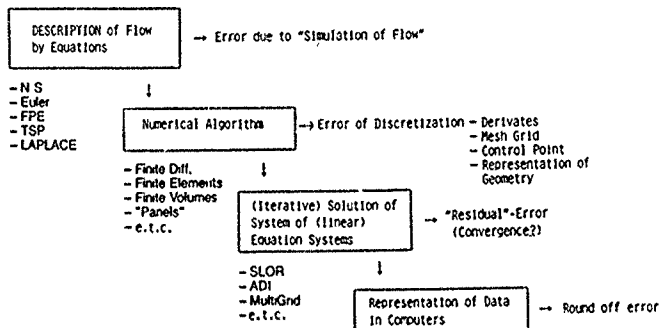


Fig. 5 Sources of errors in computational flow simulation codes

In consequence many attempts have been undertaken to validate computer codes using carefully selected "test-cases". The prediction of drag has been proven to be still the most critical problem. Fig. 6 shows a compilation of data obtained in an early attempt (GAMM 1981) to validate computer codes for a simple NACA 0012 airfoil at transonic speed. Even for the prediction of pressure-drag results obtained from various classes of solutions (non-conservative, full conservative full potential flow and Euler equation solvers) differ significantly, but even in the same category solutions of different codes predict values for drag within 100% deviation.

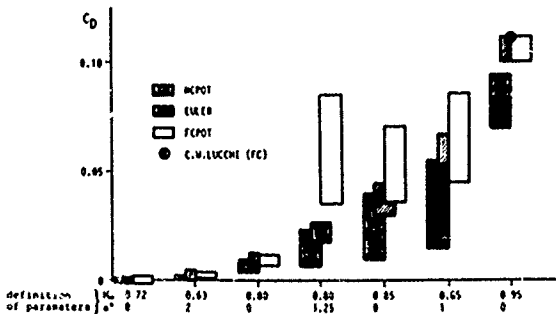


Fig. 6 Test-cases for code validation (NACA 0012)
Prediction of drag using CFD codes

Since that time the situation has improved but even using Navier-Stokes flow solvers, the prediction of drag remains the toughest challenge for CFD.

On the other hand experimental work has also been done to "validate" experimental data obtained in different windtunnels. The situation is not so different from theoretical work. As Fig. 7 shows, pressures and coefficients differ significantly for the same simple 2-D profile section.

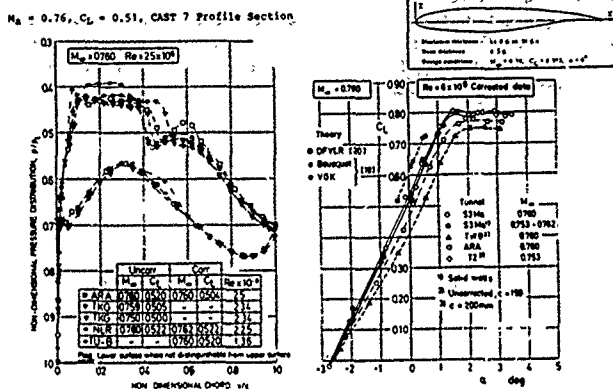


Fig. 7 Experimental approach - uncertainty and sensitivity for identical models in different windtunnels (GARTEUR AG02)

The list of activities concerning code validation during the past ten years is very impressive and AGARD has played an active role :

- 1979 AGARD AR-138/FDP WG04
Experimental data base for computer program assessment
- 1981 GAMM workshop on 2D test-cases
Full potential and Euler flow codes
- 1982 AGARD AR-702(1984 addendum No. 1)
Compendium of unsteady aerodynamic measurements
- 1984 NASA NTF delta wing model
Database for computer code development
(ATMA 84-2150)
- 1985 AGARD AR-211/FDP WG07
Testcases for inviscid flow field methods
- 1986 AGARD AR-226/FDP WG 08
Aerodynamics of aircraft afterbody
- 1986 International vortex flow experiment on Euler code validation
FFA Stockholm
- 1988 AGARD CP-437
CFD validation
- 1991 AGARD AR-270/FDP WG 13
Air intakes for high speed vehicles

In this "environment" of CFD and experiment the engineering methods during conceptual and preliminary project work will be outlined in the following chapters. Major emphasis will concentrate on the applications. Regarding detailed theoretical basic assumptions underlying engineering methods, the references will be given. It is the intention of this special course to initiate interest in the overall design procedure of a new aircraft and to give young engineers and students the opportunity to get acquainted with the "workhorses" of daily routine in aeronautical engineering.

8. Conclusion

This Special Course on "Engineering methods in aerodynamic analysis and design of aircraft has been organized at

- The Middle East Technical University (METU) of Ankara from 6.-10.May 1991
(36 Attendants)
- The Von Karman Institute (VKI) in Brussels from 13.-17.May 1991 (38 Attendants)
- Politechnical University of Madrid from 20.-24.May 1991 (60 Attendants).

In addition to the technical presentations a Round Table Discussion with the lecturers was scheduled at the end of the course. Some preliminary technical evaluation of the course was given by the course director as follows.

Six major presentation have been given during the Special Course :

- Preliminary design
- Configuration development
- Experimental techniques
- Potential flow codes
- High angle of attack aerodynamics
- Drag analysis methods

The first question at the end of the course is concerning the completeness of the content. According to the comments from the audience during the final discussions no recommendations for additional topics came up. The second question addresses the aim of the course. Did we attract a sufficient number of attendees and did we reach the "young engineer" who is about to start his professional career in aeronautical engineering? Due to the number of attendees and the contributions to the Round Table Discussion also the second question may be answered in a positive sense for all three places. The recommendation came from the floor that a similar course should be repeated each second or third year.

Some major findings from the presentations may be highlighted for better recollection.

Computational procedures for preliminary design

Pierre Perrier introduced the audience to the different definitions of design levels in the environment of the "magic triangle" of Real Flight - Experiment - and CFD. In this sense EFD stands for the simulation of the "Real World" in contrary to CFD simulation of the "Soft World". He described the "Rendez-Vous" procedure in terms of levels of quality versus time for development. According to this philosophy the state of conceptual design using simplified engineering empirical tools develops to the stage of feasibility using much more sophisticated experimental and computational tools before approaching the state of manufacturing the new aircraft.

Configuration development

Daniel Raymer stressed first of all the necessity of design trades. Basic design trades e.g. canard- versus aft-tail configuration or wing planform trades have to be repeated for any new project design. A second group of basic trades deals with "Requirement" trade-offs, e.g. max. speed versus maneuverability or maneuverability versus detectability. It is obvious that these timeconsuming trades could only be performed using automated design programmes. A major role during the application of design programmes is the definition of a so-called "Baseline-Design" configuration with known performance. To save computing time these "aircraft sizing" programmes rely to a large degree on simple empirical engineering procedures. Reference to these methods applied in design programmes have been given in detail. The result of the ap-

plication of this design programmes will be the evaluation and transparency of "design-sensibilities" depending on systematic parameter variation concerning Gross-Take-Off-Weight (GTOW).

Experimental techniques for performance prediction

Barry Haines reviewed the present state-of-the-art in experimental testing as a means of prediction of aircraft performance. Standards of accuracy are defined. The first part of the presentation deals with all aspects of data acquisition systems and discusses all effects contributing to uncertainty of measured data, (flow quality in windtunnels, windtunnel-wall interference, modelsupport interference and scale effects). In his second part the lecture discusses the types of models and test rigs used in determining the propulsion interference effects on both transport (turbofan and turboprop) and combat aircraft. Especially for recent designs the engineering problem of optimum engine-airframe-integration plays a dominant role both for civil (due to economic reasons) and for military (due to drag-performance) projects. Even airbreathing space transportation systems emerging in the near future rely to a large degree on the interdisciplinary "integrated design" of the engine components like intake and afterbody-nozzle.

Panel methods for aerodynamic analysis and design

Harry Hoeijmakers presented an extensive and complete overview on aspects of panel methods used in aerodynamic analysis and design of aircraft. This solutions of the linearized potential flow equations are today the most important "Workhorses" in the "Tool-Box" of an aeronautical engineer. They have now reached the level of personal computers for practical application. Being more complex as the methods generally understood as "empirical", the use of panel methods requires a great deal of engineering experience and personal skill. Limits of applicability have to be understood (and explored) by each individual user. The lecture starts with the detailed outline of the theoretical approach for the approximations made for the flow field and the discretisation used to deal with complex vehicle geometry. It reflects all major issues of existing panel methods and shows examples for applications both for simple and for complex geometry. Propulsion integration, viscous correction procedures and nonlinear vortical separation is referenced.

High-angle-of-attack aerodynamics

John Lamar discusses the different regimes of the CL-44 plane. Four α -segments have been identified :

- low - attached flow dominates
- moderate - combination of attached and separated or vortical flow
- high - separated or vortical flow dominates
- post-stall - vortex break-down or massive stall

Depending on the wing planform and Machnumber this segments extend to different size. The paper deals first with engineering methods for the prediction of vortical separated flow (e.g. Sychev similarity, Vortex Lattice Method-Suction Analogy, Digital Datcom and Free Vortex Filaments). Second the high angle of attack range is stressed for stability and control. The effects of different wing planforms and the effectiveness of control devices (including "vortex flaps") is discussed. Finally the subject of Post-Stall-Flight is addressed, including aerodynamic control devices, thrust vectoring and dynamic stall.

Aircraft drag analysis methods

Charles Boppe structured his lecture into two major parts :

- (1) Evaluation of drag and
- (2) Reduction of drag

First the sources of different drag contributions are discussed. Handbook methods are indispensable for prediction of drag contributions. The engineering methods are considered to be the bridge between empirism and windtunnel testing. Considerable timesavings are achievable by careful analysis and understanding the drag mechanism. For the second subject engineering methods are applied to achieve higher performance. Insight into the complex drag mechanisms is required for the desired goal. Reduction of windtunnel test time and flight tests is achieved through the use of empirical engineering drag prediction tools.

Summary

Three major statements characterize the major findings of this special course :

- (1) Engineering work in aeronautical analysis and design is traditionally performed in two ways :
 - Experimental approach,
characterized by limited simulation of flow physics (e.g. Re-Number, Machnumber, Real-Gas ...).
 - Numerical analysis,
characterized by trend to higher level codes,
high cost for viscous 3D codes,
production of high quantity of flow field data,
lack of code validation.
- (2) Interdisciplinary approach is mandatory in conceptual and preliminary design work :
 - Experiment will not be replaced by CFD,
in addition to traditional configuration testing the experiment has to provide data for CFD-code validation.
 - The role of CFD is a complimentary one with respect to the experiment,
extensive use of CFD leads to quicker and more reliable selection of the most promising configuration.
- (3) Engineering methods are indispensable because :
 - "High-level" CFD analysis is excluded in conceptual/preliminary design
 - Experimental work is not (or limited) available for configurational conception
 - Empirical (e.g. "Handbook"), low-level (potential-) flow code analysis on PC's and Workstations and extrapolation from engineering experience obtained during previous design work is the logical consequence
- (4) There is an obvious need for training young engineers to get acquainted with simple engineering methods.

ACKNOWLEDGEMENT

As director of the AGARD FDP Special Course on "Engineering Methods in Aerodynamic Analysis and Design of Aircraft" I like to express my appreciation to the lecturers which have performed their part during the course in a most professional way. It was my intention to bring together experienced experts from industry and research institutes, experts which are recognized worldwide to work successful in the related field of aerodynamic analysis and design. They all have reacted spontaneously in a positive way, shortly after having been asked to contribute to such an extensive effort of the AGARD community :

Mr. Charles W.Boppe from Grumman Aircraft Systems, New York
Mr. Barry Haines retired from ARA, Bedford
Dr. Harry W.M.Hoelijmakers from NLR, Amsterdam
Dr. John W.Lemar from NASA Langley Research Center, Hampton VA
M. Pierre Perrier from Aviation Marcel Dassault, Paris
Mr. Daniel P.Raymer from Conceptual Research, Sylmar CA

In addition I wish to express my gratefulness to the local coordinators. They have provided excellent local arrangements and perfect organisation of the Special Course during the meetings :

Prof. Dr. Cahit Ciray from the Middle East Technical University in Ankara
Prof. Dr. Mario Carbonaro from the Von Karman Institute in Brussels
Prof. Rodriguez Martinez-Val from the Polytechnical University in Madrid.

This Course could have not been organized without the outstanding support of the Fluid Dynamics Panel Executive Mr. Winston Goodrich and his Secretary Mdm. Annemarie Riveaull, from AGARD Headquarters, Paris.

Computational procedures for preliminary design

P. PERRIER

Chef du Département d'Aérodynamique Théorique

DASSAULT AVIATION -

CEDEX 300 - 92552 SAINT-CLOUD - FRANCE

0. - INTRODUCTION

Preliminary design of aircraft has evolved largely on the past ten years. The main origin of evolution came from rationalization and broadening of the preliminary phases of development of a new project. Has to be evaluated sooner the interest of the project in its capability to fulfill the requirements of a program ; has to be proposed the strategy for making its development : with what funding, with what national or international collaboration, with what long term calendar. Moreover the level of technology involved is to be evaluated : not only as the state of the art available but also as requiring an ad-hoc effort to be included in the total cost or time schedule.

Rationalization of national or international large programs has led to definitions of a succession of well-defined levels of freezing of the design ; of common use is for example the following succession of four definitions :

Definition 0 is the first complete tentative definition for which the drawings include all the main ingredients necessary for freezing the architecture in details : volume for equipments, correct geometry of main parts fixed or moving (undercarriage ; removable parts, external stores ...). It is highly hoped that the center of gravity be at a reasonable position relative to aerodynamic center of pressure in the flight envelope ; in the same effort of having a reasonable first design, main requirements are to be fulfilled on flying qualities, performances (volume of tanks) weapon system (antenna locations), payload (volume, center of gravity,

accommodation of passengers ...). Such definition can therefore be the firm basis for a complete study : it includes trade-off for the aircraft as a system and an evaluation of critical aerodynamic problems to be studied.

Definition 1 is the product of an improved design ; it results of the complete analysis of the definition 0 after first wind tunnel testing and first analysis of the critical points. It can be the basis for the first feasibility study on the nominal aircraft ; it can give valuable support to the first evaluation of main uncertainties. It is clear that it is the first definition where a realistic evaluation of the probable performances and of efforts needed for having them, plus risks associated, can be given. Performances may be determinated not as state of the art preliminary estimation but a comprehensive set of data coming both from CFD and from experiments. Research and Development. Efforts needed are related to criticality of the problems compared to the objectives of the program and on available technology for solving them. Risks assessment are based on the difficulty of solving the problems with the funding and the time scale allowed, and on the existence of alternate solutions.

Definition 2 can be frozen when iteration with detailed requirements (including maintainability, economic trade-offs, fabrication requirements...) clear the way to first detailed design of major or long-cycle parts of the aircraft. Progressive freezing of definition 2 can allow some extra time for aerodynamic work, mainly on the more complex phenomena ; but geometrical shapes need to be stable now for avoiding costly changes. Final geometrical data can be a definition 3 near the definition 2.

Here we will cover mainly the preliminary design work needed for the production of definition 0. However a part of the trade-off studies and of the continuing work of refinement of definition 1 and 2 can be done with the same tools. Analysis of critical problems on definition 1 can lead to a reassessment of some alternate design ; again such variants 1.1, 1.2... have to be built quickly, so with the same tools.

One main philosophy that has emerged from repeated experience of such preliminary cycles of design is the concept of "same level of quality of design comparison". There is a clear difficulty to extract valuable comparisons of data obtained on different designs with different tools and different levels of convergence ; it leads to mixing of evaluation of different designs with the evaluation of quality of the output of different design tools. A conservative design may seem poorer than a promising but not yet compromised new design. It is particularly true, but in the opposite direction for direct experimental comparisons of designs that are not at the same level of improvement by LFO : if design for example a wing has been optimized, a large variation of main parameter (sweep angle, location of nacelle...) can be selected without new optimization ; but the derivative will be probably poorer when the derivative are issued from preliminary design tools or when design is sensitive to quality of design (e.g. transonic, laminar...). Anyway the computational procedures are central in the evaluation of a design not only before but also for analysis after W.T. testing.

1 - GENERAL DESIGN COMPUTATIONAL PROCEDURES

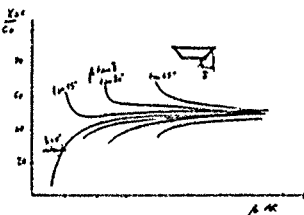
1.10 - We will cover successively the computational procedures for the first iteration of design before the selection of definition 0, as referred before, and in the preliminary the freezing after definition 0. Of main importance are evaluation of center of gravity position and of thrust-minus-drag, and L/D for general performances. So these items will be covered first.

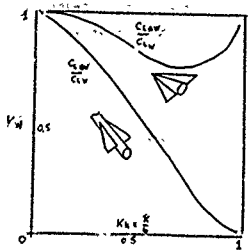
1.1 - Center of pressure evaluation

It is the first main aerodynamic characteristic that is needed from the beginning. Without it the work of the design office cannot be realistic. Some trends are needed for balancing the general architecture of the aircraft. The size of the wing can be deduced from rough estimates of the realistic wing loadings and the size of the fuselage is generally coming from volume constraints, but the balance of the mass require quotation from the start of the project definition. So a progressive approach by three procedures each being more complex and more accurate than the preceding one seem necessary and have to be used successively.

The first is an old but efficient rule of determination of approximate subsonic center of pressure on the drawing table. It relies on the assumption that the repartition of the lift on the different elements of the aircraft is elliptic or slightly distorted from elliptic distribution as given by figure 1 versus the aspect ratio, sweep angle and taper ratio. And we can assure that wing + fuselage characteristics are obtained from wing alone plus interaction. Conventionally K_w is the factor of wing lift increment when fuselage-body is present, K_b is the percentage of lift transferred to the body. Figure 2 gives an estimation of K_w and K_b (coming from low aspect ratio or slender body estimation) versus ratio of equivalent cylinder to wing span.

The aerodynamic center can be built by assuming that its local position for a slice in span is on a 25 % position on current chord and is distorted to 25% $\pm \frac{q}{2} \pi$ by the symmetry conditions. So the curve upon which can be put the load given by figure 1 and 2 can be easily approximated.



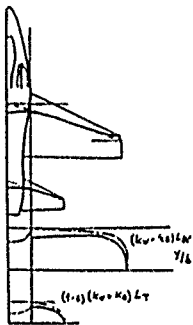


If there is a tail, the same approach is useful but a reduction of efficiency coming from deflection is needed and Fig. 3 gives typical figures vs separation distance between tail and wing. The absolute value of tail or wing alone lift is usually not far from Diederich formula

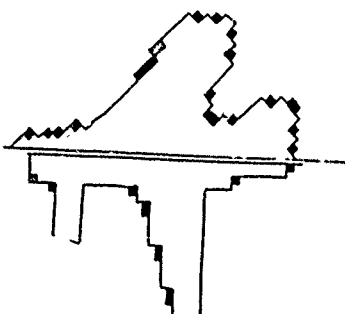
$$\text{ACL} = \frac{2 \gamma'}{1 + \left(\frac{C_L}{\gamma'}\right)^2 AR}$$

Such first level of aerodynamic center estimation is also used for quick evaluation of trade-offs during first interaction on the design. The hand procedure here described can appear in a code for a PC such code is useful for avoiding errors but it engineers may loose understanding of the complexity of interaction and of their approximation ; moreover inputs may be complex due to their numbers and may be source of errors.

such job is to retain on a P.C., with extended core memory and arithmetic coprocessor two simplified codes : one, in subsonic, make use of vortex-lattice method, the second one is linearised supersonic planform evaluation. Both require a limited time of computation but also precise rules for input of geometry for the quality of the results. On the vortex-lattice method it is absolutely required to well known the following rule : a one quarter singularity plus three quarter control point is mandatory for each cell retain in the discretisation process. On the supersonic linearised method, an efficient way is to use the quadrilateral meshing along the characteristics lines ; if the mesh is regular the matrix of influence coefficients can be inverted a priori and such furnish a very cost-effective computation procedure ; however such regular predetermined grid (with an affinity factor for span adjustment) implies difficulty with irregular planforms ; that can be improved by local refinement. Another advantage of such linearised procedure is to give an approximation of the C_p distribution in chord and span and of lift and pitching moment ; such data are useful for first determination of some critical problems ; it supposes a first definition of a camber or control deflection needed for balance at a given angle of attack. So it is the first way of asking evaluation of camber or twist. Inputs become more complex with an important number of cells ; that can be the source of (often complex to analyse) errors in data.



The second level of estimation of the position of the aerodynamic center is based on the use of small computers. A good way of doing



The third level of estimation of position of the aerodynamic center is to go to 3D computation without linearisation on the planform. Such procedure is soon required for any aircraft difficult to balance. In the past, the cost of such approach was excessive ; now it is no more true and we are able to notice that the typical 3D-code that can be retained is defined by the capacity of in-house workstation. Current practice will now be to devote such workstation to the design group for such specific task as the aerodynamic and stress analysis at the level of the preliminary design. Probably the complete transonic design will be excluded of such preliminary work ; however the main limitation comes from the interface with geometrical definition and the time for having a good mesh for computations. It is clear that singularity on panel method is well adapted to such work ; this is because such panel method requires only the discretisation of the surface of the aircraft. Subsonic and supersonic panel methods are the basic tools, but more complex 3D computations may be more useful.

In the third level of codes to be used in preliminary design is the level of 3D complete viscous codes ; their use is questionable. In fact, their effective cost is directly associated with the cost of preparation of the computation : mesh definition on geometrical data, subdomains definition, checking of the quality and correct mesh refinement as locally required. So finite element method, taking into account the total complexity of the geometry, seems well adapted to fast answer except if mesh is too costly or long to obtain.

Intermediate codes, for that point of view, are the 3D codes involving no direct meshing. Typically the mesh is a regular rectangular mesh ; the solver generally takes advantage of such regularity-it can be linear finite difference or spectral ; local application of boundary conditions can be done directly or with local regular refinement. At the other extremity of boundary conditions are the codes devoted to the complex non structured mesh around any irregular body ; that will ask for finite element solver on any complex geometry, as needed on final computations, on final aircraft shapes. We will

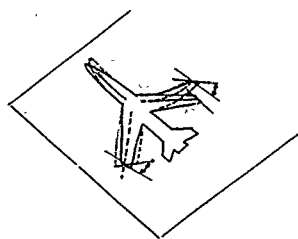
review the tools against below, but we can summarize from now the three levels in the following table.

Table I. Levels of Complexity of preliminary design tools		
LEVEL 1 Hand-books - Hand estimation - P.C codes for first estimation (Assumption : lifting lines + slenderbody + interaction linearized).		
LEVEL 2 Linearized codes - Use on workstations (Assumption : lifting surfaces + linearization of boundary conditions) A B C		
vortex method	Finite difference	space marching
2D mesh generation restricted to the surface	3D regular grid no mesh generation, direct or by SC projection on neighbouring regular points	unstructured grid with simplified mesh generation
singularity methods Subsonic Supersonic	subsonic spectral	Subsonic potential Supersonic Euler
Transonic with flowfield correction	Subsonic trans relaxation	Supersonic space marching

1.2 - Lift evaluation

In the same manner, the codes used in the 1.1 can deliver elements for lift. However, we have to distinguish between 3 different aerodynamic data : linear lift angle of attack prediction, lift mainly obtained with high-lift-devices and high angle of attack lift. The three are of main importance for different parts of the flight envelope. We will cover the three successively.

Good linear lift vs. incidence prediction is achieved by the three level of codes described before. It is clear that such prediction is useful for high dynamic pressure that corresponds to low values of angle of attack. Some concern may appear in such flight regimes with aeroelasticity effects for such aeroelastic effects a simplified procedure use the long beam approximation : flexion and torsion of wing and fuselage can be estimated by projection of efforts and moments on neutral line of the equivalent beams. A Newton iterative procedure will help to converge towards final deflection. Main contributors are coming from twist-induced by flexion of neutral lines of box of wings with sweep fig. 5.



High lift characteristics, without or with high-lift devices, mainly rely on dissipation of main wakes and mixing of viscous wakes and of boundary layers with or without separation. So it cannot be predict by inviscid flow computations. However a first assessment can be done in the approximation of lifting line. So if we return to the preceding procedure of lifting line wing + interaction + fuselage we can use the following iterative computation :

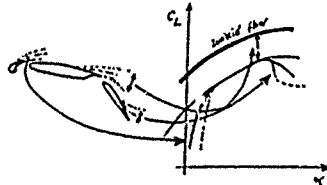
- compute the 2 D lifting correction due to viscosity + stall estimation
- compute the 3D lifting line lift distribution. It is obtain by iterative non linear spanwise induced downwash computations until convergence towards equilibrium.

So a three step procedure can be used : 1st estimation of inviscid contribution to high lift by the previously defined codes : e.g. singularities, with non linear boundary conditions.

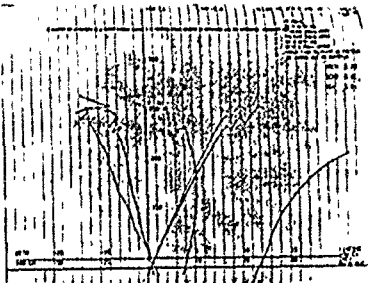
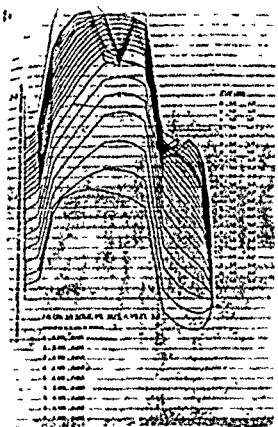
On figure 6, we have put the non-linear inviscid value of 2D lift and the experimental values for increasing camber of wing section. We have put also the angle of incidence related to maximum lift and the equivalent angle of attack having the same maximum lift as the section but on the inviscid curve. A lot of empirical criteria for determination of these two data have been proposed. We will retain the two following procedures :

- If no viscous computations are available, use of experimental results on similar wing section will help to define the "state of the art" loss of lift and angle of attack achieved for stall.
- If can be fulfilled the computation of boundary layer on upper surface of the wing section we can make the following assumption : on one element section the maximum lift is obtained when separation occurs at 85% of the chord with inviscid pressure distribution. Such figure is a mean value but can be very useful at the preliminary design level.

On multi-elements airfoil, same figure can be retained for the main section separation at the last element. Revaluable data are obtained with a value of 50% on its own chord. But when the camber increases, the C_p distribution does not change any more with angle of attack near the trailing edge : total separation on the slot is the best criteria for stall prediction.

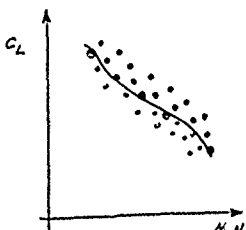


Better way of design is to use a complete iterated code taking into account the shape of the separated wake and interaction between boundary layer and wakes downstream of each slot. If the work is done in 2:50 (that is to say with account for sweep angle and local tapering of the wing) a complete set of lift (and moment) versus local angle of attack is available. Adding a lifting line computation of induced velocity will allow to be simplified 3D code to give a very precise predictor of high lift devices when aspect ratio is not too low and sweep angle not too high (say $AR \geq 3$, $\delta < 45^\circ$). On fig. 8 is given such a rebuilding of a typical subsonic aircraft by a genuine Dassault code.



For very high sweep angle another approach is to use the Poitamus approximation where the suction is assumed lost and transform in a vortex lift. Best procedure for suction predictions can be done by a vortex lattice method making the suction effective ; however maximum lift related to vortex bursting is only empirically chosen.

In transonic, fast answer can be obtained with wing alone or wing + simplified body finite volume computation. The time of computation is not so large and a complete set of data can be obtained by survey of maximum local Mach number normal to the shock-wave. A simplified rule assuming shock-wave/boundary layer separation when Mach number is larger than 1,4 gives a good approximation of the buffet angle of attack (fig. 9). If the complexity of the aircraft does not allow reasonable answer by wing alone computation (and in order to fix the CL aircraft versus CL wing) some complete aircraft computations are needed, for example by panel method.



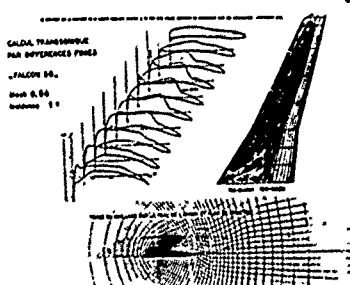
1.3 - Drag evaluation

Drag evaluation is the more complex and difficult task of any engineer in charge of preliminary design. Some probable evaluation can be done for friction and induced drag, but more complex components as those drags related to engine airframe integration and at the drag of miscellaneous, can be highly empirical at the preliminary stage of definition of an aircraft.

Friction and form-drag is obtained with good accuracy, from the data books ; such curves are well established (see for example the friction drag of Van Driest data book). But some corrections are needed ; they are directly related to square of thickness ratio for taking in account true local velocities larger than infinite value. Some concern are to be given to the roughness drag, particularly for low altitude mission prediction. A drag breakdown taking in account local chord and their Reynolds number effect is important in the selection of configuration with large variation of chords.

Preliminary estimations of friction drag only based on wetted area is dangerous except at the very preliminary stage of study.

Wave drag can be obtained at low cost in the approximation of linearized flow for wings and of axisymmetric flow for equivalent area distribution on the body. But an interaction process is needed for area ruling effect related to transonic and supersonic interaction. Fig. 10 gives such rebuilding process obtained by a Dassault genuine code used in preliminary design. It is to be noticed that correction for highly non linear effect is needed for canopy, pylons... If such correction is to be added, however such procedure gives a much better answer particularly in transonic range than the transonic or supersonic area rule formula based on trans-supersonic area rule distribution ; it was shown that such formula is only applicable with success to very slender configuration (variable geometry aircraft with high sweep angle configuration) without troubles coming from trailing edge contributions.



We will discuss the evaluation of drag related to engine installation in the next chapters.

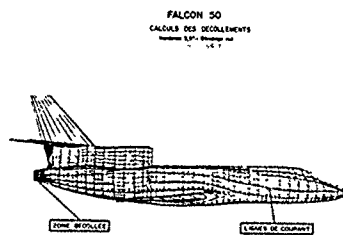
2 - DETAILED DESIGN ENGINEERING PROCEDURES

2.0 - Evaluation of first preliminary design quality can no more be done actually without a quick survey of separated area of design. We will cover successively the evaluation of local separated area, frontiers between non-separated and separated regions. Such evaluation includes the necessary first survey of air-intake integration and of afterbody integration. Many times it is at the level of induced separations that one has to predict the interaction with non aerodynamic requirements as those coming from RCS signature reduction.

2.1 - Separated areas evaluation

It is of main importance to survey for some critical points of design the boundaries of separated areas of the wetted total area ; all the skin cannot be examined versus all angles of attack and mach number of interest for separation of boundary layers.

Preliminary design has to lead directly to selection of aircraft configuration : obviously one main element of choice of configuration is generally the cleanliness of design or the boundary of such cleanliness from an aerodynamic point of view. The best preliminary design tool is the survey of one streamline after the other with a 3D boundary layer code ; fig. 11 gives an example of a flow survey at the wall for a Falcon oriented towards rear fuselage separation estimation by streamline analysis. Such code can be operated on a workstation using an inviscid pressure distribution coming from panel methods in subsonic or finite element in transonic. Of main importance are the ability of the code to give indication of the local determination of boundary layer by shape parameter $\frac{y}{\delta}$ and 3D shear angle versus the local convergence and curvature parameters of the streamlines. Easy surveys of the origine of streamline that separates is needed.

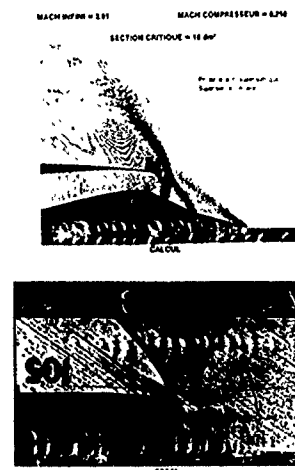


On supersonic or transonic design, the problem is generally much more related to existence of high intensity shock wave and on corresponding upstream shock-boundary layer interactions. Checking of validity of criteria of design by direct Navier-Stokes solution with simple turbulence modelling is out of the budget of preliminary design and has to be replaced by empirical evaluations.

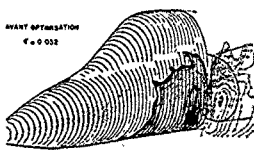
2.2 - Air-intake integration

Large difficulty in design comes from engine-inlet integration ; soon in the design is the necessity to define preliminary stage at least roughly for the boundary layer diverter. The necessity to evaluate the volume and position to be reserved to the air-intake is much mandatory for internal architecture of any project. A simple one dimensional analysis code is needed for evaluation of the area distribution of the duct and of the throat area required in different flight regimes. Another code has to help prediction of supersonic recovery factor taking account of losses in the external or internal shock waves and boundary layers. A simple 2D axisymmetric code is needed that uses the correct area distribution of the duct for preliminary design of possible internal divergence, and out of design external spillage drag. Fig. 12 shows a typical result of such axisymmetric code that helps a lot in the preliminary design phasis when intake area, external and internal devices are to be selected.

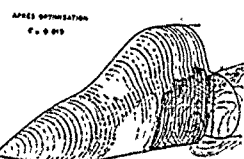
Particular insistence has to be put on accuracy of such finite difference code for evaluation of the drag because the too-rough evaluation of "suction" recovery directly extracted of 1D momentum equation, as so-called "additive drag", is dangerous. It is better to rely on integration of pressure of such code which take correctly in account the internal-external "recovery" on the lips. Conventional ram drag, as put in the definition of the thrust delivered by engine manufacturer generally given in its brochures, is to be compared to true pressure integrals. Equivalent axisymmetric air intake can furnish better data if careful duplication of local slope and duct area distribution are done.



Complementary work has to be performed from the beginning of the design related to incoming flowfield. Some external recompressions of the flow many times are coming from the shape of the aircraft. Effort are to be devoted, from the beginning of the design, to clarify what is the interaction has the forward fuselage or wing on the flowfield at the entrance of the air intake. Selection of front fuselage shape cannot be done without such preliminary study. It can be fulfilled by simple finite difference code as described in 13.



Air intake flowfield
(Cdarage 2000) optimisation



2.3 - Afterbody Integration

Symmetric work on afterbody has to be fulfilled. However it is clear that axisymmetric or monodimensional codes are not convenient for such study for twin engine integrated afterbody. For such study the delimitation of separated areas are to be done systematically with the procedure of 2.1. For more complex shapes the analysis is out of the scope of simplified inviscid or uncoupled viscous-inviscid flows. Some codes exist that can take advantage of simple correlation based on reattachment criteria or on mixing-layer development, but there are generally of limited values. Progress are to be done, but they will come from simplification of much more complete Navier-Stokes solutions. Such results are to be validated in wind-tunnel and in flight ; work are in progress.

2.4 - Interaction with non aerodynamic requirements

More are to be done in future design for integration of RCS or IR reduction in the aerodynamic design. It is to be assumed that equivalent simplified Maxwell solvers are at the disposal of designers and that interaction can take place between aerodynamicists and Maxwell specialists. Integration in the same team is mandatory. As an example this is probably more important than in the past when efforts had been push forward for integration of the aeroelastic

effects or for interaction with the stress analysis department. However the selection of position, shape, volume to be devoted to antennas are a part of the same effort towards complete Maxwell integration at the preliminary design phasis. Internal and external weapons or tanks are also part of such general effort for integration but specific tools are not needed except for preliminary evaluation of separation problems.

3 - CONCLUSION

We can summarize all the engineering tools used in the preliminary design in the following table

	AC/CP	Lift	Drag	Engine inlet-exhaust fore and after-body
Level 1	S.G.C	S.G.C	S.G.C + E.R	E.R
Level 2	L.M	P and FDM 2.S.P and FDM	L + NLC	AXI 2D INVISED CODE
Level 3	3DP and FEM	3 DP and FEM	3 DPM and FEM	3DP FF 3D S and S

SGC : Simplified graphic data-sheet and computing; ER : Expenses's rules ; L.M : Linearized method ; P.M. : Panel Method ; FDM : Finite difference method ; FEM : Finite element method ; L + NLC : Linearized + non linear corrections ; AM : Approximate methods ; FF : Flow field ; S and s : Streamline and separation.

It is clear that recent reduction of cost of computation by the minisuper computer and advanced workstation has shift the CFD computation from detailed analysis work to the preliminary design phase. Numerous tools are now used in such phase, it will improve greatly the quality of the 0.0 definition of any new project.

Références

1. W.R. Sears : High-speed Aerodynamics and jet propulsion Vol. VI General theory of high speed Aerodynamics.
2. A.F. Donovan, H.R. Lawrence : Aerodynamics components of aircraft at high speed Vol. VIII
3. Royal Aeronautical Society Aerodynamic data book.
4. E.G. Covert and all : Thrust and Drag : its prediction and verification. Progress in Astronautics and Aeronautics Vol. 98.1986
5. H.L. LOPEZ : Aerodynamics and performance characteristics of wing lift augmentation system. VKI lecture series 60,1973.
6. B. Haines : Aerodynamic interference - A general overview AGARD lecture Series Report 712, 1983
- 7 - P. Perrier - M. Lavenant : PROGRESS REPORT ON MECHANICAL FLAPS - AGARD - CP 143 - 24-26 April 1974
8. P. Perrier - J.J. DEVIERS : Calculs tridimensionnels d'hypersustentation - Colloque d'aérodynamique appliquée de l'AFITAE (AAAF) 1972.
- 9 - R. Eppler : Airfoil - Design and data - Springer Verlag - 1990
- 10 - B. Dillner and C. Koper : The role of computational aerodynamics in airplane configuration development - Agard C.P. N° 280 1979.
- 11- H. Carlson and Miller D. : The influence of leading Edge Thrust in Twisted and Cambered wing design for Supersonic cruise-AIAA Paper 81 - 16 56 - 1981 -
12. F.W. Bursham, D.R. Bellman : A flight investigation of steady state and dynamic pressure phenomena in the air inlets of supersonic aircraft AGARD CP 91 - 71.
13. W. Schmidt : Aerodynamic Subsonic/Transonic aircraft design studies by numerical methods AGARD CP 285 - 1980.
14. L.R. Harper : The subsonic Performance of Practical Military Variable area convergent Nozzles AGARD CP 301 - 1981.
- 15 - I.H. Rettie : Aerodynamic design for overall vehicle performance AGARD report n° 712 - 1983
- 16 - Rossow, Kroll, Radespiel, Schen : Investigation of the accuracy of finite volume methods for 2 and 3 dimensional flows AGARD CP n° 437 - 1988.
- 17 - P.W. Sacher : Fundamentals of fighter Aircraft Design Agard Report 740 - 1986

CONFIGURATION DEVELOPMENT

Daniel P. Raymer
P.O. Box 923156
Sylmar, CA, USA 91392-3156

NOTE:

The following material, presented as part of the AGARD FDP SPECIAL COURSE ON ENGINEERING METHODS IN AERODYNAMIC ANALYSIS AND DESIGN, is excerpted and summarized from the author's textbook, "AIRCRAFT DESIGN: A Conceptual Approach" (Copyright © 1989, published by the American Institute of Aeronautics and Astronautics, 370 L'Enfant Promenade, Washington, D.C., U.S.A., 20024). The lecture charts are part of the five day Short Course on Aircraft Conceptual Design which is regularly presented by the author. The author retains full copyright protection of this material, and further publication or reproduction beyond this AGARD short course is strictly forbidden without prior written approval.

INTRODUCTION & SUMMARY

Aircraft conceptual design is a complex, multidisciplinary process involving science, history, art, and magic, in sometimes equal proportions. In this AGARD special course, we are focused upon the aerodynamic aspects of aircraft design, but the overall configuration of the aircraft must both provide good aerodynamics and reflect a wide variety of other considerations. In this lecture number three, we will discuss configuration development and its key role in aerodynamic design.

CONFIGURATION DEVELOPMENT PROCESS

Aircraft design can be broken into three major phases depicted in figure one. Conceptual design is the phase where the basic questions of configuration arrangement, size and weight, and performance are answered.

The first question is "can an affordable aircraft be built which meets the requirements?" If the answer seems to be "no", the customer may wish to change the requirements. This is not too unusual, for the customer sets the requirements as a compromise between what experience says is feasible and what the end-users of the new airplane would like to get.

Conceptual design is a very fluid process. New ideas and problems emerge as a design is investigated in ever-increasing detail. Each time the latest design is analyzed and sized, it must be redrawn to reflect the new gross weight, fuel weight, wing size, engine size, and other changes. Early wind tunnel tests often reveal problems requiring some changes to the configuration.

Preliminary design can be said to begin when the major changes are over. The big questions such as whether to use a canard or an aft tail have been resolved. The configuration arrangement can be expected to remain about as shown on current drawings, although minor revisions may occur. At some point late in preliminary design, even minor changes are stopped when a decision is made to freeze the configuration.

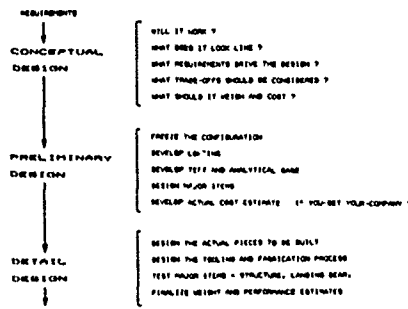


Fig. 1 Three phases of aircraft design.

During preliminary design the specialists in areas such as structures, landing gear, and control systems will design and analyze their portion of the aircraft. Testing is initiated in areas such as aerodynamics, propulsion, structures, and stability and control. A mockup may be constructed at this point.

Assuming a favorable decision for entering full-scale development, the detail design phase begins. Here, the actual pieces to be fabricated are designed. For example, during conceptual and preliminary design, the wing box is designed and analyzed as a whole. During detail design, that whole is broken down into individual ribs, spars, and skins, each of which must be separately designed and analyzed.

Detail design ends with fabrication of the aircraft. Frequently the fabrication begins on part of the aircraft before the entire detail design effort is completed. Hopefully, changes to already-fabricated pieces can be avoided.

The actual design effort usually begins with a conceptual sketch (figure 2). This

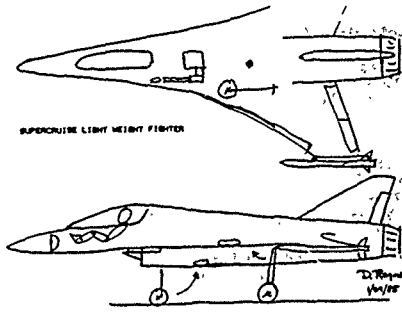


Fig. 2 Initial sketch.

is the "back of a napkin" drawing of aerospace legend, and gives a rough indication of what the design may look like. The sketch is used to make a first estimate of the required total weight and fuel weight to perform the design mission, by a process called "sizing".

The "first-order" sizing provides the information needed to develop an initial design layout (figure 3). This is a scaled three-view drawing complete with the more important internal arrangement details, including typically the landing gear, payload or passenger compartment, engines and inlet ducts, fuel tanks, cockpit, major avionics, and any other internal components which are large enough to affect the overall shaping of the aircraft. Enough cross-sections are shown to verify that everything fits.

This initial layout is analyzed to determine if it really will perform the mission as indicated by the first-order sizing. Actual aerodynamics, weights, and installed propulsion characteristics are analyzed and subsequently used to do a detailed sizing calculation. Furthermore, the performance capabilities of the design are calculated and compared to the requirements mentioned above. Optimization techniques are used to find the lightest or lowest-cost aircraft that will both perform the design mission and meet all performance requirements.

WING PLANFORM SELECTION

Before the design layout can be started, the wing geometry must be selected, including parameters such as aspect ratio, sweep, taper ratio, dihedral, and thickness. While all these parameters will be numerically optimized at some later date, that optimization will proceed from a "baseline" aircraft arrangement and that baseline must include some initial guess as to these parameters. Thus, designers have evolved a number of "first-order" methods which are provided below.

The "reference", or "trapezoidal" wing is the basic wing geometry used to begin the layout. Figures 4 and 5 show the key geometric parameters of the reference wing. Note that the reference wing is fictitious, and extends through the fuselage to the aircraft centerline.

There are two key sweep angles, as shown in figure 5. The leading edge sweep is the angle of concern in supersonic flight. To reduce drag it is common to sweep the leading edge behind the mach cone. The sweep of the quarter chord line is the sweep most related to subsonic flight.

Airfoil pitching moment data in subsonic flow is generally provided about the quarter-chord point. That is the point about which the airfoil pitching moment is essentially constant with changing angle of attack (ie, the "aerodynamic center"). In a similar fashion, such a point is defined for the complete trapezoidal wing. This is based on the concept of the "mean aerodynamic chord".

The mean aerodynamic chord, shown in figure 6, is the chord "c" of an airfoil, located at some distance "y" from the centerline. Figure 6 illustrates a graphical method for finding the mean aerodynamic chord of a trapezoidal wing planform.

The entire wing has its mean aerodynamic center at approximately the same percent location of the mean aerodynamic chord as that of the airfoil alone. In subsonic flow, this is at the quarter chord point on the mean aerodynamic chord. In supersonic flow, the

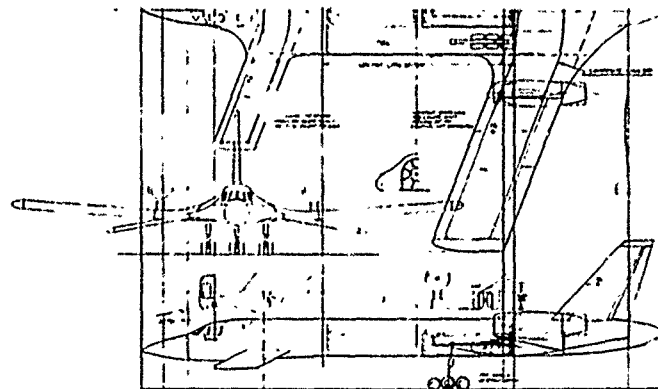


Fig. 3 Configuration layout

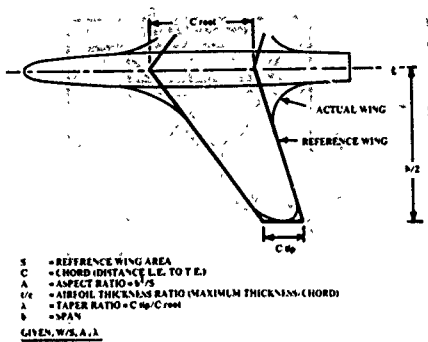


Fig. 4 Wing geometry.

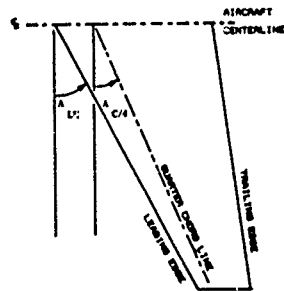


Fig. 5 Wing sweep A.

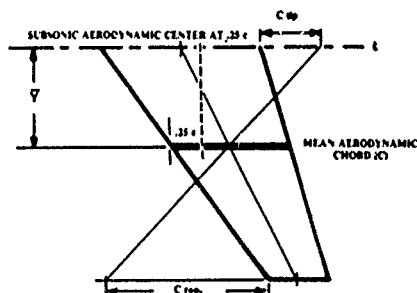


Fig. 6 Mean aerodynamic chord.

aerodynamic center moves back to about 40 percent of the mean aerodynamic chord. The mean aerodynamic chord and the resulting aerodynamic center point is used to properly locate the wing.

The shape of the reference wing is determined by its aspect ratio, taper ratio, and sweep. These will be determined now, along with the desired dihedral.

The first to investigate aspect ratio in detail were the Wright brothers, using a wind tunnel they constructed. They found that a long, 'skinny' wing (high aspect ratio) has less drag for a given lift than a short, fat wing (low aspect ratio). This is due to the three-dimensional effects.

When a wing is generating lift, it has a reduced pressure on the upper surface and an increased pressure on the lower surface. The air would like to "escape" from the bottom of the wing, moving to the top. This is not possible in two dimensional flow. However, for a real, three-dimensional wing, the air can escape around the wing tip.

When air escapes around the wing tip, the pressure difference between the upper surface and the lower surface is decreased. This reduces lift. Also, the air flowing around the tip flows in a circular path when seen from the front, and in effect, pushes down on the wing near the tip, which reduces the effective angle of attack of the airfoils near the tip. This circular, or "vortex" flow pattern continues downstream behind the wing.

A wing with a high aspect ratio has the wing tips further apart than an equal area wing with a low aspect ratio, so the amount of the wing affected by the tip vortex is less than for a low aspect ratio wing, and the strength of the tip vortex is reduced. Thus, the high aspect ratio wing suffers less loss of lift and increase of drag due to tip effects than the low aspect ratio wing of equal area.

Most early wings were rectangular in shape, the aspect ratio was initially defined as simply the span divided by the chord. For a tapered wing, the aspect ratio is defined as the span squared divided by the area (which defaults to the earlier definition for a wing with no taper).

The maximum subsonic lift to drag ratio of an aircraft increases approximately by the square root of an increase in aspect ratio. On the other hand, the wing weight also increases with increasing aspect ratio, by about the same factor.

Later in the design process, the aspect ratio will be determined by a trade study in which the aerodynamic advantages of a higher aspect ratio are balanced against the increased weight. For initial wing layout, the values and equations provided in table one can be used. There were determined through statistical analysis of a number of aircraft, using data from Jane's All The World's Aircraft.

Wing sweep is used primarily to reduce the adverse effects of transonic and

Table 1 Aspect ratio

Sailplane equivalent* aspect ratio = $4.464 (best L/D)^{1/4}$		Equivalent aspect ratio
Propeller aircraft		
Homebuilt	6.0	
General aviation—single engine	7.6	
General aviation—twin engine	7.8	
Agricultural aircraft	7.5	
Turboprop	9.2	
Flying boat	8.0	
Equivalent aspect ratio = $AM_{\infty}^{1/4}$		
Jet aircraft	A	C
Jet trainer	4.737	-0.979
Jet fighter (dogfighter)	5.416	-0.622
Jet fighter (other)	4.110	-0.622
Military cargo/bomber	5.570	-1.073
Jet transport	7.50	0

*Equivalent aspect ratio = wing span squared/(wing and canard area)

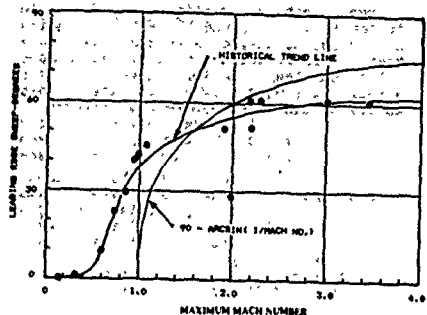


Fig. 8 Wing sweep historical trend.

supersonic flow. Theoretically, shock formation on a swept-wing is determined not by the actual velocity of the air passing over the wing, but by the air velocity in a direction perpendicular to the leading edge of the wing. This allows an increase in critical mach number by the use of sweep.

At supersonic speeds the loss of lift associated with supersonic flow can be reduced by sweeping the wing leading edge aft of the mach-cone angle ($\arcsin(1/\text{mach no.})$).

Figure 8 shows a historical trend line for wing leading edge sweep versus mach number. The historical trend differs from this theoretical result for two reasons. In the high speed range, it becomes structurally impractical to sweep the wing past the mach cone. In the transonic speed regime (roughly mach .9 to 1.2), the desire for subsonic airflow velocity over the airfoil (when measured perpendicular to the leading edge) is more important than the mach cone effect, which would indicate zero sweep for mach one.

The wing sweep and aspect ratio together have a strong effect on the wing-alone pitchup characteristics. "Pitchup" is the highly undesirable tendency of some aircraft, upon reaching an angle of attack near stall, to suddenly and uncontrollably increase the angle of attack. The aircraft continues pitching up until it stalls and departs totally out of control.

Figure 9 provides boundaries for pitchup avoidance for combinations of wing quarter-chord sweep angle and aspect ratio. Pitchup avoidance should be considered for military fighters, aerobatic aircraft, general aviation aircraft, and trainers.

Wing taper ratio is the ratio between the tip chord and the centerline root chord. Most wings of low sweep have a taper ratio of about 0.4 to 0.5, while most swept wings have a taper ratio of about 0.2 to 0.3.

Taper affects the distribution of lift along the span of the wing. As proven by the Prandtl wing theory early in this century, minimum drag due to lift, or "induced" drag, occurs when the lift is distributed in an elliptical fashion. For an untwisted and unswept wing, this occurs when the wing planform is shaped as an ellipse. This result was the basis of the graceful wing of the Supermarine Spitfire.

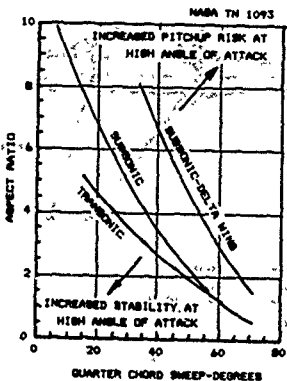


Fig. 9 Tail-off pitchup boundaries.

An elliptical wing planform is difficult and expensive to build. The easiest wing to build is the untapered rectangular wing. However, the untapered wing has constant chord length along the span, and so has excessive chord towards the tip when compared to the ideal elliptical wing. This "loads up" the tip, causing the wing to generate more lift towards the tip than is ideal. The end result is that an untwisted rectangular wing has about seven percent more drag due to lift than an elliptical wing of the same aspect ratio.

When a rectangular wing is tapered, the tip chords become shorter, alleviating the undesired effects of the constant-chord rectangular wing. In fact, a taper ratio of 0.5 almost completely eliminates those effects for an unswept wing, and produces a lift distribution very close to the elliptical ideal (figure 10). This results in a drag due to lift which is less than one percent higher than the ideal, elliptical wing.

A wing swept aft tends to divert the air outboard, towards the tips. This loads up the tips, creating more lift outboard than for an equivalent unswept wing. To return the lift distribution to the desired elliptical lift distribution, it is necessary to increase the amount of taper (ie, reduce the taper ratio).

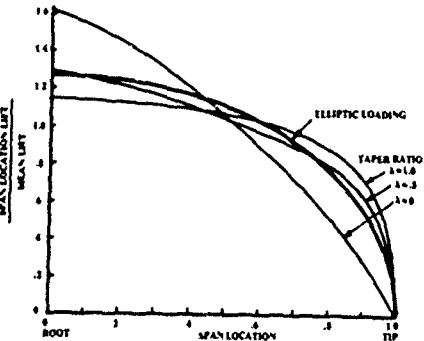


Fig. 10 Effect of taper on lift distribution.

Figure 11 illustrates the results of NACA wind tunnel tests to determine the taper ratio required to approximate the elliptical-lift distribution for a swept, untwisted wing. However, it should be noted that taper ratios much lower than 0.2 should be avoided for all but delta wings, as a very low taper ratio tends to promote tip stall.

Wing dihedral is the angle of the wing with respect to the horizontal when seen from the front. Dihedral tends to roll the aircraft level whenever it is banked. This is frequently and incorrectly explained as the result of a greater projected area for the wing which is lowered.

Actually, the rolling moment is caused

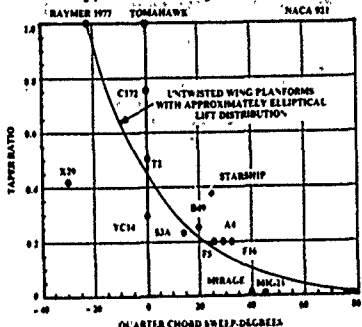


Fig. 11 Effect of sweep on desired taper ratio.

by a sideslip introduced by the bank angle. The aircraft "slides" towards the lowered wing, which increases the angle of attack of the lowered wing. The resulting rolling moment is approximately proportional to the dihedral angle.

Wing sweep also produces a rolling moment due to sideslip, caused by the change in relative sweep of the left and right wings. This creates an effective dihedral which is added to any actual geometric dihedral. Roughly speaking, ten degrees of sweep provides about one degree of effective dihedral.

In addition, the position of the wing on the fuselage has an positive influence on the effective dihedral, with the greatest effect provided by a high wing. Table 2 provides initial estimates of dihedral.

Wing airfoil thickness ratio has a direct effect on drag, maximum lift, stall characteristics, and structural weight. The subsonic drag increases with increasing thickness due to increased separation, and the critical Mach number reduces with increased thickness. The thickness ratio affects the maximum lift and stall characteristics primarily by its effect on the nose shape. For a wing of fairly high aspect ratio and moderate sweep, a larger nose radius provides a higher stall angle and a greater maximum lift coefficient.

Table 2 Dihedral guidelines

	Wing position		
	Low	Mid	High
Untwisted (civil)	3 to 7	3 to 4	0 to 2
Subsonic sweep wing	3 to 7	-2 to 2	-1 to -2
Supersonic sweep wing	0 to 5	-5 to 0	-5 to 0

The reverse is true for low aspect ratio; swept wings, such as a delta wing. Here, a sharper leading edge provides greater maximum lift due to the formation of vortices, which delay stalling.

Thickness also affects the structural weight of the wing. Statistical equations for wing weight show that the wing structural weight varies approximately inversely with the square root of the thickness ratio.

For initial selection of the thickness ratio, the historical trend shown in figure 12 can be used.

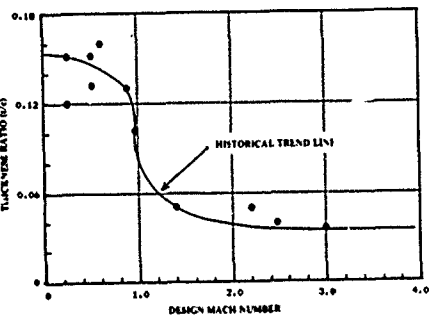


Fig. 12 Thickness ratio historical trend.

WING LOADING AND THRUST-TO-WEIGHT RATIO

The thrust-to-weight ratio (T/W) and the wing loading (W/S) are the two most important parameters affecting aircraft performance.

The thrust-to-weight ratio directly affects the performance of the aircraft. An aircraft with a higher thrust-to-weight ratio will accelerate more quickly, climb more rapidly, reach a higher maximum speed, and sustain higher turn rates. On the other hand, the larger engines will consume more fuel throughout the mission, which will drive up the aircraft's takeoff gross weight to perform the design mission.

Thrust-to-weight ratio is closely related to maximum speed. Table three provides curve fit equations based upon maximum mach number or velocity for different classes of aircraft which can be used as a first estimate for thrust-to-weight ratio.

For an aircraft which is designed primarily for efficiency during cruise, a better initial estimate of the required thrust-to-weight ratio can be obtained by "thrust matching". This refers to the comparison of the selected engine's thrust available during cruise to the estimated aircraft drag.

In level unaccelerating flight, the thrust must equal the drag. Likewise, the weight must equal the lift (assuming that the thrust is aligned with the flight path). Thus, the thrust-to-weight ratio must equal the inverse of the lift-to-drag ratio. An estimate of L/D obtained through one of several methods is thus used to determine minimum T/W for cruise.

Table 3 - T/W_0 vs M_{∞}

$T/W_0 = A M_{\infty}^2$	A.	C.
Jet trainer	0.484	0.728
Jet fighter (dogfighter)	0.648	0.594
Jet fighter (other)	0.514	0.141
Military cargo/bomber	0.244	0.341
Jet transport	0.367	0.363

There are many other criteria which can set the thrust-to-weight ratio, such as climb rate, takeoff distance, and turning performance. These other criteria also involve the wing loading and are described later.

The wing loading is the weight of the aircraft divided by the area of the reference (not exposed) wing. As with the thrust-to-weight ratio, the term "wing loading" normally refers to the takeoff wing loading, but can also refer to combat and other conditions.

Wing loading affects stall speed, climb rate, takeoff and landing distance, and turn performance. The wing loading determines the design lift coefficient, and impacts drag through its effect upon wetted area and wing span.

Wing loading has a strong effect upon sized aircraft takeoff gross weight. If the wing loading is reduced, the wing is larger. This may improve performance, but the additional drag and empty weight due to the larger wing will increase takeoff gross weight to perform the mission.

To maximize range during cruise, the wing loading should, if possible, be selected to provide a high L/D at the cruise conditions. L/D is a function of dynamic pressure. The wing loading for best L/D increases directly with increasing dynamic pressure.

A propeller aircraft, which loses thrust efficiency as speed goes up, gets the maximum range when flying at the speed for best L/D, while a jet aircraft maximizes range at a somewhat higher speed where the L/D is slightly reduced. The speed for best L/D is that speed at which the parasite drag exactly equals the induced drag. Therefore, to maximize range a propeller aircraft should fly such that equation one is satisfied.

$$qSC_{D_0} = 45 \frac{C_L}{Ae}$$

During cruise, the lift equals the weight, so the lift coefficient equals the wing loading divided by the dynamic pressure. Substitution into equation one allows solution for the required wing loading to maximize L/D for a given flight condition. This result (equation 2) is the wing loading for maximum range for a propeller aircraft.

$$\text{Maximum Prop Range: } W/S = q\sqrt{Ae C_{D_0}}$$

As the aircraft cruises, its weight reduces due to the fuel burned, so the wing loading reduces during cruise. To optimize the cruise when the wing loading is steadily reducing requires reducing the dynamic pressure by the same percent. This can be done by reducing velocity, which is undesirable, or by climbing to reduce the air density. This range optimizing technique is known as a "cruise-climb".

A jet aircraft flying a cruise-climb at a constant thrust setting will maximize

range by flying at a wing loading such that the parasite drag is exactly twice the induced drag. This yields equation 3 for wing loading selection for constant-thrust range optimization.

$$\text{Maximum Jet Range: } W/S = q\sqrt{Ae C_{D_0}/3}$$

An aircraft designed for air-to-air dogfighting must be capable of high turn rates. When air-to-air missiles are in use, the first aircraft to turn towards the other aircraft enough to launch a missile will probably win. In a guns-only dogfight, the aircraft with the higher turn rate will be able to maneuver behind the other. A turn rate superiority of two degrees per second is considered significant.

There are two important turn rates. The "sustained" turn rate for some flight condition is the turn rate at which the thrust of the aircraft is just sufficient to maintain velocity in the turn.

If the aircraft turns at a greater rate, the drag becomes greater than the available thrust so the aircraft begins to slow down. The "instantaneous" turn rate is the highest turn rate possible, ignoring the fact that the aircraft will slow down.

The "load factor", or "g-loading", during a turn is the acceleration due to lift expressed as a multiple of the standard acceleration due to gravity (32.2 ft/sec squared). Load factor ("n") is equal to the lift divided by the aircraft's weight. The required wing loading to attain a required turn load factor can be solved as follows:

$$\frac{W}{S} = \frac{qC_{L_{max}}}{n}$$

The sustained turn rate is also important for success in combat. Sustained turn rate is usually expressed in terms of the maximum load factor at some flight condition that the aircraft can sustain without slowing. For example, the capability for sustaining five "g's" at 0.9 Mach number at thirty thousand feet may be specified.

The wing loading to exactly attain a required sustained load factor "n" using all of the available thrust can be determined by equating the thrust and drag, and using the fact that the lift coefficient during maneuver equals the wing loading times "n", divided by the dynamic pressure. This yields equation 5.

$$\frac{W}{S} = \frac{(T/W) + \sqrt{(T/W)^2 - (4n^2 C_{D_0}/qAe)}}{2n/qAe}$$

The stall speed of an aircraft may also define the required wing loading, and is directly determined by the wing loading and the maximum lift coefficient. Stall speed is a major contributor to flying safety, with a substantial number of fatal accidents each year due to "failure to maintain flying speed".

Civil and military design specifications establish maximum allowable stall speeds for various classes of aircraft. In some cases, the stall speed is explicitly stated.

$$W = L = q_{\text{ref}} S C_{\text{Lmax}} = \frac{1}{2} \rho V_{\text{ref}}^2 S C_{\text{Lmax}}$$

$$W/S = \frac{1}{2} \rho V_{\text{ref}}^2 S C_{\text{Lmax}}$$

Equation 6 states that lift equals weight in level flight, and that at stall speed, the aircraft is at maximum lift coefficient. Equation 7 solves for the required wing loading to attain a given stall speed with a certain maximum lift coefficient. The air density, ρ , is typically the sea level standard value (.00238 slugs/cubic-foot) or sometimes the 5000 foot altitude, hot day value (.00189) to ensure that the airplane can be flown into Denver during summer.

The remaining unknown is the maximum lift coefficient. This can be very difficult to estimate. Values range from about 1.2 to 1.5 for a plain-wing with no flaps to as much as 5.0 for a wing with large flaps immersed in the propwash or jetwash.

Maximum lift coefficient depends upon the wing geometry, airfoil shape, flap geometry and span, leading edge slot or slat geometry, Reynolds number, surface texture, and interference from other parts of the aircraft such as the fuselage, nacelles, or pylons. The trim force provided by the horizontal tail will increase or reduce the maximum lift, depending upon the direction of the trim force. If the propwash or jetwash impinges upon the wing or the flaps, it will also have a major influence upon maximum lift during power-on conditions.

For an initial estimate of maximum lift, it is usually necessary to resort to test results and historical data. Figure 13 provides maximum lift trends versus sweep angle for several classes of aircraft. Note that the maximum lift using the takeoff flap setting will typically be about 80 percent of these landing maximum values.

Frequently the takeoff distance will determine the required wing loading. Figure 14 permits estimation of the takeoff ground roll, takeoff distance to clear a 50 foot obstacle, and FAR balanced field length over a thirty-five foot obstacle.

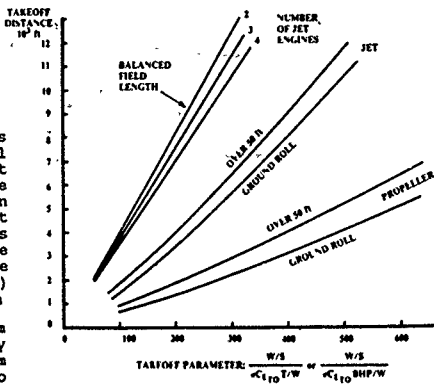


Fig. 14 Takeoff distance estimation.

Landing distance can also sometimes determine the required wing loading. Wing loading affects the approach speed, which determines the touchdown speed, which in turn defines the kinetic energy which must be dissipated to bring the aircraft to a halt. The kinetic energy, and hence the stopping distance, varies as the square of the touchdown speed.

In fact, a reasonable first-guess of the total landing distance in feet, including obstacle clearance, is approximately 0.3 times the square of the approach speed in knots.

Equation 8 provides a better approximation of the landing distance which can be used to estimate the maximum landing wing loading. The first term represents the ground roll to absorb the kinetic energy at touchdown speed. The constant term, S_0 , represents the obstacle clearance distance.

$$S_{\text{total}} = 80 \left(\frac{W}{S} \right) \left(\frac{1}{C_{L\text{max}}} \right) + S_0$$

where

$$\begin{aligned} S_0 &= 1000 \text{ (airliner-type, 3-deg glideslope)} \\ &= 600 \text{ (general aviation type power-off approach)} \\ &= 450 \text{ (STOL, 7-deg glideslope)} \end{aligned}$$

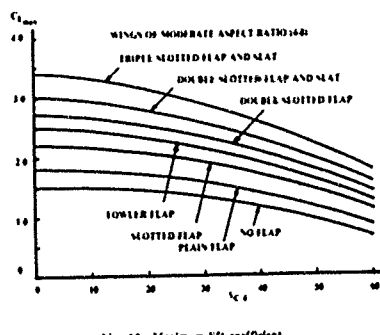


Fig. 13 Maximum lift coefficient

OTHER AERODYNAMIC CONSIDERATIONS

The overall arrangement and smoothness of the fuselage can have a major effect upon aerodynamic efficiency. A poorly designed aircraft can have excessive flow separation, transonic drag rise, and supersonic wave drag. Also, poor wing-fuselage arrangement can result in lift losses or disruption of the desired elliptical lift distribution.

The major requirement for good aerodynamic design during fuselage layout is the maintenance of smooth longitudinal contours. These can be provided by the use of smooth longitudinal control lines. Generally, longitudinal breaks in contour should follow a radius at least equal to the fuselage diameter at that point.

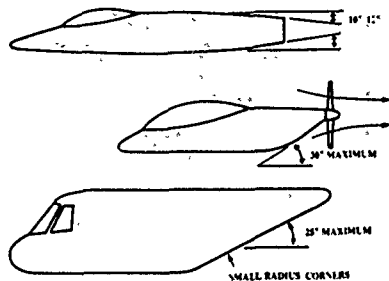


Fig. 15 Longitudinal contour guidelines.

To prevent separation of the airflow, the aft-fuselage deviation from the freestream direction should not exceed 10 to 12 degrees (figure 15). However, the air inflow induced by a pusher-propeller will prevent separation despite contour angles of up to 30 degrees or more.

A lower-surface upsweep of about 25 degrees can be tolerated for a rear-loading transport aircraft provided that the fuselage lower corners are fairly sharp. This causes a vortex flow pattern which reduces the drag penalty. In general, aft-fuselage upsweep should be minimized as much as possible, especially for high-speed aircraft.

For improved aerodynamic efficiency, the wing-fuselage connection of most aircraft is smoothly blended using a "wing fillet" (figure 16). A wing fillet is generally defined by a circular arc of varying radius, tangent to both the wing and fuselage. Typically a wing fillet has a radius of about 10 percent of the root chord length.

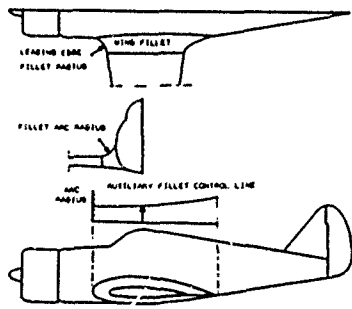


Fig. 16 Wing fillet layout.

Low wing, high-speed aircraft will frequently have a modified wing root airfoil to further minimize fuselage interference and shock-induced drag increases. This modification takes the form of an uncambered or even negatively-cambered airfoil set at a high positive angle of incidence.

For supersonic aircraft, the greatest aerodynamic impact upon the configuration layout results from the desire to minimize supersonic wave drag. Wave drag is a pressure drag due to the formation of shocks, and is analytically related to the

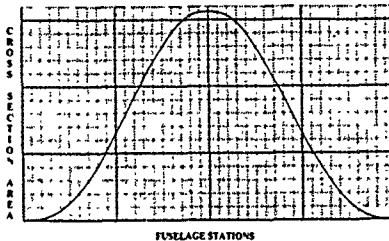


Fig. 18 Sears-Haack volume distribution.

longitudinal change in the aircraft's total cross-sectional area. In fact, wave drag is proportional to the second derivative (ie, curvature) of the volume distribution plot;

Thus, a "good" volume distribution from a wave drag viewpoint is one in which the required total internal volume is distributed longitudinally in a fashion which minimizes curvature in the volume distribution plot. Several mathematical solutions to this problem have been found for simple bodies-of-revolution, with the "Sears-Haack" body (figure 18) having the lowest wave drag.

If an aircraft could be designed with a volume plot shaped like the Sears-Haack volume distribution it would have the minimum wave drag at mach one for a given length and total internal volume. However, it is usually impossible to exactly or even approximately match the Sears-Haack shape for a real aircraft. Fortunately, major drag reductions can be obtained simply by smoothing the volume distribution shape.

As shown in figure 19, the main contributors to the cross-sectional area are the wing and the fuselage. A typical fuselage with a trapezoidal wing will have an irregularly-shaped volume distribution with the maximum cross-sectional area located near the center of the wing. By "squeezing" the fuselage at that point, the volume distribution shape can be smoothed and the maximum cross-section area reduced.

This design technique is referred to as "area-ruling" or "coke-bottling" and can reduce the wave drag by as much as fifty percent. Note that the volume removed at the center of the fuselage must be provided elsewhere, either by lengthening the fuselage or by increasing its cross-section area in other places.

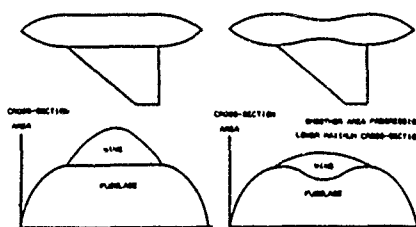


Fig. 19 Design for low wave drag

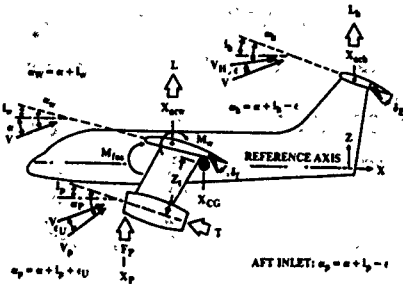


Fig. 20 Longitudinal moments.

STABILITY AND CONTROL CONSIDERATIONS

The basic concept of stability is simply that a stable aircraft, when disturbed, tends to return by itself to its original state (pitch, yaw, roll, velocity, etc.). "Static stability" is present if the forces created by the disturbed state (such as a pitching moment due to an increased angle of attack) push in the correct direction to return the aircraft to its original state.

Most aircraft are symmetrical about the centerline, so that moderate changes in angle of attack will have little or no influence upon the yaw or roll of the aircraft. This permits the stability and control analysis to be divided into longitudinal (pitch only) and lateral-directional (roll and yaw) analysis.

Figure 20 shows the major contributors to aircraft pitching moment about the center of gravity, including the wing, tail, fuselage, and engine contributions. The wing pitching moment contribution includes the lift through the wing mean aerodynamic chord ("MAC"), and the wing moment about the MAC. Another wing moment term is the change in pitching moment due to flap deflection.

The long moment arm of the tail times its lift produces a very large moment which is used to trim and control the aircraft. While this figure shows tail lift upwards, under many conditions the tail lift will be downwards to counteract the wing pitching moment.

The fuselage and nacelles produce pitching moments which are difficult to estimate without wind tunnel data. These moments are influenced by the upwash and downwash produced by the wing.

The engine produces three contributions to pitching moment. The obvious term is the thrust times its vertical distance from the center of gravity. Less obvious is the vertical force ("F_p") produced at the propeller disk or inlet front face due to the turning of the freestream airflow. Finally, the propwash or jet-induced flowfield will influence the effective angle of attack of the tail and possibly the wing.

Equation 9 expresses the sum of these moments about the CG. The effect of elevator deflection is included in the tail lift term. Equation 10 expresses the moments in coefficient form by dividing all terms by (q S_w c) and expressing the tail lift in coefficient form.

$$M_{cg} = L(X_{cg} - X_{sw}) + M_w + M_{nac} \delta_j + M_{inlet} - L(X_{sw} - X_{cg}) + T_z + F_p(X_{cg} - X_{sw})$$

$$C_{M_{cg}} = C_l \left(\frac{X_{cg} - X_{sw}}{c} \right) + C_{m_w} + C_{m_{nac}} \delta_j + C_{m_{inlet}} - \frac{qS_w}{qS_c} C_{L_{cg}} \left(\frac{X_{sw} - X_{cg}}{c} \right) + \frac{T_z}{qS_c} + \frac{F_p(X_{cg} - X_{sw})}{qS_c}$$

$$\eta_2 = q/c$$

$$C_{M_{cg}} = C_l \left(\bar{X}_{cg} - \bar{X}_{sw} \right) + C_{m_w} + C_{m_{nac}} \delta_j + C_{m_{inlet}} - \eta_2 \frac{S_w}{S_c} C_{L_{cg}} \left(\bar{X}_{sw} - \bar{X}_{cg} \right) + \frac{T_z}{qS_c} \bar{Z}_t + \frac{F_p}{qS_c} \left(\bar{X}_{cg} - \bar{X}_{sw} \right)$$

To simplify the equations, all lengths can be expressed as a fraction of the wing mean chord ('c'). These fractional lengths are denoted by a bar. This leads to equation 11.

For a static "trim" condition, the pitching moment must equal zero. The main flight conditions of concern are the takeoff and landing with flaps and landing gear down and the maximum speed. Usually the most-forward CG position is critical for trim while the aft-CG position is most critical for stability as discussed below.

For static stability, any change in angle of attack must generate moments which oppose the change. In other words, the derivative of pitching moment with respect to angle of attack (eq 12) must be negative. Note that the wing pitching moment and thrust terms have dropped out as they are essentially constant with respect to angle of attack.

$$C_m = C_l \left(\bar{X}_{cg} - \bar{X}_{sw} \right) + C_{m_{inlet}} - \eta_2 \frac{S_w}{S_c} C_{L_{cg}} \frac{\partial \bar{Z}_t}{\partial \alpha} \left(\bar{X}_{sw} - \bar{X}_{cg} \right) + \frac{F_p}{qS_c} \frac{\partial \bar{Z}_t}{\partial \alpha} \left(\bar{X}_{cg} - \bar{X}_{sw} \right)$$

Due to downwash effects the tail angle of attack does not vary directly with aircraft angle of attack, so a derivative term is included which accounts for the effects of wing and propeller downwash, as described later. A similar derivative is provided for the propeller or inlet normal force term (F_p).

The magnitude of the pitching moment derivative changes with CG location. For any aircraft there is a CG location which provides no change in pitching moment as angle of attack is varied. This "airplane aerodynamic center", or "neutral point (X_{np})" represents neutral stability and is the most-aft CG location before the aircraft becomes unstable.

Equation 13 solves for the neutral point. Equation 14 then expresses the pitching moment derivative in terms of the distance in percent MAC from the neutral point to the center of gravity. This percent distance is called the "static margin", and is the term in parenthesis in equation 14.

$$X_{np} = C_{l_{cg}} - C_{m_{inlet}} + \eta_2 \frac{S_w}{S_c} C_{L_{cg}} \frac{\partial \bar{Z}_t}{\partial \alpha} X_{cg} + \frac{F_p}{qS_c} \frac{\partial \bar{Z}_t}{\partial \alpha} X_{cg}$$

$$C_{l_{cg}} + \eta_2 \frac{S_w}{S_c} C_{L_{cg}} \frac{\partial \bar{Z}_t}{\partial \alpha} + \frac{F_p}{qS_c}$$

$$C_{l_{cg}} = -C_l \left(\bar{X}_{np} - \bar{X}_{cg} \right)$$

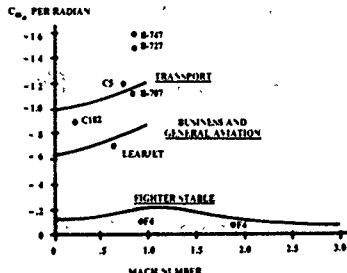


Fig. 21 Typical pitching moment derivative values.

If the CG is ahead of the neutral point (positive static margin), the pitching moment derivative is negative, so the aircraft is stable. At the most-aft CG position, a typical transport aircraft has a positive static margin of 5 to 10 percent.

While current fighters typically have positive static margins of about 5 percent, new fighters such as the F-16 are being designed with "relaxed static stability (RSS)" in which a negative static margin (zero to -15 percent) is coupled with a computerized flight control system which deflects the elevator to provide artificial stability. This reduces trim drag substantially.

Figure 21 illustrates pitching moment derivative values for several classes of aircraft. These may be used as targets for conceptual design. Dynamic analysis during later stages of design may revise these targets.

Lateral-directional analysis proceeds in a fashion similar to the above, and is discussed in my textbook.

For the initial layout, a historical approach is used for the estimation of tail size. The effectiveness of a tail in generating a moment about the center of gravity is proportional to the force (ie, lift) produced by the tail, and to the tail moment arm.

The force due to tail lift is proportional to the tail area. Thus, the tail effectiveness is proportional to the tail area times the tail moment arm. This product has units of volume, which leads to the "tail volume coefficient" method for initial estimation of tail size. The "vertical tail volume coefficient" is defined by equation 15. The "horizontal tail volume coefficient" is shown by equation 16.

$$S_{Vt} = C_{Vt} b_w S_w / L_{Vt}$$

$$S_{Ht} = C_{Ht} \bar{C}_w S_w / L_{Ht}$$

The definition of tail moment arm is shown in figure 22, along with the definitions of tail area. Observe that the horizontal tail area is commonly measured to the aircraft centerline, while a canard's area is commonly considered to include only the exposed area. If twin vertical tails are used, the vertical tail area is the sum of the two.

Table 4 provides typical values for volume coefficients for different classes of aircraft. These values are conservative averages, and are used in equation 81 or 82 to calculate tail area.

Table 4 Tail volume coefficient

	Horizontal C_{Ht}	Vertical C_{Vt}
Sailplane	0.50	0.02
Homebuilt	0.50	0.04
General aviation—single engine	0.70	0.04
General aviation—twin engine	0.80	0.07
Agricultural	0.50	0.04
Twin turboprop	0.90	0.08
Flying boat	0.70	0.06
Jet trainer	0.70	0.06
Jet fighter	0.40	0.07
Military cargo/bomber	1.00	0.06
Jet transport	1.00	0.09

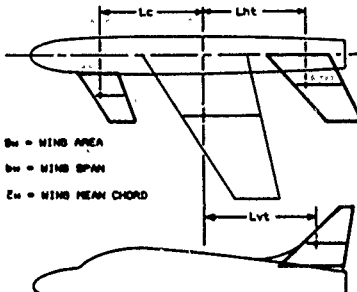


Fig. 22 Initial tail sizing.

One of the most important aspects of handling qualities is the behavior of the aircraft at high angles of attack. As the angle of attack increases, a "good" airplane experiences mild buffeting to warn the pilot, retains control about all axis, and stalls straight ahead with immediate recovery and no tendency to enter a spin. If a spin is forced, the "good" airplane can be immediately recovered.

A "bad" airplane loses control in one or more axis as angle of attack increases. A typical bad characteristic is the loss of aileron roll control and an increase in aileron adverse yaw. When the aircraft is near the stall angle of attack, any minor yaw may slow down the inboard wing enough to stall it. With only one wing generating lift, the "bad" airplane will suddenly depart into a spin or other uncontrolled flight mode from which recovery is impossible.

There have been many criteria proposed for good departure characteristics, based upon various aerodynamic derivatives. One useful one is the "Lateral Control Departure Parameter (LCDP)", sometimes called the "lateral control spin parameter" or the "aileron alone divergence parameter" (equation 17). The LCDP focuses upon the relationship between adverse yaw and directional stability.

$$LCDP = C_{A_{\text{yaw}}} - C_{Y} \frac{C_{A_{\text{yaw}}}}{C_Y}$$

$$C_{A_{\text{yaw}}} = C_A \cos \alpha - \frac{1}{f_m} C_Y \tan \alpha$$

Equation 18 shows another departure parameter, 'C-n-beta-dynamic', which includes the effects of the mass moments of inertia. Both of these parameters should be positive for "good" departure resistance.

Figure 23 shows a crossplot of the LCDP and 'C-n-beta-dynamic' as angle of attack is increased, showing the boundaries for acceptable departure resistance as determined from high-g simulator tests using experienced pilots. The earlier Weissman criteria is also shown.

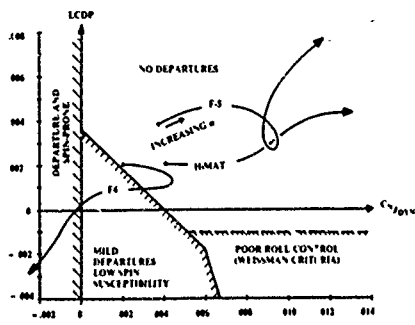


Fig. 23 Departure susceptibility.

Once an aircraft has departed into a spin, recovery becomes a high priority! The vertical tail plays a key role in spin recovery. Figure 24 illustrates the effect of tail arrangement upon rudder control at high angles of attack. At high angles of attack the horizontal tail is stalled, producing a turbulent wake extending upward at approximately a forty-five degree angle which can blanket the rudder. It is considered desirable that at least one-third of the rudder be un-blankedeted. An empirical method for estimating if an aircraft will in fact recover from a spin is provided in my textbook.

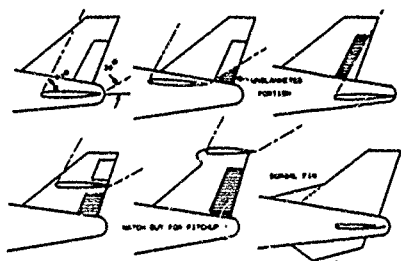


Fig. 24 Tail geometry for spin recovery.

STRUCTURAL CONSIDERATIONS

The primary concern in the development of a good structural arrangement is the provision of efficient "load paths". A load path is the structural elements by which opposing forces are connected. The primary forces to be resolved are the lift of the wing and the opposing weight of the major parts of the aircraft, such as the engines and payload. The size and weight of the structural members is minimized by locating these opposing forces near to each other.

Carried to the extreme, this leads to the Flying Wing concept. In a flying wing the lift and weight forces can be located at virtually the same place. In the ideal case, the weight of the aircraft would be distributed along the span of the wing exactly as the lift is distributed (figure 25). This is referred to as "spanloading".

While ideal spanloading is rarely possible, the spanloading concept can be applied to more-conventional aircraft by spreading some of the heavy weight items

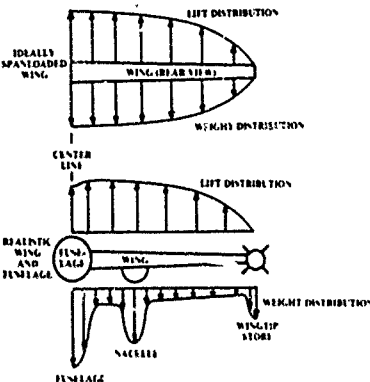


Fig. 25 Spanloading for weight reduction.

such as engines out along the wing. This will yield noticeable weight savings, but must be balanced against the possible drag increase.

If the opposing lift and weight forces cannot be located at the same place, then some structural path will be required to carry the load. The weight of those structural members can be reduced by providing the shortest, straightest load path possible.

Figure 26 illustrates a structural arrangement for a small fighter. The major fuselage loads are carried to the wing by "longerons", which are typically "I" or "H"-shaped extrusions running fore and aft and attached to the skin. Longerons are heavy, and their weight should be minimized by designing the aircraft so that they are as straight as possible.

For aircraft such as transports which have fewer cutouts and concentrated loads than a fighter, the fuselage will be constructed with a large number of longerons, or "stringers", which are approximately evenly distributed around the circumference of the fuselage. Weight is minimized when the stringers are all straight and uninterrupted.

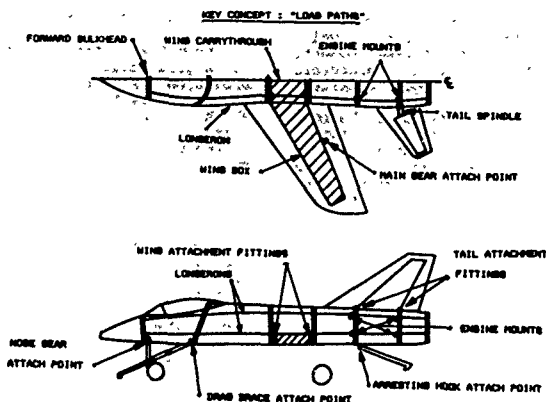
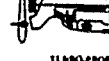
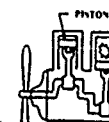
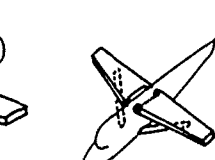
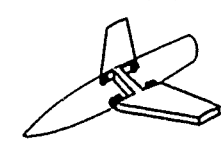
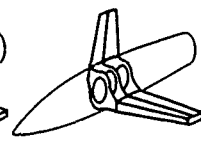
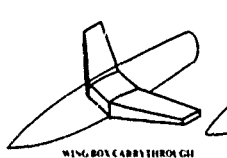


Fig. 26 Structural arrangement.



GEARBOX

BYPASS AIR

TURBO-PROP

TURBOFAN

Turbojet and turbofan engines are incapable of efficient operation unless the air entering them is slowed to a speed of about mach 0.4 to 0.5. This is to keep the tip speed of the compressor blades below sonic speed relative to the incoming air. Slowing down the incoming air is the primary purpose of an inlet system.

The installed performance of a jet engine greatly depends upon the air inlet system. Roughly speaking, a one percent reduction in inlet pressure recovery (total pressure delivered to the engine divided by freestream total pressure) will reduce thrust by about 1.3 percent.

There are four basic types of inlets, shown in figure 30. The NACA flush inlet was used by several early jet aircraft but is rarely seen today for aircraft propulsion systems due to its poor pressure recovery (ie, large losses).

The pitot inlet is simply a forward facing hole. It works very well subsonically and fairly well at low supersonic speeds. This inlet is also called a "normal shock inlet" when used for supersonic flight ("normal" meaning perpendicular in this case). The pitot inlet is seen on most subsonic jet aircraft.

The remaining inlet types are for supersonic aircraft, and offer improvements over the performance of the normal shock inlet at higher supersonic speeds. The conical inlet (also called a spike, round, or axisymmetric inlet) is based upon the shock patterns created by supersonic flow over a cone. Similarly, the two-dimensional ramp inlet (also called a "D-inlet") is based upon the flow over a wedge.

External compression inlet types are shown in figure 31. The greater the number of oblique shocks employed, the better the pressure recovery.

Figure 32 illustrates a typical three-shock external compression inlet. Note

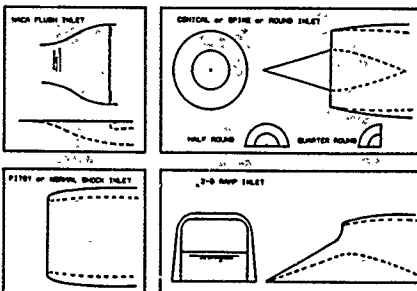


Fig. 30 Inlet types.

that the second ramp has a variable angle, and can collapse to open a larger duct opening for subsonic flight.

Figure 33 summarizes the selection criteria for different inlets, based upon design mach number. Note that these are approximate criteria, and be overruled by special considerations.

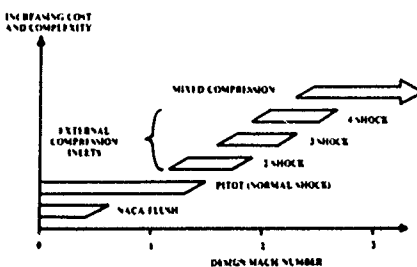


Fig. 33 Inlet applicability.

The inlet location can have almost as great of an effect on engine performance as the inlet geometry. If the inlet is located where it can ingest a vortex off the fuselage or a separated wake from a wing, the resulting inlet flow distortion can stall the engine. The F-111 had tremendous problems with its inlets, which were tucked up under the intersection of the wing and fuselage. The A-10 required a fixed slot on the inboard wing leading edge to cure a wake ingestion problem. Figures 34 and 35 illustrate the various options for inlet location.

To design the inlet for a particular application, capture area must be known. Figure 36 provides a quick method of estimating the required inlet capture area. This method is statistical and is based upon the design mach number and the engine mass flow in pounds per second. A more detailed discussion of inlet location options and capture area estimation is available in my textbook.

The aircraft's forebody builds up a thick boundary layer. If this low-energy, turbulent air is allowed to enter the engine, it can reduce engine performance subsonically and prevent proper inlet operation supersonically. Unless the aircraft's inlets are very near the nose (2-4 diameters), some form of boundary layer removal should be used just in front of the inlet.

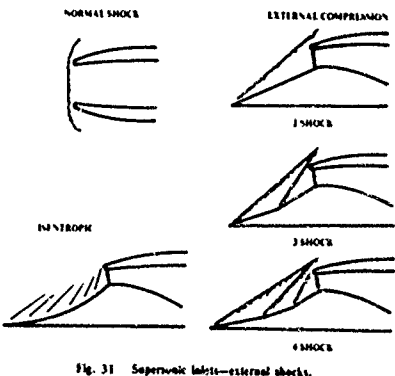


Fig. 31 Superwedge Inlets—external shocks.

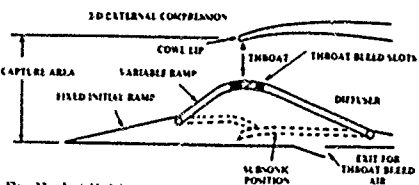


Fig. 32 Variable inlet geometry.

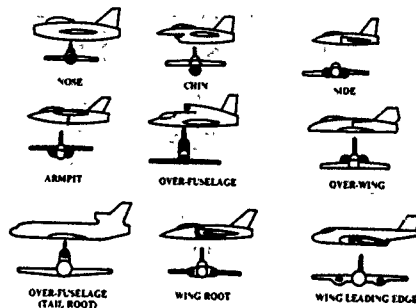


Fig. 34 Inlet locations—buried engines.

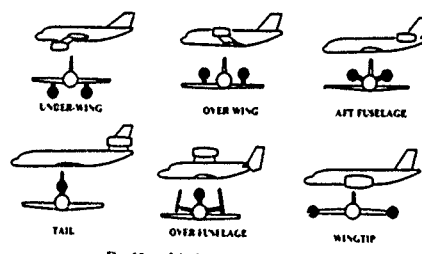


Fig. 35 Inlet locations—padded engines.

INLET CAPTURE AREA = $\pi D^2 / 4$ (square inches)
ENGINE MASS FLOW = \dot{m} (lb / sec)

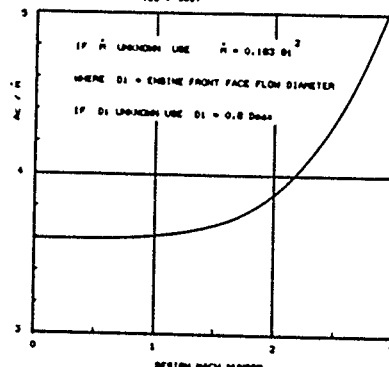


Fig. 36 Preliminary capture area sizing.

The four major varieties of boundary layer diverter are shown in figure 37. The step diverter is suitable only for subsonic aircraft, and relies upon the boundary layer itself for operation. The boundary layer bypass duct is simply a separate inlet duct which admits the boundary layer air and ducts it to an aft-facing hole. The suction form of boundary layer diverter is similar. The boundary layer air is removed by suction through holes or slots just forward of the inlet

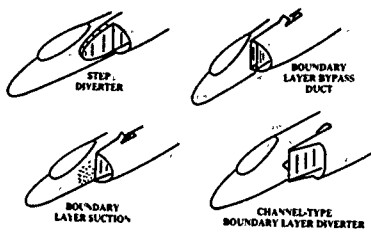


Fig. 37 Boundary layer removal.

and ducted to an aft-facing hole.

The channel diverter is the most common boundary layer diverter for supersonic aircraft. It provides the best performance and the least weight in most cases.

OBSERVABLES CONSIDERATIONS

(Note: The following material on observables has been approved for release by the U. S. Air Force.)

Ever since the dawn of military aviation attempts have been made to reduce the detectability of aircraft. During WWI, the only "sensor" in use was the human eyeball. Camouflage paint in mottled patterns was used on both sides to reduce the chance of detection.

Radar is the primary sensor used against aircraft today. "Radar" is an acronym for Radio Detection And Ranging. Radar consists of a transmitter antenna which broadcasts a directed beam of electromagnetic radio waves, and a receiver antenna which picks up the faint radio waves which bounce off objects "illuminated" by the radio beam. To avoid detection, the aircraft must return such a low amount of the transmitted radio beam that the receiver antenna cannot distinguish between it and the background radio static.

The extent to which an object returns electromagnetic energy is the object's "Radar Cross Section (RCS)". RCS is usually measured in square meters or in decibel square meters, with "zero dB_{SS}" equal to ten to the zero power, or one square meter. "Twenty dB_{SS}" equals ten to the second power, or 100 square meters.

There are many electromagnetic phenomena which contribute to the RCS of an aircraft. These require different design approaches for RCS reduction, and can produce conflicting design requirements. Figure 38 illustrates the major RCS contributors for a typical, untreated fighter aircraft.

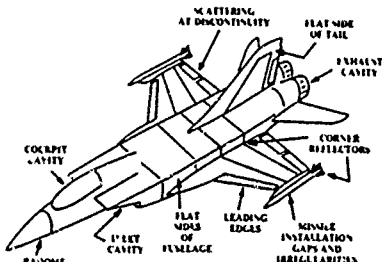


Fig. 38 Major RCS contributors

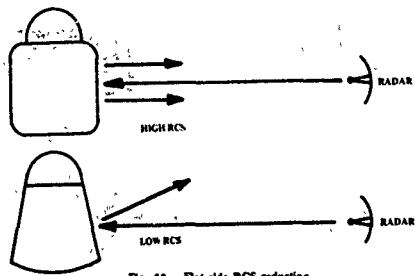


Fig. 39 Flat side RCS reduction.

One of the largest contributions to airframe RCS occurs any time a relatively flat surface of the aircraft is perpendicular to the incoming radar beam. Imagine shining a flashlight at a shiny aircraft in a dark hanger. Any spots where the beam is reflected directly back at you will have an enormous RCS contribution.

Typically this "specular return" occurs on the flat sides of the aircraft fuselage, and along an upright vertical tail (when the radar is abeam the aircraft). To prevent these RCS "spikes", the designer may slope the fuselage sides, angle the vertical tails, and so on, so that there are no flat surfaces presented towards the radar (figure 39).

Another contributor to airframe RCS occurs due to the electromagnetic currents which build up on the skin when illuminated by a radar. These currents flow across the skin until they hit a discontinuity such as at a sharp trailing edge, a wingtip, a control surface, or a crack around a removable panel or door. At a discontinuity, the currents "scatter", or radiate electromagnetic energy, some of which is transmitted back to the radar (figure 40).

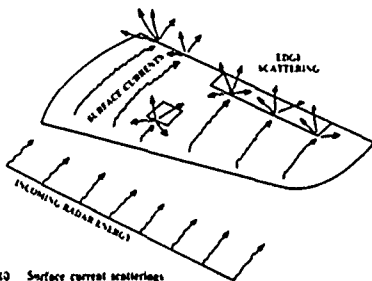


Fig. 40 Surface current scattering.

This effect is much lower in intensity than the specular return, but is still sufficient for detection. The effect is strongest when the discontinuity is straight and perpendicular to the radar beam. Thus, the discontinuities such as at the wing and tail trailing edges can be swept to minimize the detectability from the front.

In addition to reshaping the aircraft, detectability can be reduced through the use of skin materials which absorb radar energy. Such materials, called "radar absorbing materials" (RAM), are typically composites, such as fiberglass or graphite/epoxy embedded with carbon or ferrite particles.

Infrared detectability is also of concern to the aircraft designer. Many short-range air-to-air and ground-to-air missiles rely upon IR seekers. Modern IR sensors are sensitive enough to detect not only the radiation emitted by the engine exhaust and engine hot parts, but also that emitted by the whole aircraft skin due to aerodynamic heating at transonic and supersonic speeds. Also, sensors can detect the solar IR radiation which reflects off the skin and cockpit transparencies (windows).

There are several approaches for reduction of IR detectability. The most potent is the reduction of engine exhaust temperatures through use of a high-bypass engine. This reduces both exhaust and hot-part temperatures. However, depending upon the application this may result in selection of an engine which is less than optimal for aircraft sizing, which increases aircraft weight and cost.

Emissions from the exposed engine hot-parts (primarily the inside of the nozzle) can be reduced by cooling them with air bled off the engine compressor. This will also increase fuel consumption slightly. Another approach is to hide the nozzles from the expected location of the threat IR sensor. For example, the H-tails of the A-10 hide the nozzles from some angles.

Plume emissions are reduced by quickly mixing the exhaust with the outside air. As mentioned, a high-bypass engine is the best way of accomplishing this. Mixing can also be enhanced by the use of a wide, thin nozzle rather than a circular one. Another technique is to angle the exhaust upwards or downwards relative to the freestream. This will have an obvious thrust penalty, however.

CONFIGURATION LAYOUT METHODS

The process of aircraft conceptual design includes numerous statistical estimations, analytical predictions, and numerical optimizations. However, the product of aircraft design is a drawing. While the analytical tasks are vitally important, one must remember that their only purpose is to influence the drawing, for it is the drawing alone which is ultimately used to fabricate the aircraft.

The design layout process generally begins with a number of conceptual sketches. Figure 41 illustrates an actual, unretouched sketch from a Rockwell fighter conceptual design study. As can be seen, these sketches are crude and quickly done, but depict the major ideas which the designer intends to incorporate into the actual design layout.

A good sketch will show the overall aerodynamic concept and indicate the locations of the major internal

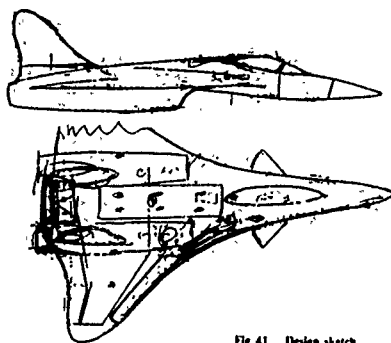


Fig. 41 Design sketch.

components. These should include the landing gear, crew station, payload or passenger compartment, propulsion system, fuel tanks, and any unique internal components such as a large radar.

The actual design layout is developed using the techniques to be discussed below. Such a design layout is shown at figure 42, courtesy of Rockwell International's North American Aircraft Operations. This drawing is typical of the initial design layouts developed by the major airframe companies during design studies.

"Lofting" is the process of defining the external geometry of the aircraft. For an initial layout the overall lofting of the fuselage, wing, tails, and nacelles must be defined sufficiently to show that these will properly enclose the required internal components while providing a smooth aerodynamic contour.

The traditional form of lofting is based upon a mathematical curve known as the "conic". A conic is a second-degree curve whose family includes the circle, ellipse, parabola, and hyperbola. The conic is best visualized as a slanted cut through a right circular cone (figure 43). The great advantage of the conic is the wide variety of curves which can be represented, and the ease with which the conic can be constructed on the drafting table.

A conic curve is constructed from the desired start and end points ("A" and "B"), and the desired tangent angles at those points. These tangent angles intersect at point "C". The shape of the conic between the points A and B is defined by some shoulder point "S". Figure 44 illustrates the rapid graphical layout of a conic curve.

To create a smoothly-lofted fuselage using conics it is necessary only to ensure that the points A, B, C, and S in each of the various cross-sections can be connected longitudinally by a smooth line. Figure 45 shows the upper half of a simple fuselage, in which the A, B, C, and S points in three cross sections are connected by smooth longitudinal lines. These are called "longitudinal control lines" because they control the shapes of

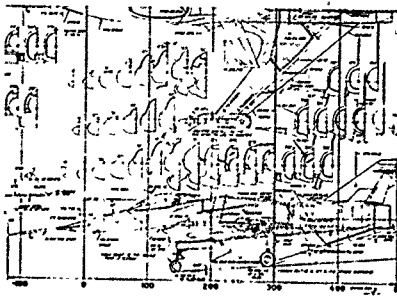


Fig. 42 XFW design layout.

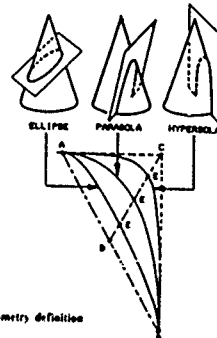


Fig. 43 Conic geometry definition.

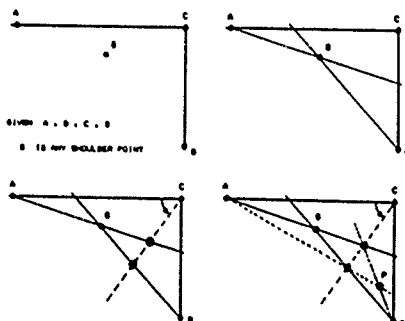


Fig. 44 Conic layout.

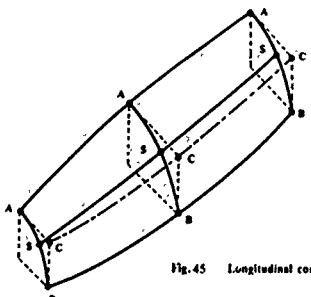


Fig. 45 Longitudinal control lines

the conic cross-sections. Figure 46 shows the side and top views of these longitudinal control lines.

In figure 46, the longitudinal control lines are used to create a new cross-section, in between the second and third cross sections previously defined. This new cross-section is created by measuring, from the longitudinal control lines, the positions of the A, B, C, and S points at the desired location of the new cross-section.

Figure 47 illustrates a common application of conic lofting to define a fighter fuselage for an initial layout. Five control stations are required for this example.

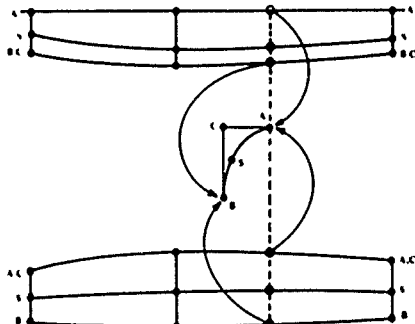


Fig. 16. Cross section drawings from longitudinal control bars.

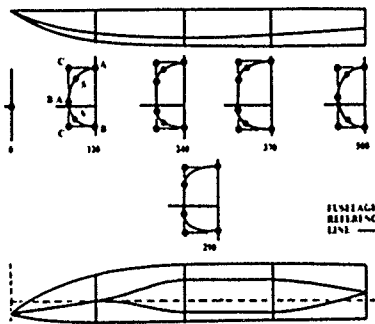


Fig. 47. Technical nuclear testing

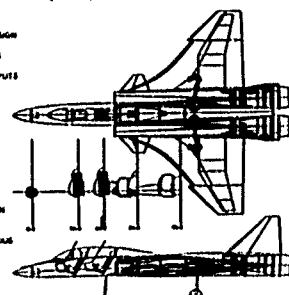
TYPICAL CONFIGURATION DEVELOPMENT TASKS	TIME/TYPE OF METHODS		CONFIGURATION DEVELOPMENT SYSTEM	
	NUMBER	COST (\$100,000)	NUMBER	COST (\$100,000)
DEVELOP WING GEOMETRY	0.5	12.50	0.1	1.50
DESIGN WING PLACEMENT	1.0	12.50	0.1	1.50
DEFINE FUSELAGE SIZE AND PLACEMENT	3.0	105.00	0.1	1.50
DESIGN MAIN ENGINE	2.5	50.00	0.1	1.75
DESIGN CARGO BAY	1.0	12.50	0.1	1.50
LOCATE CARGO GEAR	1.5	17.50	0.1	1.50
CALCULATE WING ANGLE	0.1	3.50	0.1	0.15
DESIGN TAIL PLACEMENT	1.0	12.50	0.1	1.50
CALCULATE DUCT AREAS	0.8	20.00	0.1	0.25
CHECK TAIL AND WING BELL CURVED CLEARANCE	0.5	12.50	0.1	1.50
CALCULATE TAIL SURFACE AREA	0.5	12.50	0.1	1.50
DESIGN TAIL SURFACES	0.5	12.50	0.1	1.50
CARGO GEAR RETRACTION	0.5	12.50	0.1	1.50
WING AND TAIL MACHINING	0.5	12.50	0.1	1.50
DESIGN STRUT CONNECTION	0.5	12.50	0.1	1.50
REVISED WING GEOMETRY DRAWINGS	20	200.00	0.1	35.00
ALTERNATIVE ENGINE LOCATIONS	30	300.00	0.1	35.00
ALTERNATIVE TAIL LOCATIONS	30	300.00	0.1	35.00
ALTERNATIVE AIRCRAFT DIMENSIONS	30	300.00	0.1	35.00
WEIGHTED AIRE PLAT.	1.5	52.50	0.1	1.50
WEIGHTED DESIGNER PLOT	1.5	52.50	0.1	1.50
WEIGHT ESTIMATION	1.5	52.50	0.1	1.50
WEIGHT AND COST ESTIMATION	0.5	12.50	0.1	1.50
STRUCTURE DESIGN	100	1,250.00	0.1	175.00
WING LOADS DESIGN	100	1,250.00	0.1	175.00
STRUCTURE FORGE DESIGN	100	1,250.00	20	175.00

Table 1

This traditional lofting technique is described in far greater detail in my textbook, and is very useful for obtaining an understanding of the mental process required to create smooth external contours. However, most lofting today is done on a computer-aided design (CAD) system. Such CAD systems offer substantial savings in time and cost, and also improve accuracy and save rework cost. Table 5 illustrates the time savings. Note that the biggest savings come when a design layout must be revised.

To illustrate the use of a CAD system for aircraft conceptual layout, the Rockwell Configuration Development Module (CDM—previously known as CDS) is presented in the eight figures below. Shown are capabilities for wing and fuselage creation, smoothing, cross-section reshaping, cockpit layout, landing gear kinematics, vision plotting, and display of a completed aircraft configuration design. This material is described in depth in the Notebook provided to participants in my Aircraft Conceptual Design short course.

CONFIGURATION DEVELOPMENT SYSTEM (CDS)



Page 47

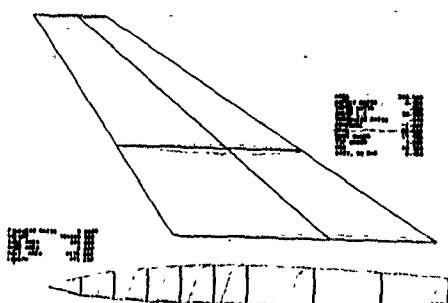
WING & FUSELAGE CREATION

Figure 49

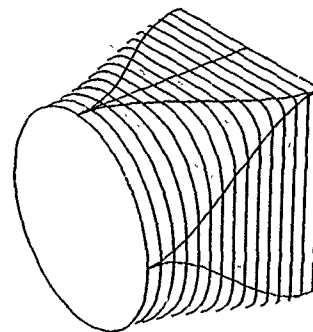
AUTOMATIC SMOOTHING

Figure 50

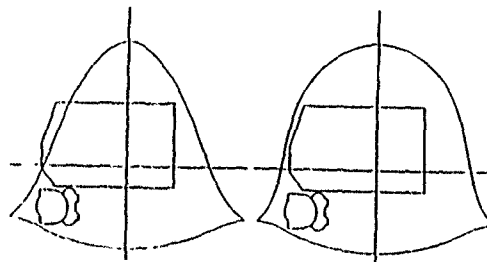
CROSS SECTION RESHAPING

Figure 51

COCKPIT REQUIREMENTS

- OVERHEAD/OVERSIDE VISION
- COCKPIT CLEARANCES

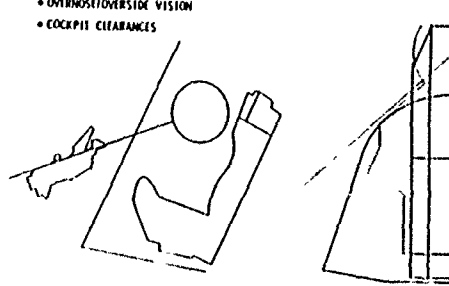


Figure 52

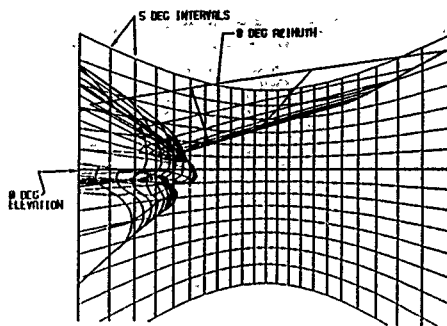


Figure 53

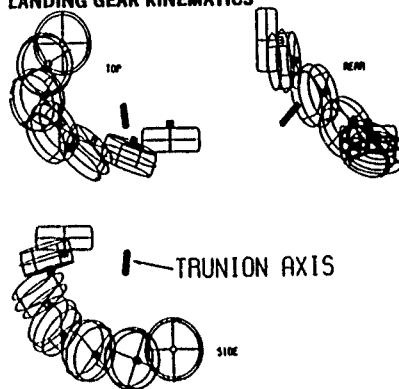
LANDING GEAR KINEMATICS

Figure 54

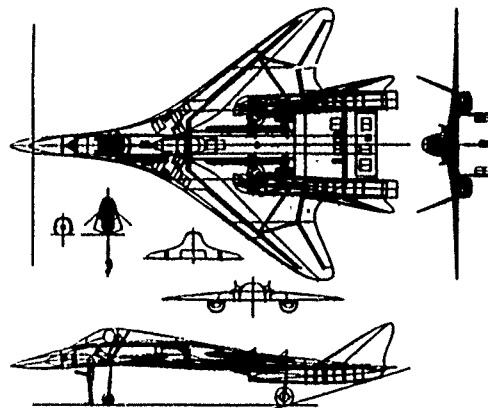


Figure 55

Table 6 Typical trade studies

Design trades	Requirements trades	Growth sensitivities
T/W and W/S	Range/payload/passenger	Dead weight
A.A	Liner time	C_D and K
I/C, A, airfoil	Speed	$C_{D_{crit}}$
High lift devices	Turn-rate, P , R_{max}	$C_{I_{max}}$
BPR, OPR, TIT, etc.	Runway length	Installed thrust and SFC
Materials	Time-to-climb	Fuel price
Configuration	Design-to-cost	
tail type		
variable sweep		
number and type of engines		
maintainability features		
observables		
passenger arrangement		
Advanced technologies		

TRADE STUDIES

Trade studies produce the answers to design questions beginning with "what if..." Proper selection and execution of the trade studies is as important in aircraft design as a good configuration layout or a correct sizing analysis. It is only through the trade studies that the true optimum aircraft is determined.

Table 6 shows a number of the trade studies commonly conducted in aircraft design. These are loosely organized into design trades, requirements trades, and growth sensitivities. Design trades are those which are conducted to reduce the weight and cost of the aircraft to meet a given set of mission and performance requirements.

Requirements trades are conducted to determine the sensitivity of the aircraft to changes in the design requirements. If it is found that one requirement is resulting in a large increase in weight, the customer may relax it.

Growth sensitivity trade studies determine how much the aircraft weight will be impacted if various parameters should increase between conceptual design and production. These are typically presented in a single graph with percent change in the parameters on the horizontal axis, and percent change in takeoff weight on the vertical axis.

It has been assumed in the above discussion that the measure of merit for trade studies is always takeoff gross weight, even though cost is the final selection measure in a design competition. Using minimum weight as the measure of merit is usually a good approximation to minimum cost because the acquisition cost is so strongly driven by the weight. However, life cycle cost is driven largely by fuel costs, which may not be minimized by the minimum weight airplane. In such cases, trade studies with life cycle cost as the measure of merit can be conducted.

SURVEY OF EXPERIMENTAL TECHNIQUES FOR PERFORMANCE PREDICTION

by

A.B.Haines
Consultant Aerodynamicist
Aircraft Research Association Ltd
Bedford
United Kingdom

SUMMARY

This lecture reviews the present state-of-the-art in experimental testing in large wind tunnels as a means of predicting aircraft performance. Desirable and attainable standards of accuracy are defined and the lecture lists and discusses in depth the factors that contribute to this accuracy. Many references are quoted to enable the reader to obtain more detailed information.

The lecture discusses

- (i) the balances and pressure scanners used for measuring the forces and pressures,
- (ii) the significant issues in the quality of the tunnel flow that can affect the accuracy of the test data,
- (iii) the methods used for correcting the test data for the effects of tunnel wall interference at subsonic and transonic speeds up to near $M=1.0$,
- (iv) the methods used establishing the corrections for model support interference in both low and high speed tunnels,
- (v) a methodology for simulating as far as possible in the model tests, the viscous flow behaviour over the full-scale aircraft and then, for extrapolating the test data to full-scale Reynolds numbers,
- (vi) the types of models and test rigs used in determining the propulsion interference effects on both transport (turbofan and turboprop) and combat aircraft. Particular attention is paid to the use of powered simulators and to the difficulties in obtaining reliable afterbody drag data.

1. INTRODUCTION

It is generally accepted that the most reliable method of predicting aircraft performance ahead of the first flight of a new aircraft is on the basis of the results of model tests in a reputable large wind tunnel. This does not mean that all wind tunnel test data are reliable. To obtain reliable results, one needs to exercise great care in both the actual testing and in the interpretation of the results. The present lecture addresses the issues that have to be borne in mind and contains a description of current testing practice in both, high and low speed tunnels. Much of the material is to be found in the published literature including earlier AGARD reports; the material has been updated where necessary, and finally, the text is supported by a substantial number of references which can be studied for further details. The experimental techniques as described are broadly those in use in UK tunnels such as the RAE 8 ft x 8 ft and 5 metre tunnels and the ARA 9 ft x 8 ft transonic tunnel, but it is hoped that the general testing philosophy and indeed, much of the detail, is a fair reflection of testing practice in other countries such as the US and France.

With most new aircraft, it is standard practice to test representative complete models in both high and low speed tunnels; this probably implies two different models at a different scale. The test results are reduced to non-dimensional form and, assuming it has been possible to test at appropriate Mach numbers, incidences and angles of sideslip, they can then be used to predict the aircraft performance. This may suggest that all that is required is to develop and use instrumentation that will measure the forces and moments on the model to the necessary standards of accuracy but this would be an over-simplified picture: there is much more to the story. The model will have been tested in an airflow that is constrained by the tunnel walls, the flow over the model will have been affected by the presence of the supporting rear sting (high speed tunnel) or under-model struts (low speed tunnel) and finally, in most cases, the model test Reynolds number will be far below the value for the full scale aircraft. Research has shown how all these three problems can be eliminated or at least greatly alleviated. adaptive walls (Refs 1-4) to reduce wall interference, magnetic suspension (Refs 5,6) to eliminate support interference and pressurised, cryogenic tunnels (Ref 7) to achieve or approach full-scale Reynolds numbers. These concepts are however not yet available for routine testing and so, corrections have to be applied for wall and support interference and methodologies (Ref 8) have to be devised to control the boundary layer development over the model in order to simulate, as far as possible, the full-scale flow. These issues are discussed in detail in this lecture.

Propulsion effects are another problem area. In general, the complete models are tested merely with free-flow nacelles although tests with turbine powered simulators are sometimes undertaken in large low speed tunnels such as the DNV tunnel. At high speeds, the normal practice with a subsonic transport aircraft with pylon-mounted underwing nacelles is to use a large half-model and to test with a powered or blown nacelle (Refs 9,10) as well as with a free flow nacelle as on the complete model. The differences between the results for these two cases provide corrections for the jet interference that is not represented in the complete model test. In theory, the same approach can be used for a subsonic transport aircraft with the nacelles mounted on the rear fuselage although this raises more questions about the use of the half-model technique. In passing, it may be noted that there is a growing trend to use a large half-

model for the basic tests to develop advanced wing designs for new subsonic transports for the sake of the higher test Reynolds number (Ref 11). The particular problems of half-model testing are discussed in detail in §II.

Propulsion effects lead to even greater complexity in the case of combat aircraft. For many years, it has been standard practice (Ref 12) to test a suite of at least three models: the normal complete model with the full-scale aircraft lines distorted as little as possible; a special intake model tested either in isolation or preferably with a partial representation of the forward fuselage and part of the wing and finally, an afterbody model to study the jet effects and the effects of the inevitable distortion of the rear fuselage on the complete model. The results from the tests on these three models have then to be combined to predict the aircraft performance. Combat aircraft have however become much more closely coupled and now, in many cases, it is no longer valid to assume that one can treat the intake, wing and jet effects as independent. One really needs a powered simulator (Ref 13) as for a transport aircraft but this is more difficult because of the geometrical constraints. The development of appropriate techniques to cope with this most difficult problem is still being addressed in research establishments.

The above discussion has introduced most of the topics to be covered in the lecture but it is appropriate to start by considering the likely aims of the wind tunnel tests, the accuracies required from the tests, and the instrumentation in use for making the measurements.

2. TYPICAL TEST AIMs

Clearly the most important test aim for the prediction of aircraft performance is to measure drag or strictly L/D to the required standard of accuracy. This is not however the only test aim: the limits of the flight envelope are usually set by considerations other than drag. To define the likely test aims in more detail:

For a transport aircraft

- 1 To measure the absolute drag and the drag increments between different configurations in the specified cruise conditions and in the second segment climb.
- 2 To define the buffet-onset boundary and, in particular, the margins to buffet in terms of C_L at the cruise Mach number or Mach number at the cruise C_L .
- 3 To measure the pressure distributions over the wing partly for comparison with theoretical predictions and, more particularly, to understand the flow in important operating conditions and, when appropriate, to suggest how the flow and performance should be improved.
- 4 To obtain the slope of the lift versus incidence curve to help in forecasting the response to gusts in cruising flight.
- 5 To establish the usable $C_{L\max}$ with and without the high-lift devices deployed at speeds appropriate to take-off and landing.

For a combat aircraft

- 1 To measure the drag in long range and loiter conditions.

- 2 To measure the drag in sustained manoeuvre and high speed dash conditions.
 - 3 To assess the likely usable lift boundary which will be determined not by buffet-onset as for the civil aircraft, but probably by stability and control considerations such as pitch-up, wing drop, nose slice, loss of directional stability, and to suggest ways of postponing these effects.
 - 4 To determine the post-stall behaviour, particularly at low and moderate Mach numbers.
 - 5 To determine the effects of external stores on overall drag and to assess the store release behaviour.
 - 6 To measure the pressure distributions over the wing for the same reasons as for the civil aircraft (and, of course, to obtain the loads in critical stressing conditions).
 - 7 To determine the low speed stalling characteristics including the drag and stability and control characteristics as a means of forecasting the usable $C_{L\max}$, with and without the high-lift devices deployed.
- There will, of course, be other test aims but the above lists give some idea of what is required in the interests of predicting performance. It will be seen that drag is the most important measurement but stability and control and also unsteady effects are all relevant.

3 ACCURACY STANDARDS

The most stringent accuracy requirements as regards performance prediction are set by civil transport aircraft. One drag count, ie 0.0001 in C_D , can be regarded as having a significant impact on the competitive prospects for a new aircraft and on the range and fuel economy of the aircraft. The most authoritative statement on the accuracy required from wind tunnel tests is that prepared by the Wind Tunnel Testing Techniques (TES) Subcommittee of the ACARD Fluid Dynamics Panel and issued (Ref 14) in 1982. This stated that the accuracy requirements for lift, drag and pitching moment, as suggested by various research and industry sources, are:

Lift coefficient : $\Delta C_L = 0.01$
 Drag coefficient : $\Delta C_D = 0.0001$
 Pitching moment coefficient : $\Delta C_m = 0.001$

In general discussions about attainable accuracy, apparently conflicting views are often expressed. On the one hand, some wind tunnel test engineers claim that they can measure drag to an accuracy of 0.00005 in C_D , ie half a drag count, while others ridicule any claim to measure to better than 10 drag counts. This confusion arises from misunderstandings as to what is meant by the word 'accuracy'. One can and should distinguish between three meanings:

- (a) Accuracy as regards ability to obtain drag increments, eg differences in drag between two different but similar configurations. Clearly, this is, to the first order, equivalent to a definition of repeatability although, as noted below, knowledge of, for example, wall interference and support interference effects may still be highly relevant.
- (b) Accuracy in obtaining the absolute drag of the model as tested in the tunnel, having corrected for support and wall interference. This is clearly more difficult than (a): it depends on knowing all the corrections precisely; bias errors as well as repeatability standards are relevant.

(c) Accuracy in the sense of forecasting the drag of the full scale aircraft. This is even more difficult because it introduces the uncertainties of predicting the scale effect between model and full scale and allowing for the aerelastic distortions of the model and full scale aircraft. Also, one has to allow for the drag of the excrescences present on the aircraft but not represented on the model.

Realistic claims about the attainable standards of accuracy in respect of (a,b,c) can be expressed as follows:

- (a) Drag differences can be discriminated in the best tunnels to an accuracy of ± 0.0001 or better in C_D .
- (b) The absolute drag of the model configuration as tested in the tunnel can be obtained to an accuracy of ± 0.0005 in C_D .
- (c) The drag of the full scale aircraft can be forecast to an accuracy of ± 0.0010 in C_D .

(a) implies that one must be able to measure drag to ± 0.00005 in C_D or better. To achieve this high standard, techniques have to be developed to remove any effects of variability or unsteadiness in the tunnel flow. It is not simply that axial force or drag has to be measured to this standard; other quantities have to be measured to similar high standards, eg

Tunnel Total and Static Pressures,
 H and $p : \pm 0.1\%$

Mach number, $M : \pm 0.0001$.

This is unlikely to be achieved in the taking of the data but the computer program should include a routine for correcting the data to this accuracy.

Lift coefficient, $C_L : 0.001$.

It should be noted that this is an order better than the figure in the AGARD report (Ref 14) quoted earlier. There are two reasons for demanding this higher standard. First, when considering the drag in cruising conditions, the wave drag is likely to be sensitive to small changes in C_L and second, in general, drag is obtained by resolving normal and axial force into lift and drag. Despite the fact that aircraft now tend to cruise at near-zero incidence, the term C_N sine may still be significant in the cruise because of a difference in angle between the balance and wind axes.

Incidence, $\alpha : \pm 0.03^\circ$ or if possible, 0.01° .

This is very important. For a typical example of a civil transport cruising at $C_L = 0.5$, $\pm 0.03^\circ$ is equivalent to 0.00003 in C_D (again as a result of the C_L sin α term).

Base pressure, $C_{pb} : \pm 0.002$.

This value is based on a fuselage base area of $0.015 \times$ wing area and should be scaled for different area ratios.

Formulae for the dependence of C_D on these and other parameters are derived in detail in Ref 14. Evidence that the claims in (a) can be achieved is provided by Figs 1, 2. Fig 1 shows the current standard of repeatability in measuring a drag polar in a given test run in the ARA transonic tunnel. Fig 2 shows the current standard of inter-test repeatability; the three polars compared are taken from the three different test series spanning almost a year with the model derigged and reassembled between the three series. The conclusions from Fig 1 and other examples that

could have been presented are that, in this ARA tunnel, it is possible, in a given test series, to repeat the polar shape to an accuracy of ± 0.00002 and to repeat the polar level to ± 0.00003 in C_D . The claim that one can, with care, discriminate drag differences between configurations to ± 0.0001 or, better therefore appears entirely reasonable.

It is important to note that accuracy in determining even differences in drag can depend on knowing what corrections to apply for tunnel wall and support interference. It is unwise to assume that these corrections remain the same for two similar configurations. This may be true in the case of wall interference (although even here it is important to associate the drag increments with the correct Mach number) but support interference can undoubtedly change significantly between two configurations of the same model. This will be discussed in detail in §9 but, even at this early stage, it may be helpful to give an example. The interference of a rear sting can seriously affect the drag of the engine nacelles if they are mounted on the rear fuselage. Sting corrections for the aircraft model shown in Fig 3a, with and without the nacelles, are presented in Fig 3b. It will be seen that the difference between the curves, ie the error, if the sting corrections are not applied, in the drag increment due to the nacelles amounts to 0.0004, ie 4 drag counts, at the cruise Mach number 0.76, also, the error varies with both Mach number and C_L . The primary reason why the nacelle drag increment is reduced by the presence of the sting is that the taper of the sting reduces the velocity and local Mach number over the nacelles. For a 4-engined aircraft such as the VC10, Fig 3c, the effect can be even greater; typically ΔC_D due to the nacelles for a 4-engined aircraft could be reduced by 0.0010 or say, 30% leading to a serious underestimate of the drag of the aircraft if the sting corrections are not applied.

It may be helpful at this point, even at the expense of some repetition, to list the main factors that contribute to success in obtaining high accuracy from wind tunnel tests:

- 1 Resolution of basic instrumentation,
- 2 Sensitivity of balances for forces and moments and of pressure transducers for pressures,
- 3 Capability in calibrating balances and in allowing for drifts,
- 4 Standards of pressure scanning equipment,
- 5 Ability to measure model attitude,
- 6 Ability to cope with any variability of unsteadiness in tunnel flow,
- 7 Geometric fidelity of model as a representation of the full scale aircraft,
- 8 Knowledge of how to correct for tunnel wall interference,
- 9 Knowledge of how to correct accurately for support interference,
- 10 Ability to correct for nacelle internal drag,
- 11 Knowledge of how to fix transition end of how to determine the transition position,
- 12 Skill in simulating the full scale boundary layer behaviour and in extrapolating the results to full scale Reynolds numbers,
- 13 Knowledge of the aeroelastic distortion of the model,
- 14 Ability to cope with other special issues in half model testing,
- 15 Finally - and most important - the skill, experience, care and dedication of the test engineers.

The special problems of propulsion testing will be addressed in §§12,13.

5 BALANCE DESIGN, SENSITIVITY AND CALIBRATION

As a general rule, balance discrimination needs to be an order greater than the required accuracy. In particular, this means that the resolution capability for drag and lift coefficients should be 0.00001 and 0.0001 respectively. This is believed in, both the ARA transonic and RAE 8 ft \times 8 ft tunnels for a typical qS (a product of dynamic pressure and model reference area) of 8000 Newtons. The basic data acquisition system does not often pose a limitation. A broad account of the system in use in the ARA tunnel up to 1989 is contained in Ref 15. This has since been replaced by a more modern system. The main improvements with the new system are that it is generally more robust with greater amplifier stability and with facilities for regular, automatic calibration of the amplifiers. On paper, the figures for discrimination given in Ref 15 still apply to the new system but the important point is that the theoretical figures should now be obtained consistently in practice. Improvements of this nature are probably typical of what is currently happening in other tunnels when and if their systems are updated.

General practice in many tunnels is to use internal strain gauge balances manufactured by the Task Corporation but in the UK, RAE and ARA have, for many years, used balances manufactured in-house to a design originally developed at RAE. Fig 4, taken from Ref 16, shows one of these balances. It is in regular use in the RAE 8 ft \times 8 ft tunnel for accurate drag measurements in tests at total pressures up to 2 bar at high subsonic speeds. In the ARA tunnel, where tests are only possible at total pressures near 1 bar, a similar but smaller balance design is used; this has a diameter of 57.15 mm or 2.25" and a normal force capacity of 7120 Newtons. These balances are machined, generally in maraging steel, from a solid block with no internal joints. The positions of the strain gauges are shown in Fig 4; the axial force is determined from the strains in the centre flexures; the other 5 components are obtained from the strain gauge bridges on the front and rear cages ahead of and behind the axial force unit. The demand over the years for ever greater accuracy has led recently to a reassessment of the basic design with the aid of finite element methods. The weakest feature of the existing design is that it is often difficult to achieve a perfect slip-free fit in the taper joints where the balance is attached to the sting and to the model wing mounting block (see Fig 5). In one recent refinement of the design the forward taper joint has been replaced by a flange joint; in another, the balance has been made integral with the sting. Also, efforts are being made to increase the length between the measuring element and the end fixations.

It is most important that these balances are calibrated regularly: ideally, before and after each test programme. The full balance matrix as generally determined in the past includes 6 direct factors, 30 first order and 126 second order terms although some of these can be taken as zero. The full calibration should be undertaken every few months and in the RAE 8 ft \times 8 ft tunnel, a check of the direct factors and the most significant interactions is made at the end of each test with the balance still installed in the model. Figs 6a,b give two examples of results from balance recalibrations at ARA: Fig 6a is considered to be a satisfactory result but the hysteresis evident in Fig 6b was not accepted and the balance was re-gauged. The aim is to achieve an accuracy of 10.33 Newtons; this corresponds to $\pm 0.05\% \times$ full scale, at the very least, one should aim for $\pm 0.15\%$.

The advent of cryogenic tunnels implies that balance calibration becomes an even more onerous requirement: one has to determine the dependence of the matrix on temperature. This is leading to the development of automatic calibration machines. In the machine described in Ref 18, calibration loads are applied to the non-metric (sting) end of the balances and these loads are measured by a machine which is similar in design to, an ex., a balance such as those commonly used in low speed tunnels. This machine has been designed as an item in the Technology Programme in support of the ETW but, although cryogenic tunnels provided the spur to this development, the machines when manufactured and available will, no doubt, be used in support of testing in conventional tunnels. The different principles of the new automatic and traditional calibration equipment are illustrated in Figs 7a,b taken from Ref 18. In the conventional rig, the balance is enclosed in a sleeve to which the loads are applied; at each loading, a realignment of the rig is needed in order to ensure that the loads are applied in the correct directions relative to the balance axes; a laborious procedure. In the new scheme, the model end of the balance is mounted to the 'external balance' which is positioned to have its reference centre at the same position as the reference centre of the balance being calibrated. The 'external balance' is a very stiff device; it measures loads applied through a system of seven load generators which are sufficient to permit the application of any single load or load combination. Interferences due to any misalignment are also measured by the 'external balance'. With the conventional rig, the first and second order interaction factors are evaluated but there are cases where this does not appear to be sufficient to represent the non-linearity in the calibration. With the new scheme, an algorithm developed at the Technical University of Darmstadt extracts a third order calibration matrix. For a six-component calibration, this matrix needs a data set of 1500 to 2000 different loading conditions. A special computer program has to be used in the tunnel since one cannot invert a third order matrix. To summarise, the primary aims of this development of are to provide

- (a) a total accuracy of about 0.02%,
- (b) a repeatability at least twice as good as the required accuracy,
- (c) resolution at least five times better than accuracy,
- (d) a rig that does not need any realignment during a calibration.

Perhaps the most crucial issue in balance design and operating practice lies in how to avoid or at least, how to allow for drifts in the signals due to temperature effects during a test run. In the ARA tunnel, the drift in the axial force balance zero can be equivalent to a drift in $C_0 = \pm 0.0003$ based on a $q = 25000$ Newtons/m². Balance drift is important in all tunnels but particularly in pressurised tunnels where there is often appreciable delay between taking the initial zeros and taking the first data point. It is standard practice to thermally match the balance bridges. This eliminates any change in sensitivity due to a uniform change in temperature but it does not compensate for changes in Young's modulus or for the really important point that the balance zeros are always sensitive, to a greater or lesser extent, to temperature gradients across the balance. Measurements of the local temperatures at points on an internal balance have shown that the changes in these local temperatures lag considerably behind the changes in tunnel total temperature. There is therefore no virtue in relating the balance drifts to the tunnel temperature. In any case, it is a temperature gradient that matters but it is not immediately

obvious what gradient controls the variation in zero. This difficulty is successfully bypassed in the ARA transonic and RAE 8 ft x 8 ft tunnels, but not necessarily in all tunnels, by relating all the data to results obtained in a special traverse through the test Mach number range at a given incidence or C_l . This special traverse is undertaken as the last traverse in the test when temperatures have tended to stabilise, these data points being computed with respect to the zeros measured at the end of the test (although there may be occasions where this appears to be the wrong approach: no general recommendation on this point can be as good as the experience of the skilled operator who knows his own equipment). In unpressurised tunnels, repeat traverses are often carried out in a special additional run and if necessary, these are repeated until satisfactory repeatability (as defined earlier) is achieved.

Drifts in the zeros are particularly troublesome with half-model balances. These balances are invariably situated outside the tunnel working section and can therefore be affected by temperature gradients between the model and tunnel structure. In the ARA tunnel, the half-model balance is submerged in a temperature-controlled oil bath but perhaps the only really satisfactory approach is to insulate the balance and to ensure that the balance chamber is free of draughts. This may be viewed as idealised advice; it is not easy to follow. In the RAE 8 ft x 8 ft tunnel a new half-model balance recently installed has improved the situation but it is still standard practice to apply corrections during the computing of the test data, for the effects of a temperature gradient between the metric and non-metric parts of the balance.

The problems of balance drift have not yet been fully solved in large low speed tunnels where the balances are, of course, much larger. This is why models in these tunnels are still often supported on under-model struts despite the consequent aerodynamic interferences (see §9).

Finally, one should note that humidity may be a significant source of error if suitable measures to combat it are not taken. Precautions that have been found to minimise these effects include: controlling the humidity in the tunnel, waterproofing the gauges, providing power to the balance at all times when the model is in the working section, and finally, storing the balance, when not in use, in dry conditions and with the power on. Even when these precautions are taken, traditional thinking and experience suggests that one should start a test on a new model with a shake-down or warm-up run. Recent evidence has indicated however that such a run may, in fact, be an excellent method of taking the initial zero for the main test at a moment when the gradients are at their most severe. Even so, the practice could still be justified on the grounds that the shake-down run is a means of exercising the balance and the joints over the range of test loads. It will however, be realised that there will be occasions when it fails because of the possibly adverse effects on the initial zero for the main run.

5. EQUIPMENT FOR PRESSURE MEASUREMENTS

5.1 Pressure Transducers

For many years, pressures have been measured by various types of pressure transducer. These convert pressure into the position of a needle on a mechanical pressure gauge or into an electrical output such as voltage or current. In wind tunnel testing, the voltage output type of sensor is used almost exclusively. The sensing element in high

quality pressure transducers is a silicon diaphragm that forms a normal Wheatstone circuit. Unfortunately, the electrical characteristics of silicon are highly dependent on temperature, resulting in both the sensitivity and offset voltage varying with time if the temperature is changing. Various methods have been used to overcome these temperature problems. The transducers can be calibrated in situ during a test; a number of accurately known calibration pressures are applied to the transducer and at least, a 2-point calibration performed to establish the sensitivity and offset on-line. Alternatively, for differential type transducers, the two pressure sensing ports can be pneumatically connected together to make a measurement of the actual offset voltage, making the assumption that the sensitivity has not changed. A third method that is not so often used is to calibrate the transducer against temperature and to measure the temperature at the moment of making the measurement. At 1990 prices, a typical quality pressure transducer costs about £350.

Particular care has to be taken about the choice of instruments to measure the tunnel reference pressures. In the RAE 8 ft x 8 ft tunnel and the ARA transonic tunnel, they are not measured by the same type of transducers as those used for pressure measurements on the actual models. In the RAE tunnel, the reference pressures are measured by self-balancing capsule manometers. The instrument measuring stagnation (total) pressure has a resolution of 0.34 mbar or 0.017% of the stagnation pressure at two atmospheres pressure and those recording static pressures have a resolution of 0.17 mbar. In the ARA tunnel, the reference pressures are measured by Ruska type DDR60000 pressure gauges (0 - 2.5 bar) which have a specified accuracy of ± 0.04 mb. The reading of these gauges is matched in the data reduction process to the output from a Druck DP1140 precision barometer at the start of every run. This barometer has a specified accuracy of ± 0.15 mbar. Thus, the maximum errors in dynamic pressure and Mach number arising from the use of these gauges are $\pm 0.02\%$ and ± 0.0001 respectively.

It is also necessary in every test to measure base pressures to high accuracy. These are measured in the ARA tunnel with 345 mbar Druck type PDCR22 differential transducers. These have a specified accuracy of 0.06% full scale which, when converted to C_D with a typical value of base area to wing reference area of 0.015, gives a possible error in C_D of only 0.00001.

5.2 Scanivalves

In general, there is not enough space to mount many individual transducers in a wind tunnel model. It is not entirely satisfactory to mount them external to the model because the length of pressure tubing between the pressure tappings where the measurement is required and the transducer itself leads to significant lags. To avoid these problems, Mechanically Scanned Pressure Scanners (MSPs) were developed by the Scanivalve Corporation in San Diego although there are others on the market.

A Scanivalve provides a means of connecting a number (typically 48) of pressure ports to a single transducer. A motor drive rotates a shaft to which is connected a rotor into which is cut a channel which pneumatically connects the centrally mounted transducer to the various input connections. In many cases, a single motor drive unit can operate several rotor units. The fact that there is only a single transducer brings several attendant advantages. First, it reduces the cost, second, it greatly reduces the space needed in the model and finally, if known calibration pressures are applied

to two or more input ports, a calibration of the pressure transducer is performed with every scan. Various establishments therefore invested heavily in Scanivalves. Pressures at more than 600 tappings on the wing have been measured at ARA in tests on complete aircraft models using 16 Scanivalves installed in the fuselage. The D- and S-type Scanivalves - the types most frequently used in wind tunnels - have diameters of 3.18 and 2.30 cm respectively.

One has to admit, however, that the physical nature of an MSP sensor such as a Scanivalve leads to some problems. The rate of taking the data is not as fast as one would like. This is partly because of its mechanical design and partly because of the need to allow the pressure to settle every time the valve is stepped. The internal volume in the rotor and transducer cavity is the main reason for the pneumatic settling time. When the rotor moves from one port to the next, a trapped volume of air is retained resulting in an error at the instant of connection to the second port and the scanner itself provides a reservoir whose pressure requires finite time to settle to the value of the external pressure to be measured. The usual method for checking whether the scanning speed is acceptable or not is to repeat a given pressure measurement on two successive ports on the valve and arrange for the previous port to be connected to a very different pressure. As an obvious example, let us imagine that two reference pressures - tunnel total pressure and free-stream static pressure - are connected to successive ports with the static pressure repeated on the following port. If the two values of the static pressure disagree, this will indicate that the scanning speed is too fast to be able to rely on successive ports coping with pressure differences as great as that between total and free-stream static pressure. The experienced engineer may still feel that the scanning speed is acceptable for all other pressure differences encountered in the test and the only action that is necessary is to ignore the first measurement of tunnel static pressure, i.e. the one immediately following the total pressure. The acceptable scanning speed is likely to vary from one facility to another because of the different tube lengths. In some facilities and with some models, for example, the Scanivalves are mounted outside the tunnel. In the ARA tunnel, experience has shown that generally, it is acceptable to scan at 10 ports per second, thus giving about 5 seconds for the complete scan at more than 5 ports per second. Even a time skew of 5 seconds can degrade the consistency and hence, accuracy of the data. This is the dominant motive behind the growing trend in the world in general to abandon MSPs in favour of Electronically Scanned Pressure Sensors (ESPs).

5.3 Electronically Scanned Pressure Sensors (ESPs)

ESPs are fundamentally different from MSPs. It is not simply that the scanning is carried out electronically rather than mechanically, each pressure port has its own separate transducer and, with an ESP, it is the output from these transducers that is scanned electronically either sequentially or randomly and then amplified to minimise electrical noise problems.

ESP sensors were first developed in the mid-1970s by several transducer manufacturers and research agencies. These included the Scanivalve Corporation, Kulte, NASA Langley Research Center and NASA Ames Research Center. The aims were to produce compact units capable of giving good accuracy and high scanning rates. Two of the above organisations - the Scanivalve Corporation and NASA Langley - produced viable products which are now available on the commercial market. The NASA Langley design having been developed and marketed

by Pressure Systems Incorporated. Early detailed descriptions of the NASA Langley design are contained in Refs 19-22. The approximate dimensions of the space required in a model for a single 48-way unit are 4.6 cm x 6.8 cm x 2.9 cm. It is possible to convert such a unit into a 96-way unit although these have only been used on rare occasions. Using these dual units, wind tunnel tests have been made on one relatively small model equipped with almost 800 pressure tappings and it is realistic to imagine that tests with 1000 or more tappings are now possible.

The output from the separate transducers is scanned by a digitally addressed analogue multiplexer. Since the transducers are being electronically scanned, data rates in excess of 20,000 measurements per second are possible. Data skew is therefore effectively eliminated. Since every pressure to be measured is permanently connected to a transducer, there is no pneumatic settling time other than that imposed by the volume of connecting piping and so, there are no 'carry-over' problems. Temperature drifts have still to be addressed but the units contain a built-in calibration facility. A pneumatically actuated calibration valve is included in each unit. This valve has two positions; normal and calibration. When in the calibration mode, a known calibration pressure (known by reference to a Ruska gauge or barometer) can be applied to all the transducers; by applying a series of say, 5 such pressures, the zero offset, sensitivity and non-linearity of each transducer is determined. It is good practice to connect at least one calibration pressure to at least one of the transducers throughout the test to monitor whether a recalibration is required. Limited UK experience suggests that a recalibration is always necessary at the end of every polar in a typical complete model test. The issue is crucial from the point of view of accuracy; without the repeated recalibrations, errors of the order of 2-3 mbar or more would be commonplace as compared with a target accuracy of 0.2 - 0.3 mbar. The time taken for an in-situ calibration depends on the volume of the tubing between the calibration pressure source and the ESP sensor and can therefore vary between seconds in a closely coupled situation to several minutes in a real wind tunnel environment. In the case of the A² tunnel the required time is about 2.5 - 3 minutes. These recalibrations, therefore, slightly erode the basic advantage of ESP sensors for speeding up the rate of data taking. Another very significant point in favour of ESP sensors is that the only moving part in them is the valve for changing to the calibration mode, this holds out the hope that they will need far less maintenance than WSPs.

The author is conscious that his personal knowledge of experience with ESP sensors is much less than that of many tunnel engineers in other countries. It seems fair to conclude however that the claims for speeding up the rate of data taking are fully justified with the qualification noted above. The only word of caution is that clearly, great care and technique discipline will have to be practised if we are going to use them and maintain the standards of accuracy to which we have become accustomed.

5.4 Measurement of Unsteady Pressures

Although this lecture concerns experimental methods for performance, it is still relevant to include a few words about the measurement of unsteady pressures, buffet onset for civil aircraft and buffet penetration for military aircraft are important considerations when determining usable lift boundaries.

Two research establishments - NLR in the Netherlands and RAE Bedford in England - have been particularly involved in developing techniques for the measurement of unsteady pressures. In the original approach at NLR, a large number of pressure tubes were connected to a small number of scanning valves (Ref 23) and each valve was connected to a group of tubes in sequence. This approach was relatively cheap but the information obtained was somewhat limited; it was not possible to measure transient pressures or to perform cross-correlations when only one scanning valve was used. The RAE approach was more expensive but provided much more information; in this approach, a large number of transducers (typically Kulite XQZ 093/25A transducers) are mounted in the actual model surface; each transducer has its own amplifier and simultaneous measurements are made of the mean pressure, the unsteady component coherent with the model motion and the random component of pressure at every point. This approach can provide transient and cross-correlation data. Details of the technique are to be found in Ref 24 where it is noted that a method had to be devised to compensate for the fact that the output from the transducers depended slightly but significantly on temperature both as regards zero and sensitivity. The RAE technique allows one to abandon the somewhat bulky compensation resistor supplied with the transducers and so to take full advantage of the very small size of the actual transducer. The data is then acquired and processed on-line into coefficient form by the Presto system described in Ref 25. Some typical results obtained by this approach are presented in Ref 26.

NLR later introduced (Ref 27) a combined system which enables comparisons to be made between results obtained with the two approaches

The above discussion should not be taken to imply that unsteady pressures have to be measured to obtain a prediction of a buffet-onset boundary. Other methods that are more likely to be used in routine testing include

- (a) measurements of the unsteady wing root bending moment by means of strain gauges mounted in pockets in the wing surface.
- (b) measurements of the steady pressures near the wing trailing edge.
- (c) noting the departures in the lift versus incidence curves from a basically linear trend, and
- (d) noting the breaks in the axial force versus incidence curve.

All these methods require considerable skill and experience in interpretation. 'Kinkology' applied to the lift curves is particularly prone to misinterpretation because flow separation giving a loss in lift (and possibly buffet) on one part of the wing may be masked in the overall results by some other change in flow on another part of the wing, giving an increase in local lift. The best advice is to realise that no one method will be successful in every situation, therefore, apply all possible methods, compare the results, interpret any discrepancies in terms of the flow behaviour over the wing and, in crucial and difficult cases, measure unsteady pressures in appropriate locations.

6 DETERMINATION OF MODEL ATTITUDE

It was noted in §3 that it is vital to be able to measure angle of attack to a high degree of accuracy. Simple examination of the equation

$$C_D = C_N \sin \alpha + C_A \cos \alpha$$

shows that α has to be known to an accuracy of $\pm 0.03^\circ$ in order to achieve ± 0.0001 in C_D at a typical cruise C_L of 0.5. This is therefore the minimum requirement for a desirable accuracy in model attitude measurement; ideally, one wants an even better resolution than $\pm 0.01^\circ$.

ARA have, for many years, used a Sunstrand QA900 accelerometer as an 'incidence meter' (Ref 15). Experience has shown that, with standard filtering techniques, these incidence meters can still be used successfully in conditions near buffet-onset. Some refinements in the technique have however been introduced since Ref 15 was published. For example, the accelerometer is now mounted integral with the balance to give added rigidity; temperatures are sensed on the instrument itself and a systematic pitch calibration from 0° to 90° is carried out before and after each test. Corrections for the change in zero and sensitivity of the instrument based on the measured temperatures are applied in the computing of the test data. The change in zero is the more significant effect, typically, this can amount to 0.00061° per degree C and a typical change in instrument temperature during a run can be about 15°C . With these refinements, the resulting accuracy in and near the cruise condition now meets the target as set out in §3.

In the RAE 8 ft \times 8 ft tunnel, on the other hand, model attitude is measured by the more traditional method of measuring the quadrant attitude and applying corrections for the deflections of the sting under load. The quadrant attitude is measured by an absolute encoder with a resolution $\pm 0.01^\circ$ and calibrations have shown that the drive is sensibly linear with no measurable hysteresis. The total deflection of the model-sting assembly can be of the order of 1° at a stagnation pressure of 2 bar and at high supersonic speeds. Typically in a calibration, there are small shifts between angles for increasing and decreasing loads owing to hysteresis effects in the joints. The mean calibration is used to determine angular misalignments between the balance and roll axes, on the one hand, and the roll axis and the fuselage datum on the other in both cases at zero-gravity conditions.

One should not dismiss the different approaches in the two tunnels as implying a difference of opinion between two groups of tunnel engineers. It is in fact a logical consequence of the different engineering characteristics of the two model support rigs. The quadrant in the RAE tunnel is very stiff and specifically much stiffer than the model cart in the ARA tunnel. On the other hand, model bounce as one approaches and enters buffet is much more noticeable in the RAE tunnel. Both these characteristics favour the use of the traditional method in the RAE tunnel and of an incidence meter in the ARA tunnel. The general message is that the best method of determining model attitude can vary from tunnel to tunnel and should be chosen in the light of experience in each particular facility.

Ability to measure model attitude to high accuracy is, of course, only part of the story, one also needs to know the tunnel flow angle to the same order of accuracy. This will be discussed in §7 below, the main approach in a complete model test is to test with the model both erect and inverted.

7 WIND TUNNEL FLOW ENVIRONMENT

It is self-evident that the accuracy of the performance data obtained from wind tunnel tests depends on the reliability and applicability of the calibration of the flow in the empty tunnel and on whether sound techniques have been developed for coping with any variability or unsteadiness in the flow. The discussion below is not intended to be comprehensive; it merely highlights some issues that have been found to be particularly important in the context of model testing to obtain performance data.

7.1 Empty Tunnel Flow Calibration

In the empty tunnel flow calibration, the flow in the working section is related to two reference pressures which usually approximate to the free stream static and stagnation pressures. In a tunnel with solid walls, the reference static pressure is usually measured on the tunnel wall at a hole which is sufficiently far upstream of the model station for the pressure not to be affected by the presence of the model when it is present. In a ventilated tunnel, i.e. a tunnel with slotted or perforated walls, the pressure in the plenum chamber surrounding the working section is usually taken as the reference static pressure. The reference stagnation pressure is usually sensed at a hole in the wall of the settling length upstream of the contraction ahead of the working section. The static pressure and hence, Mach-number distribution along the length of the working section is obtained most accurately by measuring the pressures along the side of a long tube of circular cross-section mounted in the tunnel with the rear end in the normal model support and with the forward end extending far forward ahead of the contraction (Ref 28). In this way, the presence of the tube does not modify the flow through the working section. Typical targets for this distribution are ± 0.002 in Mach number at subsonic speeds and ± 0.005 at transonic speeds. In addition, the calibration normally includes measurements of the distributions of static pressure and flow angle over the working section cross-section at various stations along the length likely to be occupied by a model.

This description of a tunnel calibration may appear to be simple textbook material but several important points should be noted.

- (i) Many tunnel calibrations were made a long time ago when standards were possibly not as stringent as they are today. For example, Ref 28 (written by the present author!) in discussing the original calibration of the ARA transonic tunnel, suggests that the Mach number based on plenum chamber static pressure can be used as a reliable indication of the free-stream Mach number at the model provided that the convergence of the working section walls does not exceed 12 minutes, however, a graph in Ref 28 shows that at 12 minutes convergence, there is a discrepancy of approaching 0.003 in Mach number. This specific point is unimportant because the ARA tunnel, in routine testing, is never operated with the walls converged but it is quoted to illustrate how standards have become more strict over the years. Today, corrections would certainly be included for differences of 0.001 or even 0.0005 in Mach number. Also, it is now recognised that tunnels should be recalibrated on a regular basis and that customers need to check that the calibration is sufficiently comprehensive to satisfy their particular requirements.

(II) The development of the boundary layer along the walls of the tunnel controls not only the velocity gradient through the tunnel (and hence the empty tunnel buoyancy corrections) but also the relationship between the free-stream Mach number at the model and the value based on the reference pressures. It follows that in a variable density tunnel, this relationship should be determined at all stagnation pressures likely to be used for testing. This point has not always been appreciated but it is now often quoted as a leading example of what has become known as a pseudo-Reynolds effect (Ref 29). This point is particularly important when the aim of the test is to determine the forces on merely part of the model installed in the tunnel. For example, when testing an afterbody model, the accuracy of the afterbody drag is critically dependent on whether the pressure on the front face of the afterbody has been related to the correct free-stream static pressure. It can be shown that an error of one drag count in afterbody drag will result from the very small errors, ΔM , in free-stream Mach number as given by the curve plotted in Fig 8a. Extreme accuracy in the tunnel calibration is therefore required for this type of testing. Ignoring the possible variation in the tunnel calibration with stagnation pressure in a variable density tunnel can result in completely wrong conclusions being drawn about the variation of afterbody drag with Reynolds number. This is shown by the example in Fig 8b taken from Ref 30. It will be seen that ignoring the change in the calibration with stagnation pressure is sufficient to change the sign of the variation of afterbody drag with Reynolds number. The surprising trend in the incorrect results puzzled researchers for many years before the error was discovered. The best discussion of the possible effects of not calibrating a variable density tunnel at all test Reynolds numbers is given in Ref 31. One should of course not go to the other extreme of dismissing all changes with Reynolds number as pseudo-Reynolds effects. Those discussed later in §10 are genuine!

(III) The emphasis in many calibrations in transonic tunnels was originally placed merely on the standard of the longitudinal distribution of Mach number and arguably, there was not enough emphasis on the uniformity of the flow, particularly as regards flow angle, over the cross-section of the working section. The trend, already mentioned to assess the performance of new civil aircraft by testing relatively large half-models, has strengthened the need to look at this uniformity, or lack of it, with a critical eye. It has been realised that, in many but not all high speed tunnels, the distribution of flow angle is far from perfect. A good example of this potential problem is to be found in Ref 11. Results are presented for the NASA Ames 11 x 11 Unitary Wind Tunnel. Fig 9 shows the variation of cross-flow angle with height above the tunnel floor, a variation of up to $\pm 03^\circ$ is indicated. The NASA Ames tunnel is certainly not unique in this respect. The existence of two vortices in the flow above the floor and below the

ceiling has been detected in other tunnels. The explanation for the presence of these vortices may vary from tunnel to tunnel but it is of interest to note that, in the ARA tunnel, this feature in the tunnel flow has been completely eliminated by the introduction of a honeycomb in the settling chamber downstream of the 4th corner. A flow angle distribution such as that shown in Fig 9 modifies the twist of a wing of a half-model mounted on a balance below the tunnel floor. Tests were made in the NASA Ames 11 ft x 11 ft tunnel on a symmetrical wing half-model with the results shown in Fig 10. The mean derived tunnel flow angle over the wing was appreciably different according to whether one used the lift-incidence or drag polars to derive the figure and hence, one cannot remove the effects of the empty tunnel flow angle by a simple change in incidence datum.

General experience shows that this flow-angle problem is less serious when testing complete models; the discrete vortices are generally not present near the centre of the tunnel stream and, to the first order, one can remove the effects of small variations in flow angle across the span of the model wing by testing the model erect and inverted. In effect, one uses the model wing as a pitch meter to determine the mean flow angle over the model. Again, it is of interest to note that the insertion of the honeycomb in the ARA tunnel appears to have had the effect of producing mean flow angles that, at a given Mach number, are virtually independent of the wing planform; this was not the case before the honeycomb was introduced. This suggests that even near the tunnel centre-plane, the introduction of the honeycomb has improved the flow angle distribution.

7.2 Variability and Unsteadiness of Tunnel Flow

As noted earlier in §5.3, the aim should be to maintain the test Mach number in a test polar to an accuracy of ± 0001 and, if this cannot be achieved, to correct the data to this standard in the post-processing routines. Fig 11 presents evidence to support this statement. At high C_L , when wave drag (or possibly, flow separation) is beginning to appear, the sensitivity of the drag to small changes in Mach number increases rapidly, the cruise condition is likely to be near or just beyond the break in this $C_D - C_L$ curve.

Regarding the effects of flow unsteadiness, fluctuations at high frequency are generally filtered out electrically. This leaves the effects of fluctuations at low frequency. Taking the ARA tunnel as an example, Fig 12 shows that the flow oscillates at low frequency, notably at 0.25 Hz and at 0.3 Hz. Particularly at the higher lift coefficient, the model incidence and the forces respond to this flow oscillation. To meet this situation, it is standard ARA practice to record 48 data point samples over a period of 4.8 - 6 seconds. The variation of C_D within these samples can be quite substantial (see Ref 15) but even so, long experience has indicated that a simple average of such samples generally gives a repeatability of better than ± 00001 in C_D . Figs 1, 2 provide the ultimate evidence that the procedure is successful, at least up to and beyond the likely cruise conditions.

7.3 Stream Turbulence and Acoustic Spectrum

The flow in any tunnel always contains a small amount of unsteadiness in the form of both velocity and pressure fluctuations. Low-speed tunnels are generally assessed in terms of their velocity fluctuations, ie their turbulence, but it has generally been assumed in many papers that, at transonic speeds, the acoustic noise spectrum is the controlling variable.

The most obvious effect of the stream turbulence and noise spectrum is on the position of boundary layer transition on a model under test. Comparative tests have therefore been made in all the major transonic tunnels in the Western world to determine the position of transition on a 10° cone (Refs 33, 34). The observed transition Reynolds numbers from these tests are shown plotted against pressure fluctuation level in Fig 13. This picture reproduced from Ref 33 appears to establish an approximate correlation with the pressure fluctuation level but it will be noted that there is a ±20% scatter about a mean line and probably, this should not be dismissed as scatter. Indeed, a later re-analysis of some of the data in Ref 35 has cast doubt on the original conclusion. In Fig 14, taken from Ref 35, the results for 4 leading NASA tunnels are plotted against both velocity and pressure fluctuation. This figure may appear difficult to understand at first sight, but the authors of Ref 35 argue that it shows that when the results are plotted against the pressure fluctuation, they show considerable scatter whereas, when they are plotted against the velocity fluctuation, they correlate much better. The authors suggest a relationship of the form:

$$R_{ff} = f(\mu u)^{-n} \text{ rms}^n$$

where (μu) is the momentum fluctuation and $n = 1/4$ for the beginning and $n = 1/6$ for the end of the transition region. Further research appears to be needed to clarify the subject; for example, the correlation in Fig 14 is proposed for the full Mach-number range from 0.1 to 2.2 whereas, if the data are analysed in terms of the tunnel noise, one often finds that R_{ff} tends to decrease with Mach number up to $M = 0.8$ and then to increase rapidly through the transonic speed range, as might have been expected since, in many tunnels, the pressure fluctuations are found to reach a maximum near $M = 0.8$ and then to decrease.

For most existing transonic tunnels, the transition Reynolds number for the 10° cone at $M = 0.8$ lies in the range $3 \times 10^4 - 5 \times 10^4$. Factors that can affect the precise value include

- (i) the noise and turbulence being propagated from upstream, eg from the valves in a blowdown tunnel and whether or not there has been any treatment in the settling chamber aimed at damping these disturbances,
- (ii) the nature of the tunnel walls, eg whether they are solid, slotted or perforated and whether there has been any attempt to alleviate their noise-generation properties,
- (iii) whether the tunnel design contains any feature such as a second throat to prevent the upstream propagation of noise from the downstream diffuser.

With the increased interest in laminar flow aircraft design, all these issues are now receiving close attention both in modifications to existing tunnels, eg the honeycomb in the ARA tunnel (Ref 32) and in the design of new tunnels, eg the T1500

tunnel at FFA, Sweden (Ref 36). The latter is a particularly interesting recent example of the detail that has to be addressed. Ref 36 shows that it is not sufficient to have a second throat at the start of the diffuser; this leaves the possibility that appreciable noise generated in the model support region can still propagate forward into the working section. Close attention has therefore to be paid to the longitudinal distribution of the tunnel cross-sectional area opposite the model support to avoid as far as possible severe decelerations in the flow that might induce a flow separation.

Differences in turbulence and/or noise in different tunnels are liable to lead to differences in natural transition position on the model under test (Ref 37). However, the recommended standard practice in transonic tunnels is to test with transition fixed artificially and this removes the risk that results from different tunnels will appear to be inconsistent because of differences in transition position. It does not follow that differences in turbulence and noise are unimportant. As will be discussed in detail in §10, a technique in common use for simulating the behaviour of the full-scale boundary layer is to test with a transition position on the model that is further aft than that expected on the full-scale aircraft. It is desirable that the stream turbulence does not place any limitation on the use of this technique. The ability to maintain an extensive length of laminar flow will be even more important when testing models of laminar flow aircraft.

Stream turbulence also has an effect on the development of a turbulent boundary layer. This has been studied by Green (Ref 38) who suggested that it was possible to transform turbulence into an effective Reynolds number. This led to the suggestion in some quarters that increasing the turbulence of the stream could be one method of increasing the effective test Reynolds number. The difficulty with this suggestion however is that increasing turbulence only increases the effective Reynolds number in respect of the boundary layer shape factor (and hence, boundary layer separation onset). In terms of boundary layer skin friction and hence, drag, it reduces the effective Reynolds number. This is illustrated by the results in Fig 15 reproduced from Ref 39.

In most transonic tunnels, the turbulence level is far less than 1% and so, the effects shown in Fig 15 can be dismissed as trivial. It has however been recognised (Ref 40) for many years that accepting too high a level of tunnel stream noise can degrade the accuracy of buffet data. Mabey suggested that, to obtain data uncontaminated by any interaction with the tunnel noise, the value of $(nf(n))^\frac{1}{2}$ should not be greater than 0.002 where n is the non-dimensional frequency for say, the model wing fundamental bending mode and where $F(n)$ is related to the non-dimensional pressure fluctuations by the equation

$$p' = q^2 \int^n F(n) dn \quad (1)$$

where p' = acoustic pressure signal

Fig 16 presents an example of how the unsteady wing-root strain can be influenced by reducing the unsteadiness of the tunnel stream. In this example, the stream unsteadiness was reduced by a change of slotted working section wall from one having a hard surface to one with a laminate, as a consequence, buffet onset became more clearly defined and the buffeting measurements showed much less scatter.

8. TUNNEL WALL INTERFERENCE

8.1 The Classical Approach

8.1.1. Closed tunnels at subsonic speeds

The presence of the tunnel walls modifies the effective angle of incidence and the effective speed of flow over the model. These effects are known respectively as tunnel constraint and blockage and the measured data from tests in a conventional tunnel must be corrected accordingly. In the classical approach to a prediction method, the model is replaced by singularities and the walls by a doubly-infinite set of images. These methods are developed in detail in Agardograph 109 (Ref 42) which is the major reference on the subject. A full set of formulae and graphs are given in this reference for closed, open and ventilated tunnels. Different standards of approximation will be needed for different types of testing in various tunnels but in the author's experience, the formulae discussed below summarise a reasonable set of corrections staying within the limitations of this classical approach which, it will be realised, is based on the assumption that the flow is uniformly of the small-perturbation type.

These formulae can be listed as follows:

(a) Tunnel constraint

In the simplest approach, the basic equation for the interference upwash angle is

$$\frac{W_1}{U} = \left[\delta_0 + \frac{x}{Bh} \delta_1 \right] \frac{SCL}{C} \quad (2)$$

Values of the factors δ_0 and δ_1 are presented in Ref 42 for square and rectangular working sections with alternatively 4 closed, 4 open and 2 closed/2 open walls. For a square section, $\delta_0 = 0.13$ and $\delta_1 = 0.25$ if the walls are closed. This simple formulation should not be used if the model wing span is greater than about $0.5 \times$ tunnel width. From the author's experience, one should then use the relations in Ref 42 in terms of a parameter $(\delta_0)_{\infty}$. If the span/tunnel width ratio is 0.8, the value of δ_0 for a square section with closed walls then becomes 0.162, i.e. an increase of 25% relative to the value for a small model.

(b) Solid and wake blockage

The presence of the tunnel walls modifies the flow around the model even at zero lift. In a closed tunnel, the flow around the model is speeded up and vice versa in an open tunnel. This interference is due to the volume of the model and its wake. In general, it is acceptable to treat solid and wake blockage as independent of each other, this is not necessarily true at high lift (see (c) below).

For the calculation of blockage by the classical methods, the model is replaced by an appropriate distribution of sources and sinks. Simple formulae are listed in Agardograph 109 but, in the UK, the standard method that has been used for many years is that produced by Evans in 1949 (Ref 44). This method was based on earlier work by Thos and Thompson (Refs 45, 46). A few points about the method are worth noting.

- (i) Empirical terms are included to allow for the effects of wing thickness/chord ratio and body fineness ratio.

(ii) Evans showed that most wings can be represented by a uniform/non-tapered wing, having the same volume, mean sweep and thickness ratio as the original wing but with a span equal to $2(3)^{\frac{1}{2}} k_x$ where k_x is the radius of gyration of the original wing about the x axis.

(iii) The value of β in the denominator of the above expression should be based on the corrected Mach number. This may seem to be a trivial point but early experience in the 1940s showed that if β was based on the uncorrected Mach number (the more straightforward procedure), the blockage corrections could be seriously underestimated. This is an important point which was not always remembered in later years.

Having determined the interference velocity, $\Delta U = cU$, corrections to the stream quantities and force and moment coefficients follow as set out in both Refs 42 and 44.

(c) Interference at high lift

The corrections for tunnel interference described above can be applied to the results of tests when the flow past the model is attached. When the flow is partially separated, however, a less rigorous approach has to be adopted. The general practice in the UK and elsewhere has been to adopt the method put forward by Maskell and described in Agardograph 109 (Ref 42). It is not possible to represent the wake as a plane sheet of streamwise trailing vortices. Maskell based his approach on a study of the flow past a bluff body. Experimental measurements described in Ref 47 confirmed that, for wings of moderate to small aspect ratio, the localised regions of separated flow that develop as such wings begin to stall, resemble axisymmetric bluff-body wakes and Maskell concluded that the tendency to axial symmetry in the separated flow region could be assumed to be universal, applying to most wings of practical interest. The formulae derived from Maskell's model of bluff body flow are applied to the separated-flow part, C_D , of the total drag, ultimately giving a blockage correction in the form

$$\frac{q_C}{q} = 1 + \frac{1}{2} \frac{S}{C} C_D + \frac{1}{2} \frac{S}{C} (C_D - C_D^* - C_D) \quad (3)$$

where C_D is given by an extrapolation of the drag-due-to-lift in the attached flow range (see Fig 17) and q_C is the corrected value of the dynamic pressure, q . The example in Fig 18 taken from Ref 42 shows that, for this case at least, the formula is very successful.

8.1.2 Tunnel with ventilated walls at subsonic speeds

Ventilated tunnel walls were introduced in the early 1950s. In general, the walls have either longitudinal slots or perforations, the primary aim is to allow air to pass between the working section and the surrounding plenum chamber and so, to relieve the choking of the flow that would otherwise occur before reaching $M = 1.0$. A supplementary aim is to reduce and, if possible, eliminate the wall interference at subsonic speeds.

Early studies showed however that it was very unlikely that complete elimination of this interference would be possible with either slotted or perforated walls.

In this early work for slotted tunnels, it was assumed that the real wall could be replaced by an equivalent homogeneous boundary having a similar influence on the flow near the model as that of the real wall. The linearised boundary condition for this equivalent wall can be expressed by the following equation:

$$\frac{\partial \phi}{\partial x} + K \frac{\partial^2 \phi}{\partial x^2} = 0 \quad (4)$$

where ϕ is the perturbation potential, x is measured in the stream direction and n along the outward normal to the surface. The boundary condition relates to inviscid flow past a slotted wall; on this assumption, there is no pressure drop across the wall and this is in direct contrast to the porous or perforated walls where there is a pressure drop through the wall giving a boundary condition of the form:

$$\frac{\partial \phi}{\partial x} + P \frac{\partial^2 \phi}{\partial n^2} = 0 \quad (5)$$

where P is a porosity parameter defined by

$$\delta p = \frac{\partial P}{P} \frac{\partial \phi}{\partial n} \quad (6)$$

Several different types of wall can be identified.

- Closed wall : $K \rightarrow \infty, P = 0$
- Open jet : $K = 0, P \rightarrow \infty$
- Ideal slotted wall : $P \rightarrow \infty$
- Real slotted wall : both K and P terms present
- Perforated wall : $K = 0, P$ dependent on wall geometry and wall boundary layer thickness

For a perforated wall with normal holes, P varies with the pressure-differential through the wall; early tests at AEDC showed that, with normal holes, the value of P was very dependent on whether there was inflow or outflow through the wall to obtain a sensibly linear characteristic for the wall porosity, one needs a wall with the holes inclined at 60° in the direction of the flow, this reduces the resistance to outflow.

Agardograph 109 (Ref 42) contains many figures showing how tunnel blockage and lift constraint vary with K and P in different types of slotted and perforated-wall tunnel. It will be realised that these estimates were made by the methods available ahead of 1966 and, numerically, could be improved today. Nevertheless, the figures still serve to illustrate some important conclusions. For example, for an ideal slotted wall, the open-area ratio for zero blockage is very different from that needed for zero lift constraint, e.g. in a working section with 2 ventilated and 2 solid walls, the open-area ratio giving zero blockage is still calculated to give a lift constraint factor of 70% of that for an open wall. However, allowing for the viscous flow in the slots in the real slotted wall, increases the chances of finding an open-area ratio that will give completely interference-free flow (Ref 49). However, the viscous flow in the slots is also predicted to give a longitudinal gradient through the working section and hence, a buoyancy correction.

Turning to a perforated tunnel, Fig 19 shows the longitudinal distribution of the blockage effect. This is a most important graph. It will be seen that the longitudinal distribution for $\beta/P = 1.28$, which gives zero blockage at the model mid-point, is strongly asymmetric. This can lead to a sizeable buoyancy effect. Calculations for a typical subsonic transport model might show that this buoyancy effect would increase the drag coefficient at high subsonic speeds by as much as $\Delta C_D = 0.0010 - 0.0020$. This is one of the main

reasons why Ref 49 concluded that slotted walls were preferable to perforated walls for tests at subsonic speeds. As noted above, this is however not a clear-cut issue because the viscous effects with a real slotted wall might produce similar (but probably smaller) effects. The results in Fig 19 are for a rectangular working section with two perforated walls; subsequently, ARA calculated values for a circular tunnel using the formulae in Ref 48; numerically, the values are slightly different but in principle and indeed, in general magnitude, the results are very similar. Finally, Fig 20 shows the variation of the constraint factors δ_0 and δ_1 with B/P for perforated walls. Compared with the ideal slotted wall, this picture at first sight looks encouraging in that δ_0 passes through zero at a value of B/P similar to the value that gives zero blockage. As noted below, however, this does not mean that one can ignore constraint effects in existing perforated-wall tunnels.

Despite the fact that all this material had been published by 1966, many operators of tunnels with ventilated walls continued for many years not to apply any corrections to their results. They hoped that if the models were kept small (i.e. blockage area ratio less than 0.5%), the corrections would be trivial except close to $M = 1.0$. They felt that they could not apply the corrections as outlined above because they did not know the porosity factors, K and P for the walls of their particular tunnel. Determining these factors directly by measuring the pressure differential and flow through the walls would indeed be a difficult task. However, to ignore the existence of the corrections simply because there may be some doubt over the precise values always seemed to the present author to be the wrong attitude. ARA almost from the outset applied lift constraint corrections, blockage and blockage buoyancy corrections. These corrections were derived as follows.

- (I) porosity factors for the walls of the ARA tunnel were obtained by interpolation of the AEDC data contained in Ref 50 for the characteristics of various perforated plates with different plate thickness, hole diameter and open-area ratio,
- (II) these values of P were then used to obtain lift constraint factors and also, the blockage at the mid-point of the model. The derived values showed that the tunnel was too open to give zero interference. As regards lift constraint, the factors were about 70% of those that would apply in an open tunnel. The blockage corrections were predicted to be about $-0.25 \times$ those that would be calculated for the corresponding closed-wall tunnel. For a typical subsonic transport model with about 0.7% blockage area ratio, this implies that $\Delta M = -0.003$ at $M = 0.85$.
- (III) finally, blockage buoyancy corrections were derived on the basis of Fig 21. To understand this figure, one has to be aware of the open-area distribution along the walls of the ARA tunnel opposite the forward part of the model, the open-area is still climbing up to its final value of 22% which is then held constant opposite the rear of the model. The suggestion in Fig 21 that the buoyancy effect is not felt by the nose of the model was confirmed in a pressure-plotting test on a civil transport model, comparing the pressures measured in two tests with the holes in the walls respectively open and sealed. In effect, this means that the buoyancy correction is only half what it would have been if the open-area ratio had been 22% along the full length of the

model; even so, the correction is still highly significant; if it were not applied, a spurious drag-creep, amounting to more than 0.0005 in C_D , would be present: a seriously misleading result.

In the same comparative test with the holes in the tunnel walls alternatively open and sealed, the wing trailing-edge pressures were measured. These results suggested that, for a model of a reasonable size, eg 0.5 - 0.7% blockage, one could assume that the blockage correction (note: not the blockage buoyancy) was zero up to $M = 0.85$. This contradicted the earlier belief that at $M = 0.85$, $\Delta M = -0.005$. The new evidence appeared at the time to be unchallengeable and it became standard practice at ARA not to apply blockage corrections for this size of model up to $M = 0.85$ and to subtract 0.005 from the values that would be calculated by the previous method for Mach numbers above $M = 0.85$. It was felt that it was better to accept the direct evidence from the comparative test than to rely on the earlier method which was based on the unproven assumption that data from the AEDC experiments on perforated plates could be used to forecast the porosity characteristics of the ARA tunnel walls. The weakness in the original method was that it rested on the unproven assumption that the boundary layer thickness on the walls of the ARA tunnel was comparable with the thickness on the AEDC plates of similar geometry; if this was true, it would be somewhat of a coincidence. The practice of taking the blockage to be zero up to $M = 0.85$ has been retained since 1968 for the sake of maintaining data-base consistency although there has always been some unease as to whether this was the correct approach. For example, the comparison between wing pressure distributions measured on a model of the Super VC10 had shown good agreement, as reported in Ref 52, with those measured in flight even though blockage corrections derived by the original method had been applied; to have assumed that $\Delta M = 0$ up to $M = 0.85$ would have reduced the standard of agreement. Recently, it has however been realised that the results of the perforated versus solid wall comparative test can, in fact, be challenged on the grounds that by $M = 0.85$, the results in the solid-wall tunnel are not correctable, to use modern terminology, by simple Δa and ΔM corrections. There should also be a wall-induced camber effect which, for a given corrected α_M , would increase the suction near mid-chord and hence, the adverse pressure gradient back to the trailing edge. This camber effect could modify the boundary layer development over the rear of the upper surface of the wing and hence, it may be wrong to expect the trailing-edge pressure to be the same in the solid and perforated-wall tunnels. Calculations suggest that this could account for the discrepancy discussed above. It should be stressed that for the majority of tests on civil transport models, where the cruise Mach number is near $M = 0.80$, this uncertainty is of trivial importance but it has been described at some length here to illustrate the difficulties that can arise in applying the classical methods. This increases the importance of adopting a more modern approach and taking full advantage of the developments in CFD methods. These methods are discussed later in §8.3.

8.2 Wall Interference at Speeds Near and Above $M = 1.0$

8.2.1 Blockage corrections

Clearly, the classical approach to the calculation of blockage corrections by which, for a ventilated-wall tunnel, $\Delta M = \text{a factor} \times (\Delta M)_{\text{closed}}$ has to be abandoned before reaching $M = 1.0$. To obtain some guidance as to the interference close to and above $M = 1.0$, a major cooperative programme was launched

in the UK in the late 1950s in which several models to the same design but at different scales were tested in two slotted-tunnels at RAE and in the ARA transonic tunnel. The results of these tests are reported in Ref 53. The model was a wing-body combination with a 6% thick symmetrical wing having an aspect ratio of 2.83, a taper ratio of 0.33 and 45° sweep on the 0.5c line. The values of blockage near $M = 1.0$ revealed by these tests are, of course, a function of the open-area ratios of the walls of the tunnels being compared. It is therefore of more general interest to compare the values derived by the analysis of the experimental data with any theoretical predictions that may be available. The only theoretical method available in 1959 was that produced by Page of NACA Ames (Ref 54). The formulae proposed by Page for the blockage correction, ΔM_0 at $M = 1.0$ are given below:

$$\Delta M_0 = -0.9g(r^*/h)^{1/2}(r^*/x^*)^{1/2}$$

for rectangular slotted tunnel, and

$$\Delta M_0 = -0.82(r^*/R)^{1/2}(r^*/x^*)^{1/2}$$

for circular perforated tunnels

where g depends on the open-area ratio,
 r^*, x^* are the coordinates of the sonic point
on the nose of the equivalent body of
revolution to the model under test,
 h is the tunnel semi-height
and R the radius of the circular tunnel.

Values are compared in the table below

	RAE slotted wall tunnel	ARA perforated wall tunnel
Predicted ΔM_0 for 0.05% blockage model (1)	-0.007	-0.020
Predicted ΔM_0 for 0.5% blockage model (2)	-0.016	-0.049
Difference between (2) and (1)	0.009	0.029
Difference as derived from experimental data	0.010	0.020

The estimates in the above table were obtained using the numerical values suggested by Page, $g = 0.35$ for the slotted tunnel and a numerical constant of 0.82 for the perforated tunnel. The comparisons suggest that the value for the slotted tunnel is reasonable but that a smaller value than that proposed should be used for the perforated tunnel. On this and other evidence obtained later, ARA have used 0.6 as the numerical constant in an expression rewritten in terms of tunnel semi-height rather than radius.

It will be seen from the above formulae that blockage area ratio is no longer a relevant parameter at $M = 1.0$. The variation of ΔM with model size is much more in sympathy with the linear dimensions of the model and the distance of the model from the tunnel walls. It follows that the tunnel interference is still significant for very small models, eg even for a pitot tube while, on the other hand, increases in model size can be tolerated without as much penalty as one might intuitively have expected. Another important point about the interference at speeds close to $M = 1.0$ is that the interference can be greater for a slender model than for a model of low fineness ratio and of the same size. This was pointed out by Berndt in Ref 55, the reason is that the lateral decay of the flow field is less and hence, the potential interference at the wall greater with the slender model.

Strictly, it is not possible to obtain meaningful results at literally $M = 1.0$. The results of the comparative tests discussed above also showed that the aft movement of the terminal shock which should reach the base of the model just above $M = 1.0$ was considerably delayed on the 0.05% blockage models. This means that, in a test at an uncorrected Mach number of say, $M = 1.05$, the flow over the front part of the model genuinely resembles what would be expected in free-air at $M = 1.05$ but the flow over the rear part of the model is more representative of what might be expected at $M = 1.0$. Such data are completely unrepresentative of the free-air results and they cannot be corrected. It cannot be emphasised too strongly that one should not test at Mach numbers very near to and just above $M = 1.0$. All test programmes should omit the range between say, $M = 0.98$ and $M = 1.05$ dependent on the size of the model. This situation would be improved if it were possible to reduce the wall open-area ratio to a very low value when testing near $M = 1.0$.

At higher Mach numbers, tunnel interference takes the form of wave reflections from the tunnel walls. Clearly, in a solid-wall tunnel, one is not in the clear until the reflection of the bow shock has passed behind the base of the model. The situation is much the same in a slotted-wall tunnel but perforated walls provide some alleviation. The 22% open-area ratio, normal holes of the ARA tunnel are successful in largely cancelling the reflections of incident shock waves at $M = 1.15$ and above (see Fig 22) but, with normal holes, expansion flow fields reflect as discrete shock waves. It follows that the data in the ARA tunnel do not become effectively interference-free until the reflections of the forebody expansion flow field have passed behind the base; inclined holes would improve this situation, for the reasons explained earlier. In any new perforated-wall tunnel, one would choose walls with inclined holes of variable open-area ratio.

8.3 The Modern Approach

It was noted in §8.1 that the classical approach to the calculation of tunnel interference at subsonic speeds suffered from several important weaknesses. To list these briefly

- the methods rely on a small-perturbation representation of the model,
- for tunnels with slotted walls, the homogeneous wall boundary condition is known (Ref 56) to be unrepresentative,
- for tunnels with perforated walls, the porosity characteristics are uncertain,
- the methods do not take proper account of the fact that the wall interference can be very dependent on the boundary layer development along the walls, and
- as one approaches $M = 1.0$, it is no longer valid to assume that the interference is correctable in terms of simple corrections to M and a .

Since 1978, there has been a major effort at many research establishments to develop new, improved methods of estimating wall interference. Most of these involve the measurement of pressures on or near the tunnel walls, most involve the use of the powerful CFD tools that have now become available. Broadly, the methods can be divided into two types

- the first type can be described as 'model representation methods'. These require only a relatively limited number of wall pressure measurements but need a reasonably accurate calculation of the

flow field around the actual model. At high subsonic speeds near $M = 1.0$, recent US work (Ref 57) has suggested that one has to undertake Navier-Stokes calculations; the results of inviscid Euler calculations can be completely misleading.

(ii)

the second type, known as two-component methods, do not require a calculation of the local flow field around the model but involve the measurement of a relatively large number of streamwise and normal velocities near the walls. Methods of the second type are therefore easier to apply in the case of solid-wall tunnels where one can make the assumption that the flow near the wall is parallel to the wall (strictly, parallel to the boundary layer on the wall) and hence, one still only needs to measure one flow component.

Methods of the first type were developed by Smith of NLR (Ref 58) and Capoller, Chevalier and Bouniol at ONERA (Ref 59). In the US, the initiative came from Kemp at NASA Langley (Ref 60) followed by Murman (Ref 61) and recent US work is described in Refs 62, 57 and 63. The second type of method was developed by Ashill and Weeks at RAE Bedford (Refs 64, 65) and currently, serious use of this technique is being explored in the RAE 5 metre tunnel (Ref 66). Historically, it can be argued that the idea of using wall pressure measurements as a guide to model blockage corrections was introduced by Coethert as long ago as 1940 (Ref 67).

A relatively simple method of the first type is being used to correct data from the RAE 8 ft x 8 ft tunnel (Ref 17). Measurements of static pressure are made at four points on the tunnel walls - two in the roof close to the model centre of volume, and a corresponding pair in the floor. The model is simulated by a distribution of point sources and sinks and calculations are made of both the increment in streamwise speed at the position of the wall holes due to both these singularities and their images, and of the blockage increment in velocity at the model. This provides the ratio of the blockage increment to the arithmetic mean of the calculated increments in speed at these four holes. It is then assumed that this ratio applies in the real tunnel flow and hence, one obtains the blockage from the wall pressure measurements. Results from applying this approach have been found (Ref 64) to be in good agreement with results obtained by a potentially more accurate two-component method and it is believed that the technique is accurate up to Mach numbers approaching the choking value.

An obvious application for a method of the second type is to the correction of data obtained at high model lift in a low speed tunnel. The flow around the model being partly separated is difficult to simulate mathematically with any accuracy but this is not needed for a method of the second type. The method developed by Ashill and Weeks (Ref 66) has therefore been applied to the results of tests on a very large half-model in a landing configuration in the 5 metre tunnel (Ref 66). Measurements of pressures were made at about 15 tappings on each of 10 streamwise rows and upwash, sidewash and streamwash corrections have been derived. Typical results are shown in Fig 23. Results obtained by using the standard correction technique are also shown for comparison. Reasonable agreement is shown for the incidence correction in Fig 23a but a significant discrepancy is evident in the streamwash correction in Fig 23b. It appears that the standard technique leads to an appreciable overprediction and these results constitute a warning that Maskell's approach may not be satisfactory for some realistic cases of partially

separated flow. It seems likely that, despite the need for a large number of pressure measurements extending far upstream and downstream of the model, two-component methods will find increasing application in the future, particularly for models with complex flows, eg models with bluff shapes, ASTOVL models, helicopters with rotor simulation and models at high lift.

Ref 64 contains an example of blockage corrections calculated by methods of both types compared with the value obtained by the classical method discussed earlier. This comparison is shown in Fig 24; the application relates to a two-dimensional aerofoil test in the 8 ft x 8 ft tunnel at RAE Bedford. Good agreement is shown between the results for the model representation and the two-component methods but all these results predict notably greater blockage than the classical method, particularly for C_D when the flow over the aerofoil is supercritical.

The recent experience at AEDC in applying these modern methods to perforated-wall interference at high subsonic Mach numbers near $M = 1.0$ is described in Ref 57. Two types of technique are discussed:

- (a) A pre-test predictive technique in which the wall boundary condition is not based on a global approach as in classical methods but allows for local variations in the porosity characteristics. This means that the slope of the characteristic is no longer a constant but is a function of the boundary layer thickness on the walls as shown in Fig 25 taken from Ref 62. This graph refers to the 60° inclined holes of the AEDC perforated walls but similar graphs could be created for other tunnels if the necessary experiments were made. Increasing the lift on the model will increase the pressure variation induced on the wall at high subsonic speeds and, as a result, the boundary layer thickness on the top wall. This is the major reason for the increase of ΔM with lift referred to above. In the pre-test predictive method, the tunnel flow-field calculation is made with the AEDC boundary condition specified on the tunnel wall.
- (b) The US WIAC approach for correcting the measured results in which the flow around the model is calculated with the pressures measured on a boundary close to the tunnel walls defining the boundary condition.

Initially, the calculations were made by an Euler code which was expected to be more than adequate for an application in which the model was a wing-body combination with 30° swept wings with NACA 0010 4 symmetrical sections. However, these calculations failed in that the derived corrections seriously overcorrected the results for the large blockage model in the small tunnel when compared against those obtained with the same model in a larger tunnel. Use of a Navier-Stokes code, however, goes a long way towards bringing the corrected results from the two tests into agreement. These comparisons are presented in Figs 26a,b, r in this figure is the wall open-area ratio. The authors of Ref 57 draw the conclusion that it is necessary to allow for viscous effects in the model flow-field calculation. This may well be true but the present author believes that the Euler code comparison could have been significantly improved if the free-air and model calculations had been made for different Mach numbers, the difference in Mach number corresponding to a first-order ΔM correction. In case the procedure of these WIAC calculations is not clear, it is worth noting that the values of C_D are obtained by integration of pressure distributions in which each

individual pressure has been corrected by interference terms which vary along the chord. In other words, the ΔM , $\Delta \alpha$ approach has been abandoned and there is now some hope that correction methods, both pre- and post-test have been developed that will remain valid up to very close to $M = 1.0$. However, research and development will have to continue for some time to come before one could claim that a correction method is available for routine use. Ref 63 notes that the WIAC procedure was apparently not completely successful in correcting some experimental data from the NASA 0.3 metre Cryogenic Tunnel, but it is possible that the lack of full agreement between a corrected experimental and theoretical result may be due to inadequacies in the turbulence modelling in the Navier-Stokes calculations, rather than any fundamental flaw in the correction method.

8.4 Adaptive Walls

None of the major transonic tunnels used for performance testing are fitted with adaptive walls and so a discussion about the development of adaptive walls is really outside the scope of this lecture. Nevertheless, for the sake of completeness, it should be noted that, in many research establishments, there has been considerable progress with adaptive walls since 1975. Achievements are described in detail in the final report of AGARD FDP Working Group 12 (Ref 4) which contains many references on the subject, and a summary of some of the main achievements is available in Ref 1.

The basic concept of an adaptive-wall wind tunnel is to match two independent flow-disturbance quantities measured at an interface in the tunnel experiment to the same quantities computed for an interference-free outer flow beyond the interface. Application of the concept has been greatly helped by advances in wind tunnel instrumentation, wall-control mechanisms, control technology, computer hardware and, more particularly, CFD algorithms and codes. In two-dimensional flow, many establishments have shown that it is possible to reduce the residual interference after shaping the walls to a very low level. The residual interference can be calculated by the methods discussed earlier using the information already available for shaping the walls. The concept has been successfully applied to Group 2 Flows (supercritical flow extending to and beyond the test-section walls). In the context of the present lecture, the most significant development has been the evidence suggesting that two-dimensional adaptive walls can be used successfully to minimise the interference in tests on three-dimensional models. This evidence is presented in detail in Chapter 4 in Ref 4, the aspect ratio of the tunnel working section is an important parameter. Experience at supersonic speeds is limited at present.

9 MODEL SUPPORT INTERFERENCE

9.1 Rear Sting Interference

In high speed and transonic tunnels, the models are usually supported on a sting from the rear of the model protruding either from the centre of the rear fuselage or as a blade from underneath or occasionally from the top of the fin. As already noted in §3, the consequent interference effects can be significant. They arise for two main reasons. First the presence of the sting itself and particularly, of any taper on the sting can have a forward influence on the flow over the rear fuselage. In general, the flow velocity is reduced and the drag reduced. Panel methods can be used to estimate these effects. Secondly, the rear

fuselage has to be truncated and distorted to admit the sting; in this respect, calculations are less effective because viscous effects are paramount.

The technique in regular use, in the UK to obtain these sting corrections experimentally is to mount the model on twin stings from the wings and then to measure the forces on the rear fuselage with and without a simulation of the rear sting. Fig 27a is a diagrammatic picture of the rear model layout for such a test. The balance measures the forces on the rear fuselage with the dummy central sting in position as shown and with the sting removed, the bore filled and the rear fuselage restored to the correct aircraft shape. The difference between the two sets of balance readings gives the sting corrections. This may sound simple but much development testing had to be undertaken before the technique gave satisfactory, repeatable results. Allowance has to be made for the pressure force acting on the internal fuselage surfaces aft of the split and, when the dummy sting is present, for the pressure force acting on the seal plate. Accurate determination of these terms is vital; in an example quoted in Ref 15, the forces acting in the drag direction were:

- (I) force on external wetted surface:
 $C_D = 0.0022$,
- (II) force on internal fuselage surface:
 $C_D = 0.0015$,
- (III) force on seal plate:
 $C_D = -0.0016$.

Thus, the unwanted pressure forces are each of similar magnitude to the actual rear fuselage drag. These corrections are obtained by measuring about 50 pressures inside the fuselage and about 10 pressures on the seal plate. Various precautions have to be taken, the gap between the forward and rear parts of the model has to be kept small, the model has to be designed to inhibit flow in and out of this gap and to give near-uniformity in pressure over the cross-section at the gap, the response characteristics on both sides of the pressure diaphragm in the transducers have to be carefully matched and finally, one has to be able to move the forward part of the dummy sting by means of a small integral actuator to locate it correctly in the bore.

The success of this twin-sting technique depends on a number of basic assumptions:

- (a) one can ignore the possible effects of the rear sting on the flow over the forward part of the model,
- (b) one can ignore the possible interference effects of the twin stings on the flow over the wing - at least to the extent that these effects might affect the difference between the two tests,
- (c) one can calculate, eg by a panel method, the possible interference effects of the yoke joining the twin stings at the rear.

On a closely coupled configuration such as that shown in Fig 27, assumptions (a) and (b) are open to question. The technique as practised in the past is only viable if there is a fair length of uniform flow upstream and downstream of the split and one cannot meet this requirement with a configuration such as Fig 27b. ARA are therefore developing a modified form of the technique as illustrated in Fig 28. The model is still mounted on twin stings but now, forces are to be measured on the complete model with balances fitted in the forward end of the pair of stings. The balances will be calibrated individually and with the model installed in the rig. Finite element analysis was

employed in the design of the new rig, the stings are very slender and have reduced torsional stiffness; the model is mounted further forward relative to the yoke. As with the previous rig, the sting corrections will be determined as the difference between the results for two configurations with alternatively the true afterbody and the distorted afterbody and dummy sting.

Some typical sting corrections were discussed earlier in §3, on the basis of the results in Figs 3a,b. It should be noted that these results relate to stings designed for tests at a stagnation pressure of 1 bar. For tests in a pressurised tunnel, it is likely that the degree of distortion of the rear-end would be greater. A recent paper (Ref 69) from NASA Langley has quoted experience which indicates that sting corrections can amount to 9-10% of total aircraft drag and can vary in a non-linear fashion with Mach number. It is therefore likely to remain as a major problem in a pressurised tunnel.

2.2 Strut Interference in Low Speed Tunnels

For most of the testing in large low speed tunnels such as the RAE 5 metre tunnel, the F1 tunnel at Le Fauga and the DNW tunnel, the models are mounted on struts from below and the forces are measured on an underfloor balance (Ref 70). Two different types of mounting are commonly used: either a 3-strut mounting with two underwing and one tail strut or a single central strut. The interference is determined experimentally in a similar fashion to that described above for sting interference. In other words, the model is mounted in a different way, ie either on a rear sting or on a strut from above, and comparative tests are made with and without dummy replicas of the standard strut supports. Possible layouts for such tests are shown in Fig 29a for the 3-strut arrangement and in Fig 29b for the central strut scheme. Such tests to determine the interference can be laborious and time-consuming and so, there is great incentive to find whether these interference corrections can be predicted by a theoretical method. This has led to much activity in recent years and it is worth including a brief summary of what has been learnt from these studies. Further details are to be found in Refs 70-73.

A typical test programme for the 3-strut case would be:

- (a) tests with the model supported on a rear sting but with no representation of the guards or struts,
- (b) tests with the model supported on a rear sting in the presence of all three dummy guards mounted on the floor, but without any struts (Fig 29a),
- (c) tests on the model, together with dummy front struts supported on the sting in the presence of all three dummy guards mounted on the floor. For these tests, the struts would be represented by replicas of the upper part of the real struts, these would be hung from the wing and would terminate just inside the guards,
- (d) tests on the exposed struts mounted on the underfloor balance with the guards mounted on the floor but with no model present, this test serving to establish the basic strut tares.

Such a test programme is clearly extensive and added complexity arises from the fact that whenever the incidence is changed, it is necessary to readjust a fitting in each dummy strut and possibly alter the fore-and-aft positions on the dummy

guards to avoid any contact between the dummy struts and guards; hence, a multiplicity of short runs are required.

A test programme as set out above recognises the need to separate the effects of the struts and of the guards. The near-field interference of the struts largely depends on viscous effects and is not readily amenable to theoretical calculations. However, the far-field effects of the guards, which are generally the more important effects numerically can be calculated by panel methods.

This is not easy: a typical calculation for a 3-guard/model configuration could need approaching 4000 panels. However, as shown in Fig 30, relatively good agreement with experiment can be obtained up to near the value of C_L at which the wing stalls, this applies to the interference on both C_L and C_D . A full panel calculation can therefore be successful but there is still a need to find whether any simpler method will give comparable results. Ref 71 presents such a method.

Ref 71 is illuminating in that it contains a detailed description of the physical nature of the interference. Four significant effects are identified:

- (i) an upwash due to the strut/guard displacement effect giving a term of the form, $\Delta C_L = \text{constant}$,
- (ii) a streamwash, again due to the guard displacement, giving a term of the form, $\Delta C_L \propto C_L$,
- (iii) an upwash induced by the effects of the trailing vortex wake from the strut guards. This wake is associated with the side force induced on the guards by the lift on the model. The ΔC_L from this term is proportional to the lift coefficient, C_{LG} , on the guards,
- (iv) and finally, a sidewash and streamwise effect again due to the guard side force. In this case, ΔC_L is proportional to the product of $C_L \times C_{LG}$.

It follows that the total lift interference is of the form

$$\Delta C_L = K_1 + K_2 C_L + K_3 C_L^2$$

where K_1 and the upwash dependent contribution to K_2 are proportional to the wing lift-curve slope and the sign of K_3 depends on the wing sweep being negative for a sweepback wing and positive for a sweptforward wing. Fig 30 shows that the new features in this analysis, viz the introduction of term (iv) and the empirical use of the measured lift-curve slope including its non-linearity at high C_L produces reasonable agreement with experiment even at and beyond the stall. This success, to quote from Ref 71, "holds out the prospect of predicting at least some aspects of the model support system lift interference on wings through the use of fairly simple panel method calculations". One has to admit, however, that this simplified method cannot provide a sufficiently accurate prediction of the drag interference due to the guards. This is thought to be due to the relatively large changes in interference over the area of the wing these effects cannot be averaged accurately in a simple fashion. Also, there is significant viscous drag interference due to the struts that has to be determined experimentally. Turning to the central single strut mounting arrangement, in general, there will be no side force on the support but, on the other hand, the blockage interference effects of the strut/guard

will be more serious than with the 3-strut arrangement. If the strut is circular, part of the underside of the model will be exposed to an interference flow field which, in principle, could be sensitive to changes in Reynolds number according to whether the flow around the strut contains a laminar or turbulent separation. Such an effect, greatly increasing the strut interference at low Reynolds number, has been found in the test range of the RAE 5 metre tunnel. Experience suggests that the interference depends strongly on the local geometry and is greatest for configurations where the underfuselage is notably non-circular (Ref 73). There can be a significant interference with the aerodynamic lateral characteristics; this can be minimised by reducing the strut diameter, ideally to $0.2 \times$ fuselage diameter or less.

10 BOUNDARY LAYER SIMULATION AND SCALE EFFECT

10.1 The Need to Fix Transition

The standard practice in most transonic and low speed tunnels operating at Reynolds numbers in the range up to $R = 15 \times 10^6$ is to test with boundary layer transition fixed artificially near the wing leading edge and body nose. The case for adopting this approach has been established for many years. There are two main reasons:

- (i) allowing transition to occur naturally would mean that the transition position could vary with both C_L and Mach number. Extrapolation of the data to full scale would be difficult unless the transition positions at all test conditions were determined accurately. To date, this would have been very laborious although there is now some hope that this may be possible in the future with the use of liquid crystals,
- (ii) it is important to ensure that, as on the full-scale aircraft, it is a turbulent boundary layer that interacts with the shock. The need to avoid a laminar or transitional boundary layer interaction was established as long ago as 1957 (Ref 74). A separated laminar boundary layer can reattach as a turbulent layer, thus giving spuriously optimistic results relative to those with a turbulent boundary layer ahead of the shock.

Examples of misleading results obtained with natural transition are shown in Fig 31. The bucket in the $C_D - M$ curve is not a genuine bucket, it is due to transition moving aft on the wing upper surface as the local supersonic region extends aft between $M = 0.72$ and 0.75 . The retention of a high lift-curve slope up to beyond $\alpha = 2^\circ$ with natural transition is related to the ability of a laminar separation to remain as a closed bubble and for the boundary layer to reattach as a turbulent layer. There is a danger that these results could have been seriously misinterpreted. For some aerofoils, buckets in the $C_D - M$ curve have been found in transition fixed results; these would have been genuine features of the aerofoil design but a bucket due to transition movements in transition free results has to be dismissed as having no relevance to the full scale performance. Similarly, without a clear understanding of what can happen with a laminar boundary layer/shock interaction one might have been tempted to treat the differences in the lift curves as an example of genuine scale effect. In fact, it is likely that the lift-curve slope in the transition-free results near $\alpha = 2^\circ$ is higher than the value that would be obtained with transition near the leading edge at any Reynolds number.

The general advice, therefore, is to test with fixed transition. There are however some cases where this advice does not necessarily apply:

- (I) as noted later in §10.4, transition-free tests can be included in test programmes for diagnostic purposes.
- (II) transition-free tests may be the appropriate choice if it is known that, for reasons of either relatively high test Reynolds number (say, $R = 15 \times 10^6$), relatively high tunnel turbulence or simply adverse pressure gradients in the pressure distribution, transition will occur naturally near the leading edge,
- (III) cases where the test objective is to measure the hinge moments on a trailing-edge control; for these, it may be important to obtain the thinnest possible boundary layer over the control,
- (IV) tests on models of aircraft designed to achieve extensive laminar flow in flight. For these, new model test techniques will have to be developed as discussed in §10.7.

10.2 Methods for Fixing Transition

The basic requirements are to fix transition with the minimum disturbance to the flow and in a consistent, repeatable manner. In the UK, the favoured method is to apply a band of glass balls known as ballotini. These are preferred to carbosilicon because they offer better control of roughness height. The ballotini balls are sieved and stuck to the model surface by blowing them lightly on to a tacky cement such as Araldite 103/951. In the search for consistency, alternatives to ballotini are favoured in certain quarters, eg

- (I) BAE Brough have used transfer characters devised for graphic work (Letraset) to produce regular transition strips.
- (II) RAE have developed a technique in which a row of holes is drilled in a tape at regular intervals and the minute mounds so formed provide a consistent distribution of roughness.
- (III) Boeing have devised a somewhat similar method whereby a tape with a row of holes drilled at regular intervals is stuck to the wing surface and then an epoxy-based filler such as Isopon is spread over the tape; the surplus filler is removed and the tape is lifted from the wing leaving a row of excrescences.

Various criteria are available to determine the required roughness height. Of these, the best known are those due to Braslow and Knox (Ref 75), Van Driess and Blumer (Ref 76), Evans (Ref 77) and Potter and Whitfield (Ref 78). The Braslow and Knox criterion states that

$$R_k' = 600$$

where R_k' is the Reynolds number based on the roughness height, k , and the flow conditions at the top of the roughness. All the criteria forecast that the required roughness height increases with Mach number by about 15-20% at $M = 1.0$, 33% at $M = 1.5$ and 80% at $M = 2$ for the Braslow and Knox criterion (with the values somewhat dependent on Reynolds number). This is an important point not merely for testing at supersonic speeds, it is also the explanation why general experience has shown that one needs a greater roughness height to fix

transition at buffet-onset than in the cruise in tests at subsonic speeds. Roughness height is not the only significant parameter; the width of the roughness band and the density of particles in the band are also important. The width of the band is usually either 2.5 mm or 1.25 mm. The required roughness height to fix transition depends on the interpretation the wind tunnel engineer places on the phrase 'a sparse roughness band'. Even a change in density from 4% to 16% can be significant; the 4% band has to have a greater height to fix transition on a given wing at a given Reynolds number. The desire to use a very sparse band (to avoid a substantial drag penalty) appears to lead, in general, to a need to use a roughness height greater than suggested by the Braslow and Knox criterion.

Traditionally, the roughness drag penalty has been predicted by a relation such as

$$\Delta C_D = 2 m \Delta \theta / c$$

where m is a magnification factor that can be estimated by Ref 79, c is the local wing chord and $\Delta \theta$ is the increment in momentum thickness at the trip and induced by the trip. However, recent trends in aerofoil and wing design are such that the effects of the trip should not be thought of simply as an increase of drag. The increase in boundary layer thickness can also give a significant reduction in rear loading and hence, often, an increase of wave drag for a given total lift. An approximate relation for the increase in momentum thickness at the trip is

$$\Delta \theta = \frac{1}{2} N A_F t C_D$$

where N is the number of excrescences per unit area, A_F is the frontal area of individual excrescences and t is the streamwise width of the transition trip. C_D is the drag coefficient of each excrescence based on its frontal area. There is little available evidence for an accurate estimate of C_D but clearly, $C_D = 1.0$ is an upper bound. On the assumption that C_D is unlikely to vary rapidly with Mach number, the values in Ref 80 can be used. The effects of the trip can then be estimated by means of a CFD calculation including $\Delta \theta$ as an input parameter.

The choice of a suitable chordwise position for the transition trip will be discussed later in §10.4 but, for the present, one can note that, to obtain a turbulent boundary layer/shock interaction without any undesirable interactions between the flow over the trip and the shock strength and position, the trip should always be at least 0.10c and preferably 0.15c ahead of the shock.

Another technique that has been used successfully (Ref 81) in research experiments is to inject air into the boundary layer in order to fix transition. This is a much more elegant technique. In a two-dimensional test with on-line monitoring of the data, it will always be possible to see whether one is being successful in fixing transition. One does not have to be very precise as to how much air one uses. In contrast with tests with distributed roughness, the penalties of using more than the minimum required amount of air are trivial.

10.3 Methods for Determining Transition Position

The standard method in most tunnels of determining the transition position and of checking whether a roughness band has been effective in fixing transition is by means of a sublimation test with say, a 10% solution of acenaphthene in Inhibisol. Closed circuit television is used to judge when the sublimate has evaporated in areas where the boundary layer is turbulent and photographs are

taken at regular intervals. There is some difference of view as to whether one should spray the entire wing surface or merely the areas downstream of the roughness band. Some believe that to spray ahead of the band and in the band reduces the effectiveness of the band. This implies that if the wing has been sprayed ahead of the band, one should accept some turbulent wedges downstream of the band; otherwise, the roughness size that is accepted will be larger than that needed to fix transition on a clean wing. If the wing is merely sprayed downstream of the band, a 'good trip' in a condition where drag is important is probably one that gives some very small wedges but in a buffet-onset condition, it may be preferable to choose a band that leaves no wedges. One should always choose the smallest possible roughness height that meets the criterion as agreed between the wind tunnel engineer and the customer for the tests and one should be consistent in what one accepts.

It may be difficult to apply a sublimation technique in a pressurised tunnel because of the time needed to pressurise the tunnel. A plot of C_D versus Reynolds number and a comparison of this plot with theoretical predictions will be useful in identifying ranges in which the transition fixing has not been fully effective but cannot be regarded as a complete answer to the problem. A decrease with Reynolds number in the excess profile drag on one part of a three-dimensional wing could, for example, mask a failure to fix transition on another part of the wing. A visual aid for use in pressurised and cryogenic tunnels is therefore needed; hence, the interest in liquid crystals. Other novel techniques are being explored. For example, Gartanberg at Old Dominion University (Ref 82) is using an infra-red imaging system. Use of such a system becomes difficult at low temperatures, partly because the difference in recovery temperature in laminar and turbulent regions decreases at low temperature and partly because the sensitivity also decreases. However, there seems to be some hope that these difficulties can be overcome by monitoring the reaction to a transient heat flux; this should be more rapid in the turbulent areas.

10.4 Simulation Methodology, Test Programme

Complete simulation of the full-scale boundary layer behaviour in a tunnel test at reduced Reynolds number is obviously never possible. All that one can hope to do is to devise a methodology that will place the testing and the extrapolation to full scale on a sound scientific basis. AGARD recognised this need and in 1984 set up Working Group to review the subject and propose an appropriate methodology. This Group reported in 1988 (Ref 8). It is hoped that, in the future, increasing use will be made of the AGARD methodology. It is based on the best of current practice and it represents an attempt to use the wind tunnel and CFD as partners in an integrated approach. The description below and in §§10.5 and 10.6 summarises the main features, for further details and a background study of the subject, the reader should consult the comprehensive treatment in Ref 8.

There is much more to a viscous simulation methodology than making decisions about whether, how and where to fix transition. The methodology as proposed requires action before, during and after the tests. It contains six steps:

1: Collection of relevant information

For example,

- What are the aims of the test?
- What are the important design and operating conditions?
- What transition Reynolds number can be achieved in the tunnel?

2: Preliminary theoretical calculations

Calculate by the most advanced theoretical method conveniently available the wing pressure distributions, boundary layer development and, if possible, the wave drag and viscous drag at the important operating conditions. The general aim of these calculations is to give the test engineer an early idea of whether and where the flow over the model is likely to be subject to scale-sensitive viscous effects, eg

- Is there likely to be a rear separation in the model tests?
- Is there likely to be a laminar separation near the leading edge ahead of any possible transition trip position?

These calculations will also provide a guide to where to locate a forward trip, eg it should not be placed at or immediately behind the peak suction position, and to the range of positions where a trip would still meet the requirement mentioned earlier of being 0.10 - 0.15c ahead of the shock.

3: Initial datum tests with forward fixed and with free transition

The aims of the test with a forward trip are

- (a) to establish the absolute drag levels free from any uncertainty due to an unknown length of laminar flow
- (b) to compare with the results of the theoretical calculations undertaken in step 2, any disagreement should be explored as it may indicate the existence of a strong viscous-inviscid interaction,
- (c) to find how the shock position varies with C_D and Mach number and so to define what will be possible in later tests with different transition positions,
- (d) to study the nature of the pressure distributions aft of the shock to establish whether any separation when present extends rearward from the shock (class A flow) or spreads forward from the trailing edge (class B flow), the distinction originally introduced by Pearcey (Ref 83). Particularly if it is a class B flow, strong scale effects are to be expected and it is only recently that theoretical methods have been developed that are capable of dealing with these (Ref 84).

The test with free transition is included largely for diagnostic purposes. For example, it will show

- (i) whether a laminar boundary layer can be maintained back to the shock,
- (ii) whether any rear separation observed in the transition fixed test is still present. If so, it will not be possible to avoid this at the model test Reynolds number,

- (III) the furthest aft shock position that can be achieved at the test incidence and Mach number, the boundary layer thickness being less in a transition-free test than in any test with a trip.

4: In-depth study of viscous effects

Steps 1-3 have in a sense all been preliminaries to step 4. The data taken in Step 4 will be the definitive data that will form the basis for the prediction of the full-scale aircraft performance. In practice, steps 3 and 4 may frequently be combined in a single test programme in the tunnel. Step 4 will be described below.

5: Interpretation of the data after the tests

This step will be discussed in §10.5.

6: Extrapolation of the data to predict the full-scale performance

This step will be discussed in §10.6.

Returning to step 4, there are two approaches to an in-depth study of the viscous effects: one can either, if possible, conduct Reynolds number sweeps with transition position held constant at the position forecast for flight at the full-scale Reynolds number or second, one can conduct a sweep through a range of transition positions at a given test Reynolds number. It will be realised that, in both cases, the tests are really a sweep through a range of boundary layer thicknesses. Whenever possible, both types of sweep should be included in the programme.

There are limitations on the use of both approaches. Reynolds number sweeps can only be accomplished satisfactorily in a variable density (or variable temperature) tunnel. Admittedly, two models at different scale, e.g. a complete and a half-model can be tested but, since it is unlikely that one could obtain precise agreement between complete and half-model data at the same Reynolds number, one still needs to be able to vary stagnation pressure (or temperature), i.e. one uses the half-model to extend a trend as indicated in Fig 35. The range of transition positions that can be covered in a transition sweep is limited by the need

- (I) to ensure a turbulent boundary layer/shock interaction,
- (II) to avoid any local interaction between the trip and the flow near the shock,
- (III) to minimise, as far as possible, any serious disturbance to the supercritical flow development over the forward part of the wing surface,
- (IV) to ensure that one can claim that there is laminar flow upstream of the trip in all test conditions, otherwise, interpretation of the results will be laborious

These limitations imply that with any one transition trip, one can obtain valid data in a corridor (Fig 32a) between two boundaries, AA and BB, corresponding to the Mach number (AA) at which the shock wave moves 0.10 - 0.15c downstream of the trip as Mach number is increased and second, the Mach number at which the shock wave has moved forward to 0.15c behind the trip under the influence of a shock-induced separation. If the wing is being pressure plotted, these boundaries can be determined easily but, even if only overall forces and moments are being measured, they can be detected with fair certainty. AA lies just beyond

a spurious hump in the drag polars as illustrated in Fig 32b. The excess drag in these humps arises because of a local interaction between the trip and the development of the supercritical flow as the shock passes over the trip as it moves downstream with increasing Mach number. As shown in the upper picture in Fig 32b, the flow accelerates over the trip and a second shock is formed downstream of the trip; with a small further increase in Mach number, the two supersonic regions combine to give a final shock wave that is stronger and lies further downstream than if there was no interference from the trip; hence, the extra spurious wave drag. Similarly, on the approach to the boundary BB, the forward movement of the shock is arrested and the shock hesitates downstream of the trip and this hesitation can be recognised by a slight increase in lift-curve slope and, generally, a nose-down blip in pitch moment.

Ideally, one needs 3 or, if possible, 4 points on a transition sweep to establish a trend. This is only possible in a relatively small part of the $C_L - M$ plane as shown in Fig 32c but fortunately, for a subsonic transport, this includes the cruise conditions and most of the buffet-onset boundary. The shock pattern over a three-dimensional swept wing is likely to create further limitations near the wing tip and root but on a transport wing, this is unlikely to be too troublesome because separation-onset generally occurs just outboard of the intersection of the 3-shock pattern near mid-span. The three-dimensional nature of the shock pattern will pose more serious problems on a combat aircraft wing of moderate aspect ratio but the technique has still been practised successfully. The above description has been somewhat simplified, e.g. as noted earlier, trips of different height may have to be used in the cruise and near buffet-onset. Using a trip that is effective (but only just effective) in the cruise, will be excellent for drag but it liable to give a spuriously optimistic estimate of buffet-onset, while using a trip that is adequate for buffet-onset will give a pessimistic idea of the drag. Other qualifications are to be found in Ref 8.

10.5 Simulation Methodology, Interpretation of Test Data

Fig 33 presents results from some two-dimensional aerofoil tests (Ref 85) where it was possible to undertake both Reynolds number and transition sweeps. The results were obtained before the ACARD Group was set up but they illustrate the way in which results should be interpreted in step 5 of the methodology. 'A' is a Reynolds-number sweep with transition near the leading edge: fixed artificially at $R = 2.3 \times 10^4$ but occurring naturally near the leading edge at higher Reynolds numbers. 'B' is a transition sweep at $R = 2.3 \times 10^4$; it appears that, by testing at $R = 2.3 \times 10^4$ with transition at 0.30c, it is possible to obtain results comparable with those that would be obtained with forward transition at about $R = 8 \times 10^4$. This example suggests that all test results from both Reynolds number and transition sweeps should be plotted as in Fig 34 against either Reynolds number or an effective Reynolds number having found how to convert transition position into an effective Reynolds number. One would not necessarily choose C_D as the 'simulation criterion' because the drag will include a strong skin friction contribution and there is no intrinsic reason why C_D should vary with R in the same manner as the wave drag and other scale-sensitive parameters. Looking at the past literature, one might be tempted to choose say, shock position, but recent research suggests that shock strength or some function of the boundary layer over generally the wing upper surface may be a better choice. Before discussing the major issue as to how to

convert transition position to R_{eff} , the aim in plotting graphs such as that illustrated diagrammatically in Fig 34 must be discussed.

Graphs such as Fig 34 are plotted as a prelude to the extrapolation to full scale Reynolds numbers in step 6. The primary aim is to compare the measured trends with the computed trends from the preliminary calculations in step 2. These calculations were made by 'the most convenient method readily available'. At the time the AGARD methodology was published, it was assumed that this phrase implied that the calculations would not be able to allow for any form of strong viscous-inviscid interaction. Methods (Ref 84) have however now become available that are capable of allowing for a limited separation near the trailing edge. This does not invalidate the main deduction from Fig 34 that below R_{crit} , where there is a major divergence between the measured and computed trends, it is probable that a strong viscous-inviscid interaction is present in the experiment. Extrapolation of the results to full scale has therefore to be based on the measured trends up to R_{crit} but can be based on computed trends above R_{crit} . Ref 8 identifies 5 simulation scenarios according to the relative values of R_{flight} , R_{crit} , and the maximum R or R_{eff} in the tests. In practice, one is most likely to encounter scenarios 3 and 4 which are defined by the relations:

Scenario 3: $R_{crit} < \text{Maximum } R \text{ or } R_{eff} \text{ in tests} < R_{flight}$

Scenario 4: $\text{Maximum } R \text{ or } R_{eff} \text{ in tests} < R_{crit} < R_{flight}$

Clearly, extrapolation is easier in scenario 3 because R_{crit} is within the test range. Indeed, one could describe the aim of the aft-fixing technique as being an attempt to bring test data which would otherwise be in scenario 4 into the orbit of scenario 3. The greater certainty in the scenario 3 situation relating to scenario 4 can be appreciated from a study of Figs 35a,b.

Returning to the issue of how to convert a transition position into an effective Reynolds number, one must consider the nature of the scale effects that may exist. Eisenman introduced the concept of direct and indirect scale effects.

- (i) direct Reynolds number (or viscous) effects arise as a result of changes in the boundary layer (and wake) development for a fixed or "frozen" pressure distribution. Examples include the variation of skin friction with Reynolds number and changes in the length of a shock-induced separation bubble for a given pressure-rise through the shock, and
- (ii) Indirect Reynolds number (or viscous) effects associated with changes in pressure distribution resulting from changes with Reynolds number in the boundary layer and wake development.

The indirect effects are surprisingly important in the context of scale effects on aircraft wings. In subcritical, attached flow, the only significant scale effects (leaving aside the changes in skin friction) are due to the changes in pressure distribution that follow from the changes in boundary layer displacement thickness. In supercritical flow, these changes become more significant: an increase in Reynolds number decreases the boundary layer displacement thickness and this leads to an increase in rear loading, a reduction in the lift contribution that is needed from the forward upper surface to achieve a given total lift and hence, in many cases, to a reduction

in wave drag. The fundamental importance of these indirect effects suggests that an appropriate parameter on which to base the equivalence of a transition position and an effective Reynolds number would be the boundary layer displacement thickness at (or near) the trailing edge on the upper surface. This has been confirmed in research undertaken since the publication of the AGARD methodology (Ref 86).

Results from this research are presented in Figs 36a,b,c. Tests had been made in the RAE (Bedford) 8 ft x 8 ft tunnel on a 14% thick aerofoil (RAE 5229) with appreciable rear camber. Tests were made at Reynolds numbers of $R = 6 \times 10^4$, 10×10^4 and 20×10^4 with transition at $0.05c$ and the range of data was then extended by calculations for other Reynolds numbers and transition positions. The first picture, Fig 36a shows

- (i) good agreement between measured and calculated results at $R = 6.05 \times 10^4$ with $x_{rg} = 0.05$ at $M = 0.735$, $C_L = 0.65$, the design condition for the aerofoil,
- (ii) appreciable indirect scale effect between $R = 6.5 \times 10^4$ and $R = 30 \times 10^4$ with transition at $0.05c$,
- (iii) a reasonable but not perfect correlation between the calculated results for $R = 6.05 \times 10^4$, $x_{rg} = 0.40c$ and $R = 30 \times 10^4$, $x_{rg} = 0.05c$. The significance of this result is that this correlation of $x_{rg} = 0.40c$ is what would have been predicted using the zero-level simulation criterion proposed in Ref 8. This criterion, the boundary layer momentum thickness on the equivalent flat plate, is often remarkably successful and, in this case, as in many others, it gives a good match as regards shock position. However, bearing in mind that the criterion is not related to the boundary layer development over the real wing, this must be somewhat coincidental. It will be seen that it does not produce close agreement in the rear loading.

Turning to the more soundly based criterion suggested above, the boundary layer displacement thickness on the upper surface of the real aerofoil, comparisons based on this criterion are presented in Figs 36b,c. This criterion yields $R_{eff} = 20 \times 10^4$ and 30×10^4 for $x_{rg} = 0.28c$ and $0.33c$ respectively. Fig 36b shows that in subcritical, attached flow, this criterion gives perfect agreement in the pressure distributions and this is maintained at the design condition, $C_L = 0.65$, except in the supercritical region on the upper surface. Analysis has confirmed that the different supercritical flow development can be explained in terms of the different boundary layer development in this region. The shock wave is further forward and weaker in the aft transition, low Reynolds number result than in the forward transition, high Reynolds number distribution. Fig 36c shows that no other choice of x_{rg} would have helped in giving agreement in wave drag. This complicates the interpretation of aft transition results by just converting to an effective Reynolds number; one cannot equate with higher Reynolds number answers, one has to include a correction to the measured wave drag. It is however possible to calculate this correction theoretically and there is no doubt that this is the correct physical approach. In other words, the procedure has to account for two distinct effects: a change in the viscous development at the rear, which is allowed for by the choice of x_{rg} and a change in supercritical flow development which is allowed for by a correction to $C_D, \text{WAVE DRAG}$.

At higher C_L , when the shock is strong enough to induce separation, the instinctive approach is to convert a transition position to an effective Reynolds number on the basis of obtaining a separation bubble of the same length. The bubble length is a function of the boundary layer momentum (or displacement) thickness at the foot of the shock (Ref 87). There is no intrinsic reason why use of the bubble length as a correlating parameter should give the same relationship between transition and effective Reynolds number as would be obtained with the boundary layer displacement thickness at the trailing edge. However, in the example discussed in Ref 86, perhaps coincidentally, this proved to be true.

In the example quoted above, it was assumed that when the transition position was moved aft at low Reynolds number, it was moved aft on both surfaces. Bearing in mind that the main effects are associated with changes in rear loading, the general conclusion is that if transition is not moved aft on the lower surface (a practice adopted in some test programmes), the change in transition position on the upper surface has to be correspondingly greater. Details of a modified criterion to allow for this point are given in Ref 86.

10.6 Simulation Methodology: Extrapolation Procedure

The general principle in the extrapolation procedure is that one should follow the measured trends up to R_{crit} and then the computed trends from R_{crit} to R_{flight} . As noted in §10.5 above, this is much easier in scenario 3 than in scenario 4. To take C_D as an example, in scenario 3, the full-scale value is obtained from a simple relation of the form

$$C_{D,flight} = (1) + (2) - (3) + (4)$$

where

- (1) = measured value for transition position that converts to R_{crit} .
- (2) = computed value for flight R and transition position.
- (3) = computed value for test conditions as in (1).
- (4) = the summation of a series of corrections for
 - (a) excrescences on the aircraft but not represented on the model,
 - (b) propulsion effects not represented in a normal complete model test,
 - (c) trimmings effects in flight,
 - (d) differences in aerelastic effects on the aircraft and the model.

In addition allowance has to be made for the increase in drag and loss in rear loading due to the presence of the roughness band. This can be done by either allowing for it in (3) or as a correction to (1).

It should be noted that the conversion from X_{Rpp} to R_{pp} plays no part in the final prediction of the full-scale value, it has merely been used in the procedure to identify that the results are in scenario 3. There is just another way of pointing out the advantages of using aft fixing to bring the results into scenario 3. If nevertheless the results are still in scenario 4, the extrapolation is necessarily more uncertain. The measured trends have to be corrected for the fact that, with forward transition at $R = R_{pp}$, the supercritical flow development and hence, the wave drag would be different and then, the trends are extrapolated to R_{crit} and this means that the conversion to R_{pp} is involved in the calculation to produce the full-scale value. It controls the slope of the measured trend. There are also problems in

determining R_{crit} . It should not be taken as the Reynolds number at which the extrapolated measured trend would intersect the computed trend. This would imply blind faith in the absolute values from the computed results which obviously would not be justified. Rather, one should extrapolate curves of, for example, skin friction near the trailing edge against R_{pp} to find the value of R_{pp} at which $C_f = 0$. In practice, the relation set out above should probably be reshaped if the results are in scenario 4 so that terms (1) and (3) are determined not for R_{crit} , but for the furthest aft transition position in the model test programme and a further correction has to be included in term (4). This extra correction term highlights why the extrapolation is uncertain in scenario 4. The correction is, in fact, an estimate of the amount by which the results at the furthest aft transition position in the model tests are affected because this value of R_{pp} lies below R_{crit} . In a very approximate fashion, this can be estimated by observing the difference between the slopes of the measured and computed trends and allowing for the effect of this difference as it would affect the extrapolation up to R_{crit} . The computed trends in C_D with Reynolds number have to allow for changes in both viscous and wave drag. Refs 88-91 should be helpful.

10.7 Simulation Methodology: Laminar Flow Aircraft

There is only one paper (Ref 92) in the open literature addressing the particular problems of obtaining wind tunnel data for aircraft designed to maintain extensive laminar flow. There are two types of problem: first, extensive laminar flow has to be achieved in the tunnel tests and second, one has to be able to forecast and simulate the full-scale transition movements with C_L and Mach number in off-design conditions.

The ability to maintain extensive laminar flow in the model tests on a suitably designed shape depends on

- (i) the tunnel flow having a low turbulence level, say, less than 0.15%,
- (ii) the tunnel being a quiet tunnel with the value of $C_{p, rms}$ ideally 0.5% or less and certainly no more than 1.0%. This depends on more than just the design of the tunnel, there is evidence (Refs 36, 92) that it can be adversely affected by the presence of the model support,
- (iii) the success in keeping the model clear of contamination from the impact of particles in the flow. The allowable roughness height is based on a roughness Reynolds number defined by the height of the roughness and the flow conditions at the top of the roughness. Critical values of about 600 for three-dimensional or 100 for two-dimensional disturbances are usually quoted but experience suggests that somewhat larger values can be tolerated near the leading edge, presumably because of favourable pressure gradients. To achieve these standards, it may be necessary to filter the flow,
- (iv) the success in inserting pressure holes in the model that do not trigger transition (Ref 93).

Ref 92 by Elsenaar contains a detailed discussion of how natural transition is likely to vary with C_L and M at both flight and model test Reynolds numbers, assuming that the points in the preceding paragraph have been negotiated successfully. Forecasting the natural transition position is

generally undertaken using the e^N method but there is still great uncertainty over what value of N to choose. If the aims of the preceding paragraph have been met, natural transition is likely to be further aft in the tunnel than in flight both at the design condition and at strongly off-design conditions, thus allowing one possibly to use normal tripping techniques. In the intermediate range of C_L , however, the forward movement of transition with C_L is likely to be delayed and to occur more abruptly on the model than in flight. If these comparative movements can be predicted, aft tripping may have a part to play in giving good simulation.

One major issue not discussed in Ref 92 arises from the fact that in flight with a laminar flow aircraft, transition is likely to be triggered by a laminar boundary/shock interaction. Little research has been undertaken to determine the scaling laws for such interactions.

11 HALF-MODEL TESTING: SPECIAL PROBLEMS

There have been several references in earlier paragraphs to the growing practice of testing large half-models of subsonic transport aircraft as a means of obtaining a higher test Reynolds number (Ref 11). This practice accentuates problems that have to be considered in all testing.

- (I) the large model mounted asymmetrically in the working section is likely to have more effect on the steadiness of the airstream,
- (II) the wall interference corrections will be more difficult to predict, particularly for tunnels with ventilated walls because, for half-model testing, one wall will have to be solid to act as a reflection plane,
- (III) buoyancy effects - both empty tunnel buoyancy and in perforated-wall tunnels, blockage buoyancy effects will be larger and more difficult to predict without extensive pressure plotting in the actual tests,
- (IV) in many tunnels, the standard of flow angle uniformity is not as good near the walls as in the centre of the stream (see §7.1).

There are also problems directly associated with the mode of testing (Ref 94). There was considerable activity in the 1960s to solve the leakage problems at the root by sealing schemes but these were often unsuccessful. The normal approach is to mount the model with the aircraft centre-line not at the tunnel wall but displaced away from the wall by a distance equal to about the wall boundary layer displacement thickness. Opinions differ as to whether one should measure the forces on the extra piece of fuselage inserted to create this displacement. Whatever one does in this respect, it is unlikely that the measured lift-curve slope will agree with what would be measured for the corresponding complete model. There are too many reasons for small differences eg the tunnel wall may not act as a fully effective reflection plane, there will be a reduction in the dynamic pressure close to the wall and, in some cases, there may be some leakage between the model and the wall. Most tunnel operators adjust the lift-curve slope to agree with that measured with the complete model and have developed semi-empirical methods for modifying these corrections for the next model having a different geometry. Clearly, this is not a fully satisfactory approach. It normally leaves a residual error in pitching moment amounting to 0.01 - 0.02c in aerodynamic centre position.

Half-models have frequently been used for tests with powered nacelles where one is merely seeking the drag increment due to the nacelle installation. Experience has shown that such tests, even on wing-mounted nacelles, should be made with a metric half-fuselage. This contradicts some early reports on the subject.

Despite the problems discussed above, it seems likely that half-models will continue to be used for

- (I) tests for determining differences in drag between two configurations,
- (II) high speed tests with powered nacelles,
- (III) tests aimed at achieving the highest possible test Reynolds number and, in particular, extending the range of a Reynolds number sweep.

12 PROPULSION INSTALLATION TEST TECHNIQUES:

SUBSONIC TRANSPORTS

12.1 Jet Turbine Engines

12.1.1 Types of simulator

The discussion in this para is taken from Ref 10. Different types of simulator are shown diagrammatically in Fig 37.

Most complete models are fitted with through-flow nacelles (TFN) - see top picture in Fig 37. This is the simplest form of simulator. They can provide the correct inlet geometry and the correct mass flow ratio if the exhaust geometry is enlarged. Alternatively, if it is felt important to retain the correct exit geometry, one has to accept a reduced inlet mass flow and it may then be necessary to modify the inlet geometry to avoid spillage drag that would not be present, full scale. With an underwing nacelle, it is probably important not to modify the exit geometry for the sake of obtaining the correct interference with the flow over the wing.

The weakness of a TFN is that the exhaust flow is unrepresentative in both total pressure and temperature and consequently in exhaust plume shape and stream shears. Attempts to include a hard shaped extension to the nacelle to represent the correct plume shape have not generally been successful. Whenever possible, the TFN should retain the geometry of the separate fan and core stream exits.

The general practice in high speed testing is to correct for the lack of jet effects with a TFN by undertaking comparative tests on a corresponding half-model with both a TFN and one of the powered simulators described below.

A blown nacelle has both practical advantages and practical disadvantages. On the one hand, since all the air that exhausts from the exits has been fed into the model, the instrumentation requirements are simplified but, on the other hand, the air requirements can be very great, eg perhaps three times those for a turbine powered simulator (TPS). Also, problems arise from the fact that the exhaust total pressure of both primary and fan are very low in comparison with the supply pressure (by perhaps 1.15). Complex pressure-dropping systems can lead to non-uniform pressure and temperature distributions. The apparent advantage of a blown nacelle to permit over-blown for calibration purposes, ie to provide the correct flight pressure ratios at the nozzles in a static calibration, may also prove to be an illusion. It is dangerous to assume that the flow distribution in the nozzle remains the same in these overblown conditions and also, this approach requires that the dependence of nozzle thrust and discharge coefficient on internal Reynolds number can be quantified.

There are also practical aerodynamic difficulties in the use of blown nacelles. A shape has to be designed for the fairing over the front of the nacelle and the flow over this shape has to be representative over a reasonable range of C_L and Mach number. The displaced intake streamtube enters the gully between the wing (or fuselage) and nacelle and the effects of this are difficult to quantify.

The great advantage of an ejector nacelle over a direct blown nacelle is that it requires much less high pressure air. Assuming that one can achieve an ejector mass ratio of about 1.5, the inlet flow with an ejector nacelle should be about 60 to 65% of the design operating value. The real challenge with an ejector nacelle is to obtain a consistent, repeatable flow at the nozzle instrumentation reference plane. This reference plane is always likely to be nearer the ejector plane than the rules of the complete mixing would allow. Proponents of the ejector nacelle would claim that this distance is nevertheless acceptable but others believe that it is too close to guarantee repeatability. The accuracy of an ejector simulator is dependent on the repeatability of the flow from a multitude of minute conical ejector nozzles and their mixing with a distorted flow field.

Finally, turbine powered simulators (TPS), these have been used extensively. Some establishments, notably ARA, DNV and ONERA have acquired a large amount of expertise in their use. Initially, in some quarters, there were some doubts about their use in view of the large number of rotating parts but in practice the units, designed and built by Tech Development Inc., have proved to be very robust. Most TPS units are associated with a particular full-scale engine and appropriate cladding is manufactured in the testing establishment or by the customer to suit a particular installation. Technically, TPS units have several distinct advantages, eg

- (i) both inlet and exhaust effects can be adequately represented in the same test. A typical figure for the intake flow is 30% of full scale.
- (ii) a linked accounting system can be used to estimate the ram drag and the gross thrust. This minimizes the potential for large errors to be present as a result of having to subtract two relatively large terms in obtaining the external drag.

Great care has nevertheless to be taken in the calibration of the units with much diagnostic instrumentation to seek out faults. These procedures are discussed in the next para.

One detailed feature worth noting is that use of an epoxy based fibre or glass cloth laminate material (Tufnol) has provided an acceptable solution to the problems of ice formations due to the very low turbine exhaust temperatures.

12.1.2 Calibration techniques

All simulators with their cladding have to be calibrated in tanks that resemble the altitude test chambers that are used for the full-scale engine. Boeing were the first to develop such a calibration tank but they now exist at many sites eg DNV, ONERA, MBB (Bremen), NASA Ames and ARA. The discussion below is based on a description of the facilities at ARA, (Ref 10).

The Mach Simulation Tanks (MST) at ARA are shown diagrammatically in Fig 38. It will be seen that the units are mounted partly in and partly out of

the tank, thus enabling the upstream nacelle stagnation pressure and the nozzle static pressure of the tunnel tests to be reproduced in the calibration whilst maintaining quiescent conditions in the flows around the inlet and downstream of the nozzles. The aim is to calibrate the gross thrust and inlet mass flow in terms of the same reference pressures and temperatures as will be used in the tunnel tests and to use the internal instrumentation to calculate the net thrust and ram drag.

The original MST1 was designed for high flow rates and relatively large models; it incorporates critical venturi monitoring of mass flow rates and two six-component balances. MST2 was developed to meet a need for greater precision for the smaller models; it uses single axial component force balances. The aims of this MST2 design were to obtain

- (i) force measurements of ± 0.1 lbf repeatability, and
- (ii) enhanced mixing of the TPS exhaust flow ahead of the tank mass flow instrumentation

To produce enhanced mixing, the flow for MST2 is first extracted from the tank into an annular mixer/plenum prior to flowing along a high velocity feed duct and into a further mixer at entry to the 'mass flow' plenum, as shown in Fig 38. The model axis is vertical and three single component Bofors 'shear force' high precision load cells are used for the measurements. A special layout of metric and non-metric components featuring annular cells was devised to compensate for the pressure area term arising on the model mounting zone due to the basic tank external to internal differential pressure. The tank top is equipped with a novel arrangement of rolling diaphragm seals specially manufactured by the patent holders, Bellofram Inc. Flat diaphragm seals tried initially did not give the required accuracy. The overall uncompensated load on the basic metric area at 6 psid is approximately 1200 lbf but the arrangement of compensating cells reduces the net metric load to less than 15 lbf at 6 psid. The RDS give an essentially linear response with ... hysteresis and good repeatability. Calibrations with external loads up to 150 lbf and with 6 psid differential have produced less than ± 0.05 lbf forces data spread.

Repeated use of MST2 has shown that it is possible to achieve 10-15% accuracy in both thrust and mass flow calibrations. This is a notable achievement but, bearing in mind that typically, ram drag, fan gross thrust and core gross thrust are respectively 300, 500 and 250 counts compared with a nacelle external drag increment of say, 20 counts, this standard of accuracy and repeatability is necessary if external drag differences are to be discriminated to the accuracy discussed in §3.

Detailed monitoring techniques have had to be developed to ensure the safety of the TPS units during the tests and to be able to diagnose the sources of any apparent inconsistency in the data. One particular feature of the reduction of the data is that they are 'power corrected'. Ref 10 contains an example where the measurements, when sampled at a finite set of duct locations, led to nozzle coefficients which showed apparent variations with rpm at fixed values of the fan nozzle pressure ratio. The 'power corrections' approach is based on the assumption that these apparent rpm effects on the nozzle coefficients are due to sampling variations as opposed to real effects. Ref 10 describes a method for correcting for these apparent power effects and, in the example discussed the spread of the nozzle

coefficients at different rpm at a given fan nozzle pressure ratio was reduced from about 0.7% to less than 0.3%. This was a case where a large number of duct pressure and temperature samples were taken. The published literature (Refs 95,96) contains examples with fewer samples where the apparent power effects before correction were as great as 3%.

Mach Simulation Tanks can, of course, be used and are used for the calibration for all forms of simulator including TFDs. The calibrations of TFDs are undertaken to determine the internal drag corrections.

12.1.3 Accounting techniques

Fig 39 shows schematically the essentials of the MST and in-tunnel bookkeeping process. The calibration phase yields a set of nozzle coefficients which represent the characteristics of the nozzle and instrumentation combination. It is important to recognise that the nozzle coefficients will change if the instrumentation is changed. It is essential, therefore, that the instrumentation remains the same in the tunnel as in the calibration. The ram drag and the fan gross thrust are computed using an identical mass flow term. Multiple methods are used to estimate the fan nozzle mass flow; comparison of the results builds up confidence in the results and helps in fault-finding.

It is important that the thrust/drag bookkeeping scheme is defined clearly and agreed. This applies even in the simplest case of tests with a through-flow nacelle. Several different definitions for the internal drag of such nacelles are in use according to whether one interprets it in terms of the change of momentum from upstream to downstream infinity or merely to the duct exit. Any definition can be used provided that other terms in the full thrust/drag scheme are adjusted to suit.

Statistical analysis techniques are applied to the results. These techniques are discussed in detail in Ref 10.

12.1.4 Propulsion integration: high-speed test programme

A number of different models and rigs have to be used in a typical test programme to study and optimise the propulsion installation on a subsonic transport. The description below is again based on the facilities at ARA but similar approaches would be followed elsewhere.

The range of possible rigs and models is illustrated in Fig 40. The pictures on the left show two special rigs for isolated component testing on respectively the external cowl shape and second, the nozzle and afterbody. The three pictures on the right show a nacelle/pylon model being tested in isolation at the top of a long swept strut, on a half-model and on a complete model. In the last three pictures the nacelle can, in principle, be any of the simulator types described above.

The cowl models tested on the isolated rig shown in the left top picture are appreciably larger than those used for the installed tests. This enables the tests to be made at a higher Reynolds number and also, the models can be a more faithful representation of the full-scale nacelle including asymmetries such as intake droop and any external bulges to house accessories on the full-scale engine. The external drag is obtained from pressures measured on a rotating rake aft of the nacelle and the mass flow is determined from pressures measured on rakes rotating in the ducts. Tests can be made on a complete cowl with a

truncated afterbody but primarily, it is a rig for refining the shape of the forecow and for checking that no avoidable spillage or wave drag is present in the important operating conditions. It can also be used for designing the modified shapes of cladding to use with powered simulators with limitations on the maximum available mass flow. It is not suitable for studies on afterbody shape because of the effect of the downstream support mounting.

The second picture shows a rig that can be used for checking the performance of the afterbody/nozzle design. It is a two-stream strut-mounted rig. The rig has been used extensively for tests on axisymmetric nozzles, the effects of a non-metric wing panel on nozzle performance and full nacelle/pylon configurations. Some typical test results are presented in Ref 10.

The main test sequence is that illustrated in the three pictures on the right. The general practice is to create a test programme including tests on:

- (a) TFD/pylons mounted on a long strut. These tests, taken in conjunction with evidence from the isolated forecow rig, will reveal whether there is any nacelle/pylon interference. Care has to be taken to avoid or at least, allow for any buoyancy effects with respect to the non-metric part of the strut.
- (b) TPS powered nacelles/pylon combinations again on the long strut. Results from these tests will form a datum for the later test data from the installed tests but also, comparison of results from (a) and (b) will be of interest as an indication of jet effects in a free-stream environment. The comparison also serves to confirm whether the design of the forecow for the TPS unit is satisfactory. Finally, carrying out these tests first will mean that one arrives at the start of the installed programme with added confidence,
- (c) a half-model fitted with alternatively TFDs and TPS units and on a corresponding complete model with TFDs. The data from these tests can be used in several ways
 - (i) comparison of results for different builds of the TPS nacelles on the half-model will indicate how to optimise the complete installation bearing in mind that all effects are represented in these tests,
 - (ii) subtraction of the results with the TFD and TPS nacelles on the half-model will yield corrections that can be applied to the data from the complete model tests to allow for the jet effects not present with the TFDs,
 - (iii) subtraction of the results with the TPS units on the half-model and those obtained in (b) will provide an idea of the aerodynamic interference present in the total installation and hence of the improvements that may, in theory, be possible. In this connection, it should be noted that zero interference is not necessarily the best that can be achieved; favourable interference is a real possibility. Fig 41 is an example taken from Ref 9. The aim should be to design a propulsion installation and wing that together give optimum performance; it is almost axiomatic that this implies that this performance is better than the sum of

the clean wing and nacelle installation performances when determined separately. This is obvious in the case of aft-mounted nacelles where the presence of the nacelles downstream of the wing can have a major influence on the position of the shock waves on the wing but it is also true of underwing nacelle installations. Ref 97 identifies 8 different sources of interference for such installations at high speed and Ref 10 adds a further 4 sources important at low speeds.

Even with half-models, the high pressure air feed to a TPS simulator has to be taken through the balance outside the tunnel wall but the associated problems are not as serious as they would be if the TPS units had been installed in a complete model. Such tests are however feasible as was shown in a research experiment on a 2-engined Lockheed 1011 model without its rear engine. An air transfer bellows system was designed successfully and the comparative test data for two configurations showed reasonable agreement with flight data (Ref 10). At low speeds, it is however more important to use complete models and, by now, DNW have acquired considerable experience in this field (Refs 98-101).

The DNW complete model tests have been made with two types of large TPS unit, one designed and manufactured by TDI and one by MBB. The aims of the tests have been:

- (I) to establish the jet interference effects on the drag in the second segment climb, the drag is needed to an accuracy of ±1% aircraft drag or about ±10 drag counts,
- (II) to determine the jet effects on the stability and control characteristics in ground effect during take-off,
- (III) to investigate the thrust reverser characteristics including braking capacity, handling qualities and reingestion boundaries, and
- (IV) to study the nature of the interference by means of surface pressures and flow field measurements.

The crucial engineering problem in the complete model testing with TPS units is how to bring the high pressure air across the balance in the fuselage. The air pipe must be flexible to minimise interactions with the balance measurements but stiff enough to maintain its position in the model and to withstand the high pressure of about 40 bar. The DNW design is shown in Ref 98, there are two air bridges, one on each side of the balance, in the models to allow for independent control of two engines.

12.2 Propellers

There has been considerable investment in recent years in new facilities and techniques for the testing of model propellers and of aircraft models fitted with propellers in both low and high speed tunnels. Many of the issues discussed above in connection with aircraft with jet engines still apply but there are some additional problems. First, model tests are needed on the propeller itself to determine its performance and aerodynamic characteristics and second, in the tests on aircraft models, the propeller thrust has to be measured directly in the wind tunnel rather than indirectly by means of reference pressures and temperatures allied with a calibration in a test

cell as with the jet engine. This introduces engineering problems in the design of rotating balances and, with modern propeller/spinner designs, there are difficulties in separating drag and thrust and, as regards propeller efficiency, there are difficulties in comparing experiment and theory because it is often not practicable to measure what one can calculate. These additional issues are considered in some detail below.

In the UK, Industry and Government cooperated in the development of new facilities (Refs 102-105) for model testing with propellers: a special Test House was built at ARA for proving trials on the model propellers ahead of the tunnel tests, three compact and powerful electric motors for testing relatively large model propellers (up to 3 ft in diameter for single rotating propellers) were acquired and have been used in tests in both the ARA and DNW tunnels, air motors were obtained for tests on aircraft models with both single and contra-rotating propellers and finally, a liner was designed to create an 8 ft x 7 ft acoustically treated working section for the ARA transonic tunnel. For convenience, the author will use the ARA experience to comment on the problems mentioned above but it is, of course, recognised that various other establishments have tested model propellers either in isolation or on aircraft models, eg the de Havilland (Canada) 30 ft x 30 ft low speed tunnel (Ref 106), the ONERA S1 tunnel (Ref 107), the NASA Lewis facilities (Ref 108), the facilities at United Technologies (Ref 107), NASA Ames and McDonnell Douglas (Ref 109) and finally, one should mention Boeing, who were the first to develop an acoustic working section for a transonic tunnel (Ref 110).

Propeller tests at ARA can be made at two different model scales. The engineering and aerodynamic problems can be illustrated by a brief discussion of the hardware and typical test programmes for tests on contra-rotating propellers at the smaller scale

(I) Fig 42a shows the rig that has been developed to obtain the basic propeller thrust in the presence of the real spinner shape but followed by an unrepresentative nacelle, being merely the minimum body required to house the TD1700 air motor. This combination is mounted on a metric strut housed in a non-metric shield. The aims of the design were to provide sufficient rigidity coupled with aerodynamic cleanliness and as small a tail drag as possible on the underfloor balance readings. The achievement of a satisfactory compromise between these conflicting requirements was a far from easy task. The propellers are cleared for tunnel testing by monitoring the output of blade mounted strain gauges which provide a means of assessing rotor dynamic disturbances, critical points and flutter. Also, the rig itself is fitted with accelerometers. The compressed air for the air motor enters the metric model in a direction perpendicular to the thrust axis but it is still necessary to insert the nacelle/nozzle system in the Mach Simulation Tank discussed earlier to determine the nozzle thrust and discharge coefficients in a quiescent environment.

(II) Fig 42b shows the hub design scheme, the attachments to both the shafts and the component propellers were designed to produce a symmetric low-stress torque and thrust path to the balance flexures. The balance electrical signals were transmitted by slipring for the front rotor and by telemetry for the rear rotor.

- (III) the shaft strain gauged balance design, Fig 42c, comprises set of flexures in a basically symmetrical layout with strain gauges placed so as to provide symmetry and duplication of the key elements. A repeatability of $\pm 1\%$ was achieved in a static calibration,
- (IV) the development of the telemetry installation provided to be a challenging task; the high CF loads dictated a specially configured housing with composite retention rings. After various structural and electrical refinements, a $\pm 1\%$ standard of signal processing was obtained,
- (V) the test programme and methodology may appear complicated but, in fact, the bookkeeping procedure as set out at the bottom has been somewhat simplified for this presentation.

For the aircraft model tests, the precise definition of propeller thrust is unimportant provided one retains consistency through the accounting in Fig 42d but, in tests on the propeller in isolation (phase A in Fig 42d), aimed at determining the propeller thrust and efficiency and comparing with theoretical prediction, the definitions become crucial. As we have seen, in the experiments, measurements are made with both a shaft and an underfloor balance. The difference between the blades-on and blades-off shaft thrust measurements yields an apparent thrust. The net thrust can be obtained in two ways either by differencing the blades-on and blades-off underfloor balance thrusts or by correcting the apparent thrust for the difference, blades-on and blades-off, in the rear nacelle axial force obtained by integrating the pressures measured on this nacelle. Assuming that this integration can be performed to the required accuracy and that allowance is made for the skin friction drag of the nacelle, these two methods of obtaining the net thrust should give the same result.

An essential element in the design of an efficient propeller installation for operation at high subsonic speeds is the slowing down of the flow over the thick root sections of the propeller by a waviness of the spinner surface opposite and ahead of the propeller (see Fig 42b). At the very least, any theoretical estimate of the propeller thrust and efficiency should allow for this effect but this is not enough to produce a theoretical estimate that can be compared directly with either the apparent or net thrusts from experiment. Any calculations by strip theory still need refinement by allowing for the effects of the pressures on the inner surfaces of the blades adjacent to the spinner and for the pressures induced on the spinner by the presence of the blades. These are obviously part of the apparent thrust from the measured results and calculations suggest that they can account for 5-10% of the final answer. All these complications suggest that a field method should be used for a comparison with experiment. The results of such a comparison using the Denton field method are shown in Fig 43 taken from Ref III. Various comments can be made about this comparison:

- (1) the apparent overprediction of the thrust and power coefficients at a given blade angle may not be the most important issue. It should perhaps be thought of as being due to a discrepancy in blade angle either because of an undetected blade twist in the experiments or because viscous effects have been ignored in the calculations. Of more direct interest in the present

context are the differences between the various curves,

- (II) the substantial difference between the blade and net thrusts in the theoretical results confirms the importance of the blade effects on the pressures on the spinner,

the differences between the apparent and net thrusts is significant in the experiment but relatively minor in the calculation. The most obvious explanation of this inconsistency is that the calculations do not include the skin friction element in the effects on the nacelle but it may also be due to detailed differences, blades-on versus blades-off in the flow through the spinner gap. More prosaically, it may merely reflect that the theory has its limitations. These comparisons have been discussed in some detail merely to emphasise that, at the present time, one is in some difficulty trying to use theory to settle uncertainties in whether the experimental data have been handled correctly. The propeller designer may wish to know the efficiency of his design to 1% or better but at present this is difficult either by experiment or theory. It is another example where comparative accuracy is better than absolute accuracy but even comparative accuracy is likely to be sensitive to the interference issues between propeller and spinner discussed above. More research is needed.

The model tests discussed above related to an aircraft with wing-mounted engines. Similar activity has been undertaken by McDonnell Douglas in connection with a design with aft-mounted engines (Ref 109). Tests on powered complete models at both low and high speeds were made. For the high speed model, the high pressure air was routed forward along a sting located below the model and then up a blade support into the forward fuselage and then back through the fuselage to the powered nacelle at the rear. A contra-rotating pusher arrangement was simulated. Power-induced effects on tail power and overall stability were measured and also, a nacelle-based rotating total pressure wake rake was used to explore the slipstream.

The final picture, Fig 44, concerned with propeller testing, shows the large scale UK rig with a contra-rotating propeller installation installed in the acoustic working section of the ARA tunnel. Points to note include

- (a) the propellers are driven by two AC induction electric motors mounted in tandem. These motors are designed and manufactured by the Able Corporation of the US and are each capable of generating 660 SHP at 7000 rpm, they are very compact, each can be contained in a volume 25" long by 14" diameter,
- (b) a co-axial system of three shafts connects the rotors and, in this case, stationary nose bullet to the Able motors,
- (c) the primary instrumentation of the rig was a pair of shaft-mounted thrust and torque balances and a set of surface pressures to enable the rotor performance to be evaluated, coupled with extensive rig and rotor 'health' instrumentation including strain gauges on the blades,

- (d) the larger size of this rig carries many advantages: a more acceptable Reynolds number on the blades and the ability to attempt a wider range of tests, eg dynamic and steady pressure measurements with transducers flush mounted on the blades and a laser system to monitor the twist and camber of the blades under load,
- (e) despite the relatively large blockage of the model and the microphone traversing rig in the tunnel with the acoustic liner, tests were possible up to $M = 0.8$. In passing, it is worth mentioning that Ref 112 is a useful reference on the effect of propeller thrust on tunnel wall interference.

In the performance tests with this large rig, supplementary tests were made with both laser anemometry and laser holography. For the laser anemometry, the flow was seeded by plumes of $0.5 \mu\text{m}$ particles of mineral oil injected from a special strut erected in the tunnel settling chamber. Two pairs of focussed beams were used, the orientation and meeting points of these beams could be rotated and translated to enable velocities to be determined in different regions of the flow field, eg the tip vortex region, the in-rotor (ie between blades) region, the between-rotors region and upstream and downstream of the rotors. In the holographic tests, features that were observed included the tip vortex path, the chopping of the front vortex by the rear rotor, the shear layer in the wake region and supercritical flow features such as the expelled blade leading edge bow shock. The measurements and tests are described in detail in Refs 105 and 113. This was a major exercise run on a cooperative basis with Rolls-Royce as the major partner. The brief description has been included here since this programme is a good example of what is going to be possible on a more regular basis in the future.

13 PROPULSION INSTALLATION TEST TECHNIQUES

COMBAT AIRCRAFT

For many years, the ACARD Fluid Dynamics Panel has devoted much attention to engine-airframe interference and, in particular, to the test techniques that are required in this field. An ad hoc committee reported (Ref 114) in 1971 on the results of a detailed study of the testing methods in use at that time and this was followed by a lecture series on the same subject in 1973 (Ref 115). In 1974, the FDP held a 4-day symposium on airframe/propulsion interference (Ref 116) as regards wind-tunnel testing; this symposium almost exclusively considered problems in afterbody testing, eg strut interference, temperature effects. More recently, two Working Groups have considered different facets of the subject. Working Group 08, which reported (Refs 12, 13) in 1986, dealt with the aerodynamics of aircraft afterbodies and Working Group 13, which is reporting in 1991, is concerned with intakes for high speed vehicles and specifically includes a chapter in its report devoted to testing methods and techniques (Ref 117). This part of the present lecture draws extensively on this recent material.

Compared with the subsonic transports discussed above, combat aircraft introduce 4 major complications

- (i) a greater speed range up to supersonic speeds,
- (ii) a greater range of angle of attack at high subsonic and transonic speeds,
- (iii) a more complicated and closely coupled geometry,
- (iv) a lack of proven engine simulators that can be used in routine testing largely due to severe geometrical constraints

The standard approach is to test a suite of at least three models:

- (a) a normal complete model of the aircraft with the best possible representation of the intake through-flow and the least possible distortion of the rear fuselage,
- (b) a partial model of the intake to a larger scale and including a faithful representation of the intake ducts back to the engine face, and
- (c) a partial model of the true afterbody shape of the real aircraft including the facility to blow the exit nozzles at representative jet pressure ratios. The distorted afterbody shape of model (a) is also tested on this afterbody model and the differences between the results for the two shapes provide corrections that can be applied to test data from (a).

Clearly, as configurations have become more closely coupled, doubts arise about the validity of this three-pronged approach. As a small move to meet this point, both intake and afterbody models now often include relevant parts of the rest of the aircraft to whatever extent is permitted by model blockage considerations. However, with a closely coupled layout it may be wrong to assume that intake and jet effects can be studied separately.

The techniques will be discussed under two headings. Intake testing, afterbody testing including a very brief description of the prospects for full simulation of the propulsion effects

13.1 Tests on Intake Models

13.1.1 Scope of intake tests

To quote from Leynaert in Ref 117, the purpose of intake testing is to qualify the flow they deliver to the engine, and to determine the effect they have (in terms of drag, lift and moment) or the external aerodynamics of the aircraft. Most testing is carried out without any engine being present. In other words, the conclusion of Ref 118 is that the engine has little effect on the intake pressure recovery, the level of turbulence, and the maximum instantaneous distortion is accepted. However, at a relatively late stage in the development of a new aircraft-engine combination, tests are sometimes made on the real intake-engine in the very large facilities at ONERA Moulouse (the SI tunnel) or AEDC Tullahoma (the 16 ft PWT) (Ref 119).

Specific aims of intake testing include

- (i) to obtain the pressure recovery/mass flow characteristics,
- (ii) to obtain the spillage drag as a function of mass-flow, Mach number and incidence,
- (iii) to refine the details of the intake design, eg to optimise the boundary layer bleeds and/or diverter,
- (iv) to study the unsteady characteristics. In this respect, one should distinguish between unsteady distortion and the surging of the intake. Distortion is related to instabilities in the intake itself and so, there is little dependence on how the internal flow valving system is arranged downstream but when surging is being studied, or any other relatively low-frequency characteristics involving wave propagation times between the engine and the intake, a valve system must be provided at the position of the first compressor stages in order to reproduce

the phenomena exactly, particularly as regards reduced frequency (which should be inversely proportional to the model scale).

13.1.2 Internal Performance: Pressure Recovery, Swirl, Dynamic Distortion

For many combat aircraft, the primary design condition for the intake will be at supersonic speeds. In two respects, this simplifies the testing: at supersonic speeds, the flow into the intake can only be influenced by the shape of the aircraft upstream of the intake plane and hence, the rest of the aircraft need not be represented on the model and second, the ratio between the stagnation pressure of the internal flow and the external static pressure is such that it is relatively easy to capture the natural flow with the intake. Figs 45a,b show two test set-ups for, respectively, an isolated and installed intake test. In both cases, the aim is to obtain the highest possible test Reynolds number. The limit on model size in the installed intake test is set by the need to keep the intake plane behind any reflected shocks from the tunnel walls. In the example illustrated, the internal flow ducts contain

- (I) Instrumentation at the engine face station (1).
- (II) a station (2) at which the flow through the duct can be controlled either by an adjustable sonic throat as shown or by a non-sonic variable pressure drop such as a butterfly valve, and finally
- (III) a station (3) at which the mass flow is measured by, for example, a flowmeter with a sonic throat.

In other cases, it may not be possible to use two throats in series at (1,2) either because the space is not available or because the internal pressure drops have to be limited to achieve the desired flow, in such cases, the mass flow is measured at station (2).

Fig 46 shows three examples of the engine face instrumentation that was adopted by BAe and MBB in one of their test programmes. It is generally believed that about 40 stagnation pressures are sufficient to obtain a reasonable mean pressure recovery and similarly, 40 pressure transducers can be used to obtain the maximum instantaneous distortions. Various methods have been proposed for estimating the unsteady distortion from a smaller number of measurements and, indeed, Ref 120 quotes a 'rule of thumb' to use in cases where no unsteady pressure measurements have been made. This rule correlates the unsteady distortion with the mean internal stagnation pressure drop through the duct starting at the diffuser. This approach conflicts, however, with the general trend which is to take more measurements than in the past. In particular, it is often considered mandatory that the test instrumentation includes measurements of swirl, eg in the case shown in Fig 46, sixteen five-hole probes were used. A parameter for quantifying the rotational deviation has been proposed in Ref 121. This is defined in an analogous manner to the DC60 definition, the swirl DS60 index is the maximum averaged value in a 60° sector of the circumferential component of the velocity, divided by the axial velocity. As long ago as 1977, Carriere (122) recommended that the differences in relative incidence of the engine face fluid stream with respect to the rotating blades - ie the distortions that give rise to the distortion effect - should be considered from a global point of view by combining the flow

deviation measurements with the local deviation measurements found by measuring the total pressure fluctuations and converting to axial velocity fluctuations but this elaborate approach has not yet been adopted.

When a flowmeter can be used as in Figs 45a,b, the mass flow can be measured directly and precisely. It is assumed that the static pressure in the settling chamber of the flowmeter is uniform and is measured at a hole in the side of the chamber and calculations are made as described in Ref 117, to determine the sonic throat area. When the test Mach number is not high enough for the flowmeter throat to be choked, or when the pressure loss accompanying a sharp reduction in mass flow leads to an unchoking of the throat, the same set-up can still be used, treating the flowmeter as a venturi. In this case, the static pressure at the throat has to be measured although ideally, a calibration should be made against a reference flowmeter.

If it is unacceptable to include both Stations (2) and (3) as separate sections, the mass flow has to be measured at the station at which it is controlled. If the throat at this station is not choked, the static pressure in the internal duct upstream has to be measured and combined with the area of the throat cross-sectional area to determine the mass flow. Ref 123 should be consulted for diagrams of sonic plugs that can be adjusted by translational movement to vary the mass flow. A unit incorporating one of these plugs is shown in Fig 47. There is no settling region upstream of the throat in this case and the aerodynamic definition of the throat is less precise. The flow measurement may therefore not be as accurate as when there is a separate section (3). When no downstream throat can be choked and the flow profile is not uniform, one can use the measurements at the engine face station (1) to compute the mass flow. The accuracy then depends on the detail in which the flow at this station has been explored. In one example where a detailed exploration was made by a rotating rake supported by a flow matching hypothesis for the wall boundary layers, Ref 124 claimed an accuracy of 1%.

In contrast to supersonic speeds, the intake flow at subsonic and transonic speeds is influenced by the entire aircraft. Strictly, therefore, one should test complete models but by comparing full-model and partial-model tests, Mach number and incidence conditions can be defined for the partial-model tests that will bring their test results close to those of the complete model. Tests at these speeds have to be extended up to very high incidences. This is normally accomplished by transferring models designed for testing in moderate size tunnels to larger tunnels for the high incidence testing. For example, a partial model of the Rafale without wings and with truncated canards that has been tested in the ONERA S2 tunnel (cross-sectional area 3 m²) was converted into a complete model of the aircraft for tests at high incidence in the S1 tunnel (cross-sectional area 40 m²).

13.1.3 External drag

In addition to the normal tests on a complete model of the aircraft, tests are made on the air intake alone or on the forward part of the aircraft including the intake. The purpose of these tests is to establish the effects of detailed changes in intake design and of intake mass flow on the external drag. The partial model allows a useful increase in Reynolds number and a more faithful representation of the detail of the intake of the full-scale aircraft. The major technique problem in such a test lies in knowing how to determine the downstream momentum accurately. Fig 48a shows one

possible experimental set-up for which another problem lies in obtaining adequate stiffness at the joint between the live and earthed parts of the model. In this case, the internal momentum at this joint is calculated from the measurements of the flow at the engine face. On the assumption that the flow is being measured more accurately elsewhere, the probe measurements at the engine face can be corrected to give better agreement with this more accurate value and a corresponding correction can then be applied to the momentum. Fig 48b illustrates another arrangement (Ref 123) in which an earthed plug is placed at the outlet of the intake duct and the momentum is evaluated a little upstream of the plug by measuring the static and total pressures in a cylindrical part of the duct and the only correction that is needed is for the drag of the cylindrical part of the tube between the measuring section and the outlet section a small friction term. The mass flow is obtained in a separate calibration.

13.1.4 Acquisition and analysis of distortion measurements

The distortion indices come from the forty unsteady transducers of the engine face rakes. The highest frequency that has to be considered is of the order of 1000 Hz full scale and this has to be divided by the scale of the model. One way of obtaining a particular distortion index is to build an analogue computer which delivers a signal proportional to the desired distortion index. These are widely used, they provide a result in real time but their usefulness is limited to the one distortion index for which they were designed. Hence, as a complement, the transducer signals are recorded on magnetic tape for off-line computer analysis. Better performance can be obtained with a PCM (Pulse-Code Modulation) record. The distortion indices can also be computed digitally using analogue-digital conversion with a suitable array processor computer.

The aircraft designer will want to know the maximum values of the various distortion indices as recorded during a given length of time of order 1 minute, full scale, for the flight conditions at which serious distortion is present. The recorded distortion can be analysed statistically to define these maximum values according to a given probability (Ref 125). A detailed map of the instantaneous flow may also be of interest but the important issue is knowing how to select from the vast amount of data that is typically taken. Systems for doing this have been developed at various establishments and in industry, eg at AEDC (Refs 126, 127).

If no analogue computers or high speed data acquisition systems are available, a first estimate of the various distortion indices can be made, based on the RMS values of each individual total pressure probe in the rake. The statistical analysis techniques employed are described in Ref 117.

13.1.5 Intake flow dynamic study

To design a control system for a variable-geometry intake, the dynamic characteristics of the internal flow have to be studied. It is also important to identify the level of the wall pressure rise, in transient flow, for the design of the intake structure. To perform such a study, high speed rotating vanes can be installed at the compressor face station to produce a periodic variation of the reduced mass flow. The intake is equipped with unsteady transducers which measure the amplitude and the phase lag of the pressure waves. One such device is described in Ref 115; in this example, a

negative mass flow was periodically injected by compressed air supplied through the vane. Comparison with flight evidence showed that a good simulation of the engine surge phenomenon and its effect on the intake was obtained in this way. Another similar device is presented in Ref 128.

13.1.6 Concluding Remarks

A major comparative test programme of intake measurements has been organised by ACARD and the results are currently being analysed. Models to a common design have been manufactured to slightly different scales and tested in wind tunnels at RAE (Bedford), ONERA and DLR. Both steady and unsteady measurements have been made over a wide range of incidence at $M = 0.8$ and at low incidence, over a wide range of Mach number up to $M = 1.8$. The models represent a simple subsonic-type pilot intake with a circular cross-section and blunt lip. Details of the instrumentation used in the various tunnels and examples of the results are given in Ref 117. The first impression from this exercise is that the results show an impressive standard of consistency, even when differences in the absolute values of the distortion indices are observed, the trends with mass flow are broadly similar. The final conclusions from this work will be presented at an ACARD symposium in September 1991. It is likely that a similar cooperative exercise will be proposed on a more complex intake design.

13.2 Tests on Afterbody Models

Wind tunnel testing to determine the true aerodynamic characteristics over the afterbody of a full-scale combat aircraft is perhaps the most difficult task in all the problem areas discussed in this lecture. The normal complete model test with the model supported on a solid sting from the rear is deficient in two respects. First, the jet effects are being ignored (since it is only in rare cases that the sting itself provides an acceptable representation of the jet plume) and second, the shape of the afterbody has probably been distorted appreciably to admit the sting. For example, if the aircraft afterbody has two nozzles with their exits at the body rear end, the gully between these two nozzles may well have been partly filled in to admit the sting. This could have a dramatic effect on the viscous flow development affecting not merely the external drag but also the effectiveness of any tail surface in the vicinity. Early flight-tunnel comparisons for aircraft such as the Lightning revealed various differences in the directional stability characteristics which were subsequently traced to the unrepresentative shape of the model afterbody. Supplementary model tests must therefore be made but many questions then arise, eg should one test a partial model or should one test the complete model with the true afterbody but mounted in a different manner and how should either of these models be supported? Also, what should one measure, eg should one test a partial model or should one test the complete model with the true afterbody but mounted in a different manner and what should one measure, eg total thrust minus drag or separate balances for thrust and drag or drag by means of a pressure integration? Further, how should the jets be simulated, eg by high pressure air ducted to the nozzles and direct blow or by use of a turbine or ejector simulator? There is no simple or unique answer to any of these questions. It all depends on the aircraft shape and on the test requirements. A study of the literature suggests that every conceivable answer has already been tried but it is still difficult to arrive at any general conclusions. The chapters (Refs 12, 13) by Bowers and Carter in the ACARD Working Group WCO8 report are the most recent

attempts to review the scene and the following text is broadly in line with their conclusions. The leading questions outlined above are discussed in turn but it will soon be realised that they are very interrelated, i.e. the answer to one question is likely to depend on what answer has been given to one of the other questions.

13.2.1 Complete or partial models?

One cannot give a general answer to this question except to comment that, as combat aircraft have become more closely coupled, the case for testing a complete model or at least a closer approximation to a complete model has strengthened. Jaarsma in Ref 129 gave a good review of the relative advantages and disadvantages of testing partial and complete models. In favour of partial models, one can quote larger scale, better potential accuracy, ability to incorporate more instrumentation, a more faithful representation of the primary and, when necessary, secondary and even tertiary jet streams and probably cheaper testing for parametric investigations. On the other hand, the common practice of using a cylindrical forebody may mean that the afterbody is being tested in a very unrealistic environment. In favour of testing a complete model, the principal advantages are better external simulation and duplication of nozzle environment, better accounting of mutual interferences and forebody influence, more accurate simulation of aircraft aerodynamics and plume interference. On the other hand, the models are smaller, the instrumentation more limited and it is difficult to include secondary and tertiary air. It is tempting to say that it is not a question of either/or but rather of deciding that one needs both the complete model for overall effects and a partial model for the development of the nozzle/aft end.

It is arguable that the past literature on this subject does not place enough emphasis on the need for a representative approach boundary layer ahead of the afterbody. The flow over the afterbody is strongly viscous and it is just as important as on an advanced wing to have a good simulation of the full scale boundary layer. The advances in CFD methods may make it possible to do this much more scientifically than in the past. This concern about the boundary layer does not necessarily favour use of a partial model despite its larger size and the probability that one can more easily modify the approach boundary layer. The pressure gradients imposed by the flow field of the rest of the aircraft may be more important factors. In determining the boundary layer development increasingly, the trend is toward a compromise between a partial and a complete model. This is shown by Fig 49 which is a picture of a new rig being developed for RAE (Pyestock) by ARA. Strictly, this is a strut-supported partial afterbody model but it can include a correctly scaled representation of the aircraft forebody, forward lifting surfaces and the inner wing which, on the underside, forms the upper part of the support strut.

13.2.2 Methods of model support

Many different types of model support have been proposed and explored, including such ideas as mounting the complete model from the nose at the tail-end of a long interference-free tube stretching from the tunnel settling chamber. In general, however, one can characterise all rigs in common use as being of one of three possible types, viz sting-mounted on an annular sting(s), wing-tip mounted and strut mounted (Figs 50a-c). Considering each of these in turn

(i) mounting the model on an annular or a pair of annular stings is perhaps the obvious method of testing a complete powered model. It certainly is the best approach for minimising support interference and, for this reason, may be the only way of obtaining data close to $M = 1.0$. However, there is one important interference consideration as to whether the free jet plume is represented correctly in the presence of the sting. This question has been studied at AEDC (Ref 130) where annular stings have been used to support large models of aircraft such as the F-16. In a research exercise at AEDC, it was found that the sting flare should be at least 3 body diameters downstream of the nozzle base with a 10' boattail and 5 diameters downstream of a cylindrical boattail. The sting interference could be determined experimentally by mounting the model, with alternatively the true rear-end and with the modified rear-end and dummy sting, on a swept support strut. The decisive final point as to whether one can use an annular sting support is the extent to which the afterbody has to be distorted to admit the sting. It is likely that to avoid serious distortion, this method of mounting can only be used for tests at low incidence.

(ii) Ref 12 concludes that wing-tip mounting is a viable alternative especially for incremental afterbody/nozzle testing but only if the Mach number range between $M = 0.8$ and $M = 1.1$ can be avoided. In one unpublished case, however, the subsonic range was extended successfully up to $M = 0.92$ by the use of specially designed bodies at the wing tip. The wing planform geometry has to be modified near the tip for structural reasons. The rig interference has to be judged on the basis of comparative tests with and without dummy wing tip support hardware with the model mounted on a slender sting. Hopefully, this interference would not change significantly between configurations while testing a series of different but similar afterbodies/nozzles.

(iii) Clearly, a strut mounting is the best scheme from the point of view of support strength, rigidity and duct space for instrumentation and high pressure air but the overriding issue is whether the aerodynamic interference is acceptable. Also, obviously, the technique cannot be used for testing under sideslip conditions and also, there may be difficulties at high incidence. Close to $M = 1.0$, very large interference drag values have been reported, e.g. 20 or even 80 drag counts, but the magnitude of this interference and the Mach number range over which it is unacceptable will depend on the geometry of the strut support and on how much of the installation is metric. A wide range of different strut geometries were compared in Ref 131. Ref 12 concluded that despite all the problems, the strut support would continue to be used but all new arrangements should be based on empirical guidelines, past experience and increasingly, theoretical CFD tools should be used in the design. It will be noted that, in the most recent design shown in Fig 49, the strut is swept forward rather than swept aft as in many past arrangements. Also, forces are being measured on the entire model/rig by means

of an accurate underfloor balance. It is hoped that the relatively large size of this rig will enable studies to be made of not merely the afterbody drag but also of the unsteady flow over the afterbody.

13.2.3 Type of measurements

To illustrate the potential variety, Fig 51a-f shows six different strut-supported model configurations with afterbody forces being measured with one or more force balances. The total metric model thrust-minus-drag arrangement (A) is considerably different from the three afterbody-only thrust-minus-drag configurations (B,C,D) and the afterbody drag balance models (E,F). Ref 12 comments that there is no convention or standard for afterbody/nozzle force balance arrangements.

Multiple force balances are often used to determine separately the forces on different parts of the model. A typical system could consist of a main balance to determine lift and thrust-minus-drag of the afterbody together with a thrust balance to measure nozzle normal and axial forces; the weakness of this approach is that drag is determined as the difference between two large quantities. Another possible way to determine the drag is to pressure plot the afterbody; this may be a sensible idea when testing relatively simple, eg cylindrical afterbodies but, in general, it may be difficult to include enough holes on a complex shape to obtain an accurate integration.

The force balances used in arrangement such as some of those illustrated in Fig 51 are often complicated and their output requires corrections to provide data with acceptable inaccuracy. In addition to the balance interferences determined in a calibration of the bare balance, corrections are needed for pressure area tare forces (including cavity, metric seal and base pressures) and for momentum tares. Any bellows system also has to be calibrated. These corrections may easily be greater than the final corrected drag. If the model includes both metric and non-metric parts the position of the break between them has to be chosen carefully, thinking of both aerodynamic and structural considerations. It should be in a region of relatively uniform pressure and at a position where any flexing of the model under load does not introduce a step at the break.

Ref 12 concludes that new model configurations and balances should be designed and built to suit the test objectives, the test facility and the configuration itself and in the light of past experience.

13.2.4 Jet simulation

The above discussion has concentrated on models with direct blow exhaust simulation, but with the close coupled nature of many modern aircraft and even more when one looks forward to ASTOVL designs, it is no longer strictly admissible to ignore possible interactions between intake and exhaust flows. The need to test inlet and exhaust flows in combination was recognised more than 10 years ago in the US and this led to the development of the model engine unit known as CMAPS (Compact Multi-mission Aircraft Propulsion Simulator). This is shown in Fig 52 and descriptions are to be found in Refs 132 and 133 and various other references quoted in Ref 13. This unit has a 4-stage axial compressor driven by the power generated by a single stage turbine. The turbine is driven by the high pressure inlet air which is then mixed with compressor air through a mixer/ejector module to provide the exhaust nozzle total pressure air supply. Performance details are summarised in Ref 13. Carter in 1986 noted that the application of

CMAPS technology in test programmes was still in its infancy and, apart from an early programme of operating tests at AEDC, the only recorded application of CMAPS is that described in Ref 132. Fig 53 shows the installation of CMAPS in the model for this application: it will be seen that a single support sting brings the drive air into the model and takes the turbine air out of the model. The sting entry is from below the fuselage at the centre of gravity up into a manifold system which distributes the high pressure air ducts out to the two earthed simulators in the wings. The live model shell is mounted on the live rear end of the balance. Considerable effort has been put into the development of CMAPS and appropriate calibration facilities at NASA Ames but the vital feature which inhibits its application to models of VSTOL combat aircraft is its geometry: an inlet to nozzle separation length of 9.5 engine diameters which is much too long to allow installation in a close-coupled configuration. Design studies for the design of a powered simulator of more relevant geometry are being made in the UK and one can express guarded optimism that, in the long term, these efforts will be successful.

The other possibility is to develop an ejector powered simulator. Carter in 1986 concluded (Ref 14) that these were capable of providing an adequate simulation of the flow requirements of current engines but that the length/diameter ratios of these simulators were likely to be even higher than for CMAPS. Hence, at the present time, for routine tests on models of combat aircraft, there is no practical alternative to the direct blow approach.

Finally, it should be noted that none of these simulators provides simulation of the full-scale jet temperature. Modern turbo-jet and turbofan effluvia operate in the region 1500° to 1700° R while the majority of model afterbody testing is conducted with a cold jet near 500° R. There are two ways in which the jet affects the afterbody drag. First the drag is reduced by the jet plume forward pressure interference and second, the drag is increased by the jet entrainment. Experimental work reported in Ref 134 studied how the jet plume shape and entrainment depended on the physical properties of the exhaust. Carter in Ref 13 concludes that the effects of jet temperature are likely to be most significant in the transonic flow range where large areas of base or separated afterbody flows occur. The effects are greater for large afterbody angles and can be as large as 35% of the jet-off afterbody drag for high jet pressure ratios. 20% is perhaps a more typical figure; the cold jet results will give pessimistic afterbody drag predictions. The effects of temperature are therefore significant and configuration-dependent but it is unlikely that any serious attempt will be made to develop methods for heating the jets in routine model testing. The effects should however not be ignored.

14 FINAL COMMENTS

This lecture has reviewed the experimental techniques in use in wind tunnel model tests for performance prediction. The review is inevitably tinged with personal bias but it is hoped that the subject is covered in detail and the large number of references will be of continued benefit. Looking to the future, we are clearly at the threshold of a large expansion in the use of non intrusive optical techniques: laser holography, laser anemometry and particle image velocimetry to study and measure the flow field. These developments are vital for the validation of new CFD methods and so, one can claim that experimental techniques and their further refinement are the key to future progress in aerodynamics in general.

Acknowledgements

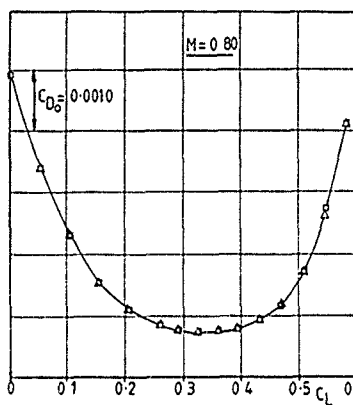
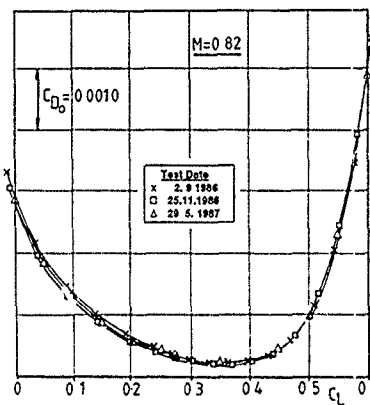
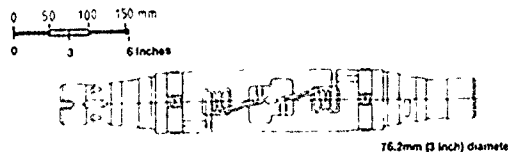
The author wishes to acknowledge gratefully the help of Mrs A Ellim and Mrs M Connolly in preparing this lecture, various useful discussions with members of the staff of ARA and RAE (Farnborough and Bedford) and the permission of MOD(PE) to publish the lecture.

References

- 1 Wolf S W, Status of adaptive wall technology for minimisation of wind tunnel boundary interferences, 1990, ICAS-90-6.2.1.
- 2 Goodyer M J, The self streamlining wind tunnel, 1957, NASA TM-X-72699.
- 3 Ganzar U, Igata Y, Ziemann J, Design and operation of TU-Berlin wind tunnel with adaptable walls, 1984, ICAS-84-2.1.1.
- 4 Hornung H (ed), Adaptive wind tunnel walls, technology and application, 1990, Report of ACARD WG12, ACARD-AR-269.
- 5 Barnwell R W, Edwards C L W, Kilgore R A, Dress D A, Optimum transonic wind tunnels, 1986, AIAA 86-0755.
- 6 Britcher C P, Progress towards large wind tunnel magnetic suspension and balance systems, 1984, AIAA 84-0413.
- 7 Kilgore R A, Lawing P L, Cryogenic wind tunnels for high Reynolds number testing, 1988, ICAS 88-3 8 4.
- 8 Lester M L (ed), Boundary layer simulation and control in wind tunnels, 1988, Report of ACARD WG09, ACARD-AR-224.
- 9 Harris A E, Carter E C, Wind tunnel test and analysis techniques using powered simulators for civil nacelle installation drag assessment, 1981, ACARD CP 301-24.
- 10 Harris A E, Palitaw K C, Civil turbofan propulsion system integration studies using powered testing techniques at ARA Bedford, 1984, AIAA 84-0593.
- 11 Goldammer M J, Steinle F W, Design and validation of advanced transonic wings using CFD and very high Reynolds number wind tunnel testing, 1990, ICAS-90-2 6 2
- 12 Bowers D L, State of the art assessment of testing techniques for aircraft afterbodies, Aerodynamics of Aircraft Afterbodies Report of WG08, 1986, ACARD AR-226
- 13 Carter E C, Jet simulation, Aerodynamics of Aircraft Afterbodies Report of WG08, 1986, ACARD-AR-226
- 14 Wind tunnel flow quality and data accuracy requirements, 1982, ACARD-AR-184
- 15 Carter E C, Pallister K C, Development of testing techniques in a large transonic wind tunnel to achieve a required drag accuracy and flow standards for modern civil transports, 1985, ACARD CP 429, Paper no 11
- 16 Wood M N, Cappa D S, The accurate measurement of drag in the 8 ft x 8 ft tunnel, 1985, ACARD CP 429, Paper no 9
- 17 Ashill P R, Private communication, 1990
- 18 Ewald B, Giesecke P, Polanski L, Schenck C, Automatic calibration machine for cryogenic and conventional internal strain gauge balance, 1990, AIAA 90-1396
- 19 Gross C, Juanarena D B, A miniature 48-channel pressure sensor module capable of in-situ calibration, 1977, ISA 23rd International Instrumentation Symposium
- 20 Juanarena D B, A distributed processing high data rate multiport wind tunnel pressure measurement system, 1977, ISA 23rd International Instrumentation Symposium
- 21 Juanarena D B, A multiport sensor and measurement system for aerospace pressure measurements, 1979, ISA 25th International Instrumentation Symposium
- 22 Gross C, Juanarena D B, Electronically scanned pressure scanners, 1981, Transducer/Tempcon '81 Conference, Wembley, England
- 23 Bergh H, Tijldean H, Theoretical and experimental results for the dynamic response of pressure measuring systems, 1965, NLR-TR-238.
- 24 Welsh B L, Pyne C R, Cripps B E, Recent developments in the measurement of time-dependent pressure, 1983, ACARD CP-348, Paper no 36.
- 25 Welsh B L, McOwat D M, PRESTO - a system for the measurement and analysis of time dependent signals, 1979, RAE-TR-79135.
- 26 Mabey D G, Welsh B L, Measurements and calculations of steady and oscillatory pressures on a low aspect ratio model at subsonic and transonic speeds, 1987, Journal of Fluids and Structures, 445-468.
- 27 Horstjen J J, Recent developments in the unsteady pressure measuring technique, 1981, NLR-TR-81-055U.
- 28 Haines A B, Jones J C M J, The centre-line Mach-number distribution and auxiliary suction requirements for the ARA 9 ft x 8 ft transonic wind tunnel, 1960, R&M 3140.
- 29 Blinton W Jr, Potentials for pseudo-Reynolds number effects, 1988, ACARD-AG-303, Chapter 2
- 30 Kennedy T L, An evaluation of wind tunnel test techniques for aircraft nozzle afterbody testing at transonic Mach numbers, 1980, AEDC-TR-80-8(AD-A091775)
- 31 Aulehla F, Pseudo-Reynolds number trends, 1987, AIAA 5th Applied Aerodynamics Conference, Monterey
- 32 Baxendale A J, Carberry J, Day J, Green J E, Replacement of the flow smoothing screen in the ARA 9' x 8' TNT by a long cell honeycomb, 1990, ARA Memo 339
- 33 Dougherty N S Jr, Fisher D F, Boundary layer transition on a 10 deg cone wind tunnel/flight data correlation, 1980, AIAA 80-0154.
- 34 Dougherty N S Jr, Steinle F W Jr, Transition Reynolds number comparisons in several major transonic tunnels, 1974, AIAA 74-627
- 35 Murthy S V, Effects of compressibility and freestream turbulence on boundary layer transition in high subsonic and transonic flows, 1986, AIAA 86-0764
- 36 Long D, An experimental evaluation of test section noise in transonic wind tunnels, 1990, AIAA 90-1419
- 37 Michel R, Coustois E, Arnal D, Transition calculations in three-dimensional flows, 1985, ONERA TP 1985-7
- 38 Green J E, On the influence of free-stream turbulence on a turbulent boundary layer, as it relates to wind tunnel testing at subsonic speeds, 1972, RAE IR 72201
- 39 Hancock P E, Bradshaw P, The effect of free-stream turbulence on turbulent boundary layers, 1983, Transactions of the ASME, Vol 105.
- 40 Mabey D G, Flow unsteadiness and model vibration in wind tunnels at subsonic and transonic speeds, 1971, ARC CP 1555
- 41 Mabey D G, A review of some recent research on time-dependent aerodynamics, 1984, Journal Royal Aeronautical Society
- 42 Garner H C, Rogers E V E, Acum W E A, Maskell E C, Subsonic wind tunnel corrections, 1966, ACARD Report 109.
- 43 Berndt S B, Wind tunnel interference due to lift for delta wings of small aspect ratio, 1950, KTH Sweden Tech Note TN 19.
- 44 Evans J Y G, Corrections to velocity for wall constraint in any 10 x 7 rectangular subsonic wind tunnel, 1949, ARC R&M 7662
- 45 Thom A, Blockage corrections in a closed high-speed tunnel, 1943, ARC R&M 2033
- 46 Thompson J S, Present methods of applying blockage corrections in a closed rectangular high speed wind tunnel, 1948, ARC Report 11385

- 47 Kirby D A, Spence A, Low-speed-tunnel model tests on the flow structure behind a delta-wing aircraft and a 40 deg swept-wing aircraft at high incidences, 1955, RAE R&M 3078.
- 48 Baldwin B S et al, Wall interference in wind tunnels with slotted and porous boundaries at subsonic speeds, 1954, NACA Tech Note 3176.
- 49 Wright R H, The effectiveness of the transonic wind tunnel as a device for minimising tunnel-boundary interference for model tests at transonic speeds, 1959, AGARD Report 294.
- 50 Goethert B H, Transonic wind tunnel testing, 1961, AGARDograph 49, Pergamon Press.
- 51 Kassner R R, Subsonic flow over a body between porous walls, 1952, WADC Tech Report 52-9.
- 52 Browne Miss G C, Bateman T E B, Pavitt M, Haines A B, A comparison of wing pressure distributions measured in flight and on a windtunnel model of the Super VC10, 1972, RAE R&M 3707.
- 53 O'Hara F, Squire L C, Haines A B, An investigation of interference effects on similar models of different size in various transonic tunnels in the UK, 1959, RAE Tech Note Aero 2606, ARA Wind Tunnel Note 27.
- 54 Page W A, Experimental study of the equivalence of transonic flow about slender cone-cylinders of circular and elliptic cross section, 1958, NACA TN 4233.
- 55 Berndt S B, Theoretical¹ aspects of the calibration of transonic test sections, 1957, FFA Report 74.
- 56 Berndt S B, Sorensen H, Flow properties of slotted walls for transonic test sections, 1975, AGARD CP 174, Paper 17.
- 57 Stickles W, Erickson J C Jr, Wall interference corrections for two dimensional transonic flows, 1990, AIAA-90-1408.
- 58 Smith J, A method for determining 2D wall interference on an aerofoil from measured pressure distributions near the wall and on the model, 1981, NLR TN 810160.
- 59 Capellier C, Chevallier J F, Bounot F, Nouvelle Méthode de correction des effets de parois en courant plan, 1978, La Recherche Aérospatiale, No 1, pp 1-11.
- 60 Kepp W B Jr, Toward the correctable-interference transonic wind tunnel, 1976, AIAA-76-1794CP.
- 61 Nurman E M, A correction method for transonic wind tunnel wall interference, 1979, AIAA-79-1533.
- 62 Kraft F M, Ritter A, Lester M L, Advances at AFDC in treating transonic wind tunnel wall interference, 1986, ICAS Proceedings, pp 748-769.
- 63 Mineck R Green L, Wall interference assessment/correction (WIAC) for transonic aerofoil data from porous and shaped wall test sections, 1990, AIAA-90-1406.
- 64 Ashill P R, Weeks D, A method for determining 1st -interference corrections in solid-wall tunnels from measurements of static pressure at the walls, 1982, AGARD CP 335.
- 65 Ashill P R, Keating R F A, Calculation of tunnel wall interference from wall-pressure measurements, 1988, RAEs Journal, pp 36-53.
- 66 Kirpatrick B, Woodward D, Priorities for high-lift testing in the future, 1990, AIAA 90-1415.
- 67 Coethert B, Windkanalkorrekturen bei hohen Unterschallgeschwindigkeiten unter Besonderer Berücksichtigung des geschlossenen Kreislaufanals 1940, Deutsche Luftfahrtforschung Forschungsbericht 1216, Translated as NACA Tech Memo 1300.
- 68 Jacocks J L, Aerodynamic characteristics of perforated walls for transonic tunnels, 1977, ADLC-TS-77-61 (AD-A040904).
- 69 Beach H L Jr, Bushnell D M, Aeronautical facility requirements into the 2000s 1990 AIAA-90-1-175.
- 70 Jelly A H, Mundell A R G, Firkins A J, Wind tunnel model support interference corrections for a three-strut mounting, 1989, RAE Tech Memo Aero 2154.
- 71 Hardy B C, A numerical study of the aerodynamic interference of a model support system used in the 8 M metre wind tunnel, 1985, RAE Tech Memo Aero 2046.
- 72 Saiz M, Quemard C, Airbus A310, essais dans la soufflerie Fl de l'ONERA, comparaison vol-soufflerie, 1984, AGARD CP 238, Paper 22.
- 73 Quemard C, Willaume J, Calculs des interactions aerodynamiques d'un montage de type '3 mats', 1987, ONERA Rapport Technique No 283/1462 CN.
- 74 Haines A B, Holder D W, Pearcey H H, Scale effects at high subsonic and transonic speeds, and methods for fixing boundary-layer transition in model experiments, 1957, RAE R&M 3012.
- 75 Braslow A L, Knox E C, Simplified method for determination of critical height of distributed roughness particles for boundary-layer transition at Mach numbers from 0 to 5, 1985, NACA TN 4363.
- 76 Van Driest E R, Blumer C B, Effect of roughness on transition in supersonic flow, 1960, AGARD Report 255.
- 77 Evans J Y G, Transition fixing techniques and the interpretation of boundary layer conditions on slender wings in supersonic flow, 1964, RAE Aero 2946.
- 78 Fother L Leith, Whitfield Jack D, Effects of unit Reynolds number, nose bluntness, and roughness on boundary layer transition, 1960, AEDC-TR 605.
- 79 Nash J F, Bradshaw P, The magnification of roughness drag by pressure gradients, 1967, RAEs Aeronautical Journal, Vol 71, pp 44-46.
- 80 Stalling R L Jr, Lamb M, Effects of roughness size on the position of boundary-layer transition on the aerodynamic characteristics of a 55° delta wing at supersonic speeds, 1969, NASA TP 1027.
- 81 Ashill P R, Fulker J L, Weeks D J, The air-injection method of fixing boundary-layer transition and investigating scale effects, 1987, RAEs Aeronautical Journal, pp 214-224.
- 82 Gartenberg E, Johnson W C Jr, Johnston C B, Carraway D L, Wright R E, Transition detection studies in the cryogenic environment, 1990, AIAA-90-3024-CP.
- 83 Pearcey H H, Osborne J, Haines A B, The interaction between local effects at the shock and rear separation - a source of significant scale effects in wind tunnel tests on aerofoils and wings, 1968, AGARD CP 35, Paper 11.
- 84 Ashill P R, Wood R F, Weeks D J, An improved, semi-inverse version of the viscous Garabedian and Korn method (VGIK), 1987, RAE Technical Report 87002.
- 85 Elsner A, Experiences with transition fixing in the high speed regime at NLR, Grenzschicht Steuerung durch Transitionfixierung, 1984, DFVLR Mitteilung 84-17.
- 86 Haines A B, Experience in the use of a viscous simulation methodology for tests in transonic tunnels, 1990, AIAA-90-1414.
- 87 Fulker J L, Ashill P R, A model of the flow over swept wings with shock induced separation, 1983, RAE IR 83086.
- 88 Lock R C, Prediction of viscous and wave drag at high subsonic speeds by viscous-inviscid interaction techniques, 1985, AGARD R-723.
- 89 A method of determining the wave drag and its spanwise distribution on a finite wing in transonic flow, 1983, ESDU IDM 83022.
- 90 Melnik R E, Chow R R, Head H R, An improved viscous/inviscid interaction procedure for transonic flow over aerofoils, 1985, NASA CR 3805.

- 91 Lock R C, Williams B R, Viscous-Inviscid interactions in external aerofoil aerodynamics, 1985, Progress in Aeronautical Sciences, Pergamon Press
- 92 Elsenaar A, The wind tunnel as a tool for laminar flow research, 1990, ICAS-90-6.1 1
- 93 Somers D M, Stack J P, Harvey W D, Influence of surface static-pressure orifices on boundary-layer transition, 1984, NASA TM 84492.
- 94 Boersen S J, Elsenaar A, Half-model tests in the MLR high speed wind tunnel HST. Its technique and application, 1983, AGARD CP 348.
- 95 Decher R, Tegeler D, High accuracy force accounting procedures for turbo powered simulator testing, 1975, AIAA 75-1324.
- 96 Pugh G, Harris A E, Establishment of an experimental technique to provide accurate measurement of the installed drag of a full span model with turbine powered engine simulators, 1981, AGARD-CP-301, Paper 25
- 97 Haines A B, Aerodynamic interference - a general overview, 1983, AGARD-R-712, Paper 9
- 98 Burgsmüller W, Akleman E, Kool J W, Engine simulation with turbo-powered simulators, 1990, DNW Colloquium.
- 99 Krenz G, Engine/airframe interference, 1983, AGARD-R-712, Paper 14
- 100 Eckert D, van Ditzhuijsen J C A, Munnikmaa B, Burgsmüller W, Low speed engine simulation on a large scale transport model in the DNW, 1984, ICAS-84-2 10.1
- 101 Burgsmüller W, Szodruch J, Benefits and costs of powered engine simulation at low speeds, 1985, AIAA-85-0381
- 102 Beavis D G, Transonic wind tunnel testing of propellers, 1987, Canadian Aeronautics and Space Institute Symposium on Aircraft Propulsion Systems, Toronto, Canada
- 103 Beavis D G, Pozniak O M, Facilities for the development of propellers and propeller installations at ARA, 1988, RAE International Conference on Advanced Propellers and their Installation on Aircraft
- 104 Wood Mrs M E, The design and commissioning of an acoustic liner for propeller noise testing in the ARA transonic wind tunnel, 1989, 1 Mech E AeroTech '89
- 105 Harris A E, Render P M, Pozniak O M, Wood M E, Recent wind tunnel testing experience of contra-rotating propellers, 1990, ICAS-90-4 1
- 106 Barber G J, Performance evaluation of full scale propellers by wind tunnel test, 1984, AGARD-CP-366
- 107 Metzger F B, Prop-fan design and test experience, 1988, RAE International Conference on Advanced Propellers and their Installation on Aircraft
- 108 Groeneweg J F, Aeroacoustics of advanced propellers, 1990, ICAS-90-4 2
- 109 Vrorno D F, Hughes J F, Aerodynamic integration of aft-mounted LHB propulsion systems, 1987, AIAA-87-2920
- 110 Bengelink R L, Doerzbacher R P, Krynytzky A J, The development and calibration of an acoustic wall transonic test section, 1986, AIAA-86-0759-CP
- 111 Wong P W C, Maina M, Forsey C R, Bocci A J, Single and contra rotation high speed propellers flow calculation and performance prediction, 1988, ICAS-88-2 4 2
- 112 Steffko G L, Jeracki R L, Porous wind tunnel corrections for counterrotation propeller testing, 1988, AIAA-88-2055
- 113 Kirker T, Procurement and test of a 1/5 scale advanced counter rotating propfan model, 1990, AIAA-90-2075.
- 114 AGARD c Committee, Engine-airplane interference and wall corrections in transonic wind tunnel tests, 1971, AGARD-AR-36-71.
- 115 Carter E C, Experimental determination of inlet characteristics and inlet and airplane interference, 1972, AGARD-LS-53, Paper 3
- 116 Carter E C, Technical evaluation report on Fluid Dynamics Panel symposium on airframe/propulsion interference, 1975, AGARD-AR-81.
- 117 Leynaert J, Air intake testing, 1991, Air intakes for high speed vehicles, AGARD Working Group 13 Report
- 118 Stevens C H, Speng E D, Hammock M S, F15 Inlet/engine test techniques and distortion methodologies studies, Vol I - technical discussion, 1978, NASA CR 144866.
- 119 Mitchell J C, Fluid dynamic aspects of turbine engine testing, 1983, AGARD-R-348.
- 120 Auhela F, Schmidt D M, Intake swirl and simplified methods for dynamic pressure distortion assessment, 1988, VKI Lecture Series 1988-04 - Intake Aerodynamics.
- 121 Guo R W, Seddon J, The swirl in an S-duct of typical air intake proportions, 1983, Aeronautical Quarterly
- 122 Carrere P, Aperçu de quelques problèmes aérodynamiques actuels posés par les prises d'air supersoniques, 1972, 1er Symposium International sur les Progrès des Réacteurs d'Avion, Marseille, ONERA TP 1102.
- 123 Seddon J, Goldsmith E L, Intake aerodynamics, 1985, Collins ed
- 124 Mackrodt P A, Schmid D M, Experimentelle Untersuchungen an einem Unterrumpf Rampeinlauf bei Überschallströmung 1986, Jahrbuch 1 der DGLR
- 125 Jockcs J L, Statistical analysis of distortion factors, 1972, AIAA-72-1100
- 126 Surber L E, Fuglenga Clay, Inlet engine compatibility, 1988, VKI Lecture Series 1988-04 - Intake Aerodynamics
- 127 Marous J, Sedlock D, An analog editing system for inlet dynamic flow distortion, DYNADEC Past, present and future, 1980, AIAA-80-1108
- 128 Lotter K, Mackrodt P A, Scherbaum R, Engine surge simulation in wind-tunnel model inlet ducts, 1988, 16th ICAS
- 129 Jaarsma F, Experimental determination of nozzle characteristics and nozzle airframe interference, 1972, AGARD LS-53
- 130 Price E A, Investigation of F-16 nozzle-afterbody forces at transonic Mach numbers with emphasis on support system interference, 1981, AEDC-TR-80-27
- 131 German R C, Strut support interference on a cylindrical model with boattail at Mach numbers from 0.6 to 1.4, 1976, AEDC-TR-76-40
- 132 Bailey R O, Krauz M, Hiley P, The design of a wind tunnel VTOL fighter model incorporating turbine powered engine simulators, 1981, AIAA-81-2635
- 133 Smith S C, Determining compressor inlet airflow in the compact multi-mission aircraft propulsion simulators in wind tunnel applications, 1983, AIAA-83-1231
- 134 Compton W B, An experimental study of jet exhaust simulation, AGARD CP 150-16

FIG 1 REPEATABILITY STANDARD WITHIN A GIVEN TEST
(ARA TRANSONIC TUNNEL, FROM REF 15)FIG 2 REPEATABILITY STANDARD BETWEEN TESTS
(ARA TRANSONIC TUNNEL, FROM REF 15)

Maximum Design Loads					
Normal Force	17.3 kN	4000 lbs	Side Force	4.18 kN	940 lbs
Axial Force	2.22 kN	500 lbs	Yawing Moment	0.73 kNm	535 lb ft
Pitching Moment	2.26 kNm	1670 lb ft	Rolling Moment	0.73 kNm	535 lb ft

FIG 4 RAE STRAIN GAUGE BALANCE

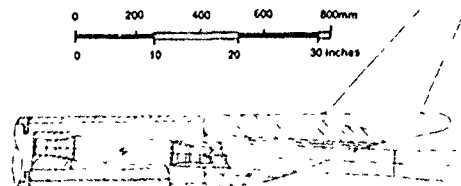


FIG 5 ARRANGEMENT OF COMPLETE MODEL ON STING/BALANCE

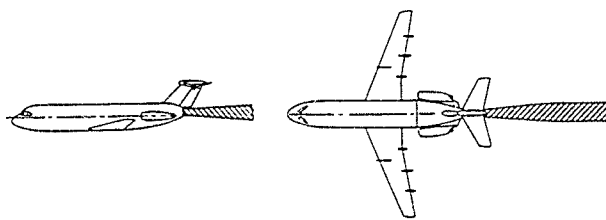


FIG 3a AIRCRAFT MODEL WITH 2 AFT-MOUNTED NACELLES

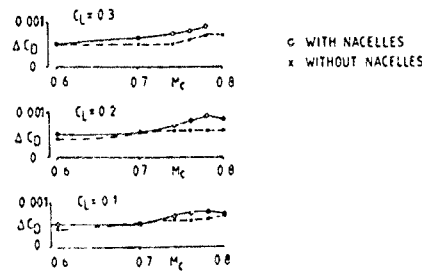


FIG 3b STING CORRECTIONS, WITH AND WITHOUT NACELLES FOR MODEL IN FIG 3a

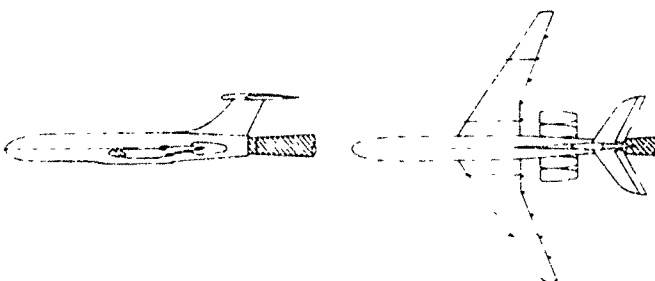
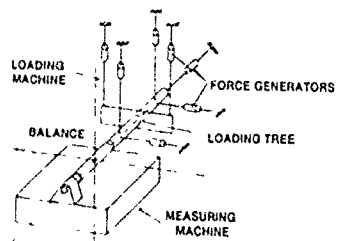
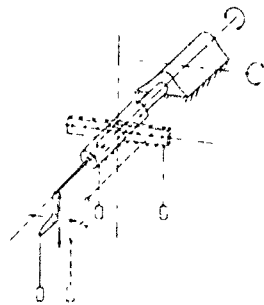
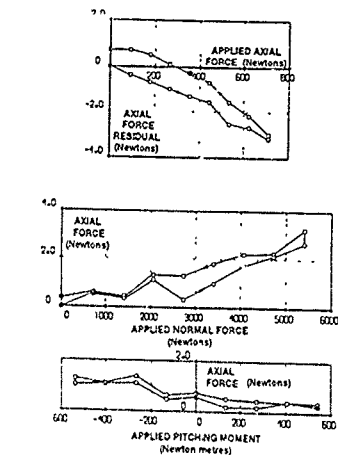
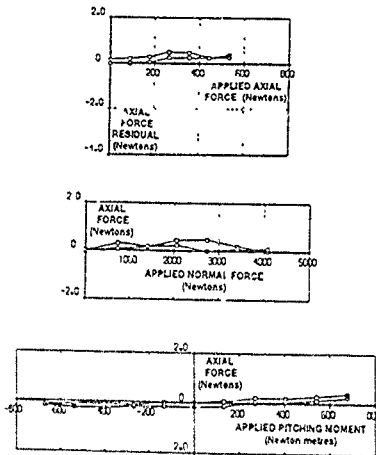


FIG 3c AIRCRAFT MODEL WITH 4 AFT-MOUNTED NACELLES



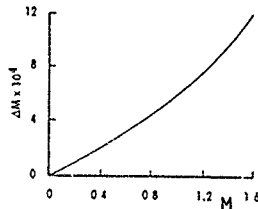


FIG 8a ERROR IN MACH NUMBER TO GIVE 1 DRAG COUNT ERROR IN AFTERBODY DRAG
(FROM REFS 29,30)

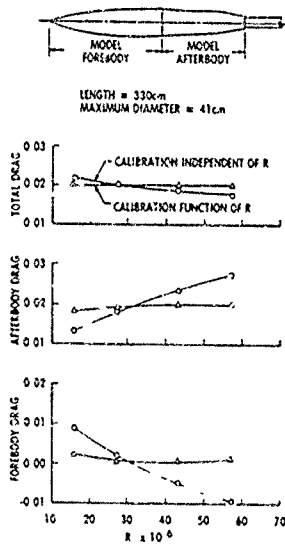


FIG 8b VARIATION OF AFTERBODY PRESSURE DRAG WITH REYNOLDS NUMBER
EFFECT OF IGNORING VARIATION IN TUNNEL CALIBRATION
(FROM REFS 29,30)

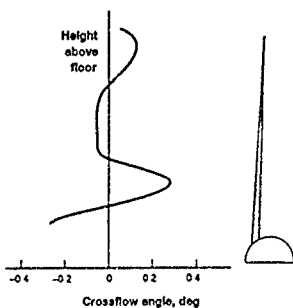


FIG 9 MEASURED WIND TUNNEL CROSSFLOW DISTRIBUTION (NASA AMES 11 x 11 TUNNEL, FROM REF 11)

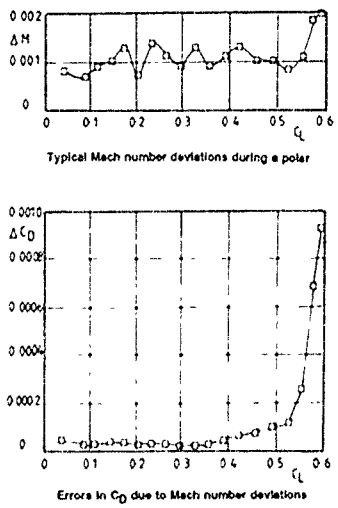


FIG 11 EFFECTS OF VARIABILITY IN MACH NUMBER (FROM REF 15)

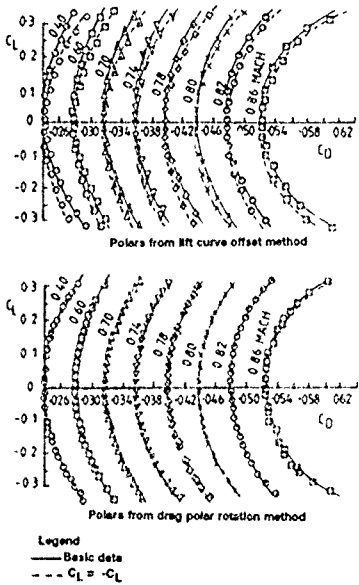
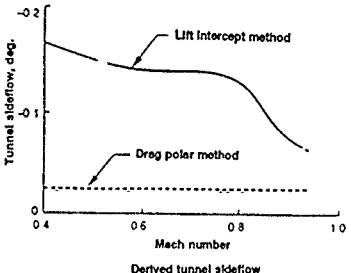


FIG 10 SYMMETRICAL AIRFOIL 'ROSSI 1% DETERMINATION (FROM REF 11)

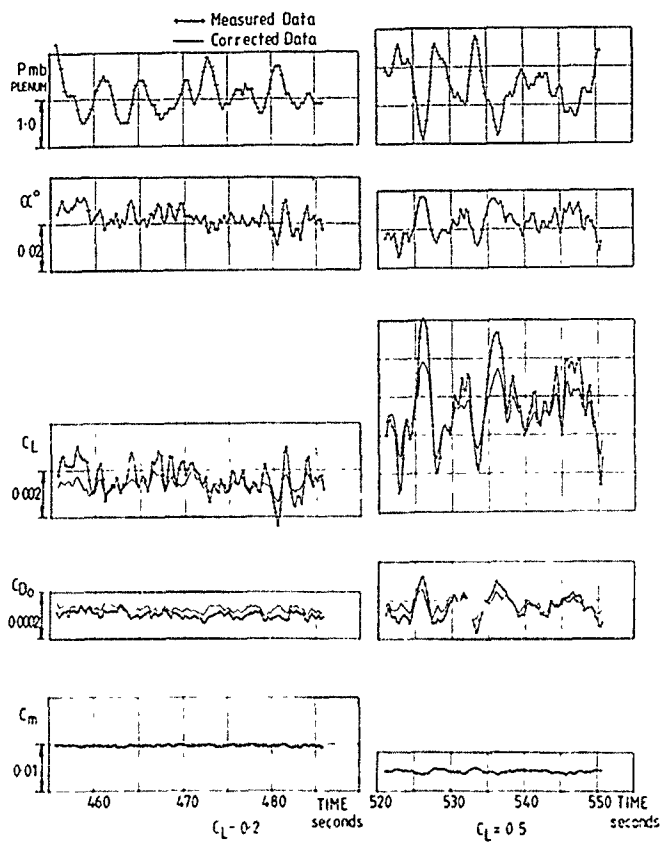


FIG 12 TIME VARIANT DATA RECORDS FOR $M = 0.8$ (ARA TRANSONIC TUNNEL, FROM REF 15)

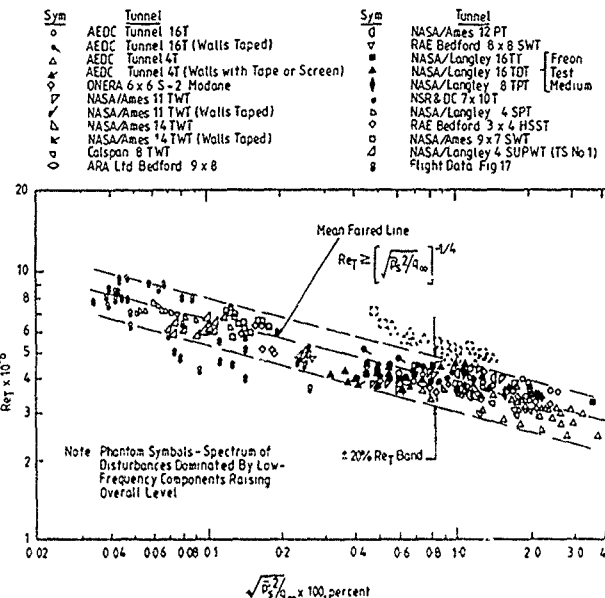


FIG 13 TRANSITION REYNOLDS NUMBERS DEDUCED FROM TESTS WITH 10° CONE (FROM REF 33)

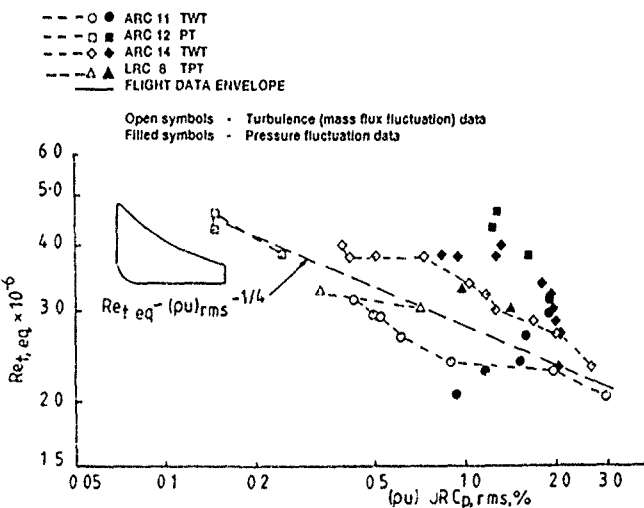


FIG 14 RESULTS OF REVISED ANALYSIS OF 10° CONE DATA (FROM REF 35)

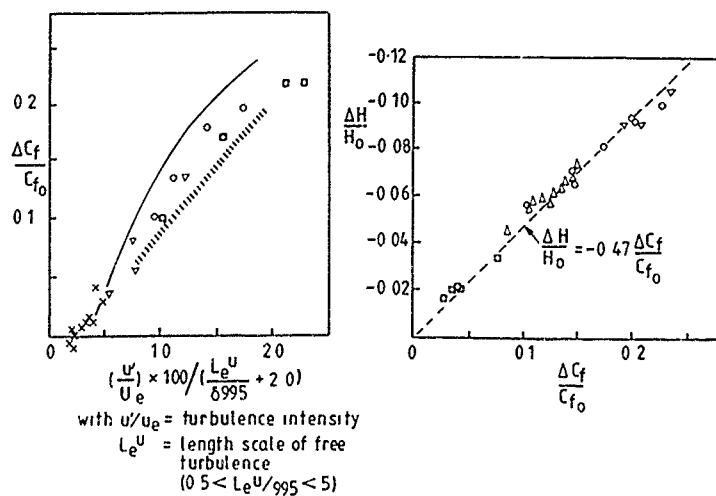
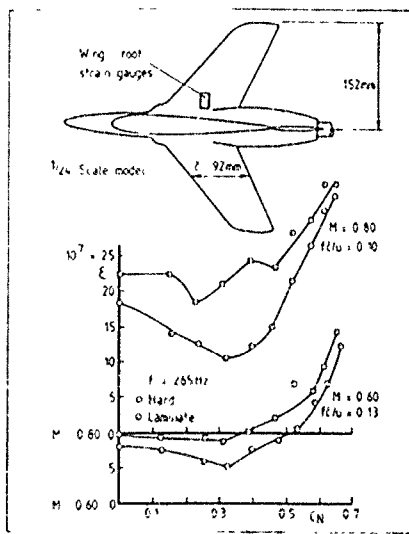


FIG 15 DEPENDENCE OF SKIN FRICTION AND SHAPE FACTOR ON TUNNEL TURBULENCE

FIG 16 DEPENDENCE OF RMS UNSTEADY WING-ROOT STRAIN ON SURFACE OF TUNNEL SLOTTED WALLS
(FROM REF 41)

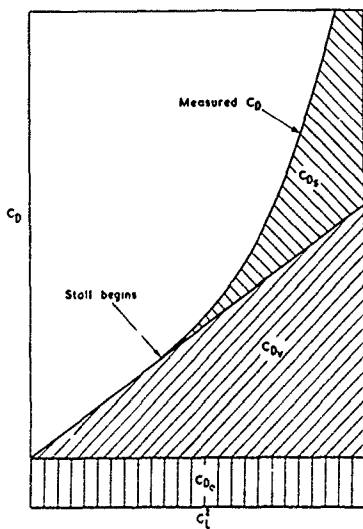


FIG. 17 DRAG ANALYSIS FOR A LIFTING WING

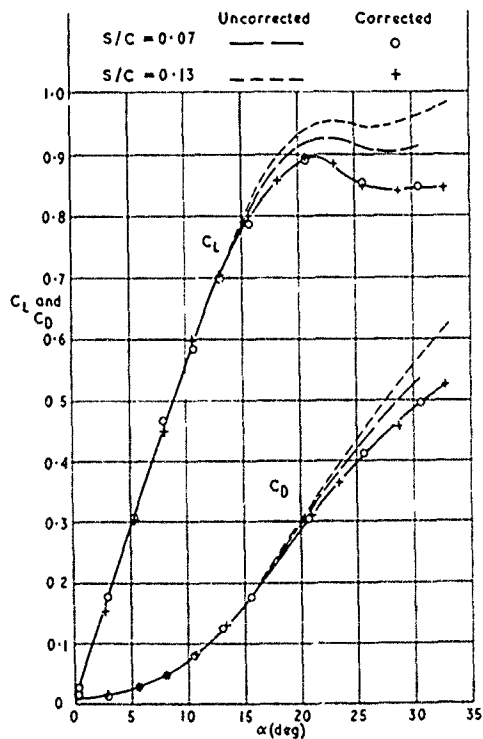


FIG. 18 APPLICATION OF BLOCKAGE CORRECTIONS AT HIGH LIFT (FROM REF. 42)

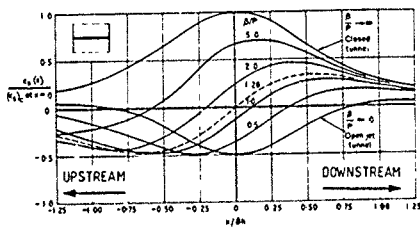


FIG 19 LONGITUDINAL DISTRIBUTION OF BLOCKAGE
IN A 2D PERFORATED WALL TUNNEL
(FROM REF 48)

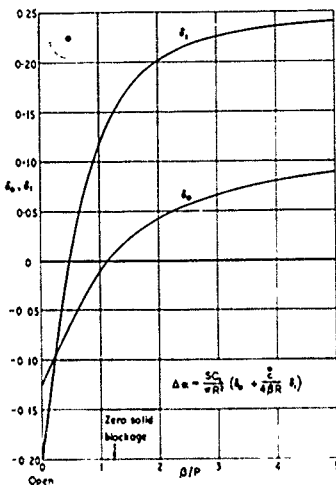


FIG 20 LIST TUNNEL CONSTRAINT FOR A SMALL
MODEL IN A PERFORATED CIRCULAR TUNNEL
(FROM REF 42)

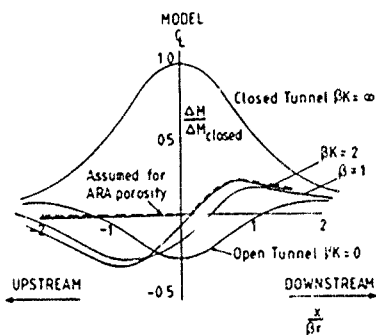


FIG 21 BLOCKAGE BUOYANCY CORRECTIONS
FOR ARA TRANSONIC TUNNEL

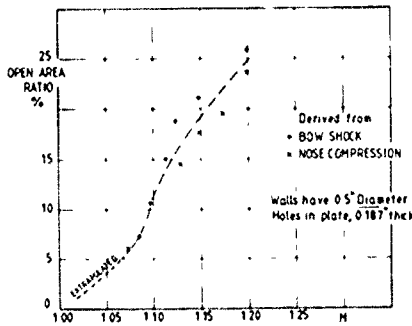


FIG 22 OPEN-AREA RATIO REQUIRED FOR
CANCELLATION OF INCIDENT SHOCK
WAVES IN THE ARA TUNNEL

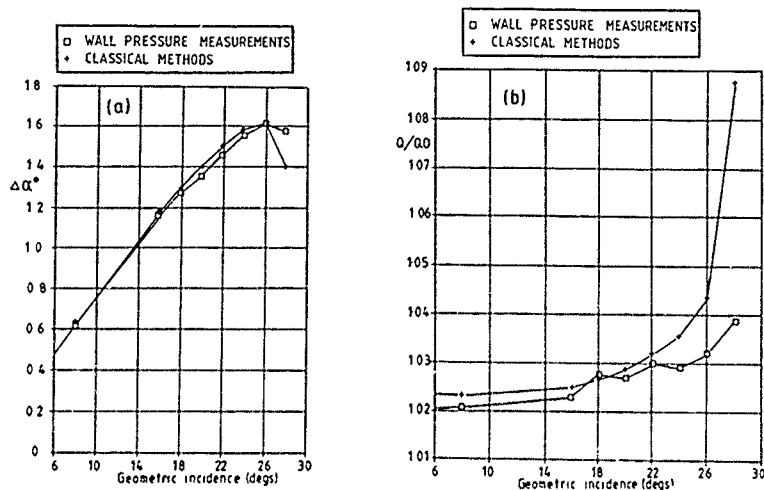


FIG 23 COMPARISON OF 2-COMPONENT WALL PRESSURE MEASUREMENTS AND CLASSICAL METHODS FOR PREDICTION OF TUNNEL INTERFERENCE (FROM REF 66)

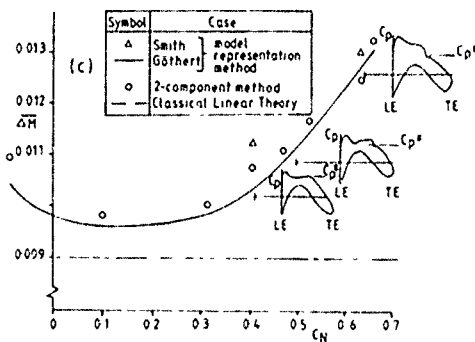


FIG 24 COMPARISON OF PREDICTIONS OF BLOCKAGE CORRECTION, 2D MODEL,
RAF 8 FT x 8 FT TUNNEL, $M = 0.73$ (FROM REF 64)

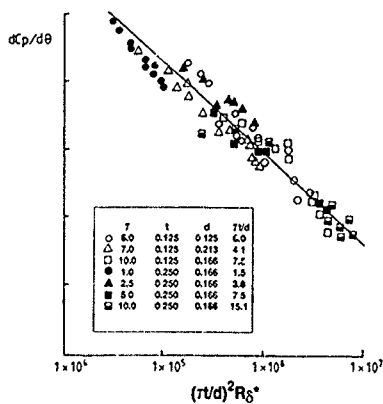
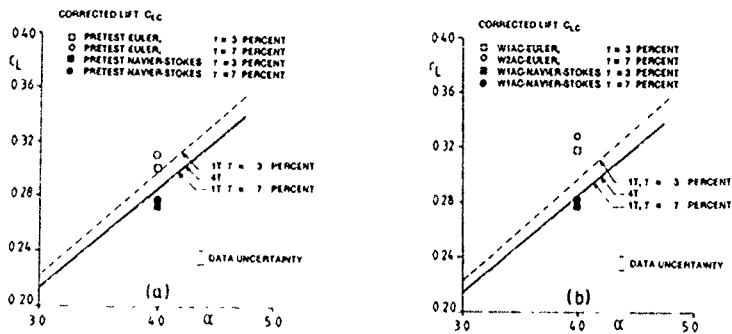


FIG 25 PERFORATED WALL CHARACTERISTIC 60° INCLINED HOLES (FROM REF 68)

FIG 26 COMPARISON OF NAVIER-STOKES AND EULER PREDICTIONS OF TUNNEL LIFT CONSTRAINT CORRECTIONS
(a) PRE TEST (b) POST TEST (FROM REF 57)

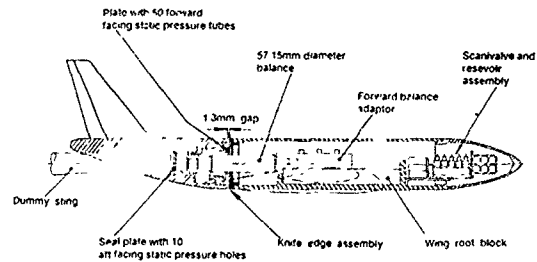


FIG 27a DETAILS OF BALANCED REAR FUSELAGE TO OBTAIN STING CORRECTIONS
USING CURRENT TWIN STING RIG AT ARA (FROM REF 15)

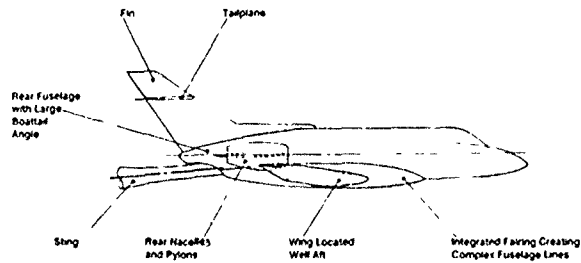


FIG 27b TYPICAL CLOSELY COUPLED FUSELAGE LAYOUT REQUIRING TEST ON ENHANCED TWIN STING RIG

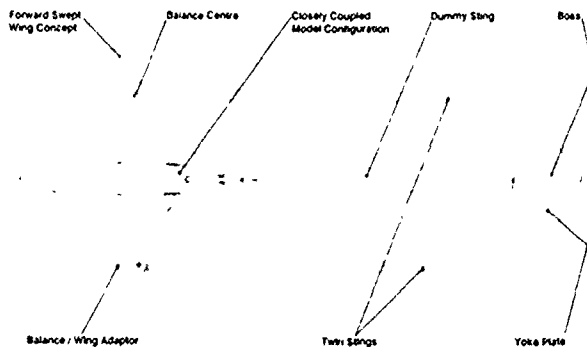
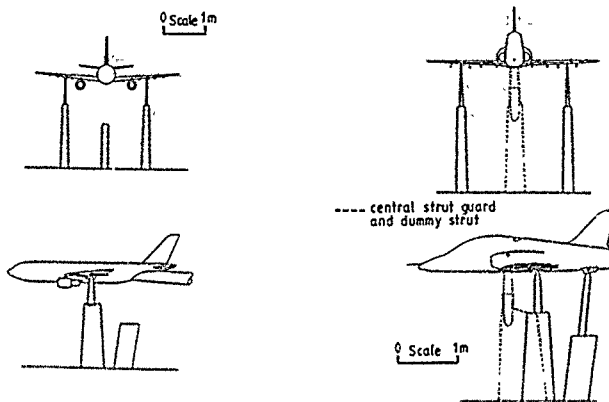


FIG 28 GENERAL LAYOUT OF MODEL IN ENHANCED TWIN STING RIG



FIC 29 (a) 3-STRUT ARRANGEMENT (b) SINGLE STRUT ARRANGEMENT LAYOUTS FOR STRUT INTERFERENCE TESTS IN RAE 5 METRE TUNNEL.

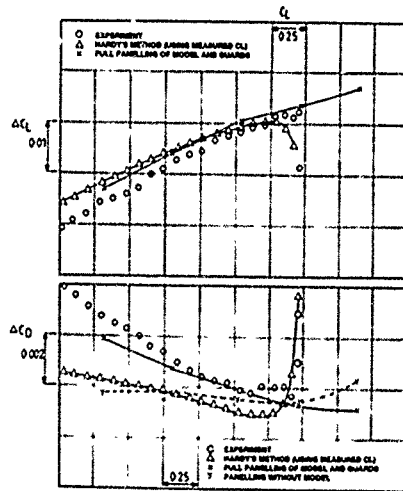


FIG. 30 COMPARISON OF GUARD INTERFERENCE CORRECTIONS

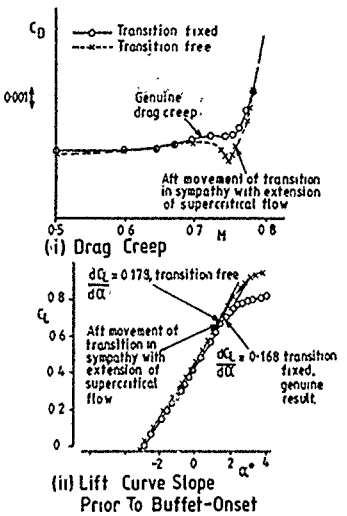


FIG 31 EXAMPLES OF SPURIOUS RESULTS WITH FREE TRANSITION

Data valid between
Boundaries AA and BB

AA Shock 0.15c aft of transition trip
BB Ditto with shock approaching trip
from rear as a result of shock induced separation.

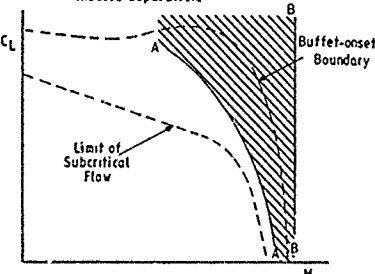


FIG 32a LIMITS ON RANGE OF VALID DATA WITH A PARTICULAR TRANSITION TRIP

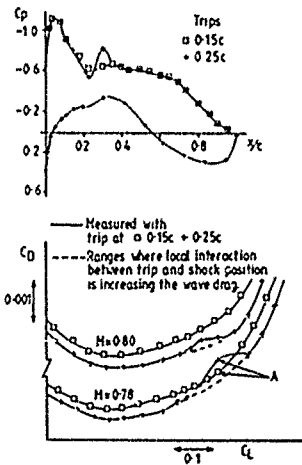
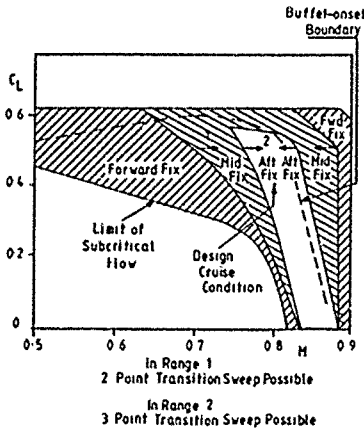
FIG 32b METHOD FOR DETERMINING LOWER $C_L - M$ LIMIT TO RANGE OF VALID DATA

FIG 32c USEFUL RANGES WITH DIFFERENT TRANSITION TRIPS

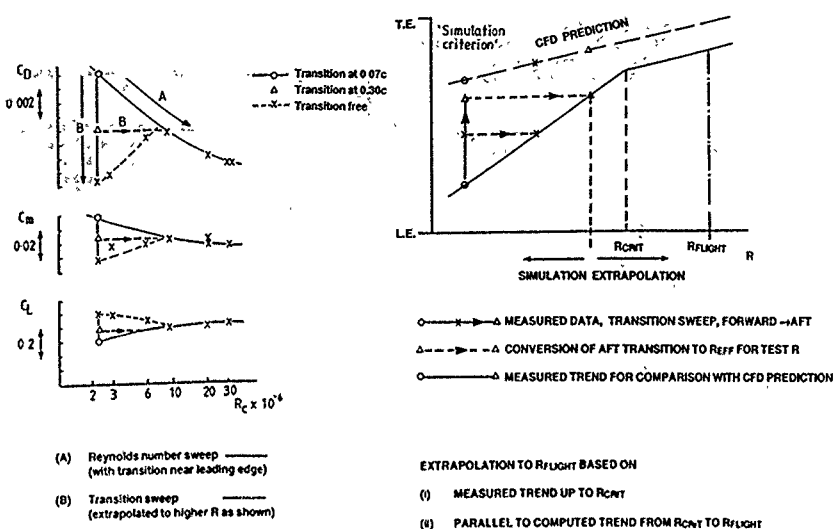
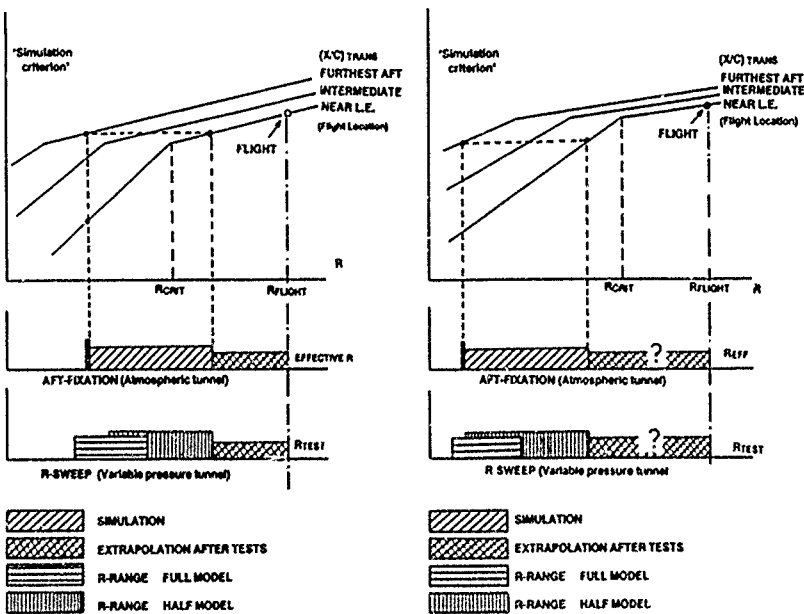


FIG 33 EXAMPLE OF TWO SIMULATION APPROACHES

FIG 34 FIRST STEP IN EXTRAPOLATION PROCEDURE TO R_{FLIGHT} 

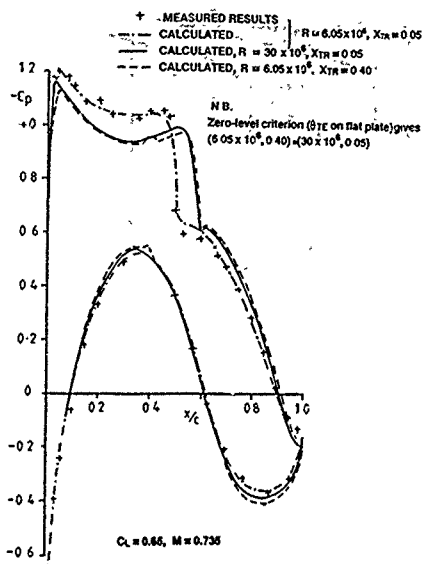


FIG 36a APPLICABILITY OF ZERO-LEVEL CRITERION (FROM REF. 86)

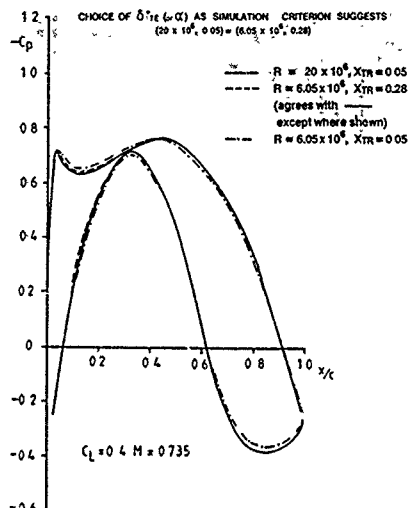
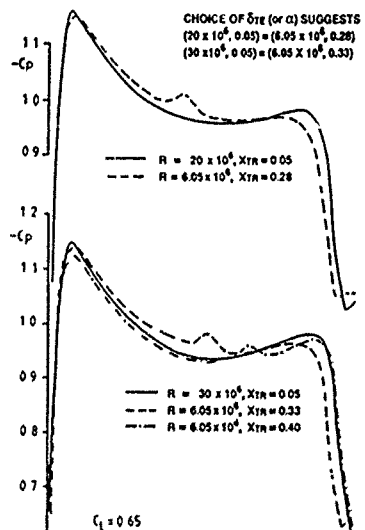
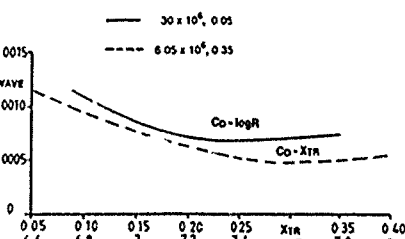
FIG 36b APPLICABILITY OF δ_{TE}^* CRITERION: $C_L = 0.4$ FIG 36c APPLICABILITY OF δ_{TE}^* CRITERION $C_L = 0.65$ 

FIG 36(d) CONSEQUENCE OF FAILURE TO SIMULATE SUPERCRITICAL FLOW DEVELOPMENT (FROM REF. 86)

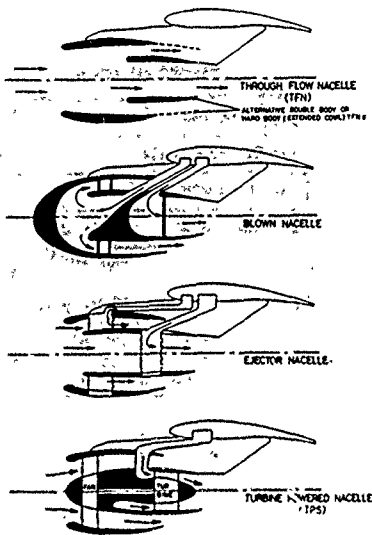


FIG 37 TYPES OF SIMULATOR (FROM REF.9)

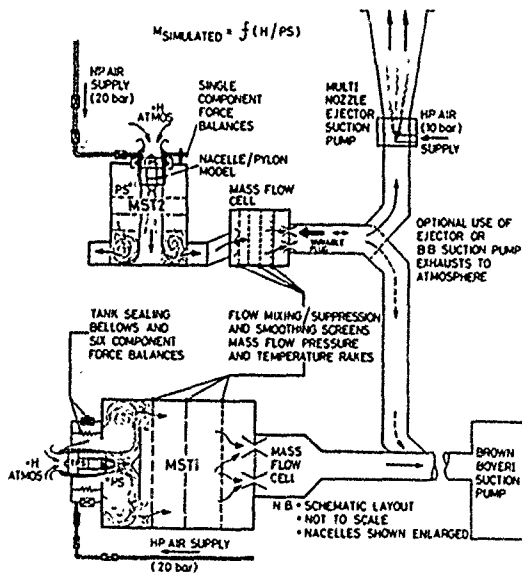


FIG 38 ARA MACH SIMULATION TANKS (FROM REF.10)

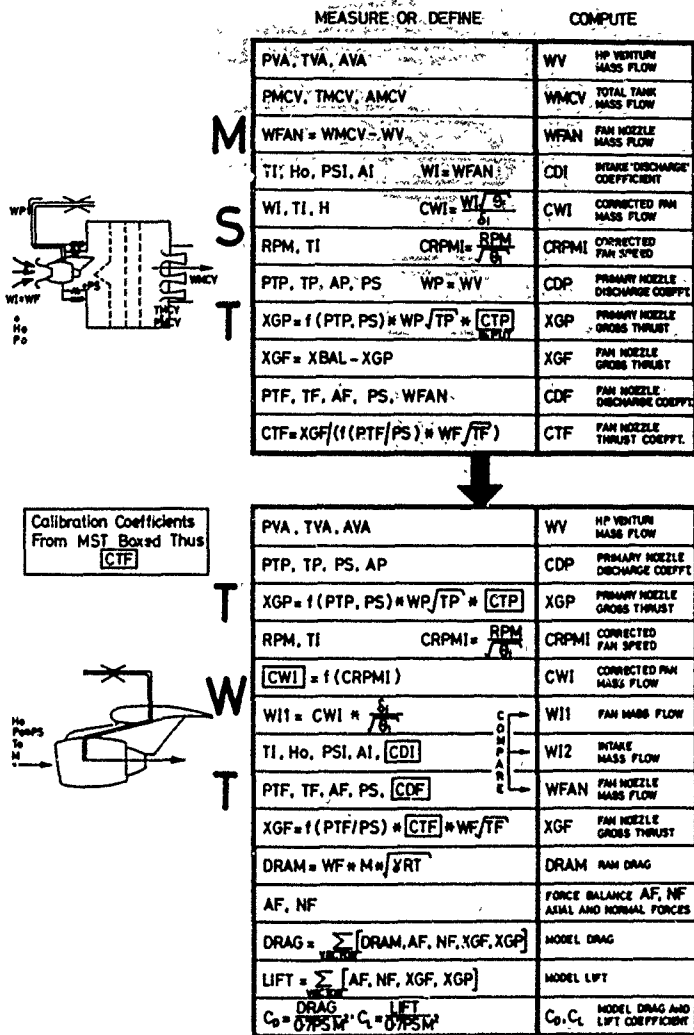


FIG 39 BOOKKEEPING PROCEDURE (FROM REF.9)

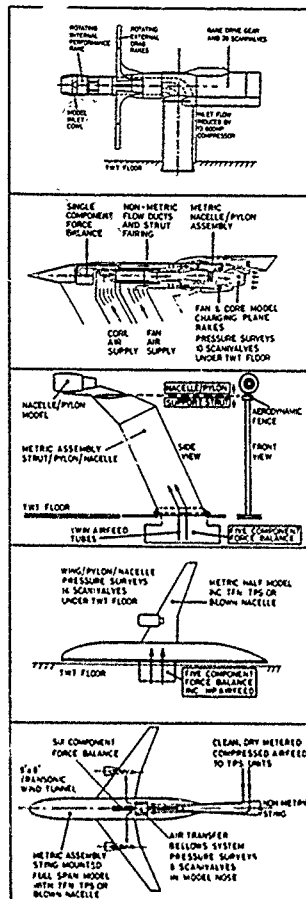


FIG 40 MODELS FOR TURBOFAN PERFORMANCE TESTING (FROM REF.10)

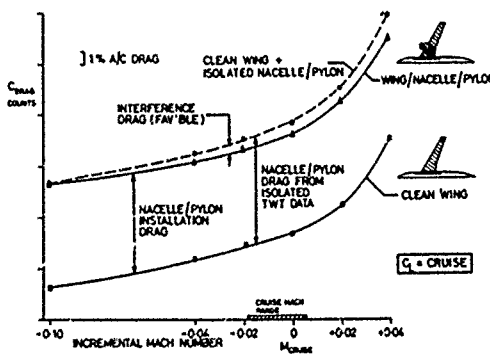


FIG 41 EXAMPLE OF FAIRVOURABLE INTERFERENCE (FROM REF.9)

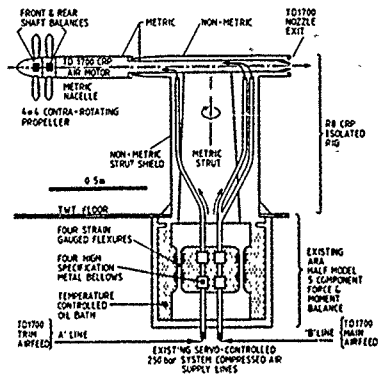


FIG 42(a) AER-DRIVEN SMALL PROPELLER R/C IN ARA TRANSONIC TUNNEL (FROM REF.105)

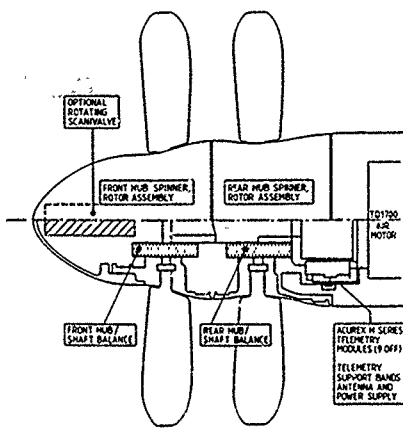


FIG 42(b) FRONT AND REAR HUB ASSEMBLIES

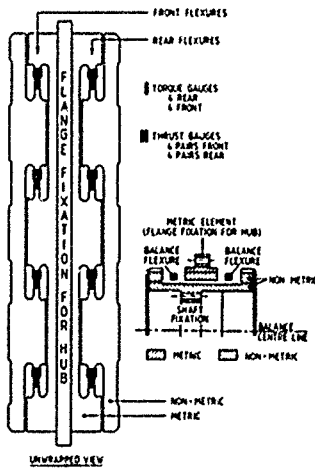


FIG 42(c) BALANCE DESIGN FOR CONTRA-ROTATING PROPELLER

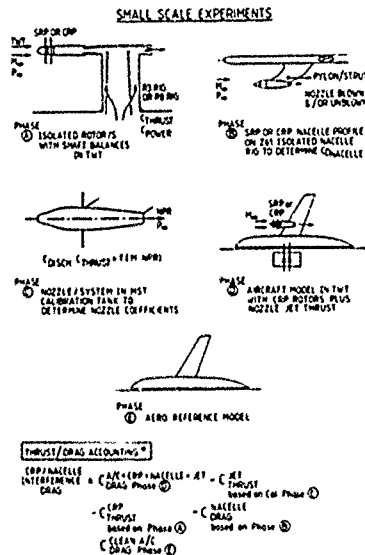


FIG 42(d) TYPICAL MODEL TEST PROGRAMME FOR TURBOPROP PROPELLER PERFORMANCE (FROM REF.105)

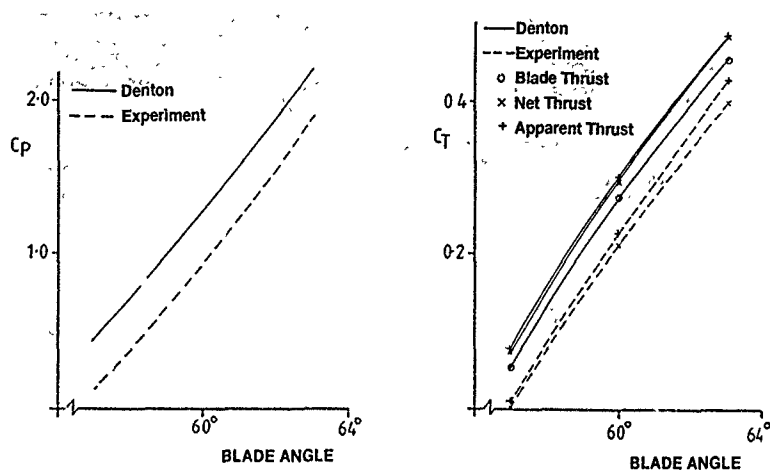


FIG 43 PROPELLER PERFORMANCE: EFFECTS OF THRUST DEFINITION (FROM REF. 111)

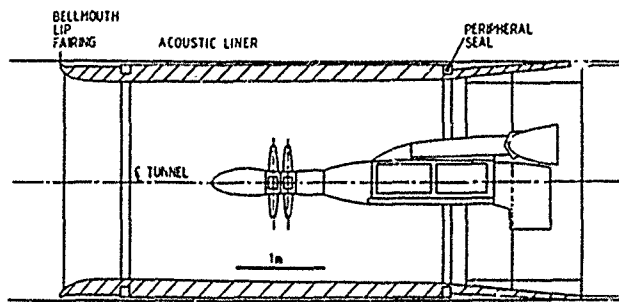
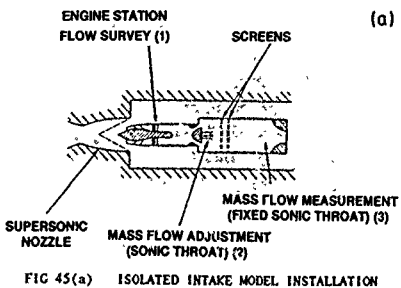
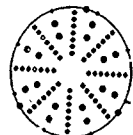


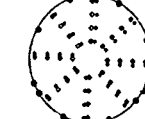
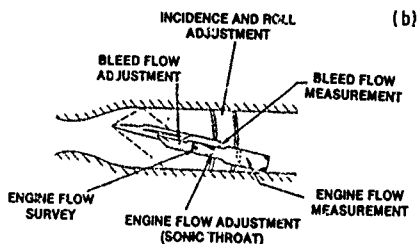
FIG 44 ELECTRIC-MOTOR DRIVEN LARGE SCALE PROPELLER RIG IN ARA ACOUSTIC TRANSONIC TUNNEL (FROM REF. 105)



- SWIRL PROBE RAKE**
- 56 Total head tubes
 - 16 Five hole probes
 - 8 Duct statics
 - 3 Endevco duct statics



- DYNAMIC DISTORTION RAKE**
- 32 Total head tubes
 - 32 Endevco dynamic tdx's
 - 8 Duct statics
 - 3 Endevco duct statics



- PERFORMANCE RAKE**
- 86 Total head tubes
 - 8 Endevco dynamic tdx's
 - 8 Duct statics
 - 3 Endevco duct statics

FIG 46 TYPICAL ENGINE FACE INSTRUMENTATION

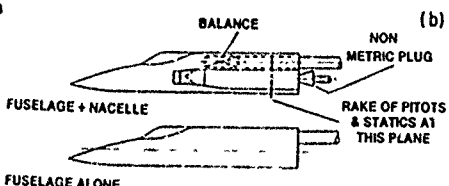
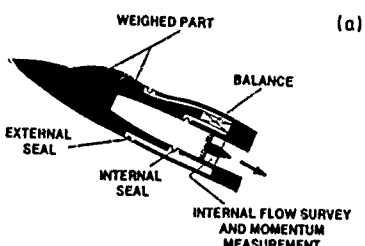
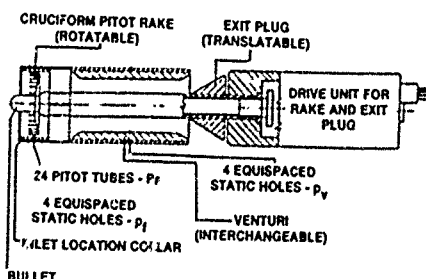


FIG 48 POSSIBLE SCHEMES FOR INTERNAL FLOW SURVEY AND FORCE MEASUREMENT

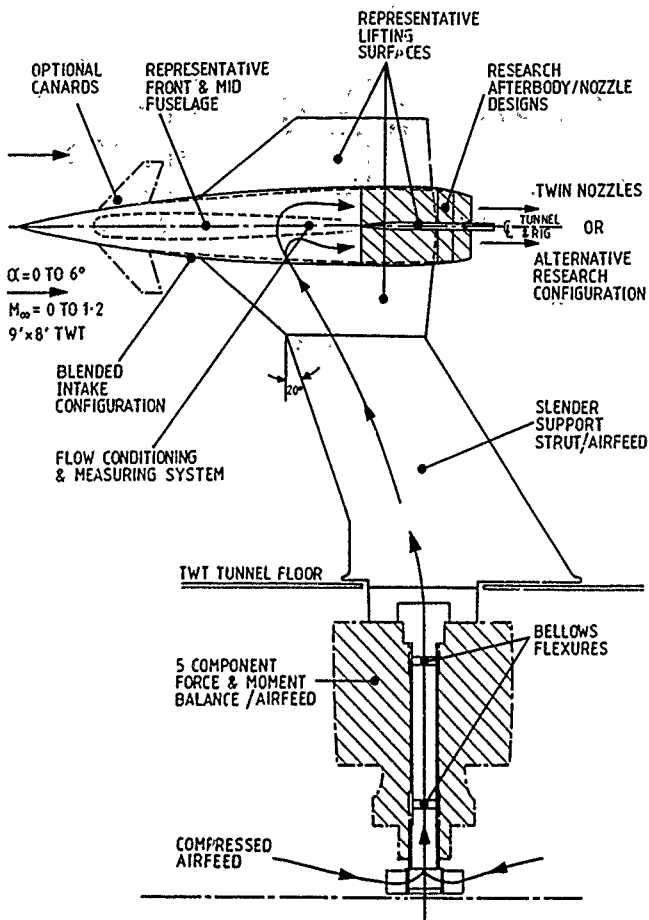


FIG 49 NEW RIG FOR AFTERBODY PERFORMANCE TESTING

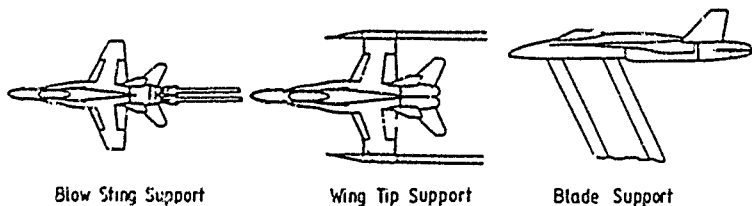


FIG 50 ALTERNATIVE RIGS FOR AFTERBODY PERFORMANCE TESTING (FROM REF 12)

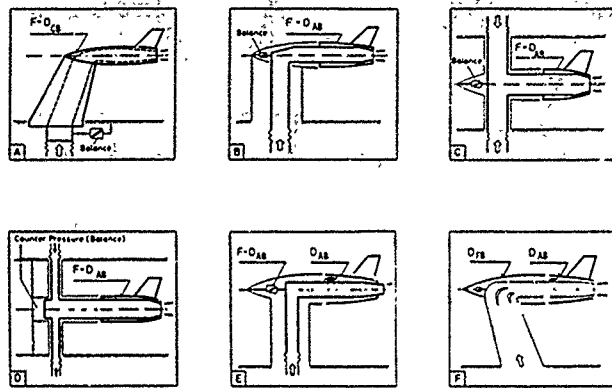


FIG 51 AFTERBODY TEST RIGS (FROM REF. 12)

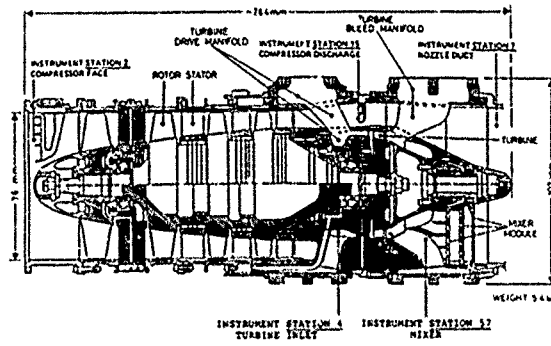


FIG 52 CROSS-SECTIONAL VIEW OF CHAPS (FROM REF. 133)

PANEL METHODS FOR AERODYNAMIC ANALYSIS AND DESIGN

H.W.M. Hoedijkmakers,
National Aerospace Laboratory NLR
Anthony Fokkerweg 2, 1059 CM Amsterdam, The Netherlands

SUMMARY

An overview is presented of several aspects of panel methods used in the aerodynamic analysis and design of aircraft or aircraft components. Panel methods can provide the flow about complex configurations and are routinely used in the analysis of the aerodynamics of realistic aircraft shapes. However, panel methods are based on a mathematical model in which much of the fluid physics is ignored. The report discusses the capabilities and limitations of panel methods, the basic concepts of panel methods, choices that can be made in the implementation of the basic concepts, as well as possible types of boundary conditions that can be utilized to creatively model subsonic and supersonic flow. The discussion also includes aspects of the accuracy of the approximations involved, consistent formulations, aspects of low-order and higher-order panel methods, etc. Also discussed are the computational aspects of panel methods and possible extensions to nonlinear compressible flows, coupling with viscous flow methods and application to other flow problems.

1.0 INTRODUCTION

The computation of the aerodynamic characteristics of aircraft configurations has been carried out by panel methods since the mid 1960's, following the pioneering work of Hess & Smith (Ref. 1) and Rubbert & Saaris (Ref. 2). But even before the availability of large-scale digital computers work was done on surface singularity methods, notably in Germany by Prager (*v.o.c.* 3) and Martensen (Ref. 4). Panel methods are presently the only computational aerodynamic tools that have been developed to an extent that they are routinely used in the aerospace industry for the analysis of the subsonic and supersonic flow about real-life, complex aircraft configurations. Panel methods have also been used for the analysis of the flow about propellers, automobiles, trains, submarines, ship hulls, sails, etc. Panel methods have been used so heavily because of their ability to provide for complex configurations linear potential flow solutions of engineering accuracy at reasonable expense. The latter applies to the computer resources required for running the computer code as well as to the manhour cost involved in preparing the input.

The relatively easy input requirement of panel methods, very important from a user's point of view, is directly related to the circumstance that a discretization is required for the surface of the 3D configuration only. This is considered to be an order of magnitude simpler than the volume discretization of the space around the configuration generally needed for finite-difference, finite-volume and finite-element methods.

It may be noted that in aircraft development projects the application of panel methods is gradually shifting from the final design phase towards the preliminary design phase and even conceptual design phase, primarily due to:

- increased demands on the accuracy of predicted aerodynamic characteristics in the earlier phases of the design process,
- the increase in computer capability (speed and memory), decrease of its costs and improvement of turn-around times,
- modern data handling techniques,
- availability of graphic displays and work stations for visualizing geometry and flow solutions.

Several panel methods, e.g. Ref. 5, 6 and 7, have been developed and are in use in the aerospace industry that are variations on the approach described in Refs. 1 and 2. Other investigators extended the panel method to linearized supersonic flow, e.g. Refs. 6 and 9. Because most of these "first-generation" panel methods do have some restrictions concerning their geometric and aerodynamic modeling capabilities and require improvement of their computational efficiency several efforts have been undertaken to develop "second-generation" panel method, e.g. Refs. 10-18.

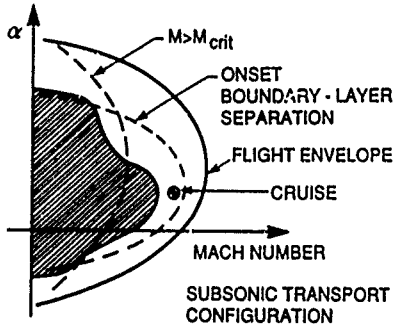


Fig. 2.1 Domain of applicability of panel method (adapted from Ref. 33)

The major drawback of the present panel methods is that their range of applicability is restricted to linear potential flow, i.e. non-linear compressibility effects are not accounted for and the important case of local regions of super-critical flow and shock waves cannot be treated. The latter occur in the high speed region in a large portion of the flow field and possibly at low speeds (at the larger incidences used in start and landing) in smaller portions of the flow field. To account for such regions of super-critical flow would require the use of a transonic finite-difference or finite-volume code (full-po-

tential or Euler) on a spatial grid covering the entire space around the configuration. However, up to the present time the spatial grid generation problem has not been solved satisfactorily for complex configurations at configurations with extended slats and flaps. In addition, the computer resources required for present-day finite difference and finite-volume codes are quite substantial. For the purpose of preliminary design, where a large number of configurations and flow conditions are to be considered, full-potential or Euler methods require far too much effort in terms of computer resources as well as in terms of man-hours.

A second drawback of current panel methods is that the computational effort, and cost, is proportional to N^2 , or even N^3 , where N is related to the number of panels. This implies that the method becomes rapidly impractical, i.e., for current mainframes for N of the order of 2000-5000, which typically are panel numbers required for the resolution required for the coupling of panel methods with boundary-layer methods. The latter is relevant for application of the method during detail design. For conceptual and for preliminary design studies, where considerably less detail is required the number of panels is typically of the order of a few hundreds. However, it is also an experience of the practice of applying panel methods that this number of panels is often quite easily "consumed", so that compromises have to be sought regarding resolution and accuracy. The latter requires insight into the flow solution, i.e. aerodynamics, but also a good perception of the numerics involved in panel methods.

In the present lecture an overview is given of several aspects related to the formulation and use of panel methods and the possibilities for extending the domain of applicability and improving the computational efficiency. The discussion deals primarily with methods for the steady flow about three-dimensional configurations in subsonic or supersonic flow. It is based on the literature on the subject and on past and current NLR research. The latter is aimed at the development of a higher-order panel method (AEROPAN) and of a panel method (PDAER) to be used in preliminary design studies. The first pertains to "the NLR panel method", the panel method workhorse used in theoretical subsonic aerodynamic analysis during the last two decades and the NIRAERO panel method for sub- and supersonic flow.

2.0 MATHEMATICAL MODEL

2.1 Background

In the aerodynamics of aircraft configurations the Reynolds-averaged Navier-Stokes equations model essentially all flow details. However, turbulence and transition need to be modeled in a manner appropriate to the flow considered. The computer resources required for numerically solving the equations on a mesh that sufficiently resolves the boundary layers, free shear layers (wakes), vortex cores, etc., are still and for some time to come will continue to be quite excessive.

For most high-Reynolds-number flow of interest in aircraft aerodynamics viscous effects are confined to thin boundary layers, thin wakes and centers of vortex cores, i.e. the global flow features depend only weakly on Reynolds number. This

implies that a model based on Euler's equations, which allow the occurrence of shock waves as well as the convection and stretching of rotational flow, provides an appealing alternative. On a local scale, some kind of model for viscous-flow dominated features will be required. This specifically at points where the flow leaves the surface (separates) and vorticity is generated and subsequently convected into the flow field ("Kutta conditions"). Although the computer requirements of Euler codes can be met by the current generation of supercomputers, routine practical application of these codes (to relatively simple configurations) starts to emerge now.

If the shocks are not too strong and if the rotational flow is confined to compact regions, the flow may be modeled as potential flow with embedded free vortex sheets and vortex filaments. Now the rotational flow regions are "fitted" explicitly into the solution, rather than "captured" implicitly as part of the solution as is the case for above flow models. Flow separation at trailing edges and at other locations has to be modelled through Kutta conditions; just like for any other inviscid flow model. Although one has to decide a priori on the presence of vortex sheets and cores and generally the topology of the vortex system must be well-defined, "fitting" still requires that both the position and strength of the vortex sheets and cores have to be determined as part of the potential-flow solution.

The treatment of vortex sheets and vortex filaments, freely floating in a fixed spatial grid, poses considerable problems for finite-difference/volume methods solving the nonlinear full-potential equation for compressible flow. The computer requirements of full-potential codes are relatively modest, but application to general aircraft configurations is hampered by the grid-generation problem.

A special class of methods for compressible potential flow is formed by the so-called transonic perturbation (TSP) methods. These methods are based on an approximation of the full-potential equation with some of the nonlinear terms retained and, with to the same order of approximation, the boundary condition applied on a planar reference surface rather than on the true surface. This eliminates the necessity of curvi-linear body-conforming grids and a much simpler Cartesian grid can be used, e.g. Boppe (Ref. 19).

In case shockwaves are absent altogether and the perturbation on the free-stream due to the presence of the configuration is small, the potential-flow model is further simplified by linearization to the linear-potential flow model, governed by the Prandtl-Glauert equation. Note that for incompressible flow the small-perturbation assumption is not required, the irrotationality condition directly reduces Euler's equations to Laplace's equation. In the linear-potential-flow model the flow and the position of the vortex sheets and filaments can be solved for by employing a boundary-integral type of formulation. In this approach singularity distributions on the surface of the configuration and on the vortex sheets are employed to simulate the flow. The formulation requires the discretization of just the bounding surfaces, i.e. a spatial grid is not required and in that sense possesses a "dimension-lowering" property. The linear-potential flow model is the model underlying the classical panel method. It is emphasized at this point that though the governing equation is linear, the problem is still nonlinear because the position of the vortex

sheets appears nonlinearly in the boundary condition on the solid surface, as well as in the boundary conditions on the vortex sheet itself. It can be argued that for most configuration in cruise condition the wakes remain fairly simple, i.e., do not roll up within one wing span down-stream of the wing trailing edge. This leads to the conventional attached flow model in which the vortex sheet is chosen as some appropriate, user-specified rigid surface, rendering the boundary conditions and therewith the resulting problem fully linear.

As far as forces and moments is concerned only Navier-Stokes methods are capable to predict the total drag, the other methods will predict the induced (vortex) and the wave component of the drag.

2.2 Domain of applicability of panel methods

The preceding discussion will have made clear that a number of substantial assumptions had to be made to finally arrive at the framework in which the panel method may be applied soundly. The assumptions are summarized here as:

- high Reynolds number, essentially inviscid flow
- no flow separation other than at the trailing edges
- compact regions with vorticity, i.e. thin wakes
- incompressible flow or small-perturbation compressible flow without shocks.

The restriction to small-perturbation compressible flow implies that the linearized potential flow panel method applies to configurations with slender bodies and thin wings at low angles of attack and sideslip. The permissible non-slenderness, wing thickness, maximum angle of attack and side slip depend on the free-stream Mach number M_∞ . No restriction for $M_\infty = 0$, severe restrictions at high free-stream Mach numbers.

In general it can be stated that the panel method provides detailed but "simplified aerodynamics" for complex configurations. This is illustrated further in Fig. 2.1, which shows, for a subsonic transport configuration, the $M_\infty - \alpha$ plane. Curves indicate the first occurrence of flow features such as shock waves and the onset of boundary-layer separation. The shaded area indicates the domain of applicability of the conventional panel method, possibly coupled with a boundary-layer method. The method is restricted to subcritical attached flow. The shaded region indicates where the method will give reasonable results, while even for the indicated design cruise condition trends in the aerodynamic characteristics will be predicted correctly to some degree. It will be clear that extension of the panel method approach into regions with transonic flow, without sacrificing its ability to treat arbitrary configurations, would greatly enhance its value for the aircraft designer.

Another area where there is still a gain to be realized is to improve upon the treatment of the wakes. For configurations with extended flaps or for combat aircraft that operate at higher incidences the rigid-wake approach adopted in most "first-generation" panel methods is rather inadequate and ways have to be found to account for the effects of non-planar wakes interacting with the flow about the configuration.

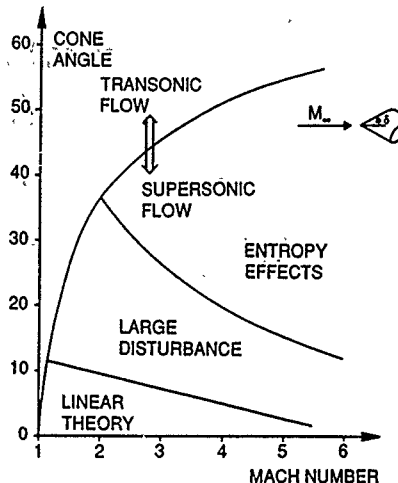


Fig. 2.2 Attached conical flow on a circular cone at zero incidence

The nonlinear flow effects can be subdivided into effects due to large disturbances and ones due to non-isentropic flow (e.g. bow shock, strong normal or oblique shocks). As far as the nonlinear effects in attached supersonic flow is concerned a guideline can be given by considering the supersonic flow over a circular cone at zero incidence. Fig. 2.2 shows a comparison of the pressure coefficient, which for this case is constant on the cone, computed by linear theory, full-potential theory and from a conical solution of Euler's equations as can be found in shock tables. It indicates the boundaries of applicability of the flow models. It shows that linear theory is valid in at least some parts of the attached flow regime.

This has been expressed by Steger (Ref. 20) in an interesting way. Here this is re-expressed as follows. An aerodynamic characteristic F of a configuration can be expressed in an asymptotic fashion as:

$$F = F_0(\text{geometry, } M_\infty, \alpha, \dots) + F_1(\text{nonlinear compressibility, viscous effects, \dots}) + \dots$$

where F_0 is the leading, $O(1)$, term and F_1 the first-order, $O(\delta)$, correction term. The $O(1)$ term is provided by the panel method solution, which can be obtained relatively easily for complex geometries since it requires the discretization of the surface of the object only. The $O(\delta)$ term is provided by the finite-difference, finite-volume or finite-element method solution, which can not be obtained so easily for arbitrary configurations because of the necessity to discretize not only the surface of the object but also the entire space surrounding the object. Of course one should realize that F_1 , the first-order effect, might dominate F_0 . This is for instance the case for the separated flow about a sphere, the transonic flow with strong shocks, hypersonic flow with real-gas effects, etc.

2.3 Governing equations

The full potential equation is with $\vec{U}_\infty = \vec{V}_\infty$, with \vec{U} the total velocity vector and ϕ the total velocity potential, written as:

$$\frac{\partial(\phi^2)}{\partial x} + \frac{\partial(\phi^2)}{\partial y} + \frac{\partial(\phi^2)}{\partial z} = 0 \quad (2.1a)$$

where

$$\rho = \rho_\infty(1 + \frac{x}{2}M_\infty^2(1 - |\vec{V}_\infty|^2/U_\infty^2))^{1/(\gamma-1)} \quad (2.1b)$$

is the density, γ the ratio of the specific heats (~ 1.4 for air), while U_∞ and ρ_∞ are the magnitude of the free-stream velocity and density, respectively. The pressure coefficient C_p follows from the isentropic formula:

$$C_p = \frac{p/p_\infty}{c_p^{\text{inc}}} \\ = \frac{2}{\gamma M_\infty^2} [(1 + \frac{x}{2}M_\infty^2)^{\text{inc}} \gamma/(\gamma-1) - 1] \quad (2.1c)$$

$$\text{with } C_p^{\text{inc}} = 1 - \frac{|\vec{V}_\infty|^2}{U_\infty^2} \quad (2.1d)$$

where $q_\infty = \frac{1}{2}\rho_\infty U_\infty^2$ and p and p_∞ are the local static pressure and the free-stream static pressure, respectively. C_p^{inc} denotes the pressure coefficient in incompressible flow.

In the case of incompressible flow $\rho = \rho_\infty$, $M_\infty = 0$ and Eq. (2.1a) reduces to Laplace's equation, i.e. with

$$\vec{U} = \vec{U}_\infty + \vec{V}_p \quad (2.2a)$$

where v is the perturbation velocity potential, one finds:

$$\frac{\partial^2 v}{\partial x^2} + \frac{\partial^2 v}{\partial y^2} + \frac{\partial^2 v}{\partial z^2} = 0 \quad (2.2b)$$

while the pressure coefficient follows from Bernoulli's equation, or equivalently from Eq. (2.1c) for the limit of $M_\infty = 0$:

$$C_p = C_p^{\text{inc}} = 1 - |\vec{U}_\infty + \vec{V}_p|^2/U_\infty^2 \quad (2.2c)$$

In the case of compressible flow Eq. (2.1a) is linearized under the assumption that \vec{V}_p is $O(\epsilon)$. In case the free stream is directed along the x -axis Eq. (2.1a) reduces to the Prandtl-Glauert equation:

$$(1 + M_\infty^2) \frac{\partial^2 \phi}{\partial x^2} + \frac{\partial^2 \phi}{\partial y^2} + \frac{\partial^2 \phi}{\partial z^2} + O(\epsilon^2) = 0 \quad (2.3a)$$

Note that this equation is elliptic for subsonic free-stream Mach numbers ($M_\infty < 1$) and hyperbolic for supersonic free-stream Mach numbers ($M_\infty > 1$). Within the scope of the linearization it may be assumed that for small angles of incidence and sideslip the compressibility axis remains the same, i.e. the x -axis rather than the direction of the free stream \vec{U}_∞/U_∞ . For incompressible flow the Prandtl-Glauert equation reduces to Laplace's equation. Further note that expanding Eqs. (2.1a-c) in the Rayleigh-Janssen expansion for small Mach number, i.e. $M_\infty = O(\epsilon)$ also results in Laplace's equation.

To the same order of approximation as used for Eq. (2.3a), Eq. (2.1b) reduces with Eq. (2.2a) to

$$\rho = \rho_\infty(1 + M_\infty^2(\vec{U}_\infty \cdot \vec{V}_p)/U_\infty^2 + O(\epsilon^2)) \quad (2.3b)$$

while the pressure coefficient follows from the linearization of Eq. (2.1c) as:

$$C_p^{\text{lin}} = -2(\vec{U}_\infty \cdot \vec{V}_p)/U_\infty^2 + O(\epsilon^2). \quad (2.3c)$$

Sometimes also a quadratic approximation is used, i.e.,

$$C_p^{\text{qua}} = C_p^{\text{lin}} + \frac{1}{4} \frac{|\vec{V}_p|^2}{U_\infty^2} + \frac{1}{4} \frac{U_\infty^2}{M_\infty^2} (C_p^{\text{lin}})^2 + O(\epsilon^3) \quad (2.3d)$$

When in practise the perturbations to the free stream are not small, Eqs. (2.3c and d) may attain nonphysical values, i.e. lower than the vacuum or exceeding the stagnation values. In most methods, using Eqs. (2.3c and d) the computed value is limited to vacuum and stagnation values:

$$(C_p)_\text{vacu} = -\frac{2}{M_\infty^2} \quad (2.3e)$$

and

$$(C_p)_\text{stag} = \frac{2}{M_\infty^2} [(1 + \frac{x}{2}M_\infty^2)^{\text{inc}} \gamma/(\gamma-1) - 1] \quad (2.3f)$$

A natural way to extend the capability of linear potential flow methods is to apply Eqs. (2.3a-d) everywhere in the flow field where the perturbation velocity is small and the full-potential flow formulation, Eqs. (2.1a-c), in the remaining small isolated regions, coupled to each other through the appropriate boundary conditions on the common boundary.

2.4 Boundary conditions

- (1) On the surface S_b of the configuration (Fig. 2.3) the condition is imposed that at the normal component of the velocity either vanishes (solid body) and is a stream surface or is prescribed. The latter is amongst others required to:

- simulate the flow through an inlet fan face;
- simulate propeller slipstream effects;
- simulate jet entrainment;
- incorporate a design option;
- account for the effect of the boundary-layer through the transpiration concept, etc., i.e.

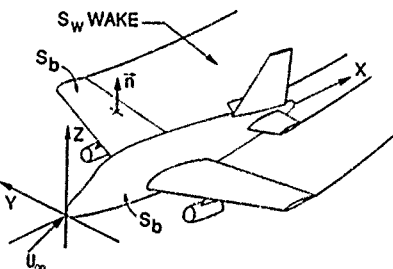


Fig. 2.3 Airplane configuration

$$(\vec{U}_\infty + \vec{V}_p) \cdot \vec{n} = v_n \quad (2.4a)$$

where \vec{n} is the normal to the surface and v_n the given normal velocity.

- (ii) On the wake vortex sheet S_v two conditions apply; the stream surface condition Eq. (2.1a), with $v = 0$ and the condition that the static pressure is continuous across the vortex sheet, i.e.

$$\Delta C_p = C_p(S_v^+) - C_p(S_v^-) = 0 \quad (2.4b)$$

which as follows from Eq. (2.1c) can be expressed as

$$C_p^{in}(S_v^+) - C_p^{in}(S_v^-) = 0 \quad (2.4c)$$

and with Eq. (2.1d)

$$(\bar{v}\phi^+ + \bar{\psi}\phi^+).(\bar{v}\phi^- + \bar{\psi}\phi^-) = 0 \quad (2.4d)$$

which leads to

$$\bar{u}_a \cdot \nabla (\phi^+ \cdot \phi^-) = 0 \quad (2.4e)$$

with \bar{u}_a the average velocity across the wake vortex sheet S_v .

- (iii) At the trailing edges of S_c the Kutta condition is applied that the flow leaves the surface "smoothly".

- (iv) At infinity upstream the perturbation vanishes. The free-stream velocity vector

\bar{U} may consist of (constant) components due to incidence and sideslip, but also ones due to (small) steady rates of pitch, yaw and roll (p, q, r). Sometimes a user-specified onset flow (and total-pressure increment) is added to model for instance propeller slipstream effects. Also other incremental velocity components can be used to model the flow about configurations which parts move with respect to each other (e.g. stores separation).

So we have:

$$\begin{aligned} \bar{U}(\vec{x}) &= U_\infty [\vec{e}_x \cos \alpha \cos \beta - \vec{e}_y \sin \alpha \cos \beta \\ &\quad + \vec{e}_z \sin \alpha] \\ &\quad + \vec{p} \times \vec{x} \\ &\quad + \bar{U}_{slip}(\vec{x}) \\ &\quad + \Delta \bar{U}(\vec{x}) + \dots \end{aligned} \quad (2.4f)$$

where α is the angle of attack, β the angle of side slip, $\vec{p} = p_x \hat{i} + p_y \hat{j} + p_z \hat{k}$ is the rotation of the configuration about the axis of the reference coordinate system, $\bar{U}_{slip}(\vec{x})$ is the onset flow due to the slipstream of a propeller, to be applied within the slipstreams, $\Delta \bar{U}(\vec{x})$ is the onset velocity due to the relative motion of a part of the configuration with respect to the global coordinate system.

- (v) No upstream influence in supersonic flow.

Above boundary-value problem is a problem in which the governing equation is linear but the boundary conditions Eqs. 2.4a and b are nonlinear.

The resulting boundary value problem will be linear only in case of the approximation in which the wake S_v is assumed to be a fixed surface in space (the rigid wake assumption) valid for high-aspect-ratio, lightly-loaded wings, the wake vortex sheet not interacting strongly with other components of the configuration or with other vortex

sheets. In case of "relaxed-wakes" boundary conditions Eqs. 2.4a and b are linear and mildly nonlinear in terms of φ , respectively, but both conditions are highly nonlinear in terms of the, also to be solved, position of the vortex wakes.

2.5 Integral representation of the solution

The solution of the potential flow problem may be represented, through Green's third identity, in terms of singularity distributions (source q and doublet μ , see Fig. 2.4 for the definition of μ) over the surface S_c of the configuration and the vortex sheets S_v in the form (see Ref. 21 for incompressible and Ref. 22 for subsonic compressible flow):

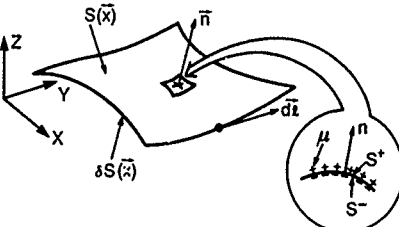


Fig. 2.4 Definition of doublet distribution

$$\varphi(\vec{x}_o) = \varphi_q(\vec{x}_o) + \varphi_\mu(\vec{x}_o) \quad (2.5a)$$

where

$$\varphi_q(\vec{x}_o) = \frac{1}{4\pi} \iint_S q(\vec{x}) \frac{dS(\vec{x})}{|\vec{R}|} \quad (2.5b)$$

$$\varphi_\mu(\vec{x}_o) = -\frac{1}{4\pi} \iint_{S+b} \mu(\vec{x}) \frac{1}{|\vec{R}|} \frac{dS(\vec{x})}{|\vec{R}|} \quad (2.5c)$$

are the velocity potential induced by the source and the doublet distribution, respectively.

In Eq. (2.5) $\vec{R} = \{B\}(\vec{x} - \vec{x}_o)$, \vec{n} is the normal directed into the flow field and the compressibility matrix $\{B\}$ is defined as

$$\{B\} = \begin{bmatrix} 1 & 0 & 0 \\ 0 & B & 0 \\ 0 & 0 & B \end{bmatrix} \quad (2.5d)$$

where $B = (1 - M_\infty^2)^{1/2}$, and

$$\{B^{-1}\} = \begin{bmatrix} 1 & 0 & 0 \\ 0 & 1/B & 0 \\ 0 & 0 & 1/B \end{bmatrix} \quad (2.5e)$$

The velocity potential as defined in Eq. (2.5) satisfies the Prandtl-Glauert equation Eq. (2.3a) exactly. They also satisfy the far-field boundary condition. The integrals in Eq. (2.5) have a singular integrand, which results, for regular q and μ , in a situation where the potential is regular everywhere, except that it has a jump across S_v , i.e.

$$\varphi(\vec{x}_o|S^+) = \varphi^P(\vec{x}_o|S) + \frac{1}{2}\mu(\vec{x}_o) \quad (2.5f)$$

where the superscript P denotes the so-called Principal-Value of the integral.

The velocity field induced by the singularity distributions follows from Eq. (2.5) through differentiation, as:

$$\vec{u}(\vec{x}_o) = \vec{\nabla}\varphi(\vec{x}_o) - \vec{u}_q(\vec{x}_o) + \vec{u}_\mu(\vec{x}_o) \quad (2.6a)$$

where,

$$\vec{u}_q(\vec{x}_o) = \frac{1}{4\pi} \int \int q(\vec{x}) \frac{\vec{n}}{|\vec{R}|^3} dS(\vec{x}) \quad (2.6b)$$

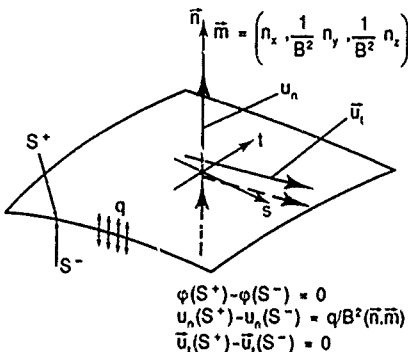
$$\vec{u}_\mu(\vec{x}_o) = \vec{u}_\gamma(\vec{x}_o) + \vec{u}_v(\vec{x}_o) \quad (2.6c)$$

with

$$\vec{u}_\gamma(\vec{x}_o) = \frac{1}{4\pi} \int \int (\vec{B}) \vec{\gamma} \times \frac{\vec{n}}{|\vec{R}|^3} dS(\vec{x}) \quad (2.6d)$$

and

$$\vec{u}_v(\vec{x}_o) = \frac{1}{4\pi} \int \int \mu(\vec{x}) \frac{\vec{n}}{|\vec{R}|^3} \times ((\vec{B}) d\vec{l}(\vec{x})) \quad (2.6e)$$



SOURCE DISTRIBUTION

Fig. 2.5 Jump conditions across source and doublet distributions

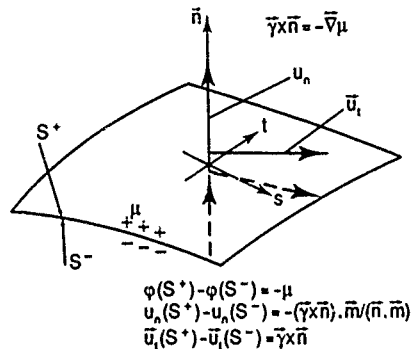
Here we used the equivalence between the velocity induced by a doublet distribution μ with that induced by a surface vorticity distribution $\vec{\gamma}$ of strength $\Gamma = -\vec{\nabla}\varphi\mu$ plus that induced by a concentrated vortex of strength $\Gamma = \mu$ along the boundary of S . Both the vorticity vector $\vec{\gamma}$ and the gradient of the doublet distribution $\vec{\nabla}\mu$ are tangential to the surface carrying the doublet distribution.

Note that in using the equivalence property it is assumed that μ is continuous everywhere on S_b and S_v except possibly at its boundary ∂S_{b+v} . The main advantage of using the doublet distribution μ rather than the surface vorticity distribution $\vec{\gamma}$ is that Kelvin's vortex law (e.g. that vortex lines only begin or end on the solid surface and are closed otherwise) are satisfied automatically. Across the surface the velocity is discontinuous, see Fig. 2.5, i.e.

$$\vec{u}(\vec{x}_o, S^\pm) = \vec{u}^p(\vec{x}_o, S) \pm \frac{1}{2}(q(\vec{x}_o) \vec{n} + \vec{\gamma} \vec{m}) / (\vec{n} \cdot \vec{m}) \quad (2.6f)$$

where $\vec{m} = \{B^{-1}\}(\{B^{-1}\}n)$, the so-called co-normal. The vector \vec{m} is parallel to the normal n in case of incompressible flow and in case of normal to or along the x -axis (= "compressibility axis").

Considering above expressions we note that the jump in the velocity potential is solely due to the doublet distribution, the velocity potential due to a source distribution is continuous across the distribution. The velocity due to the source distribution has a jump in normal direction across the distribution. The velocity induced by the doublet distribution has a jump in tangential and in normal direction, since $\vec{v} = (\vec{n}, \vec{m}) \vec{v}_n + (\vec{m}, \vec{v}) \vec{n}$. In the case of incompressible flow the velocity across the doublet distribution experiences a jump in the tangential component only. This feature has as consequence that modeling vortex sheets (which have a jump in the tangential velocity only) in compressible flow requires a composite singularity distribution consisting of a doublet distribution of strength μ and a source distribution of strength $q = -B^*(\vec{m}, \vec{v}_n)$.



DOUBLET DISTRIBUTION

2.6 Mass-flux boundary condition

In the literature sometimes reference is made to the so-called (linearized) mass-flux vector. The mass-flux is defined as

$$\vec{J} = \rho(\vec{U}_\infty + \vec{v}) \quad (2.7a)$$

$$= \rho_\infty(\vec{U}_\infty + \vec{v}) + \rho_\infty(\vec{U}_\infty \vec{v}) \frac{M^2}{U_\infty^2} \vec{J}_\infty + O(\epsilon^2) \quad (2.7b)$$

The (linearized) perturbation mass-flux vector is then defined as the difference between the total mass-flux vector and its free-stream value, $\vec{v} = \vec{U} - \rho_\infty \vec{J}_\infty$, which like $\vec{v} = \vec{\nabla}\varphi$ has order of magnitude ϵ . In the derivation of Eq. (2.7b) we used Eq. (2.3b) to order ϵ . Employing the jump relation given in Eq. (2.6f) it turns out that

$$\vec{v}(\vec{x}_o, S^\pm) = \vec{\nabla}P(\vec{x}_o, S) \pm \frac{1}{2} \rho_\infty (q \vec{v} / (\vec{n}, \vec{m}) + \vec{v} \mu) \quad (2.7c)$$

showing that the doublet distribution has associated with it a jump in the tangential component \vec{v} only, while the source distribution causes a jump in the direction of the co-normal, i.e. in general in both the normal and the tangential direction.

2.7 Correspondence between \vec{u} and \vec{u}_q

Next we point out some relations that can be utilized to reduce the computational burden. The first one is the correspondence between the velocity field $\vec{u}(\vec{x}; q)$ induced by a source distribution q , and the velocity $\vec{u}_q(\vec{x})$ induced by a vorticity distribution. Inspection of the components of Eqs. (2.6b) and (2.6d) leads that one can write:

$$\vec{u}_q(\vec{x}_o) = [B] \sum_{k=1}^3 \vec{e}_k \times ([B]^{-1} \vec{u}_q(\vec{x}_o; q - [B]\vec{e}_k)) \quad (2.8)$$

where \vec{e}_k , $k = 1, 2$ and 3 denotes the unit vector in x , y and z direction, respectively.

2.8 Symmetry

In cases with port-side/starboard-side symmetry in both geometry and the flow computing time can be saved by realizing that the singularity distribution on the port-side will be identical to the one on the starboard-side. If then the potential and the velocity induced at \vec{x}_o by the starboard-side distribution are denoted by $\varphi(\vec{x}_o)$ and $\vec{u}(\vec{x}_o)$, respectively, one finds that the potential and velocity induced at \vec{x}_o by the complete configuration are

$$\varphi(\vec{x}_o) = \varphi^*(\vec{x}_o) + \varphi^*([S]^{-1}\vec{x}_o) \quad (2.9a)$$

and

$$\vec{u}(\vec{x}_o) = \vec{u}^*(\vec{x}_o) + [S]\vec{u}^*([S]^{-1}\vec{x}_o) \quad (2.9b)$$

respectively, where $[S]$ is the so-called starboard/port-side symmetry matrix defined as

$$[S] = \begin{bmatrix} 1 & 0 & 0 \\ 0 & -1 & 0 \\ 0 & 0 & 1 \end{bmatrix} \quad (2.9c)$$

with $[S]^{-1} = [S]$.

This implies that only the starboard side of the configuration needs to be discretized and subjected to the boundary conditions.

A final point is that in case the geometry is symmetric, but the flow is not symmetric because of the boundary conditions (e.g. side-slipping configuration) the problem can be reduced by almost a factor of 2 by formulating the problem in terms of the average and the difference of the singularity distributions on port and starboard side.

In this case one can write for the velocity induced by for instance the source distribution on the complete configuration:

$$\begin{aligned} \vec{u}(\vec{x}_o) &= \vec{u}^*(\vec{x}_o; q_a) + [S]\vec{u}^*([S]^{-1}\vec{x}_o; q_a) \\ &\quad + \vec{u}^*(\vec{x}_o; q_d) + [S]\vec{u}^*([S]^{-1}\vec{x}_o; q_d) \end{aligned} \quad (2.10a)$$

with

$$q_a = (q^s + q^p)/2 \quad \text{and} \quad q_d = (q^s - q^p)/2 \quad (2.10b)$$

where q^s and q^p denote the source distribution on the starboard and the port side, respectively. In case of flow symmetry $q_d = 0$ and Eq. (2.10a) reduces to Eq. (2.9b). For the mirror-imaged point, located at $[S]\vec{x}_o$ one then gets:

$$\begin{aligned} \vec{u}([S]\vec{x}_o; q) &= [S]((\vec{u}^*(\vec{x}_o; q_a) + [S]\vec{u}^*([S]^{-1}\vec{x}_o; q_a)) \\ &\quad - (\vec{u}^*(\vec{x}_o; q_d) + [S]\vec{u}^*([S]^{-1}\vec{x}_o; q_d))) \end{aligned} \quad (2.10c)$$

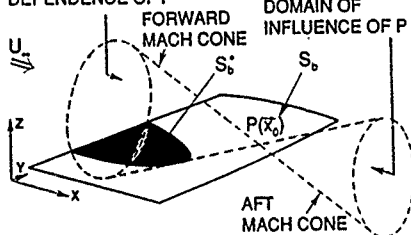
By also considering the average and the difference of the boundary conditions on the starboard and the port side ($[B]^{-1}[S]\vec{n}^*$) the integral equations for the average and the difference singularity distributions resulting from imposing the boundary conditions, decouple and can be solved for separately.

In both the fully-symmetric case and the geometric-symmetric case the surfaces that lie exactly in the plane of symmetry ($y = 0$) require special treatment.

More general cases of geometric and not necessarily aerodynamic symmetry can be formulated, like upper/lower in combination with starboard/port-side symmetry, N-lobe axi-symmetry, etc.

DOMAIN OF

DEPENDENCE OF P



MACH CONE:

$$(x_o - x)^2 + (y_o - y)^2 + (z_o - z)^2 = 0$$

Fig. 2.6 Definitions in supersonic flow

2.9 Supersonic flow

In supersonic flow the solution of the Prandtl-Glauert equation can also be written in terms of a source and a doublet distribution on the surface of the configuration, see Ref. 22. However, here the hyperbolic character of the equation is to be accounted for by restricting the surface of integration in Eqs. (2.5a), (2.5b), (2.6b), (2.6d) and (2.6e) to the area within the forward Mach cone from the point \vec{x}_o , i.e. the velocity potential induced by a source distribution becomes

$$\varphi_q(\vec{x}_o) = \frac{1}{2\pi} \iint_{S_b^*} q(\vec{x}) \frac{d\vec{x}}{|\vec{R}|} \quad (2.11a)$$

where S_b^* denotes that part of S_b falling within the forward Mach cone from \vec{x}_o (the domain of dependence of \vec{x}_o) (see Fig. 2.6). In Eq. (2.11a) a factor of $1/2\pi$ is used rather than the factor $1/4\pi$ occurring in Eq. (2.5b). This is commensurate with the circumstance that all the mass produced by a supersonic source has to flow aft through the aft Mach cone (i.e. domain of influence) rather than through both the forward and the aft Mach cone. In performing the integration in Eq. (2.11a) care should be taken to extract the proper "finite part" in the sense of Hadamard. The latter is connected with the circumstance that

$$\begin{aligned} |\vec{R}| &= |[B](\vec{x}_o - \vec{x})| \\ &= [(x_o - x)^2 + B^2((y_o - y)^2 + (z_o - z)^2)]^{1/2} \end{aligned} \quad (2.11b)$$

which with $B^2 = 1 - M^2$ being negative means that the integrand in Eq. (2.11a) is singular for all points on the Mach cone, i.e. even though in Fig. 2.3 \vec{x}_0 is not on S_0 , the integrand is singular for all points \vec{x} that lie on $\partial S_0(\vec{x})$. In subsonic flow the integrand became singular only in case the point \vec{x}_0 was on the surface $S_0(\vec{x})$.

In the same fashion one can write for the potential induced by the doublet distribution, see Eq. (2.5c)

$$\varphi_\mu(\vec{x}_0) = -\frac{B^2}{2\pi} \iint_{S_B^k ds} \mu(\vec{x}) \frac{1}{|\vec{R}|} \vec{n} \cdot d\vec{s}(\vec{x}) \quad (2.11c)$$

The expression for the velocity induced by the source and doublet distribution are found in a similar way from Eq. (2.6b), (2.6d) and (2.6e), i.e.

$$\vec{u}_q(\vec{x}_0) = \frac{B^2 f f q(\vec{x})}{2\pi S_B^k} \frac{\vec{R}}{|\vec{R}|^3} ds(\vec{x}) \quad (2.11d)$$

$$\vec{u}_y(\vec{x}_0) = \frac{B^2 f f ((B)d)}{2\pi S_B^k ds} \times \frac{\vec{R}}{|\vec{R}|^3} ds(\vec{x}) \quad (2.11e)$$

$$\vec{u}_v(\vec{x}_0) = -\frac{B^2 f f \mu(\vec{x})}{2\pi ds} \frac{\vec{R}}{|\vec{R}|^3} \times ((B)d\vec{z}(\vec{x})) \quad (2.11f)$$

Note that in above expressions B , which has an imaginary value for $M_\infty > 1$, only occurs as $B^2 = 1 - M_\infty^2$ which is negative.

It can be derived that the jumps in the velocity potential and the velocity across the source and the doublet distribution are identical to the ones given in Eqs. (2.3f) and (2.6f).

In supersonic flow one distinguishes so-called subsonic and supersonic leading and trailing edges. For a subsonic edge the component of the free-stream Mach number normal to the edge is smaller than 1.0, for a supersonic edge this component exceeds the sonic value of 1.0, i.e. for a subsonic/trailing edge the edge is swept beyond the Mach cone, for a supersonic edge the edge is swept forward of the Mach cone. As illustrated in Fig. 2.7 the behaviour of the flow near a subsonic edge is completely different from the one near a supersonic edge.

SUPersonic FLOW

UPPER-LOWER SIDE COMMUNICATION

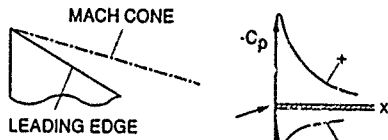


Fig. 2.7a Subsonic leading edge

SUPersonic FLOW

LEADING EDGE

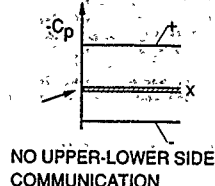
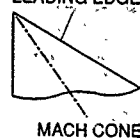


Fig. 2.7b Supersonic leading edge

For a subsonic leading edge the flow corners around the edge resulting into a singularity in the velocity field at the edge. The latter leads to the leading-edge suction force which counteracts the drag force. This also implies that there is communication between the upper and the lower wing surface, which means amongst others that at a subsonic trailing edge a Kutta condition is required to rule out expansion of the flow around the edge and force the flow to separate at the edge.

At a supersonic leading edge there is no communication possible between upper and lower side, the pressure is finite, though discontinuous, at the edge while consequently the leading-edge suction force is lost. At a supersonic trailing edge also a discontinuity in the pressure may exist because upstream influence is not possible. This implies that at a supersonic trailing edge a finite jump in the pressure is possible and also that a Kutta condition is not to be applied at such a trailing edge.

2.10 Görtler transformation

In section 2.5 the solution of the Prandtl-Glauert equation, Eq. (2.3a), was given directly in terms of elementary solutions of the Prandtl-Glauert equation. The solution can also be formulated differently by first transforming the Prandtl-Glauert equation to the Laplace equations. The transformation $\zeta = [B]\vec{x}$, i.e.

$$\xi = x, \eta = By, \zeta = Bz \quad (2.12a)$$

transforms Eq. (2.3a) with $\varphi = \psi/B^2$ into:

$$\frac{\partial^2 \varphi}{\partial \xi^2} + \frac{\partial^2 \varphi}{\partial \eta^2} + \frac{\partial^2 \varphi}{\partial \zeta^2} = 0 \quad (2.12a)$$

so that

$$\begin{aligned} \frac{\partial \varphi}{\partial \xi} &= \frac{1}{B^2} \frac{\partial \psi}{\partial \zeta} \\ \frac{\partial \varphi}{\partial \eta} &= \frac{1}{B} \frac{\partial \psi}{\partial \eta} \\ \frac{\partial \varphi}{\partial \zeta} &= \frac{1}{B} \frac{\partial \psi}{\partial \zeta} \end{aligned} \quad (2.12c)$$

This implies that one has to solve Laplace's equation for the so-called "analogous configuration" in the (ξ, η, ζ) space. The "analogous configuration" is thinner, has a smaller span and a higher sweep, than the true configuration in the (x, y, z) space.

Denoting the configuration in physical space by $F(x, y, z) = 0$, it follows that the normal vector can be expressed as:

$$\vec{n} = \left(\frac{\partial \vec{E}}{\partial x}, \frac{\partial \vec{E}}{\partial y}, \frac{\partial \vec{E}}{\partial z} \right)^T \sqrt{\left(\frac{\partial \vec{E}}{\partial x} \right)^2 + \left(\frac{\partial \vec{E}}{\partial y} \right)^2 + \left(\frac{\partial \vec{E}}{\partial z} \right)^2}^{1/2} \quad (2.13a)$$

In the transformed space the vector normal to the "analogous configuration" can be expressed as

$$\vec{v} = \left(\frac{\partial \vec{E}}{\partial x}, \frac{\partial \vec{E}}{\partial y}, \frac{\partial \vec{E}}{\partial z} \right)^T \sqrt{\left(B^2 \left(\frac{\partial \vec{E}}{\partial x} \right)^2 + \left(\frac{\partial \vec{E}}{\partial y} \right)^2 + \left(\frac{\partial \vec{E}}{\partial z} \right)^2 \right)}^{1/2} \quad (2.13b)$$

$$= (B n_x, n_y, n_z)^T f \quad (2.13b)$$

$$\left\{ \begin{array}{l} \left(\frac{\partial \vec{E}}{\partial x} \right)^2 + \left(\frac{\partial \vec{E}}{\partial y} \right)^2 + \left(\frac{\partial \vec{E}}{\partial z} \right)^2 \\ B^2 \left(\frac{\partial \vec{E}}{\partial x} \right)^2 + \left(\frac{\partial \vec{E}}{\partial y} \right)^2 + \left(\frac{\partial \vec{E}}{\partial z} \right)^2 \end{array} \right\}^{1/2}$$

where $f = \sqrt{\left(\frac{\partial \vec{E}}{\partial x} \right)^2 + \left(\frac{\partial \vec{E}}{\partial y} \right)^2 + \left(\frac{\partial \vec{E}}{\partial z} \right)^2}^{1/2}$

It follows that applying the normal-velocity condition $\frac{\partial \vec{E}}{\partial y} = -U_w n_x$ in the transformed plane, results in

$$\left(\frac{\partial^2 \vec{E}}{\partial x^2} n_x + \frac{\partial^2 \vec{E}}{\partial y^2} n_y + \frac{\partial^2 \vec{E}}{\partial z^2} n_z \right) f = -U_w n_x \quad (2.14)$$

which differs from the true boundary condition in physical space. Only if the small-perturbation assumption is made in which $f = 1 + O(\epsilon)$, and the first term on the left of Eq. (2.14), is $O(\epsilon^2)$, or for $M_\infty \rightarrow 0$, does one recover, to $O(\epsilon)$, the correct boundary condition.

An advantage from a theoretical point of view is that for above formulation, known as Göthert rule I, the uniqueness of the solution can be generally proved, which is not the case otherwise. There are further alternative Prandtl-Glauert-Göthert transformations possible, based on differences in the scalings between φ and ψ .

An alternative formulation, known as Göthert rule II, but still employing $\varphi = \psi/B$, is to solve Eq. (2.12b) in the transformed space employing incompressible source and doublet distributions, to transform the velocity components to physical space employing Eq. (2.12c) and to apply the boundary condition in physical space.

It appears that working with the direct formulation, like described in sections 2.5, 2.7 and 2.9, in which compressible source and doublet distributions are employed on the surface of the configuration in physical space, and the true boundary condition is imposed, has a slight preference. This certainly applies to the case of supersonic flow where the finite-part integration is to be performed.

2.11 Two-dimensional flow

In the present paper the emphasis is on three-dimensional flow applications. In case the panel method is to be applied to a two-dimensional configuration mostly a three-dimensional configuration is specified with a large span-chord ratio (typically of order 100). Alternatively a two-dimensional formulation can be developed directly starting from the two-dimensional Laplace or Prandtl-Glauert equation, or, as a very instructive exercise, from the three-dimensional integral formulation by taking the singularity distribution constant in spanwise direction and integrating over the interval $y \in [-\infty, \infty]$. The latter approach is taken here.

In this way one finds from Eq. (2.5b):

$$\varphi_q(\vec{x}_o) = \frac{1}{2\pi B} \int_{C_b} q(\vec{x}) \ln |\vec{R}_{2d}| dC(\vec{x}) \quad (2.15a)$$

$$\text{where } \vec{x}_o = x_o \vec{e}_x + z_o \vec{e}_z, \vec{x} = x \vec{e}_x + z \vec{e}_z,$$

$$\vec{R}_{2d} = [B] (\vec{x}_o \cdot \vec{x})$$

and C_b denotes the contour of the configuration in the x - z plane. In the derivation it has been assumed that the total integrated source-strength equals zero.

From Eq. (2.5c) it follows that in two dimensions:

$$\varphi_\mu(\vec{x}_o) = \frac{B^{-1}}{2\pi B} \int_{C_b} \mu(\vec{x}) \frac{[B^{-1}] K R}{|R_{2d}|^2} dC(\vec{x}), \quad (2.15b)$$

where $\vec{k} = n_x \vec{e}_x + n_z \vec{e}_z$ and C_{b+} is the contour of the configuration plus its wake in the x - z plane. The doublet distribution on a two-dimensional wake is constant, i.e. it serves as a cut to yield a single-valued description of the potential.

The velocity distribution due to the source and doublet distribution can be obtained in a similar way from Eqs. (2.6b), (2.6d) and (2.6e), resulting in

$$\vec{u}_q(\vec{x}_o) = \frac{|B|}{2\pi B} \int_{C_b} q(\vec{x}) \frac{\vec{R}_{2d}}{|\vec{R}_{2d}|^2} dC(\vec{x}) \quad (2.16a)$$

with $\vec{\gamma}$ directed along the y -axis, i.e. perpendicular to the x - z plane, one finds:

$$\vec{u}_q(\vec{x}_o) = \frac{|B|}{2\pi B} \int_{C_b} q(\vec{x}) \frac{\vec{R}_{2d}}{|\vec{R}_{2d}|^2} dC(\vec{x}) \quad (2.16b)$$

For the contribution due to the vortex along the edge of the doublet distribution it can be derived that

$$\vec{u}_v(\vec{x}_o) = \frac{|B|}{2\pi B} \mu(\vec{x}) \frac{\vec{R}_{2d} \times \vec{\gamma}}{|\vec{R}_{2d}|^2} \text{ for } \vec{x} \in \delta C_{b+} \quad (2.16c)$$

which is the velocity induced by a (compressible) vortex located on the edge of the distribution.

In two-dimensional flow the disturbances due to the source and doublet distributions die out less rapidly with distance from the distribution than in three-dimensional flow, i.e.

$\ln |\vec{R}_{2d}|$ versus $1/|\vec{R}|$, $|\vec{R}_{2d}|/|\vec{R}_{2d}|^2$ versus $|\vec{R}|/|\vec{R}|^3$, etc.

This corresponds with the differences in character of two- and three-dimensional flow, the two-dimensional flow being forced to remain within parallel planes and not being allowed to escape sideways.

Finally it is noted that starting from the three-dimensional formulation other, (quasi-)two-dimensional formulations can be derived. These include the case of conical flow where the geometry scales linearly with x , i.e.

$$\vec{x} = x(\vec{e}_x + \vec{e}_y(y/Kx, z/Kx))$$

with K some constant, while

$$q = q(y/Kx, z/Kx) \text{ and } \mu = \mu(y/Kx, z/Kx).$$

3. IMPLEMENTATION OF BOUNDARY CONDITIONS

3.1 Neumann condition on S_b

On the solid surface S_b of the configuration the stream-surface conditions, Eq. (2.4a), is applied, with v^* known. The most obvious manner to impose this condition is to substitute the integral representations Eqs. (2.6) directly into Eq. (2.4a). However, before this can be done one has to fix the remaining degree of freedom in the formulation, i.e. there are two singularity distributions but just one boundary condition on S_b . The degree of freedom relates to the circumstance that the flow inside the volume enclosed by S_b is arbitrary. The fictitious flow within S_b , and therefore with the degree of freedom, is fixed by specifying some relation between the two singularity distributions or by choosing one of them. In the "first-generation" panel methods the following possibilities have been implemented:

	q	μ
BODIES	Unknown	None or for LCO "Mode function"
WINGS	Unknown	

LCO: Lift-Carry-Over from WINGS to BODIES

Here "BODIES" denote parts of the configuration that have volume but no clearly defined trailing edge and do not have a wake surface associated with them. The flow over such a part in isolation would not generate any lift force. "WINGS" denote parts of the configuration that have volume or no volume, but in any case have a trailing edge and an associated wake surface, while these parts do generate lift, both in isolation and when part of a complete configuration. In case a "BODY" is attached to a "WING" the lift does not fall to zero at the junction of the body and the wing; the body carries some lift also, which is often referred to as lift-carry-over (LCO).

Most first generation panel methods started as methods that could not represent the generation of lift forces. These methods had only a source distribution on the surface of the configuration S_b and did not feature wake surfaces S_w . Later the methods were extended to cases with lift by incorporating doublet distributions (and wakes) in some relatively simple fashion, mostly in the form of what can be described as a "Mode function" approach.

The "Mode function" (given shape, unknown amplitude) doublet distribution is situated on the wing surface itself or on some auxiliary surface (often the camber surface or part of the camber surface) inside the wing, see Fig. 3.1. At the trailing edge the doublet distribution on the auxiliary surface is continued onto S_w . One of the problems encountered over and over again in the application of these first-generation panel methods is that the doublet distribution (vortex system) of the wing has to be continued into or onto appended parts without trailing edge such as fuselages, tip tanks, etc. This is necessary to avoid in a few situations, or to position in a physically correct manner in most situations, the concentrated vortex associated with the second term in Eq. (2.6a), or in other words to properly account for the lift-carry-over.

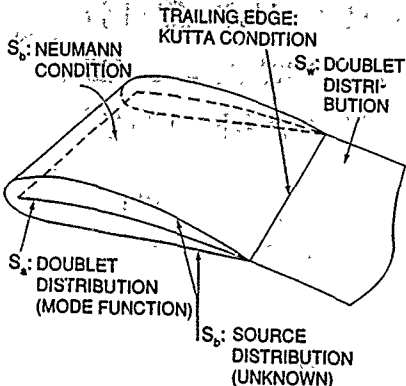


Fig. 3.1 Example of formulation of first generation panel method

Lift-carry-over occurs when the wing intersects the fuselage, the wing intersects the tip tank, the horizontal tail intersects the fuselage, the vertical tail intersects the fuselage, a pylon intersects a store or a tip tank, etc. In not all of these cases is the choice of the appropriate way to handle lift-carry-over as trivial a problem as for a simple wing-fuselage intersection of a geometrically starboard/port-side symmetric aircraft in symmetric flight.

Fig. 3.2 provides an example in which the wing intersects the fuselage and the tip tank. By introducing a LCO segment, carrying a in doublet distribution which is constant in spanwise direction and which in chordwise direction has the same distribution as the wing doublet distribution has along the section, the vortex along the wing-fuselage junction and the intersection of the wake with the fuselage is displaced to the fuselage center line. Here it will be cancelled by the vortex from the port-side LCO segment, at least for symmetric flow conditions. The vortex along the tip-tank/wing junction is displaced to the center line of the tip tank where it truthfully simulates the tip flow around the tank, and downstream of the tip tank, the wing-tip vortex. This indicates that the LCO segments are used to position the discrete vortices, associated with doublet distributions that are non-zero at their bounding edges, at physically correct locations.

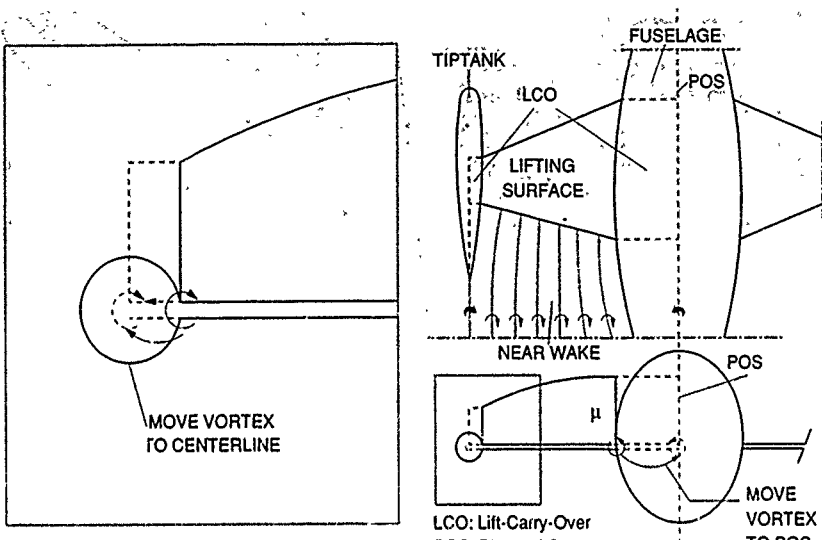


Fig. 3.2 Example of the use of lift-carry-over (LCO) segments

The formulation of the problem leads, using the direct implementation of the Neumann condition, to the following Fredholm integral equation of the second kind for the source distribution q :

$$\frac{1}{2\pi} \int \frac{q(\vec{x}_0)}{(\vec{n}, \vec{n})} + \vec{n}(\vec{x}_0) \cdot (\frac{1}{2} \iint q(\vec{x}) \vec{k}_q(\vec{x}_0, \vec{x}) dS(\vec{x}) + \vec{u}_{\text{mode } f} \cdot \vec{f}) - v_n \cdot \vec{U}_e \cdot \vec{n}(\vec{x}_0) \quad (3.1a)$$

for all $\vec{x}_0 \in S_b$.

In Eq. (3.1a) the kernel \vec{k}_q follows from Eq. (2.6b) for subsonic flow and from Eq. (2.11d) for supersonic flow, e.g. $\vec{k}_q = \vec{k}/4\pi|\vec{k}|$ for subsonic flow.

The term due to the mode function doublet distribution can be expressed as

$$\vec{u}_{\text{mode } f}(\vec{x}_0) = -\frac{1}{2} \iint_{S_{\text{aux}}} (\vec{n} \cdot \vec{\nabla} \mu) \times \vec{k}_\mu(\vec{x}_0, \vec{x}) dS(\vec{x}) - \frac{1}{2} \iint_{S_{\text{aux}}} f(\vec{x}) \vec{k}_v(\vec{x}_0, \vec{x}) \times (\frac{1}{2} dI(\vec{x})) \quad (3.1b)$$

where \vec{k}_μ and \vec{k}_v follows from Eqs. (2.6d and e) for subsonic flow and from Eqs. (2.11e and f) for supersonic flow, i.e. $\vec{k}_\mu = \vec{k}_v = \vec{k}$. In Eq. (3.1b) S_{aux} denotes the auxiliary surface carrying the mode-function doublet distribution and the wake onto which the doublet distribution is continued to infinity downstream (e.g. see Fig. 3.1). The chordwise shape of the doublet distribution is usually given, the spanwise variation of the amplitude of the mode function is found by supplementing the Neumann condition Eq. (3.1a) on S_b with a Kutta condition along the trailing edge.

The example given in Fig. 3.1 is just one of several ways in which lift can be added to a basic Neumann formulation. Other examples are a linearly varying doublet distribution on S_b , again determined by a Kutta condition at the trailing edge; defining a doublet distribution on the camber surface and applying the conditions that this surface is a stream surface for the internal flow.

The Fredholm integral equation given in Eq. (3.1) provides a sound basis for a well-conditioned discretization. Once the solution of Eq. (3.1a) is obtained the tangential velocity is computed from the evaluation of the integral representation, Eqs. (2.6b), (2.6d) and (2.6e) for subsonic flow and Eqs. (2.11d), (2.11e) and (2.11f) for supersonic flow.

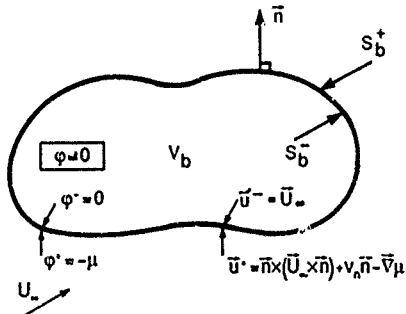


Fig. 3.3 Dirichlet condition on the perturbation potential

3.2 Dirichlet condition on S_b

Most of the "second-generation" panel methods offer an attractive alternative to the direct application of the Neumann condition described above. Utilizing the jump properties across the singularity distributions, the Neumann condition for the flow external to the volume V_b enclosed by the surface S_b , can be converted into a Dirichlet condition for the flow inside V_b . An example, see Fig. 3.3, is the formulation in which the perturbation velocity potential ϕ is set equal to zero for all points $x \in S_b$. This implies that $\phi = 0$ everywhere inside V_b and therefore also that $n \cdot \nabla \phi = 0$ for $x \in S_b$. It then follows from Eq. (2.6f) and the Neumann condition for $x \in S_b$ that

$$\vec{U}^P(\vec{x}_o) \cdot \vec{n} + \frac{1}{2}(q/b^2 + (\vec{m} \cdot \vec{\nabla} \mu)) / (\vec{n} \cdot \vec{a}) = 0 \quad (3.2a)$$

for $\vec{x}_o \in S_b^+$ and

$$(\vec{U}_n + \vec{U}^P(\vec{x}_o)) \cdot \vec{n} + \frac{1}{2}(q/b^2 + (\vec{m} \cdot \vec{\nabla} \mu)) / (\vec{n} \cdot \vec{a}) = v_n \quad (3.2b)$$

for $\vec{x}_o \in S_b^-$.

respectively. Subtraction of these two equations then yields the following relation between the source distribution q and the doublet distribution μ on S_b :

$$q = b^2(\vec{n} \cdot \vec{a})(v_n - \vec{U}_n \cdot \vec{n}) - b^2(\vec{m} \cdot \vec{\nabla} \mu) \quad (3.2c)$$

The equivalent formulation of the boundary condition that S_b should be a stream surface also leads to a Fredholm integral equation of the second kind, now for μ .

The integral equation follows directly from Eq. (2.5) as:

$$\int_{S_b \cup S_w} \mu(\vec{x}) - \iint_{S_b \cup S_w} q(\vec{x}_o, \vec{x}) dS(\vec{x}) = \iint_{S_b \cup S_w} q(\vec{x}_o, \vec{x}) dS(\vec{x}) \quad (3.3)$$

where for subsonic flow R_q and R_μ follow from Eq. (2.5c) and (2.5b), respectively, for supersonic flow from Eqs. (2.11c) and (2.11a), respectively. In case of a body with a trailing edge the wake attached to it at the trailing edge will carry a doublet distribution. The Kutta condition requires that the doublet distribution is at least continuous in function value, otherwise we would introduce a discrete vortex at the edge and consequently an infinite velocity at the edge.

This implies that at the trailing edge there is a discontinuity in the doublet distribution. Since usually trailing edges are "natural" breaks in the surface of the configuration the discontinuity in the doublet distribution will not cause additional difficulties in the discretization of the formulation.

The Dirichlet formulation does not require fictitious auxiliary internal Lift-Carry-Over surfaces. However, note that at the intersection of the wake of a wing with a body the doublet distribution on the body has a jump (equal to the wake doublet strength) (Fig. 3.4). It then means that the intersection of the wake with the fuselage should be treated explicitly as a break in the description of the cross-section of the fuselage.

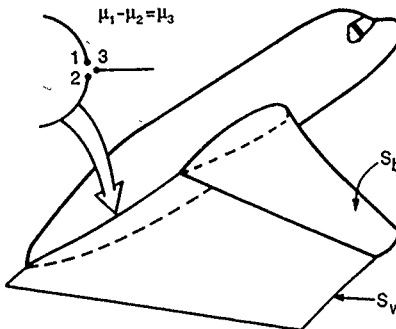


Fig. 3.4 Lift-Carry-Over in case of Dirichlet condition

Once Eq. (3.3) is solved for the doublet distribution, the tangential velocity on S_b can be obtained as follows. The Dirichlet boundary condition on S_b implies that the mean (i.e. Principal) value becomes $v^P(\vec{x}) = -\mu \vec{a}$, see Eq. (2.5f). From this same equation it follows also that

$$\vec{U}(\vec{x}_o, S_b^+) = -\mu(\vec{x}_o) \quad (3.4a)$$

and from Eq. (2.6f), solving \vec{U}^P from $\vec{U}(\vec{x}_o, S_b^-) = 0$, we find

$$\vec{U}(\vec{x}_o, S_b^-) = \vec{U}_n + (q/b^2 + (\vec{m} \cdot \vec{\nabla} \mu)) \vec{n} / (\vec{n} \cdot \vec{a}) + \vec{v}_n \quad (3.4b)$$

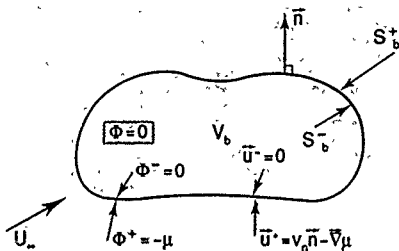
With Eq. (3.2c) this yields

$$\vec{U}(\vec{x}_o, S_b^-) = \vec{n} \times (\vec{U}_n \vec{x}_n) + v_n \vec{n} \cdot \vec{\nabla} \mu \quad (3.4c)$$

This last expression does not involve an evaluation of any integral representation, just the gradient of the doublet distribution has to be determined on the surface of the configuration together with the tangential component of the free-stream velocity (and other onset flows) and the user-specified outflow.

The latter circumstance is a clear advantage of employing the Dirichlet condition. A further advantage is that now a scalar function, v , is to be considered rather than a vector-like quantity, \vec{U} . This means that the storage problem is considerably reduced. As will be shown later on computing time required to evaluate the integral representation is not changed substantially by the approach.

In above formulation the choice was made to set the perturbation velocity potential ϕ equal to zero in the interior of V_b . This results in an internal flow field that is identical to free stream. An alternative formulation is to set the total velocity potential $\Psi(\vec{x}) = v(\vec{x}) + \vec{U} \cdot \vec{x}$ equal to zero in the interior of V_b , see Fig. 3.5.

Fig. 3.5 Dirichlet condition on S_b

Since then the total velocity is zero in the interior, Eq. (2.6f) yields for the normal component of the velocity on the inner side of S_b :

$$(\vec{U}_n + \vec{U}^P(\vec{x}_o)) \cdot \vec{n} = \frac{1}{2}(q/B^2 + (\vec{m} \cdot \vec{v}\mu)) / (\vec{n} \cdot \vec{m}) = 0, \quad (3.5a)$$

i.e. for $\vec{x}_o \in S_b$ and for the normal component of the velocity on the outer side of S_b ,

$$(\vec{U}_n + \vec{U}^P(\vec{x}_o)) \cdot \vec{n} = \frac{1}{2}(q/B^2 + (\vec{m} \cdot \vec{v}\mu)) / (\vec{n} \cdot \vec{m}) = v_n, \quad (3.5b)$$

i.e. for $\vec{x}_o \in S_b^+$, which replace Eqs. (3.2 a and b).

From these two equations it follows that now

$$q = B^2(\vec{n} \cdot \vec{m})v_n - B^2(\vec{m} \cdot \vec{v}\mu) \quad (3.5c)$$

Note that for zero outflow v_n and incompressible flow Eq. (3.5c) yields $q = 0$, i.e. for that case the potential flow solution can be found without employing a source distribution.

The integral equation to be used for the formulation of the Dirichlet condition in terms of the total potential is

$$\begin{aligned} \frac{1}{2}\mu(\vec{x}_o) + \iint_{S_{b1+b2}} \mu(\vec{x}) k_\mu(\vec{x}_o, \vec{x}) dS(\vec{x}) = \\ - \iint_{S_b} q(\vec{x}) k_q(\vec{x}_o, \vec{x}) dS(\vec{x}) + \vec{U}_n \cdot \vec{x}_o \end{aligned} \quad (3.6)$$

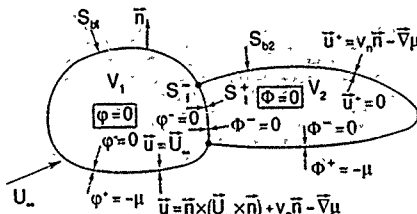
again a Fredholm equation of the second kind, differing from the integral equation Eq. (3.3) in the right-hand side only.

Once the solution of Eq. (3.6) is known it follows that

$$\Phi(\vec{x}_o, S_b^+) = -\mu(\vec{x}_o) \quad (3.7a)$$

$$\vec{U}(\vec{x}_o, S_b^+) = v_n \vec{n} - \vec{v}\mu \quad (3.7b)$$

for points on the exterior side of S_b , while in the interior of V_b the flow is at rest.

Fig. 3.6 Dirichlet condition on φ and Φ

A combination of the two Dirichlet conditions is also possible (e.g. see Fig. 3.6). In this case the flow in V_2 is stagnant flow. The boundary conditions applied are

$$\varphi = 0 \text{ on } S_b^1 \text{ and } \Phi = 0 \text{ on } S_b^2.$$

On the intersection S_1 of the two volumes we then have

$$\varphi = 0 \text{ on } S_1^+ \text{ while } \Phi = 0 \text{ on } S_1^-.$$

Carrying out the analysis as above leads to the situation in which the source distribution on S_{b1} and S_{b2} are given by Eq. (3.2c) and (3.5c), respectively. Furthermore, applying on S_1 the jump relations leads to the specification of μ , rather than q , as

$$\mu(\vec{x}_o, S_1) = \vec{U}_n \cdot \vec{x} \quad (3.8a)$$

while $q(\vec{x}_o, S_1)$ follows from an integral equation. On the whole the problem can be expressed as the following set of mixed type of integral equations to be solved simultaneously:

for $\vec{x}_o \in S_{b1}$:

$$\begin{aligned} \frac{1}{2}\mu(\vec{x}_o) + \iint_{S_{b1+b2}} \mu(\vec{x}) k_\mu(\vec{x}_o, \vec{x}) dS(\vec{x}) - \iint_{S_1} q(\vec{x}) k_q(\vec{x}_o, \vec{x}) dS(\vec{x}) = \\ - \iint_{S_{b1+b2}} q(\vec{x}) k_q(\vec{x}_o, \vec{x}) dS(\vec{x}) - \iint_{S_1} \mu(\vec{x}) k_\mu(\vec{x}_o, \vec{x}) dS(\vec{x}) \end{aligned} \quad (3.8b)$$

for $\vec{x}_o \in S_{b2}$:

$$\begin{aligned} \frac{1}{2}\mu(\vec{x}_o) + \iint_{S_{b1+b2}} \mu(\vec{x}) k_\mu(\vec{x}_o, \vec{x}) dS(\vec{x}) - \iint_{S_1} q(\vec{x}) k_q(\vec{x}_o, \vec{x}) dS(\vec{x}) = \\ - \iint_{S_{b1+b2}} q(\vec{x}) k_q(\vec{x}_o, \vec{x}) dS(\vec{x}) - \iint_{S_1} \mu(\vec{x}) k_\mu(\vec{x}_o, \vec{x}) dS(\vec{x}) \\ + \vec{U}_n \cdot \vec{x}_o \end{aligned} \quad (3.8c)$$

for $\vec{x}_o \in S_1^+$:

$$\begin{aligned} \cdot \iint_{S_{b1+b2}} \mu(\vec{x}) k_\mu(\vec{x}_o, \vec{x}) dS(\vec{x}) - \iint_{S_1} q(\vec{x}) k_q(\vec{x}_o, \vec{x}) dS(\vec{x}) = \\ - \iint_{S_{b1+b2}} q(\vec{x}) k_q(\vec{x}_o, \vec{x}) dS(\vec{x}) - \iint_{S_1} \mu(\vec{x}) k_\mu(\vec{x}_o, \vec{x}) dS(\vec{x}) \\ + \frac{1}{2}\vec{U}_n \cdot \vec{x}_o \end{aligned} \quad (3.8d)$$

Still further alternative is to apply both the external Neumann and the internal Dirichlet boundary condition. This direct approach leads to a coupled set of integral equations for the unknown source and unknown doublet distribution. Moreover, now both the velocity and the potential have to be computed resulting in a substantial increase in computational effort. This concerns not as much the computing time needed for the evaluation of the integrals but specifically the computing time involved in having to solve a system of equations with twice the dimension compared to the system resulting from the formulations discussed above, as well as the additional storage required. The possible advantage of the direct approach is that in discretized form it sometimes is more accurate than the indirect approach described above in which the source distribution is computed directly utilizing that in the inside of the body the potential is zero everywhere. This is apparently due to the circumstance that upon discretization and setting the potential equal to zero at a set of discrete points on the interior side of S_b results in an interior potential field which is not exactly zero everywhere but zero to the order of approximation employed. In case of coarse or irregular paneling it is imaginable that for a given number of panels the direct formulation involving two boundary conditions per panel might result in a more accurate simulation of the exterior flow field than the indirect formulation.

3.3 Lifting surface approximation

In the derivation of the Prandtl-Glauert equation it was implicitly assumed that bodies are pointed and slender while wings are relatively thin. Within the framework of linear theory the stream-surface condition on the upper and lower wing surfaces can be simplified to a boundary condition on a reference surface, e.g. the camber surface or any other reference surface sufficiently close to the true upper and lower wing surface (Fig. 3.7).

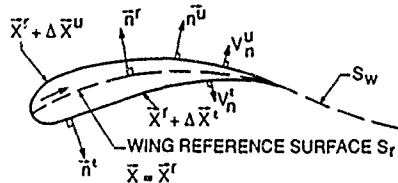


Fig. 3.7 Lifting surface approximation

In the lifting-surface approximation points on the wing surfaces are defined as

$$\bar{x} = x^r + \Delta x^r \quad (3.9a)$$

where r , u and l denote the reference ("lifting") surface, upper wing surface and lower wing surface, respectively. Under the assumptions that Δx^r and its first derivatives are small of order ϵ one may write

$$\bar{u}^{u,l} = \pm (\bar{n}^r \cdot \bar{T}^{u,l} \bar{x}^r) + O(\epsilon^2) \quad (3.9b)$$

$$\bar{u}(\bar{x}^r + \Delta \bar{x}^r) = \bar{u}_0 + \bar{u}(\bar{x}^r) + O(\epsilon^2) \quad (3.9c)$$

where \bar{n}^r denotes the vector normal to the reference surface, while the + and the - refer to the upper and lower side, respectively. $\bar{T}^{u,l}$ is of order ϵ , is tangential to the reference

surface and contains a linear combination of the first derivatives of Δx^r . The normal velocity condition on the true upper and lower wing surfaces is expanded in terms of ϵ as well, using Eq. (3.9c). In the expansion it is assumed that, to leading order of approximation, the velocity on the true surface may be replaced by the velocity on the reference surface, see Eq. (3.9c), where $\bar{u}(\bar{x}^r)$ is the perturbation velocity assumed to be of order ϵ . Adding the two expressions resulting from the approximated normal velocity boundary condition applied on upper and lower side, yields

$$\frac{1}{2} \bar{u}(\bar{x}^r) \cdot \bar{u}(\bar{x}^r) \cdot \bar{n}^r = \frac{1}{2} (\bar{v}_n^u + \bar{v}_n^l) + \frac{1}{2} \bar{u}_0 \cdot (\bar{T}^u + \bar{T}^l) \bar{n}^r \quad (3.10a)$$

where the second term on the right-hand side can be rewritten in terms of the slope of the thickness distribution of the wing. The latter one is zero in case $\Delta x^r = \Delta x$, i.e. for a wing of infinitesimal thickness. The flow problem at hand is solved by a source and a doublet distribution both situated on the reference surface, supplemented by the continuation of the doublet distribution on the wake. Substitution of the jump relation, Eq. (2.6f), then yields the following relation for q :

$$q = 2B^2(\bar{n}, \bar{u}) \left(\frac{1}{2} (\bar{v}_n^u + \bar{v}_n^l) + \frac{1}{2} \bar{u}_0 \cdot (\bar{T}^u + \bar{T}^l) \bar{x}^r \right) - B^2(\bar{m}, \bar{v}) \quad (3.10b)$$

where the last term on the right-hand side is zero for incompressible flow as well as in compressible flow in case the co-normal \bar{m} is parallel to the normal \bar{n} .

Subtracting the two expressions yields:

$$(\bar{U}_u + \bar{U}^p(\bar{x}_0)) \bar{n}^r = \frac{1}{2} (\bar{v}_n^u - \bar{v}_n^l) + \frac{1}{2} \bar{u}_0 \cdot (\bar{T}^u - \bar{T}^l) \bar{x}^r \quad (3.10c)$$

The second term on the right-hand side corresponds to the slope of the camber distribution "added" to the, not-necessarily planar, wing reference surface. The add-on camber will be zero in case $\Delta x^r = \Delta x$, i.e. in the case the reference surface is chosen to be the camber surface of the wing. It follows from Eq. (3.10c), upon substitution of Eqs. (2.6d and e), that the lifting-surface approximation leads to the following integral equation for μ :

$$\begin{aligned} \bar{n}^r (B) \int \int f(B) (\bar{n}^r \times \bar{\delta} \mu) \times \bar{k}_\mu ds - \int \mu \bar{k}_\nu \times (B) d\bar{l} &= \\ - \frac{1}{2} (\bar{v}_n^u - \bar{v}_n^l) + \bar{U}_0 \cdot \frac{1}{2} (\bar{T}^u - \bar{T}^l) \bar{x}^r - \bar{U}_0 \cdot \bar{n}^r \\ - \bar{n}^r (B) \int \int q ds \end{aligned} \quad (3.10d)$$

where \bar{k}_μ and \bar{k}_ν follow from Eqs. (2.6d and e) for subsonic flow and from Eq. (2.11e and f) for supersonic flow. Eq. (3.10d) is definitely not a Fredholm integral equation of the second kind, it probably has to be classified as an integral equation belonging to the class of Fredholm integral equations of the first kind. In above integral equation the derivative of μ appears rather than the function value itself, while also the second term on the right-hand side hampers a clear-cut classification of the integral equation. The general experience is that Fredholm integral equations of the first kind are not as easy amenable to numerical solution techniques as those of the second kind. However, at present no alternative formulation of the lifting-surface approximation is available.

The lifting-surface approximation is a thin-wing approximation with limitations in the application to arbitrary wings. It must also be mentioned that for wings with a sharp-subsonic leading edge there is formally no problem, though for most incidences there will be a singularity in the solution at the leading edge, i.e.

$$\tilde{U}(x^2; \frac{\tilde{x}}{1, e}) + 1/(x - \tilde{x}_{1,e})^{1/2}$$

For a wing with a sharp-edged supersonic leading edge there is formally no problem, but here the slope of the thickness distribution at the leading edge must be small enough to have a flow pattern with an attached shock wave. For wings with a blunt leading edge the wing-thickness source distribution becomes infinite at the leading edge, i.e. see Eq. (3.10b), invalidating the lifting-surface approximation and leading to problems in the numerical implementation. Some kind of a local treatment of blunt edges might relieve the problem.

The major advantage of the lifting-surface approximation is that now instead of the upper and the lower wing surface just one surface, with one unknown singularity distribution, is used to represent the flow about the wing. This reduces the number of panels and therewith the computational effort.

3.4 Boundary conditions on S_w

On the wake surface two boundary conditions apply: the stream-surface condition Eq. (2.4a) and the zero-pressure-jump condition Eq. (2.4b). Applying the stream-surface condition at both sides of the wake S_w gives, using Eq. (2.6f), see also Eq. (3.10a):

$$q = -b^2(\tilde{m}, \tilde{\mu}) \quad (3.11a)$$

for the source distribution (needed to cancel the jump in normal direction due to the compressible doublet distribution).

The second condition is the (average) stream-surface condition:

$$(\tilde{U}_w + \tilde{U}^*) \cdot \tilde{n} = 0 \quad (3.11b)$$

It follows from the linearized pressure formula Eq. (2.3c), again using Eq. (2.6f), that with Eq. (3.11b):

$$\Delta C_p = 2(\tilde{U}_w, \tilde{\mu})/U_w^2 + O(\epsilon^2) = 0 \quad (3.11c)$$

This latter condition leads to the classical rigid-wake approximation (see Fig. 3.8) in which the wake is directed along \tilde{U}_w (also the compressibility axis). On this surface lines with $\mu = \text{constant}$ (with the constant equal to the value of μ at the trailing edge), which correspond with the vortex lines, are directed in streamwise direction. Since now $\tilde{m}, \tilde{\mu} = 0$ this wake does not carry a source distribution, just a doublet distribution.

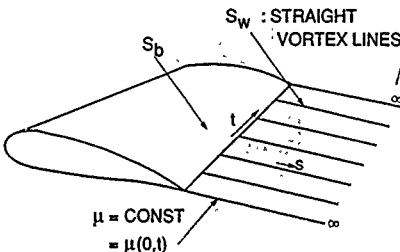


Fig. 3.8 Classical rigid-wake approximation

The classical rigid-wake approximation is so attractive because it renders the problem linear and no boundary conditions are necessary on the wake surface. Very often it yields sufficiently accurate results, such as for the case of lightly-loaded wings, for the cases without strong wing-wake/tail interaction, etc. Also, in supersonic flow very often the approximation suffices because of the absence of upstream influences.

The rigid-wake approximation with straight vortex lines fixed in space renders the problem linear. Note that though the average normal-velocity condition, Eq. 3.11b, is not satisfied on S_w , the pressure is to first order continuous across the wake implying that the wake is force free to that order of magnitude.

A frequently used slight variation on the classical planar wake is to let the user specify the vortex lines, i.e. curves along which the doublet distribution is taken as constant (Fig. 3.9), again equal to the value of μ at the trailing edge. The vortex lines on the so formed "near wake" are continued as straight lines onto the "far wake". In this case the vortex lines are still fixed in space and the problem remains linear. On the other hand one should realize that the near wake might not be force free, not even to first order.

The non-planar wake assumption, of use for low-spo, high-angle-of-attack applications, results also in a linear problem which does not require boundary conditions on the wake surface.

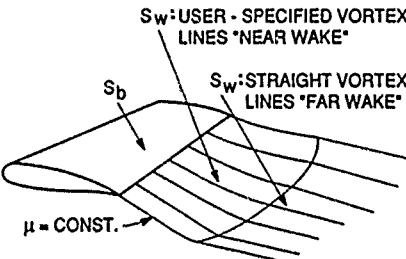


Fig. 3.9 Variation on rigid-wake approximation

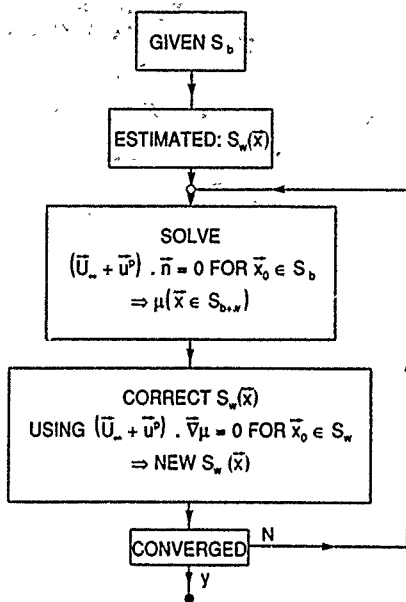


Fig. 3.10 Wake relaxation procedure

Although the user-specified near-wake option does improve the modeling capabilities of the panel method, there are cases where the interaction between the wake of one component and the flow about another nearby component of the configuration is so strong that the full nonlinear boundary conditions have to be imposed. Examples a, delta wings with leading-edge vortex flow, the flow around the side edge of a deflected flap and the flow around the wing tip. The stream-surface condition leads to the two relations given in Eqs. (3.11a and b). For the zero-pressure-jump condition substitution of Eq. (2.6f) and Eq. (3.11a and b) in Eq. (2.4e) results, without approximation into:

$$(Ū_w + Ū^p) \cdot \nabla \mu = 0 \quad (3.11d)$$

which, combined with Eq. (3.11b), implies that in incompressible flow, as well as in linearized compressible flow, the vortex lines (lines $\mu = \text{constant}$) are parallel to the local average velocity across the vortex sheet.

Note that from this exact equation Eq. (3.11c) can be obtained directly rather than via the expression for the linearized pressure coefficient.

To solve for the position of the wake and the singularity distributions on the body as well as on the wake simultaneously is a difficult task, especially for general configurations. The main difficulty is that often the topology of the wake vortex system is not known, while also specifying a successful initial guess to be input in the procedure that solves the system of nonlinear equations is a non-trivial problem. So frequently one relies on a hierarchical "wake relaxation" procedure (see Fig. 3.10) in which one first obtains the singularity distribution for a rigid wake (as in Fig. 3.9) and subsequently aligns the vortex lines with

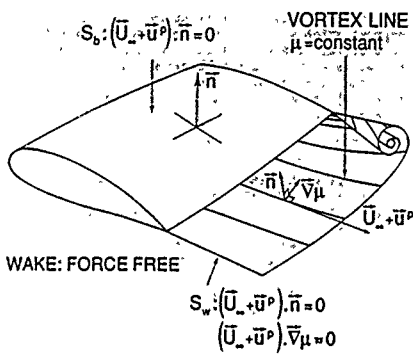


Fig. 3.11 Full wake relaxation

the local velocity, thus defining an improved estimate for the location of the wake surface, etc. However, in cases where the wake interacts very strongly with the flow about a nearby component of the configuration (e.g. the flow about slender wings with leading-edge vortex sheets) such simple hierarchical iteration scheme frequently diverges and the wake boundary conditions Eqs. (3.11b and d) have to be solved simultaneously (see Fig. 3.11). The two resulting integral equations for μ and $S_w(x̄)$ are highly nonlinear in $x̄$. In terms of μ Eq. (3.11b) leads to an integral equation not unlike a Fredholm integral equation of the first kind, similar to the lifting-surface integral equation (3.10d), while Eq. (3.11d) is nonlinear (quadratic) in the doublet distribution.

An alternative approach is to specify the shape of the "near wake" vortex sheet as in Fig. 3.9, but to allow the vortex lines to move freely within this surface such that on S_w the zero-pressure-jump condition, Eq. (3.11d) is satisfied. The resulting problem is only weakly nonlinear (μ and S_w) and a simple quasi-Newton iteration procedure can be used to solve for the doublet distribution on the near wake. For this formulation the doublet distribution on the near wake needs to be discretized into panels, see Fig. 3.12.

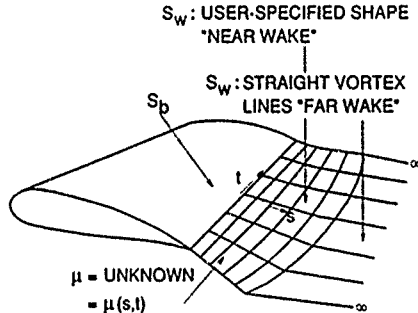


Fig. 3.12 Partial wake relaxation

As a result of the "partial wake relaxation" $U_0 + u$, the mean velocity on the vortex sheet, is perpendicular to ∇u , i.e. the velocity vector lies in a plane normal to the surface, which also contains the surface vorticity vector $\gamma = -\nabla \times u$, see Fig. 3.13. However, the normal velocity condition is not satisfied and $U_0 + u$ and γ are not parallel to each other. This then implies that there is still a force, tangential to the surface, working on the wake. This force is proportional to $(\bar{U}_0 + \bar{u})\gamma$, which with $(\bar{U}_0 + \bar{u})\cdot \nabla u = 0$ becomes $(\bar{U}_0 + \bar{u})\cdot \nabla \bar{u}$.

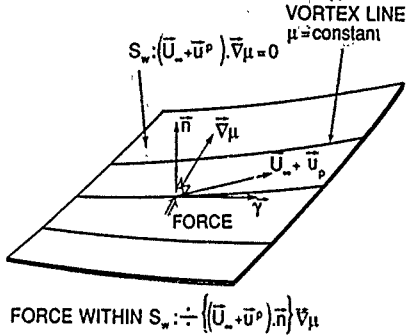


Fig. 3.13 Partial wake relaxation - Force on wake

3.5 Kutta condition

The Kutta condition is the condition that the flow leaves the surface of the configuration in a smooth fashion. This implies that the wake vortex sheet smoothly connects to the trailing edge and that the velocity is finite at the edge. In terms of the singularity distributions, this immediately implies that the doublet distribution is continuous at the edge, since any discontinuity in μ results in a discrete vortex, of strength equal to the jump in the doublet distribution, along the trailing edge which would result in an infinite velocity at the edge.

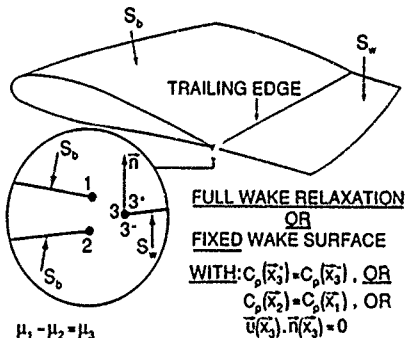


Fig. 3.14 Kutta conditions

In case the wake vortex sheet is relaxed, the Kutta condition will be satisfied in the process of the wake relaxation. In this sense, wake relaxation is the perfect Kutta condition, requiring no other input than the location of the separation line. In case the wake vortex sheet is not relaxed, but chosen as a fixed surface in space, a different procedure must be followed, see Fig. 3.14. There are several possibilities in use in panel methods:

- (i) In case the doublet distribution on the wake is relaxed ("partial wake relaxation") the pressure will already be continuous at the trailing edge point on the wake vortex sheet.

(ii) In case no condition is imposed explicitly on the wake vortex sheet some panel methods feature a nonlinear Kutta condition in which the condition is enforced that at the trailing edge the pressure on the upper wing surface equals the pressure on the lower wing surface. Note that in 2D flow this condition reduces to a linear condition.

(iii) Impose the condition that just downstream of the trailing edge the velocity vector \vec{v} is directed along the chosen wake surface S_w , i.e.

$$\vec{u} \cdot \vec{n} = 0 \text{ at } \vec{x} = \vec{x}_+^+ \quad (3.12)$$

The difficulty here is that the direction of the wake vortex sheet at S_u is directly involved in the Kutta condition. For wings with zero trailing-edge angle and for lifting surfaces the direction is uniquely determined, namely tangential to the cusped part of the wing, or tangential to S_u . For wings with a finite trailing-edge angle the wake vortex sheet is either tangential to the lower wing surface or to the upper wing surface or, at an isolated point on the trailing edge, directed along the bisector (the so-called Hangler & Smith criterion, see Ref. 23). Whether the wake vortex sheet is tangential to the lower or to the upper surface depends on the planform of the wing (the non-linearity creeping into the problem again). However, in most applications just one direction (lower or upper) is chosen.

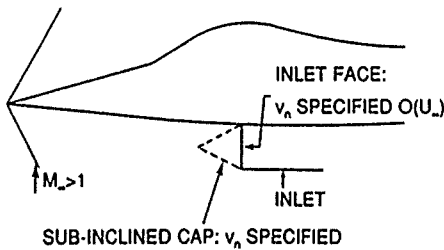
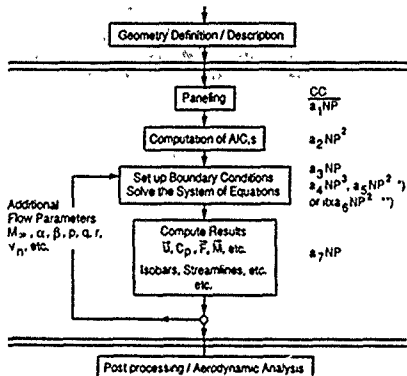


Fig. 3.15 Inlet modeling in supersonic flow

3.6 Super-inclined surface

In compressible subsonic or supersonic flow the perturbations are assumed to be small. This usually implies that the true surface is only slightly inclined with respect to the free-stream direction and generally will be sub-inclined with respect to the Mach angle in supersonic flow. However, for instance at inlet faces where an inflow is prescribed the surface will be super-inclined, but the perturbation may still be small. These super-inclined portions of the surface re-

quite special boundary specifications, not given here; or alternatively specification of an artificial sub-inclined cap or ramp covering the inlet. On the cap or ramp the specified outflow should correspond to the required mass flow into the inlet (see Fig. 3.15). However, in case of a blunt-nosed fuselage the flow near the super-inclined portion of the nose represents a region where the linearized-potential flow model is not valid. Sharpening artificially the nose for this case will alleviate the problem, but in the nose region the flow solution will be inaccurate.



CC: Computational Complexity ($a_2 \gg a_3, a_5$ or a_6)
 *) 1st solution direct solver, next solutions
 **) iterative solver

Fig. 4.1 Breakdown of tasks within a panel method

4.0 APPROXIMATION AND DISCRETIZATION

4.1 General approach

In the approach taken in panel methods the following tasks can be distinguished (see Fig. 4.1):

1. Subdivide the surface S_h of the configuration and its wake S_w into (small) quadrilateral elements, the panels. This is mostly accomplished in a hierarchical manner (Fig. 4.2) in which the configuration is subdivided into **PANELS**, each part into **SEGMENTS** (sometimes called "networks") and each segment into a number of **STRIPS** (rings) of the same number of panels. Subsequently the geometrical quantities (centroid, normal vector, curvature, twist, etc.) of each panel are computed.
2. Replace the integrals over the surface by the sum of the integrals over the NP panels. Choose on each panel, sufficiently accurate and mutually consistent, local representations for the singularity distributions μ and q . The local representations involve parameters determining the magnitude of the singularity distributions. Here Q_i , $i=1(1)NQ$ denote the NQ parameters in the source distribution, D_i , $i=1(1)ND$ denote the ND parameters in the doublet distribution. It de-

pends on the precise formulation chosen, i.e. Neumann or Dirichlet, which of the Q_i 's and D_i 's are unknown and which of these parameters are known and can be derived directly from the boundary conditions.

Also required is some local representation for the geometry of the panels, this to consistent order of approximation with respect to the representations for the singularity distributions.

In case the position of the vortex sheets is simultaneously to be solved for, also for x describing the geometry of the panels on S , a local representation is required. The latter involves 3NG further unknown parameters to be solved for, denoted here as \tilde{x}_i , $i=1(1)NG$.

3. Approximate, to the required order of accuracy, the integrals over the panel surface corresponding to the contribution of the singularity distributions on the panel in the potential or the velocity at the N (collocation) points where the boundary conditions are to be imposed.

The computational heavy ($\sim NQNP$) task, constituted by step 2 and 3, yields the so-called aerodynamic influence coefficients (AIC's), i.e., the velocity potential induced at the point \tilde{x}_0 by the singularity distribution expressed as:

$$\psi(\tilde{x}_0) = \sum_{i=1}^{NQ} a_{ki} Q_i + \sum_{i=1}^{ND} b_{ki} D_i \quad (4.1a)$$

and the velocity induced at \tilde{x}_0 as

$$\vec{u}(\tilde{x}_0) = \sum_{i=1}^{NQ} \vec{c}_{ki} Q_i + \sum_{i=1}^{ND} \vec{d}_{ki} D_i \quad (4.1b)$$

where a_{ki} , b_{ki} , \vec{c}_{ki} and \vec{d}_{ki} are the AIC's. In Eq. (4.1) Q_i , $i=1(1)NQ$ and D_i , $i=1(1)ND$ are the parameters in the panel-wise representations of the source and doublet distribution, respectively.

The AIC's are a function of \tilde{x} and of the geometric quantities describing the panel surface. This implies that the AIC's are independent of the "aerodynamic unknowns" (the Q_i 's and/or the D_i 's), but may be a function of the "geometric unknowns" of the wake vortex sheets.

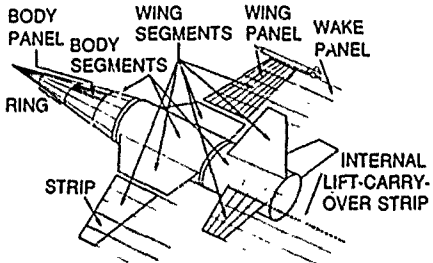


Fig. 4.2 Example of configuration paneling

4. Impose the boundary conditions at the collocation points. In most aerodynamic panel methods the collocation technique is applied

in which the boundary condition is applied at just one point per panel. Some other methods, not discussed any further here, can be classified as Galerkin methods, i.e., they involve the surface integral over the panel of the product of the boundary condition with the local representations.

In most aerodynamic panel methods the number of collocation points is equal to the number of unknown parameters and of the order of the number of panels. It should be remarked also that some of the so-called higher-order methods explicitly impose (abutment) conditions on the continuity of the singularity distributions across segment edges, which can considerably increase the number of algebraic equations to be solved, and inflate the dimension of the matrix-equation to be solved.

5. Solve the resulting non-sparse system of linear (non-linear in case of partial or full-wake relaxation) equations for the unknown parameters in the local representations for the singularity distributions (and geometry). For subsonic flow the matrix is fully populated, for $M=1$ parts of the matrix will be empty because of the forbidden upstream influence in supersonic flow. Solution of the system of linear equations requires of the order of N^3 operations in case a direct solver is used and of the order of $l \times N^2$ operations in case an iterative solver is used, with l the number of iterations required for convergence. However, in both cases the coefficient multiplying N^p , with $p = 2$ or 3 , is much smaller than the one multiplying N^{p+1} above.
6. Find to the required accuracy the velocity distribution on the surface S_b of the configuration.
7. Compute the pressure, integrated forces and moments, induced drag, (lifting surface) edge-suction forces, surface streamlines, isolars, velocity and pressure at off-body points, stability derivatives, trimmed-flight conditions, boundary-layer quantities, updated wake position, etc., etc.

The user of the method will interface with step 1., where the geometric input to the program is digested and with step 7. where the results of the flow simulation are generated. These two steps will determine the geometric capability, post-processing power and also (of utmost importance) the user-friendliness of the program. Some panel meth-

ods do not have any built-in geometric pre-processing capability and therefore fully rely on the availability of a CAD package to generate the definition of the geometry, the sub-division into parts, segments, etc. and to carry out the discretization ("paneling") of the surface of the configuration. Other methods a more stand-alone type of methods with geometric capabilities, including paneling options, definition of the geometry through basic built-in shapes, etc., all with the purpose of minimizing the amount of input data and to provide maximum flexibility.

The design and details of the remaining steps (2-6) will determine the accuracy of and computer resources required for each application. As far as the accuracy and cost is concerned, the aim in the development of any panel method to be used in preliminary design should be to obtain, for lowest costs, the surface-velocity distribution to certain accuracy, i.e.

$$\tilde{u}^h(\tilde{x}_o, S_b) - \tilde{u}(\tilde{x}_o, S_b) + O(h^n), \quad \text{for } h^n \quad (4.2)$$

Here n denotes the "order" of the panel method. Most of the "first-generation" panel methods are first-order methods, most of the "second-generation" methods are second-order methods. In the following we consider some aspects related to the formulation of a panel method of consistent order of approximation. The discussion will be restricted to first and second-order methods.

4.2 Small-curvature expansion for velocity

Consider the expression for the velocity induced by a source distribution, Eq. (2.6b). In order to simplify matters somewhat the discussion concerns the limiting case of incompressible flow, i.e.

$$\tilde{u}_q(\tilde{x}_o) = \sum_i \frac{1}{4\pi} \iint_S q(\tilde{x}) \frac{\tilde{x} - \tilde{x}_o}{|\tilde{x}|} dS(\tilde{x}) \quad (4.3)$$

where $\tilde{x} = \tilde{x}_o - \tilde{x}(s, t)$, S_i denotes the surface of the i -th panel and (s, t) is some surface coordinate system (Fig. 4.3). The integrand in Eq. (4.3) is singular for \tilde{x}_o coinciding with point $\tilde{x}(s, t)$ on S_i . In most cases the integral itself is finite, though always discontinuous across S_i . Therefore numerical quadrature is not appropriate. Hess (Ref. 25) proposed an expansion in which the characteristic singular behaviour of the integrand is conserved. The expansion results in a consistent

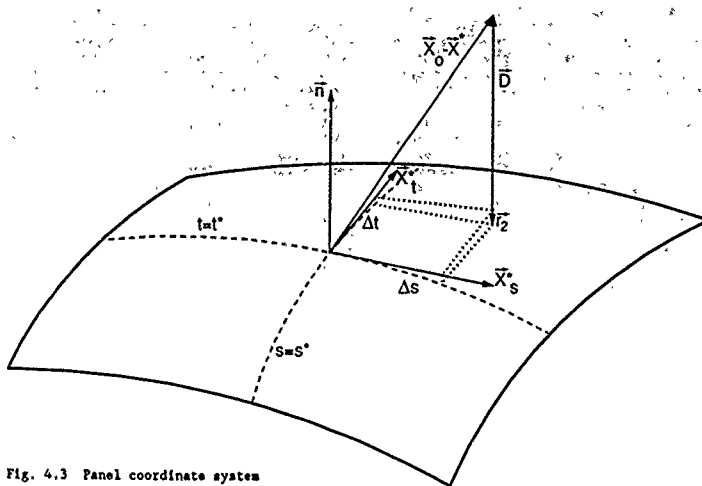


Fig. 4.3 Panel coordinate system

approximation of Eq. (4.3) thus possesses the correct behaviour as x_0 crosses the surface S_b . In the expansion the nominator is split into a linear part and a part containing the curvature and twist of the panel, i.e.

$$\vec{r} = \vec{x}_0 + (\vec{x}^* + \Delta s \vec{x}^* + \Delta t \vec{x}^*) + \vec{\epsilon}_2 + \dots \quad (4.4a)$$

$$= \vec{D} + \vec{r}_2 + O(\epsilon^3) \quad (4.4b)$$

with $\Delta s = s - s^*$ and $\Delta t = t - t^*$, with $\vec{x}^* = \vec{x}(s^*, t^*)$ denoting the so-called expansion point.

In Eq. (4.4a) the term inside the curly brackets corresponds to the equation of the plane tangential to the panel at $\mathbf{x}(s^*, t^*)$ and is defined by the vectors \mathbf{x}^s and \mathbf{x}^t , tangential to the surface coordinate directions $t = \text{constant}$ and $s = \text{constant}$, respectively.

The vector \vec{v} denotes the position of the point at which the influence is computed relative to the tangent plane. The panel curvature/twist term $I_2 = \frac{1}{2}\delta^2 x_{ss}^2 + \Delta x_{st}x_{ss} + \frac{1}{2}\delta^2 x_{tt}^2$ is of order δ^2 , where δ is a linear measure for the panel size in either direction.

The term $\tilde{D} - \tilde{x}_i - (\tilde{x}_i + \Delta x_i^{\text{near}} + \Delta x_i^{\text{far}})$ is order 5 in the "near field" of the panel and order 1 in the "far field" of the panel. In the following we denote the order of magnitude of \tilde{D} by D .

In terms of the surface coordinate system the surface element $dS = |\vec{x} \cdot \vec{x}_s| ds dt$ is expanded as:

$$dS(\vec{x}) \approx |\vec{x}_s^* \cdot \vec{x}_t^*| \{ 1 + \vec{n}^* \cdot (\Delta s \vec{T}_1 + \Delta t \vec{T}_2) + O(\delta^2) \} \quad (4.4c)$$

where \tilde{f}_1 and \tilde{f}_2 are expressions containing the curvature and twist terms evaluated at the expansion point.

$$\tilde{x}_i = (\tilde{x}_{i+1}^* \tilde{x}_{i+2}^* \dots \tilde{x}_{n+1}^* \tilde{x}_n^*) / |\tilde{x}_{i+1}^* \tilde{x}_{i+2}^*|$$

$$\vec{T}_2 = (\vec{x}^* \vec{x} \vec{x}^* - \vec{x}^* \vec{x} \vec{x}^*) / |\vec{x}^* \vec{x} \vec{x}^*|$$

The singularity distributions q and μ on S_1 are expanded in a similar fashion, i.e.

$$q = q^* + \Delta s q_s^* + \Delta t q_t^* + O(\epsilon^2) \quad (4.4d)$$

$$\mu = \mu^* + \Delta s \mu_{ss}^* + \Delta t \mu_{tt}^* +$$

$$+ \frac{1}{2} \Delta s^2 \mu_{ss}^* + \Delta s \Delta t \mu_{st}^* + \frac{1}{2} \Delta t^2 \mu_{tt}^* + O(\delta^3)$$

(4.4e)

Substitution of Eqs. (4.4a-d) into Eq. (4.3) and expansion in terms of δ and D yields

$$\begin{aligned} \hat{u}_q(\vec{x}_o) &= \frac{1}{4\pi} \sum_i \vec{x}_g^i \vec{x}_o^i \vec{\xi}_i^2, \\ \cdot \left(q^* \iint_{S_1} \frac{\vec{B}}{|\vec{B}|^3} d\sigma dt \right) &\sim O(B^2) \\ + q^* \iint_{S_1} \frac{\delta A \vec{B}}{|\vec{B}|^3} d\sigma dt + q^* \iint_{S_1} \frac{\delta B \vec{B}}{|\vec{B}|^3} d\sigma dt &\sim O(\epsilon^2 B^2) \\ + q^* \iint_{S_1} \left(\frac{\vec{v}_2}{|\vec{B}|^3} + 3\vec{v}_2 \frac{\vec{B}}{|\vec{B}|^3} \right) d\sigma dt &\sim O(KB^2 D^2) \\ + \vec{v}_1^* \iint_{S_1} (\Delta \vec{A} \vec{v}_1 + \Delta \vec{v}_2 \vec{v}_1) \frac{\vec{B}}{|\vec{B}|^3} d\sigma dt &\sim O(KB^2 D^2) \\ + O(K^2 \frac{D^2}{N^2}, K^2 \frac{D^2}{N^2}, \dots) \} &\quad (4.5) \end{aligned}$$

where K is a measure of the panel curvature and twist. All remaining integrals involve an integrand with a quadratic expression in the nominator raised to the power $1/2$, $3/2$ and $5/2$. For each of these integrals closed-form expressions can be derived.

It follows, from the order of magnitude estimate indicated for each term in Eq. (4.5), that for a first-order panel method in the near-field AIC computation a panel-wise constant representation for q in the flat-panel approximation suffices. For a first-order method the only term of importance in the "near-field" is the first term in Eq. (4.5), a term of magnitude $O(1)$. According to Eq. (4.5) a second-order panel method requires a panel-wise linear representation for q and panel curvature and twist have to be accounted for and all terms in Eq. (4.5) have to be included in the computation of the AIC's.

However, note that if the panel curvature and twist are such that $K_S \text{ [panel]} < \delta^2$, where δ is the basic length scale in the discretization, i.e. some average panel size, the terms in Eq. (4.5) due to the panel curvature and twist (the most complex ones) are small of higher order and may be omitted. Reduction of δ_{local} by sub-paneling, in which the number of sub-panels increases with increasing K but also with decreasing δ , is another possibility to formally get rid of the most complex terms in Eq. (4.5). Applying the small-curvature expansion to Eqs. (2.6d and e), the velocity induced by the doublet distribution, shows that a first-order method requires a panelwise linear representation for μ on a flat-panel approximation, while a second-order method requires a panelwise quadratic representation for μ while again panel curvature and twist have to be included.

The closed-form expressions for each of the surface integrals in Eq. (4.5) contain the same type of (computationally expensive) transcendental functions (two logarithms, one square root and one inverse tangent) multiplied by simple polynomial-type terms and summed in a way depending on the specific expression. This indicates that computationally, if carefully designed and programmed, a higher-order formulation does not need to be very much more expensive than a lower-order formulation. However, it will be clear that a third-, or even higher-order method, which amongst others will involve derivatives of the curvature, is beyond practical limits.

The small-curvature expansion warrants that the induced velocity has the proper behaviour as the point x_0 crosses the surface at $x = x(s, t^*)$, and the panel expansion point is usually chosen as the collocation point on the panel, irrespective of the location of x_0 .

Although for arbitrary configurations it cannot be proven formally, the small-curvature expansion given in Eq. (4.5) is expected to have a composite error, the error due to summing over all panels, of $O(\delta^4)$.

In considering the small-curvature expansion of the velocity induced by the doublet distribution it has to be assumed that the doublet distribution is continuous (at least to order δ , to $O(\delta^4)$ for higher-order formulations) across the panels edges, actually already implicitly used in the derivation of Eq. (2.6c). If this is not the case spurious contributions in the velocity induced by a doublet distribution will appear. Similarly the doublet distribution should be zero at the boundary of S_w , to avoid a discrete vortex at that location. However, in the description given in this paper we retained Eq. (2.6e) because of the following reason. Vortex wakes tend to roll up into concentrated vortices (e.g. near a wing tip), which are in the vortex sheet model represented by a highly rolled-up vortex sheet of infinite length.

At the edge of this vortex sheet the doublet distribution is indeed zero (see Fig. 4.4). Since it is rather impossible to discretize a vortex sheet of infinite length the tightly rolled-up part of the vortex sheet is replaced by a discrete vortex filament, connected with the remainder of S_w by a "feeding sheet" (see Fig. 4.4). The vortex, if of the correct strength and if positioned at the correct location, will provide the proper flow field away from the vortex filament but of course not near the center of the vortex core where the velocity will be singular in the numerical model.

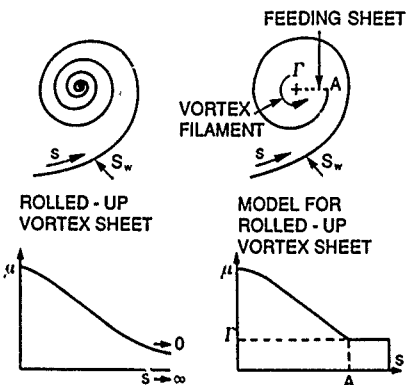


Fig. 4.4 Model for rolled-up vortex sheet

ONE HORSE-SHOE VORTEX PER PANEL

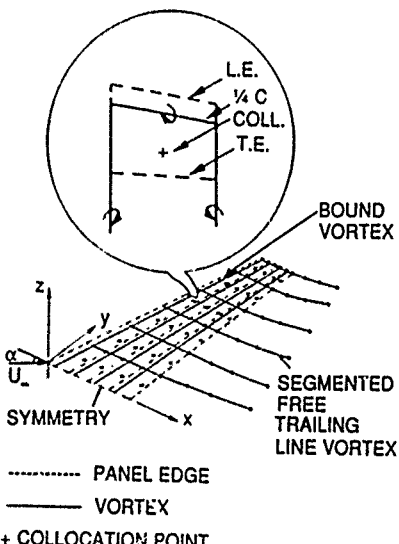


Fig. 4.5 Vortex lattice method

Under the conditions discussed above the small-curvature expansion indicates that the following consistent approximations are possible for the evaluation of the integral representation of the velocity induced by source and doublet distributions:

	To 1st order	to 2nd order
Panel geometry	$\vec{x}_s^*, \vec{x}_t^*, \vec{x}_c^*$	$\vec{x}_s^*, \vec{x}_t^*, \vec{x}_c^*, \vec{x}_{ss}^*, \vec{x}_{st}^*, \vec{x}_{ct}^*$
Source distribution	q^*	q^*, q_s^*, q_t^*
Doublet distribution	$(\mu^*), \mu_s^*, \mu_t^*$	$(\mu^*), \mu_s^*, \mu_t^*, \mu_{ss}^*, \mu_{st}^*, \mu_{ct}^*$

A further reason to retain Eq. (2.6e) is to accommodate the so-called vortex-lattice method (see Fig. 4.5), which is a lifting-surface method. In the vortex-lattice method the doublet distribution is panelwise constant, i.e.

in $\vec{U}_\mu(\vec{x}_o) = \vec{U}_\gamma(\vec{x}_o) + \vec{U}_v(\vec{x}_o)$ the first term, given in Eq. (2.6d), is zero, i.e. the second term, given in Eq. (2.6e), is the only term to be considered. This means that we have to integrate along the edges of the panel only, or rather have to consider the velocity induced by a vortex of constant strength along the perimeter of the panel.

Since the velocity distribution is singular at the vortices it is impossible to derive a consistent approximation along the lines used above. In the vortex-lattice method the point at which the velocity is to be computed has to be chosen very carefully. It turns out that if the point is chosen as the midpoint of the panel, i.e. as far away from the singularity as possible, the induced velocity is to $O(6)$ accurate. In order to avoid having a vortex located at the leading edge the vortices are shifted away from the panel edges, or as most commonly referred to, the "bound" vortex is located at the 1/4-panel-chord line of the panel, while the point where the velocity is computed is the midpoint of the 3/4-panel-chord line. This actually means that the elements with constant μ are shifted 1/4-panel chord in chordwise direction. At the trailing edge the doublet distribution is continued onto the wake as a strip of constant μ , equivalent to discrete trailing vortices along the side edges of the strip.

Similar to the shift in the vortex location at the leading edge is the usual practice to off-set the (trailing) vortex along the wing tip by 1/4-panel span.

It must be noted that in satisfying the stream surface condition at the mid point of the 3/4-panel-chord line, this probably the only point on the panel is where $\vec{u} \cdot \vec{n} = 0$. Furthermore, the velocity at that point will be continuous since the jump in the velocity associated with a doublet distribution is related to \vec{v}_0 which is zero. This implies that in order to have a jump in the tangential velocity, and therewith in the pressure and a contribution to the normal force, v_0 has to be calculated from one local non-constant representation for μ . An alternative procedure to compute the contribution of the panel in the force on the lifting surface is to apply Blasius' theorem to compute the force on the "bound" vortex along the 1/4-chord line using, see Fig. 4.6:

$$\Delta F = \rho \vec{u} \cdot \vec{v}_0 d\Gamma \quad (4.6)$$

and a similar expression for the moment.

Note that this requires that the velocity is to be computed at two points per panel, at the midpoint of the 3/4-panel-chord line and at the midpoint of the 1/4-panel-chord line. Furthermore note that \vec{F} as given in Eq. (4.6) contains both the normal and the tangential force components. For a specific two-dimensional case it can be shown analytically that the computed resulting force and moment are equal to their exact values (Ref. 24); a remarkable result indeed.

Further, note that in three-dimensional flow such a nice analytic result is not available, though it appears that above procedure yields rather satisfactory results for overall forces and moments. For swept wings axial force results can be improved by "unsweeping" the "bound" vortex segments prior to applying Eq. (4.6).

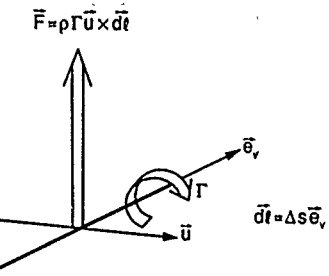


Fig. 4.6 Force on a vortex segment

4.3 Far-field expansion for velocity

Although the small-curvature expansion is uniformly valid, it is computationally expensive and therefore only applied in the region where it is really needed, i.e. in the "near field" of the panel. In the "far-field" ($|\vec{x}_o - \vec{x}^*| > 6$) of the panel the nominator of Eq. (4.3) can be expressed as

$$\vec{r} = \vec{x}_o - \vec{x}_1 - \vec{x}_2 + O(\delta^3) \quad (4.7)$$

where $\vec{x}_1 = \vec{x} - \vec{x}^*$ is $O(1)$ and $\vec{x}_2 = \Delta s \vec{x}_s + \Delta t \vec{x}_t$ is $O(6)$. Substitution in Eq. (4.3) then yields:

$$\begin{aligned} \vec{u}_q(\vec{x}_o) = & \frac{1}{6\pi} \sum_i \vec{x}_s^* \vec{x}_t^* \left[q + \frac{\vec{x}_o}{|\vec{x}_o|} \right] \iint f ds dt + O(\delta^2) \\ & + (\dots) \iint (\Delta s \text{ or } \Delta t) ds dt + O(\delta^4) \end{aligned} \quad (4.8)$$

The second term in Eq. (4.8) is zero if the expansion point (s^*, t^*) coincides with the panel midpoint. The truncation error in Eq. (4.8) is sufficiently small to guarantee a composite error of $O(4^4)$. Eq. (4.3) indicates that for the far-field expansion both a first-order and a second-order method require a panelwise constant representation for q on the flat-panel approximation, i.e., curvature and twist details of the panel or higher derivatives of the singularity distribution are of no significance for the far-field influence. For the doublet distribution it can be shown that one requires a panelwise linear representation on the flat-panel approximation.

Often the region where the near-field expansion is to be applied is reduced in size by defining an "intermediate" field in which some form of numerical (e.g., Gauss) quadrature is applied. In the intermediate field it is assumed that the integrand in Eq. (4.3) is sufficiently well-behaved to get a consistent accurate integration with a standard numerical integration procedure that is slightly more complex than Eq. (4.7) but is not as complex as Eq. (4.5).

4.4 Small-curvature expansion for potential

The expression for the velocity potential induced by a source and a doublet distribution can be expanded in a similar fashion as illustrated above for the velocity. However, in order to evaluate the velocity to $O(\delta^2)$, the velocity potential has to be evaluated to $O(\delta^3)$. As an example consider the small-curvature expansion for the velocity potential induced by a source distribution. From Eq. (2.5b) it follows (incompressible flow):

$$\begin{aligned} v_q(\vec{x}_o) = & \frac{1}{4\pi} \sum_i \vec{x}_s \cdot \vec{x}_t \\ & + q_s \iint \frac{\Delta s}{S_1 |\vec{b}|} ds dt + q_t \iint \frac{\Delta s}{S_1 |\vec{b}|} ds dt \\ & + q_s \iint \frac{\vec{r}_2 \cdot \vec{b}}{S_1 |\vec{b}|^3} ds dt + O(K_s^2 \delta^2) \\ & + O(K_s^2 \delta^2) \\ & + O(K_s^2 \delta^2) \quad (4.9) \end{aligned}$$

It follows from Eq. (4.9) and from a similar expression for the potential induced by a doublet distribution (taking continuity of doublet strength across panel edges into account) that for a first- or second-order method employing the Dirichlet condition the same type of panel-wise representations are required as for the corresponding method with the Neumann condition. The condition under which the last two terms in Eq. (4.9) may be neglected is $K_s^2 \ll \delta^2$. Comparison of Eqs. (4.5) and (4.9) indicates that the same type of integrals appear in both expressions, so that also the same transcendental functions have to be computed. This implies that computationally the formulation in terms of a Dirichlet condition will not be cheaper than the formulation in terms of Neumann conditions, but of course the Dirichlet formulation requires less storage, since a scalar influence coefficient matrix is to be computed rather than a vector influence coefficient matrix, see Eqs. (4.1a and b).

Far-field expansions can also be derived for the potential induced by source and doublet distributions, however, the details are not given here. It should be noted though that in the far-field expansion of the potential due to a source distribution use has to be made of the circumstance that the total source strength used in the simulation of the flow about a configuration is zero or a quantity of smaller order of magnitude.

In summary we get for the consistent evaluation of the integral representation of the velocity potential induced by source and doublet distributions to second- and third-order accuracy:

	To 2nd order	To 3rd order
Panel geometry	$\vec{x}_s, \vec{x}_t, \vec{x}_o$	$\vec{x}_s, \vec{x}_t, \vec{x}_o, \vec{x}_s^*, \vec{x}_t^*$
Source distribution	q^*	q^*, q_s^*, q_t^*
Doublet distribution	μ^*, μ_s^*, μ_t^*	$(\mu^*), \mu_s^*, \mu_t^*, \mu_{st}^*, \mu_s^{**}, \mu_t^{**}$

so that upon differentiation of φ one gets the velocity up to first and second order accuracy, respectively.

Some of the second-generation panel methods employ the Dirichlet condition in a so-called low-order formulation in which the doublet distribution is panelwise constant and the source distribution, if used, is also panelwise constant. Within the framework of the small-curvature expansion this implies that for the velocity potential only the leading term stemming from the contribution of μ^* is retained, so that formally the method would be $O(1)$ in the velocity potential and $O(1)$ in the velocity itself. However, it appears that upon evaluating the tangential velocity at the surface ($-n_x(\vec{x}_m) - \vec{v}_m$), employing a higher-order representation for μ to evaluate \vec{v}_m , in most cases results in a pressure distribution which is accurate as the one obtained from a first-generation panel method employing the Neumann boundary condition.

4.5 Influence coefficients for supersonic flow

The small-curvature and far-field expansions for compressible subsonic or compressible supersonic flow follow lines analogous to the ones given for incompressible flow in the preceding sections.

For subsonic flow the analytical evaluation of the resulting integrals provides no real difficulty compared with the evaluation of their incompressible counterparts. For supersonic flow matters are much more complex because now the panelwise integration is over that part of the panel which lies within the intersection of the panel with the forward Mach cone from x_o (see Fig. 2.6), while also care must be taken that the finite-part of the integral is extracted, see section 2.9. Here we consider the small-curvature near-field approximation first.

It turns out, see Refs. 8 and 9, that the following procedure is the one that leads to the desired closed-form expressions with the least effort:

- (i) Start from the closed-form expressions for the case of subsonic compressible flow, where $B = (1-M)^{1/2}$ and $B' = 1-M$, i.e. the expressions similar to the ones derived in sections 4.2 and 4.4 for the velocity and the potential, respectively;
- (ii) Replace the factor $1/4\pi$ by $1/2\pi$, which accounts for the circumstance that in supersonic flow all the influence of the singularity distribution is exercised in downstream direction only, i.e. in the aft Mach cone;
- (iii) Replace B by $i|1-M|^{1/2}$ and B' by $-i|1-M|$ everywhere in the closed-form expressions, where $i = (-1)^{1/2}$. The expressions are now

- complex-valued expressions rather than the real-valued ones we had for subsonic flow;
- (iv) Extract the real part of all the expressions. The result is the wanted finite-part of the influence exerted by the singularity distributions in supersonic flow. It should be noted that in extracting the real part the four basic transcendental functions (one square root, one arctangent and two logarithms) convert from one to the other, all such that the proper influence in the domain of influence of the singularity distribution on the panel is obtained.

From the above it will be clear that the closed-form expressions for the influence coefficients in supersonic flow are much more complicated than the ones for subsonic flow. In the coding of these expressions a rather complex logical structure is required of conditional branches, see Ref. 9, to account for the appropriate behaviour in different regions in the supersonic flow field.

As far as the far-field expansion is concerned it is remarked that the domain where the far-field expressions may be applied is situated within the aft Mach cone with the apex at some point downstream of the trailing edge of the panel. On the other hand it can be remarked that in most of the space around a panel the influence is zero, and the need for a far-field expansion for $M \gg 1$ is less urgently required than for subsonic free-stream Mach numbers.

For the case of supersonic flow much computer time can be saved by determining whether or not a complete part, segment, strip or ring of panels is located within the domain of dependence of the point where the potential or velocity is computed. If the part, etc. is not within the forward Mach cone from the point considered the AIC's can be set equal to zero directly, rather than that the program computes zeros on a panel-by-panel basis.

4.6 Numerical schemes and stability

In most aerodynamic panel methods the integral equations are solved using the collocation method, i.e. the integral equation is satisfied at just one point per panel. Compared to for instance a Galerkin method, which involves an additional integration over the surface, collocation is less expensive, but collocation may be more sensitive to the specific discretization chosen.

In most panel methods the panel midpoint or centroid is chosen as the collocation point. This leads to the simplest expressions in the far-field expansion, see Eq. (4.8). With this choice problems are also avoided with (nearly) cancelling weakly singular contributions associated with discontinuities across panel edges in the geometry and in the singularity distributions and their derivatives.

4.6.1 Numerical schemes

In the foregoing the contribution of the velocity or the potential due to the singularity distribution on a panel was expressed in terms of quantities at the panel expansion point, e.g. q^x , q^y , q^z . The next choice to be made concerns the numerical scheme to express these quantities in terms of the parameter values to be solved for. Therefore the quantities at the panel expansion point have to be expressed in terms of the parameters Q_i and D_i appearing in Eqs. (4.1a and b). For example, one could express q^x on panel (i,j) as

$$q_x(s_i, t_j) = a_1 Q_{i-1,j} + a_2 Q_{ij} + a_3 Q_{i+1,j} \quad (4.10)$$

where the Q_{ij} 's are the parameters in the representations for $q(s, t)$ on panel (i,j), in some way arranged within the array of parameters Q_i , $i=1(NQ)$ appearing in Eqs. (4.1a and b). The coefficients a_1 , a_2 , a_3 in Eq. (4.10) depend on the type of local representation chosen for. In a similar fashion q^y , q^z , \bar{u}_x , \bar{u}_y , \bar{u}_z , μ_x , μ_y and μ_z are expressed in terms of the parameters Q_i and D_i .

The geometric quantities x^x , x^y , x^z , x^x , x^y and x^z follow from the given description of the geometry of the configuration (and the user-specified wake vortex sheet). Only in case the wake vortex sheet is fully relaxed is it necessary to choose also a numerical scheme for expressing x^x , etc. in terms of a set of geometric parameters, say G_i , $i=1(NG)$.

With the choice of the numerical schemes it is now possible to write the result of the small-curvature expansion and the far-field expansion in terms of Eqs. (4.1a and b). The integral equation from the Neumann condition, Eq. (3.1), then yields using Eq. (4.1b), the following system of linear equations:

$$\sum_{i=1}^{ND} c_{ki} \cdot \bar{n}(\tilde{x}_k) Q_i + \sum_{i=1}^{ND} d_{ki} \cdot \bar{n}(\tilde{x}_k) D_i = v_n(\tilde{x}_k) \bar{U}_n \cdot \bar{n}(\tilde{x}_k) \quad (4.11)$$

where $k=1(NQ)$, while \tilde{x}_k , $k=1(NP)$ denotes the location of the NP collocation points, in principle one per panel. In almost all panel methods the number of unknown source parameters NQ equals the number of panels NP . Eq. (4.11) is to be supplemented by as many (i.e. ND) Kutta conditions (see section 3.5) as there are unknown doublet distribution parameters D_i used to describe the mode-function type of doublet distribution. The ND Kutta conditions result in ND linear equations in case Eq. (3.12) is imposed, or in ND mildly non-linear equations in case the pressure across the trailing-edge point is equated, i.e. $C_p(x=x_{c,e}) - C_p(x=x_{c,s})$.

In a similar fashion it follows from the Dirichlet condition, Eq. (3.3), using Eq. (4.1a), that:

$$\sum_{i=1}^{ND} b_{ki} D_i + \sum_{i=1}^{NQ} a_{ki} Q_i = \sum_{i=1}^{NQ} a_{ki} Q_i \quad (4.12)$$

for $k=1(ND)$, where a_{ki} and b_{ki} are evaluated at the collocation points \tilde{x}_k , $k=1(ND)$. The right-hand side in Eq. (4.12) and specific the source parameters Q_i , $i=1(NQ)$ are found from Eq. (3.2c) which specifies the source distribution q in terms of the outflow v_n and the free stream onset flow \bar{U}_n , i.e. $q = B^2(n, \bar{v}) (v_n - \bar{U}_n \cdot \bar{n})$.

The second term on the left-hand side of Eq. (4.12) stems from the contribution in the source distribution due to the doublet distribution, see Eq. (3.2c). The source parameters Q_i , $i=1(NQ)$ are through $q = B^2(n, \bar{v})$ expressed in terms of the unknown doublet parameters D_i , $i=1(ND)$, using expression like Eq. (4.10) to relate mid-point quantities to doublet parameters.

Application of the Dirichlet condition on the total potential, which leads to the integral equation given in Eq. (3.6) with the source distribution given in terms of the outflow and the gradient of the doublet distribution, see Eq. (3.5c), leads to:

$$\sum_{i=1}^{ND} b_{ki} D_i + \sum_{i=1}^{NQ} a_{ki} Q_i = \sum_{i=1}^{NQ} a_{ki} Q_i \cdot \bar{U}_n \cdot \bar{x}_k \quad (4.13)$$

for $k=1(1)ND$, Q_i^* in Eq. (4.13) follows from the known source distribution $q = \bar{B}_m^T(\bar{m}, \bar{\nu}_m)$, while now the second term on the right accounts for the free-stream onset flow, Q_0^* which follows again from the source distribution $q = -\bar{B}_m^T(\bar{m}, \bar{\nu}_m)$, is subsequently expressed in terms of the unknown doublet parameters D_i , $i=1(1)ND$:

On lifting surfaces the integral equation for the doublet distribution, Eq. (3.10d), results with Eq. (4.1b), into

$$\begin{aligned} ND \sum_{i=1}^{NO} \bar{c}_{ki} \cdot \bar{n}^T(\bar{x}_k) D_i + \sum_{i=1}^{NO} \bar{c}_{ki} \cdot \bar{n}^T(\bar{x}_k) Q_i^* &= \\ - \sum_{i=1}^{NO} \bar{c}_{ki} \cdot \bar{n}^T(\bar{x}_k) Q_i^* & \\ + \frac{1}{2} \bar{n}^T \cdot \bar{v}_n^f + \bar{U}_m \cdot \frac{1}{2} (\bar{T}^u + \bar{T}^d) \bar{x}^T(\bar{x}_k) & \\ - \bar{U}_m \cdot \bar{n}^T(\bar{x}_k) & \quad (4.14) \end{aligned}$$

for $k=1(1)ND$ and with \bar{x}_k denoting the collocation points on the lifting surfaces. In Eq. (4.14) Q_i^* follows from the known part of the expression in Eq. (3.10b), while Q_0^* is the same as described above.

For the boundary conditions on the wake, Eqs. (3.11b and d), it follows using Eq. (4.1a), that:

$$ND \sum_{i=1}^{NO} \bar{c}_{ki} \cdot \bar{n}^T(\bar{x}_k) D_i + \sum_{i=1}^{NO} \bar{c}_{ki} \cdot \bar{n}^T(\bar{x}_k) Q_i^* = - \bar{U}_m \cdot \bar{n}^T(\bar{x}_k) \quad (4.15a)$$

and

$$ND \sum_{i=1}^{NO} \bar{c}_{ki} \cdot \bar{\nu}_m(\bar{x}_k) D_i + \sum_{i=1}^{NO} \bar{c}_{ki} \cdot \bar{\nu}_m(\bar{x}_k) Q_i^* + \bar{U}_m \cdot \bar{\nu}_m(\bar{x}_k) = 0 \quad (4.15b)$$

for $k=1(1)ND$ and with \bar{x}_k , $k=1(1)ND$ denoting the collocation points on the wake vortex sheets. In Eq. (4.15b) $\bar{\nu}_m$ is to be evaluated at the collocation point \bar{x}_k on the vortex sheet, which as before can be expressed in terms of the unknown doublet distribution parameters D_i , $i=1(1)ND$. Note that Eq. (4.15b) is quadratic in terms of the D_i 's, while both Eqs. (4.15a and b) are highly nonlinear in terms of C_i , $i=1(1)NC$, the parameters occurring in the numerical schemes to express x^k , x_k , etc. at the panel midpoints in terms of the unknown geometric parameters.

In above discussion the system of equations has been derived assuming that the configuration consists of merely surfaces where the Neumann, the Dirichlet, the lifting-surface or the wake conditions are applied. The system of equations for a configuration built-up out of a mix of surfaces with Neumann, surfaces with Dirichlet, surfaces with the lifting-surface and surfaces with wake boundary conditions is easily composed from the relations given in Eqs. (4.11) through (4.13). Here we write the resulting system of equations as

$$\sum_{i=1}^{NU} a_{ij} S_j = r_i, \quad \text{for } i=1(1)NU \quad (4.16)$$

where NU is the number of unknown singularity parameters S_j , $j=1(1)NU$ and the a_{ij} 's denote the aerodynamic influence coefficients. The right-hand side r_i , $i=1(1)NU$ of Eq. (4.16) contains the free-stream onset flow, the outflow distribution and the contributions due to the known singularity distributions, all evaluated at the NU collocation

points. For Eq. (4.16) it has been assumed that we are dealing with linear boundary conditions only, i.e. with rigid wake vortex sheets consisting of fixed vortex lines.

Eq. (4.16) can be expressed in the following equivalent form:

$$[A](S) = [r] \quad (4.17)$$

where $[.]$ denotes a $NU \times NU$ matrix and $(.)$ denotes a column vector with NU elements. In Eq. (4.17) the matrix A , the so-called "aerodynamic influence coefficient matrix", depends on known geometric quantities only.

In case of "partial wake relaxation" the doublet distribution on the wake is relaxed and we have to deal with the linear equations resulting from the stream-surface condition on the solid surfaces of the configuration in combination with Eq. (4.15b) which is quadratic in terms of the unknown doublet parameters, i.e. the system of equations is now:

$$[F(S)] = [r] \quad (4.18a)$$

To solve this system of equation some iterative procedure is to be used, usually a Newton-like method. In Newton's method the solution at iteration number $it+1$ is obtained from the solution at iteration number it by solving the following system of linear equations:

$$\left[\frac{\partial F}{\partial S} \right]^{it} (S^{it+1}, S^{it}) = (r) - [F(S^{it})] \quad (4.18b)$$

The matrix on the left-hand side of Eq. (4.18b) is the so-called gradient or Jacobian matrix. It will be clear that for the linear equations contained within Eq. (4.18a) the corresponding elements in the gradient matrix are independent of S and are identical to the ones in the aerodynamic influence coefficient matrix of Eq. (4.17). The quadratic equations in Eq. (4.18a) result in elements that do depend on S and need to be re-calculated at each step of the iteration procedure.

However, at the expense of the rate of convergence of the iteration procedure, one could freeze the Jacobian at its initial value, or restrict it to the linear terms in Eq. (4.15b).

In case of full wake relaxation the doublet distribution and the position of the wake are both relaxed and we have to deal with a system of algebraic equations that is linear or quadratic in S and highly nonlinear in C , the unknown parameters of the local description of the geometry of the wake vortex sheets. So now we have

$$[F(S, C)] = [r] \quad (4.19a)$$

which leads to the following iteration procedure:

$$\begin{aligned} \left[\frac{\partial F}{\partial S} \right]^{it} (S^{it+1}, S^{it}) + \left[\frac{\partial F}{\partial C} \right]^{it} (C^{it+1}, C^{it}) &= \\ - (r) - [F(S^{it}, C^{it})] & \quad (4.19b) \end{aligned}$$

In Eq. (4.19b) the first matrix on the left-hand side contains elements of the aerodynamic influence coefficient matrix, the second one can be termed as the "geometric influence coefficient matrix". The latter represents the response of the boundary conditions to changes in the geometry of the wake vortex sheets. Its computation necessitates taking the derivatives, with respect to the

position vector; of the expressions derived in sections 4.2 through 4.4, the normal vector, etc., a rather laborious task, both from the view point of the panel method developer and from the view point of computational expense. Moreover, because of the nonlinearity with respect to G the evaluation of the right-hand side of Eq. (4.19b) requires the re-computation of the aerodynamic influence coefficients at each iteration, while also the strong nonlinearity in terms of G usually requires regular updating of the Jacobian during the iteration process.

4.6.2 Stability.

In sections 4.2 through 4.4 we discussed consistent approximations that lead to an accurate discretization of the integral equations. In order to get also an accurate solution of the discretized integral equations the panel method formulation chosen should be convergent, i.e., the difference between the solution of the continuous problem and that of the discretized problem should decrease proportional to δ^p for $\delta \rightarrow 0$, where δ is a measure for the average panel size and $p > 0$. It is well-known from numerical analysis that a consistent discretization of a well-posed problem that is stable is also convergent. Stability of a panel method is a property of the system of algebraic equations that results from the discretization of the integral equations. Therefore stability has everything to do with the chosen formulation and with the numerical scheme like Eq. (4.10) used in the discretization, and specifically with the condition number of the matrix involved in solving the system of algebraic (linear or nonlinear) equations.

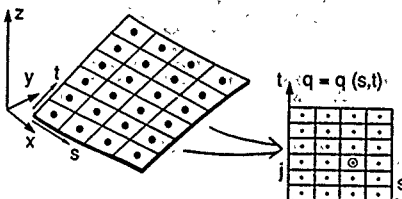
In the present context this means that for the specific choice of the panel collocation point the numerical schemes for the local representations of the unknown functions q , μ and x and their derivatives must be chosen such that the resulting method is stable. Proving stability of candidate numerical schemes for discretizing the integral equations, given in Eqs. (3.1), (3.3), (3.6), (3.6b and c), (3.10d) and (3.11d) for the Neumann, Dirichlet on ψ , Dirichlet on θ , Dirichlet on φ and θ , lifting-surface or wake boundary conditions, is a difficult task. Most investigators base their choice on arguments from what is known about the stability of interpolatory splines, supplemented with numerical experimentation.

The spline-stability arguments are useful because of the observation that commonly the application of the boundary condition at a collocation point is dominated by the function value, first or second derivative of the unknown quantity evaluated at the collocation point. Spline stability refers to the type of data to be described at a certain position to warrant a smooth non-oscillatory polynomial-type of interpolant. In the table below this is indicated for one-dimensional splines of odd and even degree.

Spline degree	Zeroth	First	Second
	derivative to be specified at		
Odd	Node	Midpoint	Node
Even	Midpoint	Node	Midpoint

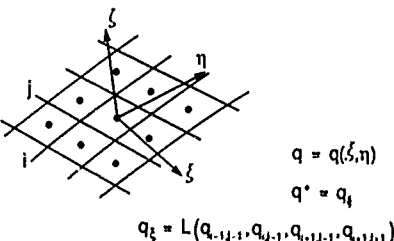
A different choice of the location at which the data is prescribed does not always lead to a complete loss of stability, for instance the conditions at the end of the interval can have a damping effect.

For interpolatory splines in two dimensions, the situation is similar, though in general more complicated. In case the data prescribed involves derivatives:



$$\text{e.g.: } q^* = q_i; q_s^* = (q_{i+1} - q_{i-1})/2\Delta s, \text{ etc.}$$

a) SEGMENT-WISE SURFACE COORDINATES



$$q_\xi = L(q_{i-1,j}, q_{i,j}, q_{i+1,j}, q_{i+1,j+1})$$

b) LOCAL REPRESENTATIONS

Fig. 4.7 Possible numerical schemes

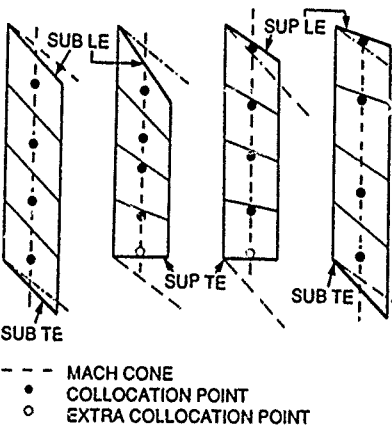


Fig. 4.8 Location of collocation points on a strip of a lifting surface in supersonic flow

For thick configurations with the Neumann boundary condition and with the source distribution as unknown, which resulted in the integral equation of Eq. (3.1), q^* is the dominant contribution. Therefore, a stable scheme is an even-degree scheme based on the function value at panel midpoints as unknown parameters. For a first-order method this is simply a constant source distribution on a flat panel approximation. For methods employing a higher-order representation the precise form of the numerical scheme can take many forms. The scheme may have been derived from finite-difference type of expressions on a segment-wise defined rectangular computational domain involving surface coordinates, or from a least-squares fit of the parameters at immediate neighbouring midpoints in terms of a local Cartesian coordinate system, etc. (see Fig. 4.7). Clearly the efficiency of a higher-order panel method will depend strongly on the compactness of the numerical scheme used.

For thick configurations with the Dirichlet boundary condition and with the doublet distribution as unknown, which resulted in the integral equation of Eq. (3.3), μ^* is the dominant contribution. A stable scheme is here also the even-degree scheme based on mid-point function values.

For lifting surfaces, for which we derived integral equation Eq. (3.10d), the choice of the numerical scheme is less trivial. It turns out that in subsonic flow the leading term of the equation imposed at $\bar{x}(s,t)$ is proportional to the second derivatives of $\bar{\mu}$ at (s,t) , so that for a second-order formulation an even-degree scheme based on mid-point function values will provide stability, which results in a second-order accurate method. Stability for a method of lower degree of accuracy, which employs a linear representation for the doublet distribution, turns out to require a shift of the collocation point to the panel edges, with its own problems related to the singular behaviour of the induced velocity at panel edges.

Apparently here the difference in the type of the underlying integral equation comes to surface. The integral equation for lifting-surfaces being not a Fredholm integral equation of the second kind, making finding a stable discretization more difficult.

The table below summarizes, for subsonic flow, the degree of the local representation for the singularity distributions leading to stable discretizations of first- and second-order panel methods.

Method*	Dominant contribution	ACCURACY	
		1st-order	2nd-order
NEUMANN	q^*	Constant	Quadratic
DIRICHLET	μ^*	Quadratic	Quadratic
LIFTING SURFACE	$\mu_{ss}^*, \mu_{st}^*, \mu_{tt}^*$	Quadratic	Quadratic

* Boundary condition applied at panel midpoint

In supersonic flow the situation is difficult again and the choice of the collocation point depends on whether the panel leading edge is subsonic or supersonic. If the panel leading edge is subsonic the collocation point is at the midpoint, if the panel leading edge is supersonic the collocation point is just downstream of the leading edge (see Fig. 4.8). Furthermore, in case the lifting surface has a supersonic trailing edge

there is no Kutta condition to be applied at the trailing edge (there is no communication between upper and lower side) and an additional collocation point is chosen just upstream of the trailing edge.

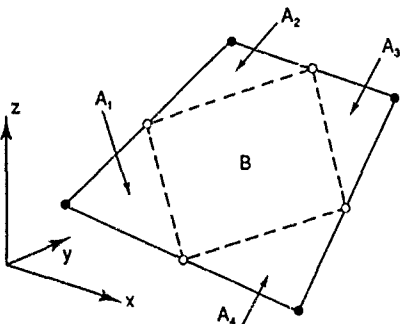
Finding a stable numerical scheme for the two coupled wake boundary conditions used in case the wake vortex sheet is fully relaxed is even more difficult. The first condition, Eq. (3.1b), is very similar to the lifting-surface condition above and is dominated by the second derivatives of μ . The second condition, Eq. (3.1d), is quadratic in μ and involves the first derivative. Both conditions are highly nonlinear in terms of the unknown geometric parameters. Usually some kind of mixed central and directionally biased numerical scheme, found by intuition and numerical experimentation is arrived at.

4.7 Some further aspects of the computational model

In the case of subsonic flow a disturbance decreases in magnitude with increasing distance from its source, specifically a discontinuity (in function value or derivatives) introduced in the numerical model usually does not cause serious problems.

- PANEL-CORNER POINTS

- PANEL-EDGE MIDPOINTS



A, i = 1(1)4: PLANAR TRIANGLES

B: CENTRAL PLANAR QUADRILATERAL

Fig. 4.9 Sub-division of a non-planar panel

In supersonic flow disturbances, due to actual discontinuities but also due to the ones introduced by the discretization, propagate undamped along Mach lines to large distances downstream of where the disturbance originated. This quite seriously hampers the application of low-order methods to complex multi-component aircraft configurations, and a higher-order method is almost obligatory for such configurations. In such higher-order methods the singularity distributions and especially the panelled geometry should be as continuous as possible in order to prevent the occurrence of not-co-sufficient degrees of accuracy cancelling spurious waves from panel edges. In this respect the subdivision of a nonplanar panel into planar sub-panels not only avoids the necessity of some of the higher-order terms due to panel curva-

ture, and twist, (see Eqs. (4.5) and (4.9), but also provides for lower-order methods geometric continuity and less severe spurious waves. An often used example of the subdivision of a quadrilateral panel into planar sub-panels is given in Fig. 4.9. The panel and each of its 5 sub-panels is planar and the sub-panels are contiguous with each other and with the sub-panels of neighbouring panels.

Another even more serious problem constitutes the waves, spurious ones or ones from truly represented breaks in the geometry, that propagate into the interior of the configuration and may give rise to a sequence of spurious internal reflections that eventually destroy the accuracy of the solution. This is illustrated in Fig. 4.10 (Ref. 9) which shows the effect of refining (in axial direction) the paneling on the aft-cone of a cone-cylinder-cone configuration at $M_\infty = 2$ and zero incidence. In the interior of the aft cone the reflecting Mach waves cause the source distribution to oscillate severely, so that actually the "best" answer

In the application of a given panel method the level of the accuracy obtained depends on many factors. Here we mention:

(i) Panel distribution. Depending on the type of the numerical schemes chosen in the local representations, the paneling may be irregular to a smaller or to a larger extent. Most panel methods use interpolating schemes that account for the non-uniformity of the paneling. In that case the paneling should have a basic panel size, say δ_b , in areas where there are no large changes in the geometry and where the singularity distributions are expected to vary smoothly.

In areas where the curvature and/or twist of the surface of the configuration are large the paneling must be refined, see also section 4.2. Also in areas where the singularity distributions are expected to vary rapidly a finer paneling is required. Truly automatic, solution-adaptive, paneling procedures have not yet been described in the literature.

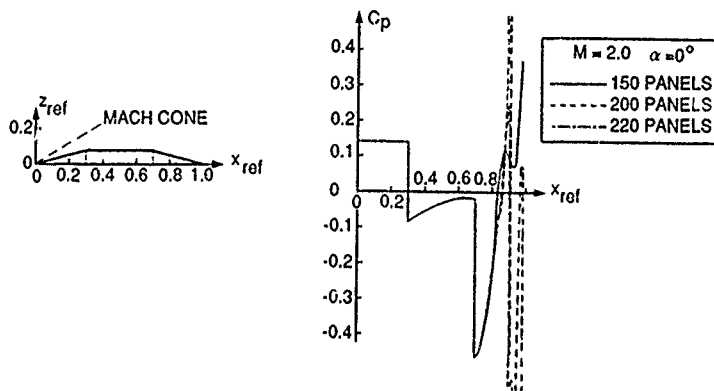


Fig. 4.10 Result of panel method with Neumann boundary conditions for supersonic flow (Ref. 9)

is obtained for the coarsest paneling. In Ref. 26 some of these problems could be alleviated by devising a special composite source-doublet (triplet) singularity distribution with the property that it has a (partially) cancelling interior velocity field. However, for multiple-component configurations spurious reflections are still present. It appears that a higher-order formulation employing the Dirichlet boundary condition, which results in a constant or stagnant flow in the interior of the configuration, is superior in avoiding much of the undesired spurious reflections discussed above.

The computing time for a specific configuration is generally less in supersonic flow than in subsonic flow. This is achieved by considering exclusively the region of dependence of the point at which the influence is computed. If the complete part, segment (or strip) is outside the upstream Mach cone from the point its influence is zero and the individual panel influences do not need to be considered. On the other hand if the panel or a part of the panel is within the domain of dependence some logic is to be executed to compute its influence.

(ii) Type of formulation. It is known that some types of formulation are not suited for specific applications. A well-known one is the application of a method with the Neumann boundary condition to the internal flow in tubes with a curved axis and/or varying cross-section, or a wind tunnel. Here the leakage through the tunnel walls can become rather excessive. A further example provides the flow through a long flow-through nozzle for which some of the first-generation panel methods have shown to produce unacceptable results. A final example is the flow about thin wings where methods employing a mode-function doublet distribution on an internal auxiliary surface and a source distribution on the wing surface may run into problems. These problems are caused by the prescribed shape of the mode function being different from the one that the solution tries to establish. This means that the source distribution has to take over part of the task of the doublet distribution, for example leading to a large value of the source strength on the upper wing surface and an accompanying large negative value of the source strength (i.e. sink) on the lower surface. The gradients associated with this phenomenon will detrimentally affect the accuracy of the solution.

(iii). Free-stream conditions. The truncation error of the method depends on the gradients of the solution. Formally, this means that increasing the incidence would require a finer paneling. However, from a practical as well as from a computational point of view this is not a desired situation and usually a paneling is set up only once and used for all flow conditions.

Apart from the point of view of numerical accuracy it should be kept in mind that the panel method is based on a relatively simple model of the real viscous and compressible flow. There are at flow conditions where viscous effects become of importance; flow conditions for which strong shocks occur; flow conditions near the condition where a wing leading edge becomes sonic, especially in case of blunt leading edges; etc., the correlation between prediction and experimental data may turn out to be unsatisfactory.

4.8 Solution of the system of equations

The solution of the system of linear equations, Eq. (4.17), can be obtained in various ways. Here we mention direct methods (Gaussian elimination, L-U decomposition, etc.) and iterative methods (Jacobi, Gauss-Seidel, etc.) operating on elements of the matrix A or on partitions (blocks) of the matrix A. In the latter case the blocks should be chosen carefully, for example as blocks containing all elements associated with the influence of a strip of the wing, or a ring of the body, on itself. In general the direct methods are more robust and a solution is almost always obtained, also in case of irregular paneling, irregular ordering of neighbouring segments or networks, etc. However, the CPU time required ($\propto N^3$) may become rather excessive on scalar mainframe computers or on workstations. Iterative methods are less computer time intensive ($\propto \text{it} \cdot N^2$), but in some cases the iterative solution procedure may converge slowly or might even diverge.

The rate of convergence depends on the choice of the iterative procedure and more specifically on the way in which the user of the method has arranged the sub-division of the configuration into parts, segments, strips, etc. Failure to converge will require a switching to an alternative procedure or a re-paneling of part or of the complete configuration, this for instance in order to get larger blocks in the iteration matrix. The rate of convergence of an iterative method depends on the diagonal dominance of the matrix A, which on its turn depends on the type of the integral equation that is being solved. It appears that the systems of equations resulting from discretization of Fredholm integral equation of the second kind, Eqs. (4.11), (4.12) and (4.13), give the least problems. The system of equations resulting from discretization of the lifting-surface integral equation, Eq. (4.14), can cause some more problems during execution of an iterative procedure. In the literature on the subject of solving iteratively nearly ill-conditioned systems of equations means are discussed to improve the rate of convergence, but most of these techniques do not apply to the matrix equations typical for panel methods.

For supersonic free-stream Mach numbers it is also noteworthy to remark that, if the paneling is arranged from nose to tail, generally convergence of iterative methods is faster than for subsonic Mach numbers.

Finally, it must be noted that in case, at fixed Mach number, many right-hand side vectors are to be considered the direct method may be preferable

over the iterative one. This since, once the L-U decomposition has been accomplished, each new solution requires just one matrix-vector multiplication, while an iterative method has to start all over again for each new right-hand side.

As far as the implementation on (super)computers is concerned it is remarked that both direct and iterative solvers are vectorizable, but that for large systems of equations the larger number of I/O operations required for the iterative solver may become a bottle-neck.

In the present report the iterative methods used to solve the system of linear and nonlinear equations occurring for configurations with partly or fully relaxed wakes is not described in more detail than given in the preceding section.

As far as the (linear) case without any form of wake relaxation is concerned it should be remarked that in order to obtain a solution for a series of free-stream conditions at fixed Mach number use can be made of the superposition principle. It can be shown that for given outflow, given onset flow due to propeller slipstreams, etc., the solution at any value of the angle of attack α , angle of side slip β , steady rate of roll p , steady rate of pitch q and steady rate of yaw r , can be obtained by combining six basis solutions, denoted here by the column vectors S_i , $i=1(1)6$, namely as:

$$\begin{aligned} S = & S_1(1 + h_1) + (S_2 \cdot S_1)h_2 + (S_3 \cdot S_1)h_3 + \\ & + (S_4 \cdot S_1)(\Delta p \cdot h_1 \tilde{r}_1) + (S_5 \cdot S_1)(\Delta q \cdot h_1 \tilde{q}_1) + \\ & + (S_6 \cdot S_1)(\Delta r \cdot h_1 \tilde{r}_1) \end{aligned} \quad (4.20)$$

where

$$\Delta p = (p - p_1)/(p_2 - p_1); \tilde{r}_1 = p_1/(p_2 - p_1)$$

$$\Delta q = (q - q_1)/(q_2 - q_1); \tilde{q}_1 = q_1/(q_2 - q_1)$$

$$\Delta r = (r - r_1)/(r_2 - r_1); \tilde{r}_1 = r_1/(r_2 - r_1)$$

$$h_1 = (\cos \beta (\sin \beta_2 - \sin \beta_1) / \sin(\beta_2 - \beta_1)) \varepsilon + g$$

$$h_2 = i \cos \beta / \cos \beta_1 \varepsilon$$

$$h_3 = S_1 + (\cos \beta \sin \beta_1 / \sin(\beta_2 - \beta_1)) \varepsilon$$

with

$$f_1 = \sin(\alpha - \alpha_1) / \sin(\alpha_2 - \alpha_1); f_2 = \sin(\alpha_2 - \alpha) / \sin(\alpha_2 - \alpha_1)$$

$$g_1 = \sin(\beta - \beta_1) / \sin(\beta_2 - \beta_1); g_2 = \sin(\beta_2 - \beta) / \sin(\beta_2 - \beta_1)$$

$$f = f_1 + f_2 - 1; g = g_1 + g_2 - 1$$

In Eq. (4.20) the basis solutions S_i , $i=1(1)6$ are solutions at pre-selected combinations of free-stream conditions, namely:

$$\begin{aligned} S_1 &= S(\alpha_1, \beta_1, p_1, q_1, r_1) \\ S_2 &= S(\alpha_2, \beta_1, p_1, q_1, r_1) \\ S_3 &= S(\alpha_1, \beta_2, p_1, q_1, r_1) \\ S_4 &= S(\alpha_1, \beta_1, p_2, q_1, r_1) \\ S_5 &= S(\alpha_1, \beta_1, p_1, q_2, r_1) \\ S_6 &= S(\alpha_1, \beta_1, p_1, q_1, r_2) \end{aligned}$$

In the case of port/starboard-side symmetry $\beta = 0$, $p = 0$ and $q = 0$ and just three basis solutions are required (S_1 , S_2 and S_3). In that case Eq. (4.20) reduces to

$$S = S_1 f_2 + S_2 f_1 + (S_3 \cdot S_1)(\Delta q \cdot \tilde{q}_1 \varepsilon) \quad (4.21)$$

Eq. (4.20) or Eq. (4.21) can also be used to obtain, analytically, the derivatives with respect to α , β , p , q and r of the solution, and therewith of the forces and moments, i.e. stability derivatives like $\partial C_l / \partial \alpha$, $\partial C_l / \partial p$, $\partial C_l / \partial q$, etc. Using above procedure we see that once for a given Mach number, the six (three) solutions have been obtained; all other solutions and their derivatives follow in O(NU) operations.

Further basic solutions can be obtained for e.g.: the mass-flow rate into an inlet characterized by one or more mode-function type parameters; the deflection of control surfaces modeled employing a lifting-surface type of approximation about a mean position of the control surface, i.e. with the paneled control surface at some fixed reference deflection and the boundary conditions on this same surface accounting for the incremental deflection; etc.

4.9 Forces and moments

Once the singularity distributions are solved for, the velocity at the panel collocation points can be computed and therewith also the pressure on the panels. Forces and moments are then determined by integration of the pressure distribution on the surface of the configuration, e.g.:

$$\vec{F} = \iint_S p(\vec{x}) \vec{n}(\vec{x}) dS(\vec{x}) \quad (4.22a)$$

$$\vec{M} = \iint_S p(\vec{x}) (\vec{x} - \vec{x}_{\text{mom}}) \times \vec{n}(\vec{x}) dS(\vec{x}) \quad (4.22b)$$

which have to be made dimensionless by $q_\infty S_{\text{ref}}$ and $q_\infty^2 S_{\text{ref}} L_{\text{ref}}$, respectively. In Eq. (4.22b) \vec{x}_{mom} denotes the moment reference center. The integrals in Eq. (4.22) can be approximated to $O(\delta^2)$ by using the simple mid-point rule, e.g.:

$$\vec{F} = \frac{NP}{i=1} \sum p(\vec{x}_i^*) (\vec{x}_i^* \vec{x}_i^*)_i \Delta s_i \Delta t_i + O(\delta^2) \quad (4.23a)$$

where there are NP panels on the solid geometry of the configuration. The integration in Eq. (4.23) should be over a closed surface. Not accounting for parts of a closed surface corresponds to assuming that $p = 0$ on the left-out part of the surface. In most panel methods the pressure coefficient C_l is integrated rather than the pressure itself, i.e.

$$\vec{F} = - q_\infty \sum_{i=1}^{NP} C_l(\vec{x}_i^*) (\vec{x}_i^* \vec{x}_i^*)_i \Delta s_i \Delta t_i \quad (4.23b)$$

and a similar expression for the moment. Since in case of a closed volume the surface integral of $n(x)$ (and the one of $a x n(x)$) vanishes, Eq. (4.23b) is identical to Eq. (4.23a). If now part of a closed surface is left out in the integration it is equivalent with assuming that $p = p_\infty$ on that part of the surface. For a body with a base this appears to be a good first estimate of the pressure in the separated flow region.

The experience of applying panel methods to configurations with a finite number of panels is that, using above integration procedure, most of the forces and moments can be computed to a sufficient degree of accuracy. However, this is generally not true for the (induced or wave) drag force. It is most obvious in the two-dimensional case where in a potential flow about a closed con-

tour the drag is identically zero, while for instance first-generation panel methods produce non-zero drag coefficients. In three-dimensional flow with lift the panel method should provide a sufficiently accurate estimate of the induced drag and for supersonic flow also of the wave drag.

For the integration of the pressure over lifting surfaces the integral over the leading edge and side edges where the pressure distribution is singular requires special care. For an accurate prediction of the contribution of lifting surfaces in the forces (and especially the induced drag) and the moments the inclusion of these edge-suction forces is crucial.

FAR-FIELD

UPSTREAM S_u

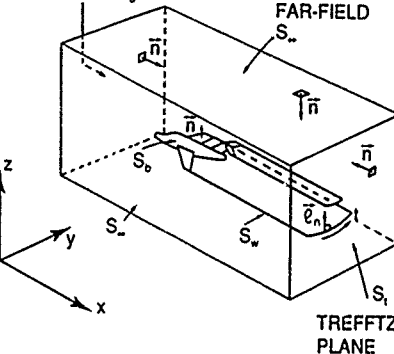


Fig. 4.11 Far-field momentum analysis

Most panel methods have an option to compute the drag from a so-called "far-field" analysis in which the drag on the configuration is obtained from the application of the law of the conservation of linear momentum in a large volume surrounding the configuration in steady flow, see Fig. 4.11. This approach automatically accounts for the edge-suction forces on lifting surfaces. Conservation of momentum applied to the fixed volume enclosed by S_u , S_v , S_b , S_t (the Trefftz plane) and both sides of the wake S_w gives

$$\iint_S (p \vec{n} + \rho (\vec{U} \cdot \vec{n}) \vec{U}) dS(\vec{x}) = 0 \quad (4.24a)$$

where $S = S_u + S_v + S_b + S_w$

with \vec{n} the normal pointing into the volume. From this it follows that the force on the configuration can be expressed as, using that the integration in Eq. (4.24a) is over a closed surface and that mass is conserved:

$$\vec{F} = \iint_S (p \cdot p_\infty) \vec{n} + \lambda (\vec{U} \cdot \vec{n}) (\vec{U} \cdot \vec{U}) dS(\vec{x}) \quad (4.24b)$$

where \vec{F} denotes the force on the body, i.e. is the surface integral of $p \cdot p_\infty$ over S_t .

In case S_u , S_v , and S_t are at an infinite distance from the configuration, one has (in subsonic flow):

$$S_u: \quad p = p_\infty, \vec{u} = \vec{U}_\infty$$

$$S_w: \quad p = p_\infty, \vec{u} = \vec{U}_\infty$$

while to sufficient degree of accuracy

$$S_v^\pm: \quad p^\pm = p_\infty, \vec{u} \cdot \vec{n} = 0$$

$$S_t: \quad \vec{u} = \vec{U}_\infty + \vec{U}_t, \rho = \rho_\infty, \vec{n} = -\vec{\epsilon}_x$$

The latter implies that the wake surface S_w is chosen to be approximately normal to the Trefftz plane S_E . This leads to:

$$\vec{F} = \iint_{S_t} ((p - p_\infty) \vec{\epsilon}_x + \rho_\infty U_\infty \vec{U}_t) dy dz \quad (4.24c)$$

where \vec{U}_t is the velocity induced in the Trefftz plane. Next employing the expression for the quadratic pressure coefficient, Eq. (2.3d), results into

$$\vec{F} = \rho_\infty \iint_{S_t} (\frac{1}{2} |\vec{U}_t|^2 \vec{\epsilon}_x + U_\infty \vec{U}_t) dy dz \quad (4.24d)$$

Upon writing \vec{U}_t in terms of the perturbation potential ψ , which to consistent order of magnitude satisfies Laplace's equation in the Trefftz plane, and using Green's theorem in this plane, one gets

$$\vec{F} = \rho_\infty \iint_{C_w} (\psi(\vec{x}') - \psi(\vec{x})) (\frac{1}{2} (\vec{U}_t \cdot \vec{\epsilon}_n) \vec{\epsilon}_x + U_\infty \vec{\epsilon}_n) dt \quad (4.24e)$$

where C_w is the trace of the wake vortex sheet(s) S_w in the Trefftz plane S_t , $\vec{\epsilon}_n$ the normal and t the arc length along C_w . Eq. (4.24e) is recognized as the classical result of the Trefftz plane, and

ysis, a result which does not depend on the free-stream Mach number directly, only indirectly through the doublet distribution.

It follows from Eq. (2.5f) that the jump in the perturbation velocity potential equals $\mu(t)$, so that:

$$\vec{F} = -\rho_\infty \int_{C_w} \mu(t) (-\frac{1}{2} (\vec{U}_t \cdot \vec{\epsilon}_n) \vec{\epsilon}_x + U_\infty \vec{\epsilon}_n) dt \quad (4.24f)$$

In order to evaluate Eq. (4.24f) one needs the velocity distribution \vec{U}_t induced by the doublet distribution on C_w in the Trefftz plane. This can be obtained by a 2D panel method applied to a system of vortex sheets with given doublet distribution.

It is general experience that obtaining the induced drag from Eq. (4.24f) (the $\vec{\epsilon}_x$ term) yields more accurate results than using Eq. (4.22a) resulting from the direct integration of the pressure distribution.

Still an alternative way to compute the forces and moments acting on the configuration is to "double-integrate" the singularity distribution. Referring to Fig. 3.13 the contribution to the force of a vortex line is found from Blasius' theorem, leading to

$$\vec{F} = \iint_{S_b} (\vec{U}_\infty + \vec{U}^P) x \vec{\epsilon}_y ds + \iint_{S_b} \rho (\vec{U}_\infty + \vec{U}^P) q ds \quad (4.25)$$

which in principle also includes all edge-suction forces, but is expensive computationally. In supersonic flow the situation on S_b is different, due to the circumstance that disturbances are propagated undamped from the configuration. Calculation of the force on the configuration from the conservation of linear momentum is much more elaborate for this case and not considered here.

	Panel	Source	Doublet	B.C.	Remarks
DOUGLAS-NEUMANN [1], 1962/1972	Flat	Const. (external)	Mode function	Neumann	$M_a < 1$
BOEING-TEA230 [2], 1967	Flat	Const.	Mode function (internal)	Neumann	$M_a < 1$ Gohert rule
NLR [6], 1969	Flat	Const.	Mode function (internal)	Neumann	$M_a < 1$ NLR comp rule
HBB [6], 1970	Flat	Const.	Mode function (internal)	Neumann	$M_a < 1$
HUNT-SEMPLE [7], 1976	Flat	Const. (internal, opt.)	Mode function	Neumann	$M_a < 1$
USSAERO [8], 1973	Flat	TB:Const. LS:Linear	- Non-polynomial	Neumann Linearized	$M_a < 1, > 1$
NLAERO [9], 1980	Flat	TB:Const. LS:Linear	- Quadratic	Neumann Linearized	$M_a < 1, > 1$
PAN ATR [10], 1975	Flat Sub-panels	Linear	Quadratic	Neumann/ Dirichlet	$M_a < 1, > 1$
DOUGLAS H O. [11], 1980	Quadratic	Linear (external, quad.)	Mode function	Neumann	$M_a < 1$
ROBERTS [12], 1975	Cubic	Cubic	Mode function (internal, Birnb.)	Neumann	$M_a = 0$
HCAERO [13], 1980	Flat Sub-panels	Linear	Quadratic	Dirichlet	$M_a = 0?$
SAAB [14], 1984	Quadratic	Linear	Quadratic	Dirichlet	$M_a = 0?$
HISSS [15], 1984	Flat Sub-panels	Linear	Quadratic	Dirichlet	$M_a < 1, > 1$
VSAERO [16], 1981	Flat	Const	Const	Dirichlet	$M_a = 0(?)$ Wake relax
QUADPAN [17], 1983	Flat	Const	Const	Dirichlet	$M_a < 1$

BC Boundary Condition

TB Thick Bodies

LS Lifting Surface

Table 1 Partial list of methods presently in use

5.0 EXISTING PANEL METHODS

5.1 Description and some general aspects

At present there are many panel methods in use capable of computing the linearized potential flow about 3D configurations (see for a partial list Table 1). Three categories can be distinguished.

- first-generation methods, Refs. 1-2, 5-9, all with the direct Neumann boundary condition applied and using the flat-panel approximation. Lift is generated through a mode-function doublet distribution on an

auxiliary surface in the interior or on the surface of thick wings, or by lifting surfaces. All these methods are first-order methods.

second-generation methods, Refs. 10-15, all accounting in some way for panel curvature and employing higher-order representations for the singularity distributions. Some methods still use the mode-function formulation, solving for q through the Neumann boundary condition, others employ the Dirichlet boundary condition and solve for μ . A number of such methods are under development, e.g. Ref 16 and at NLR AEROPAN/PDERO. advanced low-order methods, Refs. 16 and 17. These apparently quite successful methods employ the Dirichlet boundary condition on the flat-panel approximation with a constant source (if any) as well as a constant doublet distribution, claiming higher-order accuracy.

Fig. 5.1 shows a comparison (Ref. 27) of results of two first-generation methods (Refs. 5 and 7), with the higher-order (3rd order) method of Roberts (Ref. 12). The case considered is the incompressible flow about the "RAE wing" at 5° incidence for a panel scheme of 12 strips of 60 panels each. The left-hand side of the figure shows the comparison of the x- and the y-component

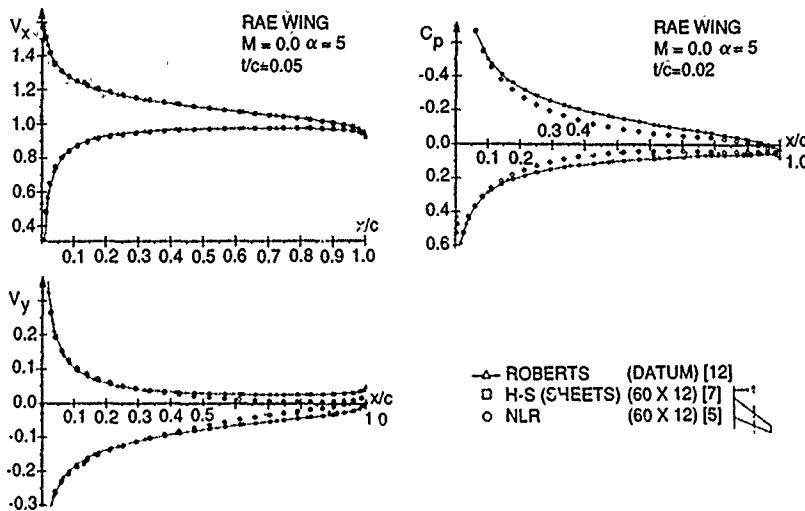


Fig. 5.1 Comparison of first-generation panel methods, Ref. 27

of the chordwise velocity distribution for a wing thickness of 5%. The x-component of the velocity does not differ much for the three methods considered. However, the y-component of the velocity computed by the method of Ref. 5, which employs an internal piecewise constant doublet distribution (equivalent to a vortex lattice, see Eq. (2.6e)), of user-specified shape, shows large deviations from the "datum" solution of Roberts and from the solution of the method of Ref. 7 which employs a more continuous "optimized" internal mode function. For even thinner wings the necessity of the more advanced internal mode function or some other formulation with less severe constraints on the mode-

(3.3), with the apparent inconsistent discretization of a panelwise constant source and constant (instead of linear) doublet distribution on the flat-panel approximation. In order to find the surface velocity, Eq. (3.4b) is to be evaluated. Using at least first-order accurate numerical differentiation to obtain ∇p , as is required for a fully consistent first order method, it is suggested that in spite of this one still finds the surface velocity with $O(h)$ accuracy. For the 2D case Oskam (Ref. 28) investigated the accuracy of a method with the internal Dirichlet condition on the total potential $\phi = 0$ (which leads to $q = 0$ if the flow is incompressible and $v_n = 0$, see Eq. (3.5c)).

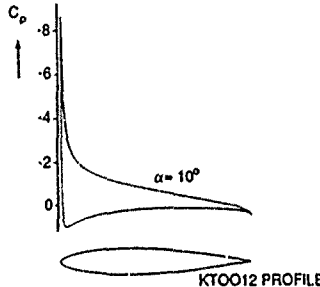
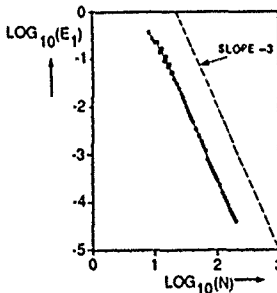


Fig. 5.2 Accuracy of solution for 2D flow using Dirichlet boundary condition and second-order formulation (Ref. 28)



In Eq. (3.6) a quadratic local representation for the doublet distribution and a curved-panel approximation was used, while in Eq. (3.7b) a 4th-order accurate numerical differentiation was employed to evaluate $\bar{V}\mu$. The method was applied to a 12% thick Karman-Trefftz airfoil section. The investigation showed that the resulting method is third-order rather than second-order accurate (Fig. 5.2) as one might have expected from the results of Refs. 16 and 17. This is a puzzling situation and one may wonder what causes this anomaly, is the analysis based on the small-curvature expansion perhaps too conservative, or is there some hidden annihilation of error terms in the process of obtaining μ from Eq. (3.6) and the surface velocity from Eq. (3.7b)? A factor that might have contributed is that the panel scheme used was highly non-uniform and adapted in the nose region where the curvature and the gradient in the solution become large.

5.2 Neumann versus Dirichlet boundary condition

In this section we consider some of the strengths and weaknesses of methods that employ the Neumann boundary condition and methods that employ the Dirichlet boundary condition. The discussion is based on the literature and on experience gained at NLR.

The methods using the Neumann boundary condition solve for the source distribution on the surface of the configuration. Lift is generated through a (mode function) doublet distribution on an artificial surface in the interior of the configuration or on the actual surface of the configuration. Alternatively, lifting components of the configuration are treated as lifting surfaces carrying a doublet distribution to be solved for and a source distribution of known strength which accounts for effects due to the wing thickness. Some positive (+) and negative (-) assets are:

- + The formulation appears to be forgiving for irregular paneling, at least for subsonic flow ($M_\infty < 1$).
- Lift-carry-over through user-specified or automatically generated auxiliary surfaces is subject to some arbitrariness.
- Thin wings may cause problems in case mode-functions are used (Fig. 5.1), the lifting-surface approximation may be inadequate for thick wings as well as for wings with a blunt leading edge.
- Internal flows cannot be modeled because of "leakage".
- Spurious Mach-wave reflections in the interior of the configuration, in case of supersonic flow.

The methods using the Dirichlet boundary condition solve for the doublet distribution on the surface of the configuration. While the source distribution (necessary in the formulation in terms of the perturbation potential ψ) follows from an algebraic relation, for this category of methods the following applies:

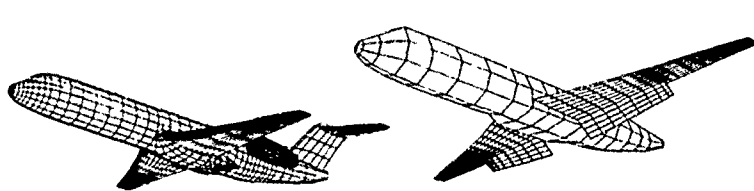
- + Lift-carry-over is implicitly accounted for. However, for a wing/body configuration, the intersection of the wake of lifting components (wings) with non-lifting components (bodies) has to be identified as the edge of a segment across which the doublet distribution is discontinuous (Fig. 3.4).
- + More accurate for the same computing cost, or for the same accuracy less computing cost?
- + Better behaved in supersonic flow.
- + Less storage required.
- More sensitive to irregular paneling and gaps in the geometry.

In view of above points it is quite evident that the methods with the Dirichlet boundary condition are considered to be a definite improvement over the (older) methods with the Neumann boundary condition in which the stream surface condition is imposed in a more direct fashion. However, much expertise in applying the latter methods to practical situations, in which the underlying assumptions are often violated locally, has been built up. This experience does not automatically carry over to the newer methods.

5.3 Lower-order versus higher-order methods

Regarding the matter of choosing (for the development and/or application) a lower-order rather than a higher-order method, several arguments, pro or contra, can be put forward. For a low-order method it can be remarked that a lower-order method:

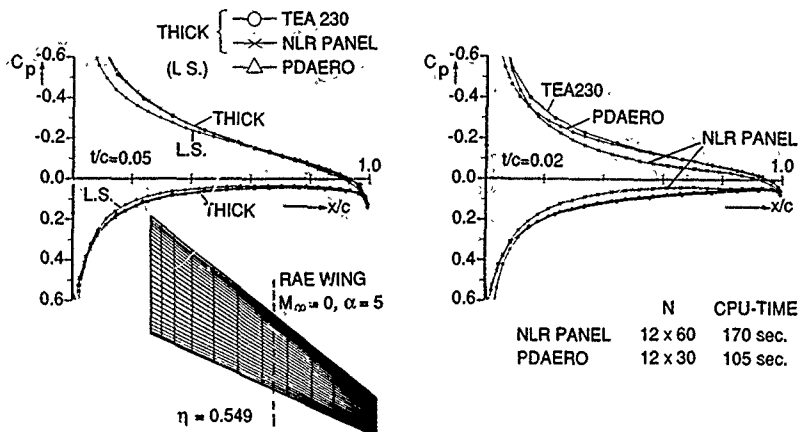
- + is less complex to design, program and maintain. Less information is required to define the geometry and less AIC expressions have to be worked out.
- + has more flexibility because no higher-order continuity is pre-assumed or required, neither in the geometry nor in the singularity distributions.
- can introduce non-physical features in the flow field such as discrete vortices which may give rise to spurious, numerical effects.
- is not suited for supersonic flow unless "triplets" (Ref. 26) or some kind of averaging (see Ref. 29) is introduced.



THICK - WING METHOD

LIFTING - SURFACE METHOD

Fig. 5.3 Type of panel method (Courtesy Fokker Aircraft B.V.)



Similarly, the higher-order methods are

- + possibly more accurate for the panel size tending to zero, i.e., in an asymptotic sense. This does not imply that for a specific (coarse) paneling the solution of the higher-order method is more accurate than the one obtained with the lower-order method using the same paneling.
- + more economic when a fine paneling is required for, for example, a subsequent computation of the boundary layer on (part of) the surface of the configuration or for cases such as close-coupled lifting components.
- + required for supersonic flow ($M > 1$), and for wake relaxation.
- less flexible because more ordering is required in the specification of the geometry.
- computationally more expensive in case continuity of geometry and singularity distributions across segment boundaries is to be enforced explicitly.
- less attractive to develop because a thorough analysis is required to minimize the computational effort.
- time-consuming to code and maintain.
- more difficult to vectorize.

It should be noted here that in many practical situations the panel scheme chosen, because of restrictions in computing budget or computer core memory, is just fine enough to resolve the relevant flow features, so that in these cases there is no advantage in using the higher-order method. However, with computing cost decreasing and core sizes increasing the user will tend to increase the number of panels and the higher-order method will eventually become more economic. It should also be realized that at locations where the solution is (nearly) singularly behaved, as frequently occurs at the edges of lifting surfaces, but also at sharp trailing edges, etc., higher-order accuracy is formally only attained if the singular parts in the solution are extracted and treated explicitly (e.g., Ref. 30). This may be pursued in 2D but is far too complicated to be extended to the general 3D framework.

5.4 What type of panel method to use

The type of panel method to be used depends strongly on the purpose of the application (Fig. 5.3). If the method is to be used during conceptual or preliminary design phases of an aircraft project, in which many possible candidate configurations are studied, there is no need to consider all the flow features in great detail. This means that a method that provides the six-component forces and moments, stability derivatives and spanwise load distributions to within a certain not too demanding level of accuracy will suffice. Also very often in these design phases the designer will look for trends rather than quantitatively accurate data. For this type of application a relatively coarse paneling is allowed which will cut down on computer run time. Also, as demonstrated in Fig. 5.4, it will be allowed to employ the lifting-surface approximation which reduces the computer cost (the number of panels required for the lifting components is halved) even further. It is also possible that for the purpose of some detail study isolated parts of the configuration are considered, e.g., the wing-flap system, utilizing a fine paneling for that part, but neglecting the interference due to other parts of the configuration. This type of considerations may lead to the for application during early design phases desired situation where the "turn-around-time" is such that the method can be used on a workstation or interactively on a mainframe computer. In addition it is required that the geometry can be handled (defined, manipulated, etc.) easily while also pre- and post-processing can be carried out fast. In such an environment the designer can investigate rapidly the effect on the aerodynamic characteristics due to for example changing the position and type of the propulsion system, changes in wing-tail lay-out, flap settings, roll angles (for missiles), etc. As far as the lifting-surface approximation is concerned Fig. 5.4 provides an insight in the accuracy of the predicted pressure distribution. It shows that for both wing thicknesses the thick-wing and the lifting-surface model give comparable results, except near the blunt leading edge where the lift-

ing-surface approximation is invalidated. For $t/c = 0.02$ the result of the NLR panel method deviates from the one of Boeing's TEA-230 as well as from the result of the lifting-surface method. This discrepancy is due to the failure of mode function to represent the doublet distribution correctly in the trailing-edge region, see also Fig. 5.1.

Fig. 5.5 gives an example of the application of a panel method (NLAERO) to an isolated component of a complete configuration. It shows the inlet region of a nacelle, and the comparison of computed and measured pressures along two sections within the inlet region. This is a type of configuration where the flow resembles an internal flow and application of a first-generation panel method employing the Neumann boundary condition resulted in unsatisfactory results. However, applying the internal Dirichlet boundary condition on the perturbation potential resulted in the rather satisfactory correlation of theory and experiment, shown in Fig. 5.5. The paneling of the nacelle is shown in Fig. 6.1.

More detailed investigations, at a later phase in an aircraft project, requiring accurate local characteristics such as pressure distributions, spanwise and axial load distributions, hinge moments, root-bending moment, etc., will ask for a finer and also for the actual wing surfaces to be modeled, or maybe even for wake relaxation. Clearly this requires an accurate, reliable and computationally efficient method.

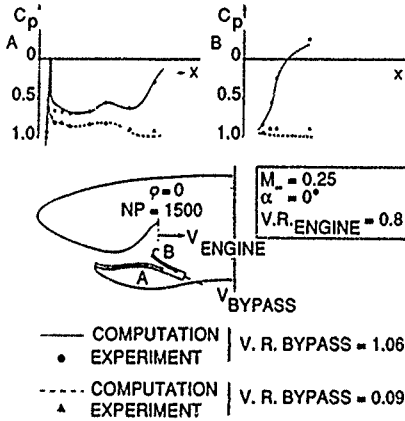


Fig. 5.5 Detail study of the flow into an engine intake

In cases where the configuration operates at both subsonic and supersonic speeds (supersonic transport aircraft, combat aircraft, missiles) it will be advantageous to use a method that applies to both subsonic and supersonic free-stream Mach numbers. The main benefit here will be the saving in manhours to prepare just one input rather than the input for a subsonic flow method and a separate one for a supersonic flow method.

Such an example application of the NLAERO method is given in Fig. 5.6. It shows the lift and drag coefficients as function of angle of attack for two subsonic and for two supersonic Mach numbers, as have been obtained in a single run of the code.

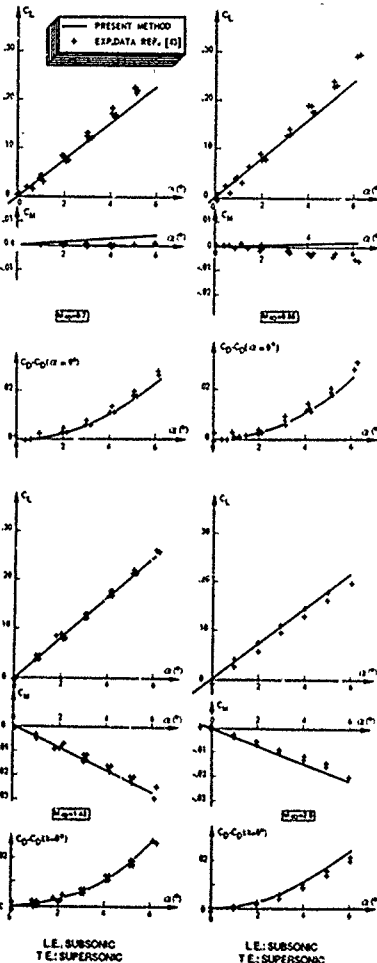
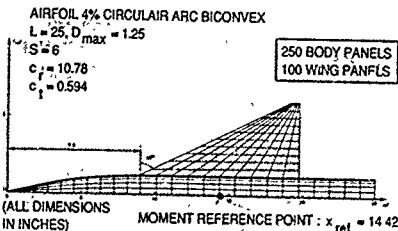


Fig. 5.6 Aerodynamic characteristics wing-body configuration predicted by NLAERO method for sub- and supersonic flow.

Above discussion leads to the conclusion that a general purpose panel method, probably second-order, with several aerodynamic modeling options as Neumann and Dirichlet boundary conditions, thick wings and lifting surfaces, default and user-specified near-wake with and without partial relaxation; inflow and outflow segments; options to model (the effect of) propeller slipstreams and jet plumes, options to account for effects due to boundary layers, option to interface with a boundary-layer method, subsonic and supersonic flow capability, etc., as well as automatic (re)-paneling options is the "aerodynamic tool" that is needed. A prerequisite for such a "building-block" system ("toolbox") is that, in spite of the many options, the computational method remains extendable, maintainable, economic and above all "user-friendly".

Regarding the latter it must be kept in mind that in the application of panel methods the costs involved in the manhours required for preparing the input and analyzing the results of the computation generally far exceed the bare computing costs.

6.0 PANEL METHOD ENVIRONMENT

As sketched in Fig. 6.1 the panel method is embedded between pre- and post-processing. The main task of the pre-processing is the generation of the input for the method, which includes:

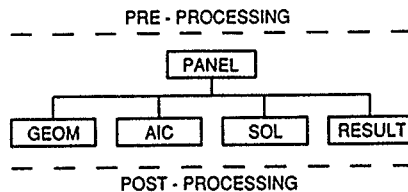


Fig. 6.1 Panel method environment

- definition of the geometry, subdivision into parts and segments, determination of intersections between wings and bodies, etc.
- paneling of the individual segments, or in case the method features automatic paneling features, specification of the panel scheme parameters
- specification of auxiliary, non-configuration surfaces such as near-wake surfaces, inlet faces, lift-carry-over segments, internal surfaces carrying the node-function doublet distribution, etc.
- inspection of the paneled configuration (e.g. Fig. 6.2)
- specification of the normal velocity component v_n , distribution that simulates viscous effects, inlet and outlet flow, etc.
- specification of slipstream data as velocity and total-pressure increment, other user-specified onset flows, etc.
- specification of free-stream direction, Mach number, steady rates of rotation (roll, pitch, yaw), incremental onset free-stream velocity due to motion of some part of the configuration, etc.

The first few items of above list require that the user has access to a geometry package for geometry manipulation. On the other hand, during preliminary design studies parts of the configuration may have a simple shape, e.g. cylindrical fuselage, constant-airfoil-section wing, zero-thickness fins, etc. Some of the panel methods available have an extensive geometry definition capability, facilitating operation of the method in a "stand-alone" fashion.

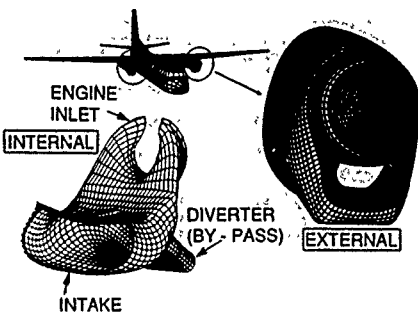


Fig. 6.2 Geometry modeling (Courtesy Fokker Aircraft B.V.)

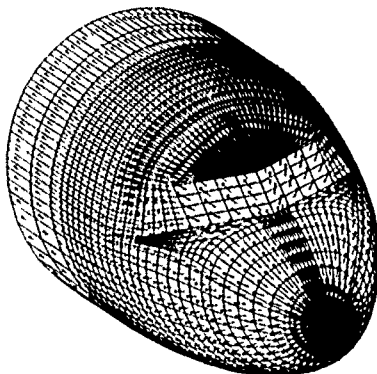


Fig. 6.3 Surface velocity vectors (Courtesy Fokker Aircraft B.V.)

Inspection will involve the visualization of the paneled geometry as a wire frame (Fig. 5.3), with or without "hidden lines", as a "solid model", as a "pin cushion" to check on the direction of the normals, etc. At present workstations with rather sophisticated graphical visualization packages are widely available. Inspection of the paneling of complex configurations using different types of visualization techniques is not a much easier task than during the early days of the application of panel methods, where printer output was the only inspection tool available.

The last couple of items on above list may require the interfacing with other methods like a boundary-layer calculation method, a method for wake relaxation, a method for isolated propeller aerodynamics, etc. As far as the incremental onset free-stream velocity is concerned it can be used to compute, in a quasi-steady approach, the separation of stores from a parent aircraft.

The main task of the post-processing is the digestion of the output of the panel method. It may involve:

- generation and visualization of pressure plots, isobars, surface (Fig. 6.3) and free streamlines/polars of forces and moments for different Mach numbers, etc.
- comparison with data from other calculations or from experiments
- (weak-interaction) boundary-layer computation
- wake relaxation
- archiving of aerodynamic data in a data-base system.

In the practical use of panel methods the rapid and user-friendly visualization of geometry and of flow results on advanced graphical (color) workstations is essential.

Panel methods run on workstations, small to large mainframe computers and on supercomputers. The basic characteristics of any panel method are the following:

- Number of lines of the code. This can run from a few thousand for a vortex-lattice method to more than one hundred thousand for a general-purpose higher-order method. In general the code can be broken down easily along the main lines indicated in Fig. 6.1 and also to deeper levels, facilitating efficient "segmented" or "capsule" loading of the object code.
 - Memory requirements. The memory requirement of panel methods is $aN^2 + O(N)$, where N is the number of unknowns (or panels) and the value of a depends on the method (Neumann or Dirichlet or lifting-surface boundary condition) but varies typically between 3 and 7. This implies that depending on N , out-of-core mass-storage is required. Some panel methods optimize the usage of main memory in order to cut down on I/O to and from disk and thereby on turn-around time. This involves amongst others the block-wise treatment of the AIC matrices.
 - CPU-time requirements. The CPU-time requirements of a panel method can be expressed as
- $$\text{CPU} = a_{\text{alc}} N^2 + (a_{\text{lu}} N^3 \text{ or } a_{\text{lu}} N^2) + O(N) \text{ sec} \quad (6.1)$$

where the coefficients depend very much on the processor speed of the computer and for supercomputers on the degree of vectorization, multi-tasking and/or of parallelization.

In the table below some values of the coefficients appearing in Eq. (6.1) are given.

	a_{alc}	a_{lu}	a_{lt}
Cyber 180-965	$(2-8) \times 10^{-4}$	1.5×10^{-6}	3×10^{-6}
NEC SX-2	$(3-7) \times 10^{-5}$	2.0×10^{-9}	$< 10^{-9}$

The values refer to the CPU requirements of NLR's PDAERO/AEROPAN code and as far as the Cyber is concerned also of the sub/supersonic NLR-AERO code, both applied to a number of test cases. The range of values given refers to different types of runs such as with or without symmetry, Dirichlet, Neu-

mann or lifting surface condition; with or without near wake, etc. The values are quoted for two computer systems, one scalar mainframe (rated at $\sim 2 \times 10^6$ flop/s) and one (one-processor) supercomputer. From these values an indication of required CPU time for any scalar computer can be deduced from the difference in the processor speed in terms of the flop rate. For a supercomputer the values of the coefficients depend very much on the degree of vectorization, multi-tasking, parallelization, etc. so that translation to other computer systems is more difficult.

Note that above table indicates that, for one solution on a scalar computer, the iterative solution procedure requires less computer time than the direct solution procedure for N 's exceeding a value of 2.0 times the number of iterations required, which is almost always the case. For the vector computer this value is even lower. However, in both cases the iterative method will require more I/O operations.

As an example consider a 500-panel case which will require less than 5 minutes CPU time on the 2-megaflop mainframe and less than one hour on a workstation with 1/10 of that processor speed.

Finally it is noted that the higher-order methods PANAIR requires, on a specific type of computer system, substantially more computer time than indicated in the table above, than other second-generation methods or than first-generation methods (see Ref. 31). Also the higher-order panel method HISSS requires relatively much computer time (e.g. Ref. 32). The reasons behind this are not easily assessed, but the elaborate way in which the numerical schemes are set up (like in Fig. 4.7b) might be an important factor.

7.0 OPPORTUNITIES FOR IMPROVEMENT

There are several areas where (existing) panel methods may be improved (see also Ref. 33). Referring to Fig. 6.1, where the various parts of a panel method are indicated, the following items are considered.

GEOM: This part of the program handles the geometric input, in "stand-alone" panel codes it also acts as pre-processor to define and subsequently panel the object considered. In this part of the method an automatic procedure for generating a (curvature- or even solution-)adaptive paneling would result in an increased accuracy of the numerical flow simulation.

AIC: In this part of the program the influence integrals are evaluated. The operational count of this part is $O(N^4)$. In panel methods, that use an iterative solver for the system of equations, this part of the program accounts for most of the total CPU time. Here attention has to be paid to the vectorization of the code, such that it runs efficiently on super-computers. As an example of the speed-up that is obtained on super-computers the table in chapter 6 gives the coefficients in the CPU-time formula, Eq. (6.1), for running the (scalar) NLR AEROPAN/PDAERO panel method on a scalar mainframe computer and on a vector computer.

It shows that even for the unmodified code a substantial speed-up of a factor of 15-20 is realized. Note that because of differences in core memory used (Cyber 962: 1 Mword in a virtual memory environment, SX-2: 16 Mword main memory), part of

the reduction of the CPU time is due to the smaller amount of I/O activity required. It is expected that the CPU-time required for AIC can be reduced further by re-arranging the computation such that a greater part of the code for computing the AIC's vectorizes. (see also Ref. 32). Another area of interest is reduction of the $O(N^2)$ operational count itself, e.g., to $O(N \log N)$, this without sacrificing the accuracy of the solution. Although some studies have been initiated in this area, e.g. Ref. 34, progress has been slow.

SOL: In this part of the program the system of equations is solved, either using an iterative procedure or a direct (LU) decomposition procedure. The direct solution requires $O(N^3)$ operations, but can be vectorized to a large extent, see the table in chapter 6 which shows a speed up by a factor of 750. The iterative solution procedure, mostly block-Jacobi or Gauss-Seidel, requires $O(10N^2)$ operations, with it the number of iterations, but this at the cost of an increase in the number of I/O operations to be carried out with the matrix during the iteration. The main problem with the iterative procedure is that for complex configurations, depending on the paneling, the number of iterations may be excessive or it may occur that the procedure fails to converge. Also for lifting surfaces in subsonic flow (which did not result in a Fredholm integral equation of second kind) the convergence is rather slow (e.g. see Ref. 9). More robust iteration procedures, as conjugate-gradient type of methods, are to be investigated.

For running a panel method on a workstation or lower-end mainframe the availability of an iterative solver remains a must. For a vector computer the CPU time required for the vectorized LU-decomposition remains relatively modest up to higher numbers of panels, but eventually the N^2 count will take over and an iterative solution procedure might be preferable. For the iterative solver one should also take into account the increase in turn-around time due to the increased I/O operations.

RESULT: In this part of the program the velocity and pressure distribution are computed and are used to compute load distributions, forces and moments on the complete configuration and on its individual components, center of pressure, vorticity and pressure at off-body points (e.g. for streamline tracing), etc. Also a file is prepared for use during post-processing.

5.0 FURTHER MODELING ASPECTS AND RECENT AREAS OF INTEREST

There are numerous areas where the panel method technique has been applied successfully. Some areas that have attracted some attention recently are considered below:

5.1 Propulsion installation effects.

The renewed interest in propeller propulsion of transport aircraft has brought along the need to predict the effects of the slipstream on the configuration aerodynamics. During preliminary design studies mostly a simple model is used in

which the flow field due to the propeller in isolation is superimposed on the free stream as an additional onset flow (see Fig. 8.1). The data for the (time-averaged) additional onset flow is obtained from a propeller program based on, for instance, blade-element momentum theory.

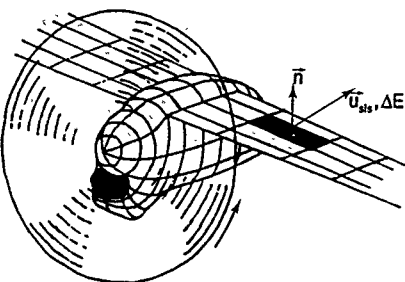


Fig. 8.1 Simple modeling of effect of propeller slipstream on flow about the wing

A panel method can also be used to compute the steady flow about the rotating isolated propeller in a blade-fixed co-rotating coordinate system, e.g. Ref 35. For this case in which the free-stream has to be directed along the propeller axis, one blade of the propeller and a segment of the axially-symmetric hub is discretized into panels. The influence of the other blades is accounted for using multi-lobe axial symmetry. The main difficulty in the model is the wake, which is a helicoidal vortex sheet interacting more strongly with the flow about the propeller blade than is the case in a conventional interaction of a wake with the flow about the wing that generated the wake. In the isolated-propeller method it is assumed that at some distance downstream of the propeller disc the wake is fully rolled up and all vorticity is contained within a cylindrical vortex sheet which forms the far-wake model of the slipstream. On the slipstream far wake the angle between the vortex lines and the axis of the slipstream is constant. From the isolated-propeller solution the additional onset flow in the configuration-fixed coordinate system is obtained from some averaging procedure.

It appears that above simple add-on onset-flow mode, in which it is assumed that the interaction is weak and the slipstream is not affected in the interaction, is not always adequate and an improved modeling is required.

One possible improved model is to approximate the propeller as an actuator disc carrying a doublet distribution of given strength (to be obtained from the time-averaged loading of the propeller blades). Downstream of the propeller a cylindrical vortex sheet, which represents the vorticity within the slipstream, trails from the edge of the actuator disc. Both the actuator disc and the trailing vortex sheet are panelled, the strength of the doublet distribution on the wake vortex sheet is determined from conditions similar to the ones used in the partial relaxation of conventional wakes. In this way at least some mutual interaction of the slipstream and the flow about the configuration is accounted for.

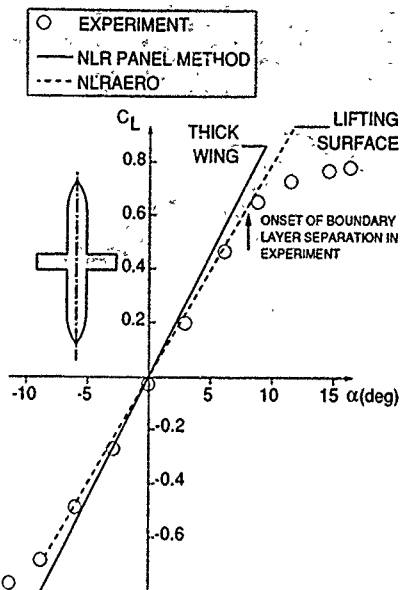


Fig. 8.2 Correlation of computed and measured lift coefficients.

8.2 Viscous effects

8.2.1. **Lifting components.** The most simple way to account for viscous effects, in an engineering fashion, is to neglect the thickness of wings altogether, i.e. consider wings merely as lifting surfaces. In this approach use is made of the general experience that wing thickness effects (which increase lift) are cancelled by viscous effects (which decrease lift through an effective de-cambering of the wing). This will yield a reasonable total lift and spanwise lift distribu-

tion. This is illustrated in Fig. 8.2, which shows the lift coefficient, as a function of angle of attack, for a simple wing-body configuration in incompressible flow. Three results are presented: the measured values; the values following from the NLR panel method which employs the thick-wing modeling and the values from NLR'AERO which employs the lifting-surface approximation. The lifting-surface method gives the best correlation with experimental data.

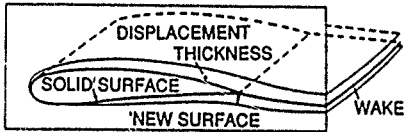
However, the latter method yields a less satisfactory representation of the chordwise pressure distribution.

A next step is to apply, for the lifting components of a configuration relatively simple formulas for the development of the boundary layer on a flat plate employing the computed inviscid velocity or pressure distribution in a stripwise fashion. This will give a first estimate of the skin friction and of the boundary-layer displacement thickness. Subsequently the displacement-thickness can be used to model the effect of the boundary layer on the inviscid flow and specifically on the lift. The latter can be accomplished in either one of two ways (see Fig. 8.3). In the first one a new wing surface is obtained by adding the boundary-layer displacement thickness to the solid wing surface. This approach is not very practical because it would require the definition and subsequent discretization of a new geometry, which is rather elaborate for a general three-dimensional configuration, while it also requires a costly re-computation of the AIC's. In the second, more practical, approach an outflow velocity distribution v_n is computed from the displacement thickness such that the actual surface transpires enough fluid to cause the resulting inviscid flow field to be displaced by the same amount as in the viscous flow. Re-computing the pressure distribution from the solution with specified v_n yields an improved estimate of the pressure distribution, lift, etc. in viscous flow.

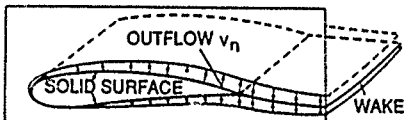
During the detail-aerodynamic design phase a more accurate procedure will be required. Now the pressure distribution re-computed by the panel method can be used to re-calculate the boundary layer on the surface of the configuration, etc. Under cruise conditions the flow will be attached, a weak interaction may be assumed and the hierarchical procedure followed, iterating between the potential flow method and the boundary-layer method, will usually converge.

However, for configurations typical for take-off and landing conditions, which feature pressure distributions with high gradients, a strong inviscid-viscous flow coupling is to be taken into account. Furthermore, for e.g. wing-flap and slat-wing configurations also the viscous wake modeling needs to be considered in more detail. An important item in any coupling of a boundary-layer method with a panel method is that typically the arbitrary-geometry capability is further developed for panel methods than for boundary-layer methods. Moreover, boundary-layer calculations require a much stronger coupling between configuration segments than one is used to in panel methods.

8.2.2 **Body-like components.** As far as accounting for viscous effects on body-like components is concerned it will be clear that in cases, such as wing-body configurations, the simple stripwise flat-plate type of approximation is not valid. Carrying out boundary-layer method calculations for an isolated body at small incidence may be feasible employing a weak-interaction technique.



a) SURFACE DISPLACEMENT (not to scale)
NEW PANELING



b) OUTFLOW FROM SURFACE NO
NEW PANELING

Fig. 8.3 Simulation of boundary-layer effects

However, at higher incidence separation might occur and also for the simple body in isolation strong-interaction type of flow phenomena have to be accounted for.

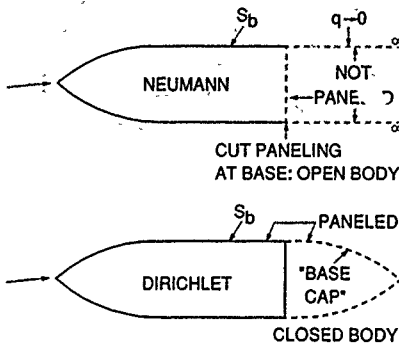


Fig. 8.4 Modeling separation from a body-like component

Within the framework of panel methods strong viscous effects, specifically at the rear end of a body-like component, can be accounted for in an engineering fashion as is shown in Fig. 8.4. In a panel method employing the Neumann boundary condition the body is extended from its base to infinity downstream. At not too high incidence it may be assumed that the resulting source distribution on the fictitious part of the body will be relatively small. This then leads to the model in which the fictitious part of the body is omitted altogether and the base of the body is not

paneled, i.e. the panel method is applied to an open-ended body.

In a panel method that employs the Dirichlet boundary condition the fictitious part of the body has to be included in the model, because the method applies to closed bodies only.

8.3 Wake relaxation.

The classical rigid-wake approximation of straight trailing vortex lines (Fig. 3.8) is totally inadequate for configurations with close-coupled components as wing-flap-tail configurations (take-off and landing) and canard-wing configurations (combat aircraft and missiles at $M_\infty < 1, > 1$). The rigid-wake approximation with a user-specified "near wake" (Fig. 3.9) will improve the modeling only if the vortex lines ($\mu = \text{const.}$) on this part of the wake are to a sufficient degree aligned with the streamlines. A possible partial alleviation of this problem is to fix the shape of the near wake and its paneling but to "relax" the doublet distribution (location of the vortex lines) on the near wake by imposing the $\Delta C_x = 0$ condition, Eq. (3.11d). This latter condition is quadratic in μ , so that an iterative procedure is required, which however does not involve a re-computation of the AIC's, see Eq. (4.15b). Because of the weak non-linearity it is usually not necessary to update the Jacobian in Eq. (4.15b) either, during partial wake relaxation. The shape of the near-wake, still to be specified by the user, might be obtained from a method that solves the non-linear problem in an approximate framework. An example of this is the method which computes, within the framework of the 2D time-dependent analogy and employing a 2D second-order panel method, the roll-up of more or less arbitrarily-structured vortex wakes (Ref. 36). In Fig. 8.5a a typical result of this method is presented, which also serves to demonstrate the complexity of the wake of configurations with deflected flaps.

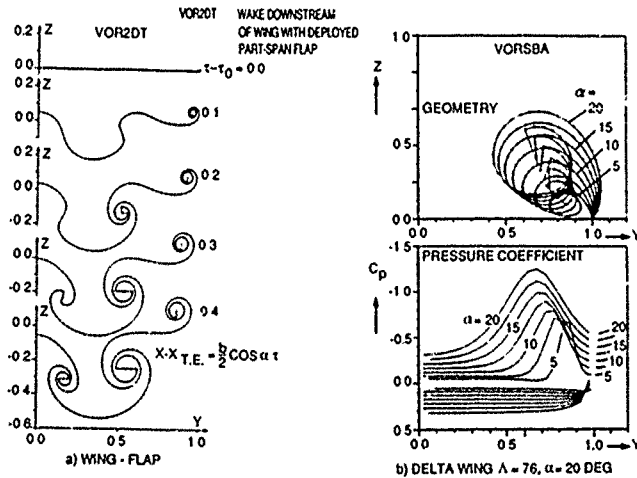


Fig. 8.5 Example of results of panel methods for configurations with free vortex sheets; approximate frame works,
a) time-dependent analogy,
b) slender-body approximation

In cases where the interaction of the wake and the solid geometry is stronger, e.g. separation from flap side edges, wing tips or for slender wings with leading-edge vortex-sheets, the two wake boundary conditions (Eqs. (3.11b) and (3.11d)) have to be solved simultaneously. The fully nonlinear 3D-wake relaxation problem is a tough problem. Here also methods formulated in an approximate framework, as slender-body theory, are used for preliminary studies or, as preprocessor for constructing the initial guess for the method for fully 3D flow. Fig. 8.5b presents the result of such a non-linear second-order panel method (Ref. 37), formulated in the slender-body approximation. Shown is the solution for the flow about a thin delta-wing of unit aspect ratio at a sequence of incidences. Subsequently such a solution is used to construct an initial guess for the method for fully 3D flow, see Fig. 8.6 for a typical result. More results and details of the vortex sheet relaxation methods using (second-order) panel methods are given in Ref. 38.

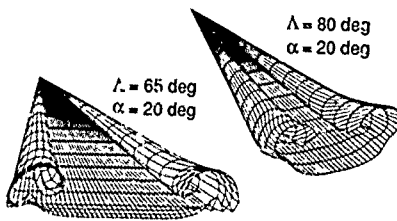


Fig. 8.6 Solution of nonlinear panel method VORSEP for 3D flow about wings with leading-edge vortex separation

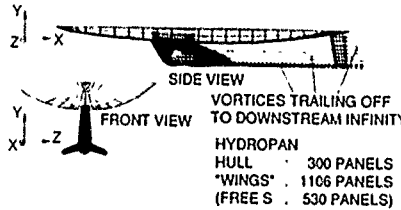


Fig. 8.7 Example of paneling of hydrodynamical application (Ref. 39)

8.4 Free-surface effects.

Panel methods are also applied in hydrodynamics. For the flow about submerged or partly submerged objects the effect due to the free surface may be substantial. At NLR the NLR panel method (Ref. 5) has been extended to hydrodynamic problems by including the free surface (Ref. 39). On the panelized free surface, which is approximated as a rigid surface, the linearized free-surface boundary conditions are applied. From the computed solution the wave resistance is deduced. Fig. 8.7 shows the paneling for the application to a realistic complex keel configuration.

9.0 EXTENSION OF DOMAIN OF APPLICABILITY

The domain of applicability of the panel method for linearized potential flow is limited to sub-critical flow. However, extension of the capability of the panel method approach to flows with regions in which nonlinear compressibility effects cannot be neglected is possible.

In one approach the integral representation for the solution of the Prandtl-Glauert equation, Eq. (2.5e), includes the contribution due to a source distribution σ in the flow field surrounding the object, i.e. the solution of Eq. (2.3a) is now expressed as

$$\varphi(\vec{x}_0) = \varphi_q(\vec{x}_0) + \varphi_\mu(\vec{x}_0) + \varphi_\sigma(\vec{x}_0) \quad (9.1a)$$

where φ_q and φ_μ are defined in Eqs. (2.5b and c) and

$$\varphi_\sigma(\vec{x}_0) = \frac{1}{4\pi} \int_V \int_{\partial V} \sigma(\vec{x}) dV(\vec{x}) \quad (9.1b)$$

In Eq. (9.1b) $V(\vec{x})$ denotes the region(s) with non linear compressibility effects and $\sigma(\vec{x})$ the spatial (field-)source distribution. In the 'field-panel' method the spatial source distribution is found by satisfying the full-potential equation Eq. (2.1a) at the points within $V(\vec{x})$. It has been shown in Ref. 40 that for the 2D (Transonic Small Perturbation) case modeling of super-critical flow with shock waves is possible. In Ref. 41 the 2D field-panel approach was extended to the full-potential equation, Eq. (2.1a), using established techniques of contemporary finite-volume methods for transonic flow.

$64 + 150 + 50 + 50 = 314$ SURFACE PANELS

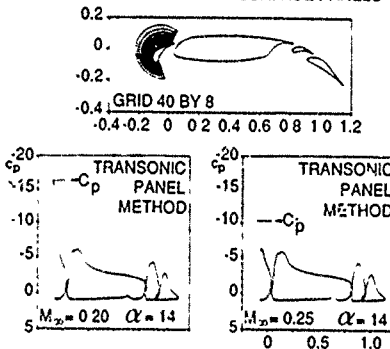


Fig. 9.1 Application of field panel method to 4-component airfoil section (Ref. 41)

Fig. 9.1 shows the result of the application of this method to the flow about a 4-component airfoil section at 14 deg incidence at $M_\infty = 0.2$ and 0.25. It is observed that, as M_∞ increases from 0.2 to 0.25, a small region of super-critical flow, terminated by a shock, develops on the highly loaded slot. This example indicates that for configurations with separate compact regions of non-negligible nonlinear compressibility effects the panel method can be applied with success, without sacrificing the capability of linear

panel methods to treat complex geometries. However, note that the number of field panels increases very rapidly as the extent of the transonic flow region(s) becomes larger.

If the field-panel method is to be applied successfully to 3D configurations the computational costs for evaluating the influence integrals will have to be reduced considerably, by vectorization or preferably by lowering the $O(N^2)$ operational count. Another point worth noting is that ideally the regions with nonlinear flow should have to be detected automatically by the program in some kind of iterative procedure. Ref. 42 describes an application of the field-panel concept to the compressible flow about delta wings with leading-edge-vortex separation, using a nonlinear vortex-lattice method to simulate the linear potential flow

An alternative for the approach using a field source distribution is the zonal (hybrid) type of approach. Here the full-potential equation Eq. (2.1a) is solved in the regions where nonlinear compressibility effects are non-negligible and the Prandtl-Glauert equation elsewhere. The two zones are coupled iteratively through the boundary conditions on the interface between the zones

At Boeing (e.g. Ref. 43) the PAN AIR code is being extended to transonic flow by superimposing onto the arbitrary surface-panel configuration a spatial rectangular grid. The volume integrals on this uniform grid, which is not body-conforming, are evaluated using Fast Fourier Transforms. Some other developments are described by Sinclair (Ref. 44) who reports on the development of a field-panel method for three-dimensional configurations with general geometric capability.

Other investigators (Ref. 28) suggest that there are prospects that the nonlinear compressible flow problem can be formulated in terms of surface integrals only, though the latter have to be re-evaluated in an iterative procedure.

10.0 INVERSE PROBLEM

In the preceding chapters the boundary conditions referred to simulating the flow about a given geometry, i.e. concerned the so-called analysis problem. Subsequently the computed surface pressure distribution was integrated to yield the forces and moments on the configuration. In the design problem the pressure distribution, and therewith the forces and moments, are specified and the geometry of the configuration is sought for solution. Sometimes not the entire geometry is unknown, only some part, e.g. the body geometry is given but the wing geometry is unknown, the geometry is given everywhere except for some part on the upper surface of the wing, the geometry of the wing box is fixed while the nose and the trailing-edge region are to be modified, etc.

In the following some methods used in the design of the geometry of aircraft configurations are discussed. Design methods based on some optimization procedure in which purely an analysis method is used as driver to find for example feasible search directions are not considered. The discussion that is presented here is far from complete, it is meant as a first introduction into the subject of the inverse (panel) methods.

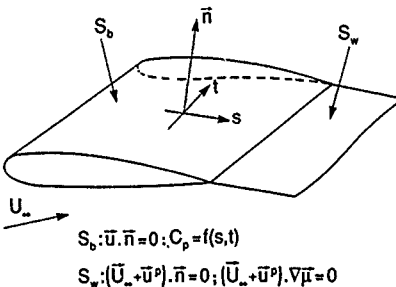


Fig. 10.1 The inverse problem

10.1 Thick wings

The problem can be formulated as follows (see Fig. 10.1). A solution of the Prandtl-Glauert equation (2.3a) is to be found subject to the conditions that the surface is a stream surface, Eq. (2.4a):

$$(\bar{U}_\infty + \bar{U}_p) \cdot \vec{n} = 0 \quad (10.1a)$$

for \vec{x} on S_b , and the condition that

$$C_p(s, t) = f(s, t) \quad (10.1b)$$

also for \vec{x} on S_w . From Eq. (2.1c) it follows that then u , which is now tangential to the surface satisfies:

$$|\dot{u}|^2 / U_\infty^2 = 1 - \frac{2}{(\gamma-1)M_\infty^2} [(1 + \frac{\dot{u}^2}{2})^{1/(\gamma-1)} - 1] \quad (10.1c)$$

where $\dot{u} = \bar{U}_\infty + \bar{U}_p$. Eq. (10.1b) is to be supplemented by some additional conditions such as that the surface is closed; the planform is given, or the position of the trailing edge and the spanwise distribution of the chord length; or some other conditions constraining the geometry. The inverse problem, which can again be expressed in terms of singularity distributions, is a nonlinear problem and resembles the wake relaxation problem. However, the main difference is that now a non-intersecting closed surface is to be found, rather than a single-surface vortex sheet. The general three-dimensional inverse problem is a complex problem with such rather difficult aspects as that the prescribed surface pressure distribution cannot be arbitrary, i.e. it should be such that the resulting flow satisfies some "ecology" rules (stagnation and separation lines), also in connection with the sign of w in Eq. (10.1c). Moreover, the resulting geometry should be closed and should not intersect itself other than at the trailing edge. Apart from aspects of uniqueness, i.e. whether or not an non-intersecting closed surface can be obtained, the resulting geometry should also be acceptable from a structural point of view (wing thickness, trailing-edge angle, leading-edge radius, etc.)

In most cases the design problem has been formulated as a constrained optimization problem in which the new geometry is obtained by minimizing a functional like

$$F = \iint_S (w_p(C_p(\vec{x})) - C_p^t(\vec{x}))^2 + v_g |\vec{x} - \vec{x}^t|^2 ds \quad (10.2)$$

supplemented by certain constraints. In Eq. (10.2) C^* and x^* are the "target" pressure distribution and the "target" geometry from which the geometry should not deviate too much, while v_j and w_j are weighting functions. Solving the problem in this way is generally more successful than solving simultaneously the two coupled nonlinear integral equations resulting from imposing Eqs. (10.1a and c) by a Newton-like iteration procedure.

Inverse panel methods have been developed for two-dimensional flow (e.g. Ref. 45) while also in PANAIR the tangential velocity distribution can be specified as boundary condition.

There are several approaches to solve the inverse problem. One possibility is the following:

- (i) Compute from the specified surface pressure distribution given on the present (initial) iterate of the geometry the velocity potential (a non-trivial task in 3D);
- (ii) Solve the Dirichlet boundary value problem;
- (iii) Compute the velocity component normal to the surface;
- (iv) Compute the geometry correction, taking all kinds of constraints into account;
- (v) Determine the next iterate of the geometry.

These steps are repeated until the geometry correction is sufficiently small. In this approach the condition on the pressure is satisfied at each step, the stream-surface condition is iterated on.

At NLR (Ref. 46) a slightly different approach is followed which can be sketched as follows.

- (i) Define the target pressure distribution, the target and the initial geometry as well as the weight factors;
- (ii) Determine the pressure distribution on the present (initial) iterate of the geometry, employing the NLR panel method (thick wings);
- (iii) Determine the difference between the target pressure distribution and the computed pressure distribution;
- (iv) Solve the inverse lifting surface problem, a linear problem (see section 10.3), to find the correction on the geometry;
- (v) Determine the next iterate of the geometry.

The items (ii)-(v) are revisited until in step (iii) the computed pressure distribution is sufficiently close to the target pressure distribution. So, in this approach the stream-surface condition is satisfied at each step, while the pressure distribution is iterated on.

10.2 Perturbation-analysis method

The method developed at McDonnell (MCAERO) has the possibility to compute for a given base-line geometry not only the solution but also the derivative of the solution with respect to geometric perturbations. This means that if $\Phi_i = \Phi(x_i)$ is the velocity potential at some point x_i on S_b , $i=1(1)NG$, also the three matrices

$$\frac{\partial \Phi}{\partial x_j}, \frac{\partial \Phi}{\partial y_j} \text{ and } \frac{\partial \Phi}{\partial z_j}, \quad i=1(1)NG \quad (10.3a)$$

are computed, all for the solution about the base-line configuration. The solution for a perturbed geometry is then obtained by linear extrapolation, i.e.

$$\Phi(\tilde{x}_i) = \Phi(x_i) + \sum_{j=1}^{NG} (\tilde{x}_j - x_j) \frac{\partial \Phi}{\partial x_j} \quad (10.3b)$$

for $i=1(1)NU$, where \tilde{x}_i , $i=1(1)NU$ denotes the location of points on the new geometry. Although this requires the computation of three additional matrices, solutions for (partly) perturbed aircraft configurations are readily obtained (no matrix equation to be solved), allowing extensive studies of for example different wing thickness and/or camber distributions, flap settings, etc. Also the effects of aircraft structural flexibility can be investigated rapidly. However, to what order of accuracy the stream-surface condition is satisfied on the perturbed configurations is not so clear.

The above perturbation analysis has been extended to the design problem. In this case the derivative of the pressure coefficient at x_i with respect to all perturbations has to be determined (like in Eq. (4.19b)), e.g.

$$\frac{\partial C_p}{\partial z_j} = \sum_{k=1}^{NS} \frac{\partial C_p}{\partial x_k} \frac{\partial x_k}{\partial z_j} \quad (10.4a)$$

where Φ_k , $k=1(1)NS$ are the Φ 's within the "stencil" (domain of dependence) of C_p at a given point on the base-line geometry. Now the pressure coefficient on a perturbed geometry becomes

$$C_p(x_i, y_i, z_i + \Delta z_i) = C_p(\tilde{x}_i) + \sum_{j=1}^{NU} \Delta z_j \frac{\partial}{\partial z_j} (C_p(\tilde{x}_i)) \quad (10.4b)$$

for $i=1(1)NU$. The perturbation Δz_i is determined from a least-squares minimization of the differences between the target pressure distribution and $C_p(x_i + \Delta z_i, z_i)$ given in Eq. (10.4b).

With the Δz_i , $i=1(1)NU$, found the pressure coefficient can be updated using Eq. (10.4b), etc. This procedure appears to work rather well for wings as well as for wing-body configurations, surprisingly also in case the deviations of the final geometry from the base-line geometry is no longer small. Constraints mostly used are that the trailing edge is fixed in space and perturbations are allowed in vertical direction only, while again it is not clear to what order of accuracy the stream-surface condition is satisfied on the designed configuration.

10.3 Lifting surfaces

As already mentioned, it is a possibility to consider the inverse problem in the framework of the lifting-surface approximation. It follows from Eq. (2.6f), see also Fig. 2.3, that across the lifting-surface (assuming incompressible flow)

$$U^T = \bar{U}(x^T) = \bar{U}(x^R) - qn^T \cdot \bar{v}_\mu \quad (10.5a)$$

with x^T denoting a point on the upper (+) and lower (-) side of the wing reference surface S_r . From the expression for the linear pressure coefficient, Eq. (2.3c), it follows then from the difference in pressure across the lifting surface:

$$\begin{aligned} \Delta C_p &= C_p(x^R) - C_p(x^T) = -2\bar{U}_u \Delta U^T / U^2 \\ &= -2\bar{U}_u \bar{v}_\mu / U^2 + O(\epsilon^2) \end{aligned} \quad (10.5b)$$

from which, for given geometry of S_r , the doublet distribution μ on S_r can be determined. From the average of the pressure on the upper and lower wing reference surface one obtains from the expression for the linear pressure coefficient, the following integral equation for the source distri-

bution on the given wing reference surface:

$$\begin{aligned} \bar{U}_w \int \int q \bar{k}_q ds - \bar{U}_w \int \int (-\bar{f} f(\bar{x}^T \bar{x}) \bar{\mu}) \bar{x}_\mu ds - \int \int \bar{\mu} \bar{v} \bar{x} d\bar{s} \\ = \frac{1}{4} U_w^2 (C_p(\bar{x}^{Tr}) + C_p(\bar{x}^{Tr})) \quad (10.5c) \end{aligned}$$

This is an integral equation resembling a Fredholm integral equation of the first kind and choosing a stable numerical scheme to express q and its derivatives at the panel expansion point in terms of a set of source parameters to be solved for is a non-trivial matter. In order to automatically satisfy the condition that the total source strength must be zero, it is advantageous to define the source distribution in terms of the gradient of a source-doublet (doublet with its axis tangential to the surface) distribution.

Once the source distribution and the doublet distribution on the wing reference surface have been determined the wing-thickness distribution follows from Eq. (3.10b), again for given wing reference surface. Finally the wing-camber surface distribution follows from Eq. (3.10d).

In above sketch of the inverse lifting-surface problem we just considered the lifting surface with unknown thickness distribution and left out the presence of any other components of the configuration. Adding these fixed geometry components in the formulation provides no real difficulty other than that now part of the matrix-equation to be solved stems from the inverse lifting-surface integral equation, Eq. (10.5c), rather than from the direct lifting-surface integral equation, Eq. (3.10d).

The lifting-surface formulation can also be used in a "partial design" option. In such an option an incremental camber is defined by for example allowing the NA airfoil sections in a segment to rotate about a given axis by a yet unknown angle C_j , $j=1(1)NA$, but still imposing the boundary condition on the fixed wing reference surface. This implies that there are NA parameters in the right-hand side of the lifting-surface integral equation, Eq. (3.10d), or its discretized form Eq. (4.14). This leads to NA basis solutions, i.e.

$$S_i = \sum_{j=1}^{NA} C_j S_{ij}, \quad \text{for } i=1(1)NU \quad (10.6)$$

where S_{ij} is the solution for the singularity parameter for which the j -th airfoil section is set at a unit incremental incidence while all the other C_j 's are set equal to zero. The NA degrees of freedom can for instance be used to prescribe the spanwise lift distribution, thus in presence of the fuselage and other fixed-geometry parts of the configuration. A further example of utilizing the linearized boundary conditions is to have control-surface deflections, and possibly also engine-inlet flow parameters or propeller-disc load parameters, as degrees of freedom to accomplish trimmed-flight conditions.

11.0 CONCLUDING REMARKS

- Panel methods are important aerodynamic tools with powerful and flexible modeling capabilities, which are used heavily in aircraft design projects. The application of the panel method is

shifting from the detailed aerodynamic design phases to the preliminary design phases.

- The extension of panel methods into the transonic flow regime and the improved handling of wakes of closely-coupled components will have a direct implication on the extension of the domain of applicability of the panel method.
- There exist possibilities for improving the computational efficiency of the panel method by: .vectorization and/or parallelization on supercomputers .reduction of operational count for the evaluation of influence integrals .new formulations and improved numerics .better, more robust (and faster) iterative procedures for solving large, non-sparse systems of equations which will lead to a further utilization of panel methods.
- Pre- and post-processing, are an essential part of the "panel-method environment".
- At all times during the application of panel methods it should be realized that panel methods are modeling the real flow under a great number of assumptions.

12.0 REFERENCES

1. Hess, J.L., Smith, A.M.O.: Calculation of Non-Lifting Potential Flow about Arbitrary Three-dimensional Bodies", Douglas Aircraft Report No. E.S. 40622 (1962), J. of Ship Res. 1, No. 2, pp. 22-44 (1964)
2. Rubbert, P.E., Saaris, G.R.: A General Three-dimensional Potential Flow Method Applied to V/STOL Aerodynamics. SAE Paper 68004 (1968).
3. Prager, W.: Die Druckverteilung an Körpern in einer Potentialströmung. Physik. Zeitschr., pp. 865-869 (1928).
4. Hartmann, E.: Die Berechnung der Druckverteilung an dicken Gitterprofilen mit Hilfe von Fredholmschen Integralgleichungen zweiter Art. Mitt. Max-Planck-Inst. Strömungs-Forschung No. 23 (1959).
5. Labruere, Th. E., Loewe, W., Slooff, J. W.: An Approximate Method for the Calculation of the Pressure Distribution on Wing-Body Combinations. AGARD CP-71 (1970).
6. Kraus, W.: Das MBB-UFE Unterschall Panelverfahren. Report MBB-UFE 633-70 (1970).
7. Hunt, B., Sempie, W.G.: The BAC(MAD) Program to Solve the 3-D Lifting Subsonic Neumann Problem using the Plane Panel Method. Report ARG 97 BAC(MAD) (1976).
8. Woodward, F.A.: An Improved Method for the Aerodynamic Analysis of Wing-Body-Tail Configurations in Subsonic or Supersonic Flow. NASA CR-2228 (1973).
9. Hoeijmakers, H.W.M.: A Panel Method for the Determination of the Aerodynamic Characteristics of Complex Configurations in Linearized Subsonic or Supersonic Flow. Report NLR TR 80124 (1980).

10. Carmichael, R.L., Erickson, L.L.: PAN AIR-A Higher Order Panel Method for Predicting Subsonic or Supersonic Linear Potential Flows about Arbitrary Configurations. AIAA Paper 81-1255 (1981).
11. Hess, J.L.: A Higher-Order Panel Method for Three-dimensional Potential Flow, Report MDC J8519 (1979).
12. Roberts, A., Rundle, K.: Computation of Incompressible Flow about Bodies and Thick Wings using the Spline-Mesh System. EAC(GAD) Rep. Aero Ma 19 (1972).
13. Bristow, D.R.: Development of Panel Methods for Subsonic Analysis and Design. NASA CR 3234 (1980). See also NASA CR-3713 (1983).
14. Löstedt, P.: A Three-Dimensional Higher-Order Panel Method for Subsonic Flow Problems - Description and Applications. SAAB-SCANIA Rep. L-0-1 R100 (1984).
15. Fornasier, L.: HISSS - A Higher-Order Subsonic/Supersonic Singularity Method for Calculating Linearized Potential Flow. AIAA Paper 84-1646 (1984).
16. Maskey, B.: Prediction of Subsonic Aerodynamic Characteristics. A Case for Low-Order Panel Methods. Journal of Aircraft, Vol. 19, No. 2, pp. 157-163 (1982).
17. Youngren, H.H., Bouchard, E.E., Coopersmith, R.H., Miranda, L.R.: Comparison of Panel Method Formulations and Its Influence on the Development of QUADPAN, An Advanced Low-Order Method. AIAA Paper 83-1827 (1983).
18. Lé, T.H., Morchoisne, Y., Ryan, J.: Techniques Numériques Nouvelles dans les Méthodes de Singularités pour l'Application à des Configurations Tri-Dimensionnelles Complexes, Paper 6, AGARD-CP-412 (1986).
19. Boppe, G.W., Stern, M.: Simulated Flows for Aircraft with Nacelles, Pylons and Winglets. AIAA Paper 80-130 (1980). See also NASA CR-3242 (1980) and NASA CR-4066 (1987).
20. Steger, J.L.: Technical Evaluation Report AGARD FDP Specialists' Meeting on "Application of Mesh Generation to Complex 3-D Configurations" AGARD-AR-268 (1991).
21. Kellogg, O.D.: Foundations of Potential Theory. Dover (1954).
22. Ward, C.N.: Linearized Theory of Steady High-Speed Flow. Cambridge University Press (1955).
23. Mangler, K.W., Smith, J.H.B.: Behaviour of the Vortex Sheet at the Trailing Edge of a Lifting Wing. RAE TR 69049 (1969).
24. James, R.M.: On the Remarkable Accuracy of the Vortex Lattice Discretization in Thin Wing Theory. Douglas Report DAC 67211 (1969).
25. Hess, J.L.: Consistent Velocity and Potential Expansions for Higher Order Surface Singularity Methods. Report MDC J6911 (1975).
26. Woodward, F.A., Landrum, E.J.: The Supersonic Triplet - A New Aerodynamic Panel Singularity with Directional Properties. AIAA Journal, Vol. 18, No. 2, pp. 138-142 (1980).
27. Sytsma, H.A., Hewitt, B.L., Rubbert, P.E.: A Comparison of Panel Methods for Subsonic Flow Computation. AGARDograph No. 241 (1979).
28. Oskam, B.: Asymptotic Convergence of Higher-Order Accurate Panel Methods. J. of Aircraft, Vol. 23, No. 2, pp. 126-130 (1986).
29. Hunt, B., Hewitt, B.L.: The Indirect Boundary-Integral Formulation for Elliptic, Hyperbolic and Non-Linear Fluid Flows. Ch. 8 of "Development in Boundary Element Methods", Vol. 4, Elsevier Applied Science Publishers (1986).
30. Hoelijmakers, H.W.M.: Aspects of Second- and Third-Order Panel Methods Demonstrated for the Two-dimensional Flat Plate Problem. NLR TR 81074 U (1981).
31. Margason, R.J., Kjelgaard, S.O., Sellers III, W.L., Morris Jr., Ch.E.K., Walkley, K.B., Shields, E.W.: Subsonic Panel Methods. A Comparison of Several Production Codes. AIAA Paper 85-0280 (1985).
32. Fornasier, L., D'Espiney, P.: Prédiction des Dérivées de Stabilité pour les Missiles avec le Code de Singularités "HISSS". La Rech. Aéronaut. - No. 1989-4, pp. 33-47 (1989).
33. Slooff, J.W.: Requirements and Developments Shaping a Next Generation of Integral Methods. Paper IMA Conf. on Num. Meth. Aerom. Fl. Dyn., Reading (1981). NLR MP 81007 U.
34. Schippers, H.: On the Evaluation of Aerodynamic Influence Coefficients. In "Panel Methods in Fluid Mechanics with Emphasis on Aerodynamics", ed. J. Ballmann et al., Notes on Numerical Fluid Mechanics, Vol. 21, Vieweg Verlag, pp. 210-219 (1987).
35. Clark, R.W., Valarezo, W.O.: Subsonic Calculation of Propeller/Wing Interference. AIAA Paper 90-0031 (1990).
36. Hoelijmakers, H.W.M.: An Approximate Method for Computing Inviscid Vortex Wake roll-up. NLR TR 85149 U (1985).
37. Hoelijmakers, H.W.M.: An Approximate Method for Computing the Flow about Slender Configurations with Vortex-Flow Separation. NLR TR 86011 U (1986).
38. Hoelijmakers, H.W.M.: Computational Aerodynamics of Ordered Vortex Flows. NLR TR 88088 U (1989).
39. van Beek, C.M., Piers, W.J., Slooff, J.W.: Boundary Integral Method for the Computation of Potential Flow about Ship Configurations with Lift and Free Surface Effects. NLR TR 85142 U (1985).
40. Piers, W.J., Slooff, J.W.: Calculation of Transonic Flow by Means of a Shock-Capturing Field Panel Method. AIAA Paper 79-1459 (1979).

41. Oskam, B.: Transonic Panel Method for the Full Potential Equation Applied to Multi-component Airfoils. AIAA Journal, Vol. 23, No. 9, pp. 1327-1334 (1985).
42. Kandil, O.A., Yates, E.C.: Transonic Vortex Flow past Delta Wings: Integral Equation Approach. AIAA Journal, Vol. 24, No. 11, pp. 1729-1736 (1986).
43. Ericksson, L.L., Strande, S.M.: A Theoretical Basis for Extending Surface-Paneling Methods to Transonic flow. AIAA Journal, Vol. 23, No. 12 (1985), pp. 1860-1867. See also AIAA Paper 87-0034 (1987).
44. Sinclair, P.M.: A Three-Dimensional Field-Integral Method for the Calculation of Transonic Flow on Complex Configurations - Theory and Preliminary Results. Aeron. J. June/July 1988, pp. 235-241.
45. Labrujère, Th.E.: MAD, a System for Computer Aided Analysis and Design of Multi-Element Airfoils. NLR TR 83136 L (1983).
46. Brandsma, F.J., Fray, J.M.J.: A System for Transonic Wing Design with Geometric Constraints Based on an Inverse Method. AGARD-CP-463, Paper 7 (1989). See also NLR TP 89179.

HIGH ANGLE OF ATTACK - AERODYNAMICS

John E. Lamar
NASA-Langley Research Center
Hampton, VA, 23665-5225, USA

SUMMARY

The ability to predict high angle-of-attack, nonlinear, aerodynamic characteristics of flight vehicles, including aircraft, has made significant progress in the last 25 years, using a variety of computational tools and insightful analyses. The key technological element which has made these analyses possible is the ability to account for the influence of the shed vortical flow, prevalent in this angle-of-attack range, on geometries of interest. Using selected analysis techniques, applications have also been made to wing design in order to improve their high-speed maneuver performance. These include a complete wing obtained by modifying the entire cambered wing, and a wing whose modification were focused on the leading- and trailing-edge flap regions.

Various techniques, associated with different levels of accuracy, exist to model this vortical flow influence. The ones included in this paper cover: suction-analogy with extensions, free-vortex-filaments, free-vortex-sheet modeling, and Euler and Navier-Stokes solutions. Associated relevant features of vortices are also addressed, including: the wing and flow conditions which cause vortex formation, and how the vortex strength varies with angle of attack and wing sweep.

Once this nonlinear vortical flow is present, the stability of the aircraft can change rapidly with increases in angle of attack. These changes need to be known early in the design process since the forces/momenta being generated can be beyond the ability of conventional controls to handle them. Depending on whether the flow is still organized, engineering methods may be able to estimate the aerodynamic effects. In general, when the flow becomes disorganized or asymmetrical and time dependent, the best engineering techniques are experimental. Furthermore, aircraft controllability may need to be found in novel aerodynamic devices or engine-thrust vectoring. This is especially true at angles of attack beyond which the onset of large-scale vortex bursting occurs over the aircraft. Work in this area is highlighted.

LIST OF SYMBOLS

A	aspect ratio of wing	C_{Lz}	longitudinal lift coefficient, $(\partial L/\partial z)/qb$
a	fractional chord location where the chord loading changes from constant value to linear varying value toward zero at trailing edge	C_{L0}	lift coefficient at $\alpha = 0^\circ$
b	span	$C_{L\alpha}$	lift coefficient curve slope
C_A	axial force coefficient, axial force/ qS	C_l	rolling moment coefficient, rolling moment/ qSb
C_D	drag coefficient, drag/ qS	C_d	damping-in-roll parameter, $\partial C_l/\partial(pb/2U)$, per radian
C_L	lift coefficient, lift/ qS	C_{ls}	rolling moment due to sideslip, per deg
		C_m	pitching moment coefficient, pitching moment/ $qS\bar{c}$
		C_{m*}	scaled nonlinear portion of pitching moment coefficient, $C_{m*}/(A \sin \alpha \cos \alpha)$
		C_N	normal force coefficient, normal force/ qS
		C_N^*	scaled normal force coefficient, $C_N^*/(A \sin \alpha \cos \alpha)$
		C_{Nv}^*	scaled nonlinear portion of normal force coefficient, $C_{Nv}^*/(A \sin \alpha \cos \alpha)$
		C_n	yawing moment coefficient, yawing moment/ qSb
		C_{n3}	yawing moment due to sideslip, per deg
		C_p	pressure coefficient, $(p - p_\infty)/q$
		C_S	leading-edge suction force coefficient, suction-force/ qS ; $(1/2)K_{v,4} \sin^2 \alpha$
		C_T	leading-edge thrust coefficient, thrust/ qS
		c_n	section normal force coefficient
		c_R	section profile nose drag coefficient
		c_s	section suction force/ q
		c_t	section thrust coefficient
		c	chord
		\tilde{c}	reference chord
		$\tilde{\epsilon}$	characteristic length in augmented vortex factor
		∞	chord at wing midspan
		ΔC_L	lift contribution from augmented vortex flow
		ΔC_p	lifting pressure coefficient, $C_{p,d} - C_{p,u}$
		$\Delta C_{p,u}$	change in upper surface pressure coefficient from $\alpha = 0^\circ$
		Δx	distance along tip chord to centroid of side-edge vortex lift
		dF_s	differential edge-suction-force
		\hat{e}	unit edge vector
		\hat{F}	force vector
		g	normal acceleration
		I_{XZ}	moments of inertia about the X and Z body axes, respectively
		K	Sychev similarity parameter, $\tan \alpha / \tan \epsilon$, also, thousands of feet altitude, and

	unsteadiness parameter defined by, $\hat{\alpha}_{\max} c_r / (2V)$, $\hat{\alpha}_{\max} (k/\Omega)$	Subscripts.
K_p	potential lift factor	a attainable
$K_{v,le}$	leading-edge-vortex-lift factor	av average
$K_{v,se}$	side-edge-vortex-lift factor	BD break down
$K_{v,ae}$	augmented-vortex-lift factor	c crossflow
k	reduced frequency; $\Omega c_0 / 2V$	cp center of pressure
L/D	lift-to-drag ratio	d design
l	distance along leading edge from apex (see fig. 24); also, inboard distance to vortex core from leading edge, inches (see fig. 41)	dyn dynamic
M, M_∞	free stream Mach number	i design variable index
M_N	component of Mach number normal to wing LE; $M \cos \Lambda (1 + \sin^2 \alpha \tan^2 \Lambda)^{1/2}$	LE, le leading edge
m	$(M^2 - 1)^{1/2} \cot \Lambda$	l lower surface
p	static pressure; also, roll rate, rad/sec	max maximum
q	free stream dynamic pressure	N normal
q_i	i^{th} velocity component in index notation	$onset$ associated with α at which significant vortex shedding begins
R_n	Reynolds number	p potential flow contribution
r	streamwise distance from leading edge to vortex action point, identified with the rotated suction force; also leading-edge radius normal to the edge	r root; also residual
S	wing reference area; also, leading-edge suction	s separation
T	leading-edge thrust	se side edge
t	time; thickness	t tip; also theoretical
U, V	free stream velocity	TE, te trailing edge
V_z	vertical velocity	tot total
u, v	perturbation backwash and sidewash, respectively	u upper surface
w_{net}	sum of induced downwash and $U \alpha$ at $\alpha = 1$ rad	v vortex
X, Y, Z	local body axes system (see fig. 37)	vac vacuum
X_f, Y_f, Z_f	vortex flap coordinate axes centered at the apex of the flap (see fig. 55)	vle vortex flow contribution from the leading edge
X	vector of design variables	vse vortex flow contribution from the side edge
\hat{z}	streamwise distance from the centroid of the area giving augmented vortex lift to the reference point	w wing
x/c	fractional distance along the local chord of the called out surface	zz, yy, zz second partial derivative with respect to x, y, z , respectively
x/c_r	fractional distance along the root chord from the actual or theoretical apex	0 value at $C_L = 0$
x'/c_r	fractional distance from local leading edge in terms of chord at $y = 0$.	1 first order expansion in perturbation quantities
$x_0(t)$	x -coordinate of vortex breakdown	2 second order expansion in perturbation quantities
\hat{x}_v/c_r	fractional distance along the root chord to the center of pressure for the non-linear portion of the normal force	∞ free stream time derivative
$y/(b/2)$	fraction of wing semispan	Greek Symbols
y/s	fraction of local semispan	
y_v^*, z_v^*	scaled lateral and vertical locations of vortex core, respectively, = $y_v/(b/2), z_v/(b/2)$	α angle of attack, deg
z	vertical distance to vortex core above upper surface, inches, also, vertical distance to called out surface	$\alpha_{C_L, \max}$ angle of attack at which $C_{L,\max}$ occurs, deg
z/c	wing camber elevation over local chord	α_l wing incidence on fuselage, deg

$\delta_{LE,s}$	leading-edge flap streamwise deflection, positive LE down (inboard/outboard), deg
δ_r	rudder deflection, deg
$\delta_{TE,s}$	trailing-edge flap streamwise deflection, positive TE down (inboard/outboard), deg
δ_t	tip rake angle, deg
ϵ	wing apex half angle, deg
ζ	surface vorticity vector
η	y/b
Λ	leading-edge sweep angle, deg
λ	wing taper ratio, c_t/c_r ; also, 2nd coefficient of viscosity
μ	Mach cone half angle, $\epsilon \text{ in}^{-1}(1/M)$, deg; also, 1st coefficient of viscosity
ρ	density of fluid
ϕ	perturbation velocity potential
Ω	trailing edge sweep angle, deg; also, circular frequency
ω	oscillation frequency, cycles/sec

Abbreviations:

ADS	Automated Design Synthesis
CFL3D	A thin layer Navier-Stokes code
FLO57GWB	An Euler equation code for generalized wing-bodies
FVS	Free-Vortex-Sheet
LE, TE	Leading Edge, Trailing Edge
LEVF	Leading-Edge Vortex Flap
NF	Normal Force
QVLM	Quasi-Vortex Lattice Method
SA	Suction Analogy
SE	Side Edge
2-D, 3-D	Two-dimensional, three-dimensional
TEAM	Three-dimensional Euler/Navier-Stokes Aerodynamic Method
TLNS	Thin Layer Navier-Stokes
VL	Vortex Lift
VLM-SA	Vortex Lattice Method coupled with Suction Analogy
VORCAM	VORTex CAMbered wings

INTRODUCTION

Since this paper focuses on engineering methods used for high angle-of-attack (α) aerodynamics, it is important to distinguish, first of all, exactly what is meant by high α . To do this, the α range from 0° to 90° will be divided into four segments, the bounds of which are determined by the dominant flow present, as shown in figure 1. These α segments are low, where attached flow dominates, moderate, where there is a combination of attached and separated or vortical flow present, high, where separated or vortical flow dominates, and higher, where the flow becomes less well structured due to vortex breakdown (bursting) or massive stall. The beginning and ending α 's for a particular segment are dependent on the Mach number and the aircraft geometry which generates the neighboring flow-field. For conventional round-edged unswept or swept

wing configurations; as used primarily in the general-aviation/sport or transport industries, respectively, the last two segments are treated as one. For configurations that are delta-like with higher values of leading-edge sweep and relatively sharp leading-edges, the low- α range may be extremely small leaving only the latter three segments to be of consequence. In addition to establishing which α segments are specifically involved, the configuration also determines whether the separated flow, which forms in the moderate α range, will ever develop into a significant, vortical-flow structure or just become wake-like at the higher values of α .

Though the emphasis of this paper is high α , the flow around configurations in the moderate and higher α ranges will also be considered. This is done, in large part, because some of the same analytical tools useful at high α have application at moderate α . The higher α range is most frequently called the post-stall range and it is of increasing research interest in order to respond to two aeronautical community needs. The first is to prevent unrecoverable spins from developing in aircraft, and the second is to enhance the operational effectiveness of fighter aircraft, as depicted in the joint U.S.A.-German X-31 research project reported by DeMeis (ref. 1). Experimental procedures or techniques, which are also classed as engineering methods, are currently the best means of obtaining the aircraft characteristics in the higher α range due to the unorganized or asymmetrical and unsteady structure of the flowfield not lending itself well to mathematical modeling. With respect to the low- α range, engineering methods for use in the analysis and design of aircraft are covered by the other papers in this AGARD special course (ref. 2).

This paper is divided into chapters which address: the prediction of vortical-separated flow, stability and control in the high- α range, and post-stall flight characteristics. The work presented here is mostly focused on engineering methods for predicting the aerodynamic forces and moments, which deals with the analysis aspect of this course, however, some of the material addresses the design aspect of the course. The thrust of this paper is on fighter configurations.

The interested reader is referred to the published results of AGARD sponsored lectures and specialists meetings over the years, in particular in 1982 (ref. 3) and 1983 (ref. 4), for additional details and supplementary information on high angle-of-attack aerodynamics.

PREDICTION OF VORTICAL-SEPARATED FLOW

This chapter contains a review of high- α vortical flows, then presents analytical methods for estimating the aerodynamic effects of this flowfield - along with representative comparisons, and ends with some design opportunities.

VORTICAL FLOW REVIEW

It is important to have a clear understanding of how vortical flows are manifested in aeronautical applications. This section reviews some of the relevant background the reader may need. It is organized into three parts: the first discusses the pertinent local conditions necessary for vortical flow onset and formation; the second examines those factors affecting vortex growth; and the third does the same for vortex diminishment.

Vortex Onset and Formation

Vorticity generation, which is simulated in inviscid flow solutions through the imposition of the TE Kutta condition, is due in fact to the action of viscosity at the TE. In addition, vorticity is introduced into an otherwise inviscid flow due to either the action of fluid viscosity along a solid boundary or behind a curve shock (see e.g. Anderson, ref. 5), with the focus of this paper being on the former. There the vorticity is contained within an attached-flow boundary layer and may lead to no other aerodynamic consequence than viscous airfoil- or wing-drag. If the airfoil boundary layer separates near the leading edge and then reattaches to form a recirculation region, this is called a bubble separation. On a swept-wing, a bubble separation often leads to the formation of a coherent, leading-edge vortex-system, due to the falling pressures from root-to-tip associated with vorticity entrainment and increased axial flow. The bubble vorticity is now confined within a small region called the core, which grows in size and vortex strength from apex to wing tip. Core growth comes about due to the addition of shed vorticity, associated with the flow satisfying the Kutta condition - a viscous statement - at the leading edge, being introduced into the vortex system along a helical path (Sketches associated with these descriptions are given in figure 2.) This general description allows for vortex onset and formation to occur at a small α , but the exact manner in which it happens is dependent on the wing camber, thickness, leading-edge radius, Mach number and planform.

The planform effect can be so powerful as to lead to novel flow situations. Consider figure 3, taken from Cunningham (ref. 6), where at moderate α this 65° sweepback trapezoidal wing has two leading edge vortex systems which merge into a single one at a slightly higher α . This generally does not happen at higher sweepback angles.

Those wings which do not generate a leading-edge shed vortex due to their planform shape being rectangular or too low in sweep still develop a vortex system at the tip. One way to describe the formation of this system is to consider it to be produced by the flow moving from the pressure side of the wing to the suction side. This well known tip-flow causes the span loading to change from a 2-D rectangular type to that approximating an ellipse and provides the theoretical base for the trailing vortices which get wrapped up into the tip vortex. Viscosity plays a role in the tip vortex initiation and in the determination of the point along the tip at which the vortex actually separates from the wing.

This lecture, however, will primarily focus on leading-edge vortices.

Figure 4, taken from McMillin et al. (ref. 7), shows regions where classical leading-edge vortical flow is to be expected in terms of the α normal to the leading edge (α_N) and the resulting Mach number normal to the edge (M_N). [This figure is the latest version of the information first quantified by Stanbrook and Squire in reference 8. These authors found it convenient to correlate the leeside, delta-wing flowfield with the quantities α_N and M_N , the primary independent variables associated with 2-D flow.] Though all this data was obtained at supersonic free streams, the figure is heuristically important in that it illustrates how the leeward flow changes with increasing α_N (or α for fixed Λ) from small to large values.

Vortex Growth

This part examines the subject of vortex growth by focusing on two of its component parts, vortex strength and core location.

Vortex strength It is well known that the strength of the vortex system from a delta wing is α and sweep dependent. However, the manner in which they are related has only recently been established theoretically by Hem� and Lucking (ref. 9) when they used an analysis based on the Sychev similarity parameter, $K (= \tan \alpha / \tan \epsilon)$. [These authors are not the first to show some relationship between vortex strength and a parameter; for example, Smith (ref. 10) used the parameter $(\alpha / \tan \epsilon)$.] The Sychev parameter is associated with slender bodies at inviscid hypersonic speeds but Hemch (ref. 11) shows it not to be limited to that situation. In particular, K has application to even moderately slender configurations developing vortical flow at low speeds. The result is that the vortex strength present at a delta-wing trailing-edge can be related to α and the wing sweep by

$$\Gamma/U \propto c_r (\tan \epsilon)^{0.8} \sin^{1.2} \alpha / \cos^{0.2} \alpha \text{ or}$$

$$\propto c_r (\sin^{1.2} \alpha / \cos^{0.2} \alpha) / (\tan \Lambda)^{0.8}$$

This equation shows for a fixed sweep and c_r that Γ/U increases monotonically with α , which is an expected result. It also shows for a fixed α and c_r that Γ/U is reduced with increasing wing sweep, a result which may seem contradictory to experience and therefore be unexpected.

The apparent contradiction is due to our intuitive understanding that in the moderate to high α range, a 75° delta wing develops more vortex lift than one with a sweep of 45°. We associate the increase in lift with an increase in vortex strength. However, the reason the 45° delta develops less vortex lift is not due to a loss in strength but to a loss in vortex coherence or stability. (This topic is covered in the vortex diminishment part.)

Figure 5, taken from Hemsch (ref. 11), shows the importance of K as a basis of analysis for vortex strength. In that solutions from the Free-Vortex-Sheet (FVS) code for three delta wings; each at a $K = 1$, yield essentially the same nondimensional value of vortex strength at the trailing edge and similar growths along the chord. This can be the basis of an engineering method.

Vortex core location: Changes in α and wing sweep affect not only vortex strength but the lateral and vertical location of the core. Combining α and sweep according to the parameter K , Hemsch (ref. 11) also determined that engineering estimates could be made for the core location as well. Figure 5 also shows that at $K = 1$ the vortex cores for these three deltas increase with distance along the c_r in a very similar manner.

Two experimental examples of vortex core/system growth are shown in figures 6 and 7. These figures (taken from Lamar et al. (ref. 12) and Lamar and Johnson (ref. 13), respectively) illustrate the α effect for two aircraft, one U.S.A. and one Soviet, as determined from in-flight vapor-screen images. [Note that the vapor screen images for the U.S.A. F-106B aircraft have been digitally enhanced after the flight.]

Vortex Diminishment

The topic of vortex diminishment is larger than just the loss of vortex-system coherence. It also includes the loss-of-influence a coherent vortex system has on surface pressures. Each is discussed.

Loss-of-vortex-coherence: The loss-of-vortex-coherence is due to vortex-core breakdown or burst, which has as its main contributors (1) α effects on core size or swirl angle, and (2) adverse pressure field disturbances. Whether the burst is of the swirl or bubble type - see Lambourne and Bryer (ref. 14) - is not of concern here, but when it does occur, the flow in that region becomes unsteady and begins to rotate like a solid body with a larger radius than that of the core; whereas, the flow ahead of the region may be steady and coherent. As burst begins to occur ahead of the trailing edge, it can lead to asymmetrical flow situations which result in an imbalance in the aerodynamic forces on the left and right sides, especially lateral ones.

Vortex breakdown occurs with hysteresis over a wing during a pitching motion with a resulting lag. This is examined later with respect to dynamic stall.

The ability to estimate under what conditions burst will occur for a configuration of interest and how to control the resulting flow or aircraft are of particular interest to the designer working in the high α regime. Much of this still must be determined experimentally. Figure 8, developed from the basic data of Wentz and Kohlman (ref. 15), shows the experimental variation of the α for vortex breakdown at both the trailing edge and apex over a large, delta-wing-sweep range. As expected, $\alpha_{BD-TG} < \alpha_{BD-Apex}$ for a given wing, however, what is revealing is how vortex breakdown at the trail-

ing edge or forward affects the maximum lifting capability of the wing, as denoted by $\alpha_{L,max}$. In particular, note that for $\Lambda > 70^\circ$ $C_{L,max}$ occurs at an α very near that for α_{BD-TG} . This shows the aerodynamic importance of vortex coherence.

However, there is one analytically determined piece of information, shown in figure 9 - taken from Lamar (ref. 16), that may be useful here. It is that the leading-edge suction distribution across the span for both delta- and cropped-delta wings have their peak value increase and occur farther outboard with increasing sweep or tip chord. By itself this doesn't help, but if a correlation is made with the quantity α_D - the α at which the measured C_L first begins to fall below the suction analogy estimate - a trend is noticeable. It is that α_D increases when the peak suction value increases and occurs more outboard, i.e., becomes increasingly triangular. This correlation can be used as a tool in trying to estimate which of several configurations will have the highest α_D by simply examining the respective suction distributions. [The quantity α_D is similar to α_{BD-TG} except that it is applicable to wings for which α_{BD-TG} data may not be available, and moreover it implicitly takes into account the loss-of-influence associated with vortex displacement.]

Loss-of-influence: The ability of the vortex system to influence the surface flow is related to its strength and the distance to the surface; hence, the greater the distance the less influence the system has. From experiments, it is well known that the vortex-system vertical displacement (see fig. 7) and strength grow for slender wings over an α range, and continue to produce a strong influence on the surface. However, after some α , and perhaps before loss of coherence, the vortex system is too far from the wing surface due either to a symmetrical or asymmetrical displacement - depending on the wing sweep and flight attitude and as indicated in the sketches in figure 10 - and thereby loses its strong influence. (Asymmetrical displacement is often associated with vortex crowding on a very slender wing at higher alphas, as shown in the right sketch, but it can also occur for most delta wing at sideslip.)

This loss-of-influence effect is apparent on a wing surface from either an oil-flow or a leeside, surface-pressure test. The effect is conspicuous from an oil-flow test by the patterns becoming more spread out and not as sharp in surface details, and from a pressure test by a reduction in suction pressure to a more positive value or to just maintaining a constant value with increasing α . Regardless of how these changes in local surface conditions are detected, the influence of the changing conditions produce corresponding global ones. These include either a reduction in lift (in particular, for α fixed at a value $> 20^\circ$ and with Λ increasing above 76° , as indicated by the basic data of Wentz and Kohlman, ref. 15) or nonzero values being developed for the aerodynamic lateral characteristics, even before vortex burst occurs.

FOR USE IN ANALYSIS

General

Various techniques, associated with different levels of accuracy and complexity, are available to model the vortical flow influence on configurational aerodynamic forces and moments to high α . The ones included herein cover suction-analogy with extensions, free-vortex-filaments, free-sheet-vortex modeling, and Euler and Navier-Stokes solutions. The latter two are known as Computational Fluid Dynamics (CFD) techniques and are not yet considered engineering methods, but may be soon. In order to demonstrate these techniques, at least one comparison with experimental data is presented for each of them.

All the techniques just listed are discussed in this section and are done so basically in the order of increasing complexity.

Suction Analogy (SA)

The leading-edge suction analogy of Polhamus (ref. 17) was originally developed for delta wings and has become known as one of the more reliable engineering tools for estimating the aerodynamic affects of separated vortical flow at subsonic and supersonic speeds. Furthermore, it is also one of the most widely implemented techniques because the information it needs can be readily obtained from analytical or computational solutions to the linearized potential-flow equations. This section reviews the basic suction-analogy concept, cites representative methods in which it is employed, details similarity use of it, and presents extensions of it.

Basics: Polhamus (ref. 17) postulated that the in-plane leading-edge suction [a force] developed in attached flow was not lost when the flow separated around a sharp leading-edge of a swept wing, instead the force only became re-oriented in the direction of the rotating vortex system. This is called the leading-edge suction analogy (LESA or just SA), in that the extra normal force developed as a result of the shed vortex system is analogously just equal to the in-plane force lost along each edge. Flow sketches depicting this change are seen at the right in figure 11, taken from reference 16.

This figure also shows an application for a $\Lambda = 75^\circ$ delta wing at $M \approx 0$. The SA allows one to use potential flow codes to compute the C_{Na} and C_S , which are then used in the lift and drag equations. In particular, the potential flow part of the lift curve is identified as involving a factor called K_p . This factor is nothing more than the low α value of $C_{L\infty}$ or C_{Na} . The vortex lift portion comes by knowing the factor $K_{v,le}$ which is determined by taking the $\partial(2 \text{one-edge } C_S)/\partial(\sin^2 \alpha)$. Figure 12, taken from reference 18, shows the K_p and $K_{v,le}$ variation for delta wings. Similar curves for arrow and diamonds wings are given by Polhamus in reference 17.

Once these factors are determined computationally or from curves, they are used in the formulas cited on the figure to obtain the total lift. The vortex drag associated with a wing

having no edge force is just $\Delta C_D = C_L \tan \alpha$. Note the good correlation obtained with the zero lift drag removed. Polhamus (ref. 17) also showed how using the Prandtl-Glauert transformations one could obtain other subsonic results from $M = 0$ solutions.

Polhamus in references 17 and 18 demonstrated that the SA was capable of making lift and drag estimates to other pointed wings than delta, i.e., diamonds, arrows and even wings with cranked leading edges. Moreover, Polhamus showed in reference 18 that this concept is not restricted in speed regime but only to the development of a leading-edge force. Since analytic solutions exists for thin delta wings with subsonic leading edges at supersonic speeds, K_p and $K_{v,le}$ can be determined and they are reported by Polhamus to be:

$$K_p = \pi A / (2E(k)),$$

where $E(k)$ is the complete elliptic integral of the second kind and $k = [1 - (\beta \cot \Lambda)^2]^{1/2}$, and

$$K_{v,le} = \pi [(16 - (A\beta)^2)[A^2 + 16]]^{1/2} / 16E^2(k).$$

Figure 13 shows two examples of measured and estimated lift at supersonic speed for an $A = 1.147$ delta, also taken from reference 16. There are two major points to be made here: (1) the reduced amount of vortex lift available at $M = 2.8$, as compared with that at $M = 1.2$; and (2) the lift is well estimated at $M = 1.2$ but not as well at $M = 2.8$. The poorer agreement at the higher Mach is due to the lower surface of the Mach cone coming near the leading edge with increasing α which effectively moves the lower surface separation line closer to the leading edge and reduces the amount of flow turning around the edge. Consequently, less vortex flow and lift are available.

Representative methods: Only two of the many methods which employ the SA are cited in this section. They are the Vortex-Lattice-Method coupled with Suction Analogy (VLM-SA), and DIGITAL DATCOM. Others are introduced in the later sections which deal with extensions or design.

VLM-SA: The NASA VLM code developed by Margason and Lamar (ref. 19) contained the ability to calculate leading-edge suction. Since then the code has been continually up-graded to include the SA effects, as indicated by the title of the report by Lamar and Gross (ref. 20), and that feature is currently embedded in the most recent VLM code release, referred to in Lamar and Herbert (ref. 21). An example of the VLM-SA code is given in figure 14, taken from Snyder and Lamar (ref. 22), in which it was used to predict the longitudinal-load-distributions - C_{LL} - for an $A = 1.147$ ($\Lambda = 74^\circ$) delta at three values of α . This work was done to address an initial concern that the success obtained with estimating lift and drag using the SA would not be repeated when trying to estimate pitching moment. The concern was based on the knowledge that to obtain reliable estimates of C_m , it was necessary to have valid predictions

of the longitudinal distributions for both potential and vortex flow, something not required by the SA.

Snyder and Lamar obtained the potential lift curves by performing a spanwise integration of lifting pressures at a variety of longitudinal locations; whereas the vortex lift portion came directly from the leading-edge-suction distribution. The resulting curves show the vortex lift contribution to become a larger fraction of the total with increasing α and the measured-and-predicted-total results to be in fairly good agreement over the α range. Based on the success of this early work, the SA concept is now used routinely to provide reasonable estimates for C_m .

Other results using this method are given later.

DIGITAL DATCOM: One well documented engineering method, developed for the USAF by Williams and Vukelich (ref. 23), is that of DIGITAL DATCOM. It is a computer-based system for obtaining "static stability, high lift and control, and dynamic derivative characteristics" over a range of aircraft geometries, Mach numbers and α 's. The computational methods are primarily linear aerodynamics with the nonlinear lift portions for some combinations of planforms and Mach numbers being accounted for using the SA. In particular, at subsonic speeds only straight-tapered, low-aspect-ratio wings are covered; and at supersonic speeds only straight-tapered wings with a subsonic-leading-edge or a supersonic-leading-edge with an attached-flow-shock at zero- α are covered. The SA is also used to estimate forebody lift and pitching moment at subsonic speeds above the α for "onset of vortex lift".

Similarity: The use of the similarity parameter K , as reported by Hemsch (ref. 11), has been previously introduced. Here the emphasis is on discussing a link between a similarity parameter $(\tan \alpha/A)$, which reduces to $K/4$ for delta wings, and SA for wings and smooth slender bodies. To assist in this effort, consider again the C_{LL} distributions presented in figure 14. Since the magnitude and shape of each distribution are dependent on α , there may be a scaling on α which would make each curve like that from another delta wing at some other α , i.e., use a similarity parameter to sort properly scaled results together.

Hemsch presents the longitudinal-normal-force distribution - a quantity similar to C_{LL} - scaled by $(A \sin \alpha \cos \alpha)^{-1}$ for a family of thin gothic wings at $M = 0$ and 0.95 for a value of the similarity parameter $(\tan \alpha/A) = 0.3$. These scaled distributions have been estimated from the Free-Vortex-Sheet (FVS) code - to be discussed later - and show close agreement to exist among the respective potential and total curves. This means that the scaled vortex normal force contribution between the various wings must have been also in close agreement. Figure 15 shows the impact of applying this same scaling to FVS estimates of the total normal force coefficient and to only the vortex flow portion as a function of $K/4$ for thin delta wings. Hemsch attributes the rationale for doing this to the fact that "several researchers have found that the velocity field of the primary vortex is nearly conical even though the wing surface pressure distribution is not

This suggests that the Sychev slender-body similarity may at least be applicable to the portion of the slender wing or body loading induced by the vortical flowfield." The result of this action is that the total C_N^* does not collapse to a single line, whereas the vortex portion, $C_{N_v}^*$, does. What is also interesting is that the theory shown for the $C_{N_v}^*$ curve is a "best one-term power law fit" given by

$$C_{N_v}^* = 3.07(\tan \alpha/A)^{0.93},$$

which is very close to the Polhamus result, written in similarity form, as

$$C_{N_v}^* = K_{v,le}(\tan \alpha/A),$$

where $K_{v,le}$ is known to become only slightly greater than π over this sweep range.

This figure also shows the fractional distance to the center of pressure of the nonlinear portion of the normal force as a function of $K/4$. Hemsch notes that this term "does not scale very well", which "means that the aspect-ratio range over which one can expect to scale or extrapolate subsonic pitching moment data is considerably smaller than it would be for supersonic flows."

Regarding smooth slender bodies, the resulting $C_{N_v}^*$ and $C_{m_v}^*$ estimates are dependent on M and on whether the body is an elliptical cone or derived from a power law. The general results are that,

$$C_{N_v}^* \propto [\tan \alpha/A - (\tan \alpha/A)_{onset}],$$

elliptical cone for $M < 1, M > 1$; also
power law body for $M < 1$

$$\propto (\tan \alpha/A)^{\text{Function}(M)},$$

power law body for $M > 1$

and

$$C_{m_v}^* \propto [\tan \alpha/A - (\tan \alpha/A)_{onset}],$$

elliptical cone, for $M < 1, M > 1$; also
power law body for $M < 1$

$$\propto (\tan \alpha/A)^{\text{Function}(M)},$$

power law body for $M > 1$.

Extensions: The LESA has spawned a variety of extensions. An early one was the estimation of the vortex flow effect for wings with finite tip chords. Another dealt with estimating the effect of a vortex system on a downstream area not associated with its generation - it is called an augmented vortex term. Others have addressed more general geometries, which include wings with camber, non-zero edge radius, thickness effects, combinations of a wing with a canard, strake or body, and asymmetrical flow situations. For cambered wings developing vortex flow, the concept of the vortex action point is discussed because of its importance. Many of the other listed items are detailed in the following paragraphs.

the term ΔC_L with known terms, the Kutta-Joukowski relationship was used for the differential leading-edge force, dF_y , as shown. The result is that another factor is identified, $\bar{K}_{v,se}$, which can contribute to the vortex flow aerodynamics, based on quantities already known, and which uses the same trigonometric functions in its' computations for the force/moment characteristics, as $K_{v,le}$ and $K_{v,se}$.

The only quantity not specifically known is \bar{c} and it is used to provide a representative length onto which the forward shed vortex system acts. This quantity is a geometric term defined to be the streamwise distance from the tip leading edge to the apex of the trailing edge, and can be positive or negative depending on the tip-chord length and the trailing-edge sweep. For pitching moment estimation the streamwise distance from the centroid of the "affected area" to the reference point is needed, a quantity called \bar{z} .

Figure 25, taken from reference 16, shows the relative size of the vortex lift factors and that the augmented factor is too large for these wings to be ignored. The cropped delta configuration at the top right is the same as shown in figure 23, but the results are for a lower Mach number. Note the improved C_L agreement up to the highest test α . For the cropped diamond at the left, the augmented factor is the same size as the other vortex lift factors and leads to good agreement with data, again to the highest test α .

The other two wings, having notched trailing edges, will not have such large values for the $\bar{K}_{v,se}$. Furthermore, both the $A = 1.069$ and 1.917 wings have C_L results which show a lift falloff by 24° and 19° , respectively. Even for a coherent leading-edge vortex system, notching the trailing edge reduces the room onto which flow reattachment can occur which will lead to a reduction in measured C_L .

Figure 26, taken from reference 28, shows the definition of \bar{c} to yield generally good agreement for α less than 16° , yet it leads to an underprediction of the C_L in the moderate α range for this 45° cropped arrow wing. In that range the tip chord itself better represents the length onto which the forward shed vortex system acts. These points are illustrated by oil-flow sketches shown at moderate and high α values. Above $\alpha = 16^\circ$ one of three things happens to this vortex system which cause C_L to fall off. They are: (1) the leading-edge vortex system bursts - on the basic delta breakdown at the TE would occur at a much lower angle than 16° , (2) the system gets so large that its influence is diminished due to vertical displacement, and (3) the loss of reattachment area.

The points being made here are that there is an additional vortex flow factor beyond those of $K_{v,le}$ and $K_{v,se}$, it is called the augmented lift term, and when used with judgment about what the leading-edge vortex system is doing can lead to good aerodynamic estimates. A good example of this is for the strake-wing combination depicted in figure 27, taken from Lamar and Campbell (ref. 29). Here one can see that the number and size of the lift augmentation regions can vary with α to reflect the actual flow. Cranked-wings and wing-canards are other configurational examples

which may employ this type of flow-modeling α -variation, as reflected in the construction of both the $\bar{K}_{v,se}$ and $K_{v,le}$ terms. Sample results are given in the next chapter.

Wing camber: Vortex flows and their effects on cambered wings are of increasing importance due to emphasis on vortex flow control devices, such as leading-edge vortex flaps (LEVFs). Extensions have been made to the VLM-SA code to account for these effects (ref. 21). Other SA methods which have also been extended, including one which uses the Quasi-Vortex Lattice Method (QVLM) as a potential flow base, as described by Lan in reference 30. Another one developed by Lan and Chang (refs. 31 and 32) is called VORCAM (Vortex lift of CAMbered wings) and is derived from an improved version of the chord-plane aerodynamic-panel method of Woodward (ref. 33). This code uses the SA to calculate the vortex induced aerodynamic effects on cambered wings, including those with vortex flaps, and is valid at those subsonic and supersonic speeds where the linearized governing equations apply.

An application of the VORCAM code to a conically cambered delta wing at $M = 1.4$ is shown in figure 28. The inclusion of the vortex contribution is seen to provide some improvement with the measured data over this restricted α range.

VORCAM also has an option for designing a portion of a contiguous wing surface to represent an integral vortex flap inset into the wing. An example of using VORCAM in LEVF design is given later.

Vortex action point: Lan and Chang (ref. 31) have also modeled the effect of the center of the vortex, called the vortex action point, moving inboard/downstream with α . This is physically correct and not accounted for in the original suction analogy modeling schemes. In these earlier schemes, as previously noted, the vortex was assumed to remain small and along the leading edge regardless of the α value. The vortex action point movement produces no aerodynamic effects for a planar wing, but for a camber/twisted wing there will be differences. They are associated with the local mean-camber slope varying along the chord, thereby causing the local contributions to lift and drag, calculated from the suction force, to differ from earlier results. This can be understood by examining the right-hand sketch in figure 29, taken from (ref. 31).

This concept was derived by comparing measured vertical velocities present near the wing leading edge with those associated with potential flow. The difference is attributed to the action of the vortex system and its magnitude based on data for one wing at one value of α and was determined to be $V_\infty/2$. From this concept the streamwise flow model was developed which has the characteristics outlined in the left and center sketches on this figure. The basic assumption is that the exchange of linear momentum into and out of a control surface of length $2r$ would be just balanced by the section leading-edge suction force. Physically, it says that the force required to keep the control surface from moving

the term ΔC_L with known terms, the Kutta-Joukowski relationship was used for the differential leading-edge force, dF_x , as shown. The result is that another factor is identified, $\tilde{K}_{v,se}$, which can contribute to the vortex flow aerodynamics, based on quantities already known, and which uses the same trigonometric functions in its' computations for the force/moment characteristics, as $K_{v,le}$ and $K_{v,se}$.

The only quantity not specifically known is \tilde{c} and it is used to provide a representative length onto which the forward shed vortex system acts. This quantity is a geometric term defined to be the streamwise distance from the tip leading edge to the apex of the trailing edge, and can be positive or negative depending on the tip-chord length and the trailing-edge sweep. For pitching moment estimation the streamwise distance from the centroid of the "affected area" to the reference point is needed, a quantity called \tilde{x} .

Figure 25, taken from reference 16, shows the relative size of the vortex lift factors and that the augmented factor is too large for these wings to be ignored. The cropped delta configuration at the top right is the same as shown in figure 23, but the results are for a lower Mach number. Note the improved C_L agreement up to the highest test α . For the cropped diamond at the left, the augmented factor is the same size as the other vortex lift factors and leads to good agreement with data, again to the highest test α .

The other two wings, having notched trailing edges, will not have such large values for the $K_{v,se}$. Furthermore, both the $A = 1.069$ and 1.917 wings have C_L results which show a lift falloff by 24° and 19° , respectively. Even for a coherent leading-edge vortex system, notching the trailing edge reduces the room onto which flow reattachment can occur which will lead to a reduction in measured C_L .

Figure 26, taken from reference 28, shows the definition of \tilde{c} to yield generally good agreement for α less than 16° , yet it leads to an underprediction of the C_L in the moderate α range for this 45° cropped arrow wing. In that range the tip chord itself better represents the length onto which the forward shed vortex system acts. These points are illustrated by oil-flow sketches shown at moderate and high α values. Above $\alpha = 16^\circ$ one of three things happens to this vortex system which cause C_L to fall off. They are, (1) the leading-edge vortex system bursts - on the basic delta breakdown at the TE would occur at a much lower angle than 16° ; (2) the system gets so large that its influence is diminished due to vertical displacement; and (3) the loss of reattachment area.

The points being made here are that there is an additional vortex flow factor beyond those of $K_{v,le}$ and $K_{v,se}$, it is called the augmented lift term, and when used with judgment about what the leading-edge vortex system is doing can lead to good aerodynamic estimates. A good example of this is for the strake-wing combination depicted in figure 27, taken from Lamar and Campbell (ref. 29). Here one can see that the number and size of the lift augmentation regions can vary with α to reflect the actual flow. Cranked-wings and wing-canards are other configurational examples

which may employ this type of flow-modeling α -variation, as reflected in the construction of both the $\tilde{K}_{v,se}$ and $K_{v,se}$ terms. Sample results are given in the next chapter.

Wing camber: Vortex flows and their effects on cambered wings are of increasing importance due to emphasis on vortex flow control devices, such as leading-edge vortex flaps (LEVFs). Extensions have been made to the VLM-SA code to account for these effects (ref. 21). Other SA methods which have also been extended, including one which uses the Quasi-Vortex Lattice Method (QVLM) as a potential flow base, as described by Lan in reference 30. Another one developed by Lan and Chang (refs. 31 and 32) is called VORCAM (Vortex lift of CAMbered wings) and is derived from an improved version of the chord-plane aerodynamic-panel method of Woodward (ref. 33). This code uses the SA to calculate the vortex induced aerodynamic effects on cambered wings, including those with vortex flaps, and is valid at those subsonic and supersonic speeds where the linearized governing equations apply.

An application of the VORCAM code to a conically cambered delta wing at $M = 1.4$ is shown in figure 28. The inclusion of the vortex contribution is seen to provide some improvement with the measured data over this restricted α range.

VORCAM also has an option for designing a portion of a contiguous wing surface to represent an integral vortex flap inset into the wing. An example of using VORCAM in LEVF design is given later.

Vortex action point: Lan and Chang (ref. 31) have also modeled the effect of the center of the vortex, called the vortex action point, moving inboard/downstream with α . This is physically correct and not accounted for in the original suction analogy modeling schemes. In these earlier schemes, as previously noted, the vortex was assumed to remain small and along the leading edge regardless of the α value. The vortex action point movement produces no aerodynamic effects for a planar wing, but for a camber/twisted wing there will be differences. They are associated with the local mean-camber slope varying along the chord, thereby causing the local contributions to lift and drag, calculated from the suction force, to differ from earlier results. This can be understood by examining the right hand sketch in figure 29, taken from (ref. 31).

This concept was derived by comparing measured vertical velocities present near the wing leading edge with those associated with potential flow. The difference is attributed to the action of the vortex system and its magnitude based on data for one wing at one value of α and was determined to be $V_{\infty}/2$. From this concept the streamwise flow model was developed which has the characteristics outlined in the left and center sketches on this figure. The basic assumption is that the exchange of linear momentum into and out of a control surface of length $2r$ would be just balanced by the section leading-edge suction force. Physically, it says that the force required to keep the control surface moving

away from the wing, due to the linear momentum exchange, is just balanced by an additional force on the wing. These forces are both caused by a suction pressure present above the wing and leads to $r = c_s c$. The sketch at the right shows the reorientation of the suction force due to the movement of the vortex action point.

Round LE simulation: For a round leading-edge wing, not all of the suction force is converted into an additional lift when the flow separates. Some of it remains as a "residual" suction force that acts in the plane of the leading edge. Polhamus showed for uncambered wings in the late 1960's (published with permission later by Kulfan in ref. 34) that there was experimental evidence to demonstrate the sum of the residual leading-edge suction and vortex normal force to be essentially the same as the theoretical value of the thin-wing leading-edge suction. Figure 30 shows one example prepared by Polhamus from existing data for an $A = 1$ delta wing with a round leading edge and $t/c = 0.10$, which supports the preceding statement. The sketch on the left illustrates the forces involved, and the equation at the bottom shows the algebraic relationship. Henderson, in reference 35, later demonstrated experimentally that there was evidence to render this statement true over a wide Reynolds number range.

The two main methods of simulating the effect of round leading edges use this Polhamus concept as a basis for determining the vortex forces, however, they differ widely in the basic assumptions and computational procedures. Kulfan (ref. 34) uses a theoretical procedure for determining the vortex normal force, then employs the equation in figure 30 to find the residual suction, whereas, Carlson and Mack (ref. 36) and Carlson and Walkley (ref. 37) use empirical formulas to determine the residual suction at supersonic and subsonic speeds, then employ this equation to determine the vortex normal force.

Kulfan's procedure, developed in a Boeing research effort, is depicted in figure 31 and which has been implemented in the VLM-SA and other codes. It is based on the assumptions that (1) the airfoil nose section is parabolic and (2) separation begins wherever the local value of theoretical leading-edge suction exceeds the parabolic nose drag value, $c_{f,0}$. The vortex and its associated normal force are assumed to occur when the local α exceeds that required for local separation, α_s , and $\alpha | \sin(\alpha - \alpha_s) | \sin(\alpha - \alpha_s)$.

Carlson assumes that the thrust at the leading edge is limited by the amount of pressure that can be attained there. An example of how the limiting pressure can reduce the leading-edge thrust to its "attainable" value is shown on figure 32. Here the limiting pressure is vacuum and its impact can be clearly seen with increasing α or the theoretical section thrust coefficient, $c_{f,t}$. (Note, if the limiting pressure were ∞ , $c_{f,t}/c_{f,s}$ would be 1.00 for all values of $c_{f,t}$.) By analyzing airfoil data, Carlson correlated the experimental residual thrust with normal Mach number, airfoil thickness and leading-edge radius ratios, and limiting pressure. The proper values for limiting pressure were determined empirically from an airfoil data base that covered a wide range of

Mach and Reynolds numbers. This procedure is extended to wings by using simple sweep theory.

Unsteady flow: Lan in reference 38 has extended the SA to unsteady flow by coupling the Unsteady QVLM method (ref. 39) with the idea of "vortex lag." Vortex lag is associated with the phase lag angle that exists between the wing motion and the buildup of the vortex strength at the leading edge. Lan determined the phase lag angle and with that was able to estimate the unsteady suction force, and hence the vortex flow aerodynamics.

Others: The reader is referred to Lan (ref. 40) and to Lamar and Campbell (ref. 29) for additional extensions to the SA.

Free-Vortex-Filaments

Free-vortex-filament models are used to represent the shed vortex system off the leading edge by using discrete vortex filaments which interact in a manner similar to that shown in figure 33. Various researchers in many countries have developed methods based on this model for both steady and unsteady flow. They include Mehrotra and Lan (ref. 41), Pao and Lan (ref. 42) and Kandil and Yates (ref. 43) for steady flow; and Katz and Maskew (ref. 44) for unsteady flow. The method of Kandil and Yates is highlighted because of its transonic application.

This method uses an integral equation approach and a shock-capturing technique to establish the features of transonic flow above the wing and in the vortex system. These include shock location and the determination of its shape and influence. One interesting result reported (for a thin, $A = 1.5$ delta at $\alpha = 15^\circ$ and $M = 0.7$) is that the captured shock is curved, attached to the vortex sheet and doesn't extend to the leeward wing surface but towards the core. This is seen at the right of figure 34 along with a favorable comparison of predicted and experimental pressure at $x/c_r = 0.80$.

The left side of the figure shows three views of the leading- and trailing-edge free-vortex lines on the wing along with the inviscid LE and TE cores. This method defines the core to be the centroid of the cross-sectional area and after the filament has made one revolution it is terminated and its vorticity added to that of the core. The fact that there are two cores may seem unusual but they result from different vortex sheets. The leading-edge sheet produces a counter-clockwise rotation about its core - when looking upstream, whereas the trailing-edge sheet produces a clockwise rotation about its core on the right wing panel due to the span loading not decreasing monotonically to zero under the influence of leading-edge vortical flow. The cross-sectional shape of the system appears mushroom-like in the trailing-edge region.

Free-Vortex-Sheet

Code description: The free-vortex-sheet (FVS) code, developed by Johnson et al. (ref. 45), satisfies the Laplace equations by using higher-order panel technology to represent the loading on the wing and differs from attached flow methods

by virtue of the more complicated boundary conditions. The chief difference is associated with the free sheet having to simultaneously satisfy both the no-load and no-flow boundary conditions, this renders the subject problem nonlinear. A second difference is associated with the near-wake boundary condition. This condition needs to be satisfied to second order accuracy in order to obtain correct results. Figure 35, taken from Luckring et al. (ref. 46), shows these features on a representative wing.

Solutions have been obtained with this code for a variety of configurations and are catalogued in the paper by Luckring et al. (ref. 47). That paper addresses solution procedures to be employed in order to overcome convergence difficulties encountered with more complex configurations. The partial restart procedure is one of those developed. The second of the two FVS examples shown here uses this procedure.

The examples, cited in order of presentation, are an $A = 1$ delta wing and the F-106B configuration.

Application to $A = 1$ delta: Figure 36 (Luckring et al., ref. 47) provides a comparison between the measured and predicted lift curve and spanwise pressure distribution results for an $A = 1$ delta wing. [The measured results have come from an experimental study reported by Hummel in reference 48.] Good C_L agreement is noted over the α range up to 30° . After this the flow physics begin to change from that assumed by the FVS method to that which encompasses vortex breakdown. The reference also shows similarly good agreement with drag and pitching moment over the C_L range up to 1.1.

Regarding the spanwise pressure distributions, the peak suction pressure is overestimated and the distribution near the leading edge missed due to the FVS having no means of accounting for the influence of the secondary vortex. The major measurable effects of the secondary vortex are twofold, firstly, displacing the primary vortex upward, thereby reducing the influence of the primary, and secondly, increasing the suction pressure near the leading edge, due to the presence of the secondary.

Application to F-106B. The partial restart procedure enables a starting vortex sheet geometry, which has either been specified by the user or previously obtained on a similar (wing, wing-fuselage, etc.) configuration, to be applied to the current one, here the F-106B. This procedure has been used in a three-step process, outlined at the top of figure 37, to obtain a converged solution (ref. 12).

The first step is to acquire a converged free-vortex-sheet solution for a flat, δ delta wing. Secondly, that sheet is attached to the same wing mounted onto a generic cylindrical fuselage with a cone-like forebody. Lastly, the converged vortex-sheet solution from the previous step becomes the initial guess for the final configuration. The final configuration models the actual airplane by making three geometrical changes. They include changing the wing planform from one with no trailing-edge sweep to one with 5° of forward sweep (going from delta to a diamond), introducing a close approx-

imation to the actual wing camber, and incorporating a more realistic fuselage model. In particular, the actual forebody, canopy, fairing-over inlet are well represented and the afterbody is closely approximated.

Steps one and two gave no evidence of convergence difficulties, however, some were manifested when a very precise modeling of the actual wing camber, which exists outboard of 80% local semispan, was attempted. To circumvent this problem an alternate method of modeling the cambered-wing was employed. This method was analytical and made the leading-edge coordinates of the cambered-and flat-wing to be the same. The effect of this was to cause the wing to be placed on the fuselage at a negative incidence (approximately 1.25°) as shown in the sketch at the bottom of figure 37.

Figure 38 shows the surface panel representation of the wing-fuselage and the converged free-vortex-sheet solution at $\alpha = 19^\circ$ and subsonic speeds. Also shown is the flight location of a vapor-screen light sheet and where it intersects the converged free-vortex-sheet. [Light sheet is oriented 11.2° ahead of perpendicular to the fuselage centerline, as documented by Lamar and Johnson (ref. 13).] Since force and pressure comparisons have not been made nor published for this configuration - due in part to the small number of α solutions made - only the vortex core location will be reported and that, subsequently.

Euler and Navier-Stokes

General Currently, methods which model either the inviscid Euler or the viscous Navier-Stokes equations fall under the classification of "expert codes". This is due in large part to the special attention required in developing an acceptable grid, and the knowledge required to stipulate suitable parameters to the flow solver. [However, this situation is improving by the introduction of CFD codes that have suitable documentation and sample cases to assist the new user in their application, e.g., the TEAM code of Raj et al. (ref. 49).] In addition, due to the large requirements of computer memory and time, these codes are most often run to either assist in understanding experimental results or to help guide the experimentalist areas where unanticipated phenomenon may be present. After the Euler and Navier-Stokes equations are presented in tensor form - summation convention implied by repeated index, example solutions are given. [It should be noted that each of these sets of three equations contains no body force and includes 5 and 7 independent variables, respectively. To obtain closure, the equations of continuity, total energy, perfect gas equation-of-state for static pressure, Stokes hypothesis for bulk viscosity and Sutherland's law for molecular viscosity are also used, as needed.]

Euler Eqns

$$\partial(\rho q_i)/\partial(t) + (\rho q_i q_j + p \delta_{ij})_j = 0$$

Navier-Stokes Eqns

$$\frac{\partial(\rho q_i)}{\partial(t)} + (\rho q_j + p \delta_{ij})_j - \lambda q_{ij} - \mu(q_{ij} + q_{ij}) = 0$$

Euler Code. Three-dimensional Euler codes, like the FLO57GWB code developed by Raj and Brennan (ref. 50), have demonstrated not only the capability to capture shock waves at transonic and supersonic speeds but can capture regions of rotational flow at these and lower speeds on generalized geometries. Unlike potential flow methods, such as the FVS, Euler codes do not require an explicit model of the vortices. Instead, they appear automatically as a part of the solution. The reasons are twofold: firstly, geometrical; and secondly, computational.

The geometrical issue is an easy one to understand in that for a real flow one expects a separated flow to be generated at the wing leading-edge if it is sharp, regardless of the Reynolds number, due to the natural enforcement of the Kutta condition there. Thus, if the geometry to be modeled has a sharp leading-edge, one can also expect this condition to be enforced computationally. This brings in the computational issue, namely, that the "discretized" Euler equations are diffusive near the leading-edge, due to truncation error and added artificial viscosity", according to Powell and Murman in reference 51. Since the Kutta condition owes its existence to the effects of viscosity or a diffusive effect, it is understandable that these authors note "any computational model that has a diffusive effect at the leading-edge that mimics real diffusive effects should trigger separation, regardless of the magnitude of the diffusion". Thus, a method employing the inviscid Euler equations is able to predict, in a fairly reliable manner, the leading-edge vortex-separation effects even for the very complex geometries, provided the wing has a sharp leading-edge (See Murman et al., ref. 52)

Two solutions using the Euler equations are given, one is for a 74° delta wing ($A = 1.147$) using the TEAM code in its Euler mode, and the other for the F-106B aircraft - basically a 6° delta wing with cone-like camber - using an earlier version of the TEAM code called FLO57GWB [It may be surprising to the reader that some CFD codes can accommodate configurations having a high degree of geometrical generality, see also Flores and Chaderjian (ref. 53) and Ghaffari et al. (ref. 54)]. Strictly speaking, this code should only be applied to geometries in which there is reason to expect a leading-edge vortex-system to be formed. Reference 12 shows that the F-106B aircraft and models meet this criteria even though they do not have a sharp leading-edge.

Application to $A = 1.147$ delta wing, Raj (ref. 55) present comparisons, similar to that of figure 39, between measured and predicted lift and surface pressures at $M = 0.3$, where the predicted values have been obtained with a H-O grid of $30 \times 37 \times 20$ points. The lift agreement is good up to $\alpha = 30^\circ$. Above this a converged steady-state solutions were not obtained.

This figure also shows predicted spanwise pressure distributions at two longitudinal locations. Primary vortex capture is noted in the computational solutions, though the peak values for suction are over-estimated. This is due in part to the inviscid Euler equations having no mechanism for modeling the secondary and tertiary vortices generated on the surface.

The secondary vortex is the more influential of these two and its effects have already been detailed in the FVS section.

Application to F-106B. The reason a representative vortex system is expected for this wing is that its leading-edge radius is small; i.e. streamwise radius-to-chord ratio reported to be less than 0.2% across the span (ref. 13). Furthermore, a discretized representation of a radius will yield an acute angle at this or any other edge. The FLO57GWB code was also selected because, at the time the work was being done, this code was both readily available and fairly straightforward to use in assessing the flowfield on a geometry as complex as the F-106B.

The basic F-106B was analyzed by Pao (ref. 56) using a C-H grid of $129 \times 25 \times 25$ with points clustered around the wing section. The surface grid representation of F-106B wing-fuselage configuration and a typical C-H grid around a wing station are shown in figure 40. The conditions of interest are $M = 0.4$ and $\alpha = 19^\circ$. Lift and surface pressure results are presented in figure 41, and vortex core location at the same position as measured from flight vapor-screen images is given in figure 42.

Regarding figure 41, the agreement between measured and predicted lift curve slopes is good over the α range from 10° to 20° . This is only important within the context that the Mach number for the experiment was 0.2 and for the computational solution was 0.4. The preceding leads to the conclusion that there is no significant Mach number effect at this low speed. At α 's above 20° even the lift curve slopes begin to differ significantly. It is known that vortex breakdown occurs at the trailing edge for a sharp-edged flat 60° delta wing at α 's greater than 14° (Wentz and Kohlman, ref. 15). Therefore, for the F-106B configuration the lift differences at the higher alphas may be due to the inability of the code to model the flow physics accurately with the number of points available. Regarding the computational solution at $\alpha = 30^\circ$, it is known that this one did not converge to a steady state value.

The major difference noted in the 10° to 20° α range is the actual level in C_L . This difference may also be attributable to the relatively few number of computational points available to resolve the configuration and flow field.

Examining the pressure data portion of this figure, it should be noted that there are no measured pressure data available for comparison with the computed values. The results at $\alpha = 19^\circ$ show the expected drop in suction peak in going from x/c of 0.51 to 0.89. The relatively high suction pressures near the air location leading edge is attributed in part to a modeling difficulty associated with the solution of

the Euler equations at a leading edge and in part to the small number of grid points available.

Figure 42 provides a comparison of the vortex core result and that from the FVS solution discussed previously. The vortex system chosen from the flight test is the one associated with the vortex nearest the leading edge, and it appears at the extreme right in the enhanced photograph shown at the top right in this figure. The selection was based on the fact that only the outer vortex extended to the leading-edge at the light-sheet station and had the necessary progressive inboard movement with increasing α . (See McGregor, ref. 57.)

On the left side of figure 42 the theoretical core locations from the FVS and Euler codes are shown. The core for the FVS is at the end of the free-vortex- sheet and is indicated by the triangle. For the Euler code a cross section of the flow-field velocity vectors just behind the light sheet plane is shown. Superimposed on it is the core location, indicated by the square, as determined from static pressure contours. To establish the core location along the light sheet plane, linear interpolation was used.

The core locations from the preceding are summarized at the lower right of figure 42 for $M \approx 0.4$ and $\alpha = 19^\circ$. The measured location in flight was made during a 1-g acceleration maneuver at 25,000 feet, and has an accuracy of + or - one inch. A comparison of the lateral core positions shows that they are all within 30 inches of the leading edge with the measured location slightly inboard and nearer the FVS result. Regarding the height of the core, it is seen to be well predicted by the Euler code.

In searching for the causes of the disagreement between the predicted and measure core location, it is clear that the differences are associated with unmodeled and/or unresolved effects. This suggests that the F-106B configuration needs to be run in a Navier-Stokes code with a sufficiently fine grid in order to resolve the geometry and subsequently all appropriate flow features.

Navier-Stokes code The Navier-Stokes (N-S) equations differ from the inviscid Euler ones in that viscosity is inherent regardless of the numerical solution. Hence, these equations naturally admit and can resolve the viscous, wing-surface, flow-field. This allows the previously missing secondary and tertiary vortices effects to be estimated. Often, a thin layer approximation to the Reynolds averaged N-S equations is sufficient for many aerodynamical problems. The term thin layer means that the viscous effects are focused near the solid boundaries, in a manner similar to the boundary layer approximations. An example code which does this is CFL3D, due to Thomas et al. (ref. 58).

A computational example of this code is for the same $A = 1$ delta wing (Hummel, ref. 48) previously examined with the FVS code.

Application to $A = 1$ delta. This $A = 1$ delta wing is modeled with a grid of $129 \times 65 \times 65$ at $M = 0.3$ and a $R_n = 0.95 \times 10^6$ in laminar flow. The lift and surface

pressure results for this wing are presented in figure 43. This figure shows that good absolute lift agreement exists up to $\alpha = 33^\circ$ and that the proper lift trend is reproduced at the higher values of α . Since the predictions over-estimate the peak C_L value, there exists an apparent offset between the two sets of lift results. The offset is associated with a flow modeling difficulty in the vortex breakdown regime which exists for $\alpha > 33^\circ$.

Regarding the suction pressures at $\alpha = 20.5^\circ$, it is noted that for the forward stations, the overall level under the primary and secondary vortices agrees closely with the experimental results. The differences at the aftmost pressure station are attributed to the presence of unmodeled turbulent flow.

This figure illustrates the possible improvements available over the previous delta wing results, in both the lift curve and surface pressures, when one uses a code which incorporates approximations to the N-S equations.

FOR USE IN DESIGN

Complete Wing

General: Two example methods are highlighted which yield low drag solutions for a complete wing design in the presence of leading-edge vortical flow. The first is associated with Lamar et al. (ref. 59) and begins with an attached-flow, complete wing camber and twist design. Then this shape is operated on by a geometrical constraint and the VLM code coupled with the Suction Analogy (VLM-SA), in a manual design-by-analysis mode, to achieve the final shape. The second code (WINGDES2) associated with Carlson and Darden (ref. 60), is subsonic or supersonic, shares some features with the first method but the whole process is more automated. The method of reference 60, also based on a vortex-lattice representation, has two design modes known as "whole wing" and "mission-adaptive". The latter mode which has a special provision for the design of flaps will be presented here.

Each method is illustrated by an application, a cranked wing for Lamar and a swept trapezoidal wing for Carlson.

Lamar The assumptions and design procedure of Lamar et al. (ref. 59), along with the resulting comparison between predictions and measured data for a Pre-SCAMP cranked wing follow.

Assumptions The inherent assumption, basic to the use of the suction analogy for a cambered-wing, is that the leading-edge vortex system would promote reattached flow near the leading edge. As is well known with the addition of positive camber to a wing, the potential-flow lift will increase at a positive angle of attack. This increase is, however, coupled with a condition in which the flow is more nearly aligned with the leading edge. The "alignment" does two things in the real flow: 1) the leading-edge vortex that is formed near the edge will not only reattach near it, but on a surface which is inclined so as to yield an effective suction or negative drag, and 2) reduces the lift associated with vortex flow. Hence, there exists a dichotomy which

must be balanced. A related assumption is that this vortex system will be small, not be shed inboard but extend to the tip, and begin to come into play only on the upper surface as the design C_L is approached. Therefore, the procedure to be followed is based on the flow being not far from the smooth on-flow condition. Hence, an attached-flow solution for smooth on-flow is obtained from a mean camber design method (the VLM technique of Lamar (ref. 61) is employed herein) and used as the initial warped surface

Design Procedure and Application: The design conditions sought for the joint NASA-General Dynamics cranked wing were $C_{L,d} = 0.5$ and $M_\infty = 0.9$. In addition, a rooftop ΔC_p distribution ($\alpha = 0.7$) was initially specified along the chord. It should be further noted that the resulting solution for span load from the VLM attached-flow design code was elliptical in keeping with minimum vortex-drag considerations. The method employed uniformly 20 horseshoe vortices chordwise at each of 10 equally spaced spanwise stations on a semispan. This pattern was also used in the VLM-SA code.

The preceding conditions led to the smooth on-flow incidence distribution shown in figure 44 for the "wing box". The term wing-box incidence refers to the incidence of the center portion of the wing chord (for this study assumed to lie between 15 and 75% of the local wing chord). The extreme variation of the structural box twist, depicted in this figure, from the side of the fuselage to the tip required for smooth on-flow would be impractical for any real aircraft configuration. In order to provide a more practical design from structural and aerodynamic standpoints, the final box incidence distribution (restricted to 12°) was used, as shown in this figure. Here the structural box remains at an essentially constant incidence and is twisted only over the outermost 15% of the semispan.

Lines connecting the wing-box leading and trailing edges at four different span stations for the final incidence are shown in figure 45. Though the x/c and x/c scales are different, the relative incidence variation across the span is discernable. Associated with each of these lines, as well as the other stations across the wing, is the initial smooth on-flow camber rotated by the difference of the two α_i curves in figure 44 and passing through the trailing edge. This combination of incidence and camber was then analyzed using the VLM-SA procedure to determine lift, drag, and the strength of the suction force along the leading edge and to provide a reference for successive modifications. The camber ahead of the wing box (the 15% chord) was then represented by five equal semispan cambered leading-edge flap segments whose deflection angles were adjusted parametrically while monitoring the VLM-SA drag level. Even though these levels were optimistic, they were considered reliable in estimating the proper trend of lowering drag with flap deflection angle. After a set of angles was obtained about the 15% chord line which produced a minimum drag value, the resulting camber was smoothed and the process was repeated about the 2.5% chord line. These smoothed camber lines are shown in figure 45 and labeled the final designed camber. It should be noted that the final camber shapes are

changed in the direction of the initial incidence distribution (shown in figure 44).

In order to put this camber on the wing, two things were done. The first was to shift the local camber distribution vertically to provide a constant elevation along the wing midchord. The second was to match the fuselage incidence to the final inboard wing incidence to provide an even wing-fuselage juncture. (Note that the $C_{L,d}$ occurs at an α of

about 9.4°.) Photographs of the designed wing mounted on an existing fuselage appear in figure 46.

For the final camber, the VLM-SA code indicates that $C_{L,d}$ occurs at a wing α slightly larger than required for smooth on-flow all across the span. If the flow features which are indicated are largely realized, then this should enable a large amount of the available leading-edge suction to be recovered at the design point.

Data obtained for the cranked wing, whose design was just detailed, are compared in the next section with theory, and an assessment of the design procedure is made therein.

Lift The lift comparison presented in figure 46 shows that the VLM-SA method (solid curve), obtained by combining the potential-flow results with the vortex lift from the leading and side edges, predicts the measured lift well over an α range of 3° - 12°. Above $\alpha = 12^\circ$, there is a loss in the amount of vortex lift realized, partially due to the lack of flow reattachment in the region of the wing-tip trailing edge as a consequence of the real flow having insufficient chord there to permit the finite-sized vortex to develop reattached flow and full lift. (For wings with trailing-edge notching this lift loss is increased.) Regarding the comparison with the solution from potential theory plus 100% leading-edge suction, it is apparent that up to about $\alpha = 8^\circ$ the effect of the vortex flow is to reduce the lift, indicative of reattachment on the lower surface. Another interesting feature of obtaining $C_{L,d} (= 0.5)$ with vortex flow is that in comparison with the potential-flow solution for this same cambered wing an angle of attack of about 2° less is required. Of course, it is realized that this wing was not designed to reach $C_{L,d}$ with potential flow. Still it is interesting to realize that theoretically there is an angle-of-attack reduction possible if vortex flow is present on the slender cambered wing, especially since vortices would tend to form naturally on such a wing.

With regard to the 0% suction with no vortex lift and the 100% leading-edge suction solutions, it is note-worthy that the presence of the potential flow leading-edge suction on the highly cambered leading edge actually reduces the C_L over the α range shown. This is, of course, due to the edge force acting tangentially to the highly cambered leading edge, thereby creating a negative lift force.

Drag polars Figures 46 to 48 present the drag data and other data to aid in its interpretation. For example, figure 46 shows both the planar and cambered wing drag polars in comparison with two theoretical curves. Over most of

the C_L range the planar-wing data follow the upper or zero edge-force curve as expected. The cambered-wing data are generally much lower than the planar-wing data and approach the lower bound polar in the C_L range of about 0.35 - 0.45, even though the wing is thin (maximum thickness/chord ratio = 3.2%) and the leading edge is sharp. Furthermore, at the design C_L the data reach a level equivalent to 77% of full leading-edge suction. This large value of equivalent suction is remarkable for such a slender wing, particularly at this high Mach number maneuver condition. The data further show that a larger fraction of leading-edge suction is realized at $C_L = 0.4$, indicating that the wing mean camber surface has not been fully optimized at the design C_L .

Figure 47 displays the same cambered-wing drag data but here in place of the planar-wing lower bound polar are two attached flow polars obtained from the VLM-SA code. One is for full edge force, 100% leading-edge suction and the other for no edge force, 0% leading-edge suction. It is well known that a planar wing of the same shape will have more edge force than a corresponding cambered wing under the same conditions, because a portion of the suction available on the cambered wing is distributed chordwise over the surface. Thus, the figure shows that the displacement between the full- and no-edge-force curves to be smaller than for the planar wing. Further, the data are quite close to the full-edge-force curve for C_L values equal to or less than C_{L4} . This is in keeping with the original idea of being at an angle of attack slightly above that for smooth on-flow, in that at smooth on-flow full suction is realized but is distributed over the cambered surface. In terms of the suction available, this cambered wing achieves a level of effective leading-edge suction of about 67%.

Axial force Another way to establish when flow changes occur on the wing, beyond examining the lift curve, is to examine the axial force, since it is a sensitive measure of the edge flow. Figure 48 shows the axial-force coefficient variation for the cranked cambered wing as a function of $\sin^2 \alpha$, because both the edge-force and vortex-flow terms have this dependency. It is interesting to note the sharp change in the C_A variation near $\alpha \approx 9^\circ$, because at this same α the lift data of figure 46 show a rapid change

The faired straight lines in figure 48 have associated with them labels describing the types of flow which are hypothesized to be present. From the insets of planview oil photographs, it is clear that at both $\alpha = 5^\circ$ and 10° the flow on the upper surface appears to be attached even though the C_A curve shows that some change in the data has occurred. It needs to be remembered here that, since this leading edge is highly cambered, the flow at the edge cannot easily be seen from the top. At $\alpha = 15^\circ$ there is a definite indication of vortex activity on the upper surface, which means that the vortex system has just formed or become strong enough to be noticeable.

Carlson the "mission-adaptive" design-mode method of Carlson of Darden (ref. 60), to be illustrated here, has a feature which allows it "to provide a twisted and cambered

surface restricted to specified wing regions". The resulting cambered regions near the leading- and trailing-edges may then be represented with flaps. The basic premise is that with most of the wing fixed, say due to structural constraints, there exists a particular combination of leading- and trailing-edge flap deflection angles which will yield the lowest drag or highest effective suction. The concepts of attainable thrust, suction analogy and vortex action point are all employed in this design mode of Carlson's method.

This method is applied to the 60° swept trapezoidal wing shown mounted on a body in figure 49 in the following way. Firstly, the "whole-wing" design mode is employed at specified values of C_L , M and R_n . These results provide a camber surface, which the designer may find helpful in selection of "mission-adaptive" or flap system design areas consistent with structural or other considerations. The "whole-wing" solution also provides a design moment, $C_m = -0.17$, which in the absence of any other specific C_m constraint is used in the next step to insure an effective contribution of trailing-edge flaps to the overall lifting efficiency. Secondly, the program is run in the "mission-adaptive" mode with C_L , M , R_n and C_m specified along with a definition of the design area in the form of spanwise leading- and trailing-edge chord distributions. The results of this second run provide a "mission-adaptive" wing camber surface shown in figure 49. Superimposed on each of the mean-camber surface wing sections are the flap-hinge-line locations and the limits of the design area. The code also provides for automation of a flap-fitting strategy, illustrated in figure 50. The idea is to replace the smooth program generated camber surface with straight line segments to approximate the design camber surface and its loadings. The resulting schedule of leading- and trailing-edge flap deflections is referred to as "code" in the inset sketches of figure 49. Thirdly, the designer selects an appropriate flap segmentation plan. On this figure it is labeled "modified" and consists of four leading-edge and two trailing-edge flap segments. Fourthly, using these segmented flaps a separate but related analysis code SUBAERF2 may be used to provide an estimate of the actual flap system performance [Much of the text in this paragraph has been contributed by Carlson in a private communication.]

No direct comparison with data is given in reference 60; however, an off-design situation is analyzed for a two segment leading-and trailing-edge flap model and the results shown in figure 51. The analysis predicts the measured values well.

[The analysis code SUBAERF2 can also be used in a design mode. It is done by varying the leading- and trailing-edge flap angles systematically while recording the suction level achieved for each combination. The suction levels and flap angles are then used as basis data in developing a "thumbprint" or an "optimization" chart to help select the best combination.]

Leading-Edge Vortex Flap

General: Designing a wing with leading-edge vortex flaps (LEVFs) is distinguished from that of Carlson's complete wing method in that for this design problem the hinge line is assumed known but the flap shape (leading-edge outer boundary) and its deflection are not. The reader is reminded that the LEVF is just a special purpose leading-edge device, as discussed by Lamar and Campbell in reference 62 and illustrated in figure 52. Initially, the function of these flaps was envisioned to be that of drag reduction for slender wings while maneuvering at moderate to high α . Since then other functions have been conceived, as detailed in the cited reference. Regarding the accomplishment of the initial function, it was to occur as a result of the flap providing appropriated capture area and orientation for the entire separation-induced shed vortex system above itself. Due to the downward deflected orientation on the forward facing surface of the flap, a substantial suction force was generated in the thrust direction to provide the drag reduction. Furthermore, the "captured" vortex also functions as a rotating fluid cylinder to turn the flow around the leading edge onto the wing upper surface, thereby promoting a smooth transition to attached flow on the wing near the hinge line.

Two methods are highlighted for designing the planform of the LEVF. The first is that of Frink (ref. 63) given in concept form, and the second is that of Huebner (ref. 64) given in some detail. An example of each is given for a F-106B configuration. [For other applications the interested reader may refer to the three conference publication volumes dealing with Vortex Flow Aerodynamics (refs. 65 to 67).]

Frink: As illustrated in figure 53 this concept was originally validated in 1978 on a highly cambered Pre-SCAMP design, just discussed. It was further demonstrated during the same wind tunnel test that comparable levels of maneuver performance improvement could be achieved by deflecting certain combinations of simple planar leading-and trailing-edge flaps on a planar wing of the same planform. The simple flap results were very attractive from a practical design and fabrication standpoint and warranted further study. As represented in figure 53, many additional experimental and analytical studies were conducted on the simple flap concept. An examination of the results from these and other studies led Frink in 1982 to the development of a LEVF design procedure - published as reference 63. A typical result is shown on the lower right of this figure.

Another example is given by Lamar et al. in reference 12 for the F-106B aircraft. There the aerodynamic design of the LEVF was developed through an iterative process that encompassed Frink's procedure, wind-tunnel results, and practical considerations and constraints. A flight photograph of the LEVF mounted on the aircraft is shown in figure 54. The associated flight test program - in which pressure and flight performance data and vapor-screen images are recorded - is scheduled for completion by the spring of 1991. [The housing for the rotating-light-sheet system - one of three systems needed in order to obtain vapor screen images -

is seen on this photograph to be located just ahead of the vertical tail. Details of this system are also provided in reference 12.]

Huebner: The design procedure of Huebner (ref. 64) is based on the analysis method of VORCAM and shares with Carlson's wing method the idea of arriving at an appropriate amount of flap area and deflection angle. However, as previously noted, this procedure differs from Carlson's method in that the shape of the leading edge is a part of the solution. This procedure also differs from that of Frink in that the flap geometry can extend beyond the wing leading edge, i.e. a "bolt-on" flap implementation, and uses a numerical optimizing procedure. The primary goal of this effort was to develop the vortex flap planform, deflection angle, and wing angle of attack to maximize L/D and satisfy $C_{L,A}$ at $M = 1.5$ for the F-106B. This speed was chosen as typical of a supersonic maneuver for an advanced tactical fighter. The F-106B was chosen as the application aircraft since its 60° swept leading edge is capable of generating measurable amounts of vortex flow.

Analytical Flap Modeling: Figure 55 shows the modeling of a typical flap with its design variables (geometrical features) in flap coordinates. The X_f axis corresponds to the wing leading edge (hinge line) in global axes, and the dimensions of the flap have been normalized to have a range of zero to one. The Y_f variable determines the flap planform shape. Using the VF-D4 flap - developed by Frink - as an initial guess, this procedure models the planform shape in three regions. Regions one and three are parabolas which are uniquely defined by their two end points and a slope condition at the points where they meet with region two, which is a straight line. The specific design variables needed to define this flap are shown in the figure. $X(1)$ and $X(2)$ determine the extent of the three regions in the X direction, $X(3)$ through $X(5)$ provide actual planform chord length and ultimately planform shape, $X(6)$ specifies the flap deflection angle and $X(7)$ is the model angle of attack.

It is worthy to note a few things about this method. The apex of the flap is shown to be at the origin of the flap axes. In reality, the chord length at this point need not be zero, but it is not a design variable and remains constant throughout the design process. The value of $X(1)$ can go to zero while the value of $X(2)$ can go to one. Thus, the possibility exists that a flap design solution could yield a constant chord, taper, or inverse taper flap. Furthermore, the value of $X(6)$ was chosen in such a way that it represents the arctangent of the flap deflection angle.

Certain geometrical constraints arise based on this method. In order to restrict the flap to a reasonable size, $X(3)$ through $X(5)$ are constrained such that their maximum values are no more than 10% of the leading-edge hinge-line length. Also, to avoid meaningless flap shapes, the value of $X(2)$ must be greater than or equal to $X(1)$.

Procedure. The flap-design-optimization process is given in outlined form in figure 56 with additional details provided in both Huebner (ref. 64) and Lamar (ref. 68).

Application. An application for the F-106B is given at the design condition of $M = 1.5$ and $C_L = 0.223$.

The initial geometric design variable values $X(1) - X(5)$, associated with the supersonic application, were taken from the design solution of vortex flap VF-D4 at $M = 0.3$, along with $X(6)$ which specifies flap deflection angle. The design variable $X(7)$, which determines α was started at an arbitrary value corresponding to $\alpha = 4^\circ$.

Figure 57 shows the initial and final planform shapes and other pertinent results from this design study. The flap chord has decreased for most of the flap, designated VF-DO1, except near the flap tip where it increased slightly. Flap planform area decreased by 6.5%. The flap deflection angle converged at 18.47° , which is quite close to the slope value at and perpendicular to the leading edge of the cambered wing. Finally, the angle of attack converged at 5.06° .

A comparison of the computed aerodynamic performance of VF-DO1 and VF-D4 on the F-106B is shown in figure 58. The VF-DO1 design shows an improvement in L/D at $C_{L,d}$ of 0.6, or 9% over VF-D4 at 10° deflection. Further, the improved L/D values extend throughout the entire C_L range. The initial design solution is also included to show the total performance improvement from the beginning to the end of the design process.

Figure 59 shows the aerodynamic characteristics of these two flap designs at $\delta_{LE} = 30^\circ$ and $M = 0.3$. The purpose of this is to determine the aerodynamic characteristics of flap VF-DO1 at an off-design Mach number. Minor variations occur for C_L and C_m versus α , however, a measurable improvement in L/D,max is noted. Thus, this figure indicates that the flap optimized for $M_d = 1.5$ would be quite satisfactory at $M = 0.3$.

A vortex flap designed for the F-106B at subsonic speeds is also given by Huebner in reference 64.

STABILITY AND CONTROL IN HIGH-ALPHA RANGE

This chapter examines stability and control both analytically and experimentally in the α range up to high- α . The analytical results presented are based on the analysis methods described in the preceding chapter, are focused more on stability rather than control, and are compared with experiments. The experimental stability-and-control results presented are not restricted to those situations that can be predicted, but include those from devices which are likely to be successful in providing either longitudinal and/or lateral control in this α range.

PREDICTIONS FROM ANALYSIS METHODS

General

Selected longitudinal stability results have already been presented with the introduction of the various analysis methods

In this section only predictions from SA methods will be shown since it is very general and has been widely applied. [Though SA only applies to the vortex flow contribution to force and moments computed by potential flow methods, in this chapter its usage is sometimes broaden, for reporting purposes, to include the potential flow contribution.] The examples shown cover geometries from isolated planforms to interfering wing surfaces and at speeds up to supersonic. The order of presentation will be (steady) longitudinal, including some configurations for which only C_L is presented, and then lateral characteristics, which include both a steady and an unsteady example. [Other examples can be found in the cited references.]

Longitudinal

Simple shapes: Comparisons are presented here for six pointed wings with round and sharp leading-edges at subsonic speeds. The configurations range from arrow to diamond

Delta wing with LE radius. Figure 60, taken from Lan and Hsu (ref. 69), shows an application of the QVLM-SA method to a 60° delta wing with a round leading edge at low speeds. The SA predictive curve is labeled "thin-sharp" and is seen to estimate the measured C_L and C_m results well up to 10° and 16° , respectively. When the round leading-edge effects are accounted for by using Kulfan's technique, Lan estimates a noticeable aerodynamic effect. This leads to an extension of the α range for which the C_L and C_m agreement is good, 16° and 20° , respectively. The lack of agreement beyond these α values means that there is still an unmodeled effect. It is obviously associated with vortex breakdown, which is known to commence at the TE on a thin-sharp delta wing of this sweep near $\alpha = 12^\circ$. Lan and Hsu (ref. 69) developed a procedure for quantifying this effect with α and when employed for this wing produces good agreement over the entire α test range.

Pointed wings: Figure 61, taken from reference 16, and figures 62 and 63, taken from reference 28, present experimental and predicted C_L data for a variety of pointed wings. Regarding figure 61, it should be noted that since these wings have no tip chord the $K_{v,te}$ values are all zero, however, this does not preclude there being an augmented, $K_{v,te}$, term. In fact, since the sign of the augmented term depends on the sign of \bar{c} it is interesting to note that three of these wings have positive values and one has a negative value. Positive augmented values produce lift above that of SA, whereas the converse is also true. Note the improved agreement at $M = 0.6$ achieved when the augmented terms are included in the C_L estimate.

Figures 62 and 63 present the C_L and C_m results for the top two wings in figure 61, but at a lower and higher subsonic Mach number. These figures show that the ability to predict the experimental C_L is similarly improved at these Mach numbers. Both figures also show that this extension to the SA gives a tremendous improvement in the ability to predict the experimental C_m . This is more true for the diamond wing than for the arrow, since the diamond wing effectively

adds area in the region where reattachment can occur, whereas, the arrow effectively removes area. In addition, the trailing-edge wake from the arrow wing can interact with the leading-edge vortex system so as to move it farther from the wing, thereby further decreasing its influence in the aft region.

Geometrical combinations Comparisons are presented here for five combinations of wings. They include a cropped-double-arrow wing, a wing-canard, a strake-wing-body, a cambered-thick lifting-body and wing combination, and a cropped-delta-wing body. The speed range covered is both subsonic and supersonic.

Cropped-double-arrow wing: The thin, sharp, uncambered, complex configuration of figure 64, taken from Lamar (ref. 70), provides a good illustration of how the various vortex-flow terms can be used to estimate the longitudinal aerodynamics at low speed. (Note that the figure legend groups these terms by moderate or high α , which just recognizes that the particular elements of each group differ according to the local flow features, as outlined in figure 27.) In particular, at moderate α 's there are two $K_{v,le}$ and $K_{v,ae}$ terms (an inner and outer pair associated with each vortex system) and a $K_{v,se}$ term. At higher α 's, the two leading-edge vortex systems are expected to merge into only one which extends from the apex along the wing leading edge to the tip. This system can be represented by a single $K_{v,le}$ and $K_{v,ae}$ term which is then combined with the previous $K_{v,se}$ term to produce a total vortex flow effect.

The determination of the \bar{c} term used in $K_{v,se}$ and \bar{x} used in estimating C_m needs to be further detailed for completeness (The reader may find it useful to refer to figure 26 for the \bar{c} variation with α justification.) In particular, at moderate α 's \bar{c} for the inboard system is just the streamwise distance from the leading edge to trailing edge at the span location where the wing sweep changes, and for the outer system \bar{c} is the tip chord. Each associated \bar{x} term is the halfway distance along \bar{c} since the area being represented is rectangular. At higher α 's \bar{c} is the streamwise distance from the tip leading edge to the trailing edge apex, which for this wing is a small positive number. The associated \bar{x} is computed the same way as before since the area represented is also rectangular.

Considering now the predicted and measured results presented in figure 64, it is clear that the high α theory gives better overall agreement than either the moderate α or potential theories, as expected. The C_L experimental data are well predicted up to nearly 28° and the C_m up to 16° . For higher α 's the vortex system grows in size and moves farther from the surface overall the wing, especially in the aft region. This gives rise to the forward part of the wing still lifting well, whereas the aft portion responds to the effects of vortex diminishment and finally breakdown.

Other examples of complex wings are given in reference 70.

Wing canard Figure 65, taken from reference 16, presents applications of the SA to a wing-forebody and a wing-canard at low speeds. Only the wing C_L results are shown, on the

left in the presence of the forebody, and on the right in the presence of a high canard ($z/\bar{c} = 0.185$). The wing-forebody comparison shows a variation typical of wings with moderate sweep because they are known to have a low α departure and vortex breakdown, which leads to the SA overestimating the experimental results at α 's above 8° . However, in the presence of the high canard, a favorable interference results, and even with the reduction in $C_{L,p}$ on the wing, due to canard downwash, the predicted amount of vortex lift is developed on the wing. The measured results are well predicted over the α range and reach higher C_L values than those for the wing in the presence of the forebody.

Strake-wing-body: Figures 66 and 67, taken from Lamar (ref. 68), present comparisons between experimental and theoretical data for a complete strake-wing-body and for its components, strake-forebody and wing-afterbody. The theoretical results, called high- and moderate- α have already been developed and outlined on figure 27. (Additional modeling details can be found in reference 71.) For the complete configuration (fig. 66) at $M = 0.2$ it is seen that up to $C_{L,max}$ the measured C_L data is better predicted by the high- α method. Above the corresponding α , neither theory appropriately models the flow. It is also seen that the two theories generally bracket the C_m data, again up to $C_{L,max}$ or vortex breakdown. The ability of these two simple theories to do this is encouraging, in that they are able to estimate collectively the general nonlinear C_m versus $C_{L,tot}$ characteristics for this class of configuration. It can be noted that the moderate- α theory may, in general, estimate better the C_m results than those obtained with the high- α theory. This occurs because the moderate- α theory produces a load center farther aft at a particular value of $C_{L,tot}$ even though this value is larger than the data at the same angle of attack. The potential-flow curve is added to the $C_{L,tot}$ versus α plots for reference.

The wing afterbody and strake-forebody longitudinal aerodynamic data and the high- α and moderate- α theories are given in figure 67 for $M = 0.2$. Just as for the complete configuration, the individual data components are generally well estimated by the high- α theory or a collective combination of theories up to $C_{L,max}$ or large-scale vortex breakdown. What is particularly useful is that the individual C_m components are tightly bracketed by the high α and moderate- α theories. The C_L data for the strake-forebody are, in general, reasonably well estimated by the two closely spaced theories until the strake vortex begins to break down on the stike at the higher values of α . The spacing between the two theories is larger for the wing afterbody, with the data tending to be generally on or above the estimates from the high- α theory. This continues until the strake vortex begins to break down ahead of the wing trailing edge. From this figure it is seen that, in general, this configuration has its aerodynamic components better estimated by the high- α theory. Lastly, note that at the higher angles of attack the wing-afterbody lift variations follow the potential curve even though the flow is closer to a Helmholtz type.

Cambered thick lifting body and wing A proposed hypersonic research aircraft configuration composed of a

cambered-thick lifting body and a cambered wing is shown in figure 68 (taken from Lamar, ref. 72). Several different ways of modeling the various wing, body and augmented vortex-lift effects developed on this configuration at $M = 0.2$ were examined using the VLM-SA code. The method which worked best in estimating the experimental data was the one which only included the cambered-wing leading- and uncambered-wing side-edge vortex-lift terms - added to the potential terms - and is given in figure 69 by the solid curve. The VLM-SA computational model for this configuration included the body and wing mean-camber slopes, wing dihedral, but not thickness.

This representation is seen to be sufficient to well predict the values of C_L, C_m , and C_D . A comparison of the results also shows that reasonably good overall lift and drag agreement is achieved. However, both the C_L and C_m are only well estimated up to an α of about 16° . For larger α 's, the influence of the vortex system is evidently getting smaller over the aft portion, most likely due to vertical displacement, which causes the measured C_L and C_m to decrease and become more nose-up than predicted, respectively. However, the overall results are quite encouraging given the modeling of the configuration.

Cropped delta-wing body: Figure 70, taken from reference 16, presents a comparison of the aerodynamic characteristics obtained on a cropped-delta wing-body model tested at $M = 1.2$ with the SA method results for the wing alone at the same Mach number. The comparison shows that inclusion of the leading-edge-, side-edge-, and augmented-vortex-lift effects leads to improved agreement with the C_L , C_m and C_D measured results over this restricted α range. The vortex flow contributions to C_m are obtained by having the respective lifts act at their centroids, and by performing the analytic surface integration, both inside and outside of the tip cone, of the product of the potential-flow lifting pressure and its chordwise position [All C_D curves have the experimental value of $C_{D,0}$ added in]

Lateral

Steady. The QVLM-SA method, with allowance for leading-edge vortex breakdown, has been applied to a cropped delta wing by Lan and Hsu in reference 69 to determine the lateral aerodynamic characteristics. Figure 71 shows the agreement with the experimental results to be remarkable. Lan points out that the inclusion of the side-edge vortex terms is important to get this good agreement. (The steps noted in the theory curves are due to the vortex breakdown criteria - developed in this reference - affecting each side of the model differently at α with $\beta \neq 0$, i.e., dependent upon the local flow conditions present.)

Unsteady. Figure 72 shows results obtained by applying the unsteady suction analogy of Lan (ref. 38) to the prediction of oscillatory roll damping for a gothic wing. Shown are experimental and theoretical data for C_l versus α for reduced frequencies of $k = (\omega b/2U) = 0.75$ and 1.20 . The theoretical results predict the experimental data quite well primarily due to an appropriate modeling of the vortex lag

and convective effects. Note the reduction in roll damping which occurs at high α 's due to a vortex-induced effect. This feature offers a possible explanation of the wing rock phenomenon encountered by slender wings geometries operating at those attitudes.

EFFECTIVENESS OF CONTROL DEVICES

General

Conventional control devices on aircraft may be effective in this α range if they have been properly integrated into the dominant flowfield of the configuration. Alternatively, non-conventional devices which work with vortical flowfields should prove effective. A few selected devices are examined to illustrate these points.

Aileron

The rolling moment generated by a single trailing-edge aileron tip-mounted onto a cropped delta wing is illustrated on the left side of figure 73, taken from reference 68, as a function of α . This aileron is immersed in the vortical flowfield off the wing leading-and side-edges and at a 5° deflection its effectiveness at generating rolling moment is constant to the highest test α . Deflection angles higher than 5° were tested, but the growth in rolling moment does not increase linearly with deflection. Therefore, the effectiveness is degraded at the higher deflection settings.

Vortex-Flow Roll-Control Device

The vortex-flow roll-control device, in proof-of-concept form, is also shown in figure 73. This device seeks to develop useful lateral characteristics by generating flow asymmetries through a planform geometry modification. In particular, the intent of the geometrical change is to alter the symmetrical flow situation by modulating the leading- and/or side-edge vortex system on the raked-tip side and by regulating the amount of area downstream of the tip leading-edge on which the vortex system has to act. The experimental results in the middle of the figure show the significant and linear, left-wing-down, rolling-moment growth with α for a tip rake angle of 5° . Though zero rolling moment is produced at zero deflection, the middle figure shows the C_l value for this device to first exceed that of the aileron, just discussed, near α of 12° .

The effect of increasing the tip rake angle at an α near 18° , shown on the right in figure 73, is also to produce an almost linear increase in rolling moment. The results of the preceding indicates a potentially useful device, which would work best when both tips were deployed in the same direction - either right or left. Another feature of this device, though not shown, is that it produces either no- or a perverse-yawing moment.

The potential theory curves shown here were determined from combinations of symmetrical model analyses, and are seen to account for only a small portion of the measured rolling moment.

Leading-Edge Vortex Flap

Rao and Campbell in reference 73 discuss many vortical flow devices which can be used to manage this flowfield in a useful manner. Among them are full-span or segmented leading-edge vortex flaps which operate on the lower or upper surface. The lower surface LEVF have already been discussed in the design section, so the upper surface type, shown in figure 74 (taken from ref 73), will be considered here. This figure shows a full-span LEVF and how it functions at moderate and high α 's. Rao reports that at moderate α 's "a vortex forms inboard of the flap whose suction generates drag on the flap, but also increases lift on the exposed wing area." [Rao actually used the term "low", but the term "moderate" is employed here for textual consistency in this lecture.] Thus, the LEVF behaves very similar to a thin, unflapped, highly-swept wing with a sharp leading edge in the same α range. Whereas, at a high α condition Rao notes that "a dominant vortex develops in front of the flap while the inboard vortex tends to weaken, the net effect being a thrust force." This is a relatively new flow feature, and therefore one which has not been fully exploited. Since the local vortex flowfields behave differently in these two α ranges, Rao suggests that this device has "potential applications in different flight regimes".

Figure 75, also taken from reference 73, shows some potential uses of a segmented version of this device at high α 's. The top sketch indicates how it can provide a drag reduction by deploying all four segments at a high lift condition in order to get the thrust benefit off the front surface of the flap. The middle sketches show how pitch-up or pitch-down can be managed by deploying only the rearward or forward pair, respectively. By manipulating the flaps in this manner the lift is maximized ahead of or behind the center-of-gravity, respectively, giving rise to the associated moments. The bottom sketches display how roll and yaw control can be accomplished through deployment of the devices on one side only and a coupling of the right-front segment with the left-back one, respectively. The right roll is produced due the deflected flap vortex-system being farther outboard than that for the undeflected side. The right yaw is associated with the thrust on the deployed flaps being properly oriented with respect to the center-of-gravity. These examples highlight single degree-of-freedom motions, but it is clear that with an appropriate-control-system and with properly sized flap segments controlled maneuvers about more than one axis at a time are possible.

POST-STALL-FLIGHT CHARACTERISTICS

This chapter examines the problem of post-stall flight, or flight at higher α 's, and offers some potential solutions. In addition the benefits associated with "dynamic stall" are introduced and an engineering method given for estimating the effects. Lastly, since flight at the higher α 's impacts not only the aircraft aerodynamics but also the engine/inlet flowfield, a brief discussion is given of ways to minimize this effect.

PROBLEM STATEMENT

Aircraft operating at post-stall-flight conditions are susceptible to quickly occurring, unusual motions - including tumbling, spinning, coning, wing rock and nose slice. These motions are caused by the flowfield around the vehicle becoming asymmetrical, unorganized and/or unsteady. Associated with the change in flowfield is a degradation in aircraft control, primarily lateral, even at zero sideslip. This is illustrated in figure 76, taken from Mumford and Rao (ref. 74), as a loss in available yaw control at higher α 's just when the requirement for control is increasing. The significance of the flow/control changes, with respect to current fighter aircraft, is better understood when one considers the evolution in design which has occurred for this class of airplanes in the last 50 years. In particular, these aircraft now have a substantial portion of the vehicle ahead of the center of gravity, as reported by Chambers (ref. 75) and shown here as figure 77. The consequence of this is to make the aircraft very susceptible to differential changes in the lateral flowfield over the forward part of the configuration. [The reader is referred to the two papers by Chambers (refs. 76 and 75) for a discussion of high α effects and experimental solutions, in particular stall/spin, on fighter and general aviation aircraft.]

Apart from lateral solutions suggested by novel flow control methods on an aircraft, it is still possible to use design criteria for the "prevention of directional departure due to either stability or control characteristics", as noted by Chambers (ref. 76). In particular, military aircraft are more likely to be resistant to directional departure if both $C_{n_{2g}}$ and the Lateral Control Divergence Parameter (LCDP) are > 0 . These criteria - defined in figure 78, are not absolutes but should be viewed as a useful guide with which to examine each new aircraft design because they are based on a large collection of correlated data. Even if a proposed design fails these criteria, there are still alternative solutions to address the post-stall-flight problem.

POSSIBLE SOLUTIONS

Possible solutions to the problem of reduced aircraft lateral control in this α range do not lend themselves well to analytical treatment with a resulting mathematical approach. Therefore, the engineering method to use is that of an experimental process, like that depicted in figure 79 - taken from Nguyen and Gilbert (ref. 77). A successful pass through this process would be one in which potential problems are identified early on and solutions verified. This section, therefore presents some possible solutions to this problem through either novel aerodynamic or powered devices.

Aerodynamic Devices

Several novel devices have been studied which offer the potential to increase the lateral control at the higher α 's. The ones presented in this section work to control the relatively small nose vortex on the long forebody, and are called nose devices. Some of the devices discussed previously, e.g., vortex-lift roll control device and LEVF (plus others)

presented in reference 68), should also be considered for flight control in this α regime.

The nose devices considered include an actuated forebody strake, jet blowing, tangential slot blowing and jet suction, as shown in figure 80, taken from reference 77. Though different in activation, all seek to change the local fluid mechanics in such a way that the nose vortex on one side of the forebody will be closer to the surface than on the other. One can view this as removing vortex symmetry. The closer the vortex is to a surface the more "suction force" it generates and the larger the yawing moment from that side. Figure 81, taken from reference 77, shows the results from one of these devices. Note how effective the actuated-forebody strake deployed on the left side of a generic model is at generating a nose right yawing moment. The effect is seen to increase with strake deflection and to peak between 40° to 55°, depending on the deflection.

Thrust vectoring

Thrust vectoring has been employed for many years on the Harrier aircraft to provide total lift at zero (and low forward) airspeed, lift enhancement during "ski-jump" takeoff and flight, and in-flight thrust reversal. Since this aircraft can "fly" at low airspeed, there is a need to augment the aerodynamic controls with a dedicated reaction control system (DRCS). Without a requirement for flight at zero air-speed, the need would no longer exist to have the engine thrust vectored (deflected) near the aircraft's center-of-gravity nor for a DRCS. In particular, if the nozzles are located in the region of aircraft rear closure, as in a conventional engine arrangement, this puts the thrust in a logical location for its deflection in order to provide effective longitudinal and/or lateral control. The preceding is the current focus in thrust-vectoring research where the deflected thrust is to impart some, if not all, of the needed aircraft control at α^* for which conventional aerodynamic controls are ineffective. The importance of this focus is reflected in the current flight research programs utilizing the F-15 SMTD, F-18 HARV and X-31 aircraft.

Figure 82, taken from reference 77, illustrates how a rudder, deflected 30°, becomes increasingly ineffective at generating yawing moment as α is increased. This is caused by the rudder flowfield not experiencing free air, but instead being exposed to increasing amounts of "the low energy separated wake" which comes from the wing and fuselage, as noted by Nguyen and Gilbert. Figure 82 also shows the contribution to yawing moment due to thrust vectoring at 10° yaw and maximum power. It is interesting to note that this effect is only weakly dependent on α . In order to minimize fuel burned during a maneuver, it would be beneficial to have the yaw-control-transition occur gradually from being fully dependent on the rudder at lower α 's to being fully dependent on thrust vectoring at the higher α 's - in a manner similar to that depicted by the idealized, aero-yaw-control curve.

The blending of aerodynamic controls, deployment of novel aerodynamic devices and engine thrust vectoring over a wide

α range is an active area of controls research.

[The reader interested in learning more about the aerodynamic and non-aerodynamic reasons for using thrust vectoring is referred to the comments by Poisson-Quinton in reference 78.]

DYNAMIC STALL

There is another aspect of flight in this flow regime that can well have a positive benefit. It is called "dynamic stall" and is associated with a pitching motion, in which the slender configuration reaches a given α rapidly before the vertical flowfield can change character, e.g. breakdown. This can occur because the vortex system has a hysteresis response during a pitching motion, as noted by Lowson (ref. 79), and leads to the phenomenon known as vortex lag with its attendant effect of keeping the vortex system coherent to a higher α . All this can lead to aerodynamic forces/momenta in excess of the static values. The study of "dynamic stall" effects has received increasing emphasis in recent years by many researchers, not only because of its positive effects but there are concerns of its impact on higher- α stability and control of flight vehicles. See, for example, the papers by Naumowicz et al. (ref. 80), Brandon and Shah (ref. 81) and Nguyen (ref. 82).

Ashley et al. (ref. 83) have put together a simple empirical theory to estimate the C_N and C_m effects of sinusoidal pitching - α motion of $(-\cos \Omega t)$ between 0° and 90° - on low aspect ratio wings. The key ingredients are to keep track of the fluid physics and an unsteadiness parameter they call K , which is related to the circular frequency and the maximum of $d\alpha/dt$. Their analysis follows. The wing's normal aerodynamic force per unit chordwise distance is assumed to consist of three parts. (1) a portion determined from the rate of change of crossflow momentum, as in slender wing theory, but with slabs of incompressible fluid oriented normal to the wing surface at α , (2) a portion calculated on a quasi-steady basis by rotating the leading-edge section through 90° (Polhamus, ref. 18) and (3) a portion dominant at the higher α 's and found by crossflow-drag considerations. In the range of α 's where instability is present above the wing, the first two parts are assumed to act only ahead of the point x_{BD} . The third part acts only behind that station and is proportional to $C_{Dc} \sin^2 \alpha$, where C_{Dc} is taken to be the measured drag (or normal force) at $\alpha = 90^\circ$. For pitching $\alpha(t)$ about an axis fixed at the two-thirds chordline [c_f], the normal force and moment about that axis are given as:

$$\begin{aligned} C_N &= \frac{\pi}{6} \left(\frac{x_{BD}}{\alpha} \right)^2 \frac{1}{\tan \Lambda} (6 \sin 2\alpha - 8 \alpha c_0/V) \cos \alpha \\ &\quad + 16(\alpha c_0/V)(x_{BD}/\alpha) \cos \alpha \\ &\quad + (\dot{\alpha} c_0^2/V^2) [3(x_{BD}/\alpha)^2 - 8x_{BD}/\alpha] \} \\ &\quad + \frac{\pi}{6} \omega \Lambda \left(\frac{x_{BD}}{\alpha} \right)^2 (6 \sin^2 \alpha \\ &\quad + 8(\dot{\alpha} c_0/V)(x_{BD}/\alpha) - 1] \sin \alpha \\ &\quad + (\alpha c_0/V)^2 [3(x_{BD}/\alpha)^2 + (8/3) - (16x_{BD}/3\alpha)] \\ &\quad + C_{Dc} [\sin^2 \alpha + (1/18)(\alpha c_0/V)^2] \end{aligned}$$

and

$$\begin{aligned}
 C_m = & -2\pi(z_{BD}/c_0)^2(c_0/\bar{c}) \frac{1}{\tan \Lambda} \{ [(z_{BD}/c_0) - 1] \sin 2\alpha \\
 & + (\dot{\alpha}c_0/V)[3(z_{BD}/c_0)^2 - 4(z_{BD}/c_0) + (4/3)] \cos \alpha \\
 & + (\dot{\alpha}c_0^2/V^2)[(3/5)(z_{BD}/c_0)^3 - (z_{BD}/c_0)^2 \\
 & + (4z_{BD}/9c_0)] \} \\
 & - \left(\frac{\pi}{6 \sin \Lambda} \right) \left(\frac{z_{BD}}{c_0} \right)^2 \left(\frac{c_0}{\bar{c}} \right) \{ 4[(z_{BD}/c_0) - 1] \sin^2 \alpha \\
 & + (\dot{\alpha}c_0/V)[3(z_{BD}/c_0)^2 - (16z_{BD}/3c_0) + (8/3)] \sin \alpha \\
 & + (\dot{\alpha}c_0/V)^2[-(16/9) + (16z_{BD}/3c_0) - 6(z_{BD}/c_0)^2 \\
 & + (12/5)(z_{BD}/c_0)^3] \} \\
 & - C_{D_c}(c_0/\bar{c}) \{ (1/9)(\dot{\alpha}c_0/V) \sin \alpha - (1/135)(\dot{\alpha}c_0/V)^2 \}
 \end{aligned}$$

Figure 83, taken from Ashley et al (ref. 83), shows measured and predicted results at a value of $K = 0.04$ where the C_m has been corrected to be about 77% c_r . They note: "The fair agreement between corresponding plots is clear." [Only one shown here.] "One can perhaps conclude that this very elementary attempt reproduces quite well that qualitative behavior of the airloads and might serve as the basis of methods for preliminary-design estimation on lifting surfaces of supermaneuvering aircraft."

ENGINE/INLET

In order to minimize the pressure or Mach number distortion across the face of an engine or inlet, a successful integration with the airframe is needed. This is especially true for fighters and is done by taking into account, early in the design cycle, the flowfield in which the inlet is to be immersed. Perner (ref. 84) illustrates this process on the Mirage 2000 where with forebody reshaping alone flowfield distortions were reduced 30%. Beyond reshaping, Leynaert (ref. 85) shows how the fuselage-boundary-layer flowfield can be kept out of the inlets through diverters (as for the Rafale, F-111A, etc.), splitter plates (as for the Rafale), or bleeds (as for the YF-17 or F/A-18). At high α 's, minimizing the distortions becomes more difficult because of flow separation which can occur at the inlet lip.

Leynaert notes that for a fixed sharp-inlet lip there are at least two basic solutions: either add vortex generators to control the separated flow in the inlet duct or bleed the boundary layer at the lip, as per Concorde. For movable inlets, there is a potential weight/mechanism problem but also a significant benefit. This benefit is documented in figure 84 for the auxiliary-door device, along with two other types of movable inlets. The rotating cowl lip (or cowl lip droop) has also been studied, as reported in a summary by Nguyen and Gilbert (ref. 77), and the results shown in figure 85. This figure shows the measured improvements in pressure recovery, average turbulence and distortion obtained by increasing the cowl lip droop angle at the higher α 's.

CONCLUDING REMARKS

This lecture focuses on aircraft high angle-of-attack aerodynamics with their attendant vortical flowfields. In order to

perform analytical or experimental work in this α range, it is imperative that the fundamental features of the dominant flowfield be well understood. Therefore, an extended discussion concerning how these flowfields form, grow and decay has been given. This was followed by a representative sample of various analysis methods used to predict the effects of vortical flow, along with examples of each. The methods presented include the suction-analogy with extensions, free-vortex-filaments, free-vortex-sheet, and modeling of the Euler and Navier-Stokes equations.

Vortical flow can also be used in the design process using engineering methods. Four examples have been given which include a complete wing, a portion of a wing and leading-edge vortex flap systems. Each of these was subsequently analyzed or analyzed and wind-tunnel-tested. Upon examining the aerodynamic results, the conclusion is reached that the salient flow features have been captured in the design process.

Stability and control in this α range has been examined with methods which employ the suction-analogy with extensions. The result of which is to establish that these methods are able to make reasonable and quick engineering estimates of both longitudinal and lateral global characteristics as long as the vortex system is coherent, and sometimes even beyond overall coherency. A general rule is that once large-scale vortex breakdown occurs, the experimental procedures with their emphasis on a sequential process and/or redundancy should currently be viewed as the method of choice, provided all of the test parameters and length-scales are well understood. Novel control devices, such as forebody nose devices which utilize vortical flows and which (as of yet) have not been modeled analytically, have been shown to make a significant contribution to the lateral characteristics in the higher- α range or post-stall flight-regime. Thrust vectoring is also shown to make a significant contribution in this α range where conventional lateral control surfaces fail.

An engineering method, which also employs the suction analogy, is provided to estimate the normal force and pitching moment of delta wings undergoing dynamic stall. Though exact agreement is not achieved with measured data, this method does capture the qualitative behavior of the loadings.

REFERENCES

- (1) DeMers, R. X-31 will turn on a dime. Aerospace America, October 1990, pp. 26-29
- (2) Many authors Engineering Methods in Aerodynamics Analysis and Design of Aircraft AGARD Report-R-783, May 1991
- (3) Many authors High Angle-of-Attack Aerodynamics AGARD-LS-121 March 1982

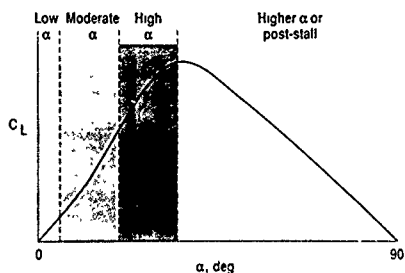
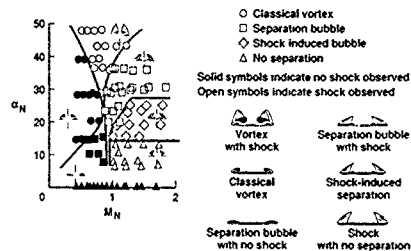
- (4) Many authors: Aerodynamics of Vortical Type Flows in Three Dimensions AGARD-CP-342, April 1983.
- (5) Anderson, J. D., Jr.: Modern Compressible Flow with Historical Perspective McGraw-Hill Book Co., p. 166, 1982.
- (6) Cunningham, A. M., Jr.: Practical Problems: Airplanes. In: Unsteady Transonic Aerodynamics, Prog. in Astronautics and Aeronautics, Vol. 120, p. 92, 1989.
- (7) McMillin, S. N.; and Thomas, J. L.; and Murman, E. M.: Navier-Stokes and Euler Solutions for Lee-Side Flows Over Supersonic Delta Wings, A Correlation With Experiment NASA TP 3035, December 1990.
- (8) Stanbrook, A.; and Squire, L. C.: Possible Types of Flow at Swept Leading Edges. *Aeronaut. Q.*, Vol. XV, Pt. 1, February 1964, pp. 72-82.
- (9) Hensch, M. J.; and Luckring, J. M.: Connection Between Leading-Edge Sweep, Vortex Lift, and Vortex Strength for Delta Wings. *J. of Aircraft*, Vol. 27, No. 5, May 1990, pp. 473-475.
- (10) Smith, J. H. B.: Calculations of the Flow over Thick, Conical, Slender Wings with Leading-Edge Separation. Aeronautical Research Council R&M 3694, March 1971.
- (11) Hensch, M. J.: Similarity for High-Angle-of-Attack Subsonic/Transonic Slender-Body Aerodynamics. *J. of Aircraft*, Vol. 26, No. 1, January 1989, pp. 56-66.
- (12) Lamar, J. E.; Hallissy, J. B.; Frank, N. T.; Smith, R. H.; Johnson, T. D., Jr.; Pao, J.-L.; and Ghaffari, F.: Review of Vortex Flow Flight Projects on the F-106B. *AIAA Paper No. 87-2346 CP*, August 1987.
- (13) Lamar, J. E., and Johnson T. D., Jr.: Sensitivity of F-106B Leading-Edge-Vortex Images to Flight and Vapor-Screen Parameters. *NASA TP 2818*, June 1988.
- (14) Lambourne, N. C., and Bryer, D. W.: The Bursting of Leading Edge Vortices, Some Observations and Discussion of the Phenomenon. Aeronautical Research Council R&M 3282, 1962.
- (15) Wentz, W. H., Jr., and Kohlman, D. L.: Vortex Breakdown on Slender Sharp-Edged Wings. *J. of Aircraft*, Vol. 8, No. 3, March 1971, pp. 156-161.
- (16) Lamar, J. E.: Some Recent Applications of the Suction Analogy to Vortex-Lift Estimates In Aerodynamic Analyses Requiring Advanced Computers, Pt. II, NASA SP-347, pp. 985-1011, March 1975.
- (17) Polhamus, E. C.: A Concept of the Vortex Lift of Sharp-Edge Delta Wings Based on a Leading-Edge-Suction Analogy. *NASA TN D-3767*, December 1966.
- (18) Polhamus, E. C.: Predictions of Vortex-Lift Characteristics Based on a Leading-Edge Suction Analogy. *J. of Aircraft*, Vol. 8, No. 4, April 1971, pp. 193-199.
- (19) Margason, R. J.; and Lamar, J. E.: Vortex-Lattice FORTRAN Program for Estimating Subsonic Aerodynamic Characteristics of Complex Planforms. *NASA TN D-6142*, February 1971.
- (20) Lamar, J. E.; and Gloss, B. B.: Subsonic Aerodynamic Characteristics of Interacting Lifting Surfaces with Separated Flow Around Sharp Edges Predicted by a Vortex-Lattice Method. *NASA TN D-7921*, September 1975.
- (21) Lamar, J. E.; and Herbert, H. E.: Production Version of the Extended NASA-Langley Vortex Lattice FORTRAN Computer Program - Volume I User's Guide. *NASA TM-83303*, April 1982.
- (22) Snyder, M. H., Jr.; and Lamar, J. E.: Application of the Leading-Edge-Suction Analogy to Prediction of Longitudinal Load Distribution and Pitching Moments for Sharp-Edged Delta Wings. *NASA TN D-6994*, October 1972.
- (23) Williams, J. E., and Vukelich, S. R.: THE USAF STABILITY AND CONTROL DIGITAL DATCOM, Volume II, Implementation of Datcom Methods AFFDL-TR-76-45, Vol. II, November 1976.
- (24) Lamar, J. E.: Extension of Leading-Edge-Suction Analogy to Wings with Separated Flow Around the Side Edges at Subsonic Speeds. *NASA TR R-428*, October 1974.
- (25) Bradley, R. G.; Smith, C. W., and Bhateley, I. E.: Vortex-Lift Prediction for Complex Wing Planforms. *J. of Aircraft*, Vol. 10, No. 6, June 1973, pp. 379-381.
- (26) Lan, C. E.; and Mehrotra, S. C.: An Improved Woodward's Panel Method for Calculating Leading-Edge and Side-Edge Suction Forces at Subsonic and Supersonic Speeds. *NASA CR-3205*, November 1979.
- (27) Lamar, J. E.: Prediction of Vortex Flow Characteristics of Wings at Subsonic and Supersonic Speeds. *J. of Aircraft*, Vol. 13, No. 7, July 1976, pp. 490-494.
- (28) Lamar, J. E.: Recent Studies of Subsonic Vortex Lift Including Parameters Affecting Stable Leading-Edge Vortex Flow. *J. of Aircraft*, Vol. 14, No. 12, December 1977, pp. 1205-1211.
- (29) Lamar, J. E., and Campbell, J. F.: Recent Studies at NASA-Langley of Vortical Flows Interacting with Neighboring Surfaces AGARD CP 342, Paper No. 10, 1983.
- (30) Lan, C. E.: A Quasi-Vortex-Lattice Method in Thin Wing Theory. *J. of Aircraft*, Vol. 11, No. 9, September 1974, pp. 518-527.

- (31) Lan, C. E.; and Chang, J.-F.: Calculation of Vortex Lift Effect for Cambered Wings by the Suction Analogy. NASA CR-3449, July 1981.
- (32) Lan, C. E.; and Chang, J.-F.: VORCAM - A Computer Program for Calculating Vortex Lift of Cambered Wings by the Suction Analogy. NASA CR-165800, November 1981
- (33) Woodward, F. A.; Tinoco, E. N.; and Larsen, J. W.: Analysis and Design of Supersonic Wing-Body Combinations, Including Flow Properties in the Near Field. Part I - Theory and Application. NASA CR-73106, August 1967.
- (34) Kulpan, R. M.: Wing Airfoil Shape Effects on the Development of Leading-Edge Vortices. AIAA Paper No 79-1675, 1979
- (35) Henderson, W. P.: Effects of Wing Leading-Edge Radius and Reynolds Number on Longitudinal Aerodynamic Characteristics of Highly Swept Wing-Body Configurations at Subsonic Speeds. NASA TN D-8361, December 1976
- (36) Carlson, H. W.; and Mack, R. J.: Studies of Leading-Edge Thrust Phenomena. AIAA Paper No 80-0325, 1980
- (37) Carlson, H. W.; and Walkley, K. B.: A Computer Program for Wing Subsonic Aerodynamic Performance Estimates Including Attainable Thrust and Vortex Lift Effects. NASA CR-3515, March 1982
- (38) Lan, C. E.: The Unsteady Suction Analogy and Applications. AIAA Paper No 81-1875, August 1981
- (39) Lan, C. E.: The Unsteady Quasi-Vortex Lattice Method with Applications to Axial Propulsion. J. of Fluid Mechanics, Vol. 93, Pt. 4, 1979, p. 747
- (40) Lan, C. E.: Applied Airfoil and Wing Theory. Cheng Chung Book Co., R.O.C., pp. 459-574, 1988
- (41) Mehrotra, S. C., and Lan, C. E.: A Theoretical Investigation of the Aerodynamics of Low-Aspect-Ratio Wings with Partial Leading-Edge Separation. NASA CR-145304, January 1978
- (42) Pao, J. L., and Lan, C. E.: A Vortex-Filament and Core Model for Wings with Edge Vortex Separation. NASA CR-165847, February 1982
- (43) Kandil, O. A., and Yates, E. C., Jr.: Transonic Vortex Flows Past Delta Wings. Integral Equation Approach. AIAA J., Vol. 24, No. 11, November 1986, pp. 1729-1736
- (44) Katz, J., and Markow, B.: Unsteady Low-Speed Aerodynamic Model for Complete Aircraft Configuration. J. of Aircraft, Vol. 25, No. 4, April 1988, pp. 302-310
- (45) Johnson, F. T., Lu, P., Tinoco, E. N., and Epton, M. A.: An Improved Panel Method for the Solution of Three-Dimensional Leading-Edge Vortex Flows. Volume I - Theory Document. NASA CR-32/8, July 1980
- (46) Luckring, J. M.; Schoonover, W. E., Jr.; and Frink, T.: Recent Advances in Applying Free Vortex Sheet Theory for the Estimation of Flow Aerodynamics. AIAA Paper No. 82-0095, January 1982.
- (47) Luckring, J. M.; Hoffler, K. D.; and Grantz, A. C.: Recent Extensions to the Free-Vortex-Sheet Theory for Expanded Convergence Capability. NASA CP-2416, pp. 85-114, 1986.
- (48) Hummel, D.: On the Vortex Formation Over a Slender Wing at Large Angles of Incidence. In AGARD-CP-247, Paper No. 15, January 1979.
- (49) Raj, P.; Olling, C. R.; Sikora, J. S.; Keen, J. M.; Singer, S. W.; and Brennan, J. E.: Three-dimensional Euler/Navier-Stokes Aerodynamic Method (TEAM), Vol. I: Computation Method and Verification. AFWAL-TR-87-3074, June 1989.
- (50) Raj, P., and Brennan, J.: Improvements to an Euler Aerodynamic Method for Transonic Flow Simulation. AIAA Paper No. 87-0040, January 1987
- (51) Powell, K. G., and Murman, E. M.: A Comparison of Experimental and Numerical Results for Delta Wings with Vortex Flaps. AIAA Paper No. 86-1840, June 1986.
- (52) Murman, E. M.; Powell, K. G.; and Miller, D. S.: Comparison of Computations and Experimental Data for Leading Edge Vortices - Effects of Yaw and Vortex Flaps. AIAA Paper No. 86-0439, January 1986
- (53) Flores, J., and Chaderjian, N. M.: The Numerical Simulation of Transonic Separated Flow about the Complete F-16A. AIAA Paper No. 88-2506, June 1988
- (54) Gaffan, F.; Luckring, J. M.; Thomas, J. L.; and Bates, B. L.: Navier-Stokes Solutions About the F/A-18 Forebody-Leading-Edge Extension Configuration. J. of Aircraft, Vol. 27, No. 9, September 1990, pp. 737-748
- (55) Raj, P.: An Euler Code for Nonlinear Aerodynamic Analysis: Assessment of Capabilities. SAE Technical Paper Series 881486, October 1988
- (56) Pao, J. L.: Vortical Flow Analysis for F-106B Configuration. AIAA Paper No. 88-3745-CP, July 1988
- (57) McGregor, I.: The Vapour-Screen Method of Flow Visualization. J. of Fluid Mechanics, Vol. 11, Pt. 4, December 1961, pp. 481-511
- (58) Thomas, J. L.; Knst, S. T.; and Anderson, W. K.: Navier-Stokes Computations of Vortical Flows over Low-Aspect-Ratio Wings. AIAA J., Vol. 28, No. 2, February 1990, pp. 205-212
- (59) Lamar, J. E.; Schemensky, R. T.; and Reddy, C. S.: Development of a Vortex Lift Design Procedure and Application to a Slender Maneuver-Wing Configuration. J. of Aircraft, Vol. 18, No. 4, April 1981, pp. 259-266

- (60) Carlson, H. W.; and Darden, C. M Validation of a Pair of Computer Codes for Estimation and Optimization of Subsonic Aerodynamic Performance of Simple Hinged-Flap Systems for Thin Swept Wings. NASA TP 2828, November 1988
- (61) Lamar, J. E.: A Vortex-Lattice Method for the Mean Camber Shapes of Trimmed Noncoplanar Planforms with Minimum Vortex Drag. NASA TN D-8090, June 1976
- (62) Lamar, J. E.; and Campbell, J. F.: Vortex Flaps - Advanced Control Devices for Supercruise Fighters. Aerospace America, January 1984, pp. 95-99.
- (63) Frink, N. T.: Concept for Designing Vortex Flap Geometries (U) NASA TP-2233, December 1983.
- (64) Huebner, L. D : Performance Analysis and Supersonic Design of Wing Leading-Edge Vortex Flaps for the Convair F-106B. Masters Thesis, The George Washington University School of Engineering and Applied Science, September 1985.
- (65) Vortex Flow Aerodynamics, Vol I NASA CP-2416, 1986
- (66) Vortex Flow Aerodynamics, Vol II NASA CP-2417, 1986
- (67) Vortex Flow Aerodynamics, Vol III NASA CP-2418, 1986
- (68) Lamar, J. E.. Nonlinear Lift Control at High Speed and High Angle of Attack Using Vortex Flow Technology In. AGARD-R-740 Special Course on Fundamentals of Fighter Aircraft Design, February 1986
- (69) Lan, C. E., and Hsu, C. H Effects of Vortex Breakdown on Longitudinal and Lateral-Directional Aerodynamics of Slender Wings by the Suction Analogy. AIAA Paper No 82-1385, August 1982.
- (70) Lamar, J. E.. Analysis and Design of Stake-Wing Configurations J of Aircraft, Vol. 17, No.1, January 1980, pp 20-27
- (71) Lamar, J. E.; and Frink, N. T.: Experimental and Analytical Study of the Longitudinal Aerodynamic Characteristics of Analytically and Empirically Designed Stake-Wing Configurations at Subcritical Speeds. NASA TP 1803, June 1981
- (72) Lamar, J. E.: Summary of Some Recent Studies of Subsonic Vortex Lift and Parameters Affecting The Leading-Edge Vortex Stability. AIAA Paper No. 76-414, July 1976
- (73) Rao, D. M., and Campbell, J. F. Vortical Flow Management Techniques In. Prog Aerospace Science Vol. 24, pp 173-224, 1987
- (74) Munn, D. G., and Rao, D. M Exploratory Studies of Actuated Forebody Strakes for Yaw Control at High Angles of Attack AIAA Paper No. 87-2557, August 1987.
- (75) Chambers, J. R : High-Angle-of-Attack Aerodynamics Lessons Learned AIAA Paper No. 86-1774-CP, June 1986.
- (76) Chambers, J. R.. Overview of Stall/Spin Technology AIAA Paper No 80-1580, August 1980.
- (77) Nguyen, L. T.; and Gilbert, W. P.: Impact of Emerging Technologies on Future Combat Aircraft Agility. AIAA 90-1304, May 1990.
- (78) Poisson-Quinton, P.: Comments on Propulsion/Airframe Integration for Improving Combat Aircraft Operational Capabilities In: AGARD- R-740 Special Course on Fundamentals of Fighter Aircraft Design, February 1986.
- (79) Lowson, M. V.. The Separated Flow on Slender Wings in Unsteady Motion Reports & Memoranda No 3448, Aeronautical Research Council, London, U. K , September 1963
- (80) Naumowicz, T, Jarrah, M. A., and Margason, R. J.. Aerodynamic Investigation of Delta Wings with Large Pitch Amplitude. AIAA Paper No 88-4332, August 1988
- (81) Brandon, J. M ; and Shah, G. H. Effect of Large Amplitude Pitching Motions on the Unsteady Aerodynamics Characteristics of Flat- Plate Wings AIAA Paper No 88-4331, August 1988
- (82) Nguyen, L. T.. Flight Dynamics Research for Highly Agile Aircraft. SAE Technical Paper Series 892235, September 1989.
- (83) Ashley, H., Katz, J., Jarrah, M. A ; and Vaneck, T Unsteady Aerodynamic Loading of Delta Wings for Low and High Angles of Attack Proceedings of the International Symposium on Nonsteady Fluid Dynamics, ASME FED Vol 92, Toronto, Canada, June 1990, pp 61-78
- (84) Perrin, P Techniques for Performance Optimisation in Cruise and Manoeuvrability In AGARD-R-740 Special Course on Fundamentals of Fighter Aircraft Design, February 1986
- (85) Leynert, J Fundamentals of Fighter Aircraft Design Engine Intake and Afterbody In AGARD-R-740 Special Course on Fundamentals of Fighter Aircraft Design, February 1986

ACKNOWLEDGEMENTS

The author wishes to thank all colleagues who contributed information for use in this lecture, also, Mr. H W Carlson, Dr M J Hemsch, Mr L T Nguyen, Dr E. C. Yates, Jr., and my wife, Joyce, for their many helpful suggestions regarding the manuscript, and Mr Peter F Jacobs and Mrs Connie Smith for manuscript preparation.

Fig. 1. Schematic of lift curve by α ranges.

Ref. 7.

Fig. 4. Classification of experimental data for sharp-leading-edge delta wings.

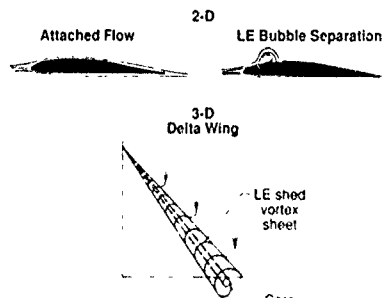
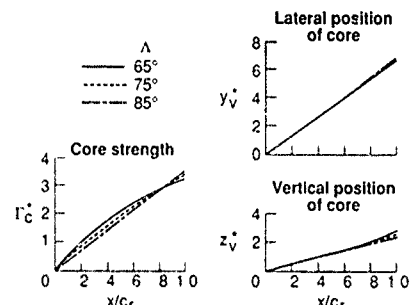
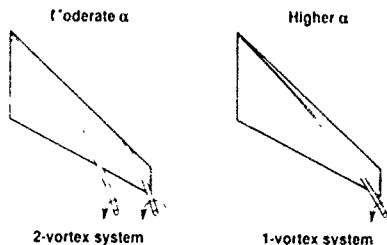


Fig. 2 Flow sketches



Ref 11

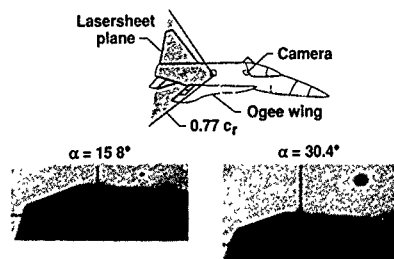
Fig. 5 Leading-edge vortex characteristics for thin delta wings, $M = 0$, $K = 1$ 

Ref. 8

Fig. 3 Vortex systems on high aspect ratio wing, $\Lambda = 65^\circ$ 

Ref. 12

Fig. 6 Multiple vortices found above wing of F-106B during flight, alt = 25,000 ft, $M = 0.4$, $R_n = 33 \times 10^6$



Ref. 13.
Fig. 7. Vapor screen applied to Soviet research aircraft

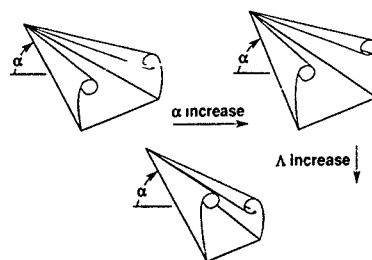


Fig. 10. Effect of α and delta-wing sweep on vortex system displacement.

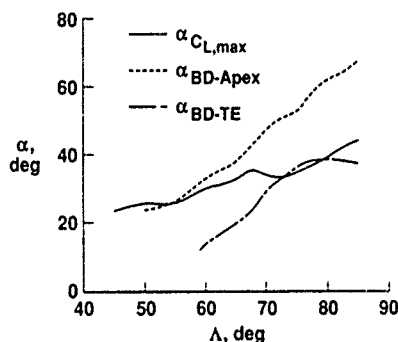
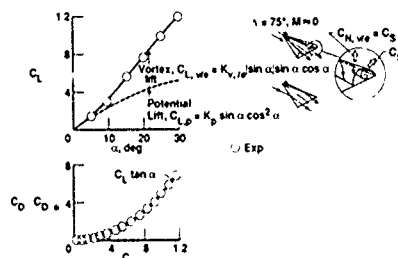
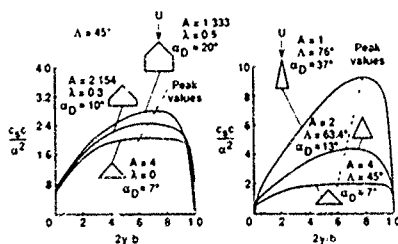


Fig. 8. Variation of α for vortex breakdown and $C_{L,\max}$ for delta wings

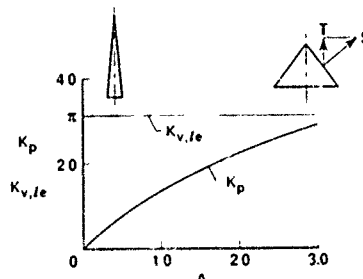


Ref. 16
Fig. 11. Original application of suction analogy



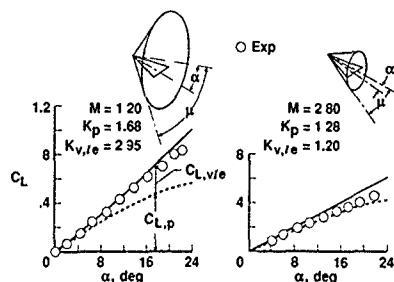
Ref. 16

Fig. 9. Leading-edge suction distributions and α for departure $M \approx 0$

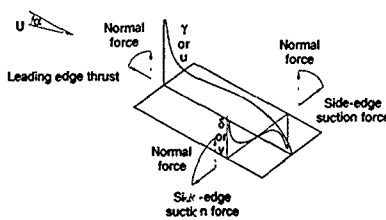


Ref. 18

Fig. 12. Variation of K_p and $K_{v,le}$ with A for delta wings, $M = 0$

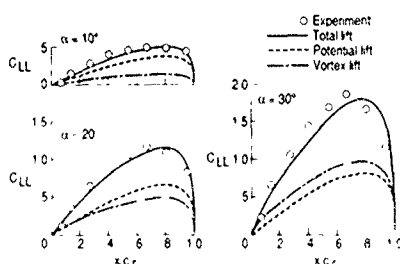


Ref. 16.

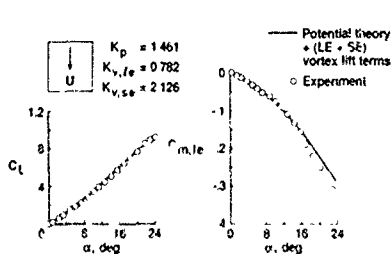


Ref. 24

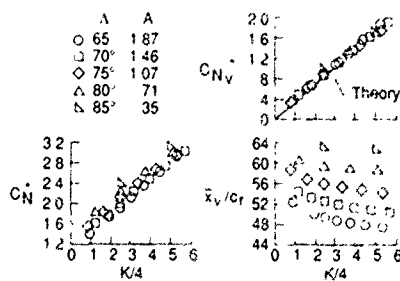
Fig. 16. Vortex-lift concept, suction analogy applied to LE and SE.



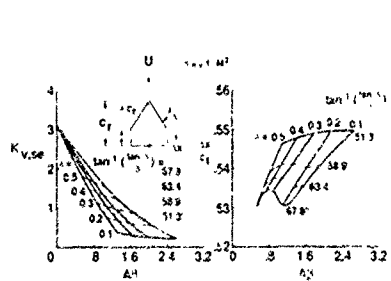
Ref. 22



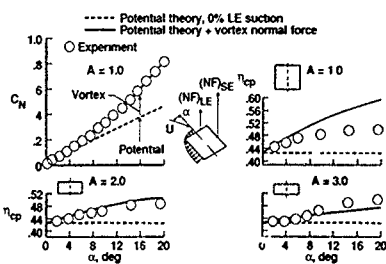
Ref. 24

Fig. 17 Aerodynamic characteristics of $A = 1$ rectangular wing, $M \approx 0$ 

Ref. 11

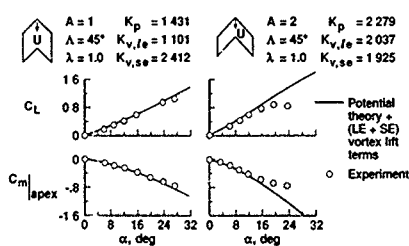
Fig. 15 Similarity for computational solutions for thin delta wings, $M = 0$ 

Ref. 27



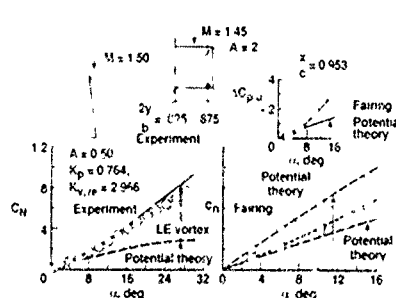
Ref. 28.

Fig. 19 Effect of vortex normal force on spanwise load center; $M \approx 0$



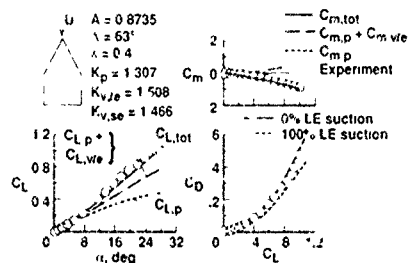
Ref. 27.

Fig. 22 Aerodynamic characteristics of two sheared rectangular wings, $M \approx 0$.



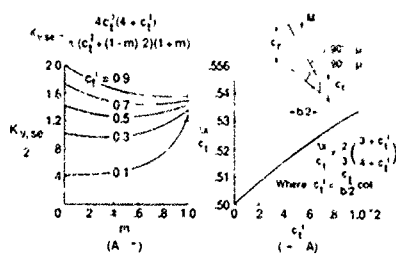
Ref. 27

Fig. 20 Vortex lift at supersonic speeds



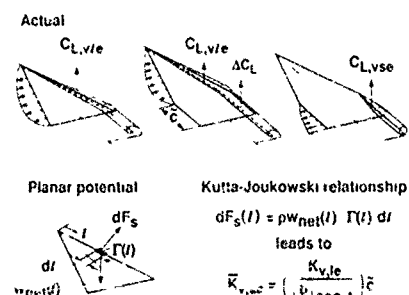
Ref. 27

Fig. 23 Aerodynamic characteristics of a cropped delta wing, $M = 0.6$



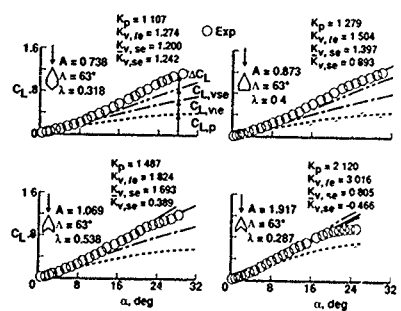
Ref. 27

Fig. 21 Theoretical values of $K_{v,se}$ and $\Delta x/c_1$ for wings with subsonic leading edges and sonic trailing edges

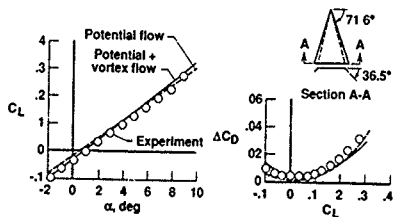


Ref. 28

Fig. 24 Augmented vortex lift development

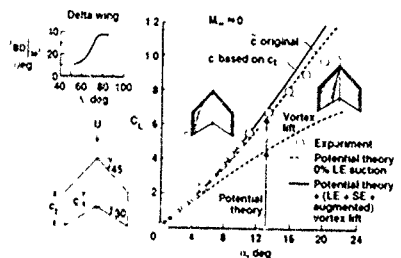


Ref. 16



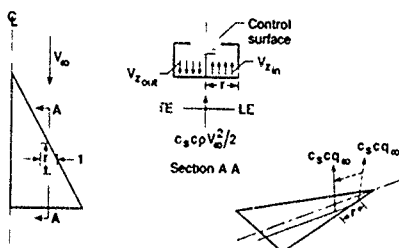
Ref. 31.

Fig. 28. Longitudinal aerodynamic characteristics of delta wing with conical LE flap; $A = 1.333$, $M = 1.4$, VORCAM.



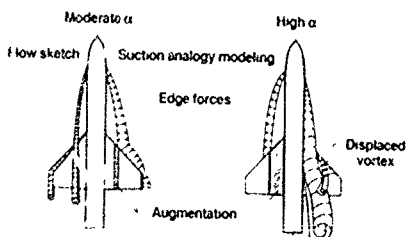
Ref 28

Fig. 26 Effect on \bar{c} definition on estimated C_L



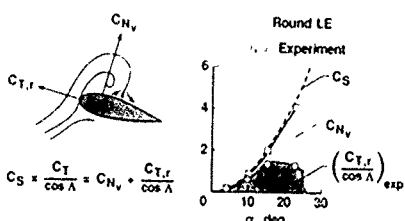
Ref 31

Fig. 29 Vortex action point concept, Lan



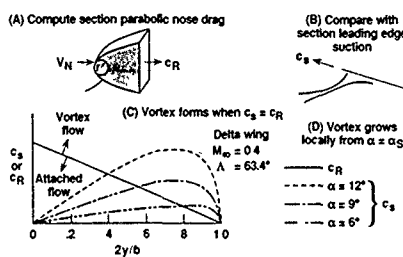
Ref 29

Fig. 27 Effect of α on vortex flow models for complex configurations, VLM-SA



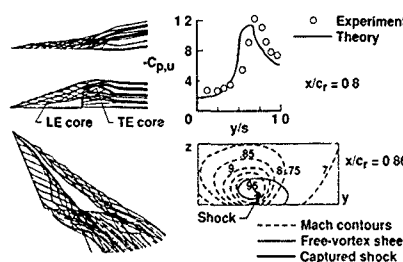
Ref 29

Fig. 30 Relationship between vortex normal force and residual thrust, $A = 1.0$, $\Lambda = 76^\circ$, $t/c = 0.1$, FFA 104-5601 airfoil



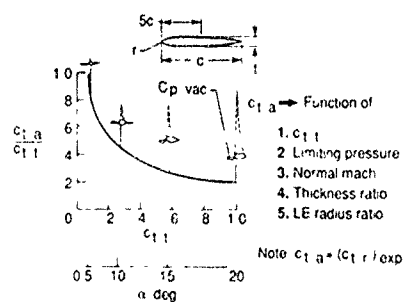
Ref. 34

Fig. 31. Kulfan's method of predicting vortex normal force.



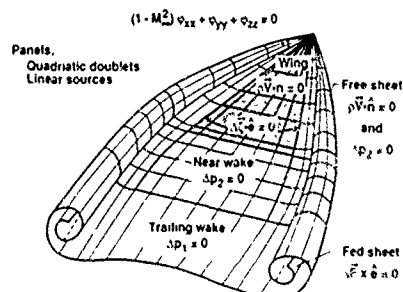
Ref. 43.

Fig. 34. Typical free vortex filament solution, $A = 1.5$ delta, $M = 0.7$, $\alpha = 15^\circ$.



Ref. 36

Fig. 32. Carlson's method for predicting residual thrust, $M = 0.6$, $t/c = 0.12$, $r/c = 0.0048$



Ref. 46.

Fig. 35. Theoretical formulation - panel method - FVS

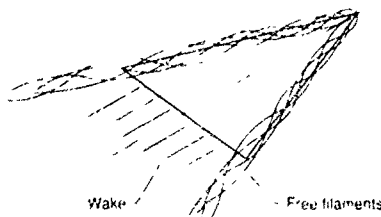
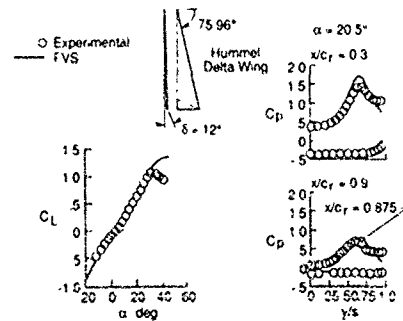
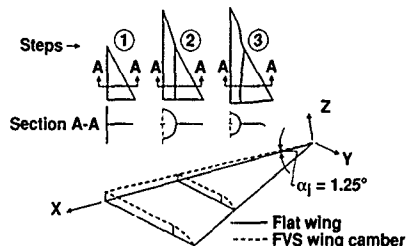


Fig. 33. Free vortex filament methods



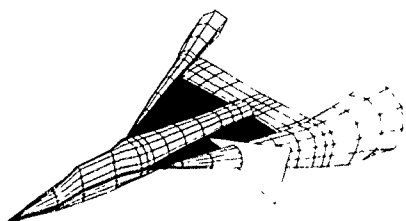
Ref. 47

Fig. 36. FVS solution, $A = 1$ delta, $M \approx 0$



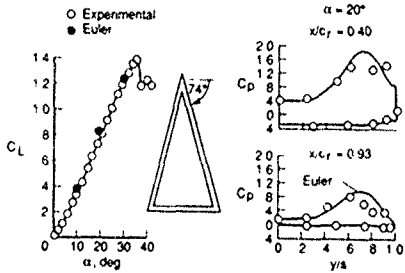
Ref. 12.

Fig. 37 FVS solution steps and camber representation

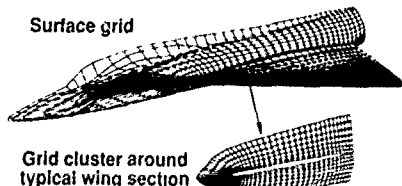


Ref. 12.

Fig. 38. Free vortex sheet paneling for F-106B

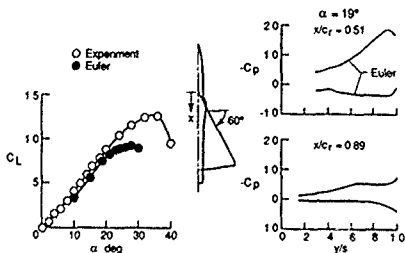


Ref. 55

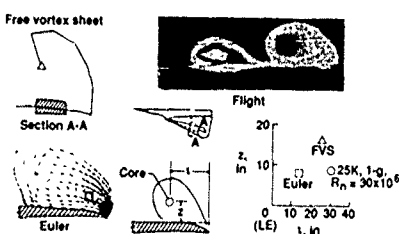
Fig. 39 Euler solution, $A = 1\ 147\ \delta$, $M = 0.3$ 

Ref. 56

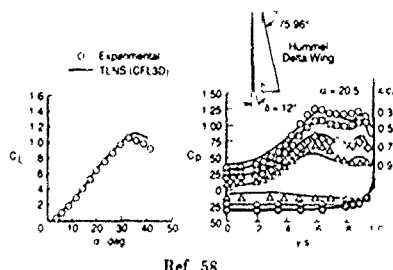
Fig. 40 C-H grid application to F-106B for Euler code



Ref. 56

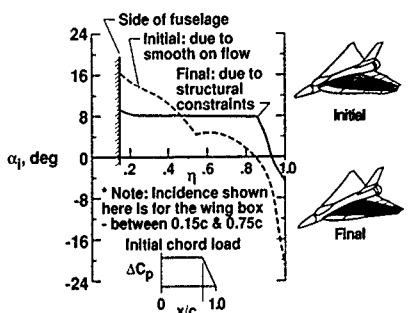
Fig. 41. Euler solution, F-106B, $M \approx 0.3$ 

Ref. 12.

Fig. 42. Measured and calculated core locations; $M \approx 0.4$, $\alpha = 19^\circ$ 

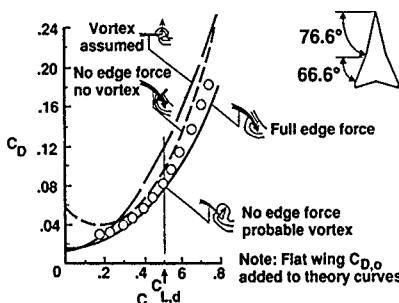
Ref. 58

Fig. 43. Thin layer N-S solution, $A = 1\ \delta$, $M \approx 0$, $R_n = 0.95 \times 10^6$

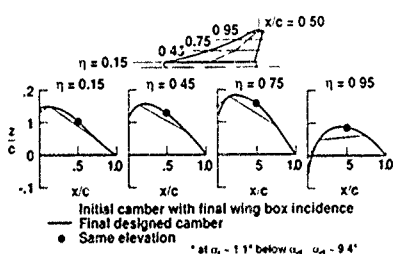


Ref. 59.

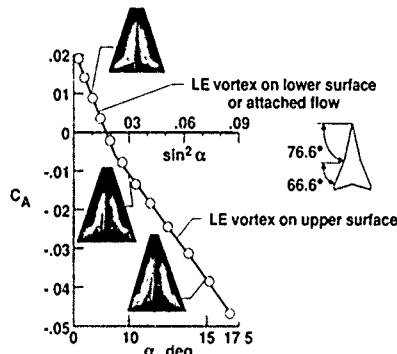
Fig. 44. Incidence distribution for cranked cambered wing.



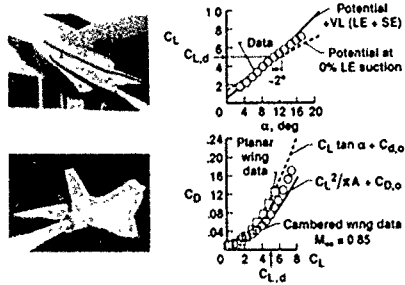
Ref. 59.

Fig. 47. Edge force recovery on transonically cambered wing; $M = 0.85$.

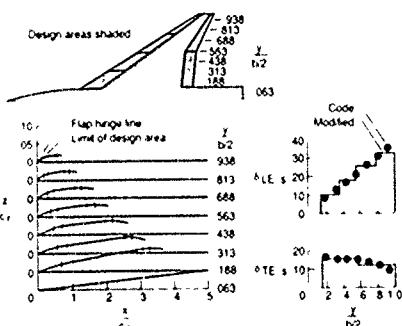
Ref. 59.

Fig. 45. Cranked wing mean camber shapes; $A = 1.383$, $C_{L,d} = 0.5$, $M_d = 0.9$, $\alpha = 0.7$ 

Ref. 59.

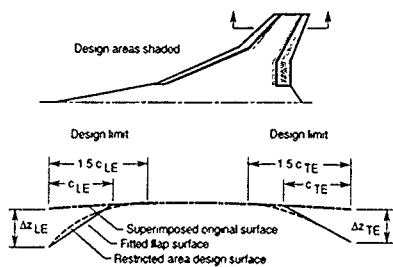
Fig. 48. Effect of flow type on transonically cambered wing, $M = 0.85$.

Ref. 59.

Fig. 46. Longitudinal aerodynamic characteristics for designed transonic-maneuver wing, $A = 1.383$, $\Delta_{LE} = 76.6^\circ/66.6^\circ$, $C_{L,d} = 0.50$, $M_d = 0.90$, VLM-SA

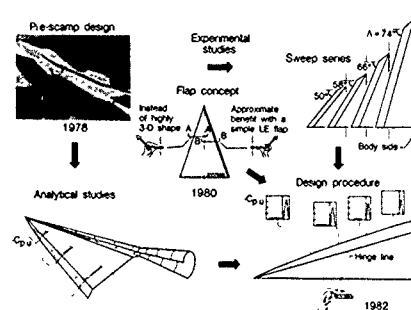
Ref. 60

Fig. 49. Restricted-area-design camber surface for 60-degree swept trapezoidal-wing fighter, $C_{L,d} = 0.73$, $C_{m,d} = -0.17$, $M = 0.5$, $R_n = 2.9 \times 10^6$.



Ref. 60.

Fig. 50 Fitting of flap surfaces to wing-design surface.

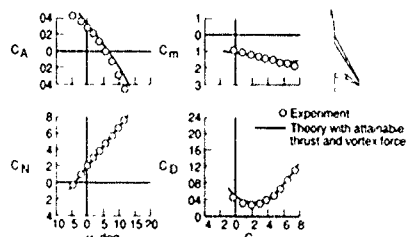


Ref. 12.

Fig. 53. Vortex flap history; transonic aerodynamics.

$$\delta_{LE,s} = \tan^{-1} \left(\frac{\Delta z_{LE}}{c_{LE}} \right)$$

$$\delta_{TE,s} = \tan^{-1} \left(\frac{\Delta z_{TE}}{c_{TE}} \right)$$



Ref. 60

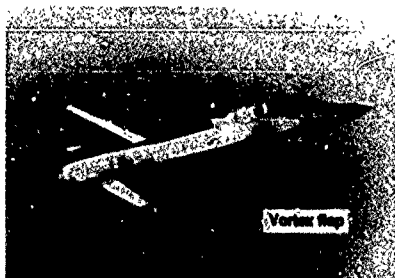
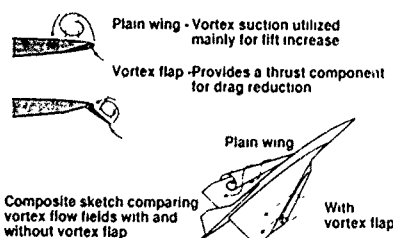
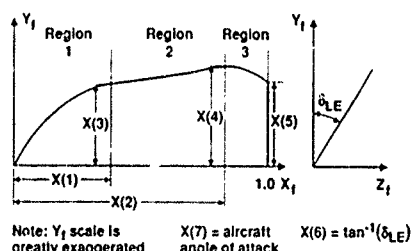
Fig. 51 Theoretical and experimental data for 60°-swept trapezoidal wing fighter; $M = 0.3$, $R_n = 1.9 \times 10^6$, $\delta_{LE,s} = 15^\circ/20^\circ$, $\delta_{TE,s} = 15^\circ/12^\circ$ 

Fig. 54. F-106B with leading-edge vortex flap in flight



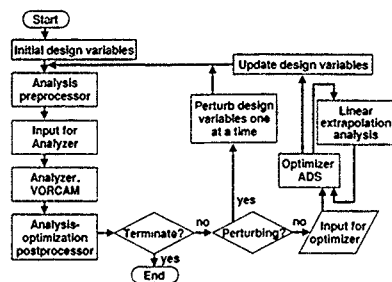
Ref. 62

Fig. 52 The vortex flap concept



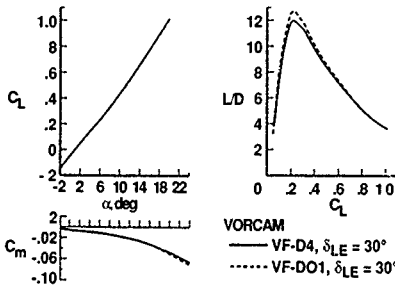
Ref. 64

Fig. 55 Analytical vortex flap model with design variables



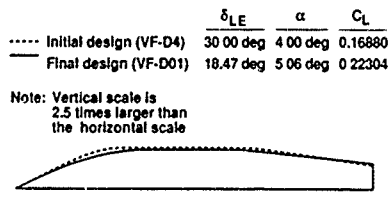
Ref. 64.

Fig. 56. Supersonic design method flow chart using analysis-optimization process



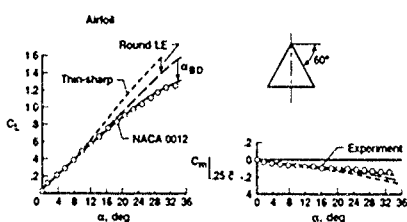
Ref. 64.

Fig. 59 Assessment of longitudinal aerodynamics for two vortex flaps F-106B at $M = 0.3$



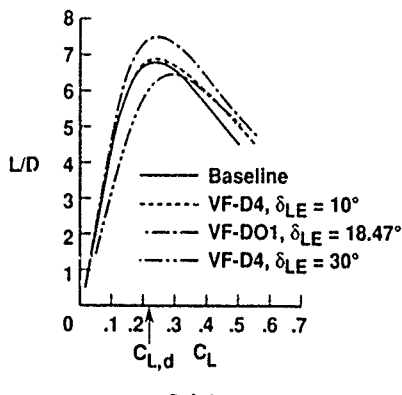
Ref. 64.

Fig. 57 Initial and final vortex flap design results for the F-106B; $M_d = 1.5$, $C_{L,d} = 0.223$



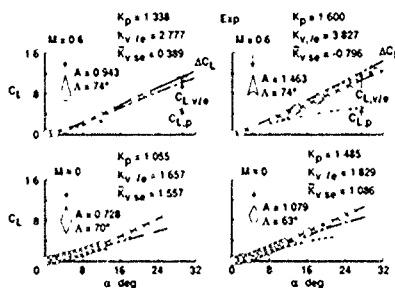
Ref. 69

Fig. 60 Longitudinal aerodynamic characteristics of a 60° delta with round LE; $A = 2.31$, $M \approx 0$



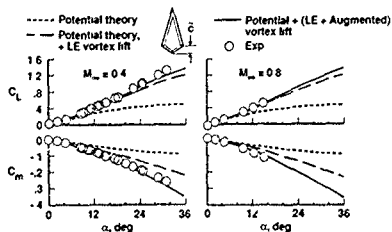
Ref. 64

Fig. 58. Performance of VF-DO1 with VF-D4 on F-106B at $M = 1.5$



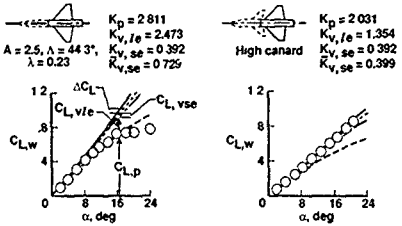
Ref. 16

Fig. 61 Lift characteristics of pointed wings.



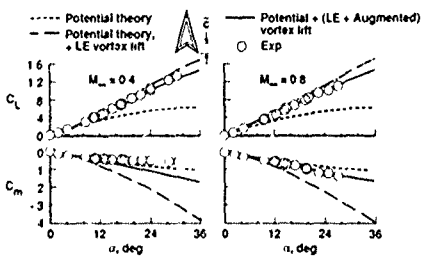
Ref. 28.

Fig. 62. Effect of Mach number on augmented vortex lift and pitch; diamond wing, $A = 0.943$, $\Lambda = 74^\circ$



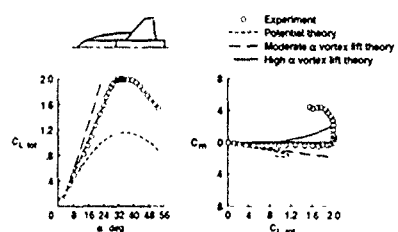
Ref. 16.

Fig. 65. Suction analogy applications to configurations; $M = 0.3$



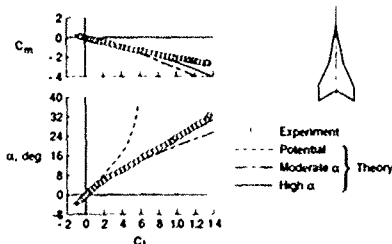
Ref. 28.

Fig. 63. Effect of Mach number on augmented vortex lift and pitch. arrow wing, $A = 1.463$, $\Lambda = 74^\circ$



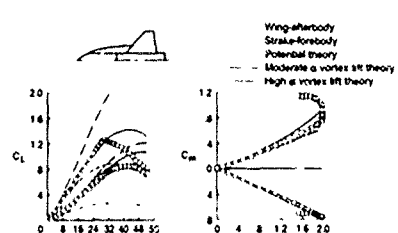
Ref. 68

Fig. 66. Complete longitudinal aerodynamic characteristics for strake-wing-body, strake AD 24, $\Lambda = 44^\circ$, $M = 0.2$



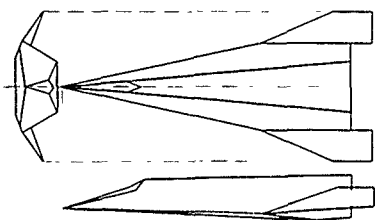
Ref. 70

Fig. 64. Longitudinal aerodynamic characteristics for cranked wing, $A = 1.10$, $\Lambda = 80^\circ/65^\circ$, $M \approx 0$, VLM-SA



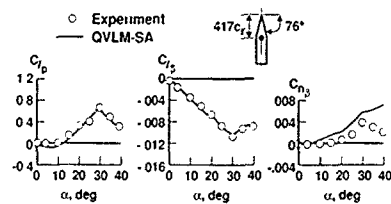
Ref. 68

Fig. 67. Component longitudinal aerodynamic characteristics for strake-wing-body, strake AD 24, $\Lambda = 44^\circ$, $M = 0.2$



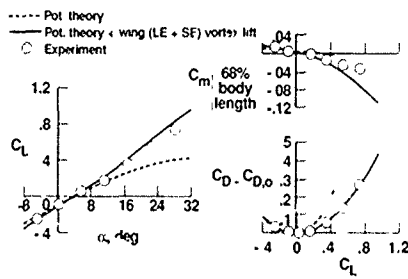
Ref 72.

Fig 68 Cambered-thick lifting-body and wing combination.



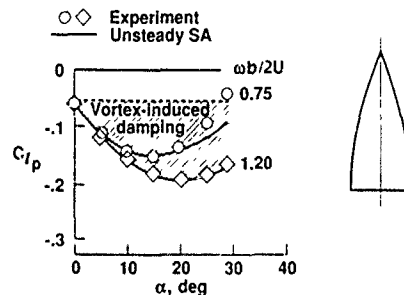
Ref 69.

Fig 71 Stability derivatives for cropped delta, $A = 0.333$, $\lambda = 0.5$, $\beta = 5^\circ$, $M \approx 0$.



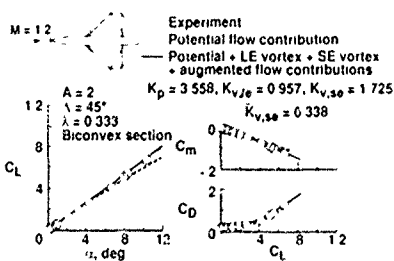
Ref 72

Fig 69 Longitudinal aerodynamic characteristics for cambered thick-body-wing combination, $M = 0.2$



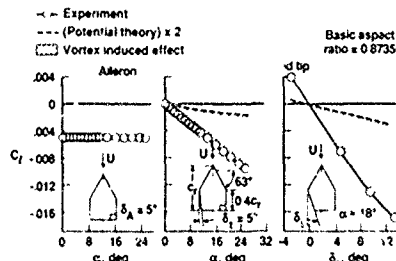
Ref 38

Fig 72 Oscillatory roll damping for gothic wing, $A = 0.75$, $M \approx 0$



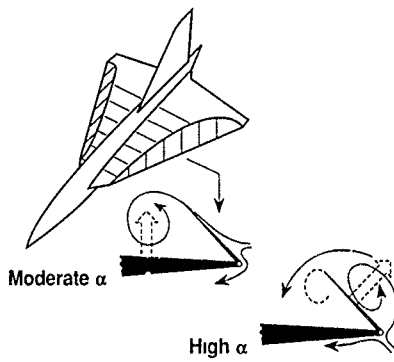
Ref 16

Fig 70 Aerodynamic characteristics of a cropped delta wing body, $M = 1.2$

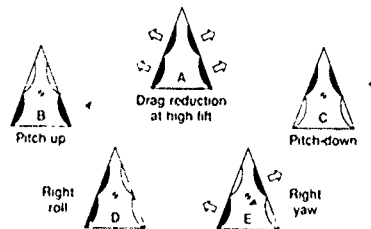


Ref 68

Fig 73 Roll-control device effectiveness on cropped delta wing, $M = 0.0$

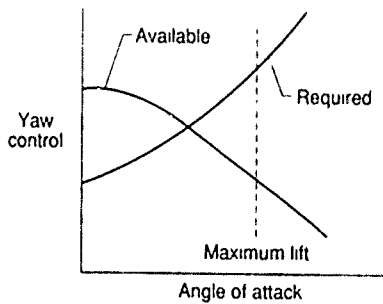


Ref 73
Fig. 74 Upper vortex flap concept



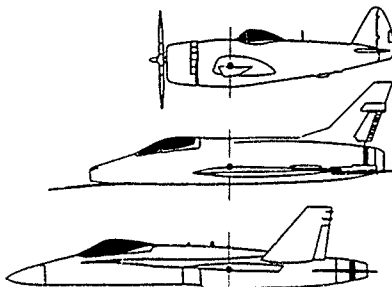
Ref 73

Fig. 75 Hypothesized application of segmented upper vortex flaps for drag reduction and aerodynamic control at high angles of attack, filled segment denotes deployed



Ref 74

Fig. 76 Typical yaw control requirements for maneuvering



Ref 75
Fig. 77 Fighter design evolution.

Military Airplanes

- Stability:

$$C_{n\beta} \sin \alpha = C_{n\beta} \cos \alpha - (l_z/l_x) C_{l\beta} \sin \alpha > 0$$

- Control:

Aileron alone.

$$LCDP - C_{n\beta} \cdot C_{l\beta} \frac{C_{n\delta a}}{C_{l\delta a}} > 0$$

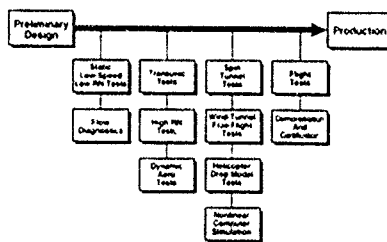
Aileron + rudder proportional to aileron.

$$LCDP - C_{n\beta} \cdot C_{l\beta} \frac{C_{n\delta a} + K_2 C_{l\delta r}}{C_{l\delta a} + K_2 C_{l\delta r}} > 0$$

$$K_2 = \delta_r / \delta_a$$

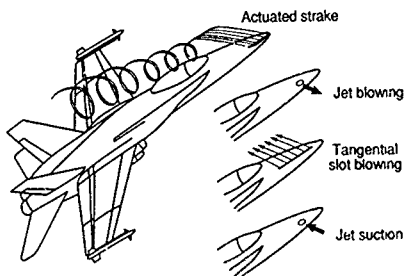
Ref 76

Fig. 78 Criteria for elimination of directional divergence for fighter airplanes, military airplanes

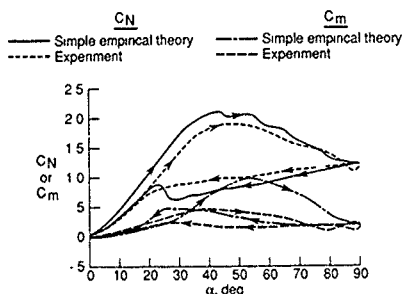


Ref 77

Fig. 79 High-alpha aero development process

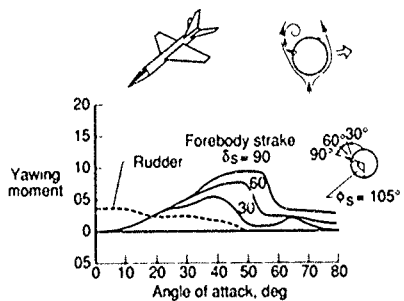


Ref. 77
Fig. 80. Forebody flow control concepts

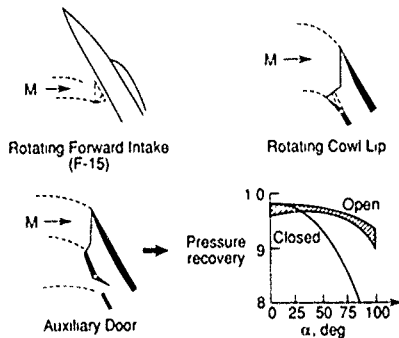


Ref. 83

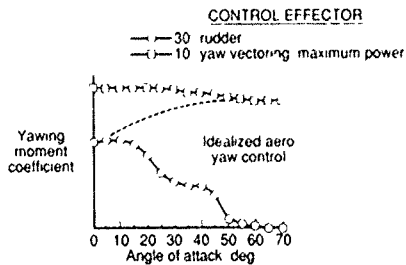
Fig. 83 Aerodynamic characteristics during pitching motion, $A = 1$ delta, $M \approx 0$, $K = 0.04$.



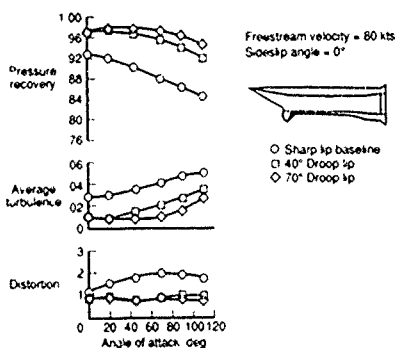
Ref. 77
Fig. 81 Generic model results



Ref. 85
Fig. 81. High α special inlet devices



Ref. 77
Fig. 82 Low-speed yaw control effectiveness,
 $alt = 20,000\text{ft}$, $M = 0.3$



Ref. 77
Fig. 85 Cowl lip droop concept

AIRCRAFT DRAG ANALYSIS METHODS

by
Charles W. Boppe

Grumman Corporation
Aircraft Systems Division
Bethpage, NY 11714

ABSTRACT

A collection of aircraft computational drag analysis methods and drag reduction techniques has been prepared for the AGARD Fluid Dynamics Panel Special Course on "Engineering Methods in Aerodynamic Analysis and Design of Aircraft" Pressure, skin friction (viscous), wave (compressibility), lift-induced (vortex), interference (multiple components, multiple flow fields), throttle-dependent (inlet and exhaust plume), and trim drag source predictions are included. Background information on complementary handbook schemes and empirical data is provided. The need to establish a computational drag prediction experience base is emphasized and illustrated. Project type applications are described in which these drag prediction tools have been implemented for drag reduction processes. The paper concludes by summarizing the role played by computerized drag prediction methods in aircraft design programs.

NOMENCLATURE

C_f	-	Incompressible Friction Coefficient	V_1/V_0	-	Required Inlet Velocity Ratio
C_{f_c}	-	Compressible Friction Coefficient	P	-	Plate Force
V	-	Velocity	q	-	Dynamic Pressure
d	-	Derivative	X ₁ , X ₂	-	Length Scales
C _p	-	Pressure Coefficient	MFR	-	Inlet Mass Flow Ratio
Γ	-	Load Distribution (C_C/C_{AVG}). Circulation	Vol	-	Volume
C	-	Chord	R	-	Correction Factor
y	-	Span Position	Log	-	Logarithm
L	-	Lift	In	-	Natural Logarithm
D _i	-	Induced Drag	ρ	-	Density
C _l	-	Local Lift Coefficient	A ₁ , A _n	-	Foiler Coefficients
α	-	Angle of Attack	Λ	-	Wing Sweep Angle
w	-	Downwash Velocity	λ	-	Wing Taper Ratio
M	-	Mach Number	eff	-	Effective
Pcrit	-	Critical Pressure	x/l	-	Non-Dimensional Axial Location
Re	-	Reynolds Number	β	-	Boat Tail Angle
C _D	-	Drag Coefficient	H	-	Height
C _L	-	Lift Coefficient	NACA	-	National Advisory Council on Aeronautics
ϵ	-	Lift-Induced Drag Efficiency Factor	SLOR	-	Single Line Over-Relaxation
C _{D,i}	-	Lift-Induced Drag Coefficient	δ^*	-	Boundary Layer Displacement Thickness
S _s	-	Suction Parameter	v/c	-	Thickness-to-chord ratio
AR	-	Aspect Ratio	D	-	Drag
δ_{LE}	-	Leading Edge Flap Deflection	U _∞	-	Free-stream velocity
δ_{TE}	-	Trailing Edge Flap Deflection	CLOC	-	Local Chord Length
δ_c	-	Canard Deflection Angle	C _{AVG}	-	Average Chord Length
GAW	-	General Aviation Wing	C _{DP}	-	Profile Drag Coefficient
l/d	-	Length/Diameter Ratio	LE	-	Leading Edge
NPR	-	Nozzle Pressure Ratio	θ	-	Shockwave Angle
C _{D,0}	-	Zero-Lift Drag Coefficient	γ	-	Ratio of Specific Heats
C	-	Chord	ϵ	-	Surface Local Orientation Angle
ζ	-	Centerline			
T	-	Temperature			
A,S	-	Area			
L	-	Length			
η	-	Non Dimensional Span Location y/b ₂			
b	-	Wing Span			
V_1/V_0	-	Calculated Open Inlet Velocity Ratio			
V_2/V_0	-	Calculated Closed-Inlet Velocity Ratio			

INTRODUCTION

Aircraft design has evolved over the past century into a process requiring increasing levels of sophistication to meet requirements for expanded speed/altitude envelopes and flexibility with improved cruise efficiency and combat maneuvering performance. Over a large portion of this period, inventors and designers combined good engineering practice with sub-scale testing programs to develop a vehicle for full-scale flight evaluation. Aviation history reveals successes and failures that were for the most part determined by the quality of the vehicle engineering design effort.

Following close behind basic stability, control, and handling qualities, performance derived by maximizing thrust and minimizing aerodynamic drag often makes or breaks a new design concept. Prediction of aerodynamic drag forces poses a formidable challenge. Elemental flow physics driving viscous and pressure resistance components can be quite complex. In addition, there is an extraordinary number of ways in which the elements can interact and combine to produce the total drag force. References 1-11 provide useful insights into the complexity of drag prediction problems. Full-scale aircraft drag prediction errors of 10-20% have occurred in the past, this is often not within the range needed for success.

One problem faced by the designer is that there is a large gap between conceptual/preliminary design "handbook" methods typically used to rough out a new configuration, and the sub-scale model testing typically used to generate the first true performance estimates. This gap exists in the form of modeling fidelity and time, so it is usually beneficial if certain key configuration characteristics are not locked-in before suitable testing and interpretation efforts are completed. It is well known, however, that sub-scale testing in wind tunnels can occasionally mislead the designer. In these cases, the problem can usually be traced back to testing anomalies caused by wall interference, flaws in simulating viscous effects, model geometry fidelity, test procedure errors, and support interference/fouling.

Over the past 20 years, computerized flow simulation methods have evolved. Applications on aircraft programs have for the most part focused on the prediction of pressure/velocity characteristics, lifting forces and moments, and boundary layer parameters. But these methods can also provide drag force predictions. If the applications engineer is careful in modeling, and can take advantage of a computational prediction experience base, multiple benefits are possible. On one level, computational predictions serve to bridge the gap between simplistic handbook methods and initial model testing results. When anomalies between sub- and full-scale testing are observed, computational predictions can be used to judge which is correct (a third source). Finally, computational methods provide a means for the design engineer to better understand the flow mechanisms that generate drag forces. This is particularly valuable for applications that radically depart from past design experience.

This paper describes the current practice used in computational drag prediction for different types of aircraft drag sources. The examples included should provide a foundation or experience base that could prove useful in future applications.

BACKGROUND

Understanding the various sources of aircraft drag becomes important since the designer or applications engineer must select the proper computational tool for the job at hand. At present, no single method is capable of simultaneously treating all drag components that are typically of interest. In addition, no single method is capable of treating a complete aircraft configuration with sufficient accuracy for all drag analyses that might be required. In view of this, it is reasonable to expect that a number of methods will be implemented with the results being combined using a component build up approach. To ensure that there is no misunderstanding about the character of different drag sources, a portion of the Background section will be set aside for descriptions and definitions.

Drag Sources

Viscous or skin friction drag is derived from the flow field shearing stresses in a region of reduced velocity near the aircraft surface. The resulting zone of velocity impairment, or boundary layer, has been sketched in Fig 1. Total pressure losses attributed to this drag mechanism can be measured in the wake downstream from the component of interest. Viscous drag can be affected by altering the boundary layer flow characteristics; this is usually accomplished by manipulating the external flow field pressure gradients. The pressure environment might also be amenable to propagating a laminar boundary layer that is thinner than a turbulent layer with an attendant reduction in viscous drag. Also, turbulent boundary layer viscous drag levels might be reduced or even approach zero in local regions if the boundary layer surface velocity and velocity gradient are very small ($CF \rightarrow 0$), but this is strictly true only for two-dimensional flows. It is possible for the boundary layer velocity to be negative. When this happens, the resulting separated flow region

(Fig 1) gives rise to another drag component - pressure drag. It should be recognized that viscous drag is unique in that it is the only drag source for which the force-generating mechanism acts tangential to the surface. All other drag sources are derived via the integrated effect of normal pressures.

Pressure or form drag is a "normal-pressure" type drag - the origins of which can be traced back to multiple sources. In the simplest case, pressure drag (or thrust) is generated any time the normal pressure integration is non-zero. Figure 2-A depicts the most common occurrence using a symmetric body-like surface

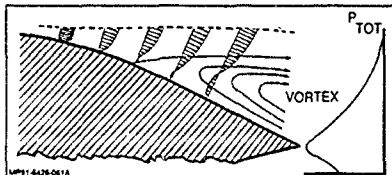


Fig 1 Boundary Layer Velocity Characteristics with Wake Total Pressure

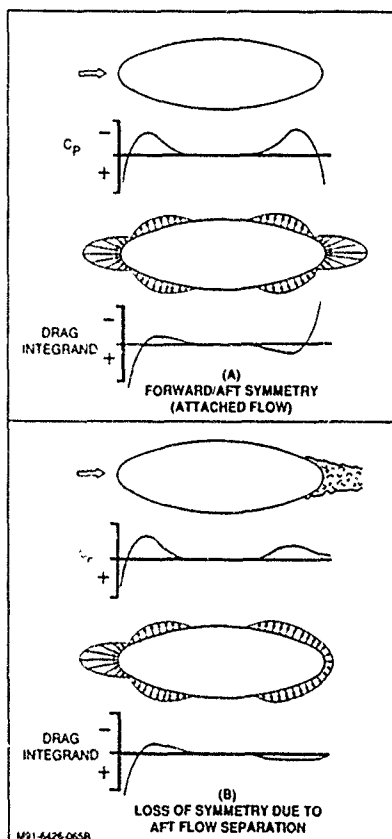


Fig. 2 Body Pressure Field With Drag Integrand

in a uniform onset flow. The resulting symmetric pressure distribution (nose to tail) is shown below the body. A third illustration shows the pressure vectors acting on the surface. Below that, the integrand to be summed to quantify the drag force can be seen. In this symmetric flow case, the pressure or form drag force is zero because the forward and aft components exactly cancel each other. Aircraft flows of this type do not exist for most applications. Typically, for body and wing shapes a flow separation region will develop aft, as depicted in Fig. 2-B. The result is that pressure symmetry is compromised and afterbody pressure recovery levels are weakened with an attendant drag increase. Form drag becomes more complex at high speeds and at lifting conditions as other drag mechanisms interact and affect the normal pressure field.

Lift-induced drag is derived from the production of lifting forces, predominantly on the wing and tail/canard surfaces. Any surface with positive lift (including body forms) will be characterized by lower pressures on the upper surface than on the lower surface. As a result, lower surface flow tends to move outward toward the surface tip, while upper surface flow moves inward toward the centerline (Fig. 3). This flow mechanism is the simple result of flow migrating from a high-pressure region to a low-pressure region. At the end of the surface, these cross-flow velocities from the upper and lower surfaces combine with the free-stream flow to form a vertical flow that is particularly strong near the surface tips or outboard regions. It is well known that the vertical flow character is dependent on the lifting surface load distribution.

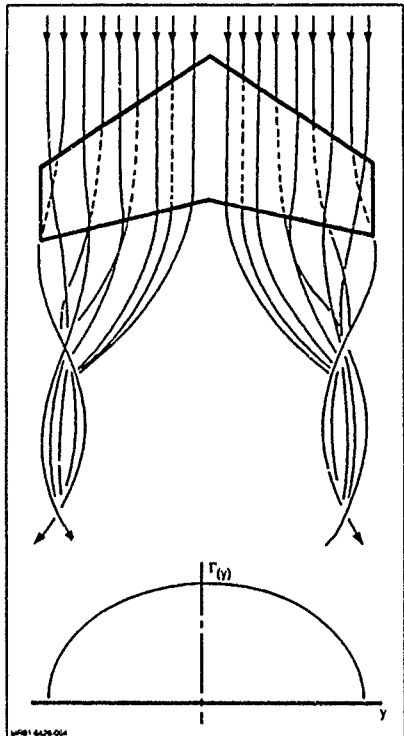


Fig. 3 Lifting Surface Upper/Lower Flow Pattern with Load Distribution

Wake vortical flow alters or induces flow velocities on the lifting surface. Most important, an upwash/downwash field can be identified (Fig. 4). When fully integrated, a net downwash exists that combines with the free-stream velocity. The resultant onset flow that the lifting surface "sees" is rotated, and the lift vector rotates with it. The component of the lift vector facing aft forms the induced drag force. Swirling flow carries energy downstream in the lifting surface wake.

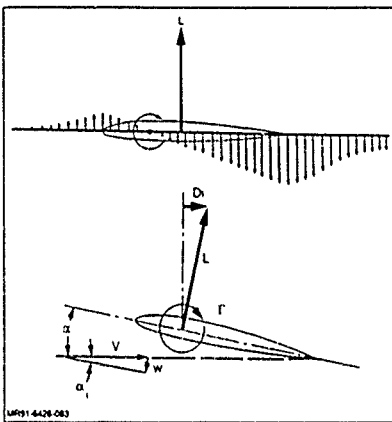


Fig. 4 Induced Upwash/Downwash Field with Rotated Lift Vector

Wave drag develops as a result of differences in the compressibility of air in subsonic and supersonic flows. A one-dimensional isentropic flow model reveals that a streamtube contraction will accelerate flow moving at subsonic speeds, while at supersonic speeds the flow will be decelerated. The opposite is true for a streamtube expansion, i.e., a subsonic flow will slow, while a supersonic flow will speed up in an expanding streamtube. Airflows about aircraft wing and body components form streamtubes with combinations of contractions and expansions.

At high subsonic speeds (beyond $M = 0.7 - 0.8$, depending on the configuration thickness and lift level), flow expansions might create a supersonic flow "bubble" embedded in the subsonic flow. If the bubble flow gains sufficient supersonic speed, a flow discontinuity (or shock wave) will permit flow parameters to return to free-stream values. Through a shock wave, flow properties (pressure, velocity vector, density, and temperature) change abruptly with an accompanying loss of total pressure downstream (Fig. 5-A). At supersonic flight speeds, a wing or body component will exhibit an array of shock waves and expansion or Mach waves (Fig. 5-B). Shock waves and the resultant effect on the aircraft wake can extend far into the flow field about the aircraft. This extent is depicted in Fig. 6 where vapor condensation about an F-14 flying at supersonic speeds can be seen. Figure 7 reveals that shock wave flow discontinuities can be large enough to disturb a water surface some distance from the aircraft.

The drag mechanisms discussed up to this point are fundamental in the sense that they cannot be broken down into simpler elements. A number of drag sources, however, are derived from combinations of fundamental drag mechanisms. Interference, throttle-dependent, and trim drag are examples.

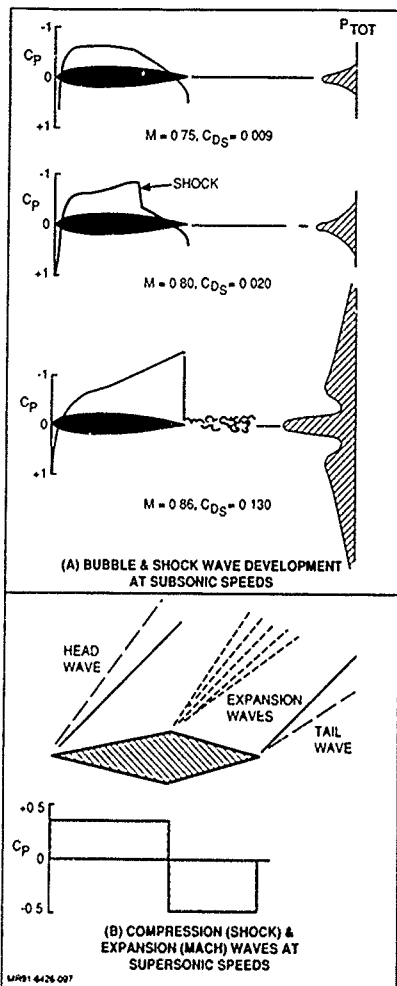


Fig. 5 Sources of Wave Drag at Subsonic & Supersonic Speeds (Ref. 16)

Interference drag takes myriad forms. The nature of the interference might be of a component or flow field type, but in all cases, a flow velocity disturbance is responsible for the drag force. An example of a pure flow field disturbance would be that of a wing immersed in the slipstream of a propeller. Dynamic pressure would be increased in the slipstream wake. In addition, a swirling flow generating an upwash on one side of the hub axis and a downwash on the other alters wing loading. At very high subsonic speeds (i.e., propfans), this interference effect will dramatically change the wing shock wave pattern. It can be appreciated by using this example that interference drag can easily have viscous, pressure, lift-induced, and wave drag components, thus greatly complicates the prediction process.

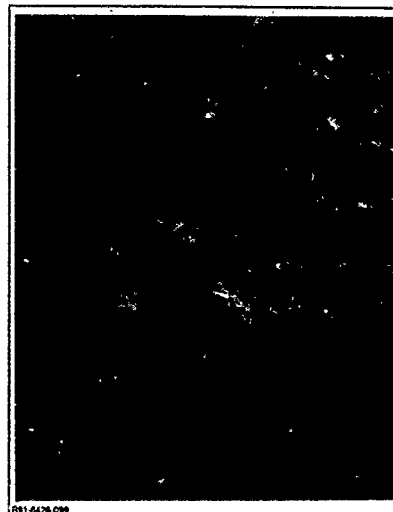


Fig. 6 Extent of F-14 Shock Wave Pattern at Supersonic Speeds



Fig. 7 Interaction of Aircraft Shock Wave with Ocean Surface

More common examples of interference drag can be found with interfering multiple body or wing and body components. Figure 8 shows the viscous flow near a component surface where a pod or some other body form has imposed a flow disturbance composed of both favorable and unfavorable pressure gradients. The effect is a weakened viscous layer that increases the probability of flow separation. Here, both viscous and pressure drag levels will be affected. Wave and lift-induced drag variations will occur if this type of interference exists on a lifting surface at high speeds.

Figure 8 provides another example of interference drag. Aircraft component junctures often present problems because a boundary layer flow along one surface, such as a fuselage, is often poorly conditioned to deal with a stagnation point (zero velocity) that might be imposed by a second surface juncture (e.g., a wing or tail surface leading edge). At this second surface stagnation point, the flow is likely to separate if proper fairings have not been implemented. A separation patch is one possibility, but another potential phenomenon is a juncture vortex. Interference drag levels are often reduced by proper fairings or fillets but the designer must minimize the use of these surfaces considering the drag penalty associated with additional wetted area.

Throttle-dependent drag is generated by disturbances predominantly near the inlet face and exhaust nozzles. Considering inlets, the engine flow rate will determine the level of inlet spillage. This in turn establishes the level of suction forces on the inlet face which may not be negligible for thick inlets with large nose radii. High levels of spillage might induce inlet flow separation. This problem is aggravated when design requirements dictate very small inlet leading-edge radii. In addition, spillage flow will interfere with wing circulation if the inlet face is near a wing surface. Nozzle flow fields are more complicated. Figure 9 is a schematic showing the elements of a typical nozzle flow. Key here is the plume entrainment region

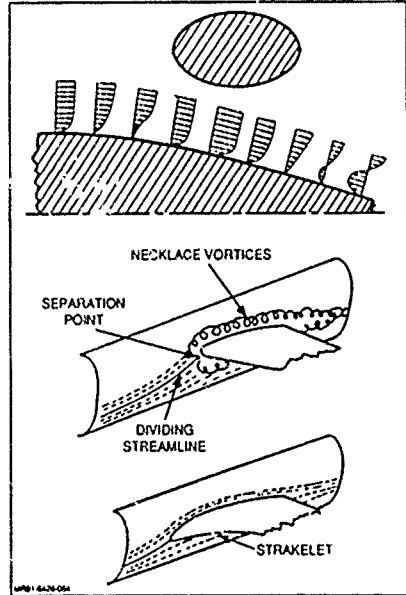


Fig. 8 Examples of Component Interference Effects

and potential flow separation region at the boattail trailing edge. Thrust variations will alter the external flow entrainment and possibly the separated flow region. At high speeds, a shock wave may exist on the boattail region with throttle changes causing the shock to migrate forward and aft. Mechanisms that alter afterbody pressure levels are important because of the relatively large surface vector component in the axial (or drag) direction.

Trim drag evolves from the need to keep the aircraft in equilibrium during cruise and maneuvering flight. It should be apparent that a trimming surface will always generate a component of lift-induced drag, but at high-speed conditions, wave drag penalties might also appear. For a conventional tail-to-trim design (Fig. 10-A), the tail surface generates a down-load requiring the wing to produce additional up-load for a given total lift level. The increased lift might result in a measurable wave drag increment at transonic conditions if the untrimmed isolated wing was designed to be optimum at the total lift level. Trimmed, the wing must now operate above the design lift level. For a canard-to-trim configuration (Fig. 10-B), a positive load to trim might eliminate this penalty, but the designer must ensure that the canard downwash field does not impair loading on the main lifting surface downstream. If it does, the trimming drag might include both lift-induced and wave drag components.

Computational Prediction Problems

It was noted in the Introduction that there are a number of factors that must be accounted for if sub-scale testing is to

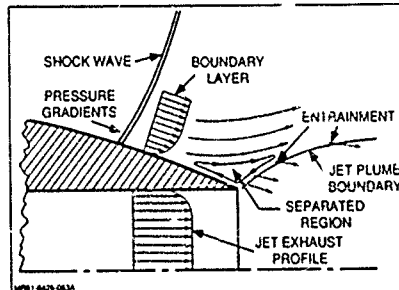


Fig. 9 Elements of Complex Nozzle/Plume Interaction Flow Fields

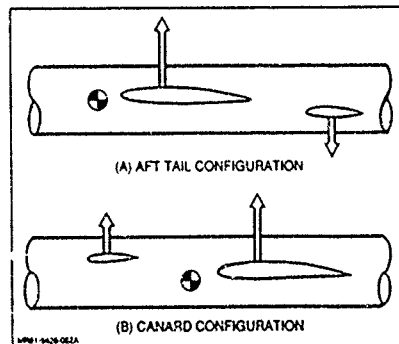


Fig. 10 Balance & Trim for Conventional Aft-Tail & Canard Configurations

provide useful drag measurements for performance estimation. The test engineer must also monitor power input during powered propulsion-type tests because drag measurement errors combine with power input measurement errors to yield a total uncertainty in resultant drag forces. Flight testing presents similar problems in that the engineer intent on establishing vehicle drag levels often has less control over flight condition variables such as speed, angle-of-attack, and true engine thrust level than he would in the wind-tunnel. Flight condition parameter accuracy is another important issue. Like sub- and full-scale testing, the determination of drag forces via computational methods presents a number of difficulties. Some of the more important problems are described in the paragraphs that follow.

Recalling Fig. 2-A, it can be appreciated that drag forces are predominantly established by summing the effects of normal pressure fields. The nose and tail portions of the body or wing component contribute disproportionately to drag because of normal vector orientation. That is to say, pressure anomalies in the mid-section often register little effect on drag, while disturbances forward and aft can have surprisingly large effects. But numerically, this characteristic magnifies another problem. Considering the integrand shown in Fig. 2-A, the drag force could be characterized as a relatively small parameter computed by taking the difference between two larger parameters, the integrated force dominating either end of the configuration. There is considerable room for error in this process because the high gradient nose and tail regions are often compromised by modeling resolution constraints inherent in the computational scheme employed. In addition, complex physical flow phenomenology characterizing these regions is approximated, to some extent, by flow simulation methods in use today. Finally, small flaws in grid or surface modeling at the nose or tail can generate numerical anomalies that register a sizable error in the drag level while revealing no apparent discrepancy in lift and moment characteristics. It can be appreciated why the developers of computational methods rarely describe the correlation of computational drag predictions with test data.

Another problem associated with computational drag prediction deals with the extraordinary differences in scale that characterize aircraft components. Table 1 summarizes what is often identified as elements of a configuration's excrescence drag. These numerous small vents, drains, probes, and antennas would require computational modeling resolution orders-of-magnitude smaller than that currently in practice today. Simultaneously modeling the global and detailed elements of complete aircraft would be impractical given current computer technology and charging algorithms. Compounding this issue is the fact that all micro physical phenomenon responsible for drag are not fully understood. In view of this and the point made earlier (that no single computational method is currently capable of treating all drag components for a complete configuration) it becomes apparent why the applications engineer is often able to predict drag increments or decrements using computational methods, but the determination of absolute drag levels is not possible.

This problem of scale and current computing hardware limitations was underscored by NASA Ames researchers (Ref. 12) who computed the smallest eddies found in a turbulent channel flow at a Reynolds number of 10,000 using a Navier-Stokes formulation. Fifty billion grid points were required for an analysis that reached a steady state after 2000 time steps. This can be compared to a typical Reynolds-Averaged Navier-Stokes analysis currently applied for aircraft applications where the grid system point count might range between 100,000 and 300,000 points. The time step count might be 500 to 1000.

Table 1. Typical Excrescence Drag

ANTENNAS (EXTERIOR)	
1 BLADE (APR-27)	10.32 IN ²
2 BLADE (AN/APX73)	AS1918/AR TACAN 44 IN ²
1 BLADE (F-111)	32 IN ² I = 30°
1 ALQ-XXX	DECM POD (F-14)
4 BLADE PDS	8 IN ² EACH
2 ECM PODS (F-111)	TAIL/WING
LIGHTS & PROBES	
2 PILOT STATIC PROBES	
2 TOTAL TEMP PROBES	
1 A-O-A TRANSMITTER	
2 BALL NOSE ALPHA PROBES	
24 STATIC DISCHARGE PROBES	
1 NAVIGATION LIGHT	
1 ANTI COLLISION LIGHT	
MISCELLANEOUS	
1 WINDSHIELD RAIN REMOVAL	
ACCESS DOOR HINGES	
1 ARRESTING HOOK	
OPENINGS	
1 FUEL DUMP - INC IN DECH POD	
1 BLEED VALVE 2 IN - 4.5 IN	
2 ENGINE DRAINS	
.3 WATER/FUEL DRAINS 1.6 - 5.8 IN DIA	
5 FUEL CELL VENTS (FUSELAGE)	
2 REFUELING SUMP DRAINS	
2 ECS GROUND COOLING LOUVERS	
2 OIL BREATHERS 14 HOLES @ 3	
COCKPIT SAFETY, GUN GAS - GAS PURGE	
1 AMMO VENT, 1-COCKPIT EXH	
2 OIL COOLER, 2 ECS EXH	
2 HYD OIL COOLER SCOOPS	
2 ENGINE & IDG OIL COOLER	
1 EPW INTAKE & EXH LOUVER	
1 APU INTAKE & EXH LOUVER	
2 BLEED AIR HEAT EXCHANGER	

WV91-6426-01

Aircraft Development Process & Computational Method Types

The aircraft development process (Fig. 11) involves a sequence of steps or design phases that is initiated by a customer specification for mission requirements and point design goals. In Conceptual Design, the configuration is "roughed out" using relatively simple tools and techniques. The emphasis here is usually on rapid turn-around. Handbook methods, experience bases, and the simplest analysis methods are typically brought to bear. For Preliminary Design, the engineering team must firm up the aircraft external contours. This stage requires both wind-tunnel testing and computational flow simulations as aides in the optimization process. The computations and sub-scale testing (both simulations) attempt to reproduce what will eventually happen in flight. The objective is to minimize design risk because anomalies identified during a flight test program are often quite expensive to resolve. The next stage, Detailed Design, is characterized by the engineering team packing the aircraft interior spaces with actuators, hydraulics, crew station, propulsors, etc. In the final stage, one or two aircraft are manufactured for flight evaluations. At this point in time, computational flow methods can play an important role in resolving flight test anomalies because it is often impractical to re-enter the wind-tunnel on very short notice.

The engineer's task of selecting the proper method for a particular stage of development and a specific design objective is extraordinarily complex. He must have an understanding of

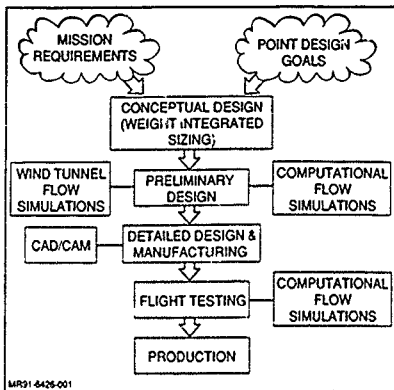


Fig. 11 Aircraft Development Process

the physical flow that is to be simulated in addition to appreciating the strengths and weaknesses of the candidate methods. The best category (see Table 2) is identified and then the proper code within that category must be properly implemented. Experience indicates that the selection of a more sophisticated code within a category or the selection of a code in a higher category may not improve the flow simulation obtained. This can be attributed to algorithm formulation characteristics and modeling constraints. Caution is necessary to ensure that prediction accidents do not occur. As codes become more complex, the probability of having a prediction accident increases and the trouble free "usage range" typically decreases. Computer resource requirements might also be a factor in the method selection process. Table 2 illustrates seven levels of analysis complexity and expense. Relative computing costs between the top and bottom entries might range between 1 and 14,000.

Table 2 Computational Method Formulation Types

CATEGORY	FORMULATION TYPE	CHARACTERISTICS
1	NEWTONIAN PRESSURE EQUATION	"POINT" PRESSURE LAW
2	LAPLACE'S EQUATION	LINEAR
3	TRANSONIC SMALL PERTURBATION EQUATION	NON LINEAR (PLANAR B.C.)
4	EXTENDED TRANSONIC SMALL PERTURBATION EQUATION	SAME AS ABOVE WITH SWEEP SHOCK WAVE MODELING
5	FULL POTENTIAL EQUATION	NON-LINEAR/ NON PLANAR B.C. (TYPICALLY REQUIRES CONFORMAL GRID)
6	EULER'S EQUATIONS	ALL ABOVE PLUS VORTICITY (NO POTENTIAL FLOW ASSUMPTION)
7	NAVIER-STOKES EQUATIONS ✓ REYNOLDS AVERAGE N.S. ✓ PARABOLIZED N.S.	COMPLETE REPRESENTATION OF PHYSICAL FLOW INCLUDING VISCOSITY & TURBULENCE

MRP-1-6426-01A

PART 1: DRAG ANALYSIS METHODS

DISCUSSION - DRAG ANALYSIS METHODS

An engineering perspective of computational drag prediction methods is now described with an attempt to identify the earliest known progress in the field and transition to techniques used on aircraft projects. This composition is not intended to represent all of the methods currently available, nor is it intended to represent the very best or optimum techniques that might be implemented. Instead, the methods are, for the most part, those with which the author has had some project-type experience and can provide some insight into applicability.

Drag Prediction Pioneers - Drag Equations

Many well-known investigators, going as far back as Newton (1642-1727), have made contributions to knowledge that is foundational to current drag prediction techniques (Ref 13). Two individuals who are particularly noteworthy for engineering applications are Smeaton and Oswald.

John Smeaton was an English experimentalist whose work focused on improving the efficiency of windmill and waterwheel blades. His technique involved rotating test specimens at the end of a 6-foot arm and measuring the resultant forces. For a flat plate oriented perpendicular to the onset flow, Smeaton's 1759 testing resulted in the following formula

$$P = 0.0049 V^2 S \quad (1)$$

where "P" was the plate force, "V" was the airspeed in miles per hour, "S" was the plate surface area in square feet, and the factor (0.0049) came to be known as "Smeaton's Coefficient" in later literature references. With a simple trigonometric relation, both lift and drag (the original terminology for drag used until the end of the 19th century) could be computed for glider wings and propeller blades

$$LIFT = 2P \frac{\cos \alpha \sin \alpha}{1 + \sin^2 \alpha} \quad 0 < \alpha < 10 \text{ deg} \quad (2)$$

$$DRAG = 2P \frac{\sin^2 \alpha}{1 + \sin^2 \alpha} \quad 0 < \alpha < 10 \text{ deg} \quad (3)$$

Smeaton's work is important since it marks the initial effort to actually compute drag forces. Also, historically, we find the first use of an empirical factor into which all the world's uncertainties and unknowns could be grouped, an approach that is still in practice today.

Lilienthal's work with gliders took advantage of Smeaton's Formula, but Lilenthal believed that Smeaton's Coefficient should have a value of 0.0055. The Wright brothers were a bit more meticulous in their work - they deduced a Smeaton Coefficient of 0.0033 from wind-tunnel testing and glider flights. This value was used for designing the Wright Flyer wing, canard, and propeller blades. It is now well known that the drag on a flat plate oriented normal to the flow will depend on the Reynolds number. At high speeds, Eiffel concluded that $CD = 1.28$ was correct, and using the relation

$$D = q C_d S \quad (4)$$

a more exact coefficient of 0.00327 is obtained, underscoring the Wrights' skill.

Over a period of 150 years, Smeaton's Coefficient varied between 0.00550 and 0.00327 - a range that might seem large, but in some complex modern applications, variations on this level can still occur when the parameter of interest is drag.

A similar evolution for the prediction of induced drag can be sketched noting the contribution of both Lanchester and Prandtl. But it is most important to recognize that the engineering prediction of induced drag was greatly simplified by NACA engineer W. Bailey Oswald. Focusing his work on providing a means to estimate aircraft performance in the late 1920's, Oswald (Ref 14) established the drag polar relation that is used to this day

$$C_D = C_{D_0} + C_L^2 / (\pi \cdot AR \cdot c) \quad (5)$$

This "airplane efficiency factor" (*c*) applied to induced drag is comparable to Smeaton's Coefficient for pressure drag

These early pressure and lift-induced drag relations might be complemented with a comparable contribution for wave drag. To that end, a useful conceptual relation developed by R. T. Jones (Ref 15) is:

$$\begin{aligned} DRAG = qSC_{D_0} + & \frac{L^2}{q\pi b^2} + \frac{(M^2 - 1)L^2}{2\pi q X_1^2} \\ & + \frac{128q}{\pi} \frac{Vol^2}{X_2^4} \end{aligned} \quad (6)$$

where "X₁" and "X₂" are length scales calculated using the supersonic area rule. This supersonic relation establishes the contribution of wave drag due to volume and wave drag due to lift consistent with friction and lift-induced components. As such, it allows the designer to establish the relative importance of various parameters.

Experimental Experience Base & Handbook Methods

A key to proper application of computational methods for drag prediction problems is the project engineer's ability to recognize the fluid mechanical features characterizing the task at hand. To this end, it is advantageous to gain some experience with "real world" aircraft project problems. This basis accrues, to some extent, in every organization as time goes on. But the applications engineer can enhance internal or organization specific experiences with those of available reports and handbooks.

Hoerner's Fluid Dynamic Drag book (Ref 16) is a compendium dominated by experimentally determined drag sources that cover an extraordinary range of applications. The empiricism found in this source can play an important role in any project application because some drag sources contributing to C_{D_0} , transonic drag rise, and interference drag defy prediction by purely computational means.

Another source that proves valuable is the USAF Stability & Control Datcom (Ref 17). This compendium summarizes prediction methods rather than test results. While not specifically created for drag prediction, the volume does identify handbook-type estimating techniques that would be applicable in the conceptual design phase of many aircraft development projects. As an example, the relation below illustrates the technique used to estimate wing C_{D_0}

$$C_{D_0} = CF [1 + L/U_c + 100(U_c)^4] \times R_u \frac{S_{act}}{S_{ref}} \quad (7)$$

where "CF" is the turbulent flat-plate skin friction coefficient, "L" is the airfoil location for maximum thickness, "U_c" is the wing section thickness ratio, "R" is a lifting surface correction factor (table look-up), and "S" represents surface areas

Similar expressions can be used to build up drag estimates for bodies, wing-body combinations, and wing-body-tail configurations with power effects and control surface deflections. The value of these handbook techniques is comparable to mathematical estimating techniques that are applied when using a desk calculator. It is useful to have some approximation of the parameter in order to pick out errors in implementing more complex or automated schemes.

In the preceding paragraphs, the importance of an empirical and handbook prediction experience base has been stressed. A similar situation exists for computations in that there is a need to establish a computational drag prediction experience base. With this in hand, an engineer will know when to trust the computational tools for absolute drag predictions, when incremental drag predictions should be used, and when to select alternate means. The subsections that follow illustrate elements of a computational drag prediction experience base.

Skin Friction & Pressure Drag

Friction drag is computed by a number of computational methods but it is important that basic formulas are in hand to put computations in proper perspective. In the USA, the Karman-Schoenherr formula (Ref 18) has been approved for use by NASA, the Navy, and the Air Force based on agreement with test results. The average incompressible turbulent skin friction coefficient relation is:

$$0.242 = \sqrt{C_{f1}} \log_{10} (C_{f1} Re_1) \quad (8)$$

Results using this formula are best tabulated for application reference, and this has been done in Table 3. In Europe, the Prandtl-Schlichting expression (Ref 19) has gained more acceptance. This relation is

$$C_{f1} = \frac{0.455}{(\log_{10} Re_1)^{2.58}} \quad (9)$$

Compressible friction coefficients can be generated from the incompressible Karman-Schoenherr coefficients by using the method of Ref 20 coupled with the charts found in Ref 21. Figure 12 is a graph that is convenient for project use.

One limitation of these relations is that it is not possible to perform configuration-specific prediction tasks where the viscous drag level depends on detailed surface shaping. This is where computational methods can complement the drag prediction process.

Eppler's method (Ref 22) can be used to design and analyze two dimensional airfoil shapes when compressibility effects are small. This formulation is well-suited to applications characterized by mixed laminar and turbulent flow. An airfoil section can be synthesized using Eppler's conformal mapping procedure by specifying regional pressure distribution characteristics. The resultant shape can then be analyzed with Eppler's distributed surface singularity scheme since it is coupled with an integral momentum/energy equation boundary layer method. But airfoils designed using Eppler's method will only be as good as the method's ability to predict drag forces. It is here that existing works in the literature do not provide sufficient information. To fill this void, Eppler's method can be applied to establish a computational prediction experience base using airfoil catalogs such as Refs 23 and 24. It can be seen that

**Table 3 Karman-Schoenherr
Average Turbulent Friction Coefficients***
(Incompressible; M = 0, Insulated Case, Smooth Flat Plate)

REYNOLDS NUMBER	0 0	0 10	0 20	0 30	0 40	0 50	0 60	0 70	0 80	0 90	1 00
$10^5 \times 1$	7 179	7 022	6 883	6 758	6 645	6 543	6 449	6 362	6 282	6 207	6 137
	2	6 137	6 072	6 011	5 953	5 899	5 847	5 798	5 751	5 706	5 664
	3	5 623	5 584	5 547	5 511	5 477	5 444	5 412	5 381	5 351	5 322
	4	5 294	5 267	5 241	5 216	5 191	5 167	5 144	5 122	5 100	5 078
	5	5 057	5 037	5 017	4 988	4 979	4 961	4 943	4 925	4 908	4 891
$10^6 \times 1$	4 875	4 859	4 843	4 827	4 812	4 797	4 783	4 768	4 754	4 741	4 727
	7	4 727	4 714	4 701	4 688	4 676	4 663	4 651	4 639	4 628	4 616
	8	4 605	4 594	4 582	4 572	4 561	4 550	4 540	4 530	4 520	4 510
	9	4 500	4 490	4 481	4 472	4 462	4 453	4 444	4 435	4 427	4 418
	6	4 409	4 330	4 258	4 194	4 136	4 083	4 035	3 990	3 948	3 909
$10^7 \times 1$	3 872	3 838	3 806	3 775	3 746	3 719	3 693	3 658	3 644	3 622	3 600
	3	3 600	3 579	3 559	3 540	3 521	3 503	3 486	3 470	3 453	3 438
	4	3 423	3 408	3 394	3 380	3 367	3 354	3 341	3 329	3 317	3 305
	5	3 294	3 283	3 272	3 261	3 251	3 241	3 231	3 221	3 212	3 202
	6	3 193	3 184	3 176	3 167	3 159	3 151	3 143	3 135	3 127	3 119
$10^8 \times 1$	3 112	3 104	3 097	3 090	3 083	3 076	3 070	3 063	3 056	3 050	3 044
	8	3 044	3 037	3 031	3 025	3 019	3 013	3 008	3 002	2 996	2 991
	9	2 985	2 980	2 974	2 969	2 964	2 959	2 954	2 949	2 944	2 939
	6	2 889	2 849	2 813	2 780	2 749	2 721	2 696	2 672	2 649	2 628
	2	2 628	2 608	2 589	2 572	2 555	2 539	2 524	2 509	2 496	2 482
$10^9 \times 1$	2 470	2 457	2 446	2 434	2 423	2 413	2 403	2 393	2 383	2 374	2 365
	4	2 365	2 357	2 348	2 340	2 332	2 324	2 317	2 310	2 302	2 295
	5	2 289	2 282	2 276	2 269	2 263	2 257	2 251	2 245	2 240	2 234
	6	2 229	2 223	2 218	2 213	2 208	2 203	2 198	2 193	2 189	2 184
	7	2 180	2 175	2 171	2 166	2 162	2 158	2 154	2 151	2 146	2 142
$10^{10} \times 1$	2 138	2 135	2 131	2 127	2 124	2 120	2 116	2 113	2 110	2 106	2 103
	8	2 103	2 100	2 096	2 093	2 090	2 087	2 084	2 081	2 078	2 075
	6	1 972	1 945	1 920	1 998	1 977	1 959	1 941	1 925	1 911	1 897
	2	1 884	1 871	1 860	1 848	1 838	1 828	1 819	1 810	1 801	1 792
	3	1 784	1 777	1 769	1 762	1 755	1 749	1 742	1 736	1 730	1 724
$10^{11} \times 1$	1 719	1 713	1 708	1 703	1 698	1 693	1 688	1 683	1 679	1 674	1 670
	5	1 670	1 668	1 662	1 658	1 654	1 650	1 646	1 642	1 639	1 635
	6	1 632	1 628	1 625	1 622	1 618	1 615	1 612	1 609	1 606	1 603
	7	1 600	1 598	1 595	1 592	1 589	1 586	1 584	1 581	1 579	1 576
	8	1 574	1 571	1 569	1 567	1 564	1 562	1 560	1 558	1 555	1 553
$10^{12} \times 1$	1 551	1 549	1 547	1 545	1 543	1 541	1 539	1 537	1 535	1 533	1 531
	6	1 531	1 513	1 497	1 482	1 469	1 457	1 446	1 435	1 426	1 416
	2	1 408	1 400	1 392	1 385	1 378	1 371	1 365	1 359	1 353	1 348
	3	1 342	1 337	1 332	1 328	1 323	1 319	1 314	1 310	1 306	1 302
	4	1 299	1 295	1 291	1 288	1 285	1 281	1 278	1 275	1 272	1 269
$10^{13} \times 1$	1 266	1 263	1 260	1 258	1 255	1 252	1 250	1 247	1 245	1 242	1 240
	6	1 240	1 238	1 236	1 233	1 231	1 229	1 227	1 225	1 223	1 221
	7	1 219	1 217	1 215	1 213	1 212	1 210	1 208	1 206	1 204	1 203
	8	1 201	1 199	1 198	1 196	1 195	1 193	1 192	1 190	1 189	1 187
	9	1 186	1 184	1 183	1 181	1 180	1 179	1 177	1 176	1 175	1 173
*Multiply Tabulated Values by 10^{-3} To Obtain C_f											
M-81-6426-002											

Airfoil thickness in this collection will vary between 6% and 24% chord. Leading edge radius range is 0.2% to over 6%. chord. Flap lengths of 17% to 30% chord are present with up to 10 degrees deflection angle. The Reynolds number range is 0.7 to 10 million. Laminar flow extent varies between 0% and 60% chord.

Consider a problem involving an aircraft component strut, vertical tail, or antenna blade for which a symmetric low drag airfoil must be designed. The Figures that follow illustrate a portion of the aforementioned experience base that would prove useful for this type of application. In all cases to be described, the results were generated using Flanders' free transition option. This allows the transition point between laminar and turbulent flow to be determined as part of the solution process. For example, increasing incidence or Reynolds number will cause

the transition point to move forward on the airfoil with an attendant increase in dr_a . The transition point is "fixed" analytically in the sense that it need not be known or fixed a priori.

Figure 13 shows computed/experimental comparisons for NACA 65 series airfoils. Airfoils with 6%, 15%, and 21% thickness are included. Here, the airfoil type is fixed and the computational method must predict the laminar/turbulent drag trending. These comparisons indicate that the method is capable of predicting drag polar break point as thickness increases. There is some error noted in laminar/turbulent drag levels for low Reynolds numbers, this is aggravated by increases in thickness. In view of this, computed results for a new airfoil within this range would have to be properly adjusted to account for observed simulation trending discrepancies.

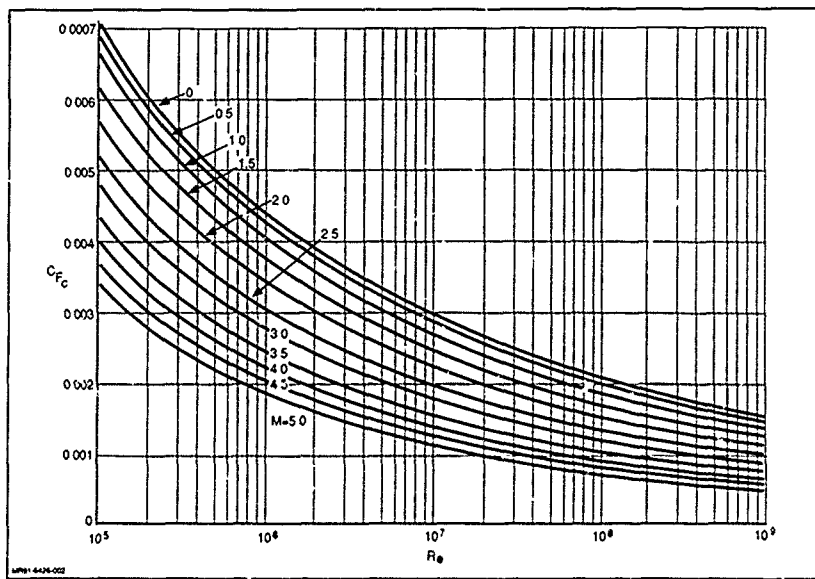
Fig. 12 Karman-Schoenherr Compressible Average Skin Friction Coefficient $T_w = T_{ad}$

Figure 14 depicts a second series. This time, airfoil thickness is fixed and the series type is changed NACA 4-Digit, 64, and 66 airfoil types are included. The method's ability to predict effects (due to position of maximum thickness, nose radius, and ultimately, the chordwise extent of laminar flow) is measured. Once again, agreement is quite good. Some discrepancy in the laminar-turbulent drag break-point can be identified for the airfoil with maximum thickness shifted aft.

For a vertical tail application, an airfoil with a simple flap might be of interest. Several airfoils featuring flap deflections have been included in Fig. 15. The first airfoil is 15% thick with a 30% chord flap deflected 0 and 10 degrees. The second airfoil is similar but the flap chord length is 20% chord. The last section features tripped turbulent flow for a 25% chord flap. Agreement is good save for small regions at low incidence where flap hinge-line gaps may be causing non-potential flow phenomena that are beyond the computational method's modeling capabilities.

With these cases, it should be apparent how computed characteristics for any newly developed airfoil might be corrected for computational simulation limitations and specific airfoil-type idiosyncrasies. Only then can a new shape and its performance be compared and evaluated within an existing family.

Eppeler's method proves easy to use in both the design and analysis mode. Solutions require only a few minutes on common personal computers.

Some design projects might require drag predictions or drag reducing surface optimization for multi-element airfoils that would be suitable for high-lift applications. Eppeler's method is constrained in viscous modeling to treating single element airfoils. Stevens' method (Ref. 25), however, does include

complex multiple stream flow mixing models needed for simulating airfoil flows with complex flap/slotted combinations. The guidance provided by this technique is derived from a demonstrated ability to permit optimization of the element gap and overlap parameters - a task that can be time consuming and costly if consigned to experimentation.

Figure 16 highlights the type of drag prediction accuracy that can be expected for a multi-element airfoil application. A Wortmann FX 67 F-141 section with a Fowler flap (Ref. 24) extended 30 degrees can be identified. Stevens' method provides the high lift result while Eppeler's method predicts the flap stowed case at lower lift levels. This comparison is useful, but the volume of data available for multi-element, high lift sections is severely limited. Interference-free wind tunnel data at very high lift levels is difficult to achieve, and many data sources are constrained to proprietary organization-specific archives. This impairs the engineer's ability to establish a complete simulation experience base.

Like Eppeler's method, Stevens' computer program can be implemented on personal computers. Solutions take about 30 minutes.

In some applications, compressibility effects can not be ignored. Eppeler's and Stevens' methods will not be applicable. One computational tool that has performed remarkably well for both low Reynolds numbers and transonic airfoil cases characterized by strong viscous inviscid interactions is that of Drela and Giles (Refs. 26 and 27). This analysis and design approach is considerably more expensive to implement than methods described so far, but some applications warrant additional effort and 2-D problems are orders of magnitude simpler to deal with than complex 3-D problems. Drela and Giles' method is discussed in the Wave Drag section.

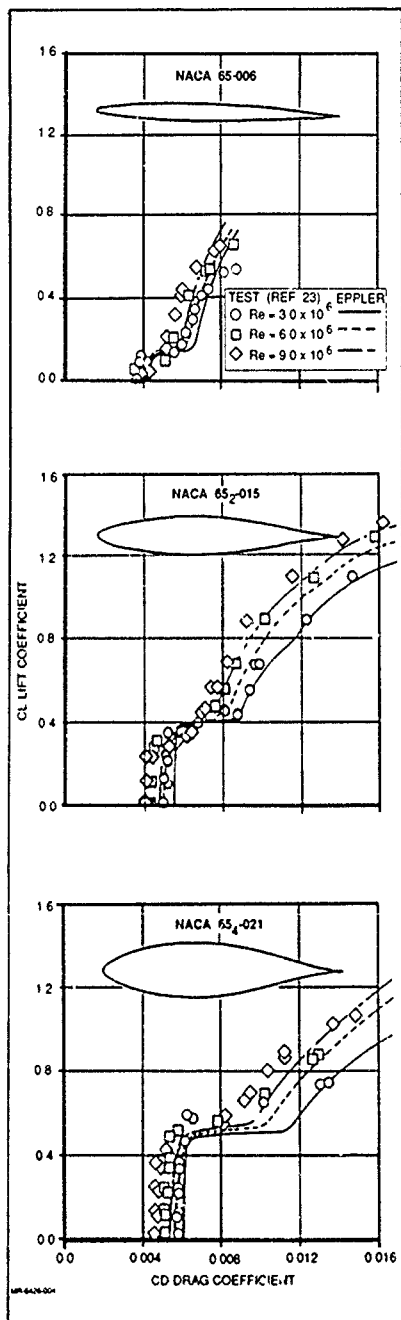


Fig. 13 2-D Airfoil Drag Correlation-Thickness Effects

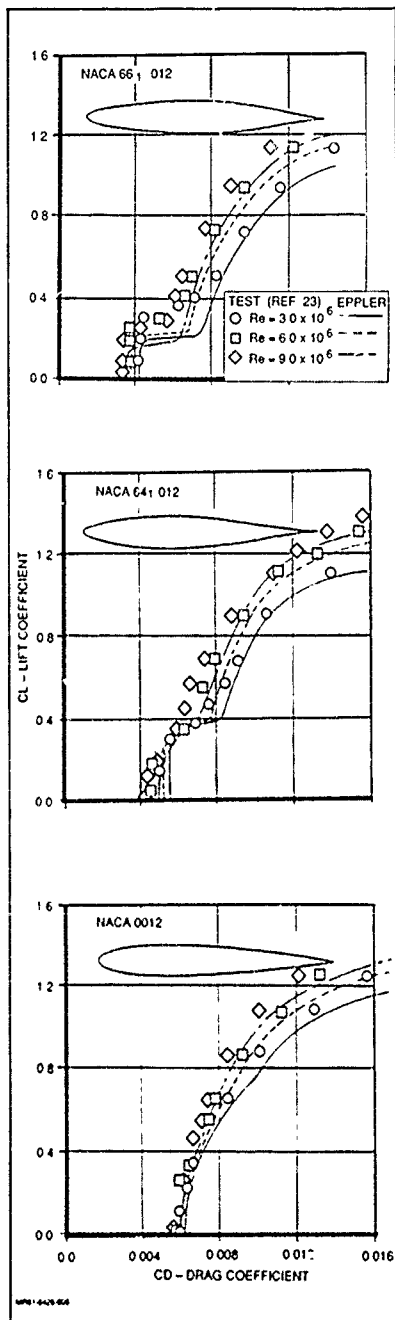


Fig. 14 2-D Airfoil Drag Correlation Laminar Flow Extent Effects

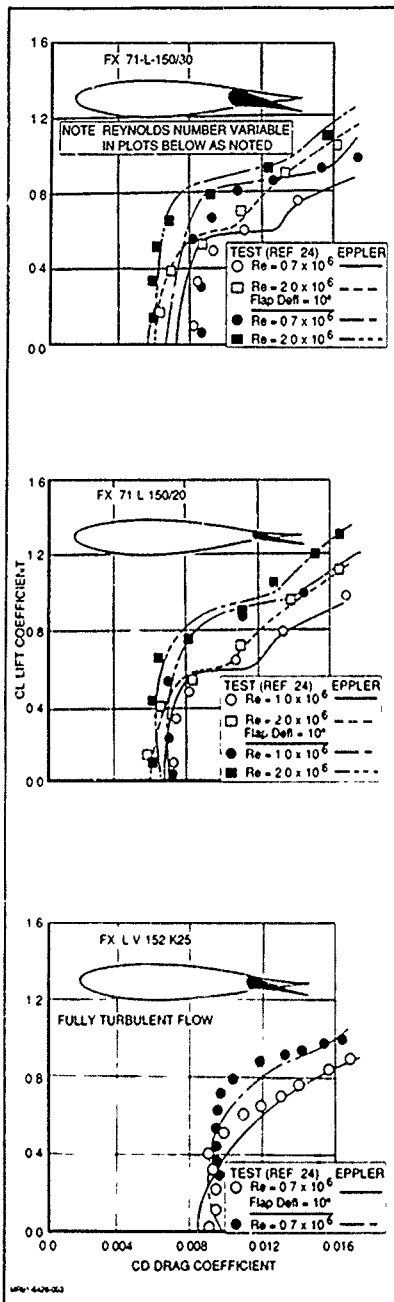


Fig. 15 2-D Foil Drag Correlation-Tab Deflection/Length Effects

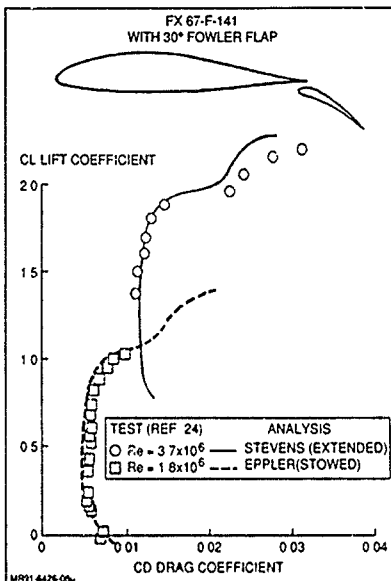


Fig. 16 Eppler & Stevens Method Prediction of Airfoil-Fowler Flap (Extended & Stowed) Drag Polars

Lift-Induced Drag

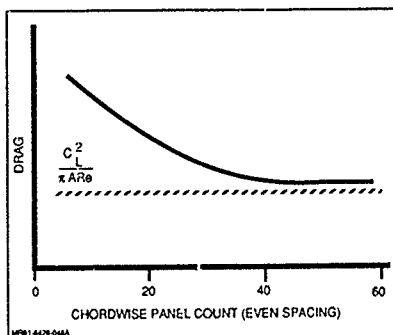
As noted in the Background section, lift induced drag registers on the aircraft surface as a form of pressure drag. Computational methods can integrate computed normal pressures to predict lift-induced drag, but in many applications where absolute drag levels are important, unsatisfactory results are obtained. This is the case because lifting surface leading edge suction forces (a component of lift-induced drag) are resolved to a degree that depends on the computational method's panel or grid resolution. As modeling element or grid density is increased, the lift induced drag level will decrease asymptotically approaching the exact or true level that would be achieved with infinite resolution (Sketch A). In a project application, pressure integration results must be used cautiously with the engineer ensuring that the computed difference between two configurations is aerodynamic in character and not numerical.

A more reliable approach (Ref. 29) to computing lift induced drag for wing-dominated configurations is that proposed by Glauert (Ref. 30). It involves integrating the load (or wake) distribution developed by the lifting configuration. For this task, the circulation would be equivalent to the spanload given by

$$\Gamma(y) = \frac{C_{loc} C_l}{C_{ref}}. \quad (10)$$

Using the notation of Ashley and Landahl (Ref. 31), the lift and induced drag can be written

$$L = \rho U_\infty \int_{b/2}^{b/2} \Gamma(y) dy \quad (11)$$



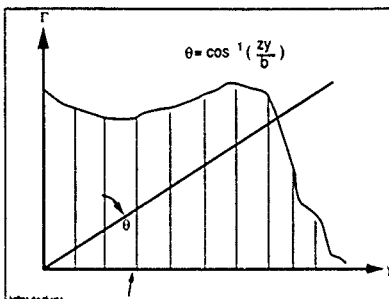
Sketch A Effect of Chordwise Panel Density on Computed Lift-Induced Drag Level

$$D_l = \frac{\rho}{4\pi} \int_{-b/2}^{b/2} \int_{-b/2}^{b/2} \Gamma(y) \frac{d\Gamma}{dy_1} \frac{dy_1 dy}{(y - y_1)} \quad (12)$$

then

$$\frac{1}{e} = \frac{\sum_n A_n^2}{A_1^2} \quad (19)$$

By expanding the full aircraft load distribution out to $\theta = 2\pi$ (Sketch B), the distribution can be Fourier analyzed to solve for the coefficients. The resulting prediction method proves very fast requiring only seconds on common personal computers.



Sketch B θ -y Relation for Fourier Analysis

and the circulation is represented by a Fourier sine series

$$\Gamma = U_\infty b \sum_{n=1}^{\infty} A_n \sin n\theta \quad (13)$$

This yields:

$$L = \frac{\rho}{4} U_\infty^2 b^2 A_1 \quad (14)$$

$$D_l = \frac{\rho U_\infty^2 b^2}{8} \sum_n A_n^2 \quad (15)$$

and in coefficient form

$$C_l = \frac{L}{\frac{1}{2} \rho U_\infty^2 S} = \frac{\pi b^2 A_1}{2 S} \quad (16)$$

$$C_{Dl} = \frac{D_l}{\frac{1}{2} \rho U_\infty^2 S} = \frac{\pi b^2 \sum_n A_n^2}{4 S} \quad (17)$$

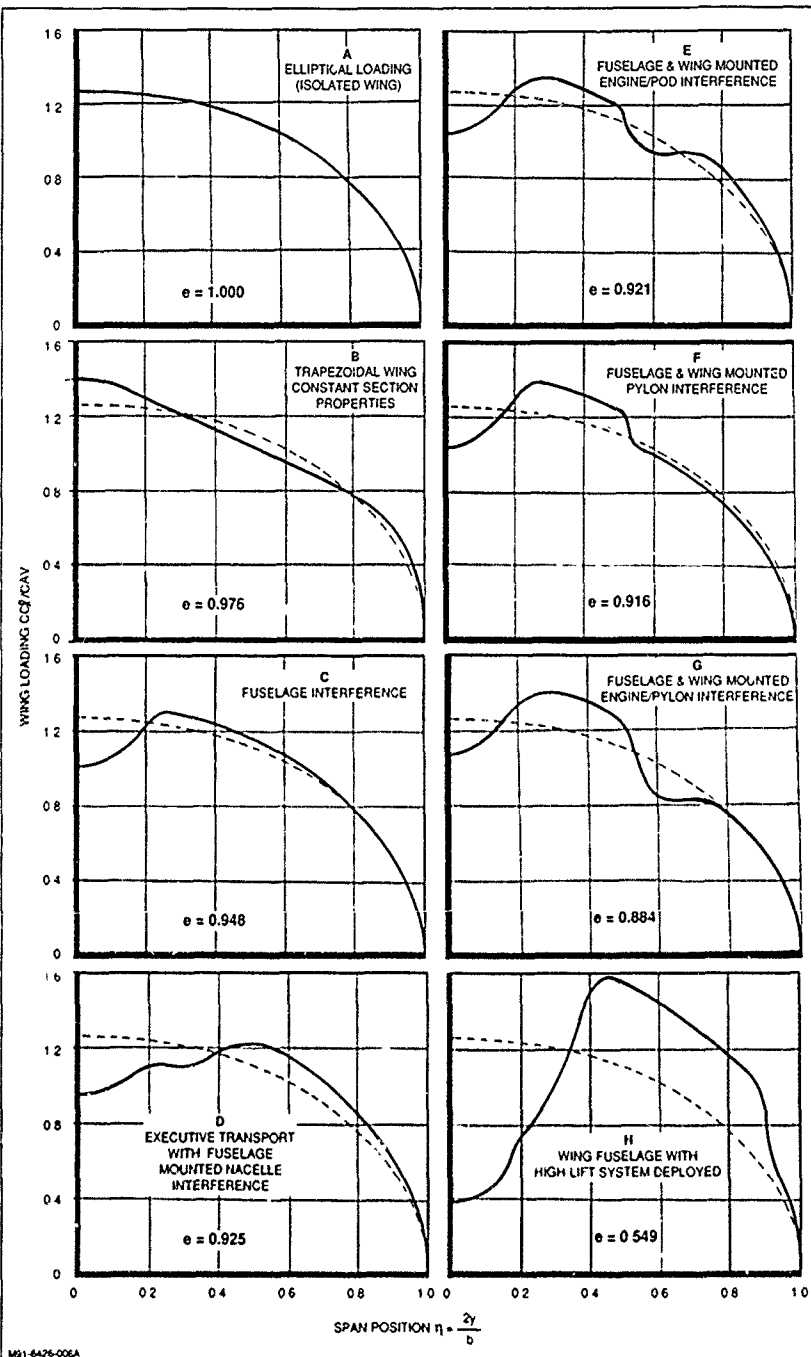
To compute a spanload efficiency factor "e" on the basis of

$$e = \frac{C_l^2}{\pi A R C_{Dl}} \quad (18)$$

Aircraft configuration spanwise load distributions can vary considerably depending on the general arrangement and flight conditions. A number of example cases for both symmetric and unsymmetric loadings have been computed using the Fourier analysis previously described. These cases illustrate the typical range of lift-induced drag "efficiency" factors that might be encountered during project applications.

Figure 17 illustrates eight cases of symmetric wing/aircraft loadings and, as such, only half of the loading is displayed. All cases represent a common lift level at $C_l = 1.0$. Note that the slope of the loading distribution is "0" at the centerline or symmetry plane. It is well known that an elliptic load distribution results in minimum lift induced drag. This load is seen in Fig. 17-A along with the computed "e" factor of 1.0. Elliptic loading is most easily attained with an isolated wing arrangement, since body or fuselage components are very inefficient in generating lift. This causes a deficit or depression in the loading curve at the body location. In many aircraft design applications, including fighters and transports, aerodynamicists attempt to achieve elliptic loading. In some applications, however, the resulting combination of induced, wave, and friction/pressure drag sources may not represent an optimum, although the conventional lift induced or vortex drag has been minimized. Another load distribution is that generated by near-constant section properties (Fig. 17-B) on a trapezoidal planform isolated wing. For this loading, drag creep (that might be generated by some local airfoil sections developing wave drag prior to others) is minimized. All wing airfoil sections approach drag divergence simultaneously. For this example, "e" drops to 0.976.

Loading on a fuselage is largely the result of wing carry-over (Fig. 17-C). Often little can be done to compensate for the load deficit that will mostly be determined by the percentage of the wing span blanketed by the fuselage surface. Figure 17 shows



MS1-6426-005A

Fig. 17 Examples of Aircraft Symmetric Loading Distributions With Lift-Induced Drag Efficiency Factor

the loading that might exist on many executive transports (business jets) where nacelles are mounted aft on the fuselage via a short pylon. The nacelle/pylon combination inhibits wing circulation near the wing-fuselage juncture. In this case, "c" might drop to a level of 0.925.

Engines are often mounted in or about the wing surface using pylons. For embedded engines or pods, an effect similar to that for the fuselage can be identified. Pylon surfaces are different. There is typically an "end-plating" effect that increases loading inboard of the pylon station and reduces loading outward. This is the case because the inboard portion behaves more two-dimensional in character while the outboard segment functions as a lower aspect ratio wing segment. Figures 17-E/F/G illustrate these possibilities. The worst case is for wing loading featuring fuselage, pylon, and engine nacelle interference.

Perhaps the largest influence on wing loading distribution will occur when effective high lift systems are deployed for landing. The spanload efficiency factor can be extraordinarily low, but, fortunately, there is little concern about drag forces during this brief segment of any flight.

Unsymmetric load distributions are generated in sideslip and when control surfaces are deflected to roll the aircraft. Figure 18 A illustrates the type of load distribution that can exist for any swept-wing aircraft in sideslip. Asymmetry is created by variations in lifting efficiency between two wing halves that now have different sweep angles. In this example, the starboard wing effective sweep is greater than the physical sweep angle, while that for the port wing is less. The resulting degradation in "c" could be subtle (0.975).

Fighter asymmetric loadings can be quite severe because a premium is placed on roll effectiveness in air-to-air combat. Lift-induced drag increases as the roll maneuver is initiated. Many aircraft designs use ailerons for roll control. While the rolling moment can be very large with control surfaces positioned near the wing tips, the resultant induced drag penalty can be high for the same reason (Fig 18 B). In other words, it is apparent from these example cases that the lift induced drag level is affected to a larger extent when a loading anomaly exists at the wing tip than when it is positioned inboard.

Another form of roll control can be derived by differential tail deflection. Figure 18 C shows the combined lifting surface load distribution that might result for this type of asymmetric configuration. Figure 18-D is a similar plot illustrating use of wing mounted spoiler deflections to generate rolling moments. It should be recognized that the cases highlighted in Fig. 17 and 18 are not specific to any particular aircraft. The true detailed loadings for an aircraft application will be a function of the configuration's geometry and design lift level. These generic examples, however, should prove useful for establishing trends linked to wing loading.

Transonic & Supersonic Wave Drag

Wave drag losses are generated by flow about the aircraft passing through shock waves. As noted in the background section, shock waves can form at subsonic speeds if wing or fuselage surfaces accelerate the free-stream flow to sufficiently large supersonic velocities. Mixed flow regions featuring an embedded supersonic flow region within a subsonic external flow (separated by a shock wave at the aft boundary) are classified as transonic. Transonic flows also exist at low supersonic speeds when small subsonic flow regions are embedded in an external supersonic flow (i.e., at the nose of a fuselage or leading edge of a wing where a stagnation point generates the reduced velocity "island"). In all high speed cases,

whether transonic or supersonic, there is an incentive to achieve shock wave surfaces that are oblique to the flow direction. This minimizes wave drag losses because the largest drag penalties are generated by flow through normal shock waves.

Many computational methods have been developed for high-speed aircraft applications, particularly at transonic speeds. But the character of complex three-dimensional mixed (subsonic/supersonic) flows presents a considerable challenge for algorithm developers. At present, computationally predicted transport cruise drag level accuracy might be on the order of 10-30 counts. At the upper end of this range, the project requirement might demand errors that are an order-of-magnitude less. Fighter applications reveal larger prediction discrepancies derived from a higher level of three-dimensionality and the complexities linked to mixed (attached, separated, vortical) flows. Computational drag prediction discrepancies greater than 100 counts are possible.

Three-dimensional computational methods have, however, demonstrated an ability to predict surface shock wave patterns. This allows the designer to develop shapes that generate weak oblique shock waves. But perhaps more important, it provides a basis for applying simpler, less expensive two-dimensional computational methods in a drag build-up process with potential for higher prediction accuracies. Figure 19 provides examples of transonic shock wave positioning for three-dimensional configurations.

Simple Sweep Theory (Ref. 32) establishes a means for relating two-dimensional airfoil characteristics to three-dimensional wing performance. Similarly, Sweep Theory can be used to translate wing performance requirements into a set of specifications suitable for two-dimensional airfoil design. The cosine relations linking two- and three-dimensional parameters are listed below:

$$M_2 D = M_3 D \cos \Lambda_{eff} \quad (20)$$

$$C_{L2-D} = C_{L3-D} / \cos^2 \Lambda_{eff} \quad (21)$$

$$V_{c2-D} = V_{c3-D} / \cos \Lambda_{eff} \quad (22)$$

$$C_{P2-D} = C_{P3-D} / \cos^2 \Lambda_{eff} \quad (23)$$

$$C_{D2-D} = C_{D3-D} / \cos^3 \Lambda_{eff} \quad (24)$$

The proper sweep angle must be identified to implement these relations. For an infinite sheared wing panel (Fig. 20 A), there is only one possibility—the panel sweep angle. This represents the original embodiment of Sweep Theory. Considering a finite tapered wing planform (Fig. 20-B), two-dimensional simulations of three-dimensional wing pressure fields at subsonic speeds reveal that the quarter-chord sweep angle serves well as an "effective" sweep angle for the five formulas listed above. The most complicated situation exists for transonic conditions where shock waves are present on the wing surface. Engineering studies (Ref. 32) performed during the HiMAT (Highly Maneuverable Aircraft Technology) Program revealed that the local sweep angle of the shock wave provided the best effective sweep angle for Sweep Theory conversions.

This definition of effective sweep at transonic conditions may at first be difficult to understand, however, it might be made more apparent by considering an example. Figure 21 shows a set of wing pressure distributions extracted from the mid section of an aspect ratio 5.8, 40 degree swept back wing with a taper ratio of 0.4. The symbols represent wind tunnel test measurements. The solid line comparisons are generated using a transonic two-dimensional airfoil analysis method (Ref. 33) with Mach and lift

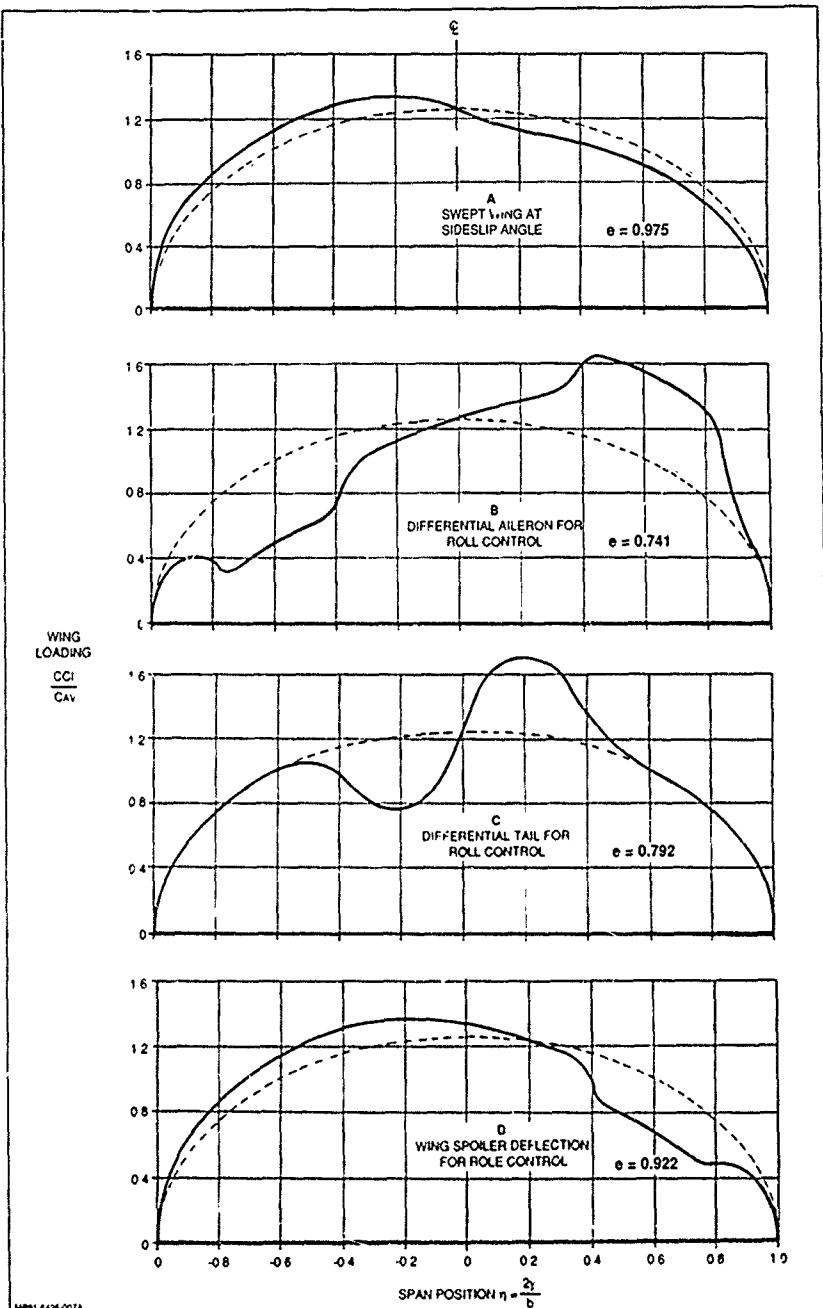


Fig. 18 Examples of Aircraft Unsymmetric Loading Distributions with Lift-Induced Drag Efficiency Factor

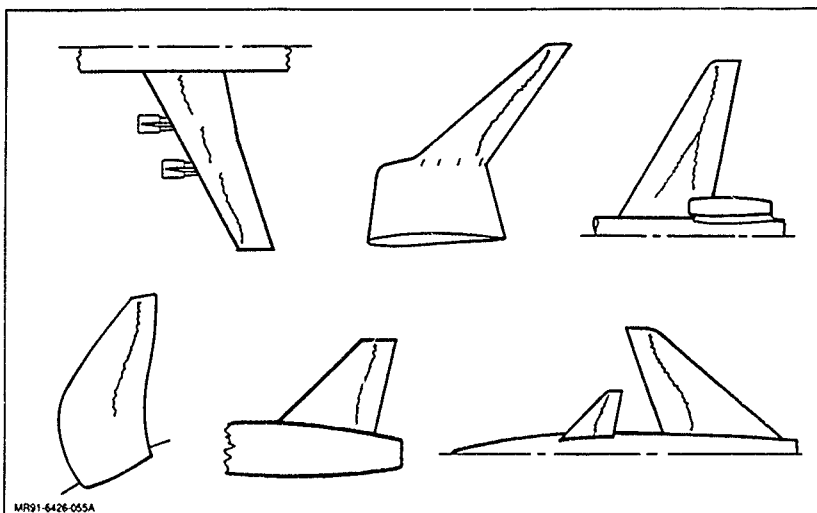


Fig. 19 Shock Wave Unsweep Regions

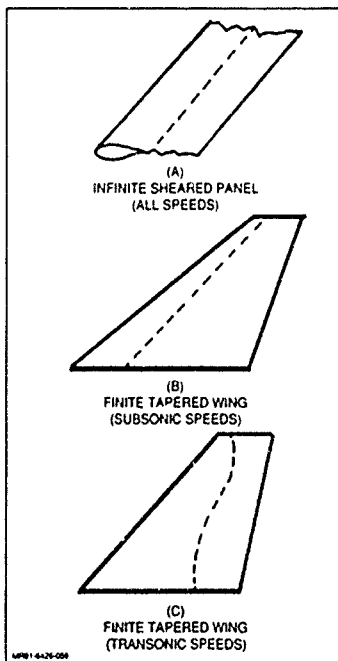


Fig. 20 Effective Sweep Basis for Different Applications

conditions specified using equations 20 and 21. The extracted airfoil shape is scaled using equation 22, taking into account the geometric local sweep lines of the tapered wing (Ref 32). Simulation agreement is excellent. But to achieve this agreement, the variability in effective sweep with local flow conditions must be accounted for. Table 4 illustrates this fact by listing the wing shock wave position, sweep angle, and the derived "effective" two-dimensional conditions used for analysis cases. Note that as the wing shock wave strengthens with increasing free-stream Mach number and moves aft, the effective sweep angle used in equations 20-24 decreases. Agreement cannot be obtained unless this variation in effective sweep with flow condition is taken into account.

An airfoil is now selected to establish wing drag prediction potential using this build-up approach. Reference 34 provides data for the RAE 2822 airfoil. The transonic design pressure distribution is seen in Fig. 22. To generate a drag rise curve, some effort is required. Data that is not all at the same lift level must be adjusted. This can be done using Kom's relation (Ref 33)

$$M + C_l/10 + v/c = K \quad (25)$$

Dr. David Kom of NYU's Courant Institute determined that he could design transonic airfoils with parameters that consistently summed to certain values depending on the level of technology (or aft loading). The design engineer can use Kom's relation to establish approximate trades between the airfoil Mach number, thickness, and design lift level. "K" levels for conventional airfoils are near 0.87 while "K" for highly aft-loaded supercritical sections can be near 0.95. Figure 23 shows an experimental drag rise curve along with the curve that results when points are adjusted to a common $C_l = 0.74$. A design point for this section (at maximum M/D) occurs near $M = 0.7$.

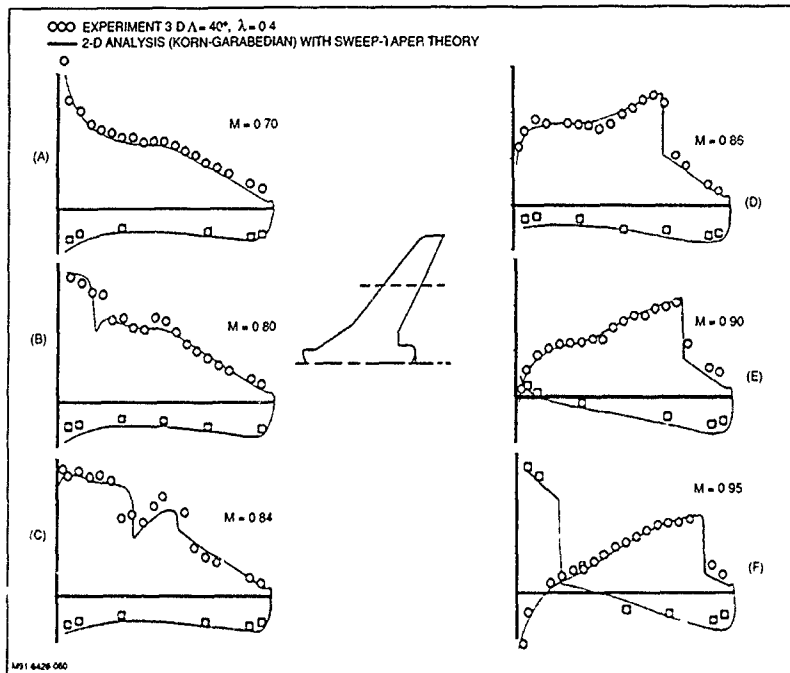


Fig. 21 Wing (3-D) Pressure Distribution Correlation using 2-D Airfoil Analysis & Sweep-Taper Theory

Table 4 Wing Effective Mach Number for 2-D Analysis

FIG	% LOCAL CHORD 2-D ANALYSIS & REDUCTION	LOCAL SWEEP ALOC	FREE-STREAM MACH M_∞	2-D NORMAL MACH M_N	EQUIV SIMPLE SWEEP THEORY M_N
21 A	25%	37.42°	0.70	0.556	0.556
21 B	25%	37.42°	0.80	0.635	0.635
21 C	30%	36.89°	0.84	0.672	0.667
21-D	70%	32.30°	0.86	0.727	0.683
21-E	70%	32.30°	0.90	0.761	0.715
21 F	85%	30.45°	0.95	0.819	0.754

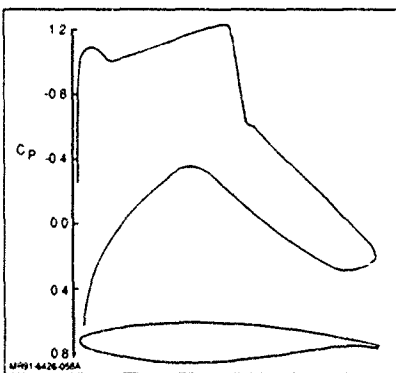


Fig. 22 RAE 2822 Airfoil Pressure Distribution at $M_\infty = 0.725$, $\alpha = 2.9^\circ$

The resulting "K" value is 0.89. Test data at $M = 0.725$ is closest to this point and there is no indication of appreciable flow separation despite a reasonably strong shock wave. The shock wave is positioned at 55% chord. A compendium of code/experiment comparisons found in Ref. 35 reveals that (considering a large number of different computational methods) two-dimensional computational drag predictions vary by approximately 5%. At the more extreme $M = 0.74$ case a 25%

variation between methods can be identified. Shock wave position varied by as much as 5% chord for $M = 0.725$ while the location spread for $M = 0.74$ was about 10% chord.

The technique for translating two-dimensional drag and shock wave location discrepancies into three-dimensional wing parameters can be illustrated by considering two wing

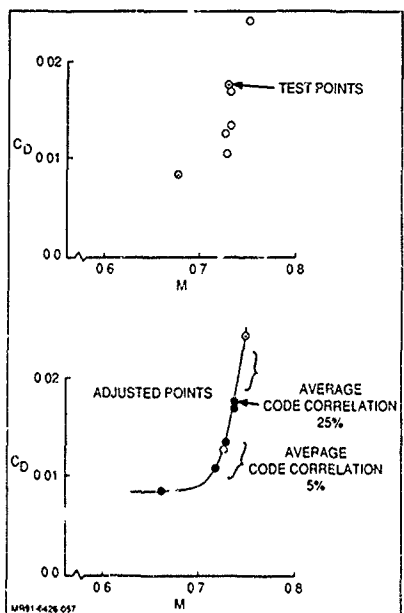


Fig. 23 RAE-2822 Airfoil Drag Divergence Curve Data & Adjusted Data ($C_L = 0.74$)

planforms one for a transport and a second for a fighter (Fig. 24). Planform parameters are listed below.

Transport Wing	Fighter Wing
$AR = 8$	$AR = 3$
$\lambda = 0.4$	$\lambda = 0.2$
$\Delta LE = 25^\circ$	$\Delta LE = 40^\circ$

Using the RAE 2822 airfoil (with shock position at 55% chord), the effective sweep angle at transonic conditions for both wing planforms is 19 degrees. Thus, for a wing design Mach number of 0.77, RAE data at $M = 0.725$ (Eq. 20) can be used. The two-dimensional section generates 107 counts ($CD = 0.0107$) of drag at $C_L = 0.74$. This translates into a 4 1/2 count error band for friction/pressure/wave drag on the transport wing using a projected 5% spread in prediction accuracy and Eq. 24. The same 4 1/2 count error band would hold for the fighter wing assuming that the design lift coefficients are identical. Now, it can be imagined that a 5% chord discrepancy in shock wave location exists. Considering the transport wing, a shock wave position at 60% chord results in a higher normal Mach number ($A_{eff} = 18.7$ deg.), about 0.73. Airfoil drag level rises to 125 counts, this effectively registers as a 6-count error for the transport wing. The fighter wing effective sweep for a 60% chord shock location is 17 degrees. The resulting two-dimensional Mach number is 0.736. From Fig. 23, the airfoil drag level rises to 157 counts yielding a wing drag level error of 34 counts - since now at the higher effective Mach number, a 25% prediction error applies.

Errors generated by this build up process using both two- and three-dimensional techniques coupled via Sweep Theory, will result in errors that are considerably smaller than those attributed

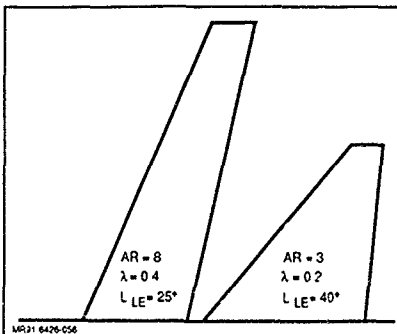


Fig. 24 Transport & Fighter Wing Planforms

to a purely three-dimensional approach. The exercise shows that both drag prediction accuracy and shock wave prediction accuracy are equally important to properly determine transonic wave drag levels. It should also be apparent why fighter wing prediction errors can be considerably greater than those for transport wings, even in applications where separated or vortical flow is not present.

Prediction discrepancies identified in the preceding paragraphs represent an average that might be obtained by selecting a computational analysis at random and applying computed results directly. These discrepancies can be considerably reduced by selecting a method that performs better than others or one that is more accurate for the particular application at hand. A Computational Airfoil Catalog can provide the flow simulation experience base needed by project applications engineers. This type of catalog would highlight the strengths and weaknesses of many computational tools and provide sufficient test-verification cases to establish correction factors for a wide range of airfoil types and design conditions.

One relatively new technique that shows promise for reducing both airfoil drag prediction error and shock location error levels is that of Drela and Giles (Refs. 26 & 27). The Drela and Giles airfoil analysis/design code is not like others in that its formulation includes an Euler solution for the outer flow region that is coupled with a two-equation integral boundary layer scheme. The set of equations is solved by a global Newton iterative process. Comparison cases reveal that the laminar/turbulent boundary layer technique works well for strong interaction cases potentially minimizing "adjustments" that might be applied at higher Mach numbers where drag prediction discrepancies are typically 25%.

From Ref. 35, it should be apparent that Navier Stokes solvers have yet to demonstrate superiority over more conventional schemes (i.e., Drela's method) for drag prediction. This is the case despite the fact that Navier Stokes methods might require two orders-of-magnitude more computing resources than current coupled methods.

Wave drag prediction at supersonic speeds often presents a simpler task than that at transonic speeds because of the applicability of supersonic linear theory and the supersonic area rule concept (Refs. 36 and 37). There are a few assumptions. One is that flow disturbances propagate outward along Mach lines and there is no dissipation with increasing distance. Another is disturbances are a function only of the cross sectional area distribution, i.e., the "flow interference" between

components due to relative positioning is not modeled. Finally, it is assumed that configuration wave drag can be predicted by computations performed for an equivalent body-of-revolution

Reference 38 provides von Karman's equation for the wave drag of a smooth, pointed body-of-revolution

$$C_D = \frac{1}{2\pi S_{REF}} \int_0^L \int_0^L \frac{d^2S}{dx^2} \frac{d^2S}{d\xi^2} \ln(x-\xi) dx d\xi \quad (26)$$

An equivalent body-of-revolution for an aircraft configuration is generated by selecting a number of longitudinal stations between the configuration nose and tail. At each station, cutting planes inclined at an angle.

$$u = \sin^{-1} (1/M) \quad (27)$$

relative to the x-axis (see Fig. 25-A) generate a planar area value that is associated with the station "x" location. This can be done graphically as shown in Fig. 25-B, or the procedure might be automated for use on digital computers. This cutting process is performed repeatedly for a number of roll angles, as depicted in Fig. 25-C. An effective drag for the equivalent body-of-revolution at each roll angle is computed and these values are then integrated to arrive at the total configuration wave drag coefficient. This procedure, combined with von Karman's relation (Eq. 26), was automated by Boeing engineers and documented with sample cases by Harris (Ref. 39). The resulting computer program has experienced application throughout the aircraft industry since its inception in 1966.

The Far Field Wave Drag Program is very simplistic by any standard. But the flexibility and complexity potential for modeling realistic aircraft shapes is extraordinary and its applicability range is quite large. Predictions for shapes that appear to exceed the bounds of linear theory are often useful for engineering purposes.

Modeling flexibility is illustrated in Fig. 26. This model of the Navy/Gruuman F-14 Tomcat was generated in the late 1960s (Ref. 40). The aircraft is modeled using a set of wing and body type components. Figure 27 shows how design engineers optimized placement of the various components to match as close as possible the optimum supersonic body area distribution. This was achieved despite a number of constraints that included overall fineness ratio, nozzle exit area, and placement of internal elements. Application of this technique is the primary reason for the F-14 being positioned in what is often called the "Third Generation of Supersonic Aircraft" (Ref. 8, and Fig. 28). It is simply too expensive and there is insufficient time to perform the wave drag minimization process with this degree of integration by experimentation alone.

One facet of drag analysis that should be noted at this point is numerical optimization. While the engineer can sequentially establish a shape modification via a "direct" computational analysis for evaluation, modification and re-evaluation, etc., there is considerable incentive to perform shape optimization using the speed of modern digital computers. In other words take the engineer out of the loop and speed up the process. Another approach might involve the use of "inverse" methods. These techniques synthesize a shape based on specified flow characteristics such as velocity or pressure fields. A useful perspective on optimization methods can be found in Ref. 41.

The methods just described can provide valuable guidance on aircraft design projects, but there are limitations that should be recognized. First, assuming that low-drag pressure/velocity

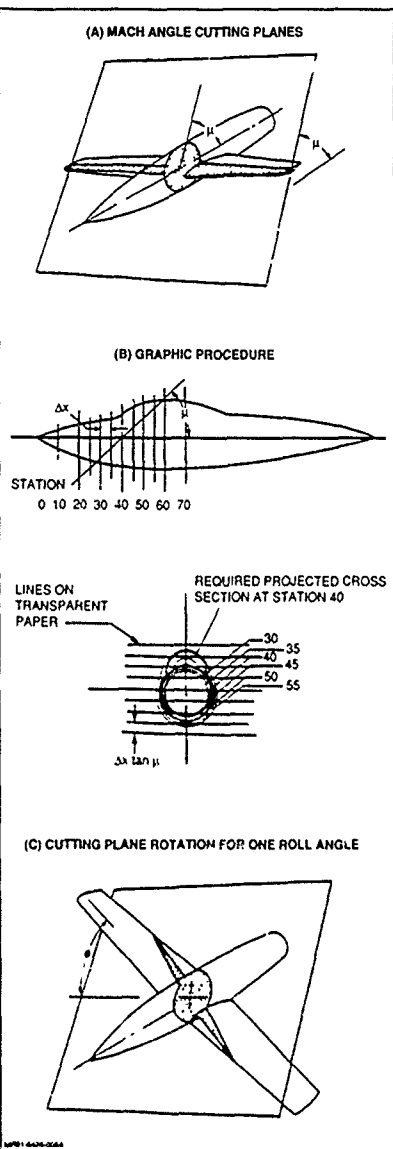


Fig. 25 Generation of Equivalent Body-of-Revolution for Supersonic Area Rule (Refs 17 and 39)

fields are properly specified, it is well known that an inverse method is simply not as robust as its direct method counterpart. In view of this, during a project application, an engineer sequentially performing direct analyses with modifications will usually be able to surpass the result generated by another engineer designing by inverse methodology. One way to circumvent this limitation is described in Ref. 42. Here, a type of

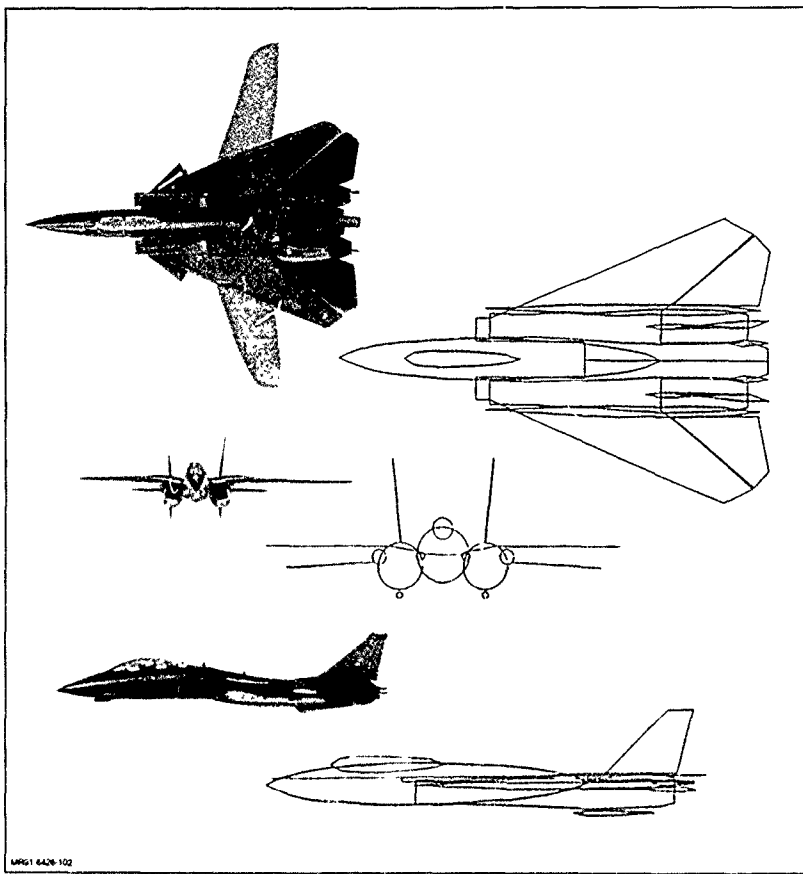


Fig. 26 F-14 Harris Wave Drag Program Model (Body & Wing Elements)

'modified direct' approach is described that is in essence an inverse technique. The key to this approach, however, is that it retains the strengths of the parent direct method.

Numerical optimization, in the classical sense, is constrained by a number of factors. First, the optimization scheme is extraordinarily expensive to implement due to the large number of analyses that are needed to establish appropriate trending. Second, reasonableness criteria are typically not applicable and as a result some lengthy computational optimization processes converge to an unrealistic or impractical shape. Finally, the parent analytical method's drag prediction fidelity is often impaired. This results in the optimizer processing deficient performance information with the outcome being a design shape that is suspect. Reference 43 describes an approach to working around these problems. In this scheme, a CONMIN optimizer (Ref. 44) is coupled with design variables that are generated using conventional inverse techniques and objective functions that are "aerodynamics specific." The resulting numerical optimization process is essentially tuned to handle aerodynamic

design applications and, as such, requires less computing resources than a method set up to treat general optimization problems.

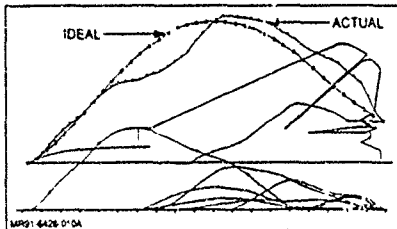
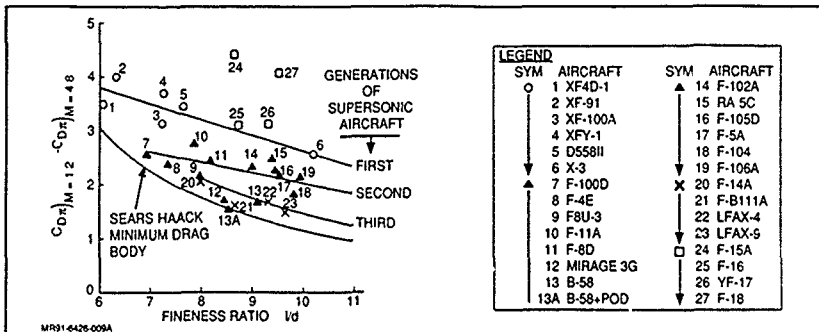


Fig. 27 F-14 Optimized Normal Area Distribution



Throttle-Dependent Drag

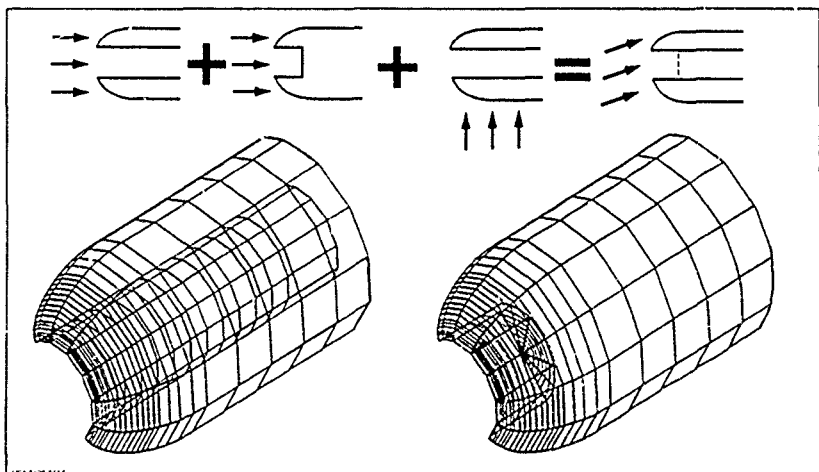
Aircraft throttle setting will affect both the inlet spillage level and the exhaust nozzle pressure ratio. The interaction of the spillage flow on inlet surfaces (Ref. 45) and any neighboring aircraft components will generate a resultant drag or thrust force. Similarly, exhaust plume interaction variations might raise or lower aircraft drag levels, depending on the particular configuration arrangement and flow characteristics. The complexity of flows associated with this drag source guarantees that on many projects the first throttle-dependent drag estimates will not be in hand until powered sub-scale testing is completed. However, two examples are included here to illustrate how computational methods can provide useful information prior to testing.

Inlet/nacelle surfaces can be modeled using a variety of subsonic, transonic, and supersonic computational methods. The example in Fig. 29 uses the subsonic "source" method of Ref. 46. The appropriate surface singularity panel model can be identified. A clever scheme outlined in Ref. 47 can be used to generate flow solutions for any incidence angle and any inlet flow rate by computing three inlet solutions and combining the

results (a form of superposition). The first inlet/nacelle model is characterized by an open or flow-through duct. The second model's duct is closed. A third model is identical to the first, but the angle of attack is set to 90 degrees. The following relation is used to compute the local surface velocities

$$V = \left[\frac{\frac{V_1 - V_2}{V_0 - V_0} \cos \alpha}{\frac{V_1 - V_2}{V_0 - V_0}} \right] V_{OPEN} + \left[\frac{\frac{V_1 - V_1}{V_0 - V_0} \cos \alpha}{\frac{V_1 - V_2}{V_0 - V_0}} \right] V_{CLOSED} + V_{CROSS} \sin \alpha \quad (28)$$

Local velocities are converted to pressure distributions that are integrated to obtain drag forces. Figure 30 reveals that this simple scheme can provide accurate pressure field details over a large range of shape, incidence angles, and flow rates. A



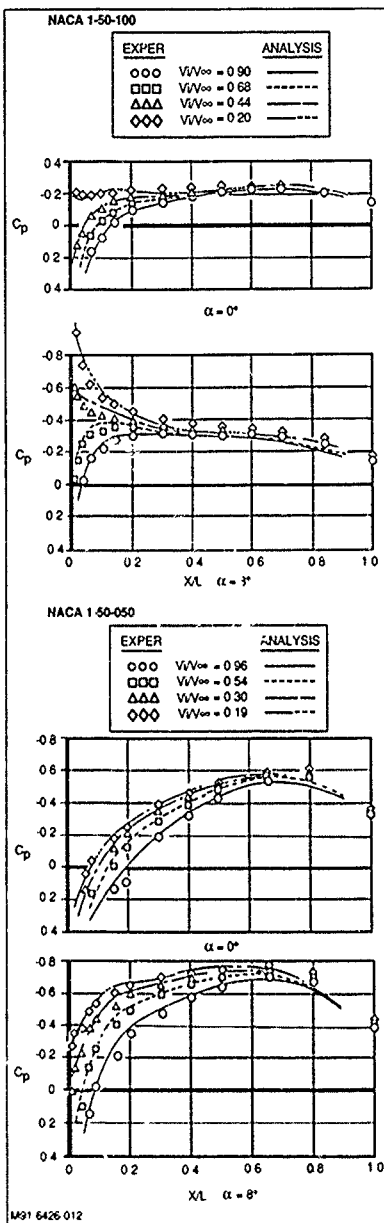


Fig. 30 Inlet Top Centerline Pressure Distribution Correlations

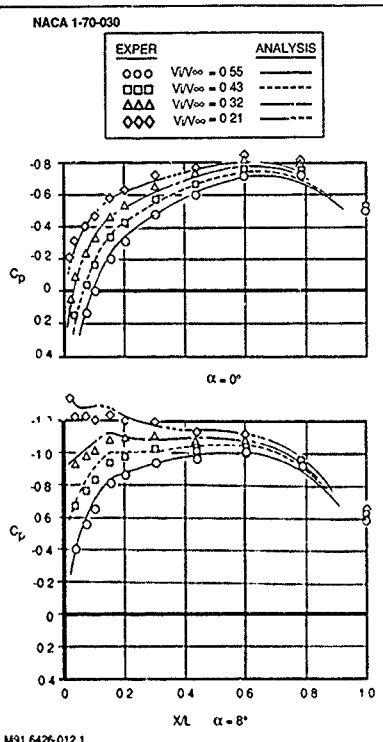


Fig. 30 Inlet Top Centerline Pressure Distribution Correlations (cont'd)

typical relation between inlet flow rate and computed drag levels is provided in Fig. 31. As inlet leading edge radii decrease, the potential for flow separation drag penalties increases. In addition, aero-propulsion bookkeeping requires that "additive drag" (a function of inlet streamtube geometry) be included to obtain total spillage drag levels. When all of these components are combined, the trend shown in Fig. 31 may be reversed, i.e., spillage drag may increase with any reduction in inlet mass flow ratio.

A key feature of this approach and the example just described is that computational modeling is not altered in generating the numerical results. In this way, the resultant drag levels are certain to be derived from configuration geometry and flow conditions, and not from numerical discrepancies that might surface when the discretized model is altered.

Afterbody drag levels, as a percentage of the total, can be quite large for fighter aircraft (Ref. 48) at certain conditions. This level might be half of the total aircraft drag level (Fig. 32). Exhaust plume interactions, an important component of the total afterbody drag, can be computed with patched solutions (Fig. 33). Two computer programs (one for transonic speeds and one for supersonic speeds) have been developed to provide this type

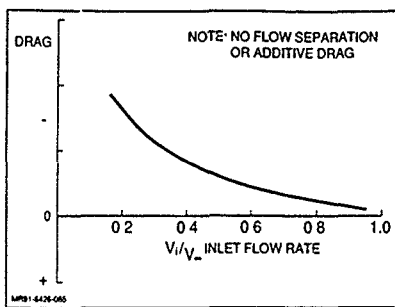


Fig. 31 Effect of Inlet Spillage on Inlet Lip Drag

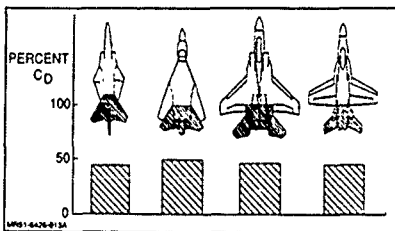
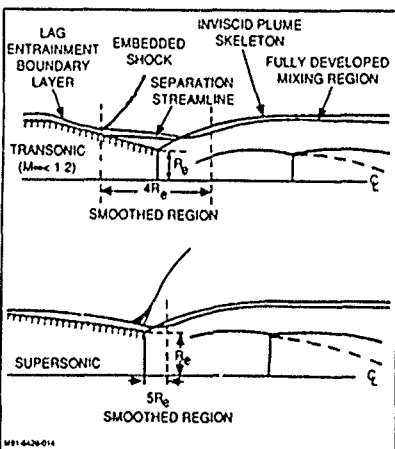
Fig. 32 Fighter Afterbody Drag Levels at Subsonic Speeds, $C_D = 0$ 

Fig. 33 Boattail Analysis Method Computational Regions

of prediction across the subsonic, transonic, and supersonic speed regimes (Refs. 49, 50, and 51). Both methods iteratively solve for five separate flow field regions found in Fig. 33. The flow regions are:

- External Inviscid Flow - Mapped region, conventional SLOR with rotated difference scheme
- Boundary Layer - Green's integral method for δ^+

- Recirculating Flow - Control volume analysis with separation and reattachment regions
- Supersonic Exhaust Plume - Salas' finite difference marching scheme
- Plume Entrainment - Mixing profile to yield equivalent displacement thickness

Figure 34 shows a typical simulation result for two boattail surfaces (Ref. 52) at supersonic speeds. The drag reduction trend that occurs with increasing nozzle pressure ratio is predicted well.

Interference Drag

Interference drag sources are complex and large in number. In some cases computational methods can predict flow qualities that will aid in the drag minimization process. In other cases, the methods can predict useful drag force information.

One example of an interference drag source that has defied accurate computational treatment is that resulting from juncture flows. The limitation appears to be associated with the inability of three-dimensional viscous flow predictors to perform well when the flow is highly three-dimensional. As a result, juncture fillets might best be optimized with guidelines applied during sub- or full-scale testing. Reference 53 provides both design guidelines and literature references that could prove useful in shaping fillets.

It should be recognized that computational methods can provide useful flow angularity and gradient information (see Fig. 35 and Refs. 54 and 55) that will help the designer conceive a shape that is quite good for the first series of experiments. Testing requirements, and therefore cost, can be minimized.

A greater level of application success is associated with simulating both propeller and rotor slipstream interactions. The former is important because of interest in high speed, high-efficiency propellers (prop-fans or unducted fans) and the latter is naturally linked to aircraft concepts like the V-22.

Figure 36 shows a propfan tractor arrangement that might exist in the future. In order to maximize the benefit of the total propfan concept, propeller slipstream and nacelle interference must be minimized. The slipstream flow is characterized by a swirling motion with discreet vorticity sheets emanating from blade trailing edges. Immersed configuration components experience increments in Mach number and flow dynamic pressure. At high transonic speeds, slipstream swirl effects will be dominant. Figure 37 reveals a test setup incorporating a

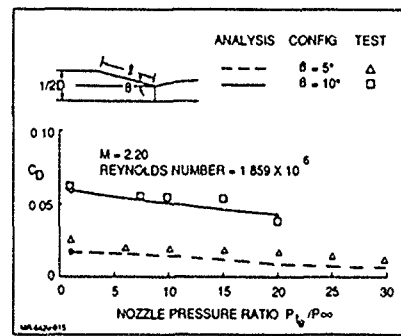


Fig. 34 Correlation of Nozzle Pressure Ratio Effects on Afterbody Drag Levels

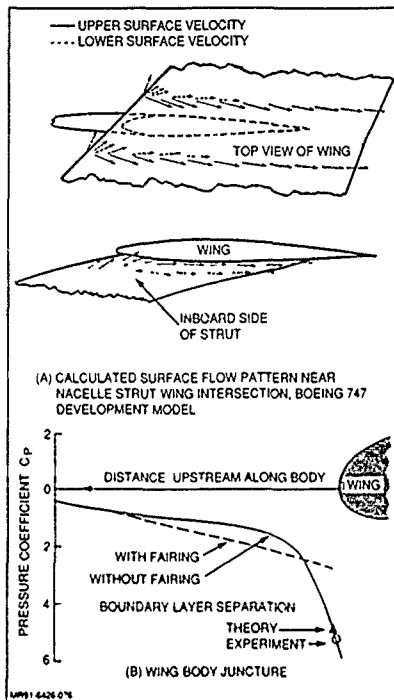


Fig. 35 Component Interference Effects (Refs 54 & 55)

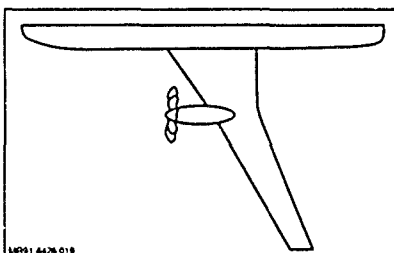


Fig. 36 Propfan Tractor Arrangement

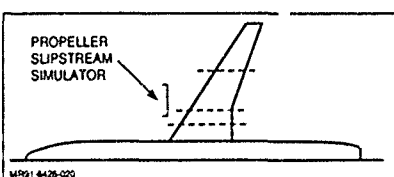


Fig. 37 Propfan Slipstream Simulator

propeller slipstream simulator positioned upstream of a supercritical wing transport model. Wing section boundary conditions were modified via "twist" angles to represent the propeller's seven-degree swirl velocity. That is to say, wing sections between the propeller centerline and the inboard radius line were modified to have seven degrees more incidence representing swirl upwash, while wing sections between the propeller centerline and the outboard radius line were altered to have seven degrees less incidence representing swirl downwash. For reverse propeller rotation, the upwash/downwash boundary conditions are interchanged. Clockwise and counter-clockwise slipstream effects on the wing pressure field are correlated in Fig. 38 using a transonic small disturbance method (Ref 56 and 57). Note that pressure field details are predicted very well despite the wing's complex double shock wave system.

The wing pressure distributions found in Fig. 38 can be integrated to generate spanwise load distributions as well as lift and drag coefficients (see Fig 39). Loading plots reveal that the slipstream interaction will affect the lift-induced drag levels, the altered shock pattern suggests that the wave drag is similarly altered. The lift level is predicted well as might be expected (good pressure simulation), but the computational drag increment is greater than that measured during the experiment. This appears to be an improvement over incompressible theory but drag levels measured in this particular experiment are suspect because of the propeller slipstream simulator hardware mounted upstream from the wing surface.

Rotor slipstream interactions are more prevalent at subsonic conditions than transonic conditions. While little success has accrued in modeling the complex flow separation patterns about helicopter fuselage shapes, some advances have been made in simulating rotor download effects on winged vehicles (Ref. 58). Figure 40 depicts this problem. It is known that the "download" or vertical drag force penalty attributable to XV-15 rotor downwash impinging on the wing surface varies between 5% and 15% of the vehicle's total gross weight. It becomes important to refine configuration components to minimize the download magnitude. Unlike most aircraft prediction applications, this case involves drag coefficient levels that are very high (on the order of 10).

The plots in Fig. 41 illustrate that wing section drag in cross-flow vanes with the flap deflection angle. The agreement between test data and the computational model is compromised by a shift in absolute drag level. If the curves are normalized by the 0-deflection drag values, it can be seen that proper trends are predicted. This trend was obtained using an unsteady panel model (Ref. 59) coupled with a free streamline representation of the separated wake. Useful design information can be extracted even though absolute drag levels predicted are in error. The speed with which computational models can be generated, coupled with relatively low cost of analysis, permits a large number of shape/orientation combinations to be examined. In this environment, out-of-the-ordinary solutions can surface that might not naturally evolve for testing based on past experience. The wing section download problem is a good example in that the minimum drag or download does not occur at 90 degrees of flap deflection, which would be the intuitive choice based on minimum area presented to the flow.

Engine nacelle interference phenomena can exhibit a degree of complexity that defies treatment with current computational methods. This in part is the result of what might be called "hard boundary" interactions that impact lift-induced, wave, and pressure drag levels. But in addition, the nacelle inlet and exhaust components add a degree of "Throttle Dependent" drag described in a preceding sub-section. An example is now described that can be used to illustrate both of these effects and the manner in which they interact.

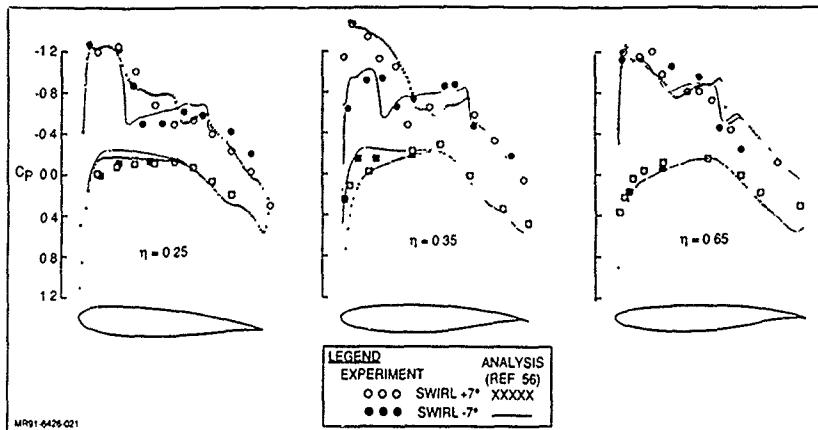


Fig. 38 Wing Pressure Distribution Correlation Illustrating Propfan Slipstream Interference Effects
($M = 0.8 \quad \alpha = 3 \text{ Deg}$)

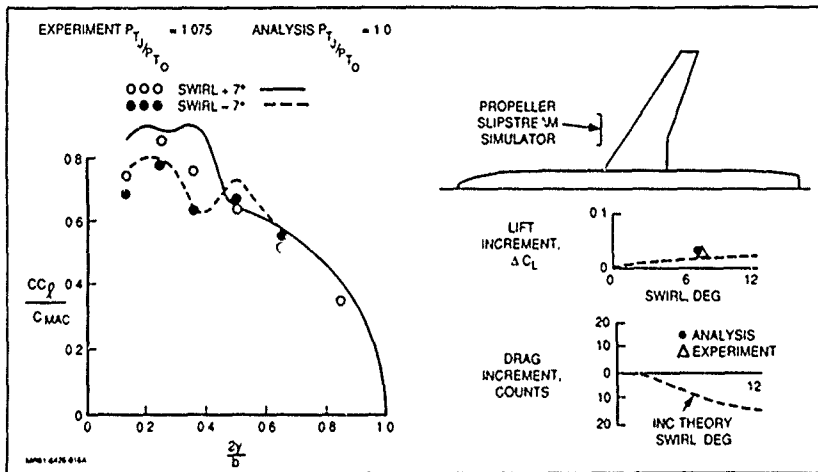


Fig. 39 Propfan Interference Effects – Wing Spanload, Lift, & Drag Increments ($M = 0.8 \quad \alpha = 3 \text{ Deg}$)

Figure 42 shows superimposed computed wing section upper surface pressure distributions for an executive jet at transonic conditions. A transonic small disturbance theory analysis (Ref 60) is used. On the left, a wing-fuselage calculation reveals a strong shock wave running along the length of the wing from the fuselage juncture to the wing tip. Just below this three-dimensional image, a wing root section cut is shown along with experimental pressure data correlation. This represents a "nacelle-off" case. Next, a comparison with the nacelle surface present can be identified. The nacelle is modeled as a closed surface in the computational method. In other words, the nacelle is a closed form as would be appropriate for a fuel tank or avionics pod. Note that the engine surface decelerates the flow in front of the nacelle and accelerates the flow just below the nacelle inlet lip forming a pressure spike. Wing pressure correlations confirm this type of character but the level of agreement is not as good as that for the nacelle-off case. This suggests that part of the nacelle interference effect is modeled

but a piece is still missing. In the third comparison (Fig. 42), the true inlet mass flow ratio (0.66) is modeled by specifying appropriate values of the flow field potential at grid points representing the inlet face. Now it can be seen that agreement with test data has improved considerably. The flow, now characterized by more negative pressures, does not slow down as much in front of the inlet face, with less spillage modeled, the flow acceleration or pressure spike at the inlet lip is reduced. Simulation agreement is dramatically improved.

As noted before, absolute drag levels predicted by a three-dimensional computational method will not yield drag accuracy levels suitable for project applications. But the information shown in Fig. 42 can be foundational for the application of simpler two-dimensional methods that might be brought to bear using superposition principles as part of a build up process. The basic ideas for this approach were described in the "Transonic and Supersonic Wave Drag" sub-section

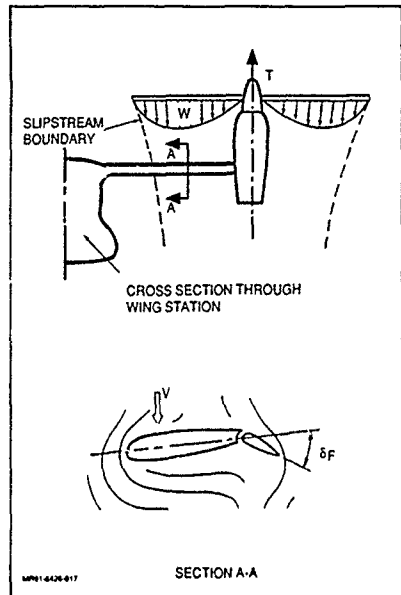


Fig. 40 Rotor Download Schematic (Ref. 58)

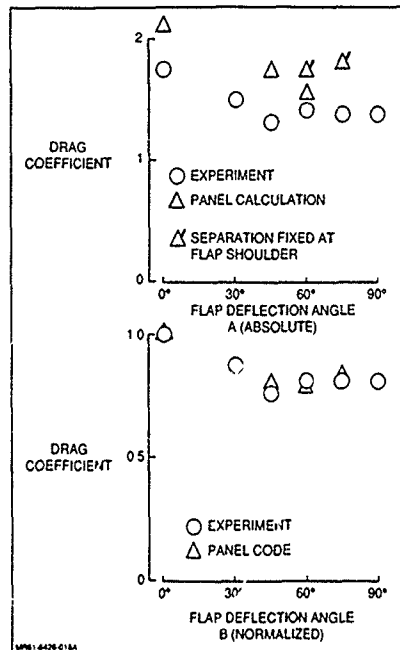
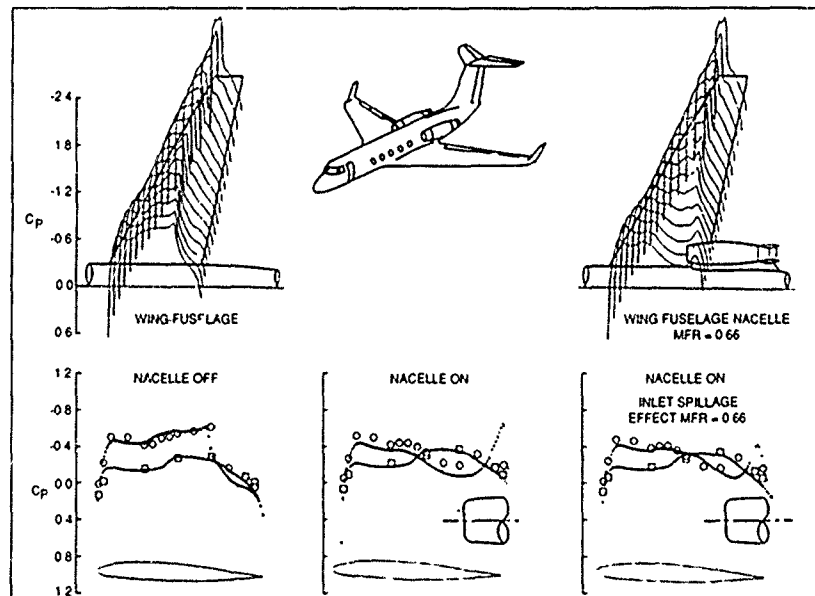


Fig. 41 Measured/Calculated Drag vs Flap Deflection Angle (Ref. 58)

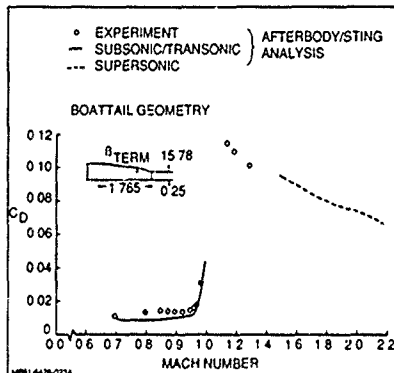
Fig. 42 Superimposed Computed Pressure Distributions & Wing Root Pressure Correlation for G-III Configuration ($M= 0.85, \alpha = \text{Deg}$)

In the following paragraphs, another interference drag source is highlighted. This source is closely related to Throttle-Dependent Drag, but the complexities of aircraft afterbody shapes require an additional level of modeling sophistication beyond what is described in that sub-section. The category to be examined now might be called "Integrated Afterbody Effects" and it can be thought of as an element of interference drag.

The boattail analysis described in the Throttle-Dependent Drag section has been implemented to treat a number of simple nozzle shapes. Figures 43 and 44 show tri-sonic drag prediction results for two boattail geometries. Applications engineers can extend the use of these axis-symmetric body computational methods by implementing the equivalent body-of-revolution technique described in Ref. 61. This approach requires that various afterbody components (e.g., multiple nozzles, inter-fairings, sponsons, horizontal and vertical tail surfaces, and fairings) be combined into a single shape with an equivalent total area distribution. A prediction generated using this technique can be seen in Fig. 45. Drag rise characteristics for a research aircraft

model have been predicted well considering the afterbody complexity. But this engineering approach is far from fool-proof as a second comparison case reveals in Fig. 46. Here, test results suggest that a drag-producing flow separation region might exist at low speeds. While this experimental trending is unusual, and may in fact be in error, this case can be used as an example to point out that the simplistic engineering method involving an unrefined equivalent body-of-revolution may not be suitable for all project applications.

Some of the shortcomings just described can be overcome by integrating a boattail analysis method, an equivalent body-of-revolution concept, and correction factors developed from test databases. Figures 47A and B present a schematic illustrating this approach. Semi-empirical corrections can be developed to account for a number of aircraft features such as empennage, inter-fairings, engine spacing, booms, base drag, and lifting surfaces. Figures 48 through 53 show examples of correction factors, configurations, models, and correlations that make up the applied experience base. A sample analysis for an F-14 afterbody using this system (Ref. 62) can be found in Fig. 54.



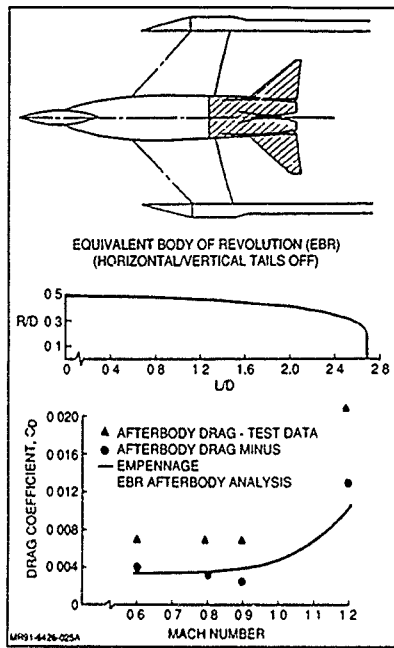


Fig. 45 Equivalent Body Approach Simulating Research Model Afterbody Drag

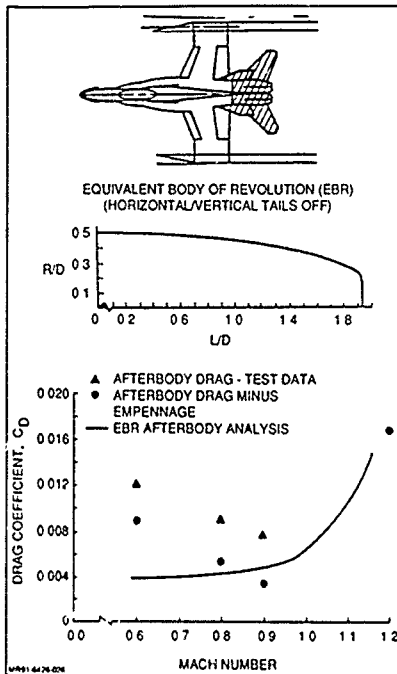


Fig. 46 Equivalent Body Approach Simulating F-18 Research Model Afterbody Drag

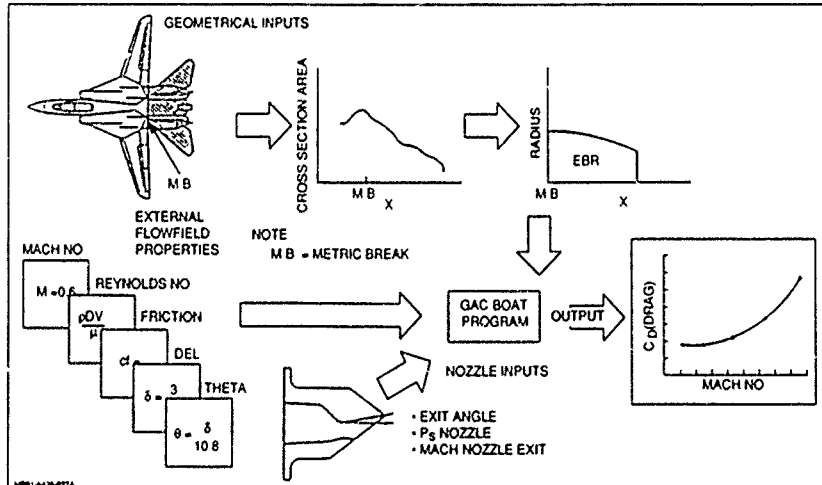


Fig. 47-A Equivalent Body of Revolution Methodology Using GAC-BOAT Code

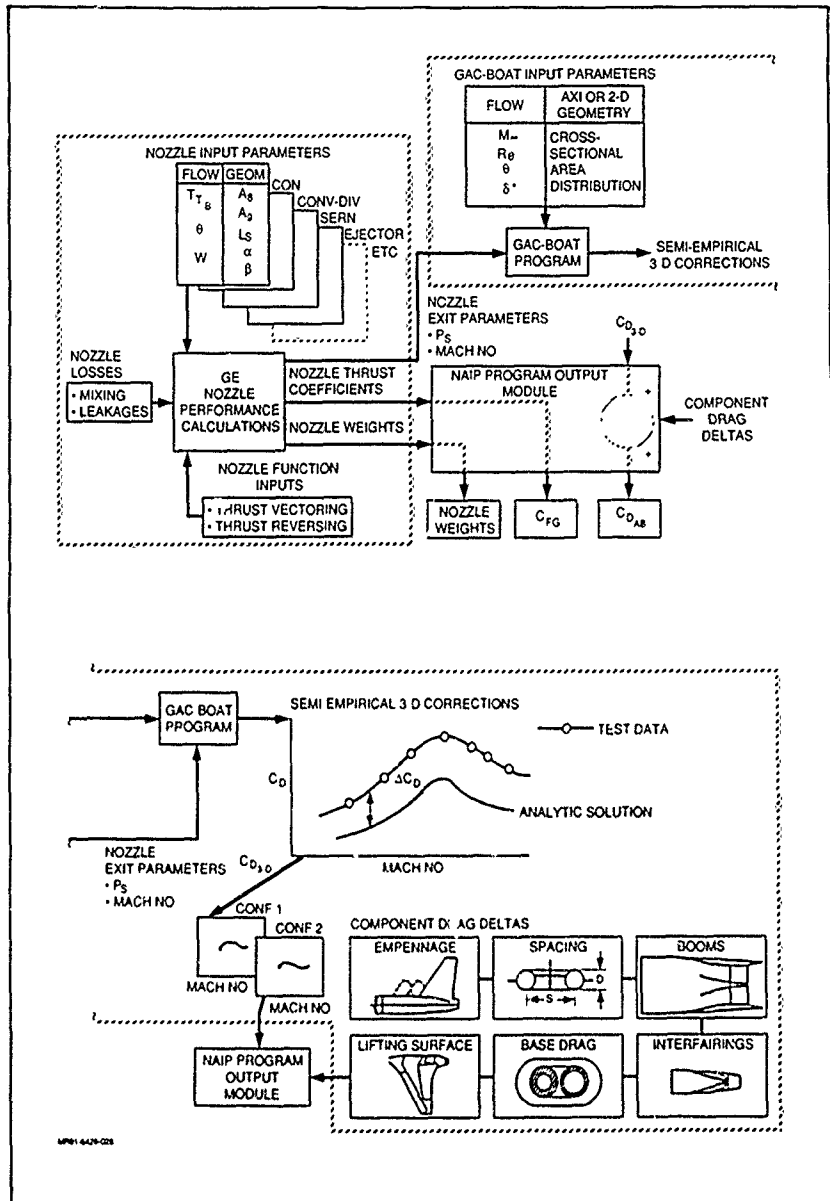


Fig. 47-B Level II Nozzle/Afterbody Installed Performance Prediction Program

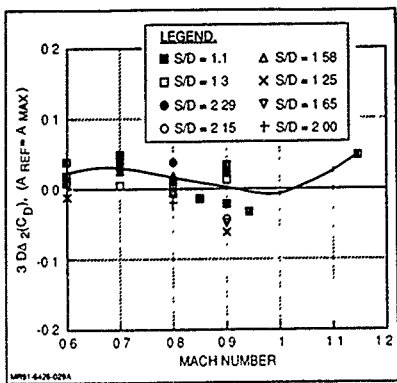


Fig. 48 ERB/Spacing Effects – Cruise Nozzle

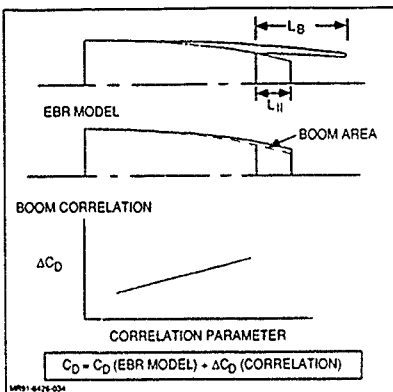


Fig. 51 Boom Methodology

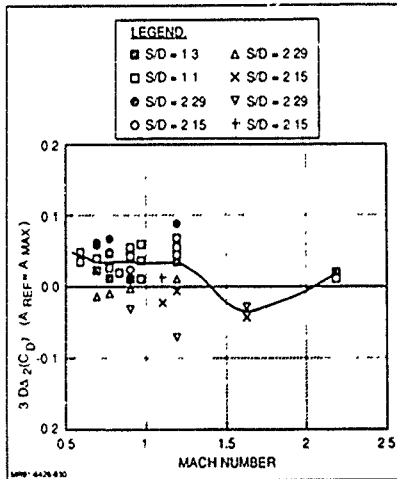


Fig. 49 ERB/Spacing Effects – Maximum A/B Nozzle

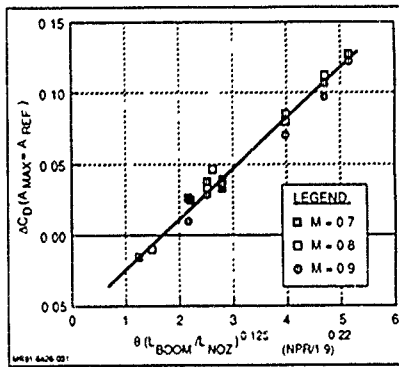


Fig. 52 Boom Correlation – Cruise Nozzle

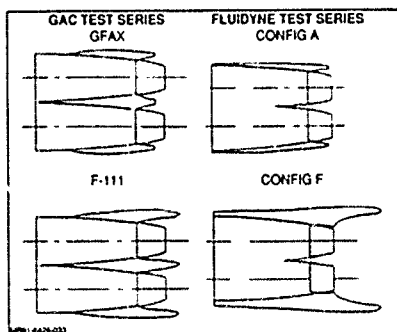


Fig. 50 Boom Configurations

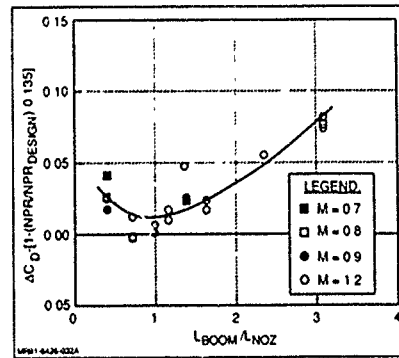


Fig. 53 Boom Correlation – Maximum A/B Nozzle

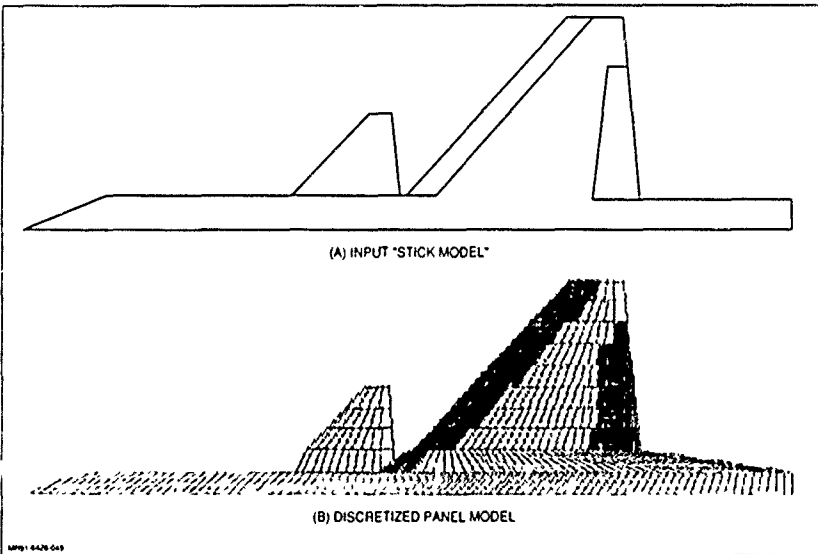
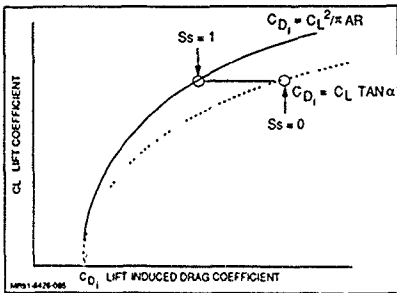
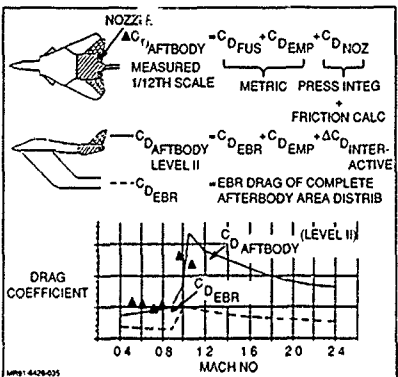


Figure 57 shows a typical set of computed results for a wing body canard configuration. Three surfaces (wing leading and trailing edge flaps and the canard) can be deflected or set to minimize drag across a range of lift, covering both cruise and maneuvering conditions. The control surface deflections, S_s parameter, and configuration pitching moment are all mapped (Fig. 57) and show the variations that occur with different total lift levels. At each of five lift values, three plots cover canard deflections of 0, 10, and 20 degrees. Each plot identifies the performance level possible with various combinations of wing leading and trailing edge flap deflections.

By combining the information in all of the plots, an optimum deflection schedule consistent with trimming the configuration can be constructed (Fig. 58). It can be seen that a more ideal polar can be generated if the configuration does not have to be trimmed. These ideal deflection combinations lead to a composite drag polar. This process is very time consuming and expensive if a complete surface deflection/orientation matrix is performed in the wind tunnel.

References 63 and 64 can be used to identify drag polar accuracy that might be expected for a range of different aircraft configuration types.

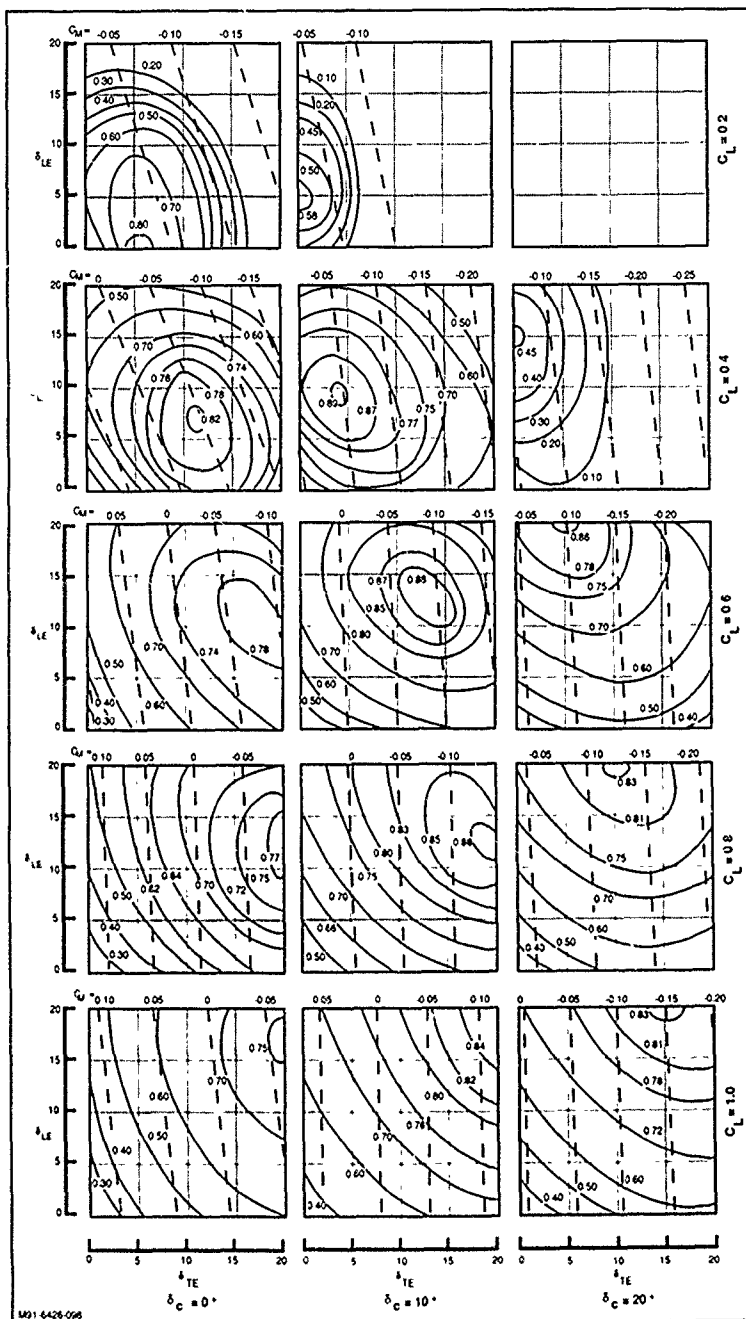


Fig. 57 Predicted Lift-Induced Drag Characteristics (S_d Contours) for a Canard Configuration at Different Lift Levels as a Function of Canard & Leading/Trailing Edge Flap Deflections

U91-6426-096

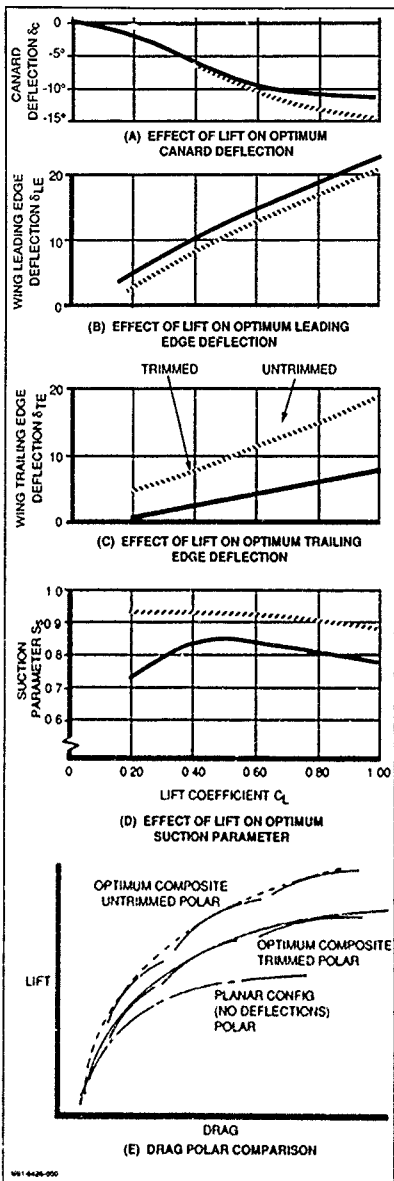


Fig. 58 Optimum Drag Polar Shape Constructed Using Multiple "Lift" Polars Generated with Control Surface Deflections

PART 2: DRAG REDUCTION/MINIMIZATION TECHNIQUES

DISCUSSION – DRAG REDUCTION/MINIMIZATION TECHNIQUES

In Part 1, a number of engineering drag prediction methods were described and example cases were used to provide some experience with the type of results that can be expected. Aircraft design teams might use these techniques in an isolated or sequential manner with experiments and handbook methods to affect drag reductions that optimize the configuration shape. The engineering methods can also be used to diagnose anomalies that surface at any time during the design or life of an aircraft. Part 2 consists of a collection of case studies that illustrate the use of computational methods for drag reduction/minimization problems and diagnostics. The topics include

- (1) Wing Tip-Mounted Winglet Design
- (2) Transonic Transport Wing Drag Minimization
- (3) Natural Laminar Flow Airfoil Design
- (4) Fighter High-Speed Drag/Buffet Reduction
- (5) Swept Wing Tip Optimization
- (6) Hypersonic Drag Source Diagnostics
- (7) Fighter Transonic Maneuver Wing Optimization

In each case, an effort is made to identify the value added to the project by the application of engineering drag analysis methods

Wing Tip-Mounted Winglet Design

Wing tip-mounted winglets provide a reduction in aircraft lift induced drag levels that can be attributed to end plate effects. A higher effective span is obtained with little increase in physical span. The resulting wing root bending moment is less than that derived from a simple wing tip extension so structural weight penalties are minimized. To be effective, however, the winglet lift induced drag benefit must not be offset by a large wetted surface friction drag penalty. This differentiates winglets from simple end-plates. It also suggests that design details are important. Further, many winglet applications require design at transonic speeds where the applications engineer must ensure that interference effects and wave drag penalties are not incurred. Once again, design details are important.

Winglet design can be initiated by taking advantage of the empirical guidelines (Ref. 65) developed by Dr. Whitcomb at NASA's Langley Research Center. Key characteristics are summarized below

- Avoid rake that would reduce wing tip region loading
- Winglet span should be comparable to wing tip chord length
- Winglet toe-out angle is comparable to wing tip twist angle
- Avoid merging of wing and winglet supersonic regions
- Winglet cant angle should be selected for optimum combination of induced drag and wing root bending moment
- Winglet juncture region should be treated like a wing root juncture region. Avoid trailing edge load build up

The final three items can be accomplished using both subsonic panel methods and transonic finite difference relaxation schemes. Figure 59 identifies typical winglet parameters

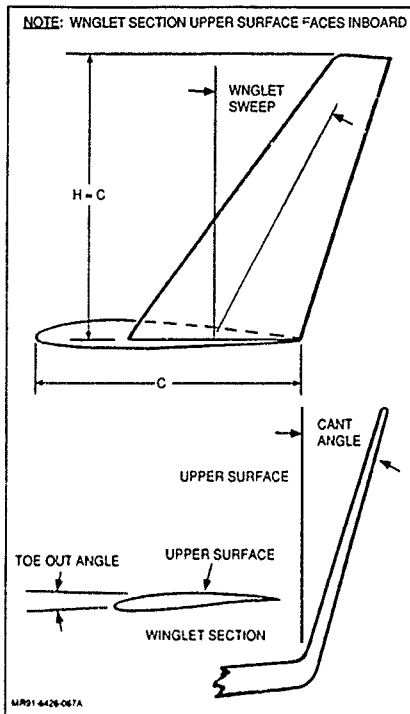


Fig. 59 Details of Winglet Geometry

During the winglet design effort for the Gulfstream III aircraft, these guidelines were followed and a recommended GAW type airfoil was implemented. The airfoil shape can be seen in Fig. 60. During the first wind tunnel test, early drag rise was observed and attributed to the GAW section shape. This effect was verified using a transonic two-dimensional transonic analysis (Ref. 33) coupled with extended sweep theory (see "Transonic and Supersonic Wave Drag" section). Iterative analyses were performed to re-contour the airfoil forward and aft regions, making the shape more supercritical in character. The improved airfoil shape (Fig. 60) was placed back in the winglet platform for wind tunnel model fabrication. All of the design goals were achieved during the second wind tunnel test.

Gulfstream III winglet drag increments are shown in Fig. 61. The benefit/penalty trade can be identified. Testing demonstrated a benefit that was slightly greater than that predicted by analysis. Also, gains are reduced by wave drag losses at a higher-than-design Mach number coupled with higher-than-design lift levels. The aircraft performance benefits that resulted from this design effort are summarized in Table 5. Applying computational methods in this case (to delay drag rise), saved considerable model and test time expenses. Further, it is judged that the final winglet drag benefit would not have been as high considering the time constraints characterizing most test programs. Designing by repetitive testing often results in compromised final configurations due to limits on the number of variables that can be assessed. This is particularly the case for aircraft with transonic design points.

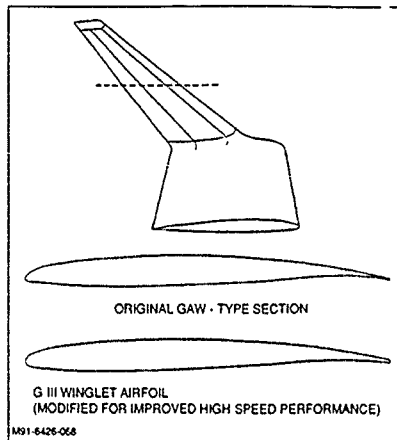


Fig. 60 Originally Proposed & Final G-III Winglet Airfoil Section

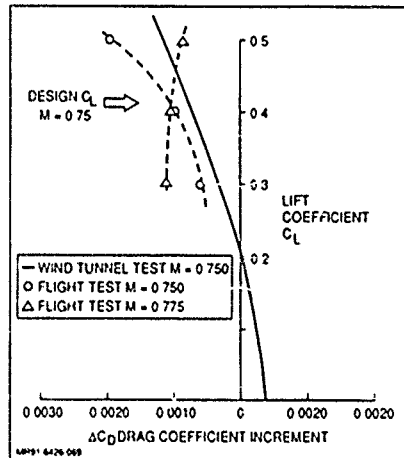


Fig. 61 G-III Winglet Drag Increment

Table 5 Results of Winglet Experimental Validation

DRAG	3 1% DRAG REDUCTION AT CRUISE CL
WEIGHT	+1/2% OF AVERAGE CRUISE WEIGHT
RANGE	+117NM (+3 3%)
FUEL	-6500 GAL/YR (BASED ON 600 HOUR USE)

M91-6426-079

Transonic Transport Wing Drag Minimization

The Gulfstream III executive jet is a good case study to demonstrate computational drag minimization techniques applied to high-speed wings. This is best accomplished by examining the series of Gulfstream designs from 1966 (Gulfstream II) to 1984 (Gulfstream IV). In 1966, design by experimentation was the means to optimize high-speed wing shapes. The Gulfstream II program fabricated eight separate wing shapes for wind tunnel testing. Including refinements to the original eight, twenty-four wing shapes were evaluated and the best was selected for the $M=0.75$ cruise design point. This may seem like a large number of wing shapes, but for that period some aircraft development programs investigated hundreds of wing shapes before settling on the final one.

The Gulfstream III configuration evolved during 1979. An effort was initiated to develop a new high-speed ($M=0.78$) wing by retaining the G-II wing box structure and flap/aileron surfaces. The G-II and G-III wing planforms are compared in Fig. 62. Leading edge and wing tip extensions increased wing area by 15%. Leading edge sweep was increased 3 degrees and aspect ratio was maintained at 6.0. The wing root chord extension decreased wing thickness from 12% to 10%. Equivalent two-dimensional airfoil sections were extracted from the original G-II wing at three span locations ($\zeta = 0.182, 0.351$, and 0.937). These shapes were refined using the transonic airfoil analysis method of Ref. 33, subject to the extent constraints identified in Fig. 62. Refinements evolved using iterative direct analysis. Figure 63 shows a wing pressure distribution "before and after" comparison where shock wave losses were reduced considerably. Initial testing revealed that G-II drag creep characteristics were eliminated and this was consistent with the specific pre-test predicted wing section drag reductions included in Fig. 64.

Clearly, a portion of the higher drag divergence Mach benefit is attributable to reductions in wing thickness ratio. Equation 25 shows that the inboard drag divergence Mach benefit of 0.04 is greater than that associated with thickness, 0.02. Figure 65 quantifies the total configuration drag reduction based on verification testing. This transonic wing design effort underscored the value of computational methods. The performance enhancement was so substantial that G-III wings were fitted to many existing G-II aircraft. These hybrid aircraft were called G-IIIs. Perhaps most intriguing, the results were achieved with a single wind tunnel test that verified computational predictions.

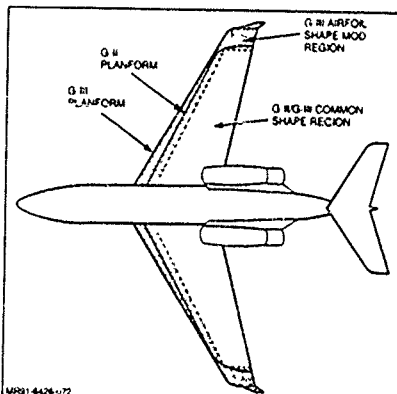


Fig. 62 Gulfstream II/III Wing Planforms with G-III Airfoil Contour Modification Region

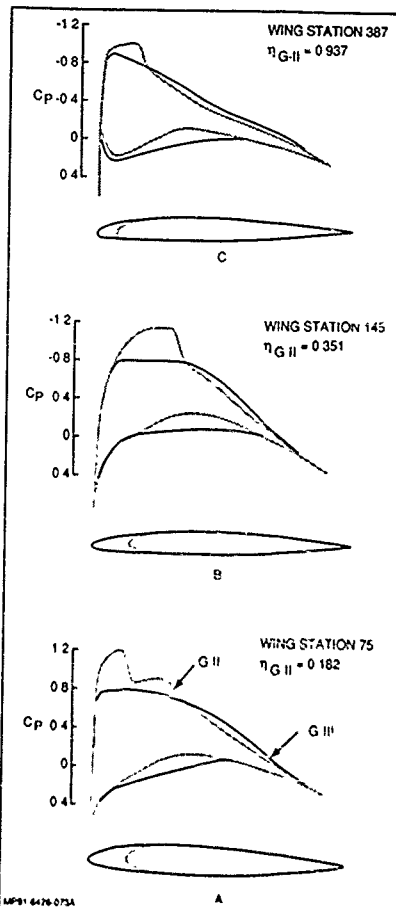


Fig. 63 Airfoil Shape/Wing Pressure Distribution Refinement for Gulfstream III

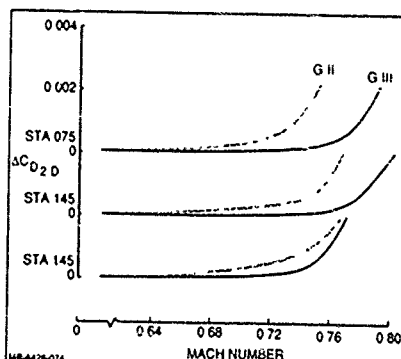


Fig. 64 Analytically Predicted Improvement in G-III Wing Section Drag Divergence Mach Number

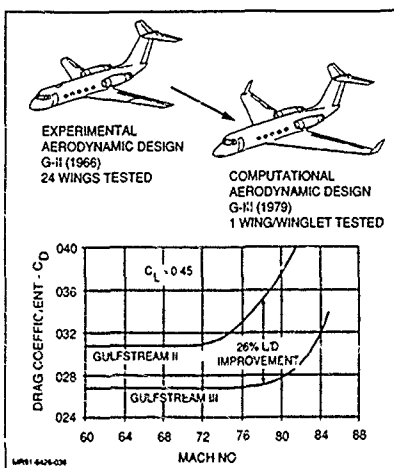


Fig. 65 G-II/G-III Drag Comparison

Gulfstream IV development (Ref. 66) was initiated in March 1983. Unlike the 1979 G-II effort, the G-IV wing would be redesigned structurally for weight reduction. This made it possible to affect additional aerodynamic refinements that could reduce drag and increase range. The primary design challenge centered on geometric characteristics of the large fuselage-mounted Tay engines with 50% more volume than the G-II's Spey engines.

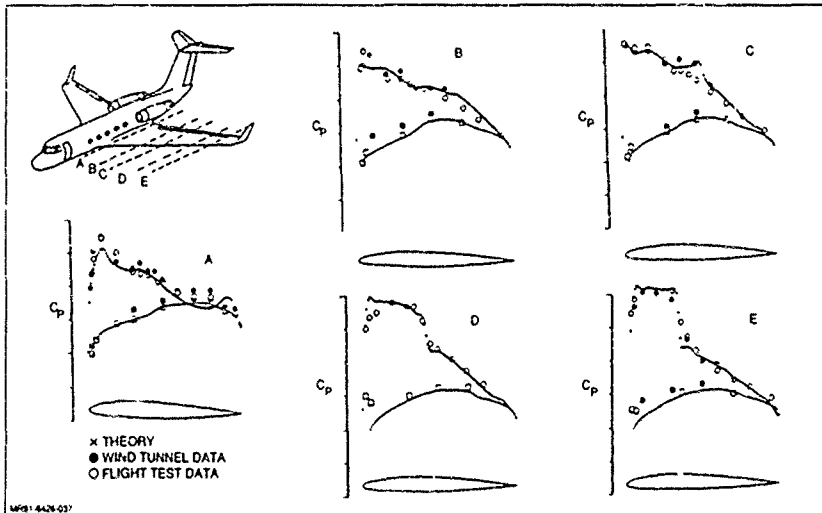
Wing shape past the 65% chord location was to be maintained in an effort to preserve G-II control surfaces and thus reduce development and manufacturing costs. Fuselage structure was left untouched by constraining the wing/fuselage juncture contours. Considering these constraints, the most effective wing design would reduce outboard shock wave strength (Fig. 66) and

shift load inward to compensate for wing load suppression induced by the larger engine nacelle. A transonic wing-body-nacelle-winglet computational analysis method (Ref. 60) was used to develop appropriate wing contour changes in the unconstrained region (Fig. 67). Care was taken to minimize a wing tip lower surface leading edge spike that evolved with the twisting needed to shift load inward. This pressure spike required treatment to avoid drag creep that would appear prior to achieving the cruise design Mach number and lift level. Figure 68 shows the refinement implemented.

G-IV design goals were achieved with testing that immediately followed the computational design program. Wind tunnel pressure distributions agreed well with pre-test projections. The wing pressure field (Fig. 69) shows a dramatic reduction in outboard shock wave strength; this raised the G-IV cruise Mach number to M=0.80. Perhaps most interesting, from the engineering design perspective, is the nature of the performance improvement shown in Fig. 70 where there is a small drag benefit when the G-III and G-IV wing/fuselage configurations are compared. With the nacelle installed, however, the performance increment is larger. This case illustrates improved component integration capabilities through computational analysis.

Natural Laminar Flow Design

Another technique for drag reduction/minimization involves achieving the lowest levels of friction drag that are derived from maintaining laminar flow over as large a surface as possible. This might involve powered concepts where suction is applied to remove low-energy boundary layer flow, or shapes might be contoured to achieve favorable gradients that delay transition to turbulent flow. This second tact, called natural laminar flow, is only applicable to some aircraft design concepts where operating circumstances and manufacturing/maintenance constraints make it feasible. Wing sweep, for example, must be moderate to inhibit instabilities in the laminar boundary layer flow. If these requirements are met, considerable advances in performance can be achieved by applying modern computational drag minimization tools.

Fig. 66 G-III Wing Pressure Distribution Comparison at Cruise Condition ($M = 0.78, \alpha = 4^\circ$)

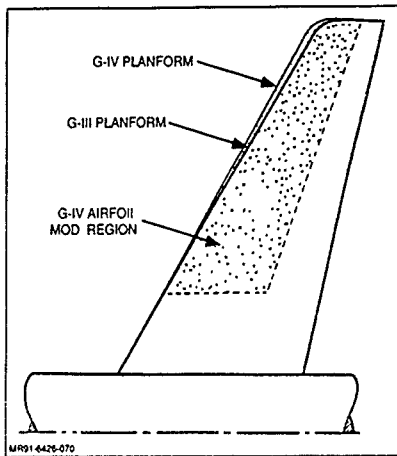


Fig. 67 Gulfstream III/IV Planforms with G-IV Airfoil Contour Modification Region

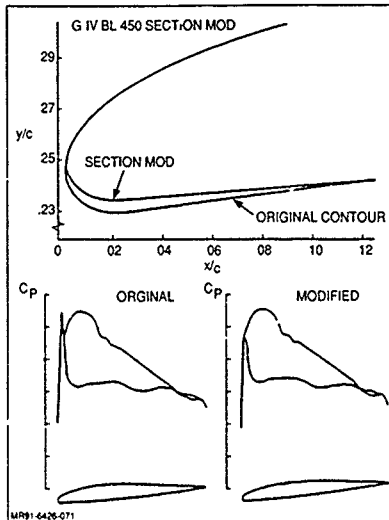


Fig. 68 G-IV Wing Tip Mod to Eliminate Lower Surface Pressure Spike, $M = 0.78$, $\alpha = 3.5^\circ$, $\eta = 0.95$

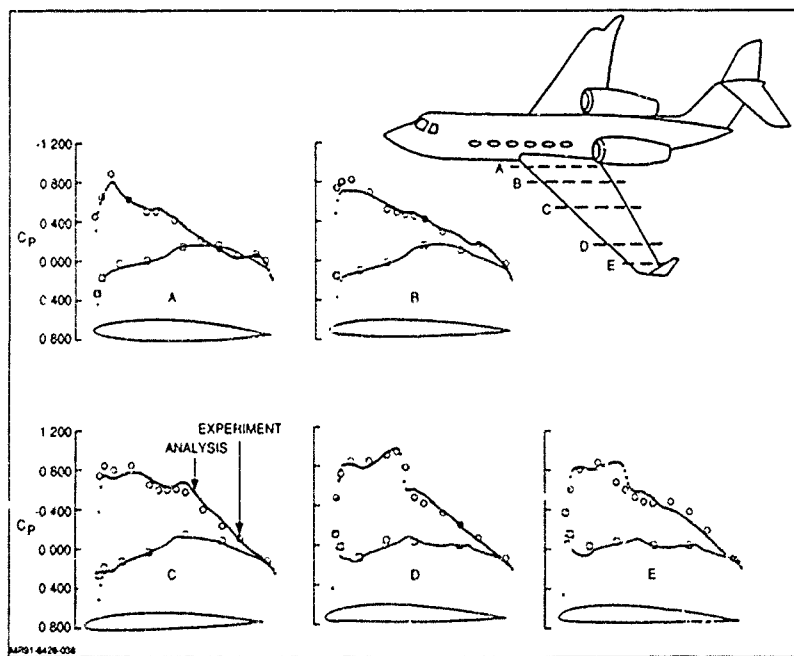


Fig. 69 Correlation of G-IV Wind Tunnel Test Pressure Distributions with Pre-Test Code Prediction ($M = 0.78$, $\alpha = 4.0^\circ$)

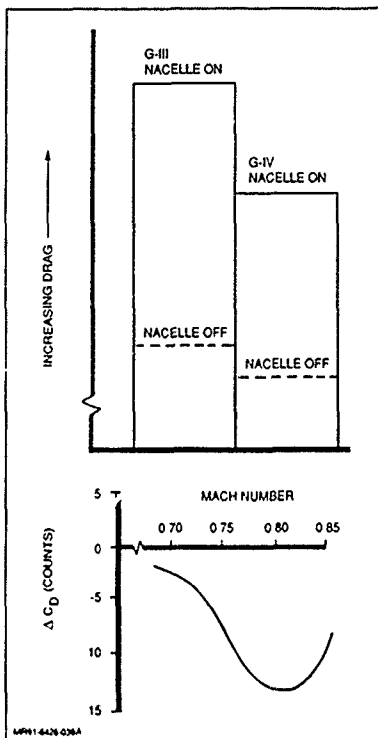


Fig. 70 C-IV/G-III Drag Reduction Showing Engine-Airframe Integration Benefit

Eppler's method (Ref 22) was discussed in the "Skin Friction and Pressure Drag" sub-section. Because of viscous flow simulation complexity, the need for a predictor/experience base was stressed. With an understanding of simulation formulation assumptions and limitations, the applications engineer can use Eppler's method to synthesize new wing section shapes for specific applications. An application is included here to illustrate the power of this engineering method.

NACA 6-Series wing sections were developed to exploit the performance gains possible with various extents of natural laminar flow. Many aircraft now in production employ NACA 6-Series sections. For this case, a NACA 64 015 symmetric section serves as a baseline. Eppler's method is used to generate an advanced section with improved drag characteristics. Figure 71 shows the NACA and advanced airfoil section shapes plotted to an expanded scale revealing details that are quite subtle. It can be seen that the improved airfoil features a comparable nose shape. It is slightly thicker between 20% and 60% chord while being somewhat thinner between 70% and 90% chord. Figures 72 A and 72 B illustrate the improved drag characteristics achieved at two Reynolds numbers. It might be expected that the largest drag reductions occur at the lower Reynolds number, and this is the case. It is important to identify that the improved performance comes in several forms. First, the extent of laminar flow is increased as evidenced by lower drag in the polar "bucket" region. Second, the incidence range over which laminar flow can be maintained is broadened. Third, once transition

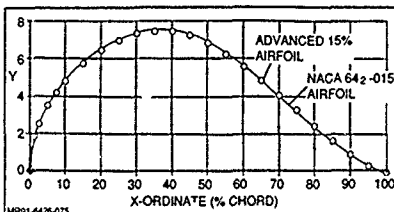


Fig. 71 NACA 64₂-015/Advanced Airfoil Shape Comparison

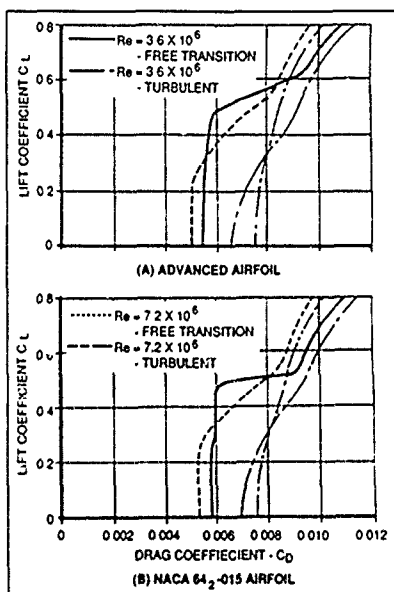


Fig. 72 Predicted Drag Polar Characteristics for NACA 64₂-015/Advanced Airfoil Sections

occurs (above $CL = 0.5$), turbulent flow drag level is lower than that for the standard NACA section. Finally, all of these beneficial characteristics are achieved with an airfoil shape having increased thickness – a characteristic that could translate into a structural weight savings.

It should be apparent that considerable progress has been made in airfoil design since the NACA sections were conceived. The advanced airfoil described here was generated with very simple parameter specifications to Eppler's method. Given some time, it is likely that section shapes with larger improvements can be synthesized. Perhaps more important than performance in some applications, computational techniques of this type allow the designer to tailor airfoil section characteristics for specific design problems with unique goals and constraints. This might be contrasted to the alternative that involves settling on an airfoil section that features some of the desired attributes but its primary benefit is derived from the fact that it already exists.

Fighter High-Speed Drag/Buffet Reduction

Flight testing revealed that subtle alterations to the F-14 nozzle, sponson, inter-fairing, and composite region (Fig. 73) required to accommodate new F110-GE-400 engines compromised the aircraft buffet boundary during acceleration at low altitudes. Transonic buffeting occurred at lower Mach numbers when comparisons were made to the original configuration. In addition, the intensity was higher. Many months of flight test diagnostics and "field fixes" resulted in no satisfactory solution of the problem. It was also unfortunate that the thrust to find a solution as soon as possible limited fluid mechanical phenomenon testing needed to develop a good physical understanding of the problem source.

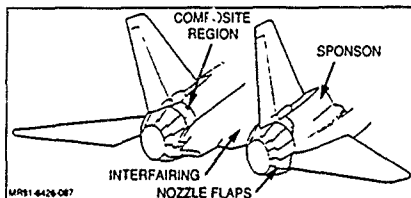


Fig. 73 Modified Afterbody Surfaces

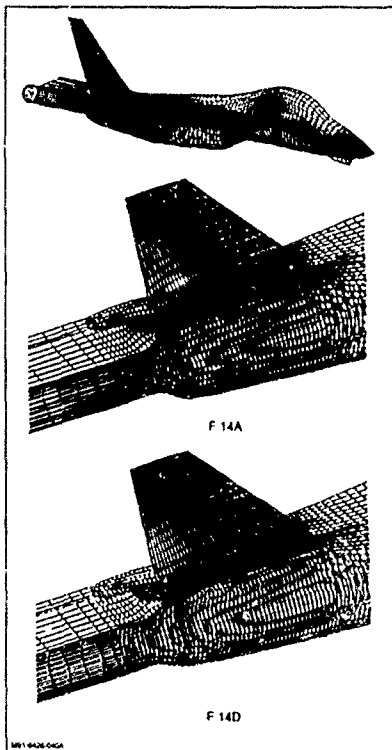


Fig. 74 Surface Gridding for Navier-Stokes Analysis

The change in buffet character was most noticeable by pilots at $M=0.95$. CFD was implemented because the closest available sub-scale test data was taken at $M=0.90$. Initial flow simulations were performed using transonic small-disturbance analyses. Unfortunately, modeling constraints precluded any representation of the vertical tails. $M=0.95$ analyses provided no insight into the relevant buffet problem flow physics.

Valuable diagnostic information (Refs. 67 and 68) was eventually obtained using the Navier-Stokes formulation PARC3D (Ref. 69). Figure 74 shows the surface gridding for the afterbody region of the original and modified F-14 configurations. Modeling sophistication was increased by adding the vertical tail surfaces. Comparisons with available $M=0.90$ wind tunnel test data (Fig. 75) proved that simulation fidelity was quite good. The only discrepancy noted can be attributed to wake modeling limitations. Computations performed at the Mach number of interest, $M=0.95$, eventually highlighted the problem area. Figure 76 illustrates a low-pressure area terminated by a shock wave on the nacelle afterbody. It was conjectured that increased shock wave strength in this region was the source of the buffet boundary shift. Computations were

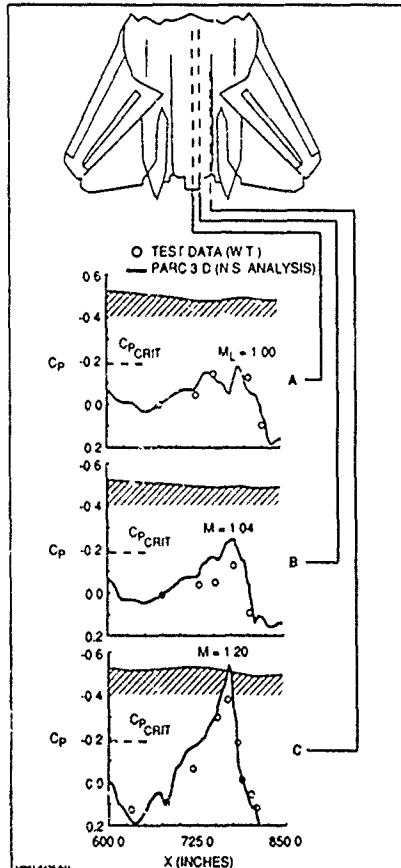


Fig. 75 F-14A Afterbody Pressure Correlation at $M = 0.90$

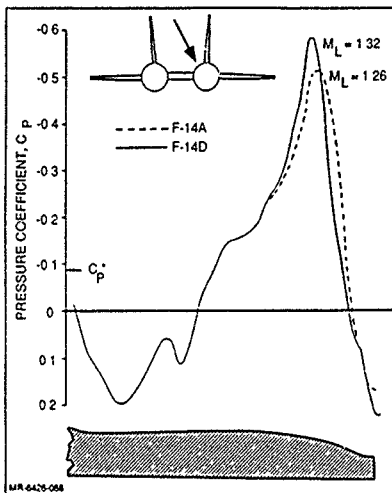


Fig. 76 Predicted F-14 Afterbody Pressure Field at $M = 0.95$

then used to identify means to weaken the shock wave. One solution involved deflecting the rudder surfaces inboard to back-pressure this region. The goal was to reduce pressure expansions to the level found on the original configuration. Figure 77 provides a complete three-dimensional view of the flow expansion/shock characteristics. Computations indicated that a rudder deflection of 4 degrees (6 degrees set to compensate for loading effects) would reduce expansion pressures as shown, but in addition, the reduction in local maximum Mach number (Figs. 78 and 79) would also result in a net drag reduction as can be seen in Fig. 80. Flight testing performed in August 1989 confirmed the computational predictions. In this case, the buffeting problem was not identified by sub-scale testing. The analysis led to a valuable engineering design solution that was not identified during a flight test program. Further, drag reductions were identified as a secondary benefit.

Swept Wing Tip Optimization

Over the past 7 years, investigators have explored the possibility of reducing lift-induced drag by severely sweeping and tapering wing tips. The motivation for doing this is derived from observing the shapes of bird wings and fish fins recognizing that these planforms have evolved naturally over millions of years to form the most efficient and competitive shapes for survival. Computational methods were applied to investigate this effect in the mid 1980s as can be identified in Refs. 70 and 71. Initial predictions identified lift induced drag reductions on the order of 30%. But this large benefit was the result of a faulty drag calculation scheme. "numerical drag" at zero-lift was not properly removed from the predictions made at incidence. When the drag force was adjusted for this problem, the benefit was closer to 3%. Performance gains in this range have also been achieved in hydrodynamic applications (Ref. 72).

Recently (Ref. 73), NASA performed tests to gain more insight into the lift induced drag reduction mechanism. The models examined have been included here as Fig. 81. Test results verify a performance improvement on the order of 3% (Fig. 82).

Drag reductions derived from swept back wing tips appear to be very controversial in a computational sense. One source (Ref

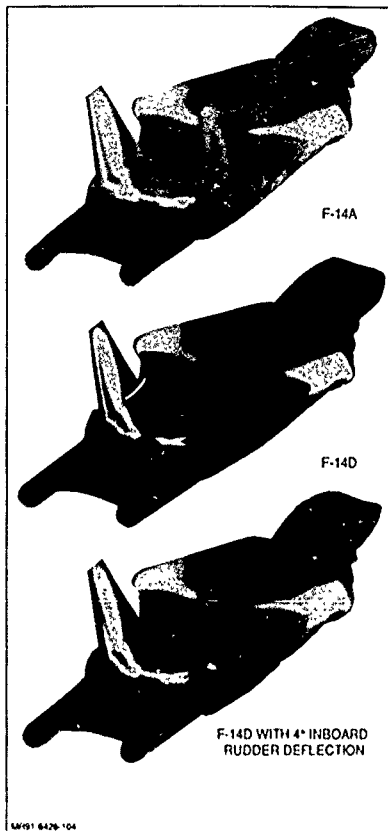


Fig. 77 Navier-Stokes Analysis for F-14 Buffet at $M = 0.95$

74) claims that there is little benefit to be derived from shapes of this type, while another (Ref. 75) believes that the benefit actually has a different character and mechanism. Other articles (Refs. 76 and 77) suggest that swept tips provide an effective end plating benefit which can be visualized by imagining a view looking upstream at a swept tip wing planform that is at some incidence angle. That is to say, a wing planform that is planar at zero incidence may not be planar or exhibit planar wing drag characteristics at incidence. Clearly there is more work to be done to ferret out a physical explanation for the drag mechanisms involved, but one aircraft designer has decided not to wait (Fig. 83).

Hypersonic Drag Source Identification

Interest in hypersonic flight has grown considerably during the last decade. It is recognized that as speed increases, aircraft dominated by wing shapes transition to vehicles that are dominated by body shapes (Fig. 84). Understanding the characteristics of body forms at hypersonic speeds becomes important, not only because of the body influence on propulsion integration, but also because the body (the largest component) generates a considerable portion of the total drag force.

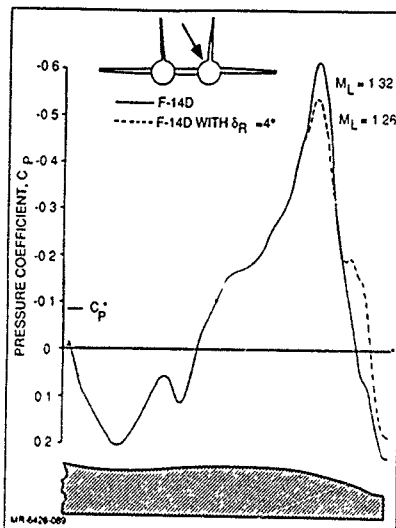


Fig. 78 Effect of Inboard Rudder Deflection on F-14 Afterbody Pressure Field at $M = 0.95$

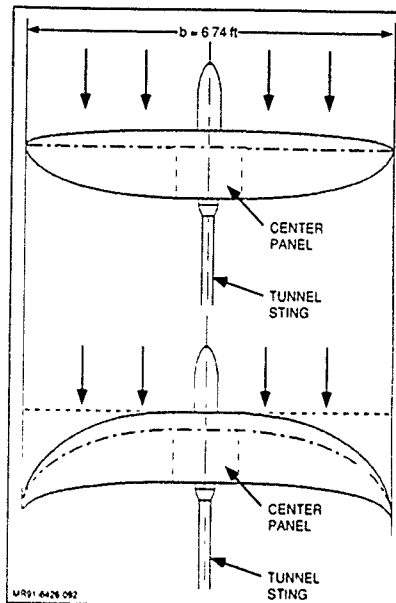


Fig. 81 Swept-Back Wing-Tip Wind Tunnel Models
(Ref. 73)

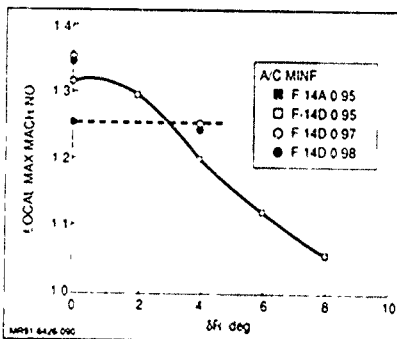


Fig. 79 Maximum Mach No. at BL 51

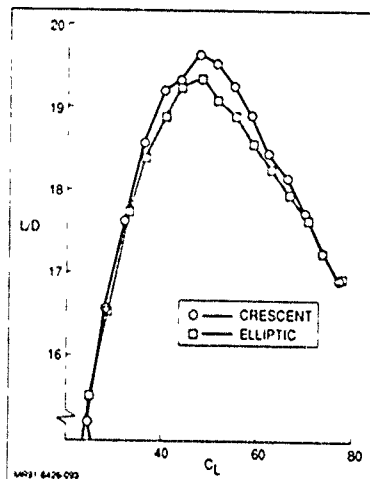


Fig. 82 Experiment Drag Reduction due to Swept-Back Wing Tips (Ref. 73)

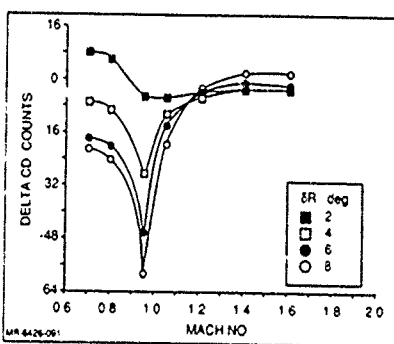


Fig. 80 F-14D Delta C_D for Rudder Deflection Angles

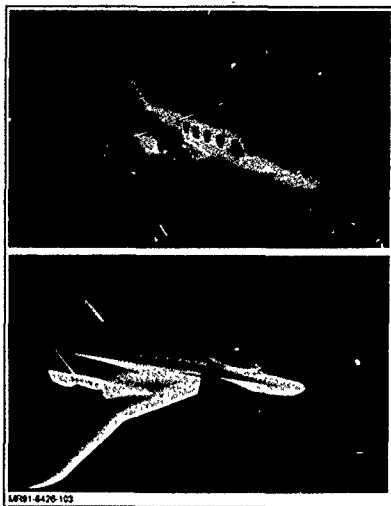


Fig. 83 Aircraft Designs Featuring Swept-Back Wing Tips

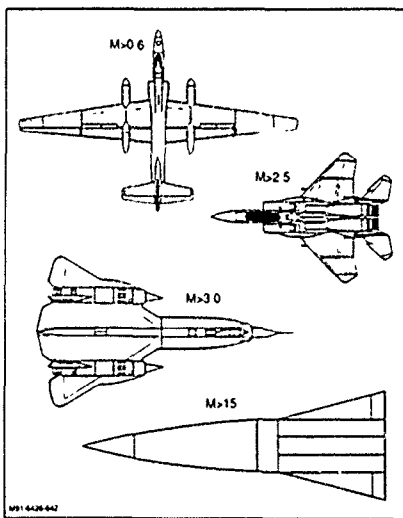


Fig. 84 Dominance of Body Shapes as Speed Increases

In 1988, a project was initiated to identify the impact of hypersonic forebody shaping on inlet flow quality. The foundation for this work was reported on in Ref 78. The new study included flight conditions at incidence and sideslip angles. A secondary objective of this effort was to better understand the nature of forebody drag characteristics at incidence (Ref 79). In other words, there was an interest in examining forebody drag to identify the elements of resistance (i.e., friction, vortex, and wave drag) as variations occur with incidence. Figure 85 shows the hypersonic vehicle forebody shapes that formed the basis for

this study. Two different types of computational methods were applied. One method (Ref. 79) was characterized by simple Newtonian Theory, while the other (Ref. 80) was a modern Navier-Stokes formulation. Experience with these methods applied to body shapes (Fig. 86 and 87) indicated that reasonably accurate absolute drag predictions could be made.

By comparing the results from two vastly different computational formulations, the nature of drag on forebody shapes at incidence could be better understood. But the computational predictions agreed closely, and the results were not what was expected. Close agreement indicated that there was probably not an appreciable amount of forebody drag attributable to vortex flows and complex viscous interactions. This is the case because the Newtonian method used did not include true viscous and vortical flow simulation capabilities. The feature not expected was a dent or hole in the drag polar shape (Fig. 88).

Since Newtonian Theory registers this effect, it might be appropriate to think in Newtonian Theory terms. Newtonian Theory is linked to perfect gas, compressible flow, oblique shock wave relations for $M \rightarrow \infty$

$$C_p \rightarrow \frac{4}{\gamma+1} \sin^2 \theta \quad (30)$$

Where for very high speeds, shock waves with angles θ will lie close to vehicle surfaces with local orientation angles ϵ . Also $\gamma \rightarrow 1$

$$C_p \rightarrow 2 \sin^2 \epsilon \quad (31)$$

This "point pressure law" is applied by breaking configuration surfaces into a large number of facets and summing for the final integrated forces and moments. Equation 31 is used for windward elements while $C_p = 0$ is used for leeward elements.

In Fig. 89, a body form is represented by a simple cone-cylinder combination. At zero incidence, a pressure field is generated on the forward-facing surface. The cylindrical portion "registers no effect". As incidence increases, the onset flow "exposes" additional body surface area and in so doing changes the effective body shape - the shape generating forces in Newtonian Theory. Finally, depending on the cone angle, an incidence angle is reached where the effective body shape is "locked in" (note the last shape in Fig. 89). It is conjectured that the irregular hypersonic forebody polar shape is a direct result of wave drag levels registering on an effective body shape that changes with angle-of-attack over a shallow incidence range. The analogy to this would be an airfoil or body shape in viscous flow where the effective shape changes with Reynolds number as the boundary layer displacement thickness varies.

It was found (Ref. 81) that experimentalists were measuring this characteristic in the past, and curve fits were used to fair the data ignoring the "dent". This occurred because, in most early hypersonic testing, data at large (five degree) increments in incidence were usually taken. This can be seen in Fig. 90. In this case, computational drag analysis served to highlight drag mechanisms and provide a basis to understand the fluid mechanical foundations of observed characteristics.

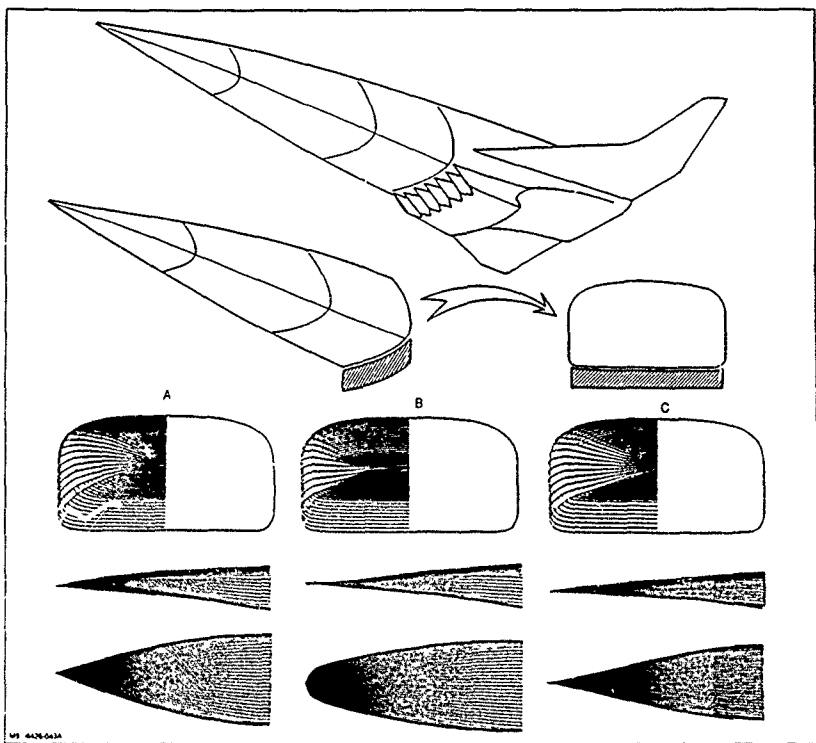


Fig. 85 Hypersonic Forebody Shapes for Drag-Due-To-Incidence Study

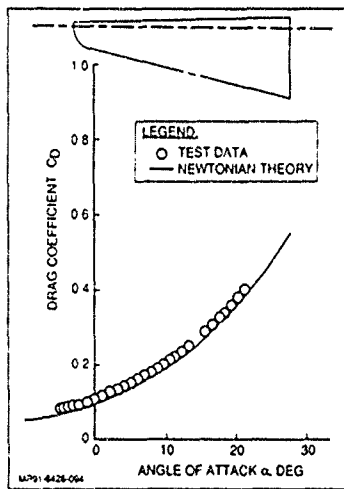


Fig. 86 Hypersonic Body Drag Polar Correlation with Newtonian Theory

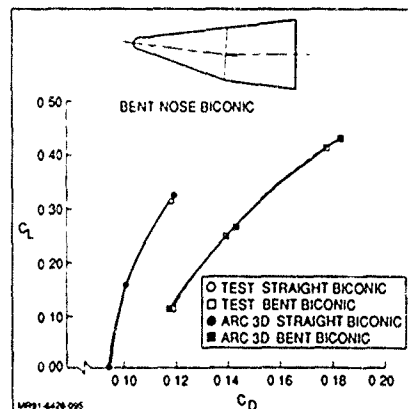


Fig. 87 Straight & Bent Biconic Drag Polar at Mach 6.0

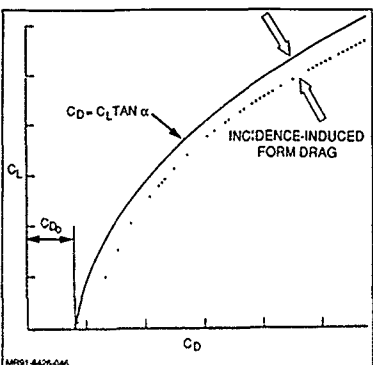


Fig. 88 Hypersonic Body Drag Polar "Dent"

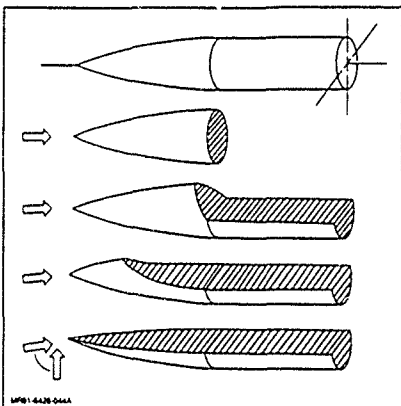
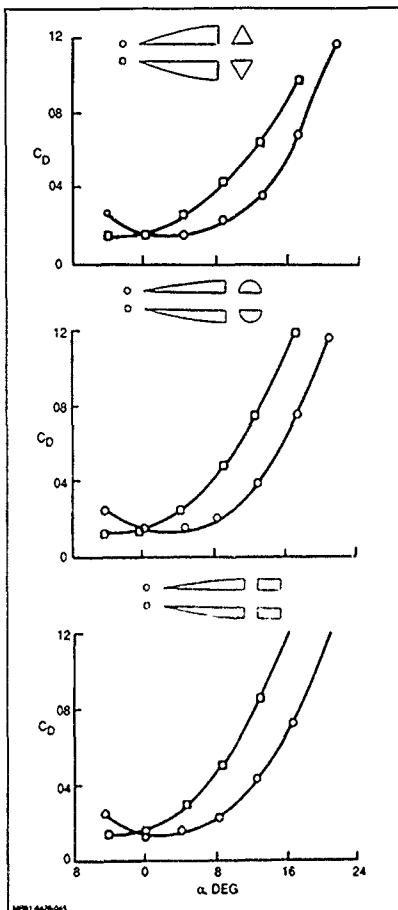


Fig. 89 Effective Body Shape in Newtonian Flow

Fighter Transonic Maneuver Wing Optimization

X-29 (Fig. 91) configuration development provides a basis for understanding the benefits that computational drag prediction methods can have when applied to high-speed fighter wing optimization. In this case, two-dimensional airfoil analyses (applied in a three dimensional wing design process) identified that wing section load was carried differently (on the upper and lower surfaces) depending on whether the wing was swept forward or aft. This has been shown in Fig. 92 A and is attributed to decoupled upper/lower flow mechanisms at transonic conditions (Ref. 82). Reduced supersonic expansion ultimately results with reduced shock wave strength and an attendant reduction in wave drag. It can also be seen that as flow conditions become more severe with increases in incidence or Mach number, the forward swept wing shock wave moves aft into a region where shock wave sweep angles are increased just the opposite of the aft swept wing situation. For aft swept wings, a shock wave moving back on the planform is forced to have lower sweep angles with an accompanying wave drag penalty (Fig. 92 B). Thus, of course, is not to say that wave drag actually decreases for forward swept wings with increasing flow severity. Instead, it suggests that there is a drag relief mechanism involved that can slow the rate that wave drag increases.

Fig. 90 Hypersonic Test Data Suggesting Polar "Dent" $M = 10$ (Ref. 81)

High-speed wing design was affected with a design procedure that coupled a two-dimensional transonic finite difference method with a three-dimensional subsonic/supersonic panel method. The two-dimensional analysis generated a streamwise wing section, while the three-dimensional method identified wing incidence or twist distribution along with any spanwise/chordwise camber modifications (Refs. 32 and 82).

The resultant sweep effects were verified by wind tunnel tests at AEDC and eventually by flight tests at NASA's Dryden Flight Research Center. A USAF study (Refs. 83 and 84) provided key insights into the impact of resulting performance levels. Figure 93 compares drag polars at two transonic Mach numbers using X-29 data and the drag polar from an existing light-weight fighter and an air superiority fighter. Figure 94 reveals that the X-29 is characterized by lower thrust-to-weight ratio but a higher maximum lift coefficient. All of this translates into an advantage in dynamic turns that might be performed during air-to-air combat engagements (Fig. 95).

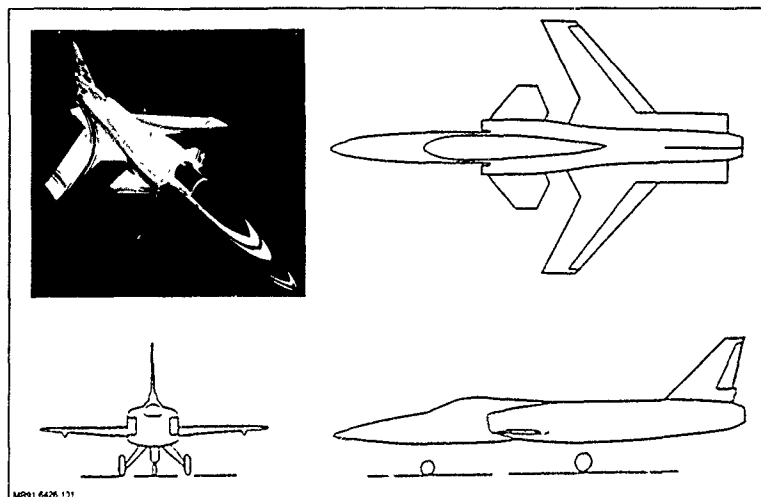


Fig. 91 X-29 Configuration

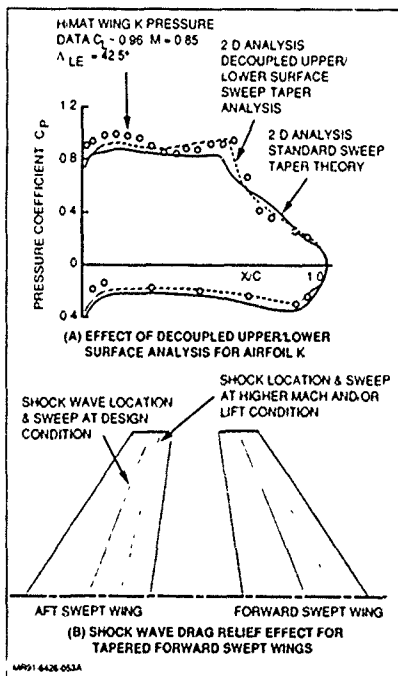


Fig. 92 Mechanism for Reduced Drag at Transonic Speeds with Forward Sweep

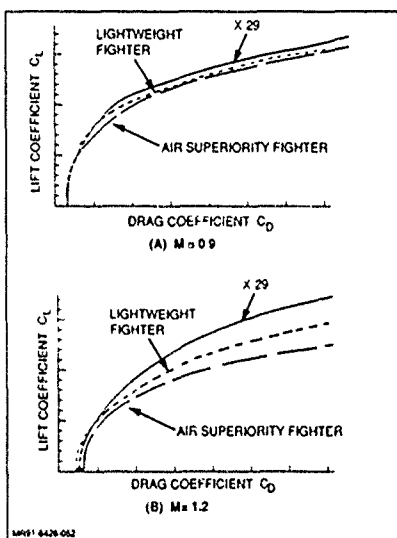


Fig. 93 Drag Polar Comparisons (Ref. 83)

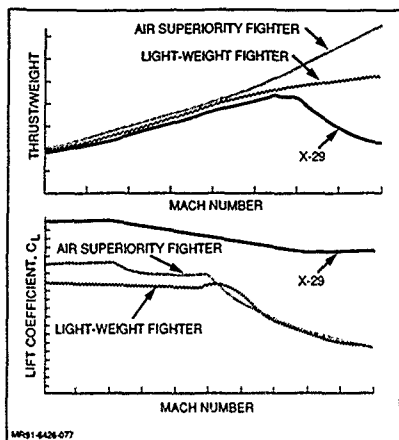


Fig. 94 Maximum Lift & Thrust/Weight Comparison
(Ref. 83)

The X-29 represents a breakthrough in advanced maneuvering technology. Not only were the original conceptual origins of modern forward sweep technology identified via computational drag prediction methodology, but computational tools were instrumental in allowing the design to move smoothly forward despite the fact that no applicable design experience base existed for swept-forward configurations which might have enhanced confidence and reduced risk levels. It is difficult to make comparisons to existing fighters since, for example, the experimental X-29 configuration is not required to perform all the functions of a tactical fighter. Notwithstanding this, it is remarkable that only 160 hours of high-speed wind-tunnel test time were required to finalize the configuration concept (Fig. 96), this is considerably less than that typically used for fighter configuration optimization (Ref. 85).

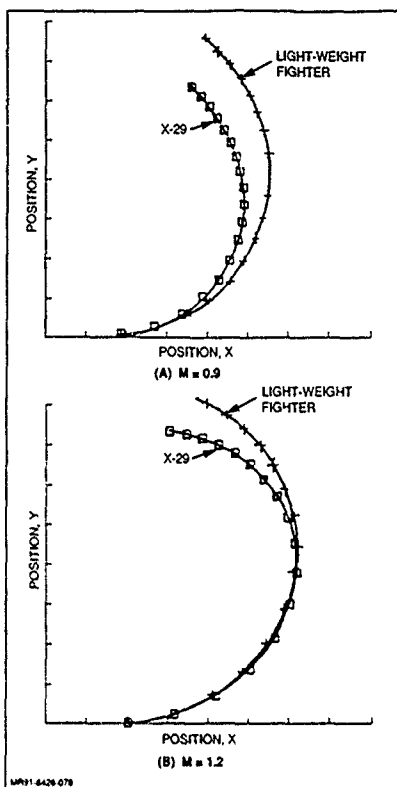


Fig. 95 Aircraft Dynamic Turn Performance at 35,000 ft
(Ref. 83)

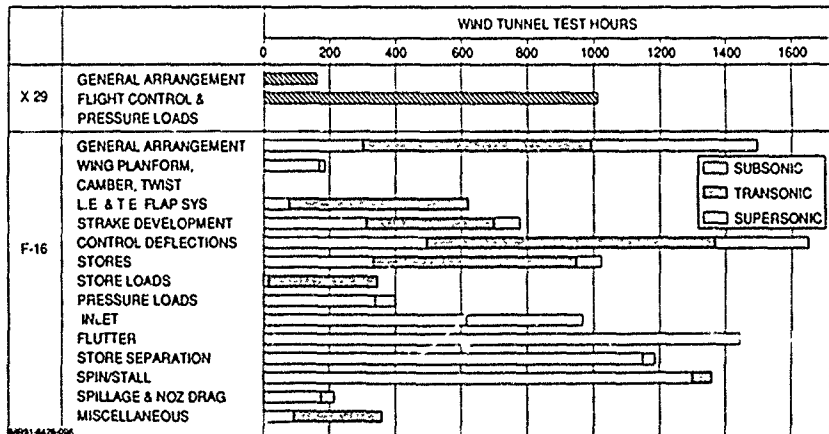


Fig. 96 Wind Tunnel Test Comparison (Ref. 85)

CONCLUDING REMARKS

A number of engineering computational methods that can play a role in predicting/analyzing drag components during aircraft development programs have been described. An attempt has been made to cover all drag components that are of interest to the design engineer and provide some basis for understanding what might be expected, i.e., typical results and accuracy levels. A key constraint in any application, however, is the fact that aircraft flows can become quite complex. Occasionally, this complexity is beyond the capabilities of current computational engineering tools. Further, it is recognized that no single method is capable of simultaneously treating all drag sources that are important. This requires that the applications engineer be clever and occasionally creative. Nothing, however, will replace the need to establish a computational drag prediction experience base - examples of which were included herein.

The role of computational engineering methods can be quite varied. It should be apparent that the drag prediction tools described can and have played an important role in bridging the gap between simple handbook methods and the performance establishing sub-scale tests that characterize aircraft development programs. Further, there are many instances where these engineering tools have provided the design team with key insights needed to advance the state-of-the-art or solve problems with considerable resource savings. This results in an element of creativity that is derived from the ability to inexpensively evaluate many ideas without the time/expense constraints associated with sub-scale testing. Finally, it should be recognized that in some cases, there may be discrepancies between wind tunnel testing and flight test results. When this happens, a third source (coming from computational engineering tools) can prove valuable in the sense that a third source of information is often needed to break ties.

There are likely to be times, however, when the best computerized methods are inadequate. A fall-back position might involve the use of Smeaton's original 1759 equation (Eq. 1). The applications engineer might also be advised to use Smeaton's coefficient (0.0049) which was shown to be conservative - since a good aerodynamicist knows that it is important to keep a few counts of "drift" in his or her back pocket. These counts are often needed as projects evolve.

ACKNOWLEDGEMENTS

The author would like to thank those at Grumman who have made significant contributions on a number of drag analysis and reduction projects. The work of P. Bavitz (G III), R. Hendrickson and W. Evans (F-14), and G. Spach (X-29) belongs to this group. D. Ives of Pratt & Whitney is to be recognized for his formulation of the symmetric lift induced drag Fourier load integration scheme. E. Tinoco and J. McMasters (Boeing) provided useful insights into the state of the art in fillet design. Finally, the author appreciates receiving permission to use photographs of Scaled Composites, Inc. design concepts.

REFERENCES

- (1) "Aircraft Drag Prediction," AGARD R 723, 1985
- (2) "Aerodynamic Drag," AGARD CP 124, 1973
- (3) "Aerodynamic Interference," AGARD CP 71-71, 1971
- (4) "Drag Prediction and Measurement," AIAA Professional Development Series, August, 1990
- (5) McCormick, B. W., *Aerodynamics, Aeronautics, and Flight Mechanics*, John Wiley & Sons, N.Y. 1979
- (6) "Technical Status Review on Drag Prediction and Analysis from Computational Fluid Dynamics: State of the Art," AGARD AR-256, June 1989.
- (7) "Aircraft Excrescence Drag," AGARD CP-264, 1981
- (8) Jobe, C. E., "Prediction of Aerodynamic Drag," AFWL-TM-84-203, July 1984
- (9) Covert, E. E., "Thrust and Drag: Its Prediction and Verification, *Progress in Astronautics and Aeronautics, Volume 98*, AIAA, New York, 1986
- (10) van der Vooren, J. and Slooff, J. W., "CFD-Based Drag Prediction, State-of-the-Art, Theory, Prospects," NLR TP 90247L, Lecture Notes Prepared for AIAA Professional Development Series on Drag Prediction and Measurement, August 1990
- (11) Slooff, J. W., "Computational Drag Analyses and Minimization, Mission Impossible?," AGARD R-723, May 1985
- (12) Rogallo, R. S. and Moin, P., "Numerical Simulation of Turbulent Flows," *Annual Review of Fluid Mechanics*, Vol 16, 1984
- (13) Hadcock, R., *Aeronautical Engineering Development, Part 1 1759-1914*, Manuscript to be Published, 1992.
- (14) Oswald, W. B., "General Formulas and Charts for the Calculation of Airplane Performance," NACA Report No 408, 1932
- (15) Jones, R. T., "Properties of Oblique Wing-Body Combinations for Low Supersonic Speeds," NASA SP-292, pp 389-407, 1971
- (16) Hoerner, S. F., *Fluid-Dynamic Drag*, Published by Author, 1965
- (17) Finch, R. D., et al, "U.S.A.F Stability & Control Datcom," Wright Research & Development Center, Flight Controls Division, April 1976
- (18) Locke, F. W. S., Jr., "Recommended Definition of Turbulent Friction in Incompressible Fluids," NAVAIR Report No 1415, June, 1952
- (19) Schlichting, H., *Boundary Layer Theory*, McGraw Hill, 1960
- (20) Sommer, S. C. and Short, B. J., "Free Flight Measurements of Turbulent Boundary Layer Skin Friction in the Presence of Severe Aerodynamic Heating at Mach Numbers From 2.8-7.0," NACA TN 3391 1955
- (21) Peterson, J. B., Jr., "A Comparison of Experimental and Theoretical Results for the Compressible Turbulent Boundary Layer Skin Friction with Zero Pressure Gradient," NASA TN-D 1795, March 1963
- (22) Eppler, R. and Somers, D. M., A Computer Program for the Design and Analysis of Low Speed Airfoils, NASA TM 80-10, August 1980
- (23) Abbott, I. A. et al, *Theory of Wing Sections*, Dover, New York, 1959
- (24) Althaus, D. et al, *Stuttgarter Profilkatalog I*, Friedr. Vieweg & Sohn, Braunschweig/Wiesbaden, 1981
- (25) Stevens, W. A. et al, Mathematical Model for Two Dimensional Multi Component Airfoils in Viscous Flow, NASA CR-1843, July 1983
- (26) Drela, M. and Giles, M. B., "Viscous Inviscid Analysis of Transonic and Low Reynolds Number Airfoils," AIAA 86-1786, January 1987
- (27) Drela, M. and Giles, M. B., "ISES A Two-Dimensional Viscous Aerodynamic Design and Analysis Code," AIAA 87-0424, January 1987
- (28) Boppe, C. W., et al, "STARS & STRIPES, Computational Flow Simulations for Hydrodynamic Design," The Eighth Chesapeake Sailing Yacht Symposium Proceedings, March 1987
- (29) Ives, D., Private Communication, Pratt & Whitney, 1983
- (30) Glauert, H., *The Elements of Aerofoil and Airscrew Theory*, Cambridge University Press, London, 1926

- (31) Ashley, H. and Landahl, M.; *Aerodynamics of Wings and Bodies*, Addison-Wesley Publishing Company, Inc., Reading, Mass 1965
- (32) Boppe, C. W.; "Computational Aerodynamic Design: X-29, The Gulfstream Series, and a Tactical Fighter," SAE 851789, October 1985 (SAE Wright Brothers Medal Award Paper - 1986).
- (33) Bauer, F., et al; "Supercritical Wing Sections II, a Handbook," *Lecture Notes in Economics and Mathematical Systems*, No 108, Springer-Verlag, 1975
- (34) Cook, P. H., et al, "Aerofoil RAE 2822 - Pressure Distributions, Boundary Layer, and Wake Measurements," AGARD AR-138, 1979
- (35) Holst, T. L., "Viscous Transonic Aerofoil Workshop Compendium Results," AIAA 87-1460, June 1987
- (36) Whitcomb, R. T., "Recent Results Pertaining to the Application of the 'Area-Rule,'" NACA RM L53I15a, 1953
- (37) Whitcomb, R. T., "A Study of the Zero-Lift Drag Rise Characteristics of Wing-Body Combinations Near the Speed of Sound," NACA Report 1273, 1956
- (38) von Karman, T., "The Problem of Resistance in Compressible Fluids," Memorie della Reale Accademia d'Italia, Classe di Scienze Fisiche, Matematiche e Naturali, Vol XIII, pp210-265, 1935
- (39) Harris, R. V., Jr., "An Analysis and Correlation of Aircraft Wave Drag," NASA TM X-947, 1964
- (40) Hendrickson, R., Private Communication, Grumman Aircraft Systems Division, November 1990
- (41) Ashley, H., "On Making Things the Best: Aeronautical Uses of Optimization," 1981 Wright Brothers Lecture, AIAA 81-1738, August 1981
- (42) Davis, W. H., Jr., Technique for Developing Design Tools from the Analysis Methods of Computational Aerodynamics," AIAA 79-1529R, also AIAA Journal, Vol 18, No 9, September 1980
- (43) Davis, W. H., Jr., et al, "A Study to Develop Improved Methods for the Design of Transonic Fighter Wings by the Use of Numerical Optimization," NASA CR-3995, August 1986
- (44) Vanderplaats, G. N., "CONMIN - A FORTRAN Program for Constrained Function Minimization Users Manual," NASA TM X-62282, August 1973
- (45) Tindell, R. and Tamplin, G., "An Inlet System Installed Performance Prediction Program Using Simplified Modeling," AIAA 83 1167, June 1983
- (46) Hess, J. L. and Smith, A. M. O., "Calculation of Non Lifting Potential Flow About Arbitrary Three-Dimensional Bodies," Douglas Report 40622, March 1962
- (47) Sherman, P. M. and Lincoln, F. W., "Ram Inlet Systems for Waterjet Propulsors," AIAA 69 418, May 1969
- (48) Henderson, W. P., "Propulsion Integration for Military Aircraft," SAE 892234, September 1989
- (49) Grossman, B. and Melnik, R., "The Numerical Computation of the Transonic Flow Over Afterbodies Including the Effect of Jet Plume and Viscous Interactions," AIAA 75-62, 1975
- (50) Salas, M. D., "The Numerical Computation of Inviscid Plume Flow Fields," AIAA 74-523, 1974
- (51) Yaeger, L. S., "Transonic Flow Over Afterbodies Including the Effects of Jet-Plume and Viscous Interactions with Separation," AIAA 77 228, 1977
- (52) Cumpton, W. B., "Jet Effects on the Drag of Conical Afterbodies at Supersonic Speeds," NASA TN D-6789, 1972
- (53) Bushnell, D. and Donaldson, C., "Control of Submersible Vortex Flows," NASA TM 102693, June 1990
- (54) Rubbert, P. and Goldammer, M., CFD in Design: An Airframe Perspective," AIAA 89-0092, January 1989
- (55) Rubbert, P. and Saars, G. R., "Review and Evaluation of a Three-Dimensional Lifting Potential Flow Analysis Method for Arbitrary Configurations," AIAA 72-188, January 1972.
- (56) Boppe, C. W.; "Transonic Flow Field Analysis for Wing-Fuselage Configurations," NASA CR-3243, May 1980
- (57) Boppe, C. W. and Rosen, B. S., "Computation of Prop-Fan Engine Installation Aerodynamics," *Journal of Aircraft*, Vol. 23, No 4, April 1986.
- (58) McCroskey, W. J., et al, "Airloads on Bluff Bodies, with Applications to the Rotor Downloads on Tilt-Rotor Aircraft," *Verifica*, Vol. 9, No. 1, 1985.
- (59) Maskew, B., "Predictions of Subsonic Aerodynamic Characteristics - A Case for Low-Order Panel Methods," AIAA 81-0252, January 1981.
- (60) Boppe, C. W., "Aerodynamic Analysis for Aircraft with Nacelles, Pylons, and Winglets at Transonic Speeds," NASA CR-4066, April 1987
- (61) Miller, E. and Delaney, F. J., "Level II Nozz'e/Aftbody Installed Performance Prediction Program," AFWAL TR-88-3004, December 1988.
- (62) Tindell, R. H.; "Computational Fluid Dynamics Applications for Jet Propulsion System Integration," ASME 90-GT-343, June 1990
- (63) Carlson, H. W., et al, "Validation of a Computer Code for Analysis of Subsonic Aerodynamic Performance of Wings and Flaps in Combination with a Canard or Horizontal Tail and an Application to Optimization," NASA TP-2961, January 1990
- (64) Carlson, H. W. and Walkley, K. B., "A Computer Program for Wing Subsonic Aerodynamic Performance Estimates Including Attainable Thrust and Vortex Lift Effects," NASA CR-3515, March 1982
- (65) Whitcomb, R. T., "A Design Approach and Selected Wind-Tunnel Results at High Subsonic Speeds for Wing-Tip Mounted Winglets," NASA TN D-8260, July 1976
- (66) Chandrasekaran, R. M., et al, "Computational Aerodynamics: Design of the Gulfstream IV Wing," AIAA 85-0427, January 1985
- (67) Davis, W. H., "Applied Transonics at Grumman," Transonic Symposium - Theory, Application and Experiment, NASA LaRC, Hampton, Virginia, April 1988
- (68) Davis, W. H., "The Role of CFD Applied to High Performance Aircraft," AIAA 90-3071, August 1990
- (69) Cooper, G. K., "The PARC Code: Theory and Usage," AEDC TR-87-24, October 1987
- (70) van Dam, C. P., "Swept Wing-Tip Shapes for Low Speed Airplanes," SAE 851770, October 1985
- (71) van Dam, C. P., "Drag Reduction Characteristics of Aft-Swept Wing Tips," AIAA 86-1824, October 1986
- (72) Boppe, C. W., "Sailboat Hydrodynamic Drag Source Prediction and Performance Assessment," The Tenth Chesapeake Sailing Yacht Symposium Proceedings, February 1991
- (73) van Dam, C. P., et al, "Wind Tunnel Investigation on the Effect of the Crescent Plantom on Lift and Drag," Proposed *Journal of Aircraft* article,(Also - AIAA 90 0300), March 1990
- (74) Smith, S. C. and Kroo, I. M., "A Closer Look at the Induced Drag of Crescent Shaped Wings," AIAA 90 3063, August 1990
- (75) Dallaan, M. A., "Induced Drag of Wings with Highly Swept and Tapered Wing Tips," AIAA 90 3062-CP, August 1990
- (76) Burkett, C. W., "Reductions in Induced Drag by the Use of Aft Swept Tips," *Aeronautical Journal*, December 1989
- (77) Burkett, C. W., "Analysis of Crescent Wings Using a Subsonic Panel Method," ICAS 90 3 6 2, September 1990

- (78) Wilson, G. J. and Davis, W. H., Jr., "Hypersonic Performance Sensitivities Based on 3-D Equilibrium Navier-Stokes Calculations," AIAA 87-2642, January 1987
- (79) Boppe, C. W. and Davis, W. H., Jr.; "Hypersonic Forebody Lift-Induced Drag," SAE 892345, September 1989 (SAE Wright Brothers Medal Award Paper 1990)
- (80) Pulliam, T. and Steger, J., "Implicit Finite-Difference Simulations of 3-D Compressible Flow," *AIAA Journal*, Vol. 18, February 1980
- (81) Spencer, B.; "Hypersonic Aerodynamic Characteristics of Minimum Wave Drag Bodies Having Variations in Cross-Sectional Shape," NASA TN D-4079, September 1967
- (82) Boppe, C. W., "X-29 Aerodynamic Design and Performance," AIAA Professional Development Series - Aerodynamics Analysis and Design, October 1988
- (83) Bursley, C. H.; "Fighter Class Aircraft Performance Comparisons," AFWAL-TR-88-3081, November 1988
- (84) Purof, S. M., "X-29 Aerodynamic Specialists Meeting Report," WRDC-TR-89-30-7, April 1989.
- (85) Bradley, R. G., "CFD Validation Philosophy," AGARD CPP-437, May 1988.

REPORT DOCUMENTATION PAGE			
1. Recipient's Reference	2. Originator's Reference	3. Further Reference	4. Security Classification of Document
	AGARD-R-783	ISBN 92-835-0652-9	UNCLASSIFIED
5. Originator	Advisory Group for Aerospace Research and Development North Atlantic Treaty Organization 7 rue Ancelle, 92200 Neuilly sur Seine, France		
6. Title	SPECIAL COURSE ON ENGINEERING METHODS IN AERODYNAMIC ANALYSIS AND DESIGN OF AIRCRAFT		
7. Presented as	an AGARD Special Course at the Middle East Technical University, Ankara, Turkey, 6th–10th May 1991, at the von Kármán Institute for Fluid Dynamics, Rhode-St-Genèse, Belgium, 13th–17th May 1991 and at the Universidad Politécnica de Madrid, Spain 20th–24th May 1991.		
8. Author(s)/Editor(s)	Various		9. Date January 1992
10. Author's/Editor's Address	Various		11. Pages 248
12. Distribution Statement	This document is distributed in accordance with AGARD policies and regulations, which are outlined on the back covers of all AGARD publications.		
13. Keywords/Descriptors	<ul style="list-style-type: none"> - Aerodynamics - Computer programs, - Aircraft Design Aerospace engineering , Computation , Cost effectiveness , 		
14. Abstract	<p>Lecture notes for the AGARD Fluid Dynamics Panel Special Course on 'Engineering Methods in Aerodynamic Analysis and Design of Aircraft' have been assembled in this report. Proven engineering methods used during conceptual and preliminary design and development of new aircraft concepts are presented. These methods focus on simple computational procedures for conceptual and preliminary design, low-level analysis computer codes, and experimental techniques for aircraft performance predictions. The course was aimed at helping train young engineers to appreciate and work with simple engineering tools to enhance the art of cost-effective preliminary design of new aircraft.</p> <p>The AGARD Fluid Dynamics Panel Special Course – for which this material was prepared – was held 6th–10th May 1991 at the Middle East Technical University, Ankara, Turkey, 13th–17th May at the von Karman Institute for Fluid Dynamics, Rhode-St-Genèse, Belgium, and 20th–24th May at the Universidad Politécnica de Madrid, ETSI Aeronáuticos, Madrid, Spain. This course was developed and conducted under the combined sponsorship of the AGARD Fluid Dynamics Panel, the AGARD Consultant and Exchange Programme, and the von Kármán Institute for Fluid Dynamics.</p>		

AGARD Report 783 Advisory Group for Aerospace Research and Development, NATO SPECIAL COURSE ON ENGINEERING METHODS IN AERODYNAMIC ANALYSIS AND DESIGN OF AIRCRAFT Published January 1992 248 pages	AGARD-R-783 Aerodynamics Computer programs Aircraft Design Aerospace engineering Computation Cost effectiveness Lecture notes for the AGARD Fluid Dynamics Panel Special Course on "Engineering Methods in Aerodynamic Analysis and Design of Aircraft" have been assembled in this report. Proven engineering methods used during conceptual and preliminary design and development of new aircraft concepts are presented. These methods focus on simple computational procedures for conceptual and PTO	AGARD Report 783 Advisory Group for Aerospace Research and Development, NATO SPECIAL COURSE ON ENGINEERING METHODS IN AERODYNAMIC ANALYSIS AND DESIGN OF AIRCRAFT Published January 1992 248 pages	Aerodynamics Computer programs Aircraft Design Aerospace engineering Computation Cost effectiveness Lecture notes for the AGARD Fluid Dynamics Panel Special Course on "Engineering Methods in Aerodynamic Analysis and Design of Aircraft" have been assembled in this report. Proven engineering methods used during conceptual and preliminary design and development of new aircraft concepts are presented. These methods focus on simple computational procedures for conceptual and PTO
AGARD Report 783 Advisory Group for Aerospace Research and Development, NATO SPECIAL COURSE ON ENGINEERING METHODS IN AERODYNAMIC ANALYSIS AND DESIGN OF AIRCRAFT Published January 1992 248 pages	AGARD-R-783 Aerodynamics Computer programs Aircraft Design Aerospace engineering Computation Cost effectiveness Lecture notes for the AGARD Fluid Dynamics Panel Special Course on "Engineering Methods in Aerodynamic Analysis and Design of Aircraft" have been assembled in this report. Proven engineering methods used during conceptual and preliminary design and development of new aircraft concepts are presented. These methods focus on simple computational procedures for conceptual and PTO	AGARD Report 783 Advisory Group for Aerospace Research and Development, NATO SPECIAL COURSE ON ENGINEERING METHODS IN AERODYNAMIC ANALYSIS AND DESIGN OF AIRCRAFT Published January 1992 248 pages	Aerodynamics Computer programs Aircraft Design Aerospace engineering Computation Cost effectiveness Lecture notes for the AGARD Fluid Dynamics Panel Special Course on "Engineering Methods in Aerodynamic Analysis and Design of Aircraft" have been assembled in this report. Proven engineering methods used during conceptual and preliminary design and development of new aircraft concepts are presented. These methods focus on simple computational procedures for conceptual and PTO

preliminary design, low-level analysis computer codes, and experimental techniques for aircraft performance predictions. The course was aimed at helping train young engineers to appreciate and work with simple engineering tools to enhance the art of cost-effective preliminary design of new aircraft

The AGARD Fluid Dynamics Panel Special Course – for which this material was prepared – was held 6th – 10th May 1991 at the Middle East Technical University, Ankara, Turkey; 13th – 17th May at the von Karman Institute for Fluid Dynamics, Rhode-Saint-Genèse, Belgium, and 20th – 24th May at the Universidad Politécnica de Madrid, ETSI Aeronáuticos, Madrid, Spain. This course was developed and conducted under the combined sponsorship of the AGARD Fluid Dynamics Panel, the AGARD Consultant and Exchange Programme, and the von Kármán Institute for Fluid Dynamics.

preliminary design, low-level analysis computer codes, and experimental techniques for aircraft performance predictions. The course was aimed at helping train young engineers to appreciate and work with simple engineering tools to enhance the art of cost-effective preliminary design of new aircraft

The AGARD Fluid Dynamics Panel Special Course – for which this material was prepared – was held 6th – 10th May 1991 at the Middle East Technical University, Ankara, Turkey; 13th – 17th May at the von Karman Institute for Fluid Dynamics, Rhode-Saint-Genèse, Belgium, and 20th – 24th May at the Universidad Politécnica de Madrid, ETSI Aeronáuticos, Madrid, Spain. This course was developed and conducted under the combined sponsorship of the AGARD Fluid Dynamics Panel, the AGARD Consultant and Exchange Programme, and the von Kármán Institute for Fluid Dynamics.

ISBN 92-835-0652-9

ISBN 92-835-0652-9

preliminary design, low-level analysis computer codes, and experimental techniques for aircraft performance predictions. The course was aimed at helping train young engineers to appreciate and work with simple engineering tools to enhance the art of cost-effective preliminary design of new aircraft

The AGARD Fluid Dynamics Panel Special Course – for which this material was prepared – was held 6th – 10th May 1991 at the Middle East Technical University, Ankara, Turkey; 13th – 17th May at the von Karman Institute for Fluid Dynamics, Rhode-Saint-Genèse, Belgium, and 20th – 24th May at the Universidad Politécnica de Madrid, ETSI Aeronáuticos, Madrid, Spain. This course was developed and conducted under the combined sponsorship of the AGARD Fluid Dynamics Panel, the AGARD Consultant and Exchange Programme, and the von Kármán Institute for Fluid Dynamics.

ISBN 92-835-0652-9

ISBN 92-835-0652-9

preliminary design, low-level analysis computer codes, and experimental techniques for aircraft performance predictions. The course was aimed at helping train young engineers to appreciate and work with simple engineering tools to enhance the art of cost-effective preliminary design of new aircraft

AGARD

NATO - OTAN
7 RUE ANCELLE 92200 NEUILLY-SUR-SEINE
FRANCE
Téléphone (1)47.38.57.00 - Telex 610.176.
Télécopie (1)47.38.57.99.

DIFFUSION DES PUBLICATIONS AGARD NON CLASSIFIÉES

L'AGARD ne détient pas de stocks de ses publications, dans un but de distribution générale à l'adresse ci-dessus. La diffusion initiale des publications de l'AGARD est effectuée auprès des pays membres de cette organisation par l'intermédiaire des Centres Nationaux de Distribution suivants. A l'exception des Etats-Unis, ces centres disposent parfois d'exemplaires additionnels; dans les cas contraire, on peut se procurer ces exemplaires sous forme de microfiches ou de microcopes auprès des Agences de Vente dont la liste suit.

CENTRES DE DIFFUSION NATIONAUX

ALLEMAGNE

Fachinformationszentrum
Karlsruhe
D-7514 Eggenstein-Leopoldshafen 2

BELGIQUE

Coordonnateur AGARD-VSU
Etat-Major de la Force Aérienne
Quartier Reine Elisabeth
Rue d'Evere, 1140 Bruxelles

CANADA

Directeur du Service des Recueillements Scientifiques
Ministère de la Défense Nationale
Ottawa, Ontario K1A 0K2

DANEMARK

Danish Defence Research Board
Ved Idrætsparken 4
2100 Copenhagen Ø

ESPAGNE

INTA (AGARD Publications)
Pintor Rosales 34
28006 Madrid

ETATS-UNIS

National Aeronautics and Space Administration
Langley Research Center
M/S 180
Hampton, Virginia 23665

FRANCE

O.NERA (Direction)
29, Avenue de la Division Leclerc
92320, Châtillon sous Bagneux

GRECE

Hellenic Air Force
Air War College
Scientific and Technical Library
Dekelia Air Force Base
Dekelia, Atena TGA 1010

LE CENTRE NATIONAL DE DISTRIBUTION DES ETATS-UNIS (NASA) NE DETIENT PAS DE STOCKS.
DES PUBLICATIONS AGARD ET LES DEMANDES D'EXEMPLAIRES DOIVENT ETRE ADRESSEES DIRECTEMENT
AU SERVICE NATIONAL TECHNIQUE DE L'INFORMATION (NTIS) DONT L'ADRESSE SUIT.

AGENCES DE VENTE

National Technical Information Service
(NTIS)
520 Port Royal Road
Springfield, Virginia 22161
Etats-Unis

ESA/Information Retrieval Service
European Space Agency
10, rue Mario Nikis
75015 Paris
France

The British Library
Document Supply Division
Boston Spa, Wetherby
West Yorkshire LS23 7BQ
Royaume Uni

Les demandes de microfichés ou de photocopies de documents AGARD (y compris les demandes faites auprès du NTIS) doivent comporter la dénomination AGARD, ainsi que le numéro de série de l'AGARD (par exemple AGARD-AG-315). Des informations analogues, telles que le titre et la date de publication sont souhaitables. Veuillez noter qu'il y a lieu de spécifier AGARD-R-xxx et AGARD-AR-xxx lors de la commande de rapports AGARD et des rapports consultatifs AGARD respectivement. Des références bibliographiques complètes ainsi que des résumés des publications AGARD figurent dans les journaux suivants:

Scientific and Technical Aerospace Reports (STAR)
publié par la NASA Scientific and Technical
Information Division
NASA Headquarters (NTI)
Washington, D.C. 20546
Etats-Unis

Government Reports Announcements and Index (GRA&I)
publié par le National Technical Information Service
Springfield
Virginia 22161
Etats-Unis

(accessible également en mode interactif dans la base de données bibliographiques en ligne du NTIS, et sur CD-ROM).

